ELSEVIER

Nuclear Physics A 710 (2002) 261–278

NUCLEAR PHYSICS A

www.elsevier.com/locate/npe

Cranked Skyrme–Hartree–Fock calculation for superdeformed and hyperdeformed rotational bands in $N = Z$ nuclei from ^{32}S to ^{48}Cr

T. Inakura [a], S. Mizutori [b], M. Yamagami [a,c], K. Matsuyanagi [a,*]

[a] *Department of Physics, Graduate School of Science, Kyoto University, Kitashirakawa, Kyoto 606-8502, Japan*
[b] *Department of Human Science, Kansai Women's College, Kashiwara City, Osaka 582-0026, Japan*
[c] *Institut de Physique Nucléaire, IN_2P_3-CNRS, 91406 Orsay Cedex, France*

Received 16 July 2002; received in revised form 13 August 2002; accepted 14 August 2002

Abstract

With the use of the symmetry-unrestricted cranked Skyrme–Hartree–Fock method in the three-dimensional coordinate-mesh representation, we have carried out a systematic theoretical search for the superdeformed and hyperdeformed rotational bands in the mass $A = 30$–50 region. Along the $N = Z$ line, we have found superdeformed solutions in ^{32}S, ^{36}Ar, ^{40}Ca, ^{44}Ti, and hyperdeformed solutions in ^{36}Ar, ^{40}Ca, ^{44}Ti, ^{48}Cr. The superdeformed band in ^{40}Ca is found to be extremely soft against both the axially symmetric (Y_{30}) and asymmetric (Y_{31}) octupole deformations. An interesting role of symmetry breaking in the mean field is pointed out.

PACS: 21.60-n; 21.60.Jz; 27.30.+t

Keywords: Cranked Skyrme–Hartree–Fock method; Superdeformation; Hyperdeformation; Non-axial octupole deformation; High-spin state; Calcium 40

1. Introduction

Nowadays, about two hundreds superdeformed (SD) rotational bands are identified in various mass ($A = 60$, 80, 130, 150, 190) regions [1–6]. Every regions of superdeformation have their own characteristics so that we can significantly enlarge and deepen our understanding of nuclear structure by systematically investigating similarities and differences

* Corresponding author.
E-mail address: ken@ruby.scphys.kyoto-u.ac.jp (K. Matsuyanagi).

0375-9474/02/$ – see front matter
PII: S0375-9474(02)01164-8

among the SD bands in different mass region. For the mass $A = 30$–50 region, although the doubly magic SD band in ^{32}S, which has been expected quite a long time [7–15], has not yet been observed and remains as a great challenge [6], quite recently, beautiful rotational spectra associated with the SD bands have been observed up to high spin in neighboring $N = Z$ nuclei; ^{36}Ar, ^{40}Ca, and ^{44}Ti. In ^{36}Ar the SD band has been identified up to its termination at $I^\pi = 16^+$ [16–18]. The SD band in the spherical magic nucleus ^{40}Ca is built on the well-known 8p–8h excited 0^+ states at 5.213 MeV and the rotational spectra have been observed up to $I^\pi = 16^+$ [19]. In ^{44}Ti a rotational spectrum associated with the excited 0^+ state at 1.905 MeV has been observed up to $I^\pi = 12^+$ [20]. This rotational band may also be regarded as belonging to a family of the SD band configurations. The fact that rotational bands built on excited 0^+ states are systematically observed is a quite important, unique feature of the SD bands in the ^{40}Ca region, as the low angular momentum portions of the SD bands in heavier mass regions are unknown in almost all cases.

In nuclei along the $N = Z$ line, effects of deformed shell structures of protons and neutrons act coherently and rich possibilities arise for coexistence and competition of different shapes. Thus, we shall be able to learn details of deformed shell structure and microscopic mechanism of shape coexistence by a systematic study of high-spin yrast structure in the sequence of $N = Z$ nuclei. Especially, yrast spectroscopy of nuclei in the $A = 30$–50 region, being relatively light compared to other regions of SD nuclei, is expected to provide detailed information about the roles of individual deformed single-particle orbits responsible for the emergence of the SD bands.

In this paper, as a continuation of the previous work on ^{32}S [21], we carry out a systematic theoretical search for SD and more elongated hyperdeformed (HD) rotational bands in $N = Z$ nuclei from ^{32}S to ^{48}Cr by means of the symmetry-unrestricted, cranked Skyrme–Hartree–Fock (SHF) method. In Ref. [21], a new computer code was constructed for the cranked SHF calculation based on the three-dimensional (3D) Cartesian-mesh representation, which provides a powerful tool for exploring exotic shapes (breaking both axial and reflection symmetries in the intrinsic states) at high spin. The algorithm of this code for numerical calculation is basically the same as in Refs. [22–31], except that various restrictions on spatial symmetries are completely removed. Namely, we do not impose parity and signature symmetries on intrinsic wave functions. Hence we call this version of the cranked SHF method "symmetry-unrestricted" one. For the development of selfconsistent mean-field models for nuclear structure, we quote Refs. [2,32,33], in which various kinds of mean-field theory, including Hartree–Fock (HF) calculations with finite-range Gogny interactions [34] and relativistic mean-field approaches [35], are thoroughly reviewed. We also mention that spontaneous symmetry breaking in rotating nuclei is reviewed in [36].

In fact, SD and HD solutions of the SHF equations we report in this paper preserve the reflection symmetries with respect to the (x, y), (y, z) and (z, x) planes, so that the symmetry-unrestricted calculation gives identical results with those evaluated by imposing such symmetries. The symmetry-unrestricted calculation, however, enables us to examine stabilities of the SD and HD states against such reflection-symmetry breaking degrees of freedom like octupole deformations. In addition, we shall show that the symmetry breaking play a quite interesting role in the crossing region between different configurations away from the local minima in the deformation parameter space.

This paper is arranged as follows: in Section 2, a brief account of the cranked SHF method is given. In Section 3, results of calculation for deformation energy curves and the SD and HD rotational bands in nuclei from ^{32}S to ^{48}Cr are systematically presented. Here, special attention will be paid to the properties of the SD bands at their high spin limits and the crossover to the HD bands with increasing angular momentum. In Section 4, an interesting role of symmetry breaking in the mean field will be pointed out in connection with configuration rearrangement mechanism. We shall further make a detailed analysis of the SD band of ^{40}Ca and show that it is extremely soft against both the axially symmetric (Y_{30}) and asymmetric (Y_{31}) octupole deformations. Main results of this paper are summarized in Section 5.

A preliminary version of this work was reported in [37,38].

2. Cranked SHF calculation

The cranked HF equation for a system uniformly rotating about the x-axis is given by

$$\delta\langle H - \omega_{\rm rot} J_x\rangle = 0, \tag{1}$$

where $\omega_{\rm rot}$ and J_x mean the rotational frequency and the x-component of angular momentum, and the bracket denotes the expectation value with respect to a Slater determinantal state. We solve the cranked HF equation for a Hamiltonian of the Skyrme type by means of the imaginary-time evolution technique [22] in the 3D Cartesian-mesh representation. We adopt the standard algorithm [22,25–27] in the numerical calculation, but completely remove various restrictions on spatial symmetries.

When we allow for the simultaneous breaking of both reflection and axial symmetries, it is crucial to accurately fulfill the center-of-mass condition

$$\left\langle \sum_{i=1}^{A} x_i \right\rangle = \left\langle \sum_{i=1}^{A} y_i \right\rangle = \left\langle \sum_{i=1}^{A} z_i \right\rangle = 0, \tag{2}$$

and the principal-axis condition

$$\left\langle \sum_{i=1}^{A} x_i y_i \right\rangle = \left\langle \sum_{i=1}^{A} y_i z_i \right\rangle = \left\langle \sum_{i=1}^{A} z_i x_i \right\rangle = 0. \tag{3}$$

For this purpose we use the constrained HF procedure with quadratic constraints [39]. Thus, we replace the "Routhian" $R = H - \omega_{\rm rot} J_x$ in Eq. (1) with

$$R' = R - \sum_{k=1}^{3} \mu_k \left\langle \sum_{i=1}^{A} (x_k)_i \right\rangle^2 - \sum_{k<k'}^{3} \mu_{k,k'} \left\langle \sum_{i=1}^{A} (x_k x_{k'})_i \right\rangle^2. \tag{4}$$

In numerical calculations, we confirmed that the constraints (2) and (3) are fulfilled to the order $O(10^{-15})$ with values of the parameters $\mu_k \sim O(10^2)$ and $\mu_{k,k'} \sim O(1)$. We solved these equations inside the sphere with radius $R = 10$ fm and mesh size $h = 1$ fm, starting with various initial configurations. We note that the accuracy for evaluating deformation energies with this mesh size was carefully checked by Tajima et al. [27,28]

(see also Ref. [40]) and was found to be quite satisfactory. The 9-point formula was used as the difference formula for the Laplacian operator. As usual, the angular momentum is evaluated as $I\hbar = \langle J_x \rangle$. For the Skyrme interaction, we adopt the widely used three versions; SIII [41], SkM* [42] and SLy4 [43].

In addition to the symmetry-unrestricted cranked SHF calculation explained above, we also carry out, for comparison sake, symmetry-restricted calculations imposing reflection symmetries about the (x, y)-, (y, z)- and (z, x)-planes. The computational algorithm for this restricted version of the cranked SHF calculation is basically the same as in [26], but we have constructed a new computer code for this purpose. Below we call these symmetry-unrestricted and -restricted cranked SHF versions "unrestricted" and "restricted" ones, respectively. Comparison between results obtained by unrestricted and restricted calculations carried out independently serves as a check of numerical results to be presented below. Physical significance of this comparison is, however, that we can, in this way, clearly identify effects of symmetry-breaking in the mean field. We shall indeed find an interesting symmetry breaking effect in the next section.

Solutions of the cranked SHF equation give minima in the deformation energy surface. In order to explore the deformation energy surface around these minima and draw deformation energy curves as functions of deformation parameters, we carry out the constrained HF procedure with quadratic constraints [39]. Namely, in addition to the constraints to fulfill the center-of-mass and principal-axis conditions mentioned above, we also introduce constraints involving relevant mass-multipole moment operators and solve resulting constrained HF equations.

As measures of the deformation, we calculate the mass-multipole moments

$$\alpha_{lm} = \frac{4\pi}{3A\overline{R}^l} \int r^l X_{lm}(\Omega)\rho(\boldsymbol{r})\, d\boldsymbol{r} \quad (m = -l, \ldots, l) \tag{5}$$

where $\rho(\boldsymbol{r})$ is the density, $\overline{R} = \sqrt{5\langle \sum_{i=1}^{A} \boldsymbol{r}_i^2 \rangle / 3A}$, and X_{lm} are real bases of the spherical harmonics

$$X_{l0} = Y_{l0}, \tag{6}$$

$$X_{l|m|} = \frac{1}{\sqrt{2}}\left(Y_{l-|m|} + Y^*_{l-|m|}\right), \tag{7}$$

$$X_{l-|m|} = \frac{-i}{\sqrt{2}}\left(Y_{l|m|} - Y^*_{l|m|}\right). \tag{8}$$

Here the quantization axis is chosen as the largest (smallest) principal axis for prolate (oblate) solutions. We then define the quadrupole deformation parameter β_2, the triaxial deformation parameter γ, and the octupole deformation parameters β_3 and β_{3m} by

$$\alpha_{20} = \beta_2 \cos\gamma, \qquad \alpha_{22} = \beta_2 \sin\gamma, \tag{9}$$

$$\beta_3 = \left(\sum_{m=-3}^{3} \alpha_{3m}^2 \right)^{1/2}, \qquad \beta_{3m} = \left(\alpha_{3m}^2 + \alpha_{3-m}^2\right)^{1/2} \quad (m = 0, 1, 2, 3). \tag{10}$$

For convenience, we also use the familiar notation $-\beta_2$ for oblate shapes with $(\beta_2, \gamma = 60^\circ)$.

3. Results of calculation

3.1. Deformation energy curves

Figs. 1–3 show deformation energy curves evaluated at $I = 0$ by means of the constrained HF procedure with the quadratic constraint on the mass-quadrupole moment. The SIII, SkM*, and SLy4 versions of the Skyrme interaction are used in Figs. 1, 2, and 3, respectively. Solid lines with and without filled circles in these figures represent results of unrestricted and restricted calculations, respectively. Let us focus our attention to the region of large quadrupole deformation β_2. In both cases, we obtain local minima corresponding to the SD states for ^{32}S, ^{36}Ar, ^{40}Ca and ^{44}Ti in the region $0.4 \leqslant \beta_2 \leqslant 0.8$. (The local minimum in ^{44}Ti is triaxial, as shown in Fig. 7 below, i.e., it is situated away from the $\gamma = 0$ section of the deformation energy surface, so that it is not clearly seen in Figs. 1–3.) The local minima in ^{32}S and ^{36}Ar involve four particles (two protons and two neutrons) in the fp shell, while those in ^{40}Ca and ^{44}Ti involve eight particles (four protons and four neutrons). These local minima respectively correspond to the 4p–12h, 4p–8h, 8p–8h and 8p–4h configurations with respect to the doubly closed shell of ^{40}Ca, and their properties have been discussed from various point of view; see Refs. [7–15] for ^{32}S, Refs. [16–18,44]

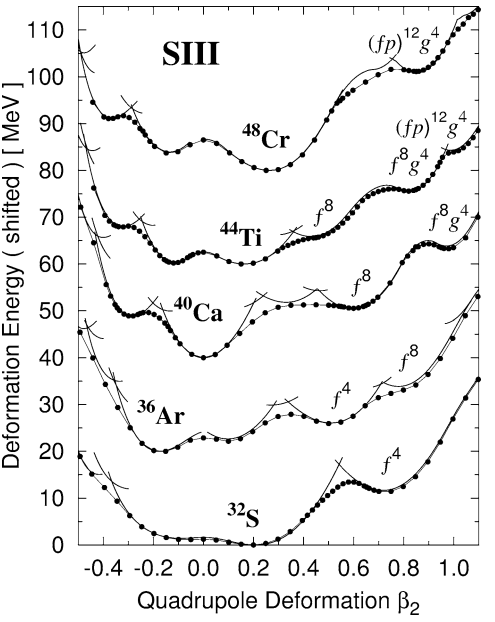

Fig. 1. Deformation energy curves as functions of the quadrupole deformation β_2 calculated at $I = 0$ by means of the constrained SHF procedure with the SIII interaction. The axial-asymmetry parameter γ is constrained to be zero. The curves for different nuclei are shifted by 20 MeV to accommodate them in a single plot. Solid lines with and without filled circles represent the results obtained by the unrestricted and restricted versions, respectively (see the text). The notations $f^n g^m$ and $(fp)^n g^m$ indicate the configurations in which the $f_{7/2}$ shell (fp shell) and the $g_{9/2}$ shell are respectively occupied by n and m nucleons.

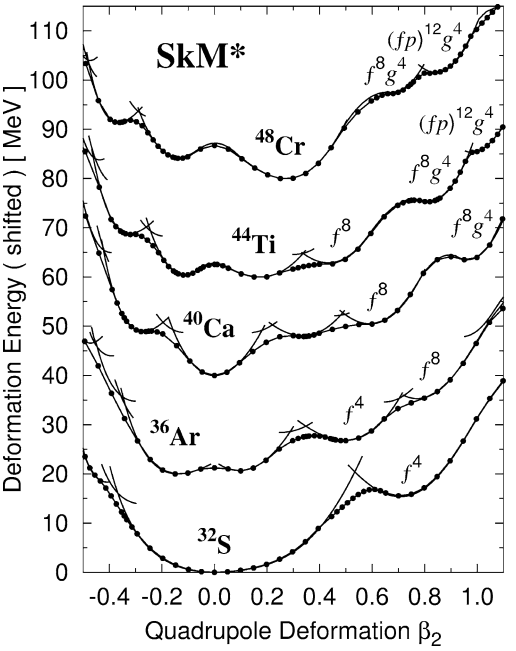

Fig. 2. The same as Fig. 1 but for the SkM* interaction.

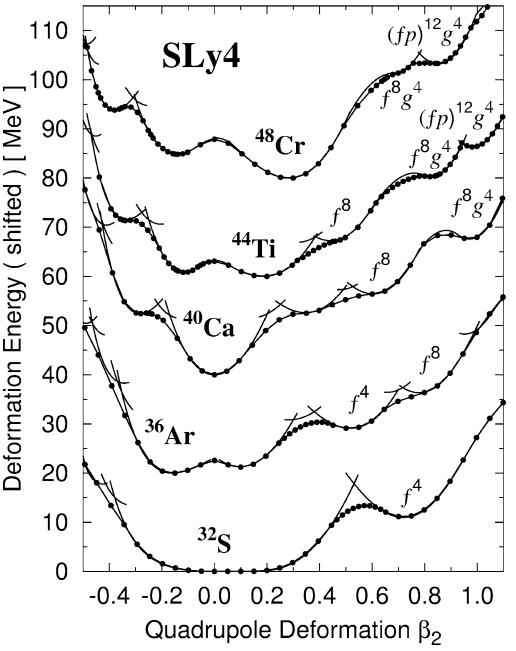

Fig. 3. The same as Fig. 1 but for the SLy4 interaction.

for ^{36}Ar, Refs. [19,45–51] for ^{40}Ca, and Refs. [20,52,53] for ^{44}Ti. These core-excited states have been reviewed in Ref. [54] as typical examples of shape coexistence phenomena.

In addition to these SD minima, we also obtain local minima in the region $\beta_2 \geqslant 0.8$ for ^{40}Ca, ^{44}Ti and ^{48}Cr. These minima involve additional four particles (two protons and two neutrons) in the single-particle levels that reduces to the $g_{9/2}$ levels in the spherical limit. Somewhat loosely we call these local minima "hyperdeformed." The HD solution in ^{40}Ca corresponds to the 12p–12h configuration. For ^{44}Ti, we obtain two HD solutions which correspond to the 12p–8h and 16p–12h configurations. The HD solution in ^{48}Cr corresponds to the 16p–8h configuration. These HD solutions well agree with those previously obtained in the SHF calculation by Zheng, Zamick and Berdichevsky [49]. We also mention that the 12p–12h configuration in ^{40}Ca and the 16p–12h configuration in ^{44}Ti agree with those obtained by the macroscopic–microscopic model calculation by Leander and Larsson [8].

In Figs. 1–3 and in the following, the above SD and HD configurations are denoted by $f^n g^m$ (or $(fp)^n g^m$), where n and m indicate the numbers of nucleons occupying the $f_{7/2}$ shell (or the fp shell) and the $g_{9/2}$ shell, respectively.

As seen in Figs. 1–3, these SD and HD minima are obtained for all calculations with the use of the SIII, SkM*, and SLy4 interactions. These local minima preserve the reflection symmetries so that the results of restricted and unrestricted calculations are the same. On the other hand, we also find a case where the two calculations give different results: we obtain a HD minimum with $\beta_2 \simeq 0.8$ for ^{36}Ar in the restricted calculations. This minimum involves eight particles (four protons and four neutrons) in the fp shell and correspond to the 8p–12h configuration, but it disappears in the unrestricted calculations and its remnant remains as a shoulder of the deformation energy curve.

Although the restricted and unrestricted calculations give identical results for the SD and HD local minima except for the HD solution for ^{36}Ar, they show different behaviors in regions away from the local minima: in Figs. 1–3, we see that the deformation energy curves obtained by the unrestricted calculations always join different local minima smoothly. On the other hand, in the restricted calculations, segments of the deformation energy curves associated with different local minima sharply cross each other in some situations, while they are smoothly joined in other situations. Closely examining the configurations involved, we notice that the sharp crossings occur between configurations having different numbers of particles excited into the fp shell. This point will be further elaborated in the subsequent section.

In Figs. 1–3 there are a number of local minima in the region of smaller values of β_2. We shall not discuss on these local minima in this paper, since the pairing correlations not taken into account here are expected to be important for these.

3.2. SD and HD rotational bands

Let us focus our attention to the SD and HD local minima shown in Figs. 1–3, and investigate properties of the rotational bands built on them. Figs. 4–6 show excitation energies, as functions of angular momentum, of the SD and HD rotational bands calculated with the use of the SIII, SkM*, and SLy4 interactions, respectively. These rotational bands are obtained by cranking each SHF solution (the SD and HD local minima in Figs. 1–3)

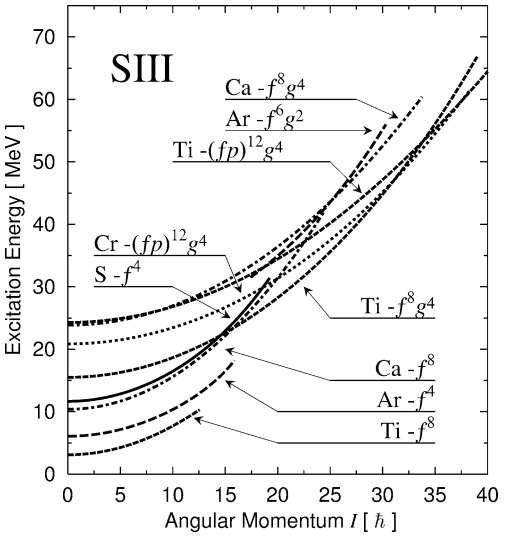

Fig. 4. Excitation energy vs. angular-momentum plot for the SD and HD rotational bands obtained by the cranked SHF calculations with the use of the SIII interaction. Their configurations are indicated by the same notations as in Fig. 1.

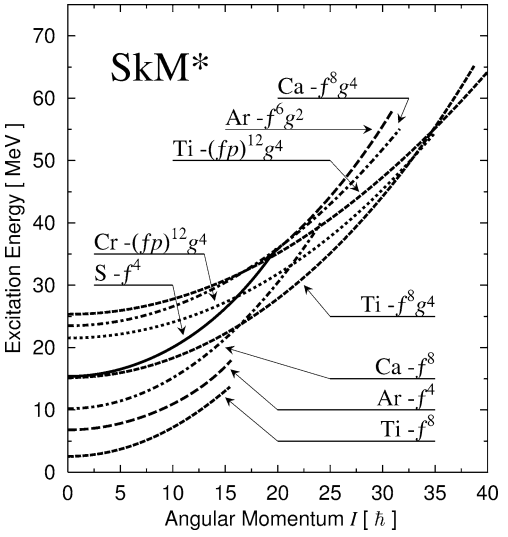

Fig. 5. The same as Fig. 4 but for the SkM* interaction.

and following the same configuration with increasing value of $\omega_{\rm rot}$ until the point where we cannot clearly identify the continuation of the same configuration any more. We note that, in ^{44}Ti, two HD bands associated with the f^8g^4 and $(fp)^{12}g^4$ configurations cross at $I = 30$–34, and the latter becomes the yrast for higher spin. (This band continues beyond $I = 40$ where the figure is cut.) In addition to the SD and HD bands built on the $I^\pi = 0^+$

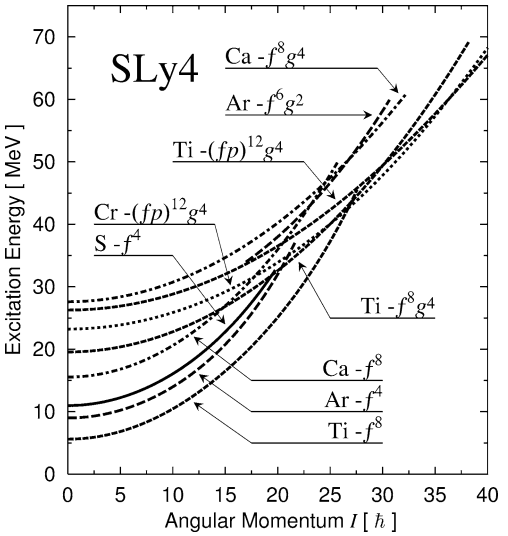

Fig. 6. The same as Fig. 4 but for the SLy4 interaction.

band-head states, we have found a HD band in ^{36}Ar, which does not exist at $I = 0$ and emerges at $I \simeq 16$ due to the rotation alignment of the $g_{9/2}$ orbit. This HD band is denoted by f^6g^2 and is included in Figs. 4–6. A similar configuration, f^4g^2, was found for ^{32}S in our previous calculation [21] and called "HD-like." This and analogous configurations in nuclei other than ^{36}Ar are not illustrated in Figs. 4–6 in order not to make the figure too complicated (drawing complete yrast spectra of individual nuclei is not the major purpose of these figures).

As is well known, according to the deformed harmonic-oscillator potential model, $N = Z = 18$ and 24 are magic numbers associated with the HD shell structure with axis ratio 3 : 1. These HD states respectively correspond to the f^4g^4 and $f^{12}g^4h^4$ configurations in our notation, where h denotes the level associated with the $h_{11/2}$ shell. Microscopic structures of the HD solutions under discussion are apparently different from these, however. We also mention that the possible existence of HD rotational bands at high spin in ^{36}Ar and ^{48}Cr have been discussed in Refs. [55,56] from the viewpoint of the cranked cluster model. The relationship between our solutions and their solutions associated with cluster structure is not clear. Molecule-like cluster structures in highly excited states of nuclei in the ^{40}Ca region have been widely discussed both experimentally and theoretically. These works are thoroughly reviewed in Ref. [57] (see, especially, Section VIII of it), putting special emphasis on reflection-symmetry breaking. The relationship between such cluster structures and the super- and hyper-deformations in the mean fields largely remains as a challenging subject in nuclear structure physics.

Calculated quadrupole deformation parameters (β_2, γ) of all bands mentioned above and their variations are displayed in Fig. 7. The rotational frequency dependence of the single-particle energy levels (Routhian) is illustrated in Fig. 8, taking the SD band in ^{40}Ca as a representative case. The excitation energies of the SD and HD bands obtained by using

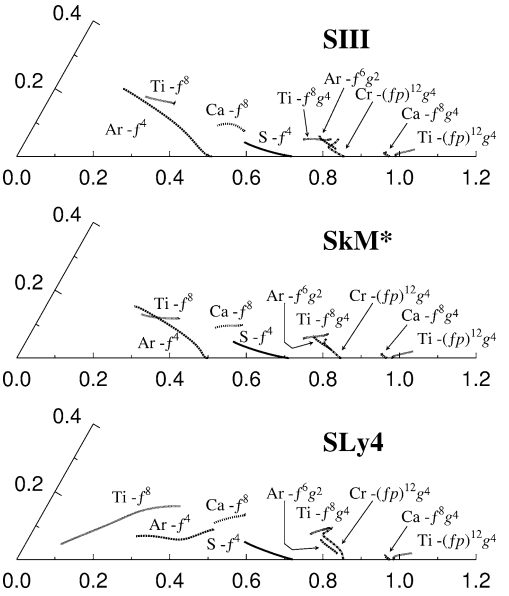

Fig. 7. Quadrupole deformation parameters (β_2, γ) and their variations for the SD and HD rotational bands in ^{32}S, ^{36}Ar, ^{40}Ca, ^{44}Ti and ^{48}Cr. The top, middle and bottom panels show the shape evolution in the (β_2, γ) plane, evaluated with the use of the SIII, SkM*, and SLy4 interactions, respectively. Notations and ranges of I for individual bands are the same as those shown in Figs. 4–6. Values of β_2 decrease with increasing I, except for the $(fp)^{12}g^4$ configuration in ^{44}Ti (where β_2 increases with increasing I).

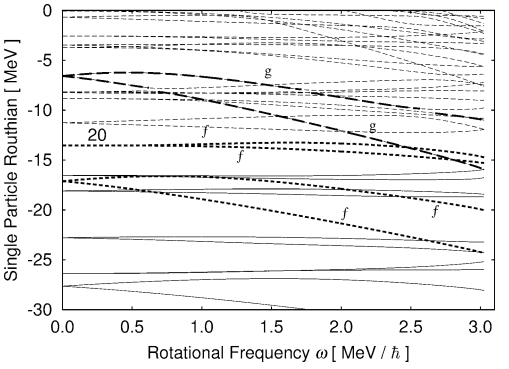

Fig. 8. Neutron single-particle energy diagram (Routhian) for the SD band in ^{40}Ca, calculated with the use of the SIII interaction and plotted as functions of rotational frequency $\omega_{\rm rot}$. The levels associated with the $f_{7/2}$ and $g_{9/2}$ shells are drawn by thick-broken and long-dashed lines, respectively.

different versions (SIII, SkM*, SLy4) of the Skyrme interaction are compared in Fig. 9 with the experimental data [16,19,20].

Examining these figures, we see that, aside from quantitative details and some subtle points to be discussed below, the results obtained by using different versions of the Skyrme

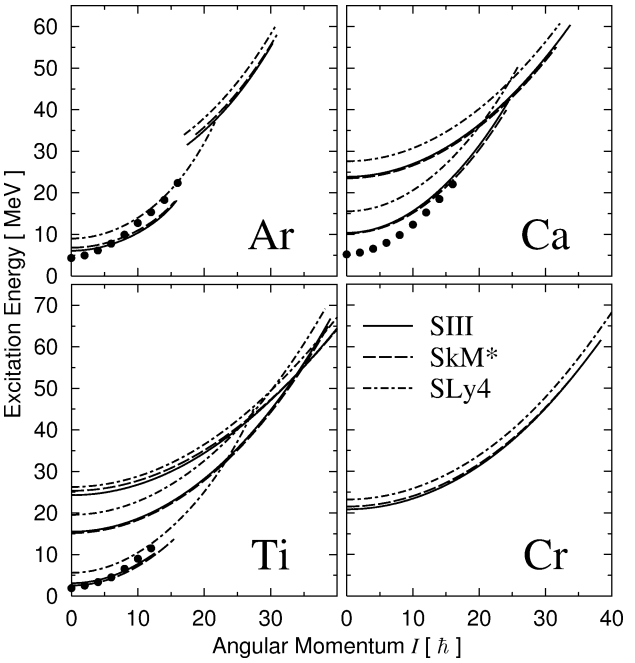

Fig. 9. Comparison between the excitation energies of the SD and HD bands in ^{36}Ar, ^{40}Ca, ^{44}Ti and ^{48}Cr, calculated by using different versions of the Skyrme interaction and the experimental data ([16] for ^{36}Ar, [19] for ^{40}Ca, and [20] for ^{44}Ti). The data are shown by filled circles and the results with the SIII, SkM* and SLy4 interactions are drawn by solid, dashed and dashed-dotted lines, respectively.

interaction are similar. This implies that the basic properties of the SD and HD bands under discussion are not sensitive to the details of the effective interaction.

As mentioned in the introduction, one of the unique features of the SD bands in the ^{40}Ca region is the possibility to observe the SD rotational level structure from the $I^\pi = 0^+$ band heads up to the maximum angular momenta allowed for the many-particle–many-hole configurations characterizing the internal structures of these bands. In fact, such a "SD band termination" has been observed at $I = 16$ in ^{36}Ar and well described by calculations in terms of the j–j coupling shell model, the cranked Nilsson–Strutinsky model [16–18], and the projected shell model [44]. On the other hand, for ^{40}Ca and ^{44}Ti, it is not clear whether or not the SD band continues beyond the highest spin states observed up to now (the 16^+ state in ^{40}Ca [19] and the 12^+ state in ^{44}Ti [20]) and, quite recently, their properties, from the 0^+ band-heads to such high-spin regions, have been discussed in terms of the spherical shell model in Ref. [51] for ^{40}Ca and in Ref. [20] for ^{44}Ti. In our calculation, except for the case of using the SLy4 interaction, the band termination phenomenon in ^{36}Ar is reproduced; the shape becomes triaxial and evolves toward the oblate shape, although the oblate limit is not reached. In the cases of ^{40}Ca, the shape is slightly triaxial with $\gamma = 6°$–$9°$ ($8°$–$9°$) and the SD band terminates at $I \simeq 24$ in the calculation with the use of the SIII (SkM*) interaction. In the case of ^{44}Ti, the shape is more triaxial with $\gamma = 18°$–$25°$ and $13°$–$19°$, and the SD bands terminates at $I \simeq 12$ and

16 for the SIII and SkM* interactions, respectively. Thus, the band termination properties appear quite sensitive to the details of the effective interaction. Concerning the SD band termination in ^{40}Ca and ^{44}Ti, the results obtained with the use of the SIII and SkM* interactions would be more reliable than that with SLy4, in view of the above discussion for ^{36}Ar. In any case, it would be very interesting to explore higher spin members of the SD rotational bands in ^{40}Ca and ^{44}Ti in order to understand the terminating properties of the SD bands at high spin limits.

As is clear from the comparison with experimental data in Fig. 9, the moments of inertia for the SD band are somewhat overestimated in the present calculation. To investigate a possible cause of this, we plan to take into account the pairing correlations by means of the cranked Skyrme–Hartree–Fock–Bogoliubov code constructed in Ref. [58]. One also notice that the excitation energy of the SD band-head state in ^{40}Ca is overestimated. It will decrease if the zero-point rotational energy correction, $-\frac{1}{2\mathcal{J}}\langle J_x^2\rangle$, is taken into account (see Ref. [49] for numerical examples). Although the calculation of this correction is rather easy, we need to evaluate, for consistency, also the zero-point vibrational energy corrections [32], and this is not an easy task. We therefore defer this task for a future publication. Inclusion of these correlations is expected to improve agreement with the experimental data.

4. Discussions

4.1. A role of symmetry breaking

Let us now discuss on the significance of the reflection symmetry breaking in the mean field. As noticed in Figs. 1–3, the crossings between configurations involving different numbers of particles in the fp shell are sharp in the restricted calculation, while we always obtain smooth configuration rearrangements in the unrestricted calculations. The reason for this different behavior between the unrestricted and restricted calculations is rather easy to understand: when the parity symmetry is imposed, there is no way, within the mean-field approximation, to mix configurations having different number of particles in the fp shell. In contrast, smooth crossover between these different configurations is possible via mixing between positive- and negative-parity single-particle levels, when such a symmetry restriction is removed. Let us examine this idea in more detail. In Figs. 10–12 octupole deformation parameters β_3 of the lowest energy states for given values of β_2 are shown. They are obtained by the unrestricted SHF calculations and plotted as functions of β_2 in the lower portion of each panel. We see that β_3 are zero near the local minima in the deformation energy surface, but rise in the crossing region between configurations involving different number of particles in the fp shell. This means that the configuration rearrangements in fact take place through paths in the deformation space that break the reflection symmetry. The importance of allowing the mean field for breaking symmetries in the process of configuration rearrangements was previously emphasized by Negele [59] in their calculations for spontaneous fission of ^{32}S by means of the imaginary time tunneling method.

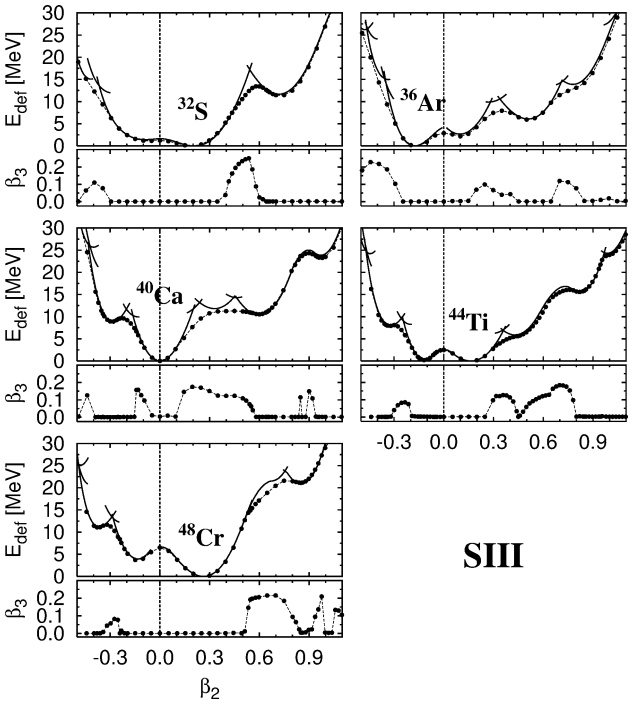

Fig. 10. Octupole deformation parameters β_3 of the lowest energy states for given values of β_2, obtained by the unrestricted SHF calculation at $I = 0$ with the use of the SIII interaction. Their values are plotted as functions of β_2 in the lower portion of each panel. To show that their values increase at crossing regions between configurations involving different number of particles in the fp shell, the deformation energy curves are also displayed in the upper portion of each panel. The latter are the same as those presented in Fig. 1.

In connection with the above finding, it may be appropriate to point out another situation in which a symmetry breaking in the mean field plays an important role. For both the restricted and unrestricted calculations, we have obtained smooth crossover between the SD and HD configurations in ^{40}Ca and ^{44}Ti (see Figs. 1–3). Since four particles are further excited into the g shell in the HD configurations, the smooth configuration rearrangement becomes possible by means of the mixing between the down-sloping levels steming from the $g_{9/2}$ shell (its asymptotic quantum number is $[440]\frac{1}{2}$) and the up-sloping levels stemming from the sd shell ($[202]\frac{5}{2}$ and $[200]\frac{1}{2}$ in the cases of ^{40}Ca and ^{44}Ti, respectively). The mixing between these single-particle levels takes place through the hexadecapole components of the mean field, and we need to break the axial symmetry to mix them in the case of ^{40}Ca. The calculations called "restricted" in this paper allow the axial symmetry breaking, so that the smooth rearrangement from the SD to HD configurations is possible also in ^{40}Ca. A very careful computation is required, however, in order to detect these mixing effects, since the interaction between the down-sloping and up-sloping levels is extremely weak.

In Figs. 10–12, one may notice that β_3 take non-zero values also in some situations other than the crossing regions. Such situations occur in some regions of the deformation energy

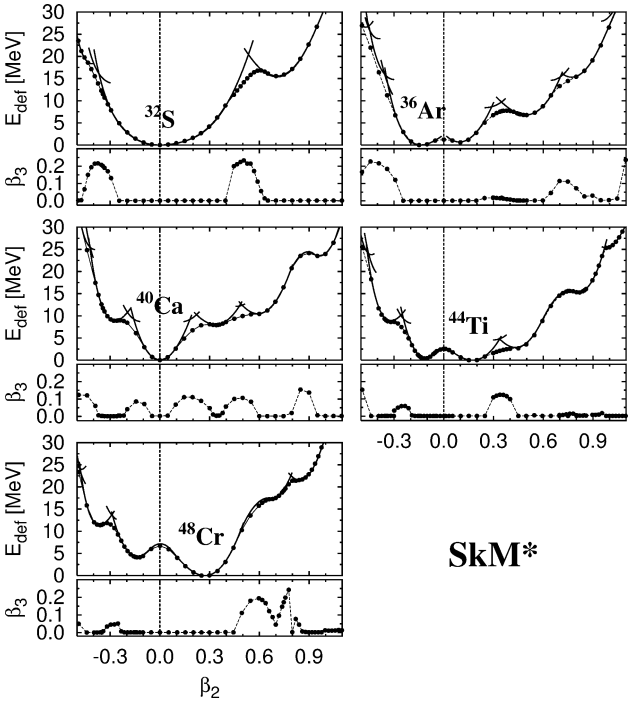

Fig. 11. The same as Fig. 10 but for the SkM* interaction.

surface where it becomes very soft with respect to the reflection-asymmetric degrees of freedom. In the next subsection, we investigate this point in detail taking the SD solution in ^{40}Ca as an especially interesting example.

4.2. Octupole softness of the SD band in ^{40}Ca

Let us examine stabilities of the SD local minimum in ^{40}Ca against octupole deformations. Fig. 13 shows deformation energy curves as functions of the octupole deformation parameters β_{3m} $(m = 0, 1, 2, 3)$ for fixed quadrupole deformation parameters at and near the SD minimum of ^{40}Ca, calculated by means of the constrained HF procedure with the use of the SIII, SkM*, and SLy4 interactions. We immediately notice that the SD state is extremely soft with respect to the β_{30} and β_{31} deformations, irrespective of the Skyrme interactions used. Although it is barely stable with respect to these directions (see curves for $\beta_2 = 0.6$), an instability toward the β_{31} deformation occurs as soon as one goes away from the local minimum point (see curves for $\beta_2 = 0.5$). In fact, the deformation energy surface is found to be almost flat for a combination of the β_{30} and β_{31} deformations already at the SD local minimum. Thus we need to take into account the octupole shape fluctuations for a better description of the SD rotational band in ^{40}Ca. It will be a very interesting subject to search for negative-parity rotational bands associated with octupole shape fluctuation modes built on the SD yrast band. We plan to make such a study in future.

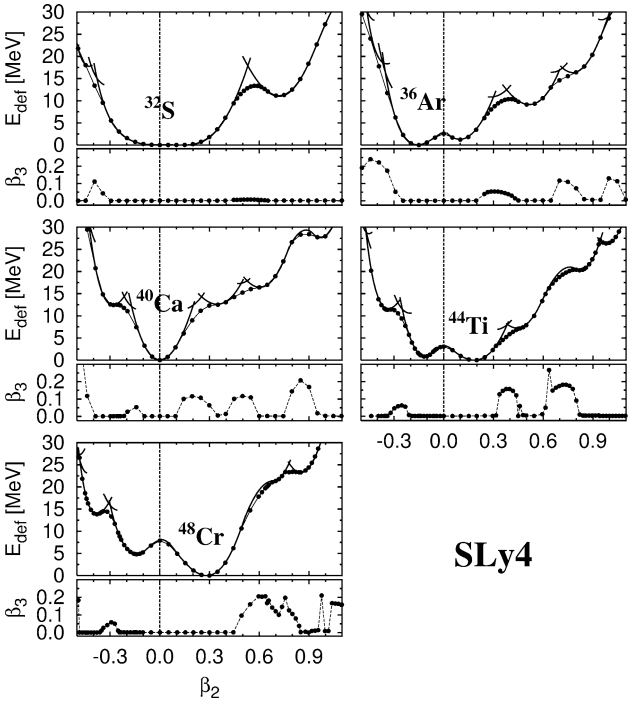

Fig. 12. The same as Fig. 10 but for the SLy4 interaction.

Quite recently, the octupole instability of the SD band in ^{40}Ca has been suggested also by Kanada-En'yo [50].

5. Conclusions

With the use of the symmetry-unrestricted cranked SHF method in the 3D coordinate-mesh representation, we have carried out a systematic theoretical search for the SD and HD rotational bands in the $N = Z$ nuclei from ^{32}S to ^{48}Cr. We have found the SD solutions in ^{32}S, ^{36}Ar, ^{40}Ca, ^{44}Ti, the HD solutions in ^{36}Ar, ^{40}Ca, ^{44}Ti, ^{48}Cr, and we have carried out a systematic analysis of their properties at high spin.

It is explicitly shown that the crossover between configurations involving different number of particles in the fp shell takes place via a reflection-symmetry breaking path in the deformation space.

Particular attention has been paid to the recently discovered SD band in ^{40}Ca, and we have found that the SD band in ^{40}Ca is extremely soft against both the axially symmetric (Y_{30}) and asymmetric (Y_{31}) octupole deformations. Thus, it will be very interesting to search for negative-parity rotational bands associated with octupole shape vibrational excitations built on the SD yrast band.

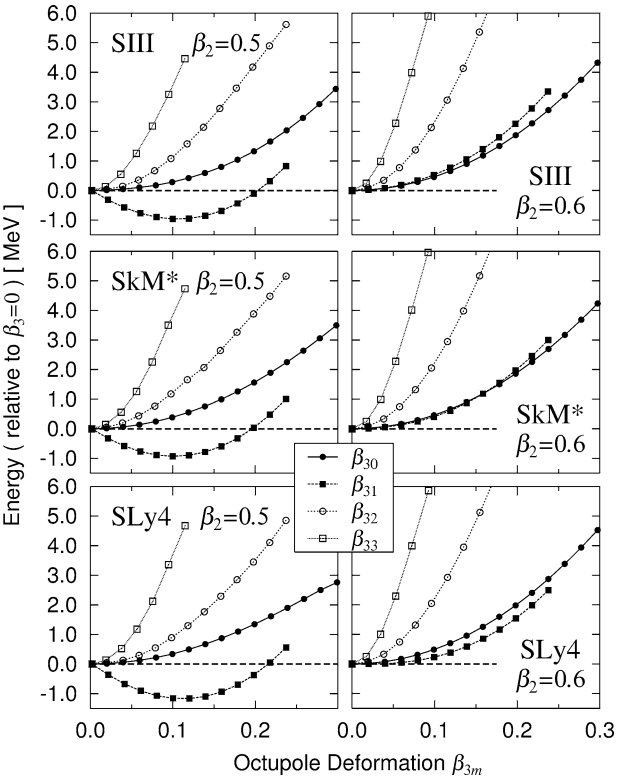

Fig. 13. Left-hand side: deformation energy curves (measured from energies at $\beta_3 = 0$) as functions of the octupole deformation parameters β_{3m} $(m = 0, 1, 2, 3)$, calculated for ^{40}Ca by means of the constrained HF procedure. The quadrupole deformation parameters are fixed at $\beta_2 = 0.5$ and $\gamma = 0$. One of the β_{3m} $(m = 0, 1, 2, 3)$ is varied while the other β_{3m}'s are fixed to zero. Right-hand side: the same as the left-hand side, except that the quadrupole deformation parameters are fixed at $\beta_2 = 0.6$ and $\gamma = 0$. Results of calculation with the use of the SIII, SkM*, and SLy4 interactions are displayed in the upper, middle and lower panels, respectively.

Acknowledgements

We would like to thank E. Ideguchi, M. Matsuo, Y.R. Shimizu and K. Hagino for useful discussions. The numerical calculations were performed on the NEC SX-5 supercomputers at RCNP, Osaka University, and at Yukawa Institute for Theoretical Physics, Kyoto University. This work was supported by the Grant-in-Aid for Scientific Research (No. 13640281) from the Japan Society for the Promotion of Science.

References

[1] P.J. Nolan, P.J. Twin, Annu. Rev. Nucl. Part. Sci. 38 (1988) 533.
[2] S. Åberg, H. Flocard, W. Nazarewicz, Annu. Rev. Nucl. Part. Sci. 40 (1990) 439.
[3] R.V.F. Janssens, T.L. Khoo, Annu. Rev. Nucl. Part. Sci. 41 (1991) 321.

[4] C. Baktash, B. Haas, W. Nazaerewicz, Annu. Rev. Nucl. Part. Sci. 45 (1995) 485.
[5] C. Baktash, Prog. Part. Nucl. Phys. 38 (1997) 291.
[6] J. Dobaczewski, in: C. Baktash (Ed.), Proc. Int. Conf. on Nuclear Structure '98, in: AIP Conference Proceedings, Vol. 481, 1998, p. 315.
[7] R.K. Sheline, I. Ragnarsson, S.G. Nilsson, Phys. Lett. B 41 (1972) 115.
[8] G. Leander, S.E. Larsson, Nucl. Phys. A 239 (1975) 93.
[9] I. Ragnarsson, S.G. Nilsson, R.K. Sheline, Phys. Rep. 45 (1978) 1.
[10] T. Bengtsson, M.E. Faber, G. Leander, P. Möller, M. Ploszajczak, I. Ragnarsson, S. Åberg, Phys. Scripta 24 (1981) 200.
[11] M. Girod, B. Grammaticos, Phys. Rev. C 27 (1983) 2317.
[12] H. Molique, J. Dobaczewski, J. Dudek, Phys. Rev. C 61 (2000) 044304.
[13] R.R. Rodriguez-Guzmán, J.L. Egido, L.M. Robeldo, Phys. Rev. C 62 (2000) 054308.
[14] T. Tanaka, R.G. Nazmitdinov, K. Iwasawa, Phys. Rev. C 63 (2001) 034309.
[15] A.V. Afanasjev, P. Ring, I. Ragnarsson, in: D. Rudolph, M. Hellström (Eds.), Proc. Int. Workshop on Selected Topics on $N = Z$ Nuclei, Lund, Sweden, June 6–10, 2000, PINGST, 2000, p. 183.
[16] C.E. Svenson, et al., Phys. Rev. Lett. 85 (2000) 2693.
[17] C.E. Svenson, et al., Phys. Rev. C 63 (2001) 061301(R) .
[18] C.E. Svenson, et al., Nucl. Phys. A 682 (2001) 1c.
[19] E. Ideguchi, et al., Phys. Rev. Lett. 87 (2001) 222501.
[20] C.D. O'Leary, M.A. Bentley, B.A. Brown, D.E. Appelbe, R.A. Bark, D.M. Cullen, S. Ertürk, A. Maj, A.C. Merchant, Phys. Rev. C 61 (2000) 064314.
[21] M. Yamagami, K. Matsuyanagi, Nucl. Phys. A 672 (2000) 123.
[22] K.T.R. Davies, H. Flocard, S.J. Krieger, M.S. Weiss, Nucl. Phys. A 342 (1980) 111.
[23] H. Flocard, P.H. Heenen, S.J. Krieger, M.S. Weiss, Nucl. Phys. A 391 (1982) 285.
[24] H. Flocard, P.H. Heenen, S.J. Krieger, M.S. Weiss, Prog. Theor. Phys. 72 (1984) 1000.
[25] P. Bonche, H. Flocard, P.H. Heenen, S.J. Krieger, M.S. Weiss, Nucl. Phys. A 443 (1985) 39.
[26] P. Bonche, H. Flocard, P.H. Heenen, Nucl. Phys. A 467 (1987) 115.
[27] N. Tajima, S. Takahara, N. Onishi, Nucl. Phys. A 603 (1996) 23.
[28] N. Tajima, Prog. Theor. Phys. Suppl. 142 (2001) 265.
[29] S. Takahara, N. Tajima, N. Onishi, Nucl. Phys. A 642 (1998) 461.
[30] S. Takami, K. Yabana, K. Ikeda, Prog. Theor. Phys. 96 (1996) 407.
[31] S. Takami, K. Yabana, M. Matsuo, Phys. Lett. B 431 (1998) 242.
[32] P.-G. Reinhard, D.J. Dean, W. Nazarewicz, J. Dobaczewski, J.A. Maruhn, M.R. Strayer, Phys. Rev. C 60 (1999) 014316.
[33] M. Bender, P.-H. Heenen, to be published in Rev. Mod. Phys.
[34] J. Dechargé, D. Gogny, Phys. Rev. C 21 (1980) 1568.
[35] P. Ring, Prog. Part. Nucl. Phys. 37 (1996) 193.
[36] S. Frauendorf, Rev. Mod. Phys. 73 (2001) 463.
[37] M. Yamagami, K. Matsuyanagi, M. Matsuo, in: Proc. Int. Workshop on Selected Topics on $N = Z$ Nuclei, Lund, Sweden, June 6–10, 2000, PINGST, 2000, p. 76.
[38] T. Inakura, M. Yamagami, S. Mizutori, K. Matsuyanagi, in: Proc. Yukawa Int. Seminar on Physics of Unstable Nuclei (YKIS01), Kyoto, Japan, November 5–10, 2001, Prog. Theor. Phys. Suppl., in press.
[39] H. Flocard, P. Quentin, A.K. Kerman, D. Vautherin, Nucl. Phys. A 203 (1973) 433.
[40] D. Baye, P.-H. Heenen, J. Phys. A 19 (1986) 2041.
[41] M. Beiner, H. Flocard, N. van Giai, P. Quentin, Nucl. Phys. A 238 (1975) 29.
[42] J. Bartel, P. Quentin, M. Brack, C. Guet, H.-B. Håkansson, Nucl. Phys. A 386 (1982) 79.
[43] E. Chabanat, P. Bonche, P. Haensel, J. Meyer, F. Schaeffer, Nucl. Phys. A 635 (1998) 231.
[44] G.-L. Long, Y. Sun, Phys. Rev. C 63 (2001) 021305(R) .
[45] W.J. Gerace, A.M. Green, Nucl. Phys. A 93 (1967) 110;
W.J. Gerace, A.M. Green, Nucl. Phys. A 123 (1969) 241.
[46] V. Metag, R. Repnow, P. von Brentano, F. Dickmann, K. Dietrich, Phys. Lett. B 34 (1971) 257.
[47] W.J. Gerace, J.P. Mestre, Nucl. Phys. A 285 (1977) 253.
[48] D.C. Zheng, D. Berdichevsky, L. Zamik, Phys. Rev. C 38 (1988) 437.
[49] D.C. Zheng, L. Zamik, D. Berdichevsky, Phys. Rev. C 42 (1990) 1004.

[50] Y. Kanada-En'yo, in: Proc. Yukawa Int. Seminar on Physics of Unstable Nuclei (YKIS01), Kyoto, Japan, November 5–10, 2001, nucl-th/0204040, Prog. Theor. Phys. Suppl., in press.
[51] E. Caurier, F. Nowacki, A. Poves, A. Zuker, nucl-th/0205036.
[52] J.J. Simpson, W.R. Dixon, R.S. Storey, Phys. Rev. Lett. 31 (1973) 946.
[53] F. Michel, S. Ohkubo, G. Reidemeister, Prog. Theor. Phys. Suppl. 132 (1998) 7.
[54] J.L. Wood, K. Heyde, W. Nazarewicz, M. Huyse, P. van Duppen, Phys. Rep. 215 (1992) 101.
[55] W.D.M. Rae, A.C. Merchant, Phys. Lett. B 279 (1992) 207.
[56] J. Zhang, W.D.M. Rae, A.C. Merchant, Nucl. Phys. A 575 (1994) 61.
[57] P.A. Butler, W. Nazarewicz, Rev. Mod. Phys. 68 (1996) 349.
[58] M. Yamagami, K. Matsuyanagi, M. Matsuo, Nucl. Phys. A 693 (2001) 579.
[59] J. Negele, Nucl. Phys. A 502 (1989) 371c.

Progress of Theoretical Physics, Vol. 108, No. 5, November 2002

Symmetry Breaking and Bifurcations in the Periodic Orbit Theory. II

— Spheroidal Cavity —

Alexander G. Magner,[1,2,3] Ken-ichiro Arita,[4] Sergey N. Fedotkin[2,3] and Kenichi Matsuyanagi[5]

[1]*Research Center for Nuclear Physics, Osaka University, Ibaraki 567-0047, Japan*
[2]*Institute for Nuclear Research, 03680 Prospekt Nauki 47, Kiev-28, Ukraine*
[3]*Institute for Theoretical Physics, University of Regensburg, D-93040 Regensburg, Germany*
[4]*Department of Physics, Nagoya Institute of Technology, Nagoya 466-8555, Japan*
[5]*Department of Physics, Graduate School of Science, Kyoto University, Kyoto 606-8502, Japan*

(Received August 5, 2002)

We derive a semiclassical trace formula for the level density of a three-dimensional spheroidal cavity. To overcome the divergences and discontinuities occurring at bifurcation points and in the spherical limit, the trace integrals over the action-angle variables are performed using an improved stationary phase method. The resulting semiclassical level density oscillations and shell energies are in good agreement with quantum-mechanical results. We find that the births of three-dimensional orbits through the bifurcations of planar orbits in the equatorial plane lead to considerable enhancement of the shell effect for superdeformed shapes.

§1. Introduction

The periodic orbit theory (POT)[1)–10)] is a nice tool for studying the correspondence between classical and quantum mechanics and, in particular, the interplay of deterministic chaos and quantum-mechanical behavior. Also, for systems with integrable or mixed classical non-linear dynamics, the POT leads to a deeper understanding of the origin of shell structure in finite fermion systems, such as nuclei,[8),11)–13)] metallic clusters,[14)–16)] and mesoscopic semiconductors.[17)–21)] Bifurcations of periodic orbits may play significant roles, e.g., in connection with superdeformations of atomic nuclei,[8),9),12),22)–24)] and were recently shown to affect the quantum oscillations observed in the magneto-conductance of mesoscopic devices.[19),20)] This phenomenon is observed for some control parameters (like the shape, magnetic field, etc.) of the potential well, for which the orbits bifurcate and new types of periodic orbits emerge from the original ones. Examples can be found, e.g., in elliptic billiard and spheroidal cavity systems.[8),9),12),23)–28)] In elliptic billiard systems, short diametric orbits with repetitions bifurcate at certain values of the deformation parameter, and new orbits with hyperbolic caustics (butterfly-shaped orbit, etc.) emerge from them. In spheroidal cavity systems, periodic orbits in the equatorial plane bifurcate, and new three-dimensional orbits emerge.

The semiclassical trace formulae connect the quantum mechanical density of states with a sum over the periodic orbits of the classical system.[1)–4)] In these formulae, divergences arise at critical points where bifurcations of periodic orbits occur or where symmetry breaking (or restoring) transitions take place. At these points, the standard stationary phase method (SSPM),[*)] used in the semiclassical evaluation of the trace integrals, breaks down. Various ways of avoiding these divergences have been studied,[3),5),29)] some of them employing uniform approximations.[29)–37)] Here we employ an improved stationary-phase method (ISPM) for the evaluation of the trace integrals in the phase-space representation, which we have derived for elliptic billiards[28)] and very recently for spheroidal cavities.[24)]

The singularities of the SSPM near the bifurcation points are due to the peculiarities of its asymptotic expansions. In the ISPM,[24),28)] the catastrophe integrals[38),39)] are evaluated more exactly within the finite integration limits in the phase-space trace formula,[3),5),9),24),28),40)] and it is possible to overcome the singularity problem due to bifurcations, which occur when the stationary points lie near the ends of the integration region in the action-angle variables. We can also take into account the stationary points outside the classically accessible region ("ghost orbits").[5)] This method is particularly useful for integrable systems in which integration limits are easily obtained. This theory is developed in Ref. 28) for the case of the bifurcations through which periodic orbit families with maximal degeneracy emerge from orbits with smaller degeneracy. The essential difference between the method presented in this paper and that with the uniform approximation of Refs. 32) and 35) is that we improve the calculation of the *angle* part of the phase-space trace integral for the orbits with smaller degeneracies. Taking an elliptic billiard system as an example, we have applied the ISPM to the integration over the angle variable for short diametric orbits and derived an improved trace formula that is continuous through all bifurcation points, including the circular limit and the separatrix. We then showed that significant enhancements of the shell effect in level densities and shell structure energies occur at deformations near the bifurcation points. Away from the bifurcation points, our result reduces to the extended Gutzwiller trace formula,[4),8)–10)] and for the leading-order families of periodic orbits, it is identical to that of Berry and Tabor.[5)]

The major purpose of this paper is to extend our semiclassical ISPM to the case of a three-dimensional (3D) spheroidal cavity,[24)] which may be taken as a simple (highly idealized) model for a heavy deformed nucleus[8),11)] or a deformed metallic cluster,[14),15)] and to specify the role of periodic orbit bifurcations in the shell structure responsible for superdeformations. Although the spheroidal cavity system is integrable, it exhibits all the difficulties mentioned above (i.e., symmetry breaking and bifurcations), and therefore it provides an exemplary case study of a non-trivial 3D system. We apply the ISPM to the bifurcating orbits and succeed in reproducing the superdeformed shell structure in terms of the POT, while observing a considerable enhancement of the shell effect near the bifurcation points.

[*)] In this paper, SSPM is understood as the standard stationary phase method and its extension to continuous symmetries.[3)–5),7)]

§2. Classical mechanics for the spheroidal cavity

The semiclassical trace formulas for the oscillating part of the level density for a spheroidal cavity are determined from the characteristic properties of the classical periodic families.[8),9),22)–27)] This section presents definitions and solutions for the classical mechanical description of the spheroidal cavity, following Refs. 8), 9), 23) and 27). They will be used for the semiclassical derivations of the trace formulas improved at the bifurcation points. We shall pay special attention to the 3D periodic orbits that emerge through bifurcations and play important roles as the semiclassical origin of superdeformed shell structure.[8),23),27)]

2.1. *General periodic-orbit formalism*

We characterize the spheroid by the ratio of its semi-axes $\eta = b/a$, keeping its volume fixed, and consider the prolate case with $\eta > 1$, where the major axis coincides with the symmetry axis. We first transform the Cartesian coordinates (x, y, z) into the usual cylindrical coordinates (ρ, z, φ), where $\rho = \sqrt{x^2 + y^2}$, which are expressed in terms of the spheroidal coordinates (u, v, φ) as

$$\rho = \zeta \, \cos u \, \sinh v, \quad z = \zeta \, \sin u \, \cosh v, \quad \zeta = \sqrt{b^2 - a^2}, \tag{2·1}$$

with

$$-\frac{\pi}{2} \le u \le \frac{\pi}{2}, \quad 0 \le v < \infty, \quad 0 \le \varphi \le 2\pi. \tag{2·2}$$

The values of $\pm\zeta$ define the positions of the foci of the spheroid lying on the z-axis. Taking into account the volume conservation condition $a^2 b = R^3$, we have $b = R\eta^{2/3}$ and $a = R\eta^{-1/3}$. As is well known, the Hamilton-Jacobi equations separate in the coordinates (u, v, φ) for a spheroidal cavity.

In the Hamilton-Jacobi formalism, the classical dynamics are determined by the partial actions. In the spheroidal coordinates, these are given by

$$I_u = \frac{p\zeta}{\pi} \int_{-u_c}^{u_c} du \sqrt{\sigma_1 - \sin^2 u - \frac{\sigma_2}{\cos^2 u}}, \tag{2·3a}$$

$$I_v = \frac{p\zeta}{\pi} \int_{v_c}^{v_b} dv \sqrt{\cosh^2 v - \sigma_1 - \frac{\sigma_2}{\sinh^2 v}}, \tag{2·3b}$$

$$I_\varphi = |l_z| = p\zeta\sqrt{\sigma_2}, \tag{2·3c}$$

where l_z is the projection of the angular momentum onto the symmetry axis, and $p = \sqrt{2m\varepsilon}$, where m is the particle mass. In Eq. (2·3) we have introduced the new "action" variables σ_1 and σ_2 related to the turning points $-u_c$, u_c and v_c, v_b along the trajectory in the (u, v) coordinates; $u = u_c$ and $v = v_c$ are the (hyperbolic and elliptic) caustic surfaces,

$$\cosh v_c = \left\{ \frac{1}{2}(1 + \sigma_1) + \left[\frac{1}{4}(1 - \sigma_1)^2 + \sigma_2 \right]^{1/2} \right\}^{1/2}, \tag{2·4a}$$

$$\sin u_c = \left\{ \frac{1}{2}(1 + \sigma_1) - \left[\frac{1}{4}(1 - \sigma_1)^2 + \sigma_2 \right]^{1/2} \right\}^{1/2}, \tag{2·4b}$$

and $v = v_b$ is the spheroid boundary, given by $\cosh v_b = \eta/\sqrt{\eta^2-1}$. The condition that the kinetic energy must be positive determines the limits for the variables σ_1 and σ_2:

$$\sigma_1^- = \sigma_2 \le \sigma_1 \le \frac{\eta^2}{\eta^2-1} - \sigma_2\left(\eta^2-1\right) = \sigma_1^+,$$
$$\sigma_2^- = 0 \le \sigma_2 \le \frac{1}{\eta^2-1} = \sigma_2^+. \tag{2·5}$$

These inequalities together with the 2π intervals for the corresponding angle variables determine the tori of the classically accessible motion with the boundaries $\sigma_1^{\pm}(\sigma_2)$ and $\sigma_2^{\pm}$.

According to Eq. (2·3), the particle energy ε is a function of only the action variables I_u, I_v and I_φ, $\varepsilon = H\left(I_u, I_v, I_\varphi\right)$, due to the integrability of the system under consideration. These relations define the partial frequencies ω_u, ω_v and ω_φ through $\omega_j = \partial H/\partial I_j$. The periodicity conditions for the classical trajectories are significantly simplified in terms of the partial frequencies ω_j. Introducing the new variables κ and θ,

$$\kappa = \frac{\sin u_c}{\cosh v_c}, \quad \theta = \arcsin\left(\frac{\cosh v_c}{\cosh v_b}\right), \tag{2·6}$$

along with the energy ε in place of the partial actions I_u, I_v and I_φ (or σ_1 and σ_2), they read

$$\frac{\omega_u}{\omega_v} \equiv \frac{1}{2}\left[1 - \frac{\mathrm{F}(\theta,\kappa)}{\mathrm{F}(\kappa)}\right] = \frac{n_u}{n_v}, \tag{2·7a}$$
$$\frac{\omega_\varphi}{\omega_u} \equiv \frac{2}{\pi}\left[\left(1-\left(\frac{\kappa}{\bar\kappa}\right)^2\right)\left(1-\bar\kappa^2\right)\right]^{1/2}\left\{\Pi\left(\left(\frac{\kappa}{\bar\kappa}\right)^2,\kappa\right) - \mathrm{F}(\kappa)\right.$$
$$\left. + \left[\Pi\left(\bar\kappa^2,\kappa\right) - \Pi\left(\theta,\bar\kappa^2,\kappa\right)\right] \Big/ \left[1 - \frac{\mathrm{F}(\theta,\kappa)}{\mathrm{F}(\kappa)}\right]\right\} = \frac{n_\varphi}{n_u}. \tag{2·7b}$$

Here, n_u, n_v and n_φ are co-prime integers: $n_u = 1, 2, \cdots$; $n_v \ge 2n_u$; $n_v \ge 2n_\varphi$, $n_\varphi = 1, 2, \cdots$, and $\bar\kappa = \sqrt{\eta^2-1}/(\eta\sin\theta)$. F and Π are elliptic integrals of the 1st and 3rd kinds (see Appendix A for their definitions). The periodicity condition (2·7) relates $\kappa(\sigma_1,\sigma_2)$ and $\theta(\sigma_1,\sigma_2)$ for a given periodic orbit β to the integers n_u, n_v and n_φ, which, together with the number of repetitions M, define this orbit; i.e., $\beta = M(n_v, n_\varphi, n_u)$.

2.2. *Three-dimensional periodic orbits*

The 3D periodic orbits (3DPO) $M(n_v, n_\varphi, n_u)$ form two-parameter ($\mathcal{K} = 2$) families for a given energy ε, because the number $\mathcal{K}$ of free continuous parameters specifying an orbit with fixed energy and a given action is two.[8),9)] The condition for 3DPO is the existence of real roots (κ, θ) of Eq. (2·7). They appear at the deformation $\eta = \eta_{\mathrm{bif}}$ given by

$$\eta_{\mathrm{bif}} = \frac{\sin(\pi n_\varphi/n_v)}{\sin(\pi n_u/n_v)}, \quad (n_u = 1, 2, \cdots,\ n_v \ge 2n_\varphi + 1,\ n_\varphi = 2, 3, \cdots) \tag{2·8}$$

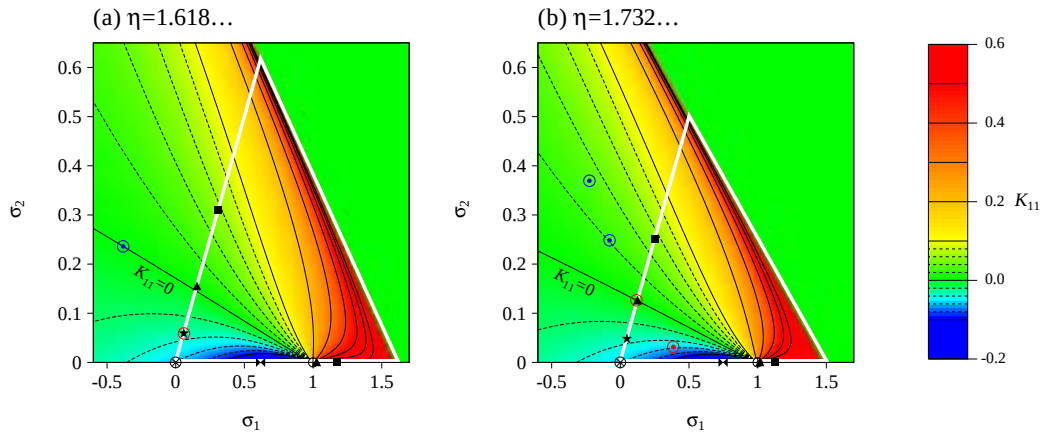

Fig. 1. The triangle of the classically accessible region determined by Eq. (2·5) is indicated by white lines in the (σ_1, σ_2) plane at the bifurcation deformations (a) $\eta = 1.618\ldots$ and (b) $\eta = \sqrt{3}$. The red and blue dots with the circles indicate the 3DPO stationary points inside (actually existing 3DPO) and outside ("ghost" 3DPO) of this triangle region, respectively. Several examples of the stationary points are indicated: on the $\sigma_2 = 0$ side, the short 2DPO (elliptic triangle, square, and hyperbolic "butterfly"); on the $\sigma_2 = \sigma_1$ side, the short EQPO (triangle, square, star and diameter (black crossed circle)). The long diameter (separatrix) is located at $(\sigma_1 = 1, \sigma_2 = 0)$. The color and contour curves indicate (in units of $p\zeta/\pi$) the curvature K_{11} defined by Eq. (3·14).

where $\kappa = 0$ and $\theta = \pi(1 - 2n_u/n_v)/2$, and exist for larger deformations $\eta > \eta_{\rm bif}$. These roots determine the caustics (the spheroid $v = v_c$ and the hyperboloids $u = \pm u_c$) of the periodic orbit $M(n_v, n_\varphi, n_u)$ through Eq. (2·6). These caustics are confocal to the boundary of the spheroid $v = v_b$.

Figure 1 displays the stationary points corresponding to the 3DPO for two bifurcation points $\eta_{\rm bif}$ given by (2·8). The physical tori region (2·5) in the variables σ_i is a triangle. At $\eta_{\rm bif} = 1.618\ldots$ (Fig. 1(a)), the stationary point for the 3DPO $(5, 2, 1)$ coincides with that for the star-shaped $(5, 2)$ orbit in the equatorial plane (discussed below) lying on the boundary with $\sigma_2 = \sigma_1$, and moves toward the inside of the physical tori region for larger deformations. At $\eta_{\rm bif} = \sqrt{3}$ (Fig. 1(b)), the stationary point for the 3DPO $(6, 2, 1)$ lies on the boundary side and coincides with that for triangular orbits in the equatorial plane. At these bifurcation deformations, the lengths of the 3DPO $(5, 2, 1)$ and $(6, 2, 1)$ coincide with those of the star $(5, 2)$ and the doubly repeated triangle $2(3, 1)$, respectively. Figure 2 illustrates some short 3DPO and their projections onto the equatorial plane.

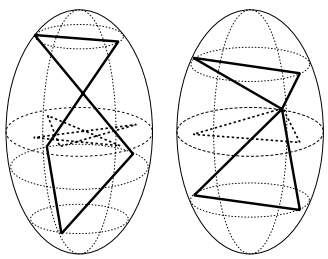

Fig. 2. Short 3D periodic orbits (5,2,1) and (6,2,1) bifurcated from the equatorial plane orbits (5,2) and 2(3,1), respectively. Their projections on the equatorial plane are also represented by thick-dashed lines.

2.3. *Orbits in the meridian plane*

Equations (2·7a) and (2·7b) have partial solutions for $\kappa(\sigma_1, \sigma_2)$ and $\theta(\sigma_1, \sigma_2)$ that correspond to the separate families of orbits, i.e. two-dimensional periodic orbits (2DPO), in the meridian planes (containing the symmetry axis z) and in the equatorial plane. First, we consider the special solutions of Eq. (2·7) corresponding to the two-parameter ($\mathcal{K} = 2$) 2DPO families in the meridian plane.[8),9)] For these orbits, $\sigma_2 = 0$ and σ_1 is in either of the regions

$$0 < \sigma_1 < 1, \qquad 1 < \sigma_1 < \frac{\eta^2}{\eta^2 - 1}, \tag{2·9}$$

for the hyperbolic 2DPO (with hyperbolic caustics $u = \pm u_c$) and the elliptic 2DPO (with elliptic caustics $v = v_c$), respectively. The periodicity condition (2·7b) becomes the identity $\omega_\varphi/\omega_u \equiv 1$ ($n_\varphi = 1$, $n_u = 1$), and θ is fixed by

$$\theta = \theta_h = \arcsin\left(\frac{\sqrt{\eta^2 - 1}}{\eta}\right), \qquad \theta = \theta_e = \arcsin\left(\frac{\sqrt{\eta^2 - 1}}{\kappa\eta}\right), \tag{2·10}$$

for the hyperbolic and elliptic 2DPO, respectively. For κ, we have only the condition Eq. (2·7a). This κ determines σ_1, and thus I_u and I_v ($I_\varphi = 0$ since $\sigma_2 = 0$), through

$$\kappa = \kappa_h = \sqrt{\sigma_1}, \qquad \kappa = \kappa_e = \frac{1}{\sqrt{\sigma_1}}, \tag{2·11}$$

for the hyperbolic and elliptic orbits, respectively.

Some examples of the hyperbolic and elliptic orbits lying along the triangular boundary side $\sigma_2 = 0$ are presented in Fig. 1 (see also their geometrical illustrations in Fig. 3). The hyperbolic and elliptic tori parts are separated by the separatrix point ($\sigma_1 = 1, \sigma_2 = 0$) related to the long diameter (see below). Another endpoint of the hyperbolic tori coincides with the stationary point ($\sigma_1 = \sigma_2 = 0$) for the diametric orbit in the equatorial plane. We can think of these hyperbolic and elliptic orbits as being periodic in the plane $\varphi =$ [const.], and we call them "meridian-plane periodic orbits".

For the elliptic case, a solution κ of Eq. (2·7) with $\theta = \theta_e(\kappa)$ exists for any $n_u = 1, 2, \cdots$ and $n_v \geq 2n_u + 1$, $(n_\varphi = n_u)$ for any deformation $\eta > 1$. Examples are

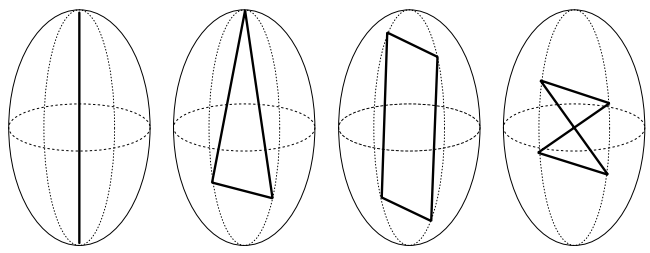

Fig. 3. Some short meridian-plane orbits in the prolate spheroidal cavity. From left to right: the isolated long diameter $(2, 1, 1)$, the elliptic triangular $(3, 1, 1)$, the elliptic rhomboidal $(4, 1, 1)$, the hyperbolic "butterfly" $(4, 2, 1)$.

the triangles ($n_v = 3, n_\varphi = 1, n_u = 1$), the rhomboids $(4, 1, 1)$ and the star-shaped orbits $(5, 2, 2)$ as one-parameter families in the meridian plane. The root κ found from Eq. (2·7) gives the elliptic caustics with $u_c = \pi/2$ in Eq. (2·6) and the semi-axes $a_c = \zeta\sqrt{1-\kappa^2}/\kappa$ and $b_c = \zeta/\kappa$.

For the hyperbolic case, the solutions κ can be found for $n_u = 1, 2, 3, \cdots$ and even n_v ($n_v \geq 2(n_u + 1)$). In Fig. 1 the "butterfly" orbit $(4, 2, 1)$ is shown as an example. The families of these orbits appear for $\eta > \eta_{\rm bif}$ with

$$\eta_{\rm bif} = \left[\sin\left(\frac{\pi n_u}{n_v}\right)\right]^{-1}. \tag{2·12}$$

This is the deformation at which the diametric orbits $M(2, 1)$ with $M \geq 2$ in the equatorial plane bifurcate, and from these orbit emerge the hyperbolic orbits. Their hyperbolic caustics are expressed in terms of the root κ of Eqs. (2·7) and (2·6) with $v_c = 0$. The parameters a_c and b_c of these caustics are given by $a_c = \zeta\sqrt{1-\kappa^2}$ and $b_c = \zeta\kappa$.

2.4. *Orbits in the equatorial plane*

In the equatorial plane with $z = 0$, the separate families of regular polygons and diameters are the same as for a circular billiard system[3)] of radius a. The restriction $z = 0$ decreases the values of $\mathcal{K}$ to 1. The single parameter in this case corresponds to the angle of rotation of the polygons and the diameters about the symmetry axis z. Figure 4 illustrates the most important (shortest) equatorial-plane periodic orbits (EQPO): the diameters $M(n_v = 2, n_\varphi = 1)$, triangles $M(3, 1)$, squares $M(4, 1)$ and star-shaped orbits $M(5, 2)$. They satisfy, from inequalities (2·5),

$$\sigma_1 = \sigma_2, \qquad 0 \leq \sigma_2 \leq \frac{1}{\eta^2 - 1}. \tag{2·13}$$

Therefore their stationary points lie along the $\sigma_2 = \sigma_1$ side in the triangle, as indicated in Fig. 1.

The caustic parameters u_c and v_c for these families are defined by $u_c = 0$ and $v_c = \operatorname{arcsinh}[a\cos(\pi n_\varphi/n_v)/\zeta]$. The solutions of Eq. (2·7) for these orbits are $\kappa = 0$ and $\theta = \arcsin\sqrt{1 - \sin^2(\pi n_\varphi/n_v)/\eta^2}$.

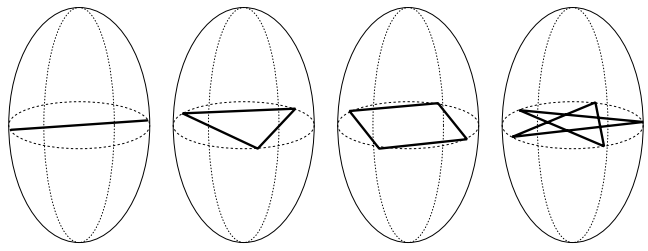

Fig. 4. Some short equatorial-plane orbits. From left to right: the short diameter $(2, 1)$, the triangular $(3, 1)$, the rhomboidal $(4, 1)$, and the star-shaped $(5, 2)$.

2.5. *Diametric orbits along the symmetry axis*

In the spheroidal cavity, there is also a diametric orbit along the z-axis (see Fig. 3). It is isolated ($\mathcal{K} = 0$), because we have two additional restrictions, $x = 0$ and $y = 0$, decreasing $\mathcal{K}$ by one with respect to the previous case. The solution of Eq. (2·7) for this orbit is $\kappa = 1$ and $\theta = \arcsin(\sqrt{\eta^2 - 1}/\eta)$. Its stationary point coincides with the separatrix values ($\sigma_1 = 1,\ \sigma_2 = 0$), corresponding formally to the caustic parameters ($u_c = \pi/2,\ v_c = 0$). (See the circle point with the vertical diameter in Fig. 1. In Fig. 1(b), this stationary point is very close to that for the elliptic orbits (3,1,1) in the meridian plane, which lies slightly on the right, along the $\sigma_2 = 0$ side.)

2.6. *Bifurcations*

At the deformations $\eta_{\rm bif}$ given by Eq. (2·8), the EQPO $M(n_v, n_\varphi)$ bifurcate, and the 3DPO or the hyperbolic 2DPO $M(n_v, n_\varphi, n_u)$ emerge. We encounter the breaking-of-symmetry problem at these bifurcation points, because the degeneracy (symmetry) parameter $\mathcal{K}$ changes there, for instance, from $\mathcal{K} = 1$ for the EQPO to $\mathcal{K} = 2$ for the 3DPO. Before the bifurcations ($\eta < \eta_{\rm bif}$), the stationary points σ_i of the 3DPO and the hyperbolic 2DPO are situated outside of the triangular tori region (2·5), and give rise to complex (κ, θ) and complex caustics. Such formal orbits are called "complex" or "ghost" orbits.[5] They cross the $\sigma_1 = \sigma_2$ boundary through the stationary points of the EQPO at bifurcations ($\eta = \eta_{\rm bif}$) and then move into the triangular tori region for larger η. In Fig. 1 are also indicated the stationary points for the 3DPO lying outside the physical tori region [(6,2,1) in Fig. 1(a), (7,2,1) and (8,2,1) in Fig. 1(b)]. The equatorial diameters $M(2,1)$ correspond to the limiting case, $\sigma_1 = \sigma_2 = 0$. They bifurcate into themselves ($\mathcal{K} = 1$) and the hyperbolic 2DPO $(2M, M, 1)$ in the meridian plane ($\mathcal{K} = 2$) at the deformations given by Eq. (2·12).

The spherical limit ($\eta = 1$) is a special bifurcation point. In this limit, the planar regular polygons and diameters have degeneracies $\mathcal{K} = 3$ and 2, respectively, and they bifurcate into the meridian 2DPO ($\mathcal{K} = 2$), EQPO ($\mathcal{K} = 1$) and the isolated long diameter ($\mathcal{K} = 0$) for deformations $\eta > 1$.

The separatrix ($\sigma_1 = 1, \sigma_2 = 0$), related to the long diameter, is a special point in the phase space. Near this point, the complicated 3DPO and elliptic and hyperbolic 2DPO having large values of (n_u, n_v) and n_u/n_v close to 1/2 appear. Similar bifurcations of the 3DPO, EQPO and elliptic 2DPO appear near other boundary values of σ_i in the triangular tori on its "creeping" side $\sigma_1 = \sigma_1^+(\sigma_2)$, where some kinds of 3D "creeping" orbits with large values of n_v but finite and generally different n_u and n_φ appear. This is in analogy to the "creeping" singularities investigated for elliptic orbits in elliptic billiard systems[28] near the maximum value of σ_1, $\sigma_1^{\rm (cr)} = \cosh^2 v_b = \eta^2/(\eta^2 - 1)$, according to Eq. (A·6) at the right vertex in the "meridian-plane orbit" side $\sigma_2 = 0$. The 3DPO with a large number of the corners n_v and finite $n_u = n_\varphi$ approach the "creeping" elliptic orbits in the meridian plane. Another vertex corresponds to the creeping EQPO that have large values of n_v and n_φ but for $n_v/n_\varphi \to 1/2$.

The bifurcation point related to the appearance of "creeping" orbits cannot

be reached for any finite deformation. However, even for finite deformations like superdeformed shapes, the solutions for σ_1 and σ_2 [related to the roots κ and θ of the periodic-orbit conditions (2·7)] can be close to the "creeping" values of σ_1 and σ_2 [related to their boundary values given in (2·5)]. In such cases, we have to take into account such bifurcations in the trace formulas for the level density. The bifurcations of the 3D and 2D diameter-like orbits with n_v/n_u close to 1/2 near the separatrix are rather long, however, so that they are not important for the shell effects discussed below.

§3. Trace formulas for the prolate spheroid

3.1. *Phase-space trace formula in action-angle variables*

The level density $g(\varepsilon)$ is obtained from the Green function $G(\boldsymbol{r}, \boldsymbol{r}'; \varepsilon)$ by taking the imaginary part of its trace:

$$g(\varepsilon) = \sum_n \delta\left(\varepsilon - \varepsilon_n\right) = -\frac{1}{\pi} \operatorname{Im} \int d\boldsymbol{r}'' \int d\boldsymbol{r}' G(\boldsymbol{r}', \boldsymbol{r}''; \varepsilon)\ \delta(\boldsymbol{r}'' - \boldsymbol{r}'), \tag{3·1}$$

where ε_n is the single-particle energy. Following Ref. 28), we now apply the Gutzwiller trajectory expansion for the Green function $G(\boldsymbol{r}, \boldsymbol{r}', \varepsilon)$.[1),2),10)] After simple transformations,[28)] we obtain the phase-space trace formula in the action-angle variables $(\boldsymbol{I}, \boldsymbol{\Theta})$,

$$\begin{aligned} g_{\mathrm{scl}}(\varepsilon) = \frac{1}{(2\pi\hbar)^3} \operatorname{Re} \sum_\alpha \int d\boldsymbol{\Theta}'' \int d\boldsymbol{I}' \delta\left(\varepsilon - H\left(\boldsymbol{I}', \boldsymbol{\Theta}'\right)\right) \\ \times \exp\left[\frac{i}{\hbar}\left(S_\alpha\left(\boldsymbol{I}', \boldsymbol{I}'', t_\alpha\right) + \left(\boldsymbol{I}'' - \boldsymbol{I}'\right) \cdot \boldsymbol{\Theta}''\right) - i\frac{\pi}{2}\nu_\alpha\right], \end{aligned} \tag{3·2}$$

where the sum is taken over all classical trajectories α, $\boldsymbol{I} = \{I_u, I_v, I_\varphi\}$ represents the actions for the spheroidal cavity, $\boldsymbol{\Theta} = \{\Theta_u, \Theta_v, \Theta_\varphi\}$ the conjugate angles, and ν_α the phases related to the Maslov indices.[39),41)–43)] The phase-space trace formula (3·2) is especially useful for integrable systems, because the Hamiltonian H does not depend on the angle variables $\boldsymbol{\Theta}$ in this case, i.e., $H = H(\boldsymbol{I})$. The action

$$S_\alpha\left(\boldsymbol{I}', \boldsymbol{I}'', t_\alpha\right) = -\int_{\boldsymbol{I}'}^{\boldsymbol{I}''} d\boldsymbol{I} \cdot \boldsymbol{\Theta}(\boldsymbol{I}) \tag{3·3}$$

is related to the standard definition,

$$S_\alpha\left(\boldsymbol{\Theta}', \boldsymbol{\Theta}'', \varepsilon\right) = \int_{\boldsymbol{\Theta}'}^{\boldsymbol{\Theta}''} d\boldsymbol{\Theta} \cdot \boldsymbol{I}(\boldsymbol{\Theta}), \tag{3·4}$$

by the Legendre transformation

$$S_\alpha(\boldsymbol{\Theta}', \boldsymbol{\Theta}'', \varepsilon) + \boldsymbol{I}'' \cdot (\boldsymbol{\Theta}' - \boldsymbol{\Theta}'') = S_\alpha(\boldsymbol{I}', \boldsymbol{I}'', t_\alpha) + \boldsymbol{\Theta}'' \cdot (\boldsymbol{I}'' - \boldsymbol{I}'), \tag{3·5}$$

t_α being the time for a particle to revolve the trajectory α. The phase ν_α is specified below.

3.2. *Stationary phase method and classical degeneracy*

It should be emphasized that *even for integrable systems*, the trace integral (3·2) is more general than the Poisson-sum trace formula, which is the starting point of Refs. 5), 32) and 35) for the semiclassical derivations of the level density. These two trace formulas become identical when the phase of the exponent does not depend on the angle variables $\boldsymbol{\Theta}$. In this case, the integral over angles in (3·2) gives simply $(2\pi)^n$, where n is the dimension of the system ($n = 3$ for a spheroidal cavity), and the stationary condition for all angle variables are identities in the 2π interval. This is true for the *most degenerate* classical orbits, like the elliptic and hyperbolic 2DPO in the meridian plane and the 3DPO with $\mathcal{K} = n - 1 = 2$. However, for orbits with smaller degeneracies, like the EQPO ($\mathcal{K} = 1$) and the isolated long diameter ($\mathcal{K} = 0$), the exponent phase depends strongly on angles and possesses a definite stationary point. Therefore, we have to integrate over such angles using the ISPM in the same way as for the bifurcations of the isolated diameters in elliptic billiard systems.[28)]

3.3. *Stationary phase conditions*

Due to the appearance of the δ-function representing energy conservation, we can perform the integral over I'_v in Eq. (3·2) exactly, and the result is

$$g_{\rm scl}(\varepsilon) = \frac{1}{(2\pi\hbar)^3}\,{\rm Re}\sum_\alpha \int d\Theta''_u \int d\Theta''_v \int d\Theta''_\varphi \int dI'_u \int dI'_\varphi \frac{1}{|\omega'_v|} \times \exp\left[\frac{i}{\hbar}\left(S_\alpha\left(\boldsymbol{I}', \boldsymbol{I}'', t_\alpha\right) + \left(\boldsymbol{I}'' - \boldsymbol{I}'\right)\cdot\boldsymbol{\Theta}''\right) - i\frac{\pi}{2}\nu_\alpha\right]. \tag{3·6}$$

The integration limits for I_u and I_φ are determined by their relations to the variables (σ_1, σ_2) and by the boundaries given by Eq. (2·5). One of the trajectories, α_0, in the sum (3·6) is a special one that corresponds to the smooth level density $g_{\rm TF}$ of the Thomas-Fermi model.[10)] For all other trajectories, we first write the stationary phase conditions for the action variables I'_u and I'_φ as

$$\left(\frac{\partial S_\alpha(\boldsymbol{I}', \boldsymbol{I}'', t_\alpha)}{\partial I'_u}\right)^* - \Theta''_u \equiv \Theta'_u - \Theta''_u = 2\pi M_u, \tag{3·7a}$$

$$\left(\frac{\partial S_\alpha(\boldsymbol{I}', \boldsymbol{I}'', t_\alpha)}{\partial I'_\varphi}\right)^* - \Theta''_\varphi \equiv \Theta'_\varphi - \Theta''_\varphi = 2\pi M_\varphi, \tag{3·7b}$$

where $\boldsymbol{M} = (M_u, M_v, M_\varphi) = M(n_u, n_v, n_\varphi)$, and M is an integer which indicates the number of revolutions along the primitive periodic orbit β. The superscript asterisk indicates that we evaluate the quantities at the stationary point with $I'_u = I^*_u$ and $I'_\varphi = I^*_\varphi$. We next use the Legendre transformation (3·5). Then, the stationary phase conditions with respect to angles $(\Theta_u, \Theta_v, \Theta_\varphi)$ are given by

$$\left(\frac{\partial S_\alpha(\boldsymbol{\Theta}', \boldsymbol{\Theta}'', \varepsilon)}{\partial \boldsymbol{\Theta}''} + \frac{\partial S_\alpha(\boldsymbol{\Theta}', \boldsymbol{\Theta}'', \varepsilon)}{\partial \boldsymbol{\Theta}'}\right)^* \equiv \boldsymbol{I}'' - \boldsymbol{I}' = 0. \tag{3·8}$$

In the following derivations, we have to judge whether the stationary phase conditions (totally or partially) given by Eqs. (3·7) and (3·8) hold identically or only

at specific stationary points. For this purpose we have to calculate separately the contributions from the most degenerate 3DPO, the 2DPO families in the meridian plane ($\mathcal{K}=2$) and those from orbits with smaller degeneracies, like EQPO ($\mathcal{K}=1$) and the isolated long diameter ($\mathcal{K}=0$). The latter two kinds of orbits are different from the former two kinds with respect to the above-mentioned two possibilities concerning the integration over angles $\boldsymbol{\Theta}$.

3.4. *Three-dimensional orbits and meridian-plane orbits*

The most degenerate 3DPO and the meridian-plane (elliptic and hyperbolic) 2DPO with equal values of the action occupy some finite 3D areas between the corresponding caustic surfaces specified above. In this case, the stationary phase conditions (3·8) for the integration over all angle variables Θ_u, Θ_v and Θ_φ hold identically. The integrand does not depend on the angle variables, and the result of the integration is $(2\pi)^3$. Because Eq. (3·8) is identically satisfied [the action does not depend on the angles like the Hamiltonian $H(\boldsymbol{I})$] we have conservation of the action variables, $I'_u = I''_u = I_u$ and $I'_\varphi = I''_\varphi = I_\varphi$, along the classical trajectory α. The integrals over all Θ in Eq. (3·2) yield $(2\pi)^3$, and we are left with the Poisson-sum trace formula,[5),10)]

$$\begin{aligned} g_{\rm scl}(\varepsilon) &= \frac{1}{\hbar^3}\,{\rm Re}\sum_{\boldsymbol{M}}\int d\boldsymbol{I}\;\delta\left(\varepsilon - H(\boldsymbol{I})\right)\;\exp\left[\frac{2\pi i}{\hbar}\boldsymbol{M}\cdot\boldsymbol{I} - i\frac{\pi}{2}\nu_M\right] \\ &= \frac{1}{\hbar^3}\,{\rm Re}\sum_{\boldsymbol{M}}\int dI_u\int dI_\varphi\;\frac{1}{|\omega_v|}\;\exp\left[\frac{2\pi i}{\hbar}\boldsymbol{M}\cdot\boldsymbol{I} - i\frac{\pi}{2}\nu_M\right]. \end{aligned} \tag{3·9}$$

It is convenient to transform the integration variables (I_u, I_φ) into (σ_1, σ_2) defined by Eq. (2·3):

$$g_{\rm scl}(\varepsilon) = \frac{1}{\hbar^3}\,{\rm Re}\sum_{\boldsymbol{M}} p\zeta\int_{\sigma_2^-}^{\sigma_2^+}\frac{d\sigma_2}{2\sqrt{\sigma_2}}\int_{\sigma_1^-}^{\sigma_1^+} d\sigma_1\;\frac{\partial I_u}{\partial\sigma_1}\;\frac{1}{|\omega_v|}\;\exp\left[\frac{2\pi i}{\hbar}\,\boldsymbol{M}\cdot\boldsymbol{I} - i\frac{\pi}{2}\nu_M\right]. \tag{3·10}$$

The integration limits are greatly simplified when written in terms of $\sigma_i^\pm$ $(i=1,2)$ and form the triangular region shown in Fig. 1. We then integrate over σ_i, expanding the exponent phase about the stationary point $\sigma_i = \sigma_i^*$,

$$\begin{aligned} 2\pi\left(\boldsymbol{M}\cdot\boldsymbol{I}\right) &\equiv S_\alpha\left(\boldsymbol{I}, \boldsymbol{I}'', t_\alpha\right) + \left(\boldsymbol{I}'' - \boldsymbol{I}\right)\cdot\boldsymbol{\Theta}'' \\ &= S_\beta(\varepsilon) + \frac{1}{2}\sum_{i,j} J_{ij}^\beta(\sigma_i - \sigma_i^*)(\sigma_j - \sigma_j^*) + \cdots, \end{aligned} \tag{3·11}$$

where $S_\beta(\varepsilon)$ is the action along the periodic orbit β,

$$S_\beta(\varepsilon) = 2\pi M\left[n_u I_u^* + n_v I_v\left(\varepsilon, I_u^*, I_\varphi^*\right) + n_\varphi I_\varphi^*\right], \tag{3·12}$$

and $I_v(\varepsilon, I_u, I_\varphi)$ is the solution of the energy conservation equation $\varepsilon = H(I_u, I_v, I_\varphi)$ with respect to I_v. Here, the single prime index is omitted for simplicity. The

quantity J_{ij}^{β} is the Jacobian stability factor with respect to σ_i along the energy surface,

$$J_{ij}^{\beta} = \left(\frac{\partial^2 S_\alpha}{\partial\sigma_i \partial\sigma_j}\right)_{\sigma_i=\sigma_i^*} = 2\pi M n_v K_{ij}^{\beta}, \tag{3·13}$$

and K_{ij}^{β} is the (2×2) curvature matrix of the energy surface evaluated at the stationary point $\sigma_i = \sigma_i^*$ (at the periodic orbit β):

$$K_{ij}^{\beta} = \frac{\partial^2 I_v}{\partial\sigma_i\partial\sigma_j} + \frac{\omega_u}{\omega_v}\frac{\partial^2 I_u}{\partial\sigma_i\partial\sigma_j} + \frac{\omega_\varphi}{\omega_v}\frac{\partial^2 I_\varphi}{\partial\sigma_i\partial\sigma_j}. \tag{3·14}$$

(See Appendix A for the explicit expressions of these curvatures.) As we see below, the off-diagonal curvature K_{12} is non-zero for variables σ_i.

Then we use the ISPM, where we keep exact finite limits for the integration over σ_i, and we finally obtain

$$\delta g^{(2)}_{\left\{{}^{\rm 3D}_{\rm 2D}\right\}}(\varepsilon) = \frac{1}{\varepsilon_0}\,{\rm Re}\sum_{\beta} A_{\beta}^{(2)}\,\exp\left(ikL_\beta - i\frac{\pi}{2}\nu_\beta\right), \tag{3·15}$$

where $\varepsilon_0 = \hbar^2/2mR^2$ ($R^3 = a^2 b$ due to the volume conservation condition). The sum runs over all two-parameter families of the 3DPO or the meridian-plane (elliptic and hyperbolic) 2DPO, and $A_{\beta}^{(2)}$ is the amplitude for a 3DPO or a 2DPO,*)

$$A^{(2)}_{\left\{{}^{\rm 3D}_{\rm 2D}\right\}} = \frac{1}{4\,\pi}\,\frac{L_\beta\zeta}{(Mn_vR)^2\sqrt{\sigma_2^*\,|\det K^\beta|}}\,\left[\frac{\partial I_u}{\partial\sigma_1}\right]_{\sigma_i=\sigma_i^*}\,{\rm erf}\left(\mathcal{Z}_1^-,\mathcal{Z}_1^+\right){\rm erf}\left(\mathcal{Z}_2^-,\mathcal{Z}_2^+\right). \tag{3·16}$$

Here, L_β represents "length" of the periodic orbit β,

$$\begin{aligned} L_\beta &= \frac{2\pi M n_v p}{m\omega_v} \\ &= 2Mn_v b\sin\theta\left[{\rm E}(\theta,\kappa) - \frac{{\rm F}(\theta,\kappa)}{{\rm F}\,(\kappa)}\,{\rm E}\,(\kappa) + \cot\theta\sqrt{1-\kappa^2\sin^2\theta}\right], \end{aligned} \tag{3·17}$$

where θ and κ are defined by the roots of the periodic-orbit equations (2·7) ($S_\beta = pL_\beta$ for cavities). This "length" taken at the stationary points σ_i^* [the real positive roots of Eq. (2·7) through Eqs. (2·4) and (2·6)] inside the finite integration range (2·5) represents the true length of the corresponding periodic orbit β. For other stationary points, the "length" is identical to the function (3·17) continued analytically outside the tori determined by (2·5). In Eq. (3·16) we also introduced the generalized error function erf $(\mathcal{Z}^-,\mathcal{Z}^+)$ of the two complex arguments $\mathcal{Z}^-$ and $\mathcal{Z}^+$,

$${\rm erf}\left(z^-,z^+\right) = \frac{2}{\sqrt{\pi}}\int_{z^-}^{z^+} dz\,e^{-z^2} = {\rm erf}(z^+) - {\rm erf}(z^-), \tag{3·18}$$

*) The expression (3·16) is valid also for the 2DPO ($\sigma_2^* = 0$), because the product $\sigma_2 K_{22}$ is finite for any σ_2 (see Appendix A).

with $\mathrm{erf}(z)$ being the simple error function.[46] The arguments of these error functions are given by

$$\mathcal{Z}_1^{\beta\pm} = \sqrt{-i\pi M n_v K_{11}^\beta/\hbar}\left(\sigma_1^\pm(\sigma_2^*) - \sigma_1^*\right), \tag{3·19a}$$

$$\mathcal{Z}_2^{\beta\pm} = \sqrt{-i\pi M n_v (\det K^\beta/K_{11}^\beta)/\hbar}\left(\sigma_2^\pm - \sigma_2^*\right), \tag{3·19b}$$

in terms of the finite limits $\sigma_i^\pm$ given by (2·5), and taken at the stationary point $\sigma_2 = \sigma_2^*$. We note that, for the 3DPO $M(3t,t,1)$ with $t = 2,3,\cdots$, the curvature K_{11}^β is zero at any deformation. For such orbits, we should use

$$\mathcal{Z}_1^{\beta\pm} = \sqrt{-i\pi M n_v (\det K^\beta/K_{22}^\beta)/\hbar}\,\left(\sigma_1^\pm(\sigma_2^*) - \sigma_1^*\right), \tag{3·20a}$$

$$\mathcal{Z}_2^{\beta\pm} = \sqrt{-i\pi M n_v K_{22}^\beta/\hbar}\,\left[\sigma_2^\pm - \sigma_2^* + \frac{K_{12}^\beta}{K_{22}^\beta}\left(\sigma_1^\pm(\sigma_2^*) - \sigma_1^*\right)\right], \tag{3·20b}$$

in place of (3·19). The latter limits (3·20) are derived by changing the integration variable σ_2 to $\sigma_2 - (K_{12}/K_{22})(\sigma_1 - \sigma_1^*)$.

Let us consider the stationary points σ_i^* positioned far from the bifurcation points. This means that they are located far from the integration limits. Accordingly, the generalized error functions can be transformed into the complex Fresnel functions with real limits and then extend the upper limit to ∞ and the lower one to $-\infty$. In this way, we asymptotically obtain the Berry-Tabor result for the standard POT,[5] which is identical to the extended Gutzwiller result[9] for the most degenerate (3D and meridian-plane) orbit families,

$$A^{(2)}_{\left\{\begin{smallmatrix}\mathrm{3D}\\ \mathrm{2D}\end{smallmatrix}\right\}}(\varepsilon) = \frac{1}{\pi}\,\frac{L_\beta \zeta}{(M n_v R)^2\sqrt{\sigma_2^*|\det K^\beta|}}\left[\frac{\partial I_u}{\partial \sigma_1}\right]_{\sigma_i=\sigma_i^*}. \tag{3·21}$$

The constant part of the phase ν_β in Eq. (3·15), which is independent of η and ε, can be found by making use of the above asymptotic expression and applying the Maslov-Fedoryuk theory.[39),41)–43)] This theory relates the Maslov index μ_β with the number of turning and caustic points for the orbit family β. For the 3DPO, the total asymptotic phase ν_β is given by

$$\nu_{3\mathrm{D}} = \mu_{3\mathrm{D}} - \frac{1}{2}\epsilon_{3\mathrm{D}} + 2(Mn_u - 1), \quad \mu_{3\mathrm{D}} = M(3n_v + 2n_u). \tag{3·22}$$

Here, μ_β denotes the Maslov index, the numbers of caustic and turning points traversed by the orbit, and ϵ_β represents the difference of the numbers of positive and negative eigenvalues of curvature K^β.*) For the hyperbolic and elliptic meridian 2DPO, we obtain

$$\nu_{2\mathrm{DH}} = \mu_{2\mathrm{DH}} - \frac{1}{2}\epsilon_{2\mathrm{DH}} + 2\left(Mn_u - 1\right), \quad \mu_{2\mathrm{DH}} = 2M\left(n_v + n_u\right) \tag{3·23}$$

*) Because the dimension of K^β is 2, ϵ_β is written $\epsilon_\beta = \mathrm{sign}(K_1^\beta) + \mathrm{sign}(K_2^\beta)$, where K_i^β is the i-th eigenvalue of K^β. It can also be calculated by $\epsilon_\beta = \mathrm{sign}(K_{11}^\beta) + \mathrm{sign}(\det K^\beta/K_{11}^\beta)$ for $K_{11}^\beta \neq 0$, and $\epsilon_\beta = \mathrm{sign}(K_{22}^\beta) + \mathrm{sign}(\det K^\beta/K_{22}^\beta)$ for $K_{22}^\beta \neq 0$. Here, $\mathrm{sign}(x) = \pm 1$ for $x \gtrless 0$ and 0 for $x = 0$.

and

$$\nu_{\rm 2DE} = \mu_{\rm 2DE} - \frac{1}{2}\epsilon_{\rm 2DE} + 2\,(Mn_u - 1)\,, \quad \mu_{\rm 2DE} = 3Mn_v \tag{3·24}$$

respectively. Note that the total phase includes the argument of the complex amplitude (3·16), and it depends on both the deformation and energy.

Near the bifurcation deformations, the stationary points σ_i^* are close to the boundary of the finite area (2·5). In such cases, the asymptotic forms of the error functions are not good approximations, and we have to carry out the integration over σ_i in the calculation of the error functions in Eq. (3·16) exactly within the finite limits. It should also be noted that the contributions from "ghost" periodic orbits are important near the bifurcation points. They make the trace formula continuous as a function of η at all bifurcations.

Also when the stationary phase points σ_i^* are close to other boundaries of the tori, the integrals have to be evaluated with finite limits; for instance, near the triangular side $\sigma_1 = \sigma_1^+(\sigma_2)$, where we have the "creeping" points for the 3DPO inside the tori (2·5) and the meridian elliptic 2DPO near the endpoint ($\sigma_1 = \sigma_1^+$, $\sigma_2 = 0$) with a large number of vertices, $n_v \to \infty$. Another example of such a special bifurcation point is the separatrix ($\sigma_1 = 1$, $\sigma_2 = 0$), where 3DPO and hyperbolic 2DPO have a finite limit $n_u/n_v \to 1/2$ for $n_v \to \infty$ and $n_u \to \infty$. In this case, the curvature K_{11} becomes infinite, and the amplitude (3·16) approaches zero. Thus, to improve the trace formula near the bifurcations, we have to evaluate the generalized error integral $\mathrm{erf}(\mathcal{Z}_i^{\beta\,-}, \mathcal{Z}_i^{\beta\,+})$ (or corresponding complex Fresnel functions[46]) in Eq. (3·16) within the finite limits $\mathcal{Z}_i^{\beta\,\pm}$ given by Eq. (3·19) or (3·20).

For a spheroidal cavity, we have another bifurcation in the spherical limit, where the "azimuthal" Jacobian J_{22}^{β} and J_{12}^{β} (3·13) ($\sigma_2 \propto I_\varphi^2$) vanish.[9] This is the reason for the divergence of the standard POT result (3·21) in the spherical limit. Our improved trace formula (3·16) is finite in the spherical limit, because the "azimuthal" generalized error function $\mathrm{erf}(\mathcal{Z}_2^{\beta\,-}, \mathcal{Z}_2^{\beta\,+})$ is proportional to $\sqrt{J_{22}^{\beta}}$ in this limit, and thus this "azimuthal" Jacobian is exactly canceled by that coming from the denominator of Eq. (3·16). Thus, as shown in Ref. 9), the elliptic 2DPO term ($\mathcal{K}$=2) in the level density approaches the spherical Balian-Bloch result for the most degenerate planar orbits with larger degeneracy ($\mathcal{K} = 3$):

$$\delta g_{\rm sph}^{(3)}(\varepsilon) = \frac{\sqrt{kR}}{\varepsilon_0} \sum_{t\geq 1,\, q>2t} \sin\left(\frac{2\pi t}{q}\right) \sqrt{\frac{\sin(2\pi t/q)}{q\pi}} \times \sin\left[2kRq\sin\left(\frac{\pi t}{q}\right) - \frac{3\pi}{2}q - (t-1)\pi - \frac{\pi}{4}\right], \tag{3·25}$$

where $t = Mn_u$ and $q = Mn_v$. Note that Eq. (3·25) can be derived directly from the phase-space trace formula (3·2) or from the Poisson-sum trace formula, both rewritten in terms of the spherical action-angle variables.

3.5. *Equatorial-plane orbits*

We cannot apply the Poisson-sum trace formula (3·9) for equatorial-plane orbits, because, although the stationary-phase conditions for Θ_φ'' and Θ_v'' in Eq. (3·8) hold

identically, this is not the case for the angle variable Θ_u''. We thus apply the ISPM for the integration over Θ_u''.

Returning to Eq. (3·6), we transform the phase-space trace formula into new "parallel" $(\Theta_v''; I_v')$ and "perpendicular" $(\Theta_u'', \Theta_\varphi''; I_u', I_\varphi')$ variables, as explained in Appendix B for more general (integrable and non-integrable) systems. We then carry out the integration over the variables (I_u', I_φ') in terms of the ISPM by transforming them into the variables σ_i. Next, we consider the integration over the *angle* variable Θ_u'' using the ISPM, as there is an *isolated* stationary point at $\Theta_u^* = 0$ (or an integer multiple of 2π). We expand the exponent phase in a power series of Θ_u'' about $\Theta_u^* = 0$,

$$\begin{aligned} &S_\alpha\left(\boldsymbol{I}, \boldsymbol{I}'', t_\alpha\right) + \left(\boldsymbol{I}'' - \boldsymbol{I}\right) \cdot \boldsymbol{\Theta}'' \\ &\quad = pL_{\mathrm{EQ}} + \frac{1}{2}\sum_{ij} J_{ij}^{\mathrm{EQ}}(\sigma_i - \sigma_i^*)(\sigma_j - \sigma_j^*) + \frac{1}{2}J_\perp^{\mathrm{EQ}}\ \left(\Theta_u''\right)^2 + \cdots, \end{aligned} \tag{3·26}$$

where the stationary point $\sigma_1^* = \sigma_2^* \equiv \sigma^*$ is given by

$$\sigma^* = \left(\frac{I_\varphi^*}{p\zeta}\right)^2 = \frac{a^2\cos^2\phi}{\zeta^2} = \frac{\cos^2\phi}{\eta^2 - 1}, \qquad I_\varphi^* = p\,a\cos\phi. \tag{3·27}$$

The length of the equatorial polygon with n_v vertices and M rotations, L_{EQ}, is given by

$$L_{\mathrm{EQ}} = 2Mn_v R\sin\phi, \quad \phi = \pi n_\varphi / n_v. \tag{3·28}$$

In this way, we finally obtain the contribution of EQPO,

$$\delta g_{\mathrm{EQ}}^{(1)}(\varepsilon) = \frac{1}{\varepsilon_0}\,\mathrm{Re}\sum_{\mathrm{EQ}} A_{\mathrm{EQ}}^{(1)} \exp\left\{i\left(kL_{\mathrm{EQ}} - \frac{\pi}{2}\nu_{\mathrm{EQ}}\right)\right\}, \tag{3·29}$$

with the amplitudes $A_{\mathrm{EQ}}^{(1)}$ given by

$$A_{\mathrm{EQ}}^{(1)} = \sqrt{\frac{\sin^3\phi}{\pi M n_v k R \eta F_z^{\mathrm{EQ}}}}\ \mathrm{erf}\left(\mathcal{Z}_1^-, \mathcal{Z}_1^+\right)\ \mathrm{erf}\left(\mathcal{Z}_2^-, \mathcal{Z}_2^+\right)\ \mathrm{erf}\left(\mathcal{Z}_3^-, \mathcal{Z}_3^+\right) \tag{3·30}$$

(see Appendix B for a detailed derivation). Here, $\mathcal{Z}_i^\pm$ are the limits given by Eq. (3·19) or (3·20) for $i = 1, 2$, and $\mathcal{Z}_3^- = 0, \mathcal{Z}_3^+ = \mathcal{Z}_\perp^+$ from Eq. (B·19). The latter is related to the finite limits $0 \le \Theta_u \le \pi/2$ for the angle Θ_u in the trace integration in Eq. (3·6), taking into account explicitly the factor 4, due to the time-reversal and spatial symmetries.

For the total asymptotic phase ν_{EQ}, we find

$$\nu_{\mathrm{EQ}} = \mu_{\mathrm{EQ}} + \frac{1}{2}, \quad \mu_{\mathrm{EQ}} = 3Mn_v, \tag{3·31}$$

where μ_{EQ} is the Maslov index. We calculated this phase using the Maslov-Fedoryuk theory[43] at a point asymptotically far from the bifurcations. Note that the total phase is defined as the sum of the asymptotic phase ν_{EQ} and the argument of the

Table I. Bifurcation points of some short periodic orbits.

periodic orbit	$\eta_{\rm bif}$	periodic orbit	$\eta_{\rm bif}$
(4,2,1)	$\sqrt{2}$	(6,3,1)	2
(5,2,1)	1.618...	(7,3,1)	2.247...
(6,2,1)	$\sqrt{3}$	(8,3,1)	2.414...
(7,2,1)	1.802...	(9,3,1)	2.532...
(8,2,1)	1.848...		

amplitude $A_{\rm EQ}$, given by Eq. (3·30), so that it depends on kR and η through the complex arguments of the product of the error functions. In the derivations of Eq. (3·30) we have taken into account the off-diagonal curvature, as in the previous subsection, but much smaller corrections due to the mixed derivatives of the action S_α with respect to Θ_u'' and σ_i are ignored, taking $\sigma_i = \sigma_i^*$ in Eq. (3·26).

The bifurcation points are associated with zeros of the stability factor $F_z^{\rm EQ}$ and given by

$$\eta_{\rm bif} = \frac{\sin\phi}{\sin\left(n\phi/M\right)}, \qquad n = 1, 2, \cdots, M. \tag{3·32}$$

The bifurcation points most important for the superdeformed shell structure are listed in Table I.

When the stationary points are located inside the finite integration region far from the ends, we transform the error functions in Eq. (3·30) into the Fresnel functions and extend their arguments to $\pm\infty$, except in the case that the lower limit is exactly zero. From the definitions of the limit, Eqs. (3·19) and (B·19), for $\mathcal{Z}_i^{\pm}$, we have asymptotically $\mathcal{Z}_i^+ \to +\infty$ $(i = 1, 2, 3)$, $\mathcal{Z}_1^- = \mathcal{Z}_3^- \to 0$ and $\mathcal{Z}_2^- \to 0$ for diameters and $\mathcal{Z}_2^- \to -\infty$ for the other EQPO. Finally, we arrive at the standard Balian-Bloch formula[3] for the amplitude $A_{\rm EQ}^{(1)}$,

$$A_{\rm EQ}^{(1)} = \frac{f_{\rm EQ}}{\sqrt{\pi kR\eta}} \sqrt{\frac{\sin^3\phi}{Mn_v F_z^{\rm EQ}}}, \tag{3·33}$$

where $f_{\rm EQ} = 1$ for the diameters and 2 for the other EQPO [$\mathrm{erf}(\mathcal{Z}_2^-, \mathcal{Z}_2^+) \to f_{\rm EQ}$ in this limit].

As seen from Eq. (3·33), there is a divergence at the bifurcation points where $F_z^{\rm EQ} \to 0$. We emphasize that our ISPM trace formula (3·29) has no such divergences. Indeed, the stability factor $F_z^{\rm EQ}$ responsible for this divergence is canceled by $F_z^{\rm EQ}$ from the upper limit $\mathcal{Z}_3^+$, Eq. (B·19), of the last error function in Eq. (3·30), $\mathcal{Z}_3^+ \propto \sqrt{F_z^{\rm EQ}}$, and we obtain the following finite result at the bifurcation point:

$$A_{\rm EQ}^{(1)} = \frac{\eta^{1/3}\sin\phi\sqrt{\eta^2 - \sin^2\phi}}{\sqrt{2i(\eta^2-1)}Mn_v}\ \mathrm{erf}\left(\mathcal{Z}_1^-, \mathcal{Z}_1^+\right)\ \mathrm{erf}\left(\mathcal{Z}_2^-, \mathcal{Z}_2^+\right). \tag{3·34}$$

It is very important to note that there is a local enhancement of the amplitude

(3·34) by a factor of order $\sqrt{kR}$*) near the bifurcation point. This enhancement is associated with a change of the degeneracy parameter $\mathcal{K}$ by one locally near the bifurcation point. In general, any change of the degeneracy parameter $\mathcal{K}$ by $\Delta\mathcal{K}$ is accompanied by an amplitude enhancement by a factor of $(kR)^{\Delta\mathcal{K}/2}$, because $\Delta\mathcal{K}$ extra exact integrations are carried out. This enhancement mechanism of the amplitude obtained in the ISPM is quite general, and it is independent of the specific choice of the potential shapes.

We mention that a more general trace formula that can be applied also to non-integrable but axially symmetric systems can be derived from the phase-space trace formula (see Appendix B).

The contribution of the equatorial diameters in Eq. (3·29) for deformations far from bifurcation points reduces to the Balian-Bloch result for spherical diameters ($\mathcal{K} = 2$),

$$\delta g^{(2)}_{\rm sph}(\varepsilon) = -\frac{1}{\varepsilon_0}\sum_M \frac{1}{2\pi M}\,\sin(4MkR). \tag{3·35}$$

The amplitudes for planar polygons in the equatorial plane vanish in the spherical limit (see Appendix B). Note that the contributions of the planar polygons in the spherical cavity, Eq. (3·25), are obtained as the limit of $A^{(2)}_{\rm 2D}$, Eq. (3·16), for elliptic orbits in the meridian plane.[9)]

3.6. *Long diametric orbits and separatrices*

As mentioned in §2, the curvatures K^{β}_{ij} become infinite near the separatrix ($\sigma_1 = 1$, $\sigma_2 = 0$) (see Appendix C). This separatrix corresponds to the isolated long diameters ($\mathcal{K} = 0$) along the symmetry axis. Thus, for the derivation of their contributions to the trace formula, the expansion up to second order in action-angle variables considered above fails, as for the turning and caustic points in the usual phase space coordinates. However, we can apply the Maslov-Fedoryuk theory[39),41)–43)] in a similar way as the calculation of the Maslov indices associated with the turning and caustic points, but with the use of the action-angle variables in place of the usual phase-space variables. This is similar to the derivation of the long diametric term in the elliptic billiard.[28)]

Starting from the phase-space trace formula (3·6), we note that the spheroidal separatrix problem differs from that for the elliptic billiard system[28)] by the integrals over the two azimuthal variables Θ''_φ and I'_φ, which are additional to the integrals over Θ''_u and I'_u. We expand the phase of the exponent in Eq. (3·6) with respect to the action I'_φ and angle Θ''_φ about the stationary points $I^*_\varphi = 0$ and an arbitrary Θ^*_φ (for instance, $\Theta^*_\varphi = 0$), and take into account the *third* order terms, in a similar way as for the variables Θ''_u and I'_u (see Appendix C). Note that we consider here small deviations from the long diameters, and Θ^*_φ determines the azimuthal angle of the final point $\boldsymbol{r}''$ of this trajectory near the symmetry axis.

---

*) The parameter of our semiclassical expansion is in practice $\sqrt{kL_\beta}\left(\propto\sqrt{kR}\right)$. It is actually large for 3D orbits ($L_\beta \sim 10R$) associated with superdeformed shell structures in nuclei.

After the procedure explained in Appendix C, we obtain

$$\delta g^{(0)}_{\rm LD}(\varepsilon) = \frac{\pi b}{2\varepsilon_0 R}\,{\rm Re}\sum_M \frac{1}{kR}\, e^{ikL_{\rm LD}-i\frac{\pi}{2}\nu_{\rm LD}} \prod_{j=1}^{2} e^{\frac{2i}{3}\left[(w_j^{\parallel})^{3/2}+(w_j^{\perp})^{3/2}\right]} \frac{\left(w_j^{\parallel} w_j^{\perp}\right)^{1/4}}{\sqrt{|c_{2,j}^{\parallel} c_{2,j}^{\perp}|}}$$
$$\times[{\rm Ai}(-w_j^{\parallel}) + i\,{\rm Gi}(-w_j^{\parallel})]$$
$$\times[{\rm Ai}(-w_j^{\perp}, \mathcal{Z}_{\perp}^{-}, \mathcal{Z}_{\perp}^{+}) + i\,{\rm Gi}(-w_j^{\perp}, \mathcal{Z}_{\perp}^{-}, \mathcal{Z}_{\perp}^{+})] \tag{3·36}$$

(see Appendix C for the notation used here).

For finite deformations and sufficiently large kR, i.e. for large $p\zeta \propto kR\sqrt{\eta^2-1}$, near the separatrix $\sigma_1 \to 1, \sigma_2 \to 0$, the incomplete Airy functions in this equation can be approximated by the complete ones. Thus, Eq. (3·36) reduces to the standard Gutzwiller result for isolated diameters,[3),9)]

$$\delta g^{(0)}_{\rm LD}(\varepsilon) = \frac{2b}{\pi\varepsilon_0 kR^2}\sum_M \frac{1}{|F^{\rm LD}_{xy}|}\cos\left[kL_{\rm LD}(M) - \frac{\pi}{2}\nu_{\rm LD}\right], \tag{3·37}$$

with the length $L_{\rm LD}(M) = 4Mb = 4M\eta^{2/3}R$ and the stability factor $F^{\rm LD}_{xy}$ for long diameters given by Eq. (C·20).

For the calculation of the asymptotic phase $\nu_{\rm LD}$, we use this asymptotic expression and calculate the Maslov indices $\mu_{\rm LD}$ using the Maslov-Fedoryuk theory,[43)] obtaining

$$\nu_{\rm LD} = \mu_{\rm LD} + 2, \quad \mu_{\rm LD} = 4M. \tag{3·38}$$

The additional phases, dependent on deformation and energy, come from the arguments of the complex exponents and Airy functions of the complex amplitude.

In the spherical limit, both the upper and lower limits of the incomplete Airy functions in Eq. (3·36) approach zero, and the angle integration has the finite limit $\pi/2$ (see Appendix C). With this, the other factors ensure that the amplitude for long diameters becomes zero; that is, the long diametric contribution to the level density vanishes in the spherical limit.

§4. Level density, shell energy and averaging

4.1. *Total level density*

In spheroidal cavity systems, the ISPM total semiclassical level density can be written as a sum over all periodic orbit families:

$$\delta g_{\rm scl}(\varepsilon) = \delta g^{(2)}_{\rm 3D}(\varepsilon) + \delta g^{(2)}_{\rm 2D}(\varepsilon) + \delta g^{(1)}_{\rm EQ}(\varepsilon) + \delta g^{(0)}_{\rm LD}(\varepsilon) = \sum_\beta \delta g^{(\beta)}_{\rm scl}(\varepsilon), \tag{4·1}$$

where the first two terms represent the contributions from the most degenerate ($\mathcal{K} = 2$) families of periodic orbits, the 3DPO and the meridian-plane 2DPO, given by Eq. (3·15), the third term the EQPO given by Eq. (3·29), and the fourth term the long diameters given by Eq. (3·36).

4.2. *Semiclassical shell energy*

The shell energy δE can be expressed in terms of the oscillating part $\delta g_{\rm scl}^{(\beta)}(\varepsilon)$ of the semiclassical level density (4·1) as[4),9),10)]

$$\delta E = \sum_{\beta} \left(\frac{\hbar}{t_\beta}\right)^2 \delta g_{\rm scl}^{(\beta)}(\varepsilon_{\rm F}), \qquad N = \int_0^{\varepsilon_{\rm F}} d\varepsilon\, g(\varepsilon). \tag{4·2}$$

Here, t_β denotes the period for a particle moving with the Fermi energy $\varepsilon_{\rm F}$ along the periodic orbit β,

$$t_\beta = MT_\beta = \frac{2\pi M}{\Omega_\beta}, \tag{4·3}$$

T_β being the primitive period ($M = 1$), M the number of repetitions, and Ω_β the frequency. The Fermi energy $\varepsilon_{\rm F}$ is determined by the second equation of (4·2), where N is the particle number.

In the derivation of Eq. (4·2) we used an expansion of the amplitudes $A_\beta(\varepsilon)$ about the Fermi energy $\varepsilon = \varepsilon_{\rm F}$. Although the $A_\beta(\varepsilon)$ are oscillating functions of the energy ε (or kR), we can apply such an expansion, because the A_β are much smoother than the oscillations coming from the exponent function of kL_β. The latter oscillations are responsible for the shell structure, while the oscillations of A_β merely lead to slight modulations with much smaller frequencies.

Thus, the trace formula for δE differs from that for δg only by the factor $(\hbar/t_\beta)^2 = (\hbar^2 k_{\rm F}/mL_\beta)^2$ near the Fermi surface, i.e. longer orbits are additionally suppressed by the factor $1/L_\beta^2$. The semiclassical shell energy is therefore determined by short periodic orbits.

4.3. *Average level density*

For the purpose of presentation of the level density improved at the bifurcations we need to consider only an average level density, thus also avoiding the convergence problems that usually arise when one is interested in a full semiclassical quantization.

The average level density is obtained by folding the level density with a Gaussian of width Γ:

$$g_\Gamma(\varepsilon) = \frac{1}{\sqrt{\pi}\Gamma} \int_{-\infty}^{\infty} d\varepsilon'\, g(\varepsilon')\, e^{-(\frac{\varepsilon-\varepsilon'}{\Gamma})^2}. \tag{4·4}$$

The choice of the Gaussian form of the averaging function is insignificant and is made here only for the sake of mathematical simplicity.

Applying now the averaging procedure defined above to the semiclassical level density (4·1), we obtain[3),9)]

$$\delta g_{\Gamma,{\rm scl}}(\varepsilon) = \sum_{\beta} \delta g_{\rm scl}^{(\beta)}(\varepsilon)\, e^{-(\frac{\Gamma MT_\beta}{2\hbar})^2} = \sum_{\beta} \delta g_{\rm scl}^{(\beta)}(\varepsilon)\, e^{-(\frac{\gamma L_\beta}{2R})^2}. \tag{4·5}$$

The latter equation is written specifically for cavity problems in terms of the orbit length L_β (in units of the typical length scale R) and the dimensionless parameter γ defined by

$$\Gamma = 2\gamma\sqrt{\varepsilon\varepsilon_0}\ , \tag{4·6}$$

where γ is the averaging width with respect to kR. Thus, the averaging yields an exponential decrease of the amplitudes with increasing L_β and γ. In Ref. 9), the value of γ is chosen to be 0.6. In this case, all longer orbits are strongly damped and only the short periodic orbits contribute to the oscillating part of the level density. For the study of the bifurcation phenomena in the superdeformed region, we need a significantly smaller value of γ.

Finally, we can say that the contribution of an orbit family to the average density of states is more important as the degeneracy of the orbit is higher, and as the volume occupied by the orbit family in the phase space is larger, and also as the length of the orbit is shorter.

§5. Quantum spheroidal cavity

5.1. *Oscillating level density*

We calculated the quantum spectrum using the spherical wave decomposition method,[50] in which wave functions are decomposed into the spherical waves as

$$\psi_m(\boldsymbol{r}) = {\sum_l}' C_l\, j_l(kr)\, Y_{lm}(\Omega). \tag{5·1}$$

Here, m denotes the magnetic quantum number, and $\sum'$ indicates that l is summed over even (odd) numbers for positive (negative) parity states. The functions j_l and Y_{lm} are the usual spherical Bessel functions and spherical harmonics, respectively. The expansion coefficients C_l are determined so that the wave function (5·1) satisfies the Dirichlet boundary condition

$$\psi_m(r = R(\Omega)) = 0, \tag{5·2}$$

or equivalently,

$$\int d\Omega Y^*_{lm}(\Omega)\psi_m(r = R(\Omega)) = 0, \quad {}^\forall l. \tag{5·3}$$

By inserting (5·1) into (5·3), we obtain the matrix equation

$${\sum_{l'}}' B_{ll'}(k)C_{l'} = 0, \quad B_{ll'}(k) = \int d\Omega Y^*_{lm}(\Omega) j_{l'}(kR(\Omega))Y_{l'm}(\Omega). \tag{5·4}$$

Truncating the summation l at a sufficiently large number l_c, we can obtain the energy eigenvalue $\varepsilon_n = \hbar^2 k_n^2/2m$ by searching for the roots satisfying

$$\det B(k_n) = 0. \tag{5·5}$$

Figure 5 displays the energy level diagram for the prolate spheroidal cavity as functions of the axis ratio $\eta > 1$. In Fig. 6, we plot shell structure energy

$$\delta E(N, \eta) = \sum_{n=1}^{N} \varepsilon_n(\eta) - \tilde{E}(N, \eta) \tag{5·6}$$

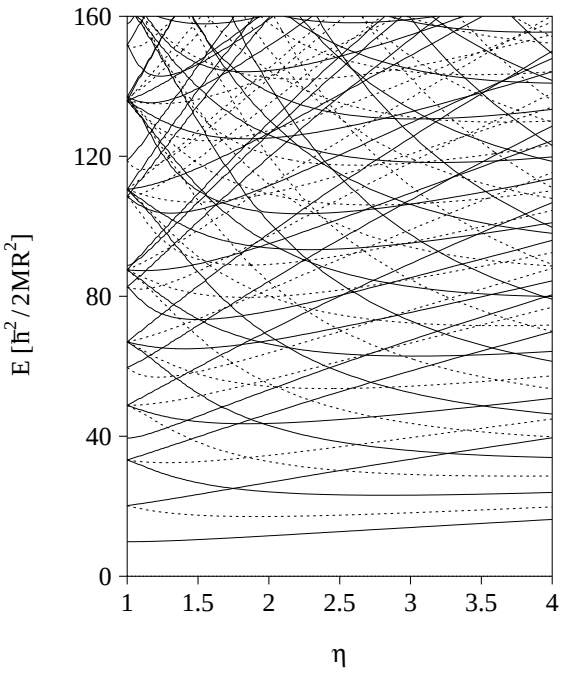

Fig. 5. Single-particle spectrum for the spheroidal cavity as a function of the axis ratio η. Solid and dashed curves represent the positive and negative parity levels, respectively.

as a function of η and particle number N. As well as the strong shell effect at the spherical shape ($\eta = 1$), one clearly sees a prominent shell structure for a superdeformed shape ($\eta \sim 2$).

Next, we calculated the coarse-grained level density with the usual Strutinsky smoothing procedure by treating the wave number k as smoothing variable:

$$g_\gamma(k) = \frac{1}{\gamma}\int_0^\infty dk' R\, f_M\left(\frac{kR - k'R}{\gamma}\right) g(k'). \tag{5·7}$$

As the smoothing function $f_M(x)$, we use a Gaussian with M-th order curvature corrections,

$$f_M(x) = \frac{1}{\sqrt{\pi}} e^{-x^2} L_{M/2}^{1/2}(x^2), \tag{5·8}$$

where $L_n^\alpha(z)$ represents a Laguerre polynomial. Equation (4·4) corresponds to the case of $M = 0$. In the following, we set the order of curvature corrections to $M = 6$ and the smoothing width to $\tilde{\gamma} = 2.5$, with which we can nicely satisfy the plateau condition.[44] A coarse-graining is also performed using the same smoothing function but with smaller γ. We define the oscillating part of the level density by subtracting the smooth part as

$$\delta g_\gamma(k) = g_\gamma(k) - g_{\tilde{\gamma}}(k). \tag{5·9}$$

The left-hand side of Fig. 7 displays $\delta g_\gamma(k)$ with $\gamma = 0.3$ as a function of η and

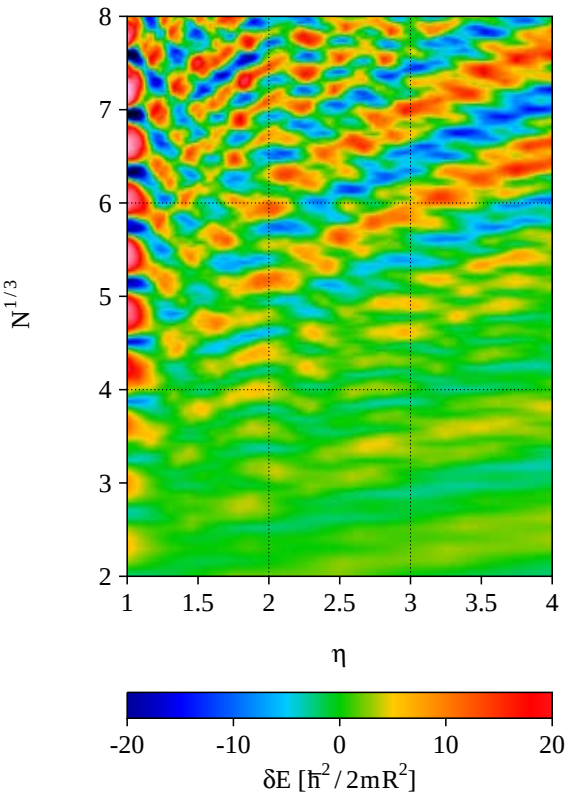

Fig. 6. Shell structure energy δE as a function of η and $N^{1/3}$, where N is the neutron (proton) number, taking the spin-degeneracy factor into account. Energies are counted in units of $\hbar^2/2mR^2$ ($\sim 30A^{-2/3}$MeV).

kR. It is seen that a clear shell structure emerges for $\eta \sim 2$, corresponding to the superdeformed shape.

Let us consider the mechanism of this strong shell effect. If a single orbit makes a dominant contribution to the periodic-orbit sum

$$\delta g_{\rm scl}(\varepsilon) = \sum_{\beta} a_\beta(k)\cos(kL_\beta - \pi\nu_\beta/2), \quad a_\beta(k) = A_\beta/\varepsilon_0, \tag{5·10}$$

the major oscillating pattern in δg should be determined by the phase factor of the dominant term. In that case, the positions of the valley curves for δg in the (η, kR) plane are given by

$$kL_\beta - \pi\nu_\beta/2 = (2n+1)\pi. \qquad (n = 0, 1, 2, \cdots) \tag{5·11}$$

The right-hand side of Fig. 7 plots the *stationary action curves* (5·11) for several periodic orbits. The green solid curves represent the triangular orbit in the meridian plane. The other longer meridian orbits exhibit the same behavior but with smaller distances. The red dashed curves represent the star-shaped orbit with five vertices in

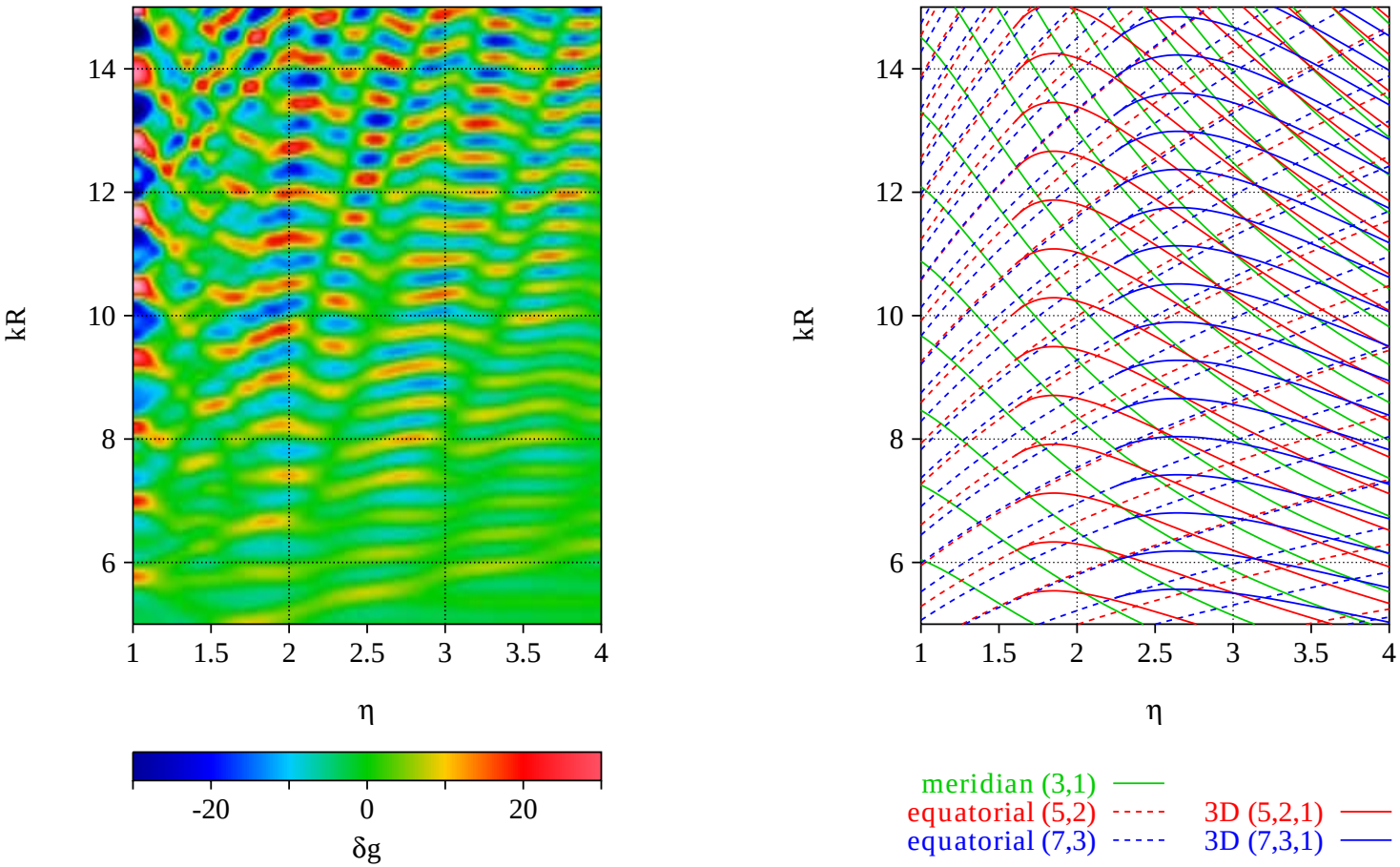

Fig. 7. Oscillating part δg of the single-particle level density as a function of η and kR (left-hand side) and stationary-action curves for several periodic orbits (right-hand side). A clear correspondence between the enhancement of the shell effect and the periodic-orbit bifurcations is seen.

the equatorial plane. It bifurcates at $\eta = 1.618\ldots$ and the 3D orbit (5,2,1) thereby appears (red solid curves). The sequence $(n, 2, 1)$ $(n = 5, 6, 7, \cdots)$ exhibit similar behaviors, shifting the bifurcation points slightly to larger η. Comparing with the plot of quantum δg, there is a clear correspondence between the superdeformed shell structure and the bifurcation of above star-shaped orbits. There is also a correspondence between the bifurcations of the equatorial-plane orbits $(n, 3)$ $(n = 7, 8, 9, \cdots)$ with the hyperdeformed shell structure emerging at $\eta \simeq 2.5$. The significant shell energy gain occurring at the superdeformed shape obtained in Fig. 6 is considered to be a result of this strong shell effect in the level density.

5.2. *Fourier analysis of the level density*

Fourier analysis is a useful tool to investigate the quantum-classical correspondence in the level density.[3)] Due to the simple form of the action integral $S_\beta = \hbar k L_\beta$, it is easy to Fourier transform the semiclassical level density $g_{\rm scl}(k)$ with respect to k. Let us define the Fourier transform $F(L)$ by

$$F(L) = \int dk e^{-ikL} g(k). \tag{5·12}$$

In actual numerical calculations, we multiply the integrand of the right-hand side of this equation by a Gaussian truncation function, obtaining

$$F_\Delta(L) = \frac{\Delta}{\sqrt{2\pi}} \int dk e^{-\frac{1}{2}(k\Delta)^2} e^{-ikL} g(k). \tag{5·13}$$

Inserting the semiclassical level density (5·10), the Fourier transform is expressed as

$$F_\Delta^{\rm scl}(L) = \bar{F}_\Delta(L) + \frac{1}{2} \sum_\beta e^{-i\pi\nu_\beta/2} a_\beta \left(i \frac{\partial}{\partial L} \right) \exp\left[-\frac{1}{2} \left(\frac{L - L_\beta}{\Delta} \right)^2 \right]. \tag{5·14}$$

This is a function that has peaks at the lengths of the classical periodic orbits $L = L_\beta$. On the other hand, we can calculate $F(L)$ by inserting the quantum mechanical level density $g(k) = \sum_n \delta(k - k_n)$ as

$$F_\Delta^{\rm qm}(L) = \frac{\Delta}{\sqrt{2\pi}} \sum_n e^{-\frac{1}{2}(k_n\Delta)^2} e^{-ik_n L}. \tag{5·15}$$

This quantity should exhibit successive peaks at orbit lengths $L = L_\beta$. Thus we can extract information concerning classical periodic orbits from the quantum spectrum. On the left-hand side of Fig. 8, we plot the Fourier transform (5·15) as a function of L and η. On the right-hand side of Fig. 8, the lengths of classical periodic orbits $L_\beta(\eta)$ are shown. There, red curves represent the orbits $M(n_v, 2, 1)$ $(n_v = 4, 5, 6, \cdots)$. We find strong Fourier peaks at $\eta \simeq 2$, corresponding to the periodic orbits (5,2,1), (6,2,1) and (7,2,1) just after the bifurcation points. We also find Fourier peaks at $\eta \simeq 2.5$, corresponding to the periodic orbits (7,3,1) and (8,3,1), etc. Thus, we can conclude that these periodic orbit bifurcations play essential roles in the emergence of superdeformed and hyperdeformed shell structures.

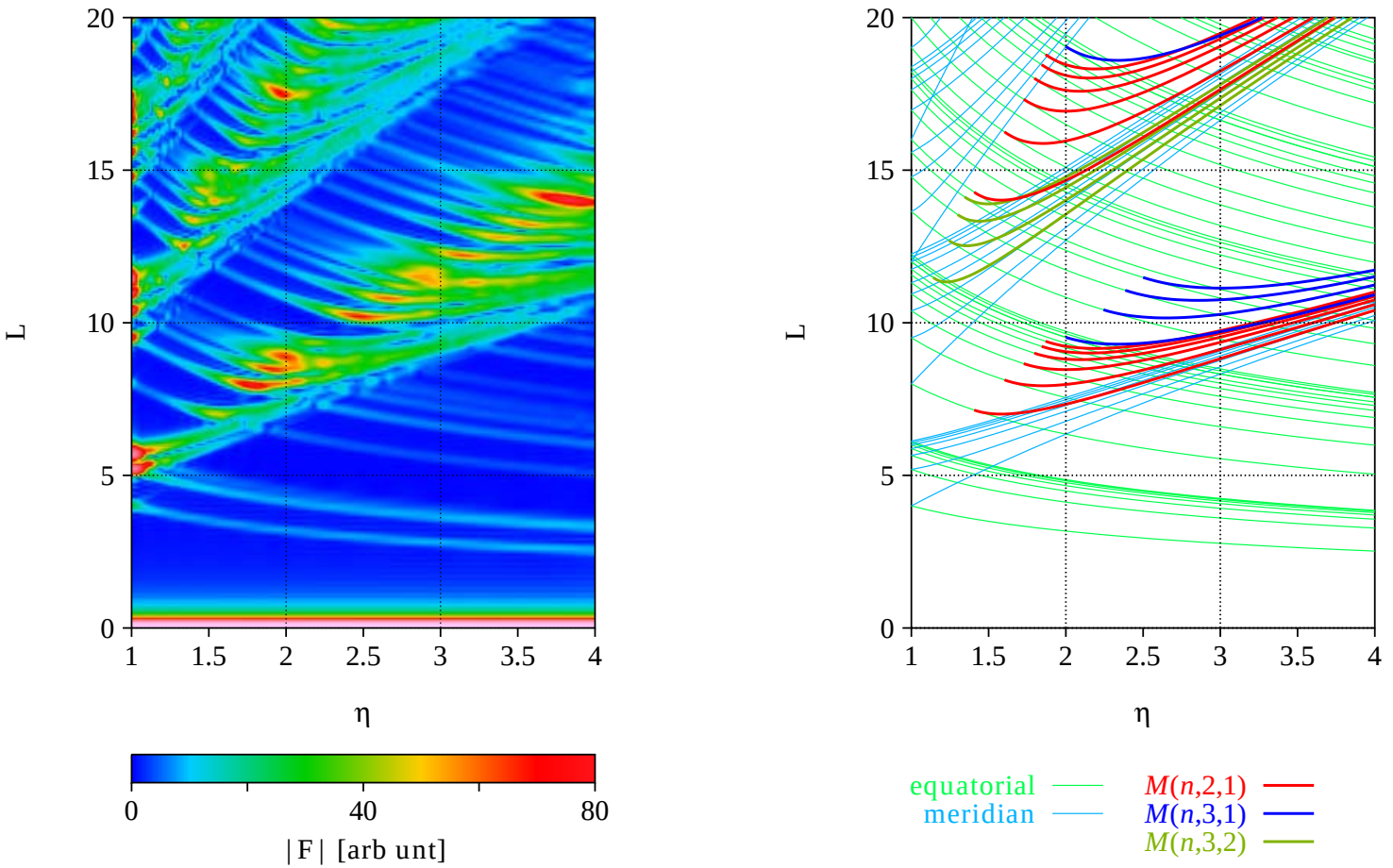

Fig. 8. Fourier amplitude $|F(L)|$ of the single-particle level density (left-hand side) and lengths of classical periodic orbits (right-hand side).

5.3. *Coarse-grained shell structure energy*

In order to prove that the shell structure at the superdeformed shape is due to the bifurcated orbits, we calculated the 'coarse-grained' shell energy defined by

$$\delta\tilde{E}_\gamma(N) = \int^{\tilde{k}_{\rm F}(\gamma)} \varepsilon(k) g_\gamma(k) dk - \int^{\tilde{k}_{\rm F}(\tilde{\gamma})} \varepsilon(k) g_{\tilde{\gamma}}(k) dk, \tag{5·16}$$

where the smoothed Fermi wave number $\tilde{k}_{\rm F}$ in each term is determined so that they satisfy the particle number condition

$$\int^{\tilde{k}_{\rm F}(\gamma)} g_\gamma(k) dk = \int^{\tilde{k}_{\rm F}(\tilde{\gamma})} g_{\tilde{\gamma}}(k) dk = N. \tag{5·17}$$

By coarse-graining with the width γ, a shell structure of resolution $\Delta kR = \gamma$ is extracted. Classical orbits relevant to such a structure are those with lengths

$$L < L_{\rm max} = \frac{2\pi R}{\gamma}. \tag{5·18}$$

Setting $\gamma = 0.6$, contributions from periodic orbits with $L \gtrsim 10R$ are smeared out. Around the superdeformed shape, bifurcated orbits have lengths $L \sim 10R$, and these contributions are significantly weakened by smoothing with $\gamma = 0.6$, and the major oscillating pattern of δE should disappear if these bifurcated orbits are responsible

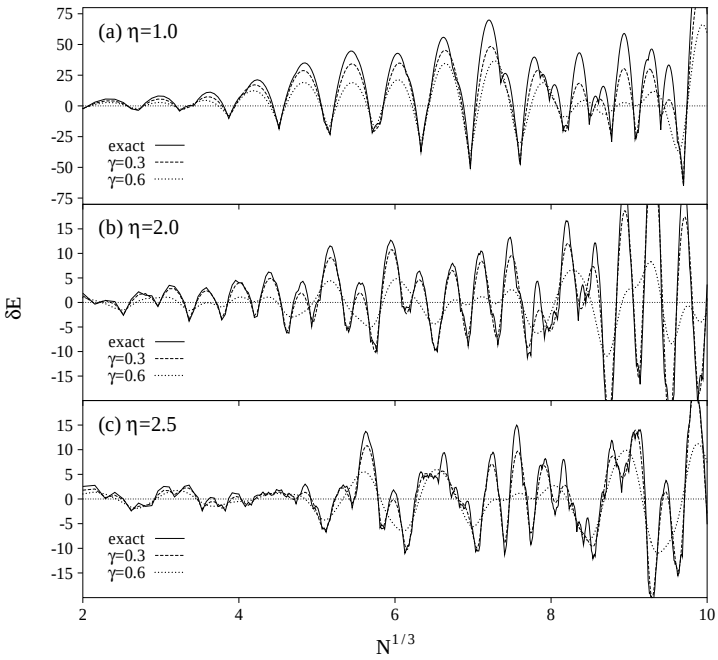

Fig. 9. Shell structure energies plotted as functions of $N^{1/3}$. Solid curves represent the exact shell structure energies. Dashed and dotted curves represent those calculated by using the coarse-grained level density $g_\gamma(k)$ with the smoothing widths $\gamma = 0.3$ and 0.6, respectively.

for the superdeformed shell effect. In Fig. 9, the coarse-grained shell energies (5·16) calculated for $\eta = 1, 2$ and 2.5 with $\gamma = 0.3$ and 0.6 are compared with the exact shell structure energies. In the upper panel, it is seen that the spherical shell structure survives after smoothing with $\gamma = 0.6$, indicating that the major structure is determined by orbits whose lengths are sufficiently shorter than $10R$. In contrast with it, the middle panel shows that the major oscillating pattern of the superdeformed shell structure is considerably broken after smoothing with $\gamma = 0.6$. The same argument is valid also for $\eta = 2.5$. This strongly supports the significance of bifurcated orbits for the superdeformed and hyperdeformed shell structures.

§6. Enhancement of semiclassical amplitudes near the bifurcation points

In this section, we present some results of the semiclassical ISPM calculation, which clearly show enhancement phenomena of the semiclassical amplitudes $|A_{3D}|$ and $|A_{EQ}|$ near the bifurcation points.

Figure 10(a) shows the modulus of the complex amplitude A_{3D} [Eq. (3·16)]

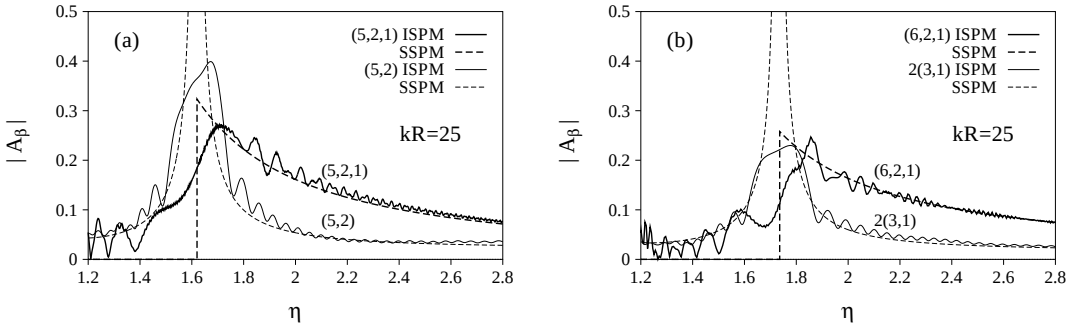

Fig. 10. (a) Semiclassical amplitudes $|A_{3D}|$ for the 3DPO (5,2,1) and $|A_{EQ}|$ for the EQPO (5,2), calculated at $kR = 25$ with the ISPM, are plotted as functions of the deformation parameter η by thick and thin solid curves, respectively. They are compared with the SSPM amplitudes (dashed curves). (b) The same as (a), but for the 3DPO (6,2,1) and the EQPO 2(3,1).

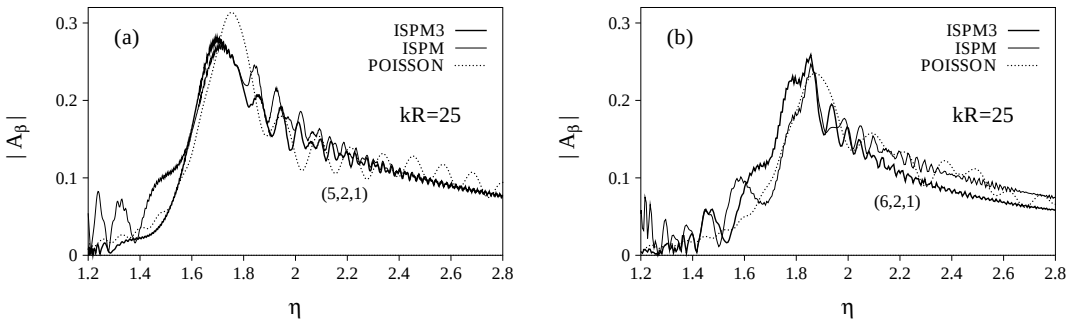

Fig. 11. (a) ISPM3 amplitudes for the 3DPO (5,2,1), calculated at $kR = 25$, are plotted as functions of the deformation η by thick-solid curves. For comparison, the ISPM amplitudes and the results of exact integration in the Poisson-sum trace formula are plotted by thin-solid and thick-dotted curves, respectively. (b) The same as (a), but for the 3DPO (6,2,1).

for the 3DPO $(5,2,1)$ and $A_{\rm EQ}$ [Eq. (3·30)] for the EQPO $(5,2)$ as functions of the deformation parameter η. They are compared with those of the SSPM. The SSPM amplitude for the EQPO $(5,2)$ is divergent at the bifurcation deformation $\eta_{\rm bif} = 1.618\ldots$, while the ISPM amplitude is finite and continuous through this bifurcation point, with a rather sharp maximum at this point. This difference is due to a local change of the symmetry parameter $\mathcal{K}$ from 1 to 2 at the bifurcation, and the associated enhancement of the amplitude is of order $\sqrt{kR}$. As seen from Fig. 10(a), the ISPM amplitude for the $(5,2,1)$ is continuous through the bifurcation point and exhibits a significant enhancement slightly to the right of it. It approaches the SSPM amplitude given by Eq. (3·21) away from the bifurcation point. The ISPM enhancement for the 3DPO is also of order $\sqrt{kR}$, because here, as in the case of the bifurcating EQPO, the degeneracy parameter $\mathcal{K}$ changes from 1 to 2. The same is true for the 3DPO (6,2,1) and the EQPO 2(3,1), as shown in Fig. 10(b).

In Fig. 11, we consider corrections from the 3rd-order terms in the expansion of the action about the stationary point. Here we incorporate the 3rd-order terms in the variable σ_1 (ISPM3) which are expected to be important for the 3DPO (6,2,1) whose curvature K_{11} is identically zero (see Appendix D). We also show results of the exact integration in the Poisson-sum trace formula (3·10) (marked "POISSON"). It is seen that the results of the ISPM3 for the $(5,2,1)$ and $(6,2,1)$ orbits are in good agreement with those of the ISPM in the most important regions, near the bifurcations, and on their right-hand sides. It is gratifying to see that the ISPM and the ISPM3 amplitudes $|A_{\rm 3D}|$ for $(5,2,1)$ and $(6,2,1)$ are also in good agreement with the results of the exact integration in the Poisson-sum trace formula. With the 3rd-order corrections, excessive ghost orbit contributions in the ISPM (bumps in the ISPM amplitudes on the left-hand side of the bifurcation point) are removed, and better agreement with the result of the exact integration is obtained. Except for this, the corrections due to the 3rd-order terms are rather small, and good convergence is achieved up to the second-order terms.

The amplitudes $|A_\beta|$ are slightly oscillating functions of kR. Because the period of this oscillation is much larger than that of the shell energy oscillation, the expansion about the Fermi energy $\varepsilon_{\rm F}$ (or $k_{\rm F}R$) can be used in the derivations of both the semiclassical ISPM shell energy $\delta E_{\rm scl}$ and the oscillating level density $\delta g_{\rm scl}$ (3·15). Figure 12 displays the semiclassical amplitudes $A_{\rm 3D}$ for the 3DPO (5,2,1) and $A_{\rm EQ}$ for the EQPO $(5,2)$ as functions of kR at $\eta = 1.618\ldots$ (top panel) and $\eta = 2$ (bottom panel). In this figure, the semiclassical amplitudes $A_{\rm 3D}$ for the 3DPO (6,2,1) and $A_{\rm EQ}$ for the EQPO 2(3,1) are also plotted as functions of kR at the bifurcation point $\eta = \sqrt{3}$ (middle panel). We see that for $\eta = 2$ the amplitudes $|A_{\rm 3D}|$ for the 3DPO $(5,2,1)$ and $(6,2,1)$ become much larger than the amplitude $|A_{\rm EQ}|$ for the EQPO.

§7. Comparison between quantum and semiclassical calculations

In this section we present results of calculations of the level densities and shell energies using the quantum Strutinsky method and the semiclassical ISPM, and make comparisons between the quantum and semiclassical calculations. In the quantum

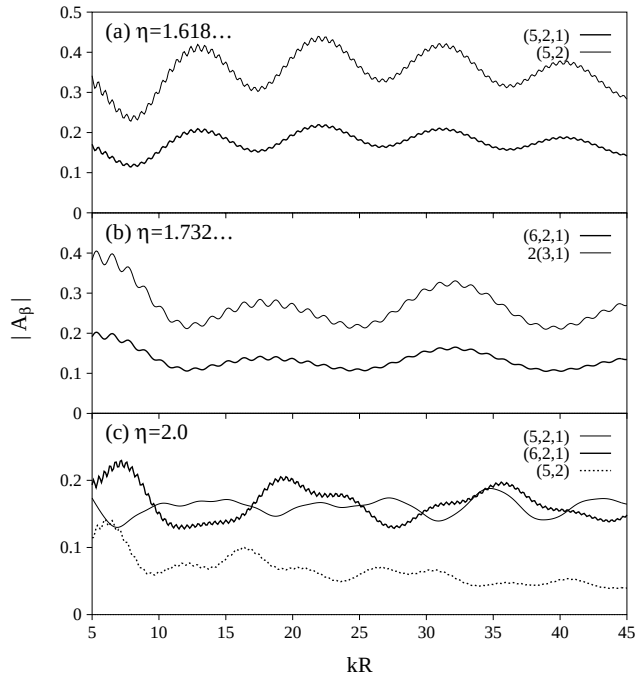

Fig. 12. (a) Semiclassical amplitudes $|A_{3D}|$ for the 3DPO (5,2,1) and $|A_{EQ}|$ for the EQPO (5,2) plotted by bold and thin solid curves, respectively, as functions of kR at the bifurcation point $\eta = 1.618\ldots$. (b) The same as (a), but for the 3DPO (6,2,1) and the EQPO 2(3,1) at the bifurcation point $\eta = 1.732\ldots$. (c) Semiclassical amplitudes $|A_{3D}|$ for (5,2,1), (6,2,1) and $|A_{EQ}|$ for (5,2) plotted by thin-solid, thick-solid and dotted curves, respectively, as functions of kR at $\eta = 2.0$.

calculations, the averaging parameter $\gamma = 0.3$ is used.

Figure 13 displays oscillating level densities δg for relatively small deformations. There, QM and ISPM denote the δg obtained with the quantum Strutinsky method and the semiclassical ISPM, respectively. For $\eta = 1.2$ we obtain good convergence of the periodic orbit sum (4·1) by taking into account the short elliptic 2DPO with $n_v \leq 12$, $n_u = 1$, the short EQPO with the maximum vertex number $p_{\max} = M(n_v)_{\max} = 14$, and the maximum winding number $t_{\max} = Mn_\varphi = 1$ ($M = 1, n_\varphi = 1$). The ISPM result is in good agreement with the quantum result. For the bifurcation point $\eta = \sqrt{2}$ of the butterfly orbit $(4, 2, 1)$ and $\eta = 1.5$ slightly to the right of it, the convergence of the periodic-orbit sum is achieved by taking into account the contributions from the bifurcating orbits, $(4, 2, 1)$ and the twice-repeated diameter $2(2, 1)$ with $t_{\max} = 2$, in addition to the 2DPO and the EQPO considered in the $\eta = 1.2$ case.

Figure 14 presents the oscillating level densities for the bifurcation deformations: $\eta = 1.618\ldots$ for the EQPO $(5, 2)$, $\eta = \sqrt{3}$ for the EQPO $2(3, 1)$, and $\eta = 2$ for the triply repeated equatorial diameters $3(2, 1)$. It is interesting to compare this figure with Fig. 15, where some results of simplified semiclassical calculations are given. In the top panel of Fig. 15, the SSPM is used instead of the ISPM. We see that the

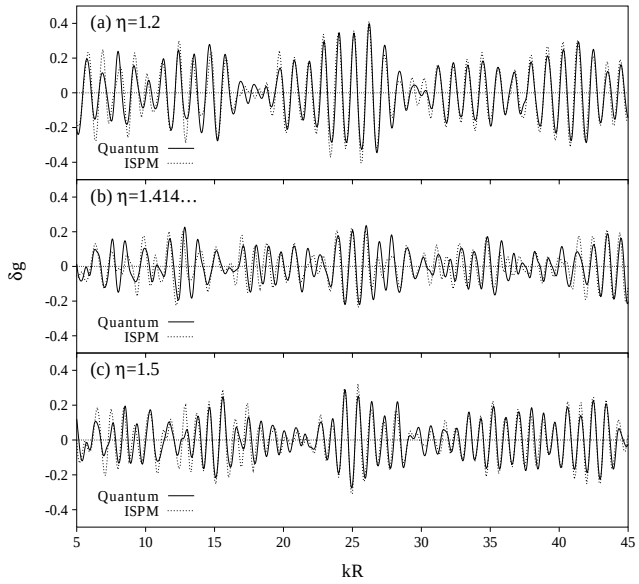

Fig. 13. Oscillating level densities evaluated with the semiclassical ISPM and a quantum mechanical method are shown by dotted and solid curves, respectively, as functions of kR for several deformations η.

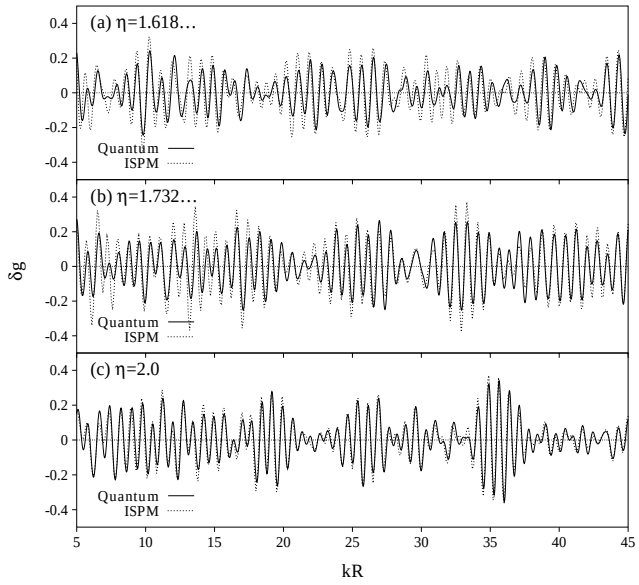

Fig. 14. The same as Fig. 13 but for larger deformations.

SSPM is a good approximation for $\eta = 1.2$. In the middle and bottom panels, only bifurcating orbits are taken into account in the periodic-orbit sum: Only the 3DPO $(5, 2, 1)$, the EQPO $(5, 2)$ and the butterfly $(4, 2, 1)$ are accounted for in the middle panel, while only the 3DPO $(5, 2, 1)$, $(6, 2, 1)$, $(7, 2, 1)$ and $(8, 2, 1)$ in the bottom panel. By comparing with the corresponding ISPM results shown in Fig. 15, we see

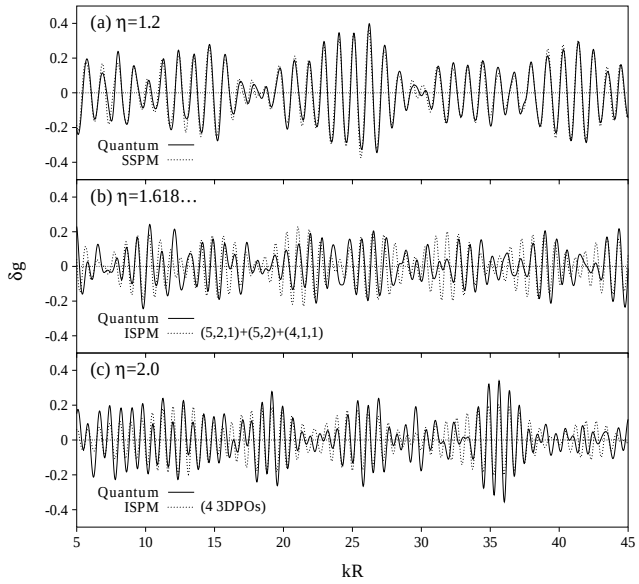

Fig. 15. Comparison of the oscillating level densities calculated with a quantum mechanical method (solid curves) and those obtained with some specific semiclassical calculations (dotted curves): (a) the top panel gives a comparison with the SSPM result for $\eta = 1.2$; (b) the middle panel displays the ISPM result in which only the bifurcating 3DPO $(5, 2, 1)$, the EQPO $(5, 2)$ and the 2DPO butterfly $(4, 2, 1)$ are taken into account for the POT sum in Eq. (3·15) for $\eta = 1.618\ldots$; (c) the bottom panel displays the ISPM result, in which only the four shortest 3DPO are taken into account for $\eta = 2.0$.

that, for $\eta = 1.618\ldots$ and 2, the major patterns of the oscillation are determined by these short 3DPO.

Figures 16 and 17 display the shell energies, which respectively correspond to the oscillating level densities shown in Figs. 13 and 14. Again, we see good agreement between the results of the semiclassical ISPM and the quantum calculations. For $\eta = 1.2$, good convergence is obtained by including only the shortest elliptic 2DPO and EQPO, in the same way as for the level density δg (see Ref. 9)). For $\eta = \sqrt{2}$ and 1.5, the properties of the ISPM shell energies are similar to those considered for the elliptic billiard system in Ref. 28). Now, let us more closely examine the bifurcation effects in the superdeformed region by comparing Fig. 17 with Fig. 18. In the top panel of Fig. 18, we show the ISPM result for $\eta = 1.618\ldots$ in which only the bifurcating 3DPO $(5, 2, 1)$, the short EQPO $(5, 2)$ and the hyperbolic 2DPO $(4, 2, 1)$ are taken into account. In the middle panel of this figure, we show the ISPM shell energies at $\eta = 1.732\ldots$, calculated by taking into account only the 3DPO $(5, 2, 1)$, the bifurcating 3DPO $(6, 2, 1)$ and the EQPO $2(3, 1)$. These comparisons clearly indicate that a few dominant periodic orbits determine the properties of the quantum shell structure at those bifurcation deformations. The bottom panel in this figure displays the dominant contributions of only the few shortest 3DPO at $\eta = 2.0$. Evidently, the short 3DPO $(5, 2, 1)$, $(6, 2, 1)$, $(7, 2, 1)$ and $(8, 2, 1)$ determine the major oscillating pattern of the shell energy. Thus, we can say that they are

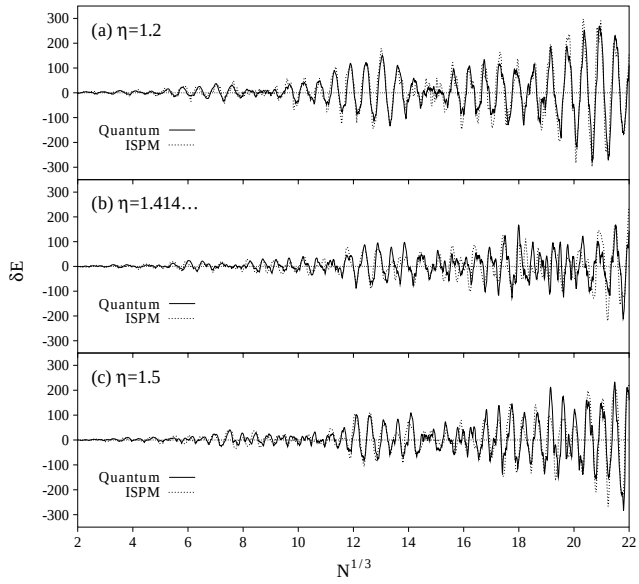

Fig. 16. Semiclassical ISPM and quantum shell energies (in units of ε_0) are plotted by dotted and solid curves, respectively, as functions of $N^{1/3}$.

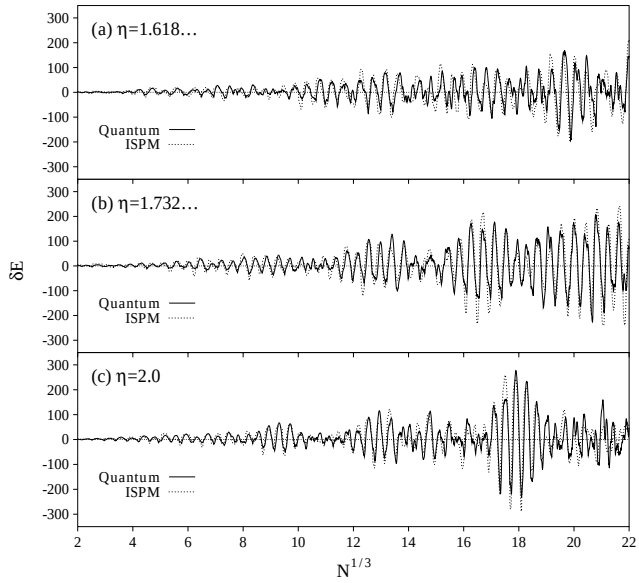

Fig. 17. The same as Fig. 16, but for larger deformations.

responsible for the formation of the shell structure at large deformations around the superdeformed shape. These results of the calculation are in good agreement with those obtained in Ref. 23) from the analysis of the length spectra (Fourier transforms of the quantum level densities).

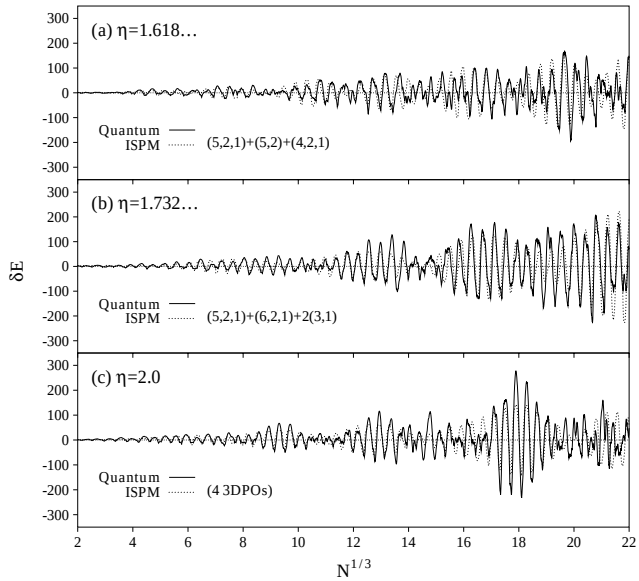

Fig. 18. Comparison of quantum shell energies (solid curves) with those obtained with specific semiclassical calculations (dotted curves): (a) the top panel presents the ISPM result for $\eta = 1.618...$, where only the bifurcating orbits (5,2,1), (5,2) and (4,2,1) are taken into account; (b) the middle panel displays for $\eta = 1.732...$ the contributions of *only* three orbits, the 3DPO $(5, 2, 1)$ and $(6, 2, 1)$, and the EQPO $2(3, 1)$; (c) the bottom panel plots for $\eta = 2.0$ the contributions of *only* the four shortest 3DPO to the ISPM sum.

§8. Conclusion

We have obtained an analytical trace formula for the 3D spheroidal cavity model, which is continuous through all critical deformations where bifurcations of periodic orbits occur. We find an enhancement of the amplitudes $|A_\beta|$ at deformations $\eta \sim 1.6$–2.0 due to bifurcations of 3D orbits from the short 2D orbits in the equatorial plane. The cause of this enhancement is quite general and independent of the specific potential shapes. We believe that this is an important mechanism that contributes to the stability of superdeformed systems, also in the formation of the second minimum related to the isometric states in nuclear fission. Our semiclassical analysis may therefore lead to a deeper understanding of shell structure effects in superdeformed fermionic systems — not only in nuclei and metallic clusters, but also, e.g., in deformed semiconductor quantum dots whose conductance and magnetic susceptibilities are significantly modified by shell effects.

Acknowledgements

A.G.M. gratefully acknowledges the financial support provided under the COE Professorship Program by the Ministry of Education, Science, Sports and Culture of Japan (Monbu-sho), giving him the opportunity to work at the RCNP and thanks

Prof. H. Toki for his warm hospitality and fruitful discussions. We acknowledge valuable discussions with Prof. M. Brack. Two of us (A.G.M. and S.N.F.) thank also the Regensburger Universitätsstiftung Hans Vielberth and Deutsche Forschungsgemeinshaft (DFG) for financial support.

Appendix A
— *Curvatures* —

A.1. *Three-dimensional orbits*

The action is written

$$S = 2\pi M \left(n_v I_v + n_u I_u + n_\varphi I_\varphi\right), \tag{A·1}$$

where I_u, I_v and I_φ are the partial actions. In a dimensionless form, they are

$$I_u = \frac{p\zeta}{\pi}\tilde{I}_u, \qquad I_v = \frac{p\zeta}{\pi}\tilde{I}_v, \qquad I_\varphi = \frac{p\zeta}{\pi}\tilde{I}_\varphi, \tag{A·2}$$

where

$$\tilde{I}_u = 2\int_0^{z_-} \frac{dz}{1-z^2}\sqrt{(z^2-z_-^2)(z^2-z_+^2)}, \tag{A·3a}$$

$$\tilde{I}_v = \int_{z_+}^{z_b} \frac{dz}{z^2-1}\sqrt{(z^2-z_-^2)(z^2-z_+^2)}, \tag{A·3b}$$

$$\tilde{I}_\varphi = \pi\sqrt{\sigma_2}. \tag{A·3c}$$

The quantities $z_\pm$ are related to the variables σ_i by

$$z_+^2 + z_-^2 = \sigma_1 + 1, \qquad z_+^2 z_-^2 = \sigma_1 - \sigma_2. \tag{A·4}$$

In terms of the elliptic integrals, (A·3) can be expressed as

$$\tilde{I}_u = \frac{2}{z_+}\left[(z_-^2-1)\mathrm{F}(k) - \sigma_2\Pi(z_-^2,k) + z_+^2\mathrm{E}(k)\right], \tag{A·5a}$$

$$\tilde{I}_v = \frac{1}{z_+}\left\{(z_+^2-z_-^2)\left[\mathrm{F}(\varphi,k) - \Pi(\varphi,n,k)\right] - z_+^2\mathrm{E}(\varphi,k)\right\} + z_b\sin\varphi, \tag{A·5b}$$

with

$$k = \frac{z_-}{z_+}, \quad n = \frac{1-z_-^2}{1-z_+^2}, \quad \varphi = \arcsin\sqrt{\frac{z_b^2-z_+^2}{z_b^2-z_-^2}}, \quad z_b = \cosh v_b = \frac{\eta}{\sqrt{\eta^2-1}}. \tag{A·6}$$

Here, we have used the standard definitions of the elliptic integrals of the first and the third kind,*)

$$\mathrm{F}(\varphi,k) = \int_0^\varphi \frac{dx}{\sqrt{1-k^2\sin^2 x}}, \tag{A·7a}$$

*) The definitions of the elliptic integrals (A·7) are related with those in Ref. 46) as $\mathrm{F}(\theta,\kappa) \equiv \mathrm{F}(\theta|\alpha)$ and $\Pi(\theta,n,\kappa) = \Pi(n,\theta|\alpha)$ ($\kappa = \sin\alpha$).

$$\mathrm{E}(\varphi,k)=\int_0^{\varphi}\sqrt{1-k^2\sin^2 x}\,dx, \tag{A·7b}$$

$$\Pi(\varphi,n,k)=\int_0^{\varphi}\frac{dx}{(1-n\sin^2 x)\sqrt{1-k^2\sin^2 x}}, \tag{A·7c}$$

and we have omitted the argument $\varphi=\pi/2$ for complete elliptic integrals.

The action (A·1) is written as

$$S=2p\zeta M\left(n_v\tilde{I}_v+n_u\tilde{I}_u+n_\varphi\tilde{I}_\varphi\right). \tag{A·8}$$

The curvatures K_{ij} of the energy surface $\varepsilon=H(\sigma_1,\sigma_2,\varepsilon)$ are defined as

$$K_{ij}=\frac{p\zeta}{\pi}\tilde{K}_{ij}=\frac{\partial^2 I_v}{\partial\sigma_i\partial\sigma_j}+\frac{\omega_u}{\omega_v}\frac{\partial^2 I_u}{\partial\sigma_i\partial\sigma_j}+\frac{\omega_\varphi}{\omega_v}\frac{\partial^2 I_\varphi}{\partial\sigma_i\partial\sigma_j}, \tag{A·9}$$

and the frequency ratios in Eq. (A·9) are given by

$$\frac{\omega_u}{\omega_v}\equiv-\left(\frac{\partial I_v}{\partial I_u}\right)_{I_\varphi}=-\frac{\partial\tilde{I}_v/\partial\sigma_1}{\partial\tilde{I}_u/\partial\sigma_1}, \tag{A·10}$$

$$\frac{\omega_\varphi}{\omega_v}\equiv-\left(\frac{\partial I_v}{\partial I_\varphi}\right)_{I_u}=-\frac{2\sqrt{\sigma_2}}{\pi}\left[\frac{\partial\tilde{I}_v}{\partial\sigma_2}+\frac{\omega_u}{\omega_v}\frac{\partial\tilde{I}_u}{\partial\sigma_2}\right]. \tag{A·11}$$

We have used here the properties of Jacobians for the transformations from the variables (I_u,I_φ) to (σ_1,σ_2). For the first derivatives of the actions (A·3) with respect to σ_1 and σ_2, we obtain

$$\frac{\partial\tilde{I}_u}{\partial\sigma_1}=\frac{1}{z_+}\,\mathrm{F}(k), \qquad \frac{\partial\tilde{I}_v}{\partial\sigma_1}=-\frac{1}{2z_+}\,\mathrm{F}(\varphi,k), \tag{A·12a}$$

$$\frac{\partial\tilde{I}_u}{\partial\sigma_2}=-\frac{1}{z_+}\,\Pi(z_-^2,k), \quad \frac{\partial\tilde{I}_v}{\partial\sigma_2}=C_{\mathrm{F}}\,\mathrm{F}(\varphi,k)+C_\Pi\,\Pi(\varphi,n,k), \tag{A·12b}$$

with

$$C_{\mathrm{F}}=\frac{z_+^2-1}{2z_+\sigma_2}=-\frac{1}{2z_+(z_-^2-1)},$$
$$C_\Pi=-\frac{z_+^2-z_-^2}{2z_+\sigma_2}=\frac{z_+^2-z_-^2}{2z_+(z_+^2-1)(z_-^2-1)}. \tag{A·13}$$

For the second derivatives of these actions, we obtain

$$\frac{\partial^2\tilde{I}_u}{\partial\sigma_1^2}=\frac{1}{2z_+^3}\left\{\frac{1}{k^2}\left[\Pi(k^2,k)-\mathrm{F}(k)\right]\left(\frac{\partial z_-^2}{\partial\sigma_1}-k^2\frac{\partial z_+^2}{\partial\sigma_1}\right)-\frac{\partial z_+^2}{\partial\sigma_1}\mathrm{F}(k)\right\}, \tag{A·14a}$$

$$\frac{\partial^2\tilde{I}_v}{\partial\sigma_1^2}=-\frac{1}{4z_+^3}\left\{\frac{1}{k^2}\left[\Pi(\varphi,k^2,k)-\mathrm{F}(\varphi,k)\right]\left(\frac{\partial z_-^2}{\partial\sigma_1}-k^2\frac{\partial z_+^2}{\partial\sigma_1}\right)\right.$$
$$\left.-\frac{\partial z_+^2}{\partial\sigma_1}\mathrm{F}(\varphi,k)+\frac{2z_+^2}{\Delta_\varphi}\frac{\partial\varphi}{\partial\sigma_1}\right\}, \tag{A·14b}$$

$$\frac{\partial^2 \tilde{I}_u}{\partial \sigma_2^2} = \frac{1}{2z_+^5 k_1^2}\left[\Pi(z_-^2,k) + 2z_+^2\,\frac{\partial \Pi(z_-^2,k)}{\partial n} + \frac{1+k^2}{k}\,\frac{\partial \Pi(z_-^2,k)}{\partial k}\right], \tag{A·14c}$$

$$\begin{aligned}\frac{\partial^2 \tilde{I}_v}{\partial \sigma_2^2} &= \frac{\partial C_{\rm F}}{\partial \sigma_2}\,{\rm F}(\varphi,k) + C_{\rm F}\left(\frac{1}{\Delta_\varphi}\frac{\partial \varphi}{\partial \sigma_2} + \frac{\partial {\rm F}(\varphi,k)}{\partial k}\frac{\partial k}{\partial \sigma_2}\right) + \frac{\partial C_\Pi}{\partial \sigma_2}\,\Pi(\varphi,n,k)\\ &\quad + C_\Pi\left(\frac{\partial \Pi(\varphi,n,k)}{\partial \varphi}\frac{\partial \varphi}{\partial \sigma_2} + \frac{\partial \Pi(\varphi,n,k)}{\partial n}\frac{\partial n}{\partial \sigma_2} + \frac{\partial \Pi(\varphi,n,k)}{\partial k}\frac{\partial k}{\partial \sigma_2}\right),\end{aligned} \tag{A·14d}$$

and

$$\frac{\partial^2 \tilde{I}_u}{\partial \sigma_1 \partial \sigma_2} = -\frac{1}{2z_+^5 k_1^2}\left[{\rm F}(k) + \frac{1+k^2}{k}\,\frac{\partial {\rm F}(k)}{\partial k}\right], \tag{A·14e}$$

$$\frac{\partial^2 \tilde{I}_v}{\partial \sigma_1 \partial \sigma_2} = \frac{1}{4z_+^5 k_1^2}\left[{\rm F}\,(\varphi,k) - \frac{(\sigma_1+1-2z_b^2)\tan\theta}{\Delta_\varphi z_b^2 \Delta_\theta^2 k_1} + \frac{1+k^2}{k}\,\frac{\partial {\rm F}(\varphi,k)}{\partial k}\right]. \tag{A·14f}$$

Here,

$$\Delta_x = \sqrt{1-k^2\sin^2 x}, \quad k_1 = \sqrt{1-k^2}, \quad \theta = \arcsin\left(\frac{z_+}{z_b}\right), \tag{A·15}$$

and

$$\frac{\partial z_\pm^2}{\partial \sigma_1} = \frac{1}{2}\left[1 \pm \frac{\sigma_1 - 1}{\sqrt{(\sigma_1-1)^2 + 4\sigma_2}}\right] = \frac{1}{2}\left[1 \pm \frac{z_+^2 + z_-^2 - 2}{z_+^2 - z_-^2}\right], \tag{A·16}$$

$$\frac{\partial \varphi}{\partial \sigma_1} = \frac{1}{2}\,\frac{\frac{\partial z_-^2}{\partial \sigma_1}(z_b^2 - z_+^2) - \frac{\partial z_+^2}{\partial \sigma_1}(z_b^2 - z_-^2)}{(z_b^2 - z_-^2)\sqrt{(z_b^2 - z_+^2)(z_+^2 - z_-^2)}}, \tag{A·17}$$

$$\frac{\partial k^2}{\partial \sigma_2} = -\frac{1+k^2}{z_+^4 k_1^2}, \tag{A·18}$$

$$\frac{\partial C_{\rm F}}{\partial \sigma_2} = \frac{z_-^2 - 2z_+^2 - 1}{4z_+^3(1-z_-^2)^2(z_+^2 - z_-^2)}, \tag{A·19}$$

$$\frac{\partial C_\Pi}{\partial \sigma_2} = -\frac{\sigma_2(3z_+^2 + z_-^2) - 2z_+^2(z_+^2 - z_-^2)^2}{4z_+^3 \sigma_2^2 (z_+^2 - z_-^2)}, \tag{A·20}$$

$$\frac{\partial \varphi}{\partial \sigma_2} = \frac{\left(2z_b^2 - (\sigma_1+1)\right)\tan\theta}{2z_b^2 z_+^4 k_1^3 \Delta_\theta^2}, \tag{A·21}$$

$$\frac{\partial n}{\partial \sigma_2} = \frac{\sigma_1 - 1}{(1-z_+^2)^2(z_+^2 - z_-^2)}, \tag{A·22}$$

$$\frac{\partial z_\pm^2}{\partial \sigma_2} = \pm\frac{1}{z_+^2 - z_-^2}. \tag{A·23}$$

Derivatives of the elliptic integrals are given by

$$\frac{\partial {\rm F}(\varphi,k)}{\partial k} = \frac{1}{k}\left[\Pi(\varphi,k^2,k) - {\rm F}(\varphi,k)\right], \tag{A·24}$$

$$\frac{\partial \Pi(\varphi,n,k)}{\partial \varphi} = \frac{1}{(1-n\sin^2\varphi)\Delta_\varphi}\,, \tag{A·25}$$

$$\frac{\partial \Pi(\varphi,n,k)}{\partial n} = \frac{1}{n}\left[\Pi_{21}(\varphi,n,k) - \Pi(\varphi,n,k)\right], \tag{A·26}$$

$$\frac{\partial \Pi(\varphi,n,k)}{\partial k} = \frac{1}{k}\left[\Pi_{13}(\varphi,n,k) - \Pi(\varphi,n,k)\right], \tag{A·27}$$

with

$$\Pi_{ij}(\varphi,n,k) = \int_0^\varphi \frac{dx}{(1-n\sin^2 x)^i (1-k^2\sin^2 x)^{j/2}}\,. \tag{A·28}$$

A.2. *Meridian-plane orbits*

For the meridian-plane orbits for which $I_\varphi = 0$ ($\sigma_2 = 0$), the actions I_u and I_v defined by Eq. (2·3) can be simplified. In the dimensionless form (A·2) we obtain for the elliptic orbits,

$$\tilde{I}_u = 2\sqrt{\sigma}\ \mathrm{E}\left(\frac{1}{\sqrt{\sigma}}\right), \tag{A·29a}$$

$$\tilde{I}_v = \sqrt{\sigma}\left[\mathrm{E}\left(\theta_e, \frac{1}{\sqrt{\sigma}}\right) - \mathrm{E}\left(\frac{1}{\sqrt{\sigma}}\right)\right] + \frac{\sqrt{\eta^2-\sigma(\eta^2-1)}}{\eta\sqrt{\eta^2-1}}\,. \tag{A·29b}$$

Here we have used the identity[47)]

$$\Pi(\varphi,k^2,k) = \left[\mathrm{E}(\varphi,k) - k^2\sin\varphi\cos\varphi/\sqrt{1-k^2\sin^2\varphi}\right]/(1-k^2)\,. \tag{A·30}$$

In this subsection, we omit the suffix "1" on the variable σ_1 for brevity. For the hyperbolic orbits, we have

$$\tilde{I}_u = 2\left[\mathrm{E}(\sqrt{\sigma}) - (1-\sigma)\ \mathrm{F}(\sqrt{\sigma})\right], \tag{A·31a}$$

$$\tilde{I}_v = (1-\sigma)\left[\mathrm{F}(\sqrt{\sigma}) - \mathrm{F}(\theta_h,\sqrt{\sigma})\right] + \mathrm{E}(\theta_h,\sqrt{\sigma}) - \mathrm{E}(\sqrt{\sigma}) + \frac{\sqrt{\eta^2-\sigma(\eta^2-1)}}{\eta\sqrt{\eta^2-1}}. \tag{A·31b}$$

Equations (A·29) and (A·31) can be regarded as parametric equations in terms of the parameter σ for the energy surface of the meridian-plane orbits, $\varepsilon(\tilde{I}_u, \tilde{I}_v, \tilde{I}_\varphi = 0)$, for its elliptic and hyperbolic parts, respectively.

The curvature K_{11} of the energy curve for the meridian-plane orbits can be obtained by differentiating Eqs. (A·29) and (A·31) implicitly through the parameter σ. In this way we obtain Eq. (3·13) with the dimensionless derivatives for the elliptic orbits

$$\frac{\partial \tilde{I}_u}{\partial \sigma} = \frac{1}{\sqrt{\sigma}}\ \mathrm{F}\left(\frac{1}{\sqrt{\sigma}}\right), \tag{A·32a}$$

$$\frac{\partial \tilde{I}_v}{\partial \sigma} = -\frac{1}{2\sqrt{\sigma}}\ \left[\mathrm{F}\left(\frac{1}{\sqrt{\sigma}}\right) - \mathrm{F}\left(\theta_e, \frac{1}{\sqrt{\sigma}}\right)\right], \tag{A·32b}$$

$$\frac{\partial^2 \tilde{I}_u}{\partial \sigma^2} = -\frac{1}{2\sqrt{\sigma^3}}\,\Pi\left(\frac{1}{\sigma}, \frac{1}{\sqrt{\sigma}}\right), \tag{A·32c}$$

$$\frac{\partial^2 \tilde{I}_v}{\partial \sigma^2} = \frac{1}{4\sqrt{\sigma^3}}\,\left[\Pi\left(\frac{1}{\sigma}, \frac{1}{\sqrt{\sigma}}\right) - \Pi\left(\theta_e, \frac{1}{\sigma}, \frac{1}{\sqrt{\sigma}}\right) + \frac{\eta\sqrt{\eta^2-1}}{\sqrt{1-(1-\sigma^{-1})\eta^2}}\right]. \tag{A·32d}$$

For the hyperbolic orbits, we have

$$\frac{\partial \tilde{I}_u}{\partial \sigma} = \mathrm{F}(\sqrt{\sigma}), \tag{A·33a}$$

$$\frac{\partial \tilde{I}_v}{\partial \sigma} = \frac{1}{2}\,\left[\mathrm{F}(\theta_h, \sqrt{\sigma}) - \mathrm{F}(\sqrt{\sigma})\right], \tag{A·33b}$$

$$\frac{\partial^2 \tilde{I}_u}{\partial \sigma^2} = \frac{1}{2\sigma}\,\left[\Pi(\sigma, \sqrt{\sigma}) - \mathrm{F}(\sqrt{\sigma})\right], \tag{A·33c}$$

$$\frac{\partial^2 \tilde{I}_v}{\partial \sigma^2} = \frac{1}{4\sigma}\,\left[\Pi(\theta_h, \sigma, \sqrt{\sigma}) - \Pi(\sigma, \sqrt{\sigma})z + \mathrm{F}(\sqrt{\sigma}) - \mathrm{F}(\theta_h, \sqrt{\sigma})\right]. \tag{A·33d}$$

Thus, for elliptic orbits, we obtain

$$\tilde{K}_{11} = \frac{1}{4\sqrt{\sigma^3}}\left[\frac{\mathrm{F}(\theta_e, \kappa)}{\mathrm{F}(\kappa)}\Pi(\kappa^2, \kappa) - \Pi(\theta_e, \kappa^2, \kappa) + \frac{\sqrt{\eta^2 - \sigma(\eta^2-1)}}{\eta\sqrt{\eta^2-1}}\right], \tag{A·34}$$

and for hyperbolic orbits,

$$\tilde{K}_{11} = -\frac{1}{4\sigma}\left[\frac{\mathrm{F}(\theta_h, \kappa)}{\mathrm{F}(\kappa)}\Pi(\kappa^2, \kappa) - \Pi(\theta_h, \kappa^2, \kappa)\right]. \tag{A·35}$$

A.3. *Equatorial-plane orbits*

For the equatorial limit $\sigma_2 = \sigma_1 \equiv \sigma$ we have, from (A·4),

$$z_-^2 = 0, \qquad z_+^2 = \sigma + 1\,. \tag{A·36}$$

We thus obtain in this limit ($k \to 0$)

$$\frac{\partial \tilde{I}_u}{\partial \sigma_1} = \frac{\pi}{2\sqrt{\sigma+1}}, \quad \frac{\partial \tilde{I}_v}{\partial \sigma_1} = -\frac{\varphi_{\mathrm{EQ}}}{2\sqrt{\sigma+1}}, \quad \frac{\partial z_\pm^2}{\partial \sigma_1} = \left\{\begin{matrix}\sigma/(\sigma+1)\\ 1/(\sigma+1)\end{matrix}\right\} \tag{A·37}$$

and

$$\frac{\partial^2 \tilde{I}_u}{\partial \sigma_1^2} = \frac{\pi(1-2\sigma)}{8(\sigma+1)^{5/2}},$$

$$\frac{\partial^2 \tilde{I}_v}{\partial \sigma_1^2} = \frac{1}{8(\sigma+1)^{5/2}}\left\{(2\sigma-1)\varphi_{\mathrm{EQ}} + \frac{1}{2}\sin(2\varphi_{\mathrm{EQ}}) - \frac{2\sqrt{\sigma+1}\,\left[z_b^2(1-\sigma) - (\sigma+1)\right]}{z_b^2\sqrt{z_b^2 - (\sigma+1)}}\right\},$$

$$\varphi_{\mathrm{EQ}} = \arcsin\frac{\sqrt{z_b^2 - (\sigma+1)}}{z_b}. \tag{A·38}$$

Substituting (A·37) and (A·38) into (A·9), we finally obtain the equatorial limit,

$$\tilde{K}_{11}^{\mathrm{EQ}} = \frac{z_b^2(2\sigma-1)+(\sigma+1)}{8z_b^2(\sigma+1)^2\sqrt{z_b^2-(\sigma+1)}}. \tag{A·39a}$$

In the same way, we obtain

$$\tilde{K}_{22}^{\mathrm{EQ}} = \frac{z_b^2(2-\sigma)+\sigma(\sigma+1)}{8z_b^2\sigma(\sigma+1)^2\sqrt{z_b^2-(\sigma+1)}}, \tag{A·39b}$$

$$\tilde{K}_{12}^{\mathrm{EQ}} = \frac{3z_b^2-(\sigma+1)}{8z_b^2(\sigma+1)^2\sqrt{z_b^2-(\sigma+1)}}. \tag{A·39c}$$

The determinant of the curvature matrix for EQPO becomes

$$\det \tilde{K}^{\mathrm{EQ}} = -\frac{1}{32z_b^2\sigma(\sigma+1)^2}, \tag{A·40}$$

which is negative for any orbit and for any deformation $\eta > 1$. This shows that bifurcations of EQPO occur only through the zeros of the stability factor F_z^{EQ}.

Appendix B

Derivation of the Trace Formula for the Equatorial-Plane Orbits

We start with the phase-space trace formula[9),28),31),40)]

$$\delta g_{\mathrm{scl}}(\varepsilon) = \mathrm{Re}\sum_{\alpha}\int \frac{d\boldsymbol{q}''d\boldsymbol{p}'}{(2\pi\hbar)^3}\,\delta\left(\varepsilon - H\left(\boldsymbol{q}',\boldsymbol{p}'\right)\right)\left|\mathcal{J}\left(\boldsymbol{p}_\perp'',\boldsymbol{p}_\perp'\right)\right|^{1/2} \times \exp\left\{\frac{i}{\hbar}\left[S_\alpha\left(\boldsymbol{p}',\boldsymbol{p}'',t_\alpha\right)+\left(\boldsymbol{p}''-\boldsymbol{p}'\right)\cdot\boldsymbol{q}''\right]-i\frac{\pi}{2}\nu_\alpha\right\}, \tag{B·1}$$

where the sum runs over all trajectories α, $\boldsymbol{q} = \boldsymbol{q}_\alpha(t,\boldsymbol{q}'',\boldsymbol{p}')$ determined by the fixed initial momentum $\boldsymbol{p}'$ and the final coordinate $\boldsymbol{q}''$, $H(\boldsymbol{q},\boldsymbol{p})$ is the classical Hamiltonian, and ν_α is the phase related to the Maslov index, number of caustics and turning points.[39),41)–43)] The function $S_\alpha(\boldsymbol{p}',\boldsymbol{p}'',t_\alpha)$ is the action in the mixed phase-space representation,

$$S_\alpha\left(\boldsymbol{p}',\boldsymbol{p}'',t_\alpha\right) = -\int_{\boldsymbol{p}'}^{\boldsymbol{p}''} d\boldsymbol{p}\cdot\boldsymbol{q}\left(\boldsymbol{p}\right), \tag{B·2}$$

related to the standard definition of the action $S_\alpha(\boldsymbol{q}',\boldsymbol{q}'',\varepsilon)$,

$$S_\alpha\left(\boldsymbol{q}',\boldsymbol{q}'',\varepsilon\right) = \int_{\boldsymbol{q}'}^{\boldsymbol{q}''} d\boldsymbol{q}\cdot\boldsymbol{p}\left(\boldsymbol{q}\right), \tag{B·3}$$

by the Legendre transformations (integration by parts),

$$S_\alpha\left(\boldsymbol{p}',\boldsymbol{p}'',t_\alpha\right) = S_\alpha\left(\boldsymbol{q}',\boldsymbol{q}'',\varepsilon\right)+\left(\boldsymbol{p}'-\boldsymbol{p}''\right)\boldsymbol{q}'', \tag{B·4}$$

t_α being the time for a particle to revolve the trajectory α. The quantity $\mathcal{J}\left(\boldsymbol{p}''_\perp, \boldsymbol{p}'_\perp\right)$ in Eq. (B·1) is the Jacobian for the transformation from $\boldsymbol{p}''_\perp$ to $\boldsymbol{p}'_\perp$. Here, we have introduced the local system of the phase-space coordinates $\boldsymbol{q} = \left\{q_\parallel, \boldsymbol{q}_\perp\right\}$ and $\boldsymbol{p} = \left\{p_\parallel, \boldsymbol{p}_\perp\right\}$, splitting the vectors into the parallel and perpendicular components with respect to the trajectory α.

For the equatorial-plane periodic orbits (EQPO), one of the components in $\boldsymbol{q}_\perp$ and $\boldsymbol{p}_\perp$ can be taken along the symmetry axis, say z and p_z, keeping for other perpendicular components the same suffix, $q_\perp$ and $p_\perp$. After the transformation to this local phase-space coordinate system and integration over the "parallel" momentum $p_\parallel = p = \sqrt{2m\varepsilon}$ by using the δ-function in Eq. (B·1), we obtain, for the contribution from the EQPO ($\mathcal{K} = 1$),

$$\delta g^{(1)}_{\rm EQ}(\varepsilon) = \frac{1}{(2\pi\hbar)^3}\,{\rm Re}\sum_\alpha \int \frac{dq''_\parallel}{|\dot q''_\parallel|}\int dq''_\perp dp'_\perp \int dz'' dp'_z \left|\mathcal{J}\left(\boldsymbol{p}'', \boldsymbol{p}'\right)\right|^{1/2} \times \exp\left\{\frac{i}{\hbar}\left[S_\alpha\left(\boldsymbol{p}', \boldsymbol{p}'', t_\alpha\right) + \left(\boldsymbol{p}'' - \boldsymbol{p}'\right)\cdot\boldsymbol{q}''\right] - i\frac{\pi}{2}\nu_\alpha\right\}, \tag{B·5}$$

where $\dot q_\parallel = \partial H/\partial p_\parallel = p/m$ is the velocity. In spheroidal action-angle variables, $q_\parallel = \Theta_v$, $p_\parallel = I_v$, $\dot q_\parallel = \omega_v$, $q_\perp = \Theta_\varphi = \varphi$, $p_\perp = I_\varphi$, $z = \Theta_u$, $p_z = I_u$, and we have

$$\delta g^{(1)}_{\rm EQ}(\varepsilon) = \frac{1}{(2\pi\hbar)^3}\,{\rm Re}\sum_\alpha \int \frac{d\Theta''_v}{|\omega_v|}\int d\Theta''_\varphi\, dI'_\varphi \int d\Theta''_u\, dI'_u \left|\mathcal{J}\left(I''_\varphi I''_u, I'_\varphi I'_u\right)\right|^{1/2} \times \exp\left\{\frac{i}{\hbar}\left[S_\alpha\left(\boldsymbol{I}', \boldsymbol{I}'', t_\alpha\right) + \left(\boldsymbol{I}'' - \boldsymbol{I}'\right)\cdot\boldsymbol{\Theta}''\right] - i\frac{\pi}{2}\nu_\alpha\right\}. \tag{B·6}$$

We now perform the integrations using the expansion of the action S_α about the stationary points:

$$S_\alpha\left(\boldsymbol{I}', \boldsymbol{I}'', t_\alpha\right) + \left(\boldsymbol{I}'' - \boldsymbol{I}'\right)\cdot\boldsymbol{\Theta}'' = S_\beta(\varepsilon) + \frac{1}{2}\sum_{ij} J_{ij}(\sigma_i - \sigma_i^*)(\sigma_j - \sigma_j^*) + \frac{1}{2}J_\perp\left(z - z^*\right)^2 + \cdots. \tag{B·7}$$

Here, we omit the corrections associated with mixed derivatives of type $\partial^2 S/\partial\Theta\partial I$ for simplicity. $J_\perp$ is the Jacobian corresponding to the second variation of the action S_α with respect to the angle variable Θ_u:

$$J_\perp^{\rm EQ} = \left(\frac{\partial^2 S_\alpha}{\partial {\Theta'_u}^2} + 2\frac{\partial^2 S_\alpha}{\partial\Theta'_u\partial\Theta''_u} + \frac{\partial^2 S_\alpha}{\partial {\Theta'_u}^2}\right)_{\rm EQ} = \left(-\frac{\partial I'_u}{\partial\Theta'_u} - 2\frac{\partial I'_u}{\partial\Theta''_u} + \frac{\partial I''_u}{\partial\Theta''_u}\right)_{\rm EQ}. \tag{B·8}$$

This quantity can be expressed in terms of the curvatures $K^{\rm EQ}$ and the Gutzwiller stability factor $F_z^{\rm EQ}$,

$$F_z^{\rm EQ} = -\left[\left(-\frac{\partial I'_u}{\partial\Theta'_u} - 2\frac{\partial I'_u}{\partial\Theta''_u} + \frac{\partial I''_u}{\partial\Theta''_u}\right)\Big/\frac{\partial I'_u}{\partial\Theta''_u}\right]_{\rm EQ} = 4\sin^2\left[\frac{1}{2}Mn_v\arccos\left(1 - 2\eta^{-2}\sin^2\phi\right)\right], \tag{B·9}$$

as

$$J_{\perp}^{\mathrm{EQ}} = -\frac{F_z^{\mathrm{EQ}}}{(J_u - J_{u\varphi}^2/J_\varphi)^{\mathrm{EQ}}} = -\frac{F_z^{\mathrm{EQ}}}{2\pi M n_v (K_u - K_{u\varphi}^2/K_\varphi)^{\mathrm{EQ}}}\,. \tag{B·10}$$

In these equations we have used the simple identical Jacobian transformations

$$\left(\frac{\partial I'_u}{\partial \Theta''_u}\right)^{-1}_{I'_\varphi} = \frac{\partial(\Theta''_u, I'_\varphi)}{\partial(I'_u, I'_\varphi)} = \frac{\partial \Theta''_u}{\partial I'_u} - \frac{\partial \Theta''_u}{\partial I'_\varphi}\frac{\partial I'_\varphi}{\partial I'_u} = J_u - J_{u\varphi}\frac{J_{u\varphi}}{J_\varphi}\,.$$

The curvature K_u^{EQ} is the quantity K_u defined in (B·13), evaluated at the stationary point $\sigma_1 = \sigma_2 = \sigma^*$ given by Eq. (3·27), and so on.

The integrand of (B·6) does not depend on the angles $(\Theta_v,\ \Theta_\varphi)$, and we obtain simply $(2\pi)^2$ for the integration over these angle variables. We transform the integration variables (I_u, I_φ) into (σ_1, σ_2) to obtain simple integration limits, and integrate over (σ_1, σ_2) using the ISPM. In this way we obtain

$$\delta g_{\mathrm{EQ}}^{(1)}(\varepsilon) = \sqrt{\frac{\pi}{2\hbar^3}}\,\mathrm{Re}\sum_\beta e^{i(kL_\beta - \pi\nu_\beta/2)}\frac{1}{\omega_v}\left|\frac{\partial(I_u, I_\varphi)}{\partial(\sigma_1,\sigma_2)}\right|\sqrt{\frac{1}{J_\perp|\det J^{\mathrm{EQ}}|}}$$
$$\times\,\mathrm{erf}(\mathcal{Z}_\perp^-, \mathcal{Z}_\perp^+; \mathcal{Z}_1^-, \mathcal{Z}_1^+; \mathcal{Z}_2^-, \mathcal{Z}_2^+), \tag{B·11}$$

where

$$\mathrm{erf}\left(x^-, x^+; y^-, y^+; z^-, z^+\right) = \left(\frac{2}{\sqrt{\pi}}\right)^3 \int_{x^-}^{x^+} dx \int_{y^-}^{y^+} dy \int_{z^-}^{z^+} dz\, e^{-x^2-y^2-z^2}. \tag{B·12}$$

Note that the integration limits for the internal integrals over y and z in $\mathrm{erf}\,(x^-, x^+; y^-, y^+; z^-, z^+)$ in general depend on the variable of the next integrations, $y^\pm = y^\pm(x)$ and $z^\pm = z^\pm(x, y)$. Here we define curvatures in the variables (I_u, I_φ) as

$$J_u = \frac{\partial^2 S_\alpha}{\partial I_u^2} = 2\pi M n_v K_u, \quad J_\varphi = \frac{\partial^2 S_\alpha}{\partial I_\varphi^2} = 2\pi M n_v K_\varphi,$$
$$J_{u\varphi} = \frac{\partial^2 S_\alpha}{\partial I_u \partial I_\varphi} = 2\pi M n_v K_{u\varphi}. \tag{B·13}$$

Using (B·10) and the relations

$$\det J \equiv J_{11}J_{22} - {J_{12}}^2 = \left|\frac{\partial(I_u, I_\varphi)}{\partial(\sigma_1,\sigma_2)}\right|^2 (J_u J_\varphi - {J_{u\varphi}}^2), \tag{B·14}$$

$$K_\varphi = \frac{1}{\pi p a \sin\phi}, \qquad \omega_v = \frac{\pi p}{m a \sin\phi}, \tag{B·15}$$

we finally obtain

$$\delta g_{\mathrm{EQ}}^{(1)}(\varepsilon) = \frac{1}{\varepsilon_0}\,\mathrm{Re}\sum_{\mathrm{EQ}} A_{\mathrm{EQ}} \exp\left(ikL_{\mathrm{EQ}} - i\frac{\pi}{2}\nu_{\mathrm{EQ}}\right), \tag{B·16}$$

$$A_{\rm EQ} = \frac{1}{2}\sqrt{\frac{\sin^3\phi}{\pi M n_v k R \eta F_z}}\,\mathrm{erf}\left(\mathcal{Z}_\perp^-, \mathcal{Z}_\perp^+; \mathcal{Z}_1^-, \mathcal{Z}_1^+; \mathcal{Z}_2^-, \mathcal{Z}_2^+\right), \tag{B·17}$$

where $L_{\rm EQ}$ represents the length of the EQPO. The "triple" error function in Eq. (B·17) can be separated into the product of three standard error functions as

$$\mathrm{erf}\left(\mathcal{Z}_\perp^-, \mathcal{Z}_\perp^+; \mathcal{Z}_1^-, \mathcal{Z}_1^+; \mathcal{Z}_2^-, \mathcal{Z}_2^+\right) \approx \mathrm{erf}\left(\mathcal{Z}_\perp^-, \mathcal{Z}_\perp^+\right)\mathrm{erf}\left(\mathcal{Z}_1^-, \mathcal{Z}_1^+\right)\mathrm{erf}\left(\mathcal{Z}_2^-, \mathcal{Z}_2^+\right) \tag{B·18}$$

by taking the limits at the stationary points for all deformations, except in a small region near the spherical shape. In this way, we obtain the simple results (3·30). The arguments of the error functions are given by (3·19) or (3·20) for $\mathcal{Z}_i^\pm$ $(i = 1, 2)$ and

$$\mathcal{Z}_\perp^\pm = \pm\frac{\pi}{2}\sqrt{-\frac{iJ_\perp^{\rm EQ}}{2\hbar}} = \pm\frac{\hbar(k\zeta)^2}{16}\sqrt{\frac{iF_z^{\rm EQ}}{M n_v k a \sin\phi\,\sigma^*(\sigma^*+1)\det K^{\rm EQ}}}. \tag{B·19}$$

The spherical limit is easily obtained by using the spherical action-angle variables $\{\Theta_\theta, \Theta_r, \Theta_\varphi; I_\theta, I_r, I_\varphi\}$. In these variables,

$$A_{\rm EQ} = \frac{1}{2}\sqrt{\frac{\sin^3\phi}{\pi M n_r k R \eta F_z}}\,\mathrm{erf}\left(\mathcal{Z}_\perp^-, \mathcal{Z}_\perp^+; \mathcal{Z}_\theta^-, \mathcal{Z}_\theta^+; \mathcal{Z}_\varphi^-, \mathcal{Z}_\varphi^+\right), \tag{B·20}$$

where $n_r \equiv n_v$ for the equatorial-plane orbits with (n_v, n_φ), and the invariant stability factor $F_\theta \equiv F_z^{\rm EQ}$ is given by (B·9):

$$\mathcal{Z}_\perp^\pm = \sqrt{\frac{-i\pi F_\theta^{\rm EQ}}{16 M n_r \hbar K_\theta^{\rm EQ}}}(z^\pm - z^*), \quad \mathcal{Z}_{\{\theta\atop\varphi\}}^\pm = \sqrt{-i\pi M n_r K_{\{\theta\atop\varphi\}}^{\rm EQ}/\hbar}\left(I_{\{\theta\atop\varphi\}}^\pm - I_{\{\theta\atop\varphi\}}^*\right). \tag{B·21}$$

The quantities $K_\theta^{\rm EQ}$ and $K_\varphi^{\rm EQ}$, given by

$$K_{\{\theta\atop\varphi\}}^{\rm EQ} = \left(\frac{\partial^2 I_r}{\partial I_{\{\theta\atop\varphi\}}^2}\right)_{\rm EQ}, \tag{B·22}$$

are the curvatures of the energy surface $\varepsilon = H(I_\theta, I_r, I_\varphi)$ in the spherical coordinate system. In that system, the maximum value of I_φ is equal to the absolute value of the classical angular momentum I_θ, $I_\varphi^\pm = \pm I_\theta$, I_θ^+ being the maximum value of $|I_\theta|$, and $I_\theta^- = 0$. We note that for the diametric orbits, the stationary points I_θ^* and I_φ^* are exactly zero and there are also specific integration limits in Eq. (B·20). In this case, the internal integral over I_φ within a small region can be evaluated approximately as $2I_\theta$, and we obtain for the "triple" error function,

$$\mathrm{erf}\left(\mathcal{Z}_\perp^-, \mathcal{Z}_\perp^+; \mathcal{Z}_\theta^-, \mathcal{Z}_\theta^+; \mathcal{Z}_\varphi^-, \mathcal{Z}_\varphi^+\right) \to \sqrt{\frac{-4iF_z}{M\pi^2 n_r \hbar K_\theta^{\rm EQ}}} = \sqrt{\frac{-4iF_z k R}{2\pi M}}. \tag{B·23}$$

Here, we have used the fact that in the spherical limit, $F_z \to 0$, the integral over $\mathcal{Z}_\theta$ can be approximated by the upper limit $\mathcal{Z}_\theta^+$ given by Eq. (B·21). We also omitted the strong oscillating value of $\int dz^2 e^{-z^2}$ at the upper limit, because it vanishes after any small averaging over kR and equals 1 in this approximation. We also accounted for the fact that $K_\theta^{\rm EQ} \to 1/(\pi pR)$ for the diameters (see Eq. (B·22) and note that $\phi = \pi/2$ for the diameters). Finally, the stability factor F_z is canceled, and we obtain the Balian-Bloch result (3·33) for the contribution of the diametric orbits in the spherical cavity.[3)]

For all other EQPO there are the stationary points $I_\varphi^* = I_\theta^* \neq 0$, and I_φ is identical to its maximum value I_θ in the spherical limit. This is the reason that there is no next order $(1/\sqrt{kR})$ corrections to the Balian-Bloch trace formula for the contribution of the planar orbits with $n_r \geq 3$. The latter comes from the spherical limit of the elliptic orbits in the meridian plane (3·16) (see Ref. 9)).

Appendix C
Separatrix

As in the case of the turning points,[39),41)–43)] we first expand the exponent phase in Eq. (3·6) with respect to I'_u:

$$S_\alpha\left(\boldsymbol{I}', \boldsymbol{I}'', t_\alpha\right) - \left(\boldsymbol{I}'' - \boldsymbol{I}'\right) \cdot \boldsymbol{\Theta}'' = c_0^{\parallel} + c_1^{\parallel} x + c_2^{\parallel} x^2 + c_3^{\parallel} x^3 + \cdots \equiv \tau_0^{\parallel} + \tau_1^{\parallel} z + \frac{1}{3} z^3. \tag{C·1}$$

Here,

$$x = \frac{1}{\hbar}\left(I'_u - I_u'^{\,*}\right), \tag{C·2}$$

$$c_0^{\parallel} = \frac{1}{\hbar}\left[S_\alpha^*\left(\boldsymbol{I}', \boldsymbol{I}'', \varepsilon\right) - \left(\boldsymbol{I}' - \boldsymbol{I}''\right)^* \cdot \boldsymbol{\Theta}''^*\right] = \frac{1}{\hbar} S_\alpha^*\left(\boldsymbol{\Theta}', \boldsymbol{\Theta}'', \varepsilon\right), \tag{C·3}$$

$$c_1^{\parallel} = \left(\frac{\partial S_\alpha}{\partial I'_u} - \Theta''_u\right)^* = \Theta'_u - \Theta''_u \to 0, \qquad \sigma_1 \to 1, \tag{C·4}$$

$$c_2^{\parallel} = \frac{\hbar}{2}\left(\frac{\partial^2 S_\alpha}{\partial I_u'^{\,2}}\right)^* = 2p\zeta M \hbar \tilde{K}_u^\alpha \to \infty, \qquad \sigma_1 \to 1, \tag{C·5}$$

$$c_3^{\parallel} = \frac{\hbar^3}{6}\left(\frac{\partial^3 S_\alpha}{\partial I_u'^{\,3}}\right)^* = \frac{2\pi^3 \hbar^2 M}{3(p\zeta^2)^2}\left(\frac{\partial \tilde{K}_u^\alpha}{\partial \tilde{I}_u}\right) < 0, \quad \sigma_\parallel \to 1, \tag{C·6}$$

where the superscript asterisk indicates the value at $I'_u = I''_u = I_u^*$. The asymptotic behavior of the constants $c_i^{\parallel}$ near the separatrix $\sigma_1 \approx 1$ is found from

$$\tilde{K}_u^\alpha \to \frac{\log\left[(1+\sin\theta)/(1-\sin\theta)\right]}{(\sigma_1 - 1)\log^3(\sigma_1 - 1)}, \qquad \sigma_1 \to 1, \tag{C·7}$$

and with $\theta \to \theta_h(\eta)$ [see Eq. (2·6)],

$$\frac{\partial \tilde{K}_u^\alpha}{\partial \tilde{I}_u} \to -\frac{2\log\left[(1+\sin\theta)/(1-\sin\theta)\right]}{\left((\sigma_1 - 1)\log^2(\sigma_1 - 1)\right)^2}, \qquad \sigma_1 \to 1. \tag{C·8}$$

The rightmost part of Eq. (C·1) is obtained using a linear transformation with some constants α and β:

$$x = \alpha z + \beta, \qquad \alpha = \left(3c_3^{\|}\right)^{-1/3}, \qquad \beta = -c_2^{\|}/(3c_3^{\|}), \tag{C·9}$$

$$\tau_0^{\|} = \left(c_0 - c_1c_2/(3c_3) + 2c_2^3/(27c_3^2)\right)^{\|}, \qquad \tau_1^{\|} = \alpha\left[c_1 - c_2^2/(3c_3)\right]^{\|}. \tag{C·10}$$

Near the stationary point for $\sigma_1 \to 1$, we obtain $c_1^{\|} \to 0$ and $\tau_1^{\|} \to -w^{\|}$, with the positive quantity

$$w^{\|} = \left(\frac{c_2^2}{(3c_3)^{4/3}}\right)^{\|} \to \left|\frac{M\log\left[(1+\sin\theta)/(1-\sin\theta)\right](\sigma_1-1)}{\hbar\log(\sigma_1-1)}\right|^{2/3}. \tag{C·11}$$

Using expansion (C·1) in Eq. (3·6) and evaluating the integral over Θ_v'' exactly (i.e., obtaining a factor of 2π for this integral), we obtain

$$\begin{aligned}
\delta g_{\rm LD}^{(0)} &= -\frac{2}{2\pi\hbar^2}\,{\rm Re}\sum_\alpha \int d\Theta_\varphi'' \int dI_\varphi' \int d\Theta_u'' \frac{1}{|\omega_v^*|} e^{i\left(\tau_0^{\|} - \frac{\pi}{2}\nu_\alpha\right)} \\
&\quad \times \sqrt{\frac{\sqrt{w^{\|}}}{c_2^{\|}}}\left[{\rm Ai}\left(-w^{\|}, \mathcal{Z}_{\|}^-, \mathcal{Z}_{\|}^+\right) + i\,{\rm Gi}\left(-w^{\|}, \mathcal{Z}_{\|}^-, \mathcal{Z}_{\|}^+\right)\right] \\
&\approx -\frac{2}{\hbar}\,{\rm Re}\sum_\alpha \int d\Theta_u'' \frac{1}{|\omega_v^*|}\sqrt{\frac{\sqrt{w^{\|}}}{c_2^{\|}}}\left[{\rm Ai}\left(-w^{\|}\right) + i\,{\rm Gi}\left(-w^{\|}\right)\right] e^{i\left(\tau_0^{\|} - \frac{\pi}{2}\nu_\alpha\right)},
\end{aligned} \tag{C·12}$$

where

$$\mathcal{Z}_{\|}^- = \sqrt{w^{\|}}, \qquad \mathcal{Z}_{\|}^+ = \sqrt{\frac{c_2^{\|}}{\sqrt{w^{\|}}}}\frac{I_u^{\rm (cr)}}{\hbar} + \sqrt{w^{\|}}. \tag{C·13}$$

Here, ${\rm Ai}(-w, z_1, z_2)$ and ${\rm Gi}(-w, z_1, z_2)$ are the incomplete Airy and Gairy functions defined by

$$\left\{\begin{matrix}{\rm Ai}\\ {\rm Gi}\end{matrix}\right\}(-w, z_1, z_2) = \frac{1}{\pi}\int_{z_1}^{z_2} dz\,\left\{\begin{matrix}\cos\\ \sin\end{matrix}\right\}\left(-wz + \frac{z^3}{3}\right), \tag{C·14}$$

${\rm Ai}(-w)$ and ${\rm Gi}(-w)$ are the corresponding standard complete functions, and $I_u^{\rm (cr)} = I_u(\sigma_1^{\rm (cr)}, \sigma_1^{\rm (cr)})$ is the "creeping" elliptic 2DPO value defined in §2. In the second equality of (C·12), we have used

$$\begin{aligned}
&\mathcal{Z}_{\|}^- \to 0, \\
&\mathcal{Z}_{\|}^+ \to 4\left[\frac{M\log\left[(1+\sin\theta)/(1-\sin\theta)\right]p\zeta}{2(\sigma_1-1)^2\log^4(\sigma_1-1)}\right]^{1/3}\left[\frac{\eta}{\sqrt{\eta^2-1}}{\rm E}\left(\frac{\sqrt{\eta^2-1}}{\eta}\right) - 1\right] \\
&\qquad \to \infty,
\end{aligned} \tag{C·15}$$

for any finite deformation η and large kR near the separatrix ($\sigma_1 \to 1$). Using an analogous expansion of the action $\tau_0^{\parallel}$ in (C·12) with respect to the angle Θ_u'' to third order and a linear transformation like (C·9), we arrive at

$$\begin{aligned}\delta g_{\rm LD}^{(0)}(\varepsilon) = {} & \frac{b}{2\varepsilon_0 \pi^2 R\hbar}\,{\rm Re}\sum_\alpha \int d\Theta_\varphi'' \int dI_\varphi' \frac{1}{kR}\frac{\left(w^{\parallel}w^{\perp}\right)^{1/4}}{\sqrt{|c_2^{\parallel}c_2^{\perp}|}} \\ & \times \left[{\rm Ai}\left(-w^{\parallel}\right) + i\,{\rm Gi}\left(-w^{\parallel}\right)\right]\left[{\rm Ai}\left(-w^{\perp},\mathcal{Z}_{\perp}^{-},\mathcal{Z}_{\perp}^{+}\right) + i\,{\rm Gi}\left(-w^{\perp},\mathcal{Z}_{\perp}^{-},\mathcal{Z}_{\perp}^{+}\right)\right] \\ & \times \exp\left\{\frac{i}{\hbar}\left[S_\alpha^*\left(\boldsymbol{I}',\boldsymbol{I}'',\varepsilon\right) - \left(\boldsymbol{I}'-\boldsymbol{I}''\right)^*\cdot\boldsymbol{\Theta}''^*\right]\right. \\ & \left. + \frac{2i}{3}\left[(w^{\parallel})^{3/2} + (w^{\perp})^{3/2}\right] - i\frac{\pi}{2}\nu_\alpha\right\}, \end{aligned} \tag{C·16}$$

where

$$w^{\perp} = \left(\frac{c_2^2}{(3c_3)^{4/3}}\right)^{\perp} \;>\; 0, \tag{C·17}$$

$$\mathcal{Z}_{\perp}^{-} = \sqrt{w^{\perp}}, \qquad \mathcal{Z}_{\perp}^{+} = \frac{\pi}{2}\left|3c_3^{\perp}\right|^{1/3} + \sqrt{w^{\perp}}, \tag{C·18}$$

$$c_2^{\perp} = \frac{1}{2\hbar}\left(J_{u,\alpha}^{\perp}\right)^* = \left(\frac{\partial^2 S_\alpha}{\partial\Theta_u'^{\,2}} + 2\frac{\partial^2 S_\alpha}{\partial\Theta_u'\partial\Theta_u''} + \frac{\partial^2 S_\alpha}{\partial\Theta_u''^{\,2}}\right)_{\rm LD}^{*} = -\frac{F_{xy}^{\rm LD}}{2\pi M K_u^{\alpha}}. \tag{C·19}$$

Here, $F_{xy}^{\rm LD}$ is the stability factor for long diameters,

$$F_{xy}^{\rm LD} = -4\sinh^2\left[M\,{\rm arccosh}\left(2\eta^2-1\right)\right]\ , \tag{C·20}$$

$$\begin{aligned} c_3^{\perp} &= \frac{1}{6\hbar}\left[\frac{\partial^3 S_\alpha}{\partial\Theta_u'^{\,3}} + 3\frac{\partial^3 S_\alpha}{\partial\Theta_u'^{\,2}\partial\Theta_u''} + 3\frac{\partial^3 S_\alpha}{\partial\Theta_u'\partial\Theta_u''^{2}} + \frac{\partial^3 S_\alpha}{\partial\Theta_u''^{3}}\right]^* \\ &= \frac{1}{6\hbar}\left[\frac{\partial J_{u,\alpha}^{\perp}}{\partial\Theta_u'} + \frac{\partial J_{u,\alpha}^{\perp}}{\partial\Theta_u''}\right]^* \;<\; 0\,. \end{aligned} \tag{C·21}$$

Note that according to (C·19), the quantity $c_2^{\perp}$ approaches zero near the separatrix ($\sigma_1 \to 1$) as in the caustic case. This is the reason that we apply the Maslov-Fedoryuk theory[39),41)–43)] for the transformation of the integral over the angle Θ_u'' from (C·12) to (C·16). The remaining two integrals over the azimuthal variables (I_φ' and Θ_φ'') can be calculated in a manner similar to that explained in the text.

The divergence of the curvature K_φ, Eq. (B·13), for the long diameters ($\sigma_1 \to 1$, $\sigma_2 \to 0$) can be easily seen from the following expression, valid for any polygon orbit with a vertex on the symmetry axis:

$$K_\varphi^{\beta} = \frac{L_0 c}{\rho_0^2 n_v M\hbar}\left[\frac{2\eta^2}{1+\eta^2\tan^2\psi} - 1\right]. \tag{C·22}$$

Here, L_0 denotes the length of the side having a vertex at the pole, ρ_0 the cylindrical coordinate of the other end of this side, and ψ the angle between this side and the symmetry axis. For the long diameters, $L_0 \to 2bM$, $\rho_0 \to 0$ and $\psi \to 0$, so that $K_\varphi^{\beta} \to \infty$.

Appendix D
Derivation of the Third-Order Term

D.1. *Third-order curvatures*

For the curvature $K_1^{(3)}$, which appears in the third-order terms in the expansion of the action $S/\hbar$ with respect to σ_1, we obtain

$$\tilde{K}_1^{(3)} = \frac{\pi}{p\zeta} K_1^{(3)} = \frac{\partial^3 \tilde{I}_v}{\partial \sigma_1^3} + \frac{n_u}{n_v} \frac{\partial^3 \tilde{I}_u}{\partial \sigma_1^3}, \tag{D·1}$$

where

$$\begin{aligned} \frac{\partial^3 \tilde{I}_v}{\partial \sigma_1^3} &= -\frac{1}{4z_+^3} \left[\frac{\partial B_v}{\partial \sigma_1} + 6z_+ \frac{\partial z_+^2}{\partial \sigma_1} \frac{\partial^2 \tilde{I}_v}{\partial \sigma_1^2} \right], \\ \frac{\partial^3 \tilde{I}_u}{\partial \sigma_1^3} &= \frac{1}{2z_+^3} \left[\frac{\partial B_u}{\partial \sigma_1} - 3z_+ \frac{\partial z_+^2}{\partial \sigma_1} \frac{\partial^2 \tilde{I}_u}{\partial \sigma_1^2} \right], \end{aligned} \tag{D·2}$$

$$B_v = \left[\Pi(\varphi, k^2, k) - \mathrm{F}(\varphi, k) \right] \tilde{\partial}_k - \frac{\partial z_+^2}{\partial \sigma_1} \mathrm{F}(\varphi, k) + \frac{2z_+^2}{\Delta_\varphi} \frac{\partial \varphi}{\partial \sigma_1}, \tag{D·3}$$

$$\begin{aligned} B_u &= \left[\Pi(k^2, k) - \mathrm{F}(k) \right] \tilde{\partial}_k - \frac{\partial z_+^2}{\partial \sigma_1} \mathrm{F}(k), \\ \tilde{\partial}_k &= \frac{z_+^2}{k^2} \frac{\partial k^2}{\partial \sigma_1} = \frac{1}{k^2} \frac{\partial z_-^2}{\partial \sigma_1} - \frac{\partial z_+^2}{\partial \sigma_1}, \end{aligned} \tag{D·4}$$

with the derivatives

$$\begin{aligned} \frac{\partial B_u}{\partial \sigma_1} &= k \left[\frac{\partial \Pi(k^2, k)}{\partial \partial k} - \frac{\partial \mathrm{F}(k)}{\partial k} \right] \frac{\tilde{\partial}_k^2}{2z_+^2} + \left[\Pi(k^2, k) - \mathrm{F}(k) \right] \left[-\frac{\tilde{\partial}_k}{z_-^2} \frac{\partial z_-^2}{\partial \sigma_1} \right. \\ &\quad \left. + \frac{1}{k^2} \frac{\partial^2 z_-^2}{\partial \sigma_1^2} - \frac{\partial^2 z_+^2}{\partial \sigma_1^2} \right] - k \frac{\partial \mathrm{F}(k)}{\partial k} \frac{\tilde{\partial}_k}{2z_+^2} \frac{\partial z_+^2}{\partial \sigma_1} - \frac{\partial^2 z_+^2}{\partial \sigma_1^2} \mathrm{F}(k), \\ \frac{\partial^2 z_\pm^2}{\partial \sigma_1^2} &= \pm \frac{2\sigma_2}{\left[(\sigma_1 - 1)^2 + 4\sigma_2 \right]^{3/2}}, \end{aligned} \tag{D·5}$$

$$\begin{aligned} \frac{\partial B_v}{\partial \sigma_1} &= \tilde{\partial}_k \left[\frac{\partial \Pi(\varphi, k^2, k)}{\partial \sigma_1} - \frac{\partial \mathrm{F}(\varphi, k)}{\partial \sigma_1} + \left(1 - \frac{1}{z_-^2} \frac{\partial z_-^2}{\partial \sigma_1} \right) \right] - \frac{\partial^2 z_+^2}{\partial \sigma_1^2} \mathrm{F}(\varphi, k) \\ &\quad - \frac{\partial z_-^2}{\partial \sigma_1} \frac{\partial \mathrm{F}(\varphi, k)}{\partial \sigma_1} + \frac{1}{\Delta_\varphi} \left[\left(2 \frac{\partial z_+^2}{\partial \sigma_1} - \frac{z_+^2}{\Delta_\varphi^2} \frac{\partial \Delta_\varphi^2}{\partial \sigma_1} \right) \frac{\partial \varphi}{\partial \sigma_1} + 2z_+^2 \frac{\partial^2 \varphi}{\partial \sigma_1^2} \right]. \end{aligned} \tag{D·6}$$

Here,

$$\frac{\partial \Pi(k^2, k)}{\partial k} = \frac{k^2 \tilde{\partial}_k}{k_1^2 z_+^2} \left[\Pi(k^2, k) + \frac{1}{2k^2} \left(\mathrm{E}(k) - \mathrm{F}(k) \right) \right], \tag{D·7}$$

$$\frac{\partial \mathrm{F}(k)}{\partial k} = \frac{1}{k}\left[\Pi(k^2,k) - \mathrm{F}(k)\right], \tag{D·8}$$

$$\frac{\partial \Pi(\varphi,k^2,k)}{\partial \sigma_1} = \frac{1}{k_1^2}\left[\frac{k^2\tilde{\partial}_k}{z_+^2}\left\{\Pi(\varphi,k^2,k) + \frac{1}{2k^2}\left(\mathrm{E}(\varphi,k) - \mathrm{F}(\varphi,k)\right)\right.\right.$$
$$\left.\left. - \frac{\sin(2\varphi)}{4\Delta_\varphi^3}\left(1+\Delta_\varphi^2\right)\right\} + \Delta_\varphi \frac{\partial \varphi}{\partial \sigma_1}\left\{1 - \frac{k^2}{4\Delta_\varphi^4}\left[4\Delta_\varphi^2\cos(2\varphi) + k^2\sin^2(2\varphi)\right]\right\}\right], \tag{D·9}$$

$$\frac{\partial \mathrm{F}(\varphi,k)}{\partial \sigma_1} = \frac{\tilde{\partial}_k}{2z_+^2}\left[\Pi(\varphi,k^2,k) - \mathrm{F}(\varphi,k)\right] + \frac{1}{\Delta_\varphi}\frac{\partial \varphi}{\partial \sigma_1}, \tag{D·10}$$

$$\frac{\partial^2 \varphi}{\partial \sigma_1^2} = \frac{1}{\sin(2\varphi)}\left\{\frac{1}{\left(z_b^2 - z_-^2\right)^3}\left[\left(\frac{\partial^2 z_-^2}{\partial \sigma_1^2}\left(z_b^2 - z_+^2\right) - \frac{\partial^2 z_+^2}{\partial \sigma_1^2}\left(z_b^2 - z_-^2\right)\right)\right.\right.$$
$$\left.\left. + 2\frac{\partial z_-^2}{\partial \sigma_1}\left(\frac{\partial z_-^2}{\partial \sigma_1}\left(z_b^2 - z_+^2\right) - \frac{\partial z_+^2}{\partial \sigma_1}\left(z_b^2 - z_-^2\right)\right)\right] - 2\cos(2\varphi)\left(\frac{\partial \varphi}{\partial \sigma_1}\right)^2\right\}, \tag{D·11}$$

$$\frac{\partial \Delta_\varphi^2}{\partial \sigma_1} = -k^2\left[\frac{\tilde{\partial}_k}{z_+^2}\sin^2\varphi + \sin(2\varphi)\frac{\partial \varphi}{\partial \sigma_1}\right]. \tag{D·12}$$

D.2. *Stationary phase method with third-order expansions*

After the expansion of the action in the Poisson-sum trace formula (3·10) up to second order with respect to σ_2 and up to third order with respect to σ_1, we obtain

$$\delta g^{(2)}(\varepsilon) = \frac{k\zeta^2}{4\pi^2 R\varepsilon_0}\,\mathrm{Re}\sum_\beta \frac{L_\beta}{M n_v R\sqrt{\sigma_2^*}}\left(\frac{\partial \tilde{I}_u}{\partial \sigma_1}\right)^* \exp\left(ikL_\beta - i\frac{\pi}{2}\nu_\beta\right)$$
$$\times \int_0^{\sigma_2^+} d\sigma_2 \int_{x^-}^{x^+} dx\, \exp\left[ik\zeta M n_v \tilde{K}_{22}\left(\sigma_2 - \sigma_2^* + \frac{K_{12}}{K_{22}}(\sigma_1 - \sigma_1^*)\right)^2\right.$$
$$\left. + i\left(c_1 x + c_2 x^2 + c_3 x^3\right)\right], \tag{D·13}$$

where

$$c_1 \to 0, \quad c_2 = k\zeta M n_v \frac{\det \tilde{K}}{\tilde{K}_{22}}, \quad c_3 = \frac{1}{3}k\zeta M n_v \tilde{K}_1^{(3)}, \tag{D·14}$$

$$x = \sigma_1 - \sigma_1^*, \quad x^\pm = \sigma_1^\pm - \sigma_1^*. \tag{D·15}$$

After transformation from σ_2 to the new variable $\mathcal{Z}_2$, defined by

$$\mathcal{Z}_2 = \sqrt{-ik\zeta M n_v \tilde{K}_{22}}\left(\sigma_2 - \sigma_2^* + \frac{K_{12}}{K_{22}}(\sigma_1 - \sigma_1^*)\right), \tag{D·16}$$

and a linear transformation from x to z through

$$x = q_1 z + q_2, \quad \text{with} \quad q_1 = (3c_3)^{-1/3}, \quad q_2 = -\frac{c_2}{3c_3}, \tag{D·17}$$

we obtain Eq. (3·15) with the ISPM3 amplitude

$$A_{3\mathrm{D}}^{(2)}(\varepsilon) = \frac{L_\beta}{8Mn_vR\left(k\zeta Mn_v\tilde{K}_1^{(3)}\right)^{1/3}}\sqrt{\frac{ik\zeta^3}{\pi Mn_vR^2\tilde{K}_{22}\sigma_2^*}}\left(\frac{\partial\tilde{I}_u}{\partial\sigma_1}\right)^*\exp\left(\frac{2}{3}i\tau^{3/2}\right)$$
$$\times\,\mathrm{erf}\left(\mathcal{Z}_2^-,\mathcal{Z}_2^+\right)\left[\mathrm{Ai}\left(-\tau,z_-,z_+\right)+i\,\mathrm{Gi}\left(-\tau,z_-,z_+\right)\right]. \qquad \text{(D·18)}$$

Here, $\mathcal{Z}_2^\pm$ is defined by Eq. (3·20b), and

$$\tau = (3c_3)^{-1/3}\left(\frac{c_2^2}{3c_3}-c_1\right), \quad z_\pm = \frac{x^\pm - q_2}{q_1}. \qquad \text{(D·19)}$$

In the limit $c_1 \to 0$, we obtain

$$\tau = \frac{c_2^2}{(3c_3)^{4/3}} = \frac{(k\zeta Mn_v)^{2/3}(\det\tilde{K}/\tilde{K}_{22})^2}{\left(\tilde{K}_1^{(3)}\right)^{4/3}}. \qquad \text{(D·20)}$$

For finite curvatures far from the bifurcations, the limits of the Airy and Gairy functions can be extended as $z_- \to 0$ and $z_+ \to \infty$, yielding the complete Airy $\mathrm{Ai}(-\tau)$ and Gairy $\mathrm{Gi}(-\tau)$ functions. Then, using the asymptotic forms of these functions for large $\tau \propto (kR)^{2/3}$ (large kR),

$$\left\{\begin{matrix}\mathrm{Ai}\\ \mathrm{Gi}\end{matrix}\right\}(-\tau) \sim \frac{1}{\sqrt{\pi}\tau^{1/4}}\left\{\begin{matrix}\sin\\ \cos\end{matrix}\right\}\left(\frac{2}{3}\tau^{3/2}+\frac{\pi}{4}\right), \qquad \text{(D·21)}$$

and that of the erf-function given in Eq. (D·18), we obtain the SSPM limit, (3·21).

References

1) M. C. Gutzwiller, J. Math. Phys. **12** (1971), 343; and earlier references quoted therein.
2) M. C. Gutzwiller, *Chaos in Classical and Quantum Mechanics* (Springer-Verlag, New York, 1990).
3) R. B. Balian and C. Bloch, Ann. of Phys. **69** (1972), 76.
4) V. M. Strutinsky, Nukleonika **20** (1975), 679.
   V. M. Strutinsky and A. G. Magner, Sov. Phys. Part. Nucl. **7** (1977), 138.
5) M. V. Berry and M. Tabor, Proc. Roy. Soc. London A **349** (1976), 101.
6) M. V. Berry and M. Tabor, J. of Phys. A **10** (1977), 371.
7) S. C. Creagh and R. G. Littlejohn, Phys. Rev. A **44** (1990), 836; J. of Phys. A **25** (1992), 1643.
8) V. M. Strutinsky, A. G. Magner, S. R. Ofengenden and T. Døssing, Z. Phys. A **283** (1977), 269.
9) A. G. Magner, S. N. Fedotkin, F. A. Ivanyuk, P. Meier, M. Brack, S. M. Reimann and H. Koizumi, Ann. of Phys. **6** (1997), 555.
   A. G. Magner, S. N. Fedotkin, F. A. Ivanyuk, P. Meier and M. Brack, Czech. J. of Phys. **48** (1998), 845.
10) M. Brack and R. K. Bhaduri, *Semiclassical Physics* (Addison-Wesley, 1997).
11) H. Frisk, Nucl. Phys. A **511** (1990), 309.
12) K. Arita and K. Matsuyanagi, Nucl. Phys. A **592** (1995), 9.
13) M. Brack, S. M. Reimann and M. Sieber, Phys. Rev. Lett. **79** (1997), 1817.
    M. Brack, P. Meier, S. M. Riemann and M. Sieber, in *Similarities and Differences between Atomic Nuclei and Clusters*, ed. Y. Abe et al. (AIP, New York, 1998), p. 17.
14) H. Nishioka, K. Hansen and B. R. Mottelson, Phys. Rev. B **42** (1990), 9377.

15) M. Brack, S. Creag, P. Meier, S. Reimann and M. Seidl, in *Large Cluster of Atoms and Molecules*, ed. T. P. Martin (Kluwer, Dordrecht, 1996), p. 1.
M. Brack, J. Blaschke, S. C. Creag, A. G. Magner, P. Meier and S. M. Reimann, Z. Phys. D **40** (1997), 276.
16) S. Frauendorf, V. M. Kolomietz, A. G. Magner and A. I. Sanzhur, Phys. Rev. B **58** (1998), 5622.
17) S. M. Reimann, M. Persson, P. E. Lindelof and M. Brack, Z. Phys. B **101** (1996), 377.
18) J. Ma and K. Nakamura, Phys. Rev. B **60** (1999), 10676; ibid. **60** (1999), 11611.
19) J. Blaschke and M. Brack, Europhys. Lett. **50** (2000), 294.
20) J. Ma and K. Nakamura, Phys. Rev. B **62** (2000), 13552.
21) J. Ma and K. Nakamura, cond-mat/0108276, submitted to Phys. Rev. Lett.
22) A. Sugita, K. Arita and K. Matsuyanagi, Prog. Theor. Phys. **100** (1998), 597.
23) K. Arita, A. Sugita and K. Matsuyanagi, Prog. Theor. Phys. **100** (1998), 1223.
24) A. G. Magner, S. N. Fedotkin, K. Arita, K. Matsuyanagi and M. Brack, Phys. Rev. E **63** (2001), 065201(R).
25) H. Nishioka, M. Ohta and S. Okai, Mem. Konan Univ. Sci. Ser. **38** (2) (1991), 1 (unpublished).
26) H. Nishioka, N. Nitanda, M. Ohta and S. Okai, Mem. Konan Univ. Sci. Ser. **39** (2) (1992), 67 (unpublished).
27) K. Arita, A. Sugita and K. Matsuyanagi, *Proc. Int. Conf. on "Atomic Nuclei and Metallic Clusters", Prague, 1997*, Czech. J. of Phys. **48** (1998), 821.
28) A. G. Magner, S. N. Fedotkin, K. Arita, K. Matsuyanagi, T. Misu, T. Schachner and M. Brack, Prog. Theor. Phys. **102** (1999), 551.
29) S. C. Creagh, Ann. of Phys. **248** (1997), 60.
30) S. Tomsovic, M. Grinberg and D. Ullmo, Phys. Rev. Lett. **75** (1995), 4346.
D. Ullmo, M. Grinberg and S. Tomsovic, Phys. Rev. E **54** (1996), 136.
31) M. Sieber, J. of Phys. A **30** (1997), 4563.
32) P. J. Richens, J. of Phys. A **15** (1982), 2110.
33) P. Meier, M. Brack and C. Creagh, Z. Phys. D **41** (1997), 281.
34) H. Waalkens, J. Wiersig and H. R. Dullin, Ann. of Phys. **260** (1997), 50.
35) M. Sieber, J. of Phys. A **29** (1996), 4715.
36) H. Schomerus and M. Sieber, J. of Phys. A **30** (1997), 4537.
M. Sieber and H. Schomerus, J. of Phys. A **31** (1998), 165.
37) M. Brack, P. Meier and K. Tanaka, J. of Phys. A **32** (1999), 331.
38) C. Chester, B. Friedmann and F. Ursell, Proc. Cambridge Philos. Soc. **53** (1957), 599.
39) M. V. Fedoryuk, Sov. J. of Comp. Math. and Math. Phys. **4** (1964), 671; ibid. **10** (1970), 286.
40) A. D. Bruno, preprint Inst. Prikl. Mat. Akad. Nauk SSSR Moskva (1970), 44 (in Russian).
41) V. P. Maslov, Theor. Math. Phys. **2** (1970), 30.
42) M. V. Fedoryuk, *Saddle-point method* (Nauka, Moscow, 1977, in Russian).
43) M. V. Fedoryuk, *Asymptotics: Integrals and sums* (Nauka, Moscow, 1987, in Russian).
44) V. M. Strutinsky, Nucl. Phys. A **122** (1968), 1; and earlier references quoted therein.
45) M. Brack et al., Rev. Mod. Phys. **44** (1972), 320.
46) M. Abramowitz and I. A. Stegun, *Handbook of mathematical functions* (Dover publications INC., New York, 1964).
47) Paul F. Byrd and Morris D. Friedman, *Handbook of Elliptic Integrals for Engineers and Scientists* (Springer-Verlag, 1971).
48) L. D. Landau and E. M. Lifshits, *Theoretical Physics, Vol. 1, Classical mechanics* (Nauka, Moscow, 1973, in Russian).
49) I. S. Gradshteyn and I. M. Ryzhik, *Tables of integrals, series, and products, 6th ed.* (Academic Press, 2000).
50) T. Mukhopadhyay and S. Pal, Nucl. Phys. A **592** (1995), 291.

Progress of Theoretical Physics, Vol. 110, No. 1, July 2003

Application of the Adiabatic Self-Consistent Collective Coordinate Method to a Solvable Model of Prolate-Oblate Shape Coexistence

Masato KOBAYASI,[1] Takashi NAKATSUKASA,[2] Masayuki MATSUO[3] and Kenichi MATSUYANAGI[1]

[1]*Department of Physics, Graduate School of Science, Kyoto University, Kyoto 606-8502, Japan*
[2]*Physics Department, Tohoku University, Sendai 980-8578, Japan*
[3]*Graduate School of Science and Technology, Niigata University, Niigata 950-2181, Japan*

(Received April 16, 2003)

The adiabatic self-consistent collective coordinate method is applied to an exactly solvable multi-$O(4)$ model that is designed to describe nuclear shape coexistence phenomena. The collective mass and dynamics of large amplitude collective motion in this model system are analyzed, and it is shown that the method yields a faithful description of tunneling motion through a barrier between the prolate and oblate local minima in the collective potential. The emergence of the doublet pattern is clearly described.

§1. Introduction

The microscopic description of large amplitude collective motion in nuclei is a long-standing fundamental subject of study in nuclear structure physics.[1),2)] In spite of the steady development of various theoretical concepts and their mathematical formulations, the application of microscopic many-body theory to actual nuclear phenomena still remains a challenging problem[3)–30)] (see Ref. 31) for a recent comprehensive review). Shape coexistence phenomena are typical examples of large amplitude collective motion in nuclei and have been investigated from various points of view.[32)–45)] For instance, even in typical spherical nuclei, like Pb and Sn isotopes, excited deformed states have been systematically observed in low-energy regions,[32)] and the coexistence of prolate, spherical and oblate shapes has been recently reported for ^{186}Pb and ^{188}Pb.[38)] As another example, we mention a recent discovery of two rotational bands in ^{68}Se, which are associated with oblate and prolate intrinsic shapes.[39)] These are only a few examples among abundant experimental data. These data clearly reveal the need to further development of a theory that is better able to describe them and to re-examine the present theoretical understanding of nuclear structure. From the viewpoint of microscopic mean-field theory, the existence of these phenomena implies that different solutions of the Hartree-Fock-Bogoliubov (HFB) equations (local minima in the deformation energy surface) appear in the same energy region and that the nucleus exhibits large amplitude collective motion connecting these different equilibrium points. The identities and mixings of these different shapes are determined by the dynamics of such collective motion.

The self-consistent collective coordinate (SCC) method, which is based on the time-dependent Hartree-Fock (TDHF) theory, has been proposed as a microscopic theory of such large amplitude collective motion.[9] This theory was extended to the case of time-dependent HFB (TDHFB) including pairing correlations,[20] and has been successfully applied to various kinds of anharmonic vibration and high-spin rotational motions.[46)–57)] In order to apply this method to shape coexistence phenomena, however, we need to develop the theory further, because the well-known method of solving the basic equations of the SCC method (the η-expansion method[9]) assumes a single local minima, whereas, in fact, several local minima of the potential energy surface compete in these phenomena. Quite recently, a new method of solving the basic equations of the SCC method, the adiabatic SCC (ASCC) method, was proposed.[58] This new method uses an expansion in terms of the collective momentum and does not assume a single local minimum. Therefore it is believed to be suitable for the description of the shape coexistence phenomena. The ASCC method can also be regarded as a successor of the adiabatic TDHF (ATDHF) methods. It inherits the major merits of the ATDHF theory (as reviewed in Ref. 31)) and, in addition, enables us to include the pairing correlations self-consistently, removing the spurious number fluctuation modes.

The main purpose of this paper is to examine the feasibility of the ASCC method for application to actual nuclear phenomena. This is done by applying it to an exactly solvable model called the multi-$O(4)$ model and testing the results of the ASCC method against exact solutions obtained by diagonalizing the Hamiltonian in very large bases. This solvable model can be regarded as a simplified version of the well-known pairing-plus-quadrupole (P+Q) interaction model,[59),60)] because in this model, only the $K = 0$ component of the quadrupole deformation is considered in a schematic manner. This model has been widely used as a testing ground for various microscopic theories of nuclear collective motion.[61)–64)] The multi-$O(4)$ model possesses a symmetry with respect to the sign of the "quadrupole" deformation, which is analogous to the ordinary parity quantum number. Accordingly, it can be utilized as a simple model of many-body systems possessing double well structure in which large amplitude tunneling motion takes place through the barrier between two degenerate local minima of the potential (which correspond to the prolate and oblate shapes). Because of the special symmetry of the model, the "prolate" and "oblate" shapes mix completely. Of course, in contrast to ordinary parity, such an exact prolate-oblate symmetry does not exist in reality, and in this sense this solvable model is somewhat unrealistic. Nevertheless, this model provides an important test of the theory by examining its ability to describe the "parity doublet" pattern.

In this paper, we focus on the collective dynamics and the collective mass of large amplitude collective motion. It is known that the barrier penetration depends sensitively on the collective mass. A similar investigation of the collective dynamics of this model is reported in Ref. 27). In that work, the degree of freedom corresponding to the number fluctuation was explicitly removed from the model space. In the present approach, the spurious number fluctuation modes are automatically decoupled from the physical modes within the self-consistent framework of the TDHFB theory. This should be a great advantage when the method is applied to realistic

nuclear problems.

This paper is organized as follows. In §2, the basic equations of the ASCC method are presented. In §3, a brief account of the multi-$O(4)$ model is given. In §4, we apply the ASCC method to the multi-$O(4)$ model and derive explicit expressions necessary for numerical calculations. In §5, we present results of numerical analysis. Conclusions are given in §6.

§2. Basic equations of the ASCC method

In this section, instead of giving a general outline of the SCC method, we summarize its adiabatic version, formulated in Ref. 58). We assume that large amplitude collective motion is described by a set of TDHFB state vectors $|\phi(q,p,\varphi,N)\rangle$ that are parametrized by the single collective coordinate q, the collective momentum p conjugate to q, the particle number N, and the gauge angle φ conjugate to N. The time evolution of $|\phi(q,p,\varphi,N)\rangle$ is determined by the time-dependent variational principle

$$\delta \left\langle \phi(q,p,\varphi,N) \right| i\frac{\partial}{\partial t} - \hat{H} \left| \phi(q,p,\varphi,N) \right\rangle = 0. \tag{2·1}$$

As discussed in Ref. 58), we can set

$$|\phi(q,p,\varphi,N)\rangle = e^{-i\varphi\hat{N}} \left| \phi(q,p,N) \right\rangle . \tag{2·2}$$

Then, because the Hamiltonian $\hat{H}$ commutes with the number operator $\hat{N}$, the gauge angle φ is cyclic. The basic equations of the SCC method consist of (2·1), representing the invariance principle of the TDHFB equations, and the following equations for the state vectors $|\phi(q,p,N)\rangle$, representing the canonical variable condition:

$$\left\langle \phi(q,p,N) \right| i\frac{\partial}{\partial q} \left| \phi(q,p,N) \right\rangle = p, \tag{2·3a}$$

$$\left\langle \phi(q,p,N) \right| \frac{\partial}{i\partial p} \left| \phi(q,p,N) \right\rangle = 0, \tag{2·3b}$$

$$\left\langle \phi(q,p,N) \right| \hat{N} \left| \phi(q,p,N) \right\rangle = N, \tag{2·3c}$$

$$\left\langle \phi(q,p,N) \right| \frac{\partial}{i\partial N} \left| \phi(q,p,N) \right\rangle = 0. \tag{2·3d}$$

The third equation here guarantees that the particle number expectation value remains constant during the large amplitude collective motion described by the collective variables (q,p). Assuming that the large amplitude collective motion described by the collective variables (q,p) is slow, we now introduce the adiabatic approximation into the SCC method; that is, we expand the basic equations with respect to the collective momentum p. Because the particle number variable N is a momentum variable in the present formulation, we also expand the basic equations with respect to $n = N - N_0$ when we consider a system with particle number N_0. We then keep only the lowest-order term. The TDHFB state vectors are thus written

$$|\phi(q,p,N)\rangle = e^{ip\hat{Q}(q)+in\hat{\Theta}(q)}|\phi(q)\rangle, \tag{2·4}$$

where $\hat{Q}(q)$ and $\hat{\Theta}(q)$ are infinitesimal generators with respect to $|\phi(q)\rangle$. We also define an infinitesimal generator $\hat{P}(q)$ by

$$e^{-i\delta q\hat{P}(q)}|\phi(q)\rangle = |\phi(q+\delta q)\rangle. \tag{2·5}$$

We insert the TDHFB state vectors (2·4) into (2·1) and carry out an expansion with respect to p and n. Requiring that the time-dependent variational principle (the canonical variable condition) be satisfied up to second (first) order, we obtain the basic set of equations of the ASCC method to determine the infinitesimal generators $\hat{Q}(q)$ and $\hat{P}(q)$ as follows.

Canonical variable conditions:

$$\langle\phi(q)|\,[\hat{Q}(q),\hat{P}(q)]\,|\phi(q)\rangle = i, \tag{2·6a}$$
$$\langle\phi(q)|\,[\hat{\Theta}(q),\hat{N}]\,|\phi(q)\rangle = i. \tag{2·6b}$$

The other expectation values of commutators among the operators $\hat{Q}(q)$, $\hat{P}(q)$, $\hat{\Theta}(q)$ and $\hat{N}$ are zero.

HFB equation in the moving frame:

$$\delta\,\langle\phi(q)|\,\hat{H}_M(q)\,|\phi(q)\rangle = 0. \tag{2·7}$$

Here, $\hat{H}_M(q)$ is the Hamiltonian in the moving frame defined by

$$\hat{H}_M(q) = \hat{H} - \lambda(q)\hat{N} - \frac{\partial V}{\partial q}\hat{Q}(q). \tag{2·8}$$

Local harmonic equations:

$$\delta\,\langle\phi(q)|\,\big[\hat{H}_M(q),\hat{Q}(q)\big] - \frac{1}{i}B(q)\hat{P}(q)\,|\phi(q)\rangle = 0, \tag{2·9a}$$

$$\delta\,\langle\phi(q)|\,\Big[\hat{H}_M(q),\frac{1}{i}\hat{P}(q)\Big] - C(q)\hat{Q}(q) - \frac{1}{2B(q)}[[\hat{H}_M(q)\ ,\ (\hat{H}-\lambda(q)\hat{N})_A],\hat{Q}(q)] - \frac{\partial\lambda}{\partial q}\hat{N}\,|\phi(q)\rangle = 0. \tag{2·9b}$$

Here, the local stiffness $C(q)$ is defined by

$$C(q) = \frac{\partial^2 V}{\partial q^2} + \frac{1}{2B(q)}\frac{\partial B}{\partial q}\frac{\partial V}{\partial q}, \tag{2·10}$$

and $(\hat{H}-\lambda\hat{N})_A$ represents the $a^\dagger a^\dagger$ and aa parts of $(\hat{H}-\lambda\hat{N})$ containing two-quasiparticle creation and annihilation operators. The collective potential $V(q)$, the inverse mass $B(q)$, and the chemical potential $\lambda(q)$ are defined below. Equations (2·9a) and (2·9b) are linear with respect to the one-body operators $\hat{Q}(q)$ and $\hat{P}(q)$. They have essentially the same structure as the standard RPA equations, except for

the last two terms in Eq. (2·9b), which arise from the curvature term (derivative of the generator) and the particle number constraint, respectively. The infinitesimal generators $\hat{Q}(q)$ and $\hat{P}(q)$ are thus closely related to the harmonic normal modes locally defined for $|\phi(q)\rangle$ and the moving frame Hamiltonian $\hat{H}_M(q)$. The collective subspace defined by these equations is uniquely determined once a suitable boundary condition is specified.

The collective Hamiltonian is given by

$$\mathcal{H}(q,p,N) \equiv \langle\phi(q,p,N)|\,\hat{H}\,|\phi(q,p,N)\rangle \tag{2·11a}$$

$$= V(q) + \frac{1}{2}B(q)p^2 + \lambda(q)n, \tag{2·11b}$$

up to second order in p and first order in n, where

$$V(q) = \mathcal{H}(q,p,N)|_{p=0,N=N_0} = \langle\phi(q)|\,\hat{H}\,|\phi(q)\rangle\,, \tag{2·12}$$

$$B(q) = \frac{1}{2}\frac{\partial^2\mathcal{H}(q,p,N)}{\partial p^2}|_{p=0,N=N_0} = -\,\langle\phi(q)|\,[[\hat{H},\hat{Q}(q)],\hat{Q}(q)]\,|\phi(q)\rangle\,, \tag{2·13}$$

$$\lambda(q) = \frac{\partial\mathcal{H}(q,p,N)}{\partial N}|_{p=0,N=N_0} = \langle\phi(q)|\,[\hat{H},i\hat{\Theta}(q)]\,|\phi(q)\rangle\,. \tag{2·14}$$

For a system with $N = N_0$ particles, we can set $n = 0$.

§3. Multi-$O(4)$ model

The multi-$O(4)$ model can be regarded as a simplified version of the conventional P+Q interaction model,[59),60)] in which only the $K = 0$ component of the quadrupole deformation is considered in a schematic manner. This model has been used for the schematic analysis of anharmonic vibrations in transitional nuclei and of various kinds of large amplitude collective motion.[61)–64)]

We define the following bilinear fermion operators for each j-shell:

$$A_j^\dagger = \sum_{m>0} c_{jm}^\dagger c_{j-m}^\dagger, \quad B_j^\dagger = \sum_{m>0} \sigma_{jm} c_{jm}^\dagger c_{j-m}^\dagger, \tag{3·1a}$$

$$\hat{N}_j = \sum_m c_{jm}^\dagger c_{jm}, \qquad \hat{D}_j = \sum_m \sigma_{jm} c_{jm}^\dagger c_{jm}, \tag{3·1b}$$

with

$$\sigma_{jm} = \begin{cases} 1 & |m| < \Omega_j/2 \\ -1 & |m| > \Omega_j/2. \end{cases} \tag{3·2}$$

The sign of σ_{jm} is chosen so as to simulate the behavior of the quadrupole matrix elements $\langle jm|\,r^2Y_{20}\,|jm\rangle$, and we assume that the pair multiplicity $\Omega_j = j + \frac{1}{2}$ is an even integer. The set of operators $\{A_j^\dagger, A_j, B_j^\dagger, B_j, \hat{N}_j, \hat{D}_j\}$ form a Lie algebra of $O(4)$. We then define their extensions to the multi-j-shell case,

$$A^\dagger = \sum_j A_j^\dagger,\ B^\dagger = \sum_j B_j^\dagger,\ \hat{N} = \sum_j \hat{N}_j,\ \hat{D} = \sum_j d_j\hat{D}_j, \tag{3·3}$$

where the coefficients d_j in $\hat{D}$ represent the magnitudes of the reduced quadrupole matrix elements of the j-shells, and we introduce the model Hamiltonian

$$\hat{H} = \hat{h}_0 - \frac{1}{2}G(A^\dagger A + AA^\dagger) - \frac{1}{2}\chi\hat{D}^2, \tag{3·4a}$$

$$\hat{h}_0 = \sum_j e_j^0 \hat{N}_j, \tag{3·4b}$$

where the quantities e_j^0 are the single-particle energies of the j-shells, and G and χ represent the strengths of the pairing and the "quadrupole" interactions, respectively. Note that this Hamiltonian is invariant with respect to the exchange of single-particle states $(j, \pm|m|) \leftrightarrow (j, \pm(\Omega_j - |m|))$. Thus, eigenstates can be classified according to the "parity" quantum number associated with this symmetry.

If we form different combinations of these operators as

$$K_{j+} = \frac{1}{2}(A_j^\dagger + B_j^\dagger), \qquad L_{j+} = \frac{1}{2}(A_j^\dagger - B_j^\dagger), \tag{3·5a}$$

$$K_{j-} = \frac{1}{2}(A_j + B_j), \qquad L_{j-} = \frac{1}{2}(A_j - B_j), \tag{3·5b}$$

$$K_{j0} = \frac{1}{2}(\hat{N}_j + \hat{D}_j - \Omega_j), \quad L_{j0} = \frac{1}{2}(\hat{N}_j - \hat{D}_j - \Omega_j), \tag{3·5c}$$

the sets $\{K_{j+}, K_{j-}, K_{j0}\}$ and $\{L_{j+}, L_{j-}, L_{j0}\}$ separately form $SU(2)$ algebras, and any two elements of different sets commute. It is thus seen that the multi-$O(4)$ model is equivalent to the multi-$SU(2) \otimes SU(2)$ model. Therefore, we can diagonalize the Hamiltonian (3·4) in the basis set

$$\prod_j |n_{Kj}, n_{Lj}\rangle = \prod_j (K_{j+})^{n_{Kj}} (L_{j+})^{n_{Lj}} |0\rangle \tag{3·6}$$

to obtain exact eigenvalues and eigenvectors, where n_{Kj} and n_{Lj}, respectively, represent the numbers of K and L pairs in the j-shell. They satisfy the relations $0 \le n_{Kj}, n_{Lj} \le \Omega_j/2$ and $\sum_j (n_{Kj} + n_{Lj}) = N_0/2$. We note that, in the special case that the single-particle levels e_j^0 are equidistant, the d_j are equal, and $\Omega_j = 2$ for all j, this model reduces to that used in Ref. 65), in which the collective mass in finite superconducting systems is investigated.

§4. Application of the ASCC method to the multi-$O(4)$ model

4.1. *Quasiparticle representation*

We are now in a position to apply the ASCC method to the multi-$O(4)$ model. For separable residual interactions, such as those in this model, it is customary to ignore the Fock terms.[59),60)] We also do this. For this reason, in the following, we use "HB" in place of "HFB". It is readily seen that the TDHB state vectors $|\phi(q)\rangle$ in the multi-$O(4)$ model can be written in the BCS form

$$|\phi(q)\rangle = \exp\Big\{ \sum_i \theta_i(q)(A_i^\dagger - A_i) \Big\} |0\rangle, \tag{4·1}$$

where the quantities $\theta_i(q)$ are related to the coefficients u_i and v_i of the Bogoliubov transformation to the quasiparticle operators $a_i^\dagger$ and a_i,

$$\begin{pmatrix} {a_i}^\dagger \\ a_{-i} \end{pmatrix} \equiv \begin{pmatrix} u_i & -v_i \\ v_i & u_i \end{pmatrix} \begin{pmatrix} {c_i}^\dagger \\ c_{-i} \end{pmatrix}, \tag{4·2}$$

as $u_i = \sin\theta_i$ and $v_i = \cos\theta_i$. Here, $i \equiv (j, m)$, $-i \equiv (j, -m)$, and $\sum_i$ denotes the sum over levels with $m > 0$. We use these conventions hereafter.

The pair operator $A_i^\dagger \equiv c_i^\dagger c_{-i}^\dagger$ and the number operator $\hat{N}_i \equiv c_i^\dagger c_i + c_{-i}^\dagger c_{-i}$ for the degenerate single-particle levels $(i, -i)$ are written in terms of the *quasiparticle* pair, $\boldsymbol{A}_i^\dagger \equiv a_i^\dagger a_{-i}^\dagger$, and *quasiparticle* number operator, $\hat{\boldsymbol{N}}_i \equiv a_i^\dagger a_i + a_{-i}^\dagger a_{-i}$, as

$$A_i^\dagger = u_i v_i + u_i^2 \boldsymbol{A}_i^\dagger - v_i^2 \boldsymbol{A}_i - u_i v_i \hat{\boldsymbol{N}}_i, \tag{4·3a}$$

$$\hat{N}_i = 2v_i^2 + 2u_i v_i (\boldsymbol{A}_i^\dagger + \boldsymbol{A}_i) + (u_i^2 - v_i^2)\hat{\boldsymbol{N}}_i. \tag{4·3b}$$

The quasiparticle operators $\boldsymbol{A}_i^\dagger$, $\boldsymbol{A}_i$ and $\hat{\boldsymbol{N}}_i$ satisfy the commutation relations

$$\left[\boldsymbol{A}_i, \boldsymbol{A}_{i'}^\dagger\right] = \delta_{ii'}(1 - \hat{\boldsymbol{N}}_i), \tag{4·4a}$$

$$\left[\hat{\boldsymbol{N}}_i, \boldsymbol{A}_{i'}^\dagger\right] = 2\delta_{ii'} \boldsymbol{A}_{i'}^\dagger. \tag{4·4b}$$

We define the deformation $D(q)$ and the pairing gap $\Delta(q)$ for the TDHB state $|\phi(q)\rangle$ as

$$D(q) = \langle\phi(q)|\hat{D}|\phi(q)\rangle = 2\sum_i d_i \sigma_i v_i^2, \tag{4·5}$$

$$\Delta(q) = G\,\langle\phi(q)|\,A^\dagger\,|\phi(q)\rangle = G\sum_i u_i v_i. \tag{4·6}$$

4.2. *Quasiparticle RPA at local minima*

We start from the standard procedure for describing small amplitude vibrations around the local minima of the collective potential. Specifically, we apply the quasiparticle RPA about the HB equilibrium points. Because the ASCC is equivalent to the HB+RPA for equilibrium states, the quasiparticle RPA modes provide the boundary condition for solving the local harmonic equations of the ASCC method.

For the equilibrium HB state $|\phi_0\rangle$, the HB equation is given, as usual, by

$$\begin{pmatrix} e_i - \lambda_0 & \Delta_0 \\ \Delta_0 & -e_i + \lambda_0 \end{pmatrix} \begin{pmatrix} u_i \\ v_i \end{pmatrix} = E_i \begin{pmatrix} u_i \\ v_i \end{pmatrix}, \tag{4·7}$$

where Δ_0 and λ_0 denote the pairing gap and the chemical potential, and the quantities

$$e_i = e_i^0 - \chi d_i \sigma_i D_0 \tag{4·8}$$

are the single-particle energies at the equilibrium deformation D_0. The quasiparticle energy and the particle number are written $E_i = \sqrt{(e_i - \lambda_0)^2 + \Delta_0^2}$ and $N_0 = 2\sum_i v_i^2$.

Writing the RPA normal coordinates and momenta as

$$\hat{Q}_n = \sum_i Q_i^n (\boldsymbol{A}_i^\dagger + \boldsymbol{A}_i), \tag{4·9a}$$

$$\hat{P}_n = i \sum_i P_i^n (\boldsymbol{A}_i^\dagger - \boldsymbol{A}_i), \tag{4·9b}$$

we can easily solve the quasiparticle RPA equations,

$$\delta \langle \phi_0 | [\hat{H} - \lambda_0 \hat{N}, \hat{Q}_n] - \frac{1}{i} B_n \hat{P}_n | \phi_0 \rangle = 0, \tag{4·10a}$$

$$\delta \langle \phi_0 | \left[\hat{H} - \lambda_0 \hat{N}, \frac{1}{i} \hat{P}_n \right] - C_n \hat{Q}_n | \phi_0 \rangle = 0, \tag{4·10b}$$

where B_n and C_n denote the inverse mass and the stiffness for the n-th RPA solution, respectively. Note that the local harmonic equations (2·9a) and (2·9b) reduce to the RPA equations at the HB equilibrium points, because the third and fourth terms in Eq. (2·9b) vanish there. The RPA dispersion equation determining the frequencies $\omega_n = \sqrt{B_n C_n}$ is given by

$$\det(S_{kk'}) = 0, \tag{4·11}$$

where S is a 3×3 matrix whose elements are given by

$$S_{11} = \sum_i (f_i^2/(2E_i - \omega) + g_i^2/(2E_i + \omega)) - 1, \tag{4·12a}$$

$$S_{12} = \sum_i (f_i g_i/(2E_i - \omega) + g_i f_i/(2E_i + \omega)), \tag{4·12b}$$

$$S_{13} = \sum_i (f_i h_i/(2E_i - \omega) + g_i h_i/(2E_i + \omega)), \tag{4·12c}$$

$$S_{22} = \sum_i (g_i^2/(2E_i - \omega) + f_i^2/(2E_i + \omega)) - 1, \tag{4·12d}$$

$$S_{23} = \sum_i (g_i h_i/(2E_i - \omega) + f_i h_i/(2E_i + \omega)), \tag{4·12e}$$

$$S_{33} = \sum_i (h_i^2/(2E_i - \omega) + h_i^2/(2E_i + \omega)) - 1, \tag{4·12f}$$

and $S_{k'k} = S_{kk'}$, with the definitions $f_i = \sqrt{G} u_i^2$, $g_i = \sqrt{G} v_i^2$, and $h_i = 2\sqrt{\chi} d_i \sigma_i u_i v_i$. If $\chi = 0$, the above dispersion equation reduces to

$$\omega^2 \Big\{ (\omega^2 - 4\Delta^2\ ) \ \Big(\sum_i \frac{1}{2E_i((2E_i)^2 - \omega^2)} \Big)^2 - \Big(\sum_i \frac{u_i^2 - v_i^2}{2E_i((2E_i)^2 - \omega^2)} \Big)^2 \Big\} = 0, \tag{4·13}$$

which involves two well-known quasiparticle RPA normal modes, the pairing vibration ($\omega \simeq 2\Delta$) and the pairing rotation ($\omega = 0$). On the other hand, if we ignore the

residual pairing interactions, this dispersion equation reduces to

$$4\sum_i \frac{2E_i d_i^2 u_i^2 v_i^2}{(2E_i)^2-\omega^2} = \frac{1}{2\chi}, \tag{4·14}$$

which involves a normal mode analogous to the β vibrations in deformed nuclei. We note that these three kinds of normal modes are decoupled at the spherical point ($D=0$), where $\langle\phi(q)|\left[\hat{D}, A^\dagger + A\right]|\phi(q)\rangle = 0$.

4.3. *HB and local harmonic equations in the moving frame*

In order to find a collective subspace in the TDHB space, we need to solve the RPA-like equations in the moving frame, i.e, the local harmonic equations. These equations determine the generators of the collective space, $\hat{Q}(q)$ and $\hat{P}(q)$. First, we present the local harmonic equations for the multi-$O(4)$ model. With the definitions $\hat{F}_{s=1} \equiv A$, $\hat{F}_{s=2} \equiv \hat{D}$, and

$$\hat{F}_s^{(\pm)} \equiv (\hat{F}_s \pm \hat{F}_s^\dagger)/2 = \pm\hat{F}_s^{(\pm)\dagger}, \tag{4·15}$$

the multi-$O(4)$ Hamiltonian is written

$$\hat{H} = \hat{h}_0 - \frac{1}{2}\sum_{s=1,2}\kappa_s \hat{F}_s^{(+)}\hat{F}_s^{(+)} + \frac{1}{2}\sum_{s=1,2}\kappa_s \hat{F}_s^{(-)}\hat{F}_s^{(-)}, \tag{4·16}$$

where the suffices $s=1$ and 2 indicate the pairing and "quadrupole" parts, respectively, and $\kappa_1 = 2G$ and $\kappa_2 = \chi$. The equation of motion for the time-dependent mean-field state vector $|\phi(q,p)\rangle$ is written

$$\delta\,\langle\phi(q,p)|\, i\frac{\partial}{\partial t} - \hat{h}\,|\phi(q,p)\rangle = 0, \tag{4·17}$$

with the self-consistent mean-field Hamiltonian

$$\hat{h} = \hat{h}_0 - \sum_s \kappa_s \hat{F}_s^{(+)}\,\langle\phi(q,p)|\,\hat{F}_s^{(+)}\,|\phi(q,p)\rangle + \sum_s \kappa_s \hat{F}_s^{(-)}\,\langle\phi(q,p)|\,\hat{F}_s^{(-)}\,|\phi(q,p)\rangle\,. \tag{4·18}$$

The HB equation in the moving frame, (2·7), and the local harmonic equations, (2·9a)–(2·9b), then become

$$\delta\,\langle\phi(q)|\,\hat{h}_M(q)\,|\phi(q)\rangle = 0, \tag{4·19a}$$

$$\delta\,\langle\phi(q)|\,[\hat{h}_M(q), \hat{Q}(q)] - \sum_s f_{Q,s}^{(-)}\hat{F}_s^{(-)} - \frac{1}{i}B(q)\hat{P}(q)\,|\phi(q)\rangle = 0, \tag{4·19b}$$

$$\begin{aligned}\delta\,\langle\phi(q)|\left[\hat{h}_M(q), \frac{1}{i}B(q)\hat{P}(q)\right] - \sum_s f_{P,s}^{(+)}\hat{F}_s^{(+)} - B(q)C(q)\hat{Q}(q) - \sum_s f_{R,s}^{(+)}\hat{F}_s^{(+)} \\ - \sum_s [\hat{F}_s^{(-)}, (\hat{h}(q) - \lambda(q)\hat{N})_A] f_{Q,s}^{(-)} - f_N\hat{N}\,|\phi(q)\rangle = 0,\end{aligned} \tag{4·19c}$$

where $\hat{h}_M(q)$ is the self-consistent mean-field Hamiltonian in the moving frame defined by

$$\hat{h}_M(q) = \hat{h}(q) - \lambda(q)\hat{N} - \frac{\partial V}{\partial q}\hat{Q}(q), \tag{4·20a}$$

$$\hat{h}(q) = \hat{h}_0 - \sum_s \kappa_s \hat{F}_s^{(+)} \langle\phi(q)|\, \hat{F}_s^{(+)}\, |\phi(q)\rangle\,, \tag{4·20b}$$

and

$$f_{Q,s}^{(-)} = -\kappa_s \langle\phi(q)|\, [\hat{F}_s^{(-)}, \hat{Q}(q)]\, |\phi(q)\rangle\,, \tag{4·21a}$$

$$f_{P,s}^{(+)} = \kappa_s \langle\phi(q)|\, \left[\hat{F}_s^{(+)}, \frac{1}{i}B(q)\hat{P}(q)\right]\, |\phi(q)\rangle\,, \tag{4·21b}$$

$$f_{R,s}^{(+)} = -\frac{1}{2}\kappa_s \langle\phi(q)|\, [[\hat{F}_s^{(+)}, (\hat{h}(q) - \lambda(q)\hat{N})_A], \hat{Q}(q)]\, |\phi(q)\rangle\,, \tag{4·21c}$$

$$f_N = B(q)\frac{\partial \lambda}{\partial q}. \tag{4·21d}$$

We express all operators in the above equations in terms of the quasiparticle operators $\boldsymbol{A}_i^\dagger$, $\boldsymbol{A}_i$ and $\hat{\boldsymbol{N}}_i$, defined with respect to $\hat{h}_M(q)$ and $|\phi(q)\rangle$ as follows:

$$\hat{h}_M(q) = \sum_i E_i \hat{\boldsymbol{N}}_i, \tag{4·22}$$

$$\hat{F}_s^{(+)} = \langle\phi(q)|\, F_s^{(+)}\, |\phi(q)\rangle + \sum_i F_{A,s}^{(+)}(i)(\boldsymbol{A}_i^\dagger + \boldsymbol{A}_i) + \sum_i F_{B,s}^{(+)}(i)\hat{\boldsymbol{N}}_i, \tag{4·23}$$

$$\hat{F}_s^{(-)} = \sum_i F_{A,s}^{(-)}(i)(\boldsymbol{A}_i^\dagger - \boldsymbol{A}_i), \tag{4·24}$$

with

$$F_{A,1}^{(+)}(i) = \frac{1}{2}(u_i^2 - v_i^2), \qquad F_{A,2}^{(+)}(i) = 2d_i\sigma_i u_i v_i, \tag{4·25a}$$

$$F_{A,1}^{(-)}(i) = -\frac{1}{2}, \qquad F_{A,2}^{(-)}(i) = 0, \tag{4·25b}$$

$$F_{B,1}^{(+)}(i) = -u_i v_i, \qquad F_{B,2}^{(+)}(i) = d_i\sigma_i(u_i^2 - v_i^2). \tag{4·25c}$$

Note that all matrix elements are real, so that $\langle\phi(q)|\, \hat{F}_s^{(-)}\, |\phi(q)\rangle = 0$. For later convenience, we define one-body operators as

$$\hat{R}_s^{(+)} \equiv [\hat{F}_{B,s}^{(+)}, (\hat{h}(q) - \lambda(q)\hat{N})_A] = 2\sum_i R_s^{(+)}(i)(\boldsymbol{A}_i^\dagger - \boldsymbol{A}_i), \tag{4·26}$$

where $\hat{F}_{B,s}^{(+)}$ represents the last terms of Eq. (4·23) and

$$R_s^{(+)}(i) = \{2u_i v_i(e_i - \chi d_i\sigma_i D - \lambda(q)) - \Delta(u_i^2 - v_i^2)\}F_{B,s}^{(+)}(i). \tag{4·27}$$

The infinitesimal generators $\hat{Q}(q)$ and $\hat{P}(q)$ can be written

$$\hat{Q}(q) = \sum_i Q_i(q)(\boldsymbol{A}_i^\dagger + \boldsymbol{A}_i), \tag{4·28a}$$

$$\hat{P}(q) = i\sum_i P_i(q)(\boldsymbol{A}_i^\dagger - \boldsymbol{A}_i). \tag{4·28b}$$

Equations (4·19b) and (4·19c) are then reduced to linear equations for the matrix elements $Q_i(q)$ and $P_i(q)$ of the infinitesimal generators $\hat{Q}(q)$ and $\hat{P}(q)$. They are easily solved, yielding the expressions

$$\begin{aligned} Q_i(q) = {} & \frac{2E_i}{(2E_i)^2 - \omega^2} \sum_s F_{A,s}^{(-)}(i) f_{Q,s}^{(-)} \\ & + \frac{1}{(2E_i)^2 - \omega^2} \sum_s (F_{A,s}^{(+)}(i) f_{PR,s}^{(+)} + N_i f_N), \end{aligned} \tag{4·29a}$$

$$\begin{aligned} P_i(q) = {} & \frac{2E_i}{(2E_i)^2 - \omega^2} \sum_s (F_{A,s}^{(+)}(i) f_{PR,s}^{(+)} + N_i f_N) \\ & + \frac{\Omega(q)}{(2E_i)^2 - \omega^2} \sum_s F_{A,s}^{(-)}(i) f_{Q,s}^{(-)}, \end{aligned} \tag{4·29b}$$

where $N_i = 2u_i v_i$ and

$$f_{PR,s}^{(+)} = f_{P,s}^{(+)} + f_{R,s}^{(+)}. \tag{4·30}$$

Note that ω^2, representing the square of the frequency $\omega(q) = \sqrt{B(q)C(q)}$ of the local harmonic mode, is not necessarily positive. The values of $B(q)$ and $C(q)$ depend on the scale of the collective coordinate q, while $\omega(q)$ does not. In this sense, there remains an ambiguity in determining q. We therefore require $B(q) = 1$ everywhere in the collective space to uniquely determine q.

The quantities $f_{Q,s}^{(-)}$, $f_{P,s}^{(+)}$ and $f_{R,s}^{(+)}$ are easily calculated as

$$f_{Q,s}^{(-)} = 2\kappa_s \sum_i F_{A,s}^{(-)}(i) Q_i(q), \tag{4·31a}$$

$$f_{P,s}^{(+)} = 2\kappa_s \sum_i F_{A,s}^{(+)}(i) P_i(q), \tag{4·31b}$$

$$f_{R,s}^{(+)} = 2\kappa_s \sum_i R_s^{(+)}(i) Q_i(q). \tag{4·31c}$$

Inserting Eqs. (4·29a) and (4·29b) for $Q_i(q)$ and $P_i(q)$ into the above expressions, we obtain linear homogeneous equations for the unknown quantities $f_{PR,s}^{(+)}, f_{Q,s}^{(-)}$ and f_N. Similarly, the condition of orthogonality to the number operator,

$$\langle \phi(q) | [\hat{N}, \hat{P}(q)] | \phi(q) \rangle = 2i \sum_i N_i P_i(q) = 0, \tag{4·32}$$

gives another equation for $f_{PR,s}^{(+)}, f_{Q,s}^{(-)}$ and f_N. Because $f_{Q,2}^{(-)} = 0$, these equations

can be written in 4×4 matrix form as

$$\begin{pmatrix} & & & \\ & S_{kk'}(\omega) & & \\ & & & \\ & & & \end{pmatrix} \begin{pmatrix} f^{(-)}_{Q,1} \\ f^{(+)}_{PR,1} \\ f^{(+)}_{PR,2} \\ f_N \end{pmatrix} = 0, \tag{4·33}$$

where

$$S_{11} = 2GS^{(1)}(F^{(-)}_{A,1}, F^{(-)}_{A,1}) - 1, \tag{4·34a}$$
$$S_{12} = 2GS^{(2)}(F^{(-)}_{A,1}, F^{(+)}_{A,1}), \tag{4·34b}$$
$$S_{13} = 2GS^{(2)}(F^{(-)}_{A,1}, F^{(+)}_{A,2}), \tag{4·34c}$$
$$S_{14} = 2GS^{(2)}(F^{(-)}_{A,1}, N), \tag{4·34d}$$
$$S_{21} = 2G\{S^{(1)}(R^{(+)}_1, F^{(-)}_{A,1}) + \omega^2 S^{(2)}(F^{(+)}_{A,1}, F^{(-)}_{A,1})\}, \tag{4·34e}$$
$$S_{22} = 2G\{S^{(1)}(F^{(+)}_{A,1}, F^{(+)}_{A,1}) + S^{(2)}(R^{(+)}_1, F^{(+)}_{A,1})\} - 1, \tag{4·34f}$$
$$S_{23} = 2G\{S^{(1)}(F^{(+)}_{A,1}, F^{(+)}_{A,2}) + S^{(2)}(R^{(+)}_1, F^{(+)}_{A,2})\}, \tag{4·34g}$$
$$S_{24} = 2G\{S^{(1)}(F^{(+)}_{A,1}, N) + S^{(2)}(R^{(+)}_1, N)\}, \tag{4·34h}$$
$$S_{31} = 4\chi\{S^{(1)}(R^{(+)}_2, F^{(-)}_{A,1}) + \omega^2 S^{(2)}(F^{(+)}_{A,2}, F^{(-)}_{A,1})\}, \tag{4·34i}$$
$$S_{32} = 4\chi\{S^{(1)}(F^{(+)}_{A,2}, F^{(+)}_{A,1}) + S^{(2)}(R^{(+)}_2, F^{(+)}_{A,1})\}, \tag{4·34j}$$
$$S_{33} = 4\chi\{S^{(1)}(F^{(+)}_{A,2}, F^{(+)}_{A,2}) + S^{(2)}(R^{(+)}_2, F^{(+)}_{A,2})\} - 1, \tag{4·34k}$$
$$S_{34} = 4\chi\{S^{(1)}(F^{(+)}_{A,2}, N) + S^{(2)}(R^{(+)}_2, N)\}, \tag{4·34l}$$
$$S_{41} = \omega^2 S^{(2)}(N, F^{(-)}_{A,1}), \tag{4·34m}$$
$$S_{42} = S^{(1)}(N, F^{(+)}_{A,1}), \tag{4·34n}$$
$$S_{43} = S^{(1)}(N, F^{(+)}_{A,2}), \tag{4·34o}$$
$$S_{44} = S^{(1)}(N, N). \tag{4·34p}$$

Here, the functions $S^{(1)}(X, Y)$ and $S^{(2)}(X, Y)$ are defined by

$$S^{(1)}(X, Y) = \sum_i \frac{2E_i}{(2E_i)^2 - \omega^2} X_i Y_i, \tag{4·35a}$$

$$S^{(2)}(X, Y) = \sum_i \frac{1}{(2E_i)^2 - \omega^2} X_i Y_i, \tag{4·35b}$$

with X_i and Y_i each representing one of the quantities $F^{(\pm)}_{A,s}(i)$, $R^{(+)}_s(i)$ and N_i. The frequency $\omega(q)$ is determined by finding the solution of the dispersion equation

$$\det\{S_{kk'}(\omega)\} = 0 \tag{4·36}$$

for which ω^2 is minimal. The normalizations of $f^{(+)}_{PR,1}, f^{(+)}_{PR,2}, f^{(-)}_{Q,1}$ and f_N are fixed by the canonical variable condition

$$\langle\phi(q)|[\hat{Q}(q),\hat{P}(q)]|\phi(q)\rangle = 2i\sum_i Q_i(q)P_i(q) = i. \tag{4·37}$$

Note that ω^2 represents the curvature of the collective potential,

$$\omega^2 = \frac{\partial^2 V}{\partial q^2}, \tag{4·38}$$

for the choice of the coordinate scale with which $B(q) = 1$.

§5. Numerical analysis

In this section, we report the results of a numerical analysis of the oblate-prolate shape coexistence and large amplitude collective motion in the multi-$O(4)$ model.

5.1. *Procedure of the calculation*

We first solve the HB equations and find the HB equilibrium points that correspond to extrema of the collective potential $V(q)$ defined by Eq. (2·12). At these points, the HB equation in the moving frame, Eq. (2·7), and the local harmonic equations, Eqs. (2·9a) and (2·9b), coincide with the ordinary HB equation and the quasiparticle RPA equations, respectively. Let $|\phi(q_0)\rangle$ be a HB solution, which is assumed to be in the collective subspace at a particular value of the collective coordinate, $q = q_0$. Solving the quasiparticle RPA equation with respect to $|\phi(q_0)\rangle$, we find a collective normal mode, which determines the infinitesimal generators $\hat{Q}(q_0)$ and $\hat{P}(q_0)$. In the present analysis, we choose the normal mode with the lowest frequency, which represents the most collective motion with respect to the "quadrupole" operator $\hat{D}$. We then generate the state $|\phi(q_0+\delta q)\rangle$ with an infinitesimal shift of the collective coordinate as

$$|\phi(q_0+\delta q)\rangle = e^{-i\delta q\hat{P}(q_0)}\,|\phi(q_0)\rangle\,. \tag{5·1}$$

Next, we solve the local harmonic equations at $q = q_0+\delta q$, and determine $\hat{Q}(q_0+\delta q)$ and $\hat{P}(q_0+\delta q)$, and proceed to $q = q_0+2\delta q$. Repeating this procedure, we construct a collective subspace. Owing to the invariance

$$A^\dagger_i - A_i = \boldsymbol{A}^\dagger_i - \boldsymbol{A}_i, \tag{5·2}$$

we can rewrite the state vectors as

$$\begin{aligned}|\phi(q+\delta q)\rangle &= \exp\left\{\delta q\sum_i P_i(q)(\boldsymbol{A}^\dagger_i - \boldsymbol{A}_i)\right\}|\phi(q)\rangle \\ &= \exp\left\{\delta q\sum_i P_i(q)(A^\dagger_i - A_i)\right\}|\phi(q)\rangle\,.\end{aligned} \tag{5·3}$$

Combining the above expression with Eq. (4·1), we obtain the following simple relations between the coefficients u_i and v_i at $q+\delta q$ and those at q:

$$\begin{pmatrix} u_i(q+\delta q) \\ v_i(q+\delta q) \end{pmatrix} = \begin{pmatrix} \cos(P_i(q)\delta q) & -\sin(P_i(q)\delta q) \\ \sin(P_i(q)\delta q) & \cos(P_i(q)\delta q) \end{pmatrix} \begin{pmatrix} u_i(q) \\ v_i(q) \end{pmatrix}. \tag{5·4}$$

In the present calculation, we always start from the spherical equilibrium point ($q = 0$). This point is an unstable extremum (a saddle point) in the collective subspace when we choose parameter values producing deformed HB minima (see below). Note that the quasiparticle RPA equations given in §4.1 are still valid, whereas the frequency ω of the eigenmode is purely imaginary in this case.

If the collective subspace is exactly decoupled from the non-collective subspace, the state vectors $|\phi(q)\rangle$ obtained in this way should simultaneously satisfy the HB equation in the moving frame, Eq. (2·7). In general, however, the decoupling conditions may not be exactly satisfied, and we must resort to some kind of iterative procedure to construct a collective subspace in which Eq. (2·7) holds. One way of evaluating the quality of the decoupling and the accuracy of the numerical calculation is to examine the validity of Eq. (2·7) in the collective space. For the multi-$O(4)$ model under consideration, as we see in Fig. 2, this condition is found to be satisfied to a good approximation with the use of a step size $\delta q = 0.005$ in Eq. (5·4). Of course, this does not necessarily imply that such a simple algorithm will work in more realistic cases, and we need further investigations concerning numerical techniques for solving Eqs. (2·7), (2·9a) and (2·9b).

The collective Hamiltonian thus obtained, $\mathcal{H}(q,p) = \frac{1}{2}B(q)p^2 + V(q)$, is then quantized, and the collective Schrödinger equation is solved to obtain eigenvalues and transition probabilities. As we set the scale of the collective coordinate q such that $B(q) = 1$, there is no ambiguity with regard to ordering in the canonical quantization procedure, following the Pauli quantization rule. It is easily confirmed that the collective representation of the "quadrupole" operator, defined by $\mathcal{D}(q) = \langle\phi(q,p)|\,\hat{D}\,|\phi(q,p)\rangle$, does not depend on p, and transition matrix elements can be evaluated as $\int \psi_n(q)^* \mathcal{D}(q)\psi_{n'}(q)dq$, where $\psi_n(q)$ denotes the collective wave function of the n-th eigenstate.

5.2. *Parameters*

In the following, we consider a system consisting of three shells with the spherical single-particle energies $e^0_{j_1} = 0.0,\ e^0_{j_2} = 1.0,\ e^0_{j_3} = 3.5$, the pair degeneracies $\Omega_{j_1} = 14,\ \Omega_{j_2} = 10,\ \Omega_{j_3} = 4$, and the reduced quadrupole moments $d_{j_1} = 2,\ d_{j_2} = d_{j_3} = 1$. We distribute 14 pairs ($N_0 = 28$) in this shell-model space (we do not distinguish protons and neutrons). We compare numerical results obtained with different values of the pairing interaction strength, $G = 0.14,\ 0.16$ and 0.20, for a fixed "quadrupole" interaction strength, $\chi = 0.04$. These numerical examples are presented merely as representatives of similar results obtained with other sets of parameter values. Because properties of the single-shell $O(4)$ model are determined by the ratio G/χ, similar results are obtained if χ is varied instead of G. The only reason that we vary G with χ fixed is because it is intuitively easier to visualize the variation of the barrier height (between the prolate and oblate local minima) while keeping the

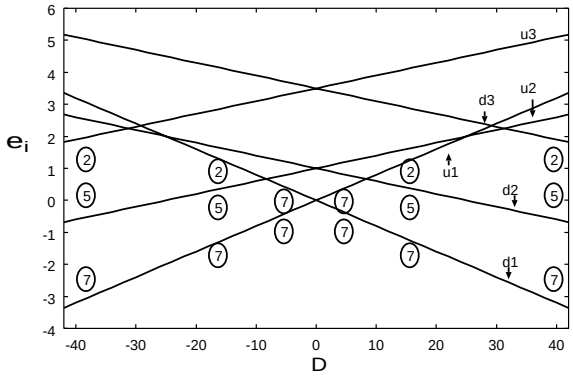

Fig. 1. Deformed single-particle energies, $e_i = e_i^0 - \chi d_i \sigma_i D$, plotted as functions of the deformation parameter D for the following set of parameter values: $e_{j_1}^0 = 0.0$, $e_{j_2}^0 = 1.0$, $e_{j_3}^0 = 3.5$, $\Omega_{j_1} = 14$, $\Omega_{j_2} = 10$, $\Omega_{j_3} = 4$, and $d_{j_1} = 2$, $d_{j_2} = d_{j_3} = 1$. The numbers enclosed by circles indicate the numbers of pairs occupying individual levels in the lowest energy configuration for a given value of D when pairing correlations are absent. Near the spherical point ($D = 0$), the lowest shell is fully occupied by 14 pairs (28 nucleons). The level diagram is invariant under the change of sign of D (prolate-oblate symmetry). The down(up)-sloping levels are referred to as d1, d2 and d3 (u1, u2 and u3), as indicated. On the prolate side ($D \geq 0$), the down-sloping level originating from the second shell (d2) crosses the up-sloping level (u1) at $D = 8.3$. After this first crossing, the lowest energy configuration involves 5 pairs occupying the second down-sloping level (d2), and 2 pairs remaining in the first up-sloping level (u1). At $D = 29.2$, the down-sloping level originating from the third shell (d3) crosses the second up-sloping level (u2). In the lowest-energy configuration after this crossing, all the down-sloping levels are fully occupied, while all the up-sloping levels are unoccupied. This configuration possesses the maximum value of the deformation parameter, $D_{\max} = 42$. The same pattern of level crossings is found also on the oblate side ($D \leq 0$). Note that this figure was obtained by treating D as a free parameter, although D in Eq. (4·5) represents the expectation value of the operator $\hat{D}$. In this sense, this figure should be regarded as a kind of Nilsson diagram.

magnitude of the equilibrium deformation D_0 almost constant.

Figure 1 plots the single-particle energy diagram as a function of D. Details of the level crossings are explained in the caption. It is certainly possible to analyze the level crossing dynamics and simulate the shape coexistence phenomena by means of a multi-$O(4)$ model consisting of only two shells. However, it is found that the inclusion of three shells yields more realistic properties in the large deformation region. In realistic situations, a number of successive level crossings take place as the deformation increases.

5.3. *Collective potentials*

We present in Fig. 2 the collective potentials calculated for three values of the pairing strength G. For $G = 0.14$, the potential exhibits a double well structure, while it possesses a single well for $G = 0.2$. The case $G = 0.16$ is intermediate between these. Note that the collective potentials are plotted here as functions of the deformation D. The relation between D and the collective coordinate q is shown explicitly below. The mechanism causing the appearance and disappearance of the double well structure is determined by the competition between the pairing and

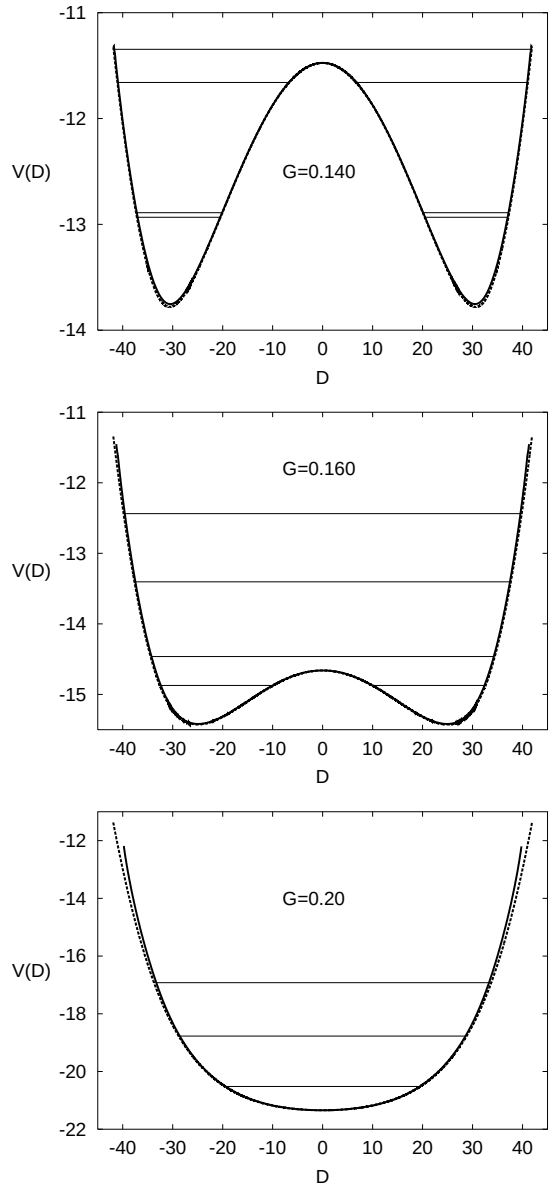

Fig. 2. Collective potentials calculated with the ASCC method for $G = 0.14$ (top), $G = 0.16$ (middle), and $G = 0.20$ (bottom) are plotted by the solid curves as functions of the deformation D. The other parameter values used in the calculation are listed in the caption of Fig. 1. For comparison, the collective potentials obtained with the CHB method are plotted by the dotted curves. The horizontal lines indicate eigenenergies of the quantized collective Hamiltonian.

"quadrupole" interactions: The pairing force favors an equal population of particles in all magnetic substates in each j-shell, whereas the "quadrupole" force favors the occupation of down-sloping levels, creating level crossings and asymmetry in the magnetic substate population. In the three j-shell system under consideration, the energy of the degenerate local minima is lower than that of the spherical point

for small values of G. As pairing correlations increase, however, the energy of the spherical point decreases, so that the barrier height decreases, and eventually the height of the barrier itself diminishes.

In Fig. 2, quantum eigenstates obtained by solving the collective Shrödinger equations are indicated. We can clearly see a parity-doublet-like pattern associated with tunneling through the central barrier in the collective potential curve. The properties of these excitation spectra are discussed in the succeeding subsection. In this figure, we also display the potential energy functions calculated by means of the conventional constrained HB (CHB) procedure, given by

$$V_{\rm CHB}(D) = \langle \phi_0^{\rm CHB}(D)|\hat{H}|\phi_0^{\rm CHB}(D)\rangle = 2\sum_i e_i^0 v_i^2 - \frac{\Delta^2}{G} - \frac{1}{2}\chi D^2, \qquad (5\cdot5)$$

where the state vectors $|\phi_0^{\rm CHB}(D)\rangle$ are determined by the constrained variational principle

$$\delta\langle \phi_0^{\rm CHB}(D)|\hat{H} - \lambda\hat{N} - \mu\hat{D}|\phi_0^{\rm CHB}(D)\rangle = 0, \qquad (5\cdot6)$$

with μ denoting a Lagrange multiplier. As seen in the figures, the collective potentials obtained with the ASCC and CHB methods are practically indistinguishable. In principle, when the collective path obtained in the ASCC method and that obtained in the CHB method go through the same HB local minima, the collective potential energies at these points should coincide. We note, however, very small differences between their values at the HB local minima with $D \neq 0$ for the cases $G = 0.14$ and 0.16. These discrepancies are due to violation of Eq. (2·7) which accumulates in the numerical calculation starting from $D = 0$, and represent the amount of error associated with the computational algorithms adopted here, as mentioned in §6.1.

In Fig. 3, the pairing gaps Δ are displayed as functions of the deformation D. It is seen that they are monotonically decreasing functions of $|D|$ and vanish at the maximum deformation, which is $D_{\rm max} = 42$ for the parameter values adopted in these calculations. In Fig. 4, occupation probabilities v_i^2 are displayed. Note that all down-sloping (up-sloping) levels are fully occupied (unoccupied) at $D_{\rm max}$. Again, the results obtained with the ASCC and CHB methods are practically indistinguishable in these figures. Thus, in the present multi-$O(4)$ model, the static mean-field properties (such as potential energy curves and the pairing gaps) obtained with the ASCC method are very similar to those obtained with the conventional CHB method. However, it should be noted that this is due to the simplicity of the multi-$O(4)$ model adopted here. In general, the collective subspace of the ASCC method may differ from that of the CHB method.[27)]

In Figs. 3 and 4, we have also plotted the BCS pairing gaps and occupation probabilities calculated using the BCS approximation. In this approximation, single-particle energies given by $e_i = e_i^0 - \chi d_i \sigma_i D$ are used to solve the BCS equations, where the deformation D is treated as a free parameter, ignoring the HB self-consistency condition, (4·5), as in phenomenological single-particle potential models. The pairing gap Δ in the BCS approximation differs from those in the CHB and ASCC methods. Note that the BCS gaps do not vanish in the $D \to D_{\rm max}$ limit, in contrast to the

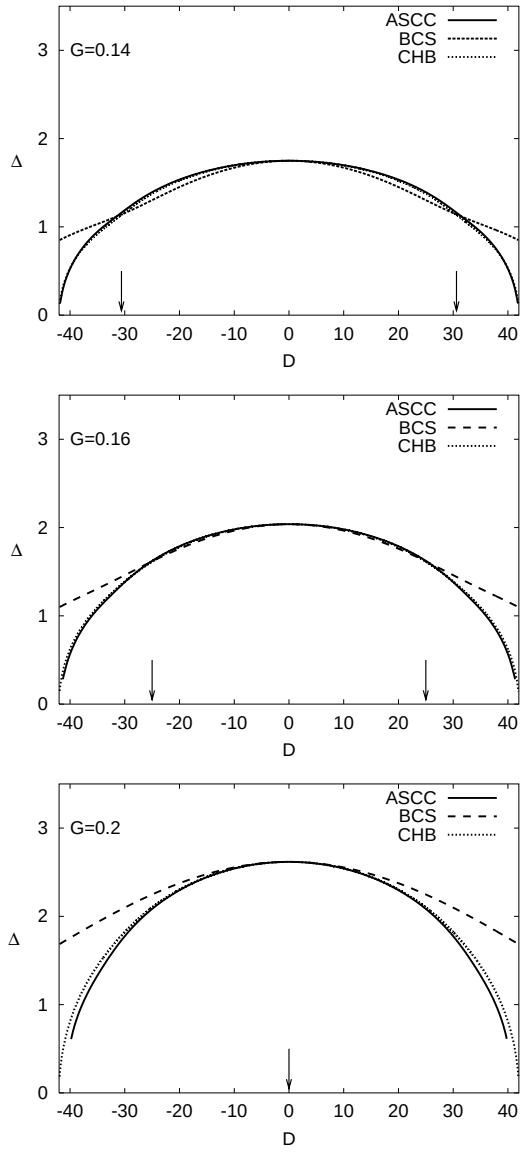

Fig. 3. Pairing gaps Δ calculated with the ASCC method for $G = 0.14$ (top), $G = 0.16$ (middle), and $G = 0.20$ (bottom) are plotted by the solid curves as functions of the deformation D. The other parameter values used are the same as in Fig. 2. For comparison, Δ calculated with the CHB method and with the BCS approximation are also plotted by the dotted and dashed curves, respectively. The solid and dotted curves deviate little. The equilibrium deformations are indicated by the arrows.

HB self-consistent pairing gaps. In the following, we focus on dynamical properties of tunneling motion between the oblate and prolate minima.

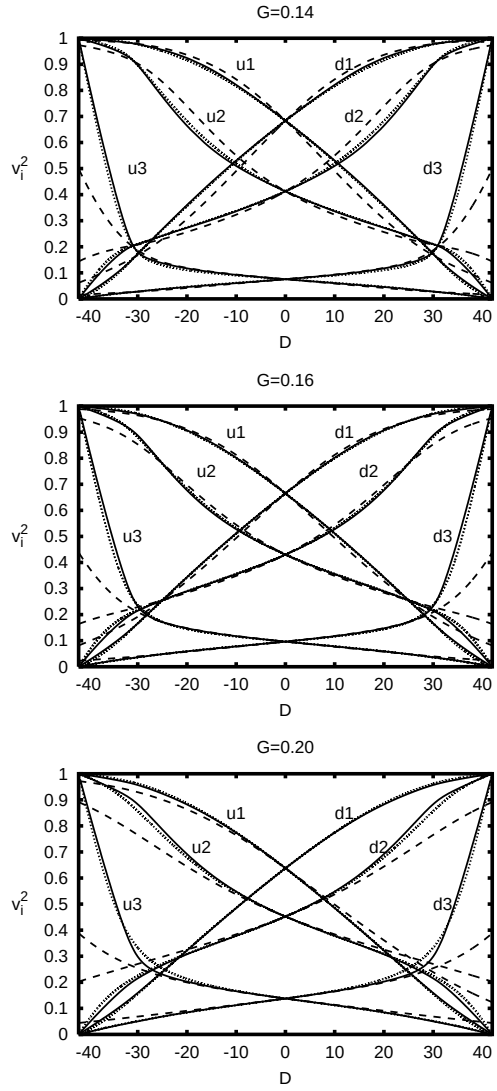

Fig. 4. Occupation probabilities v_i^2 calculated with the ASCC method for $G = 0.14$ (top), $G = 0.16$ (middle), and $G = 0.20$ (bottom) are plotted by the solid curves as functions of the deformation D. Other parameter values used are the same as in Fig. 2. For comparison, v_i^2 calculated with the CHB method and with the BCS approximation are also plotted by the dotted and dashed curves, respectively. The solid and dotted curves appear similar. Note that, in the case that D is equal to its maximal value, $D_{\max}$, all down-sloping (up-sloping) levels are fully occupied (unoccupied) in the cases of the ASCC and CHB methods, but not in the case of the BCS approximation.

5.4. *Excitation spectra and collective mass*

Figure 5 displays the excitation spectra and transition matrix elements for the ASCC method and for the case of exact diagonalization in the basis set given in Eq. (3·6). The wave functions of the low-lying states are displayed in Figs. 6 and

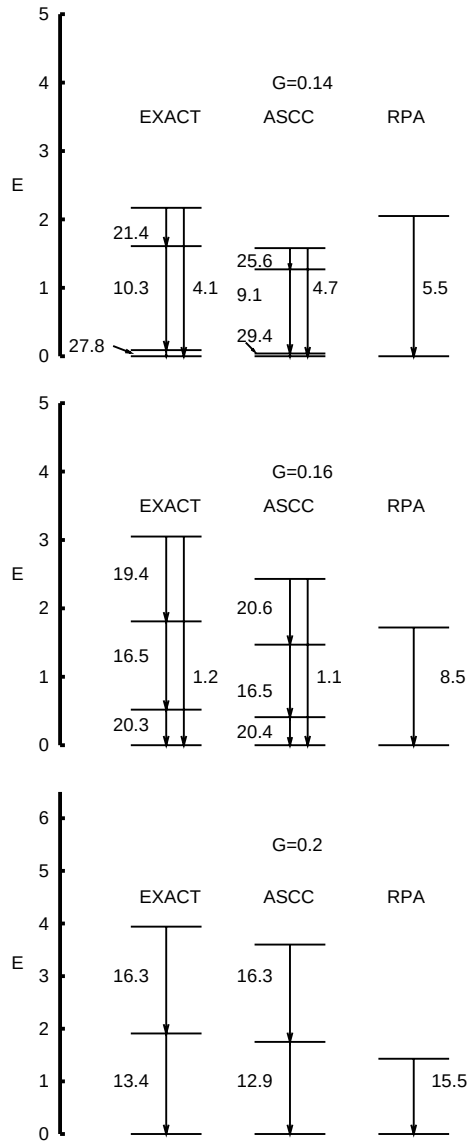

Fig. 5. Comparison of excitation spectra calculated with the ASCC method and with the exact diagonalization for $G = 0.14$ (top), $G = 0.16$ (middle) and $G = 0.20$ (bottom). For reference, the excitation energies of the lowest RPA modes in the HFB local minima are also indicated. Other parameter values used are the same as in Fig. 2. The numbers adjacent to vertical lines indicate the transition matrix elements for the "quadrupole" operator $\hat{D}$. In the top panel, the transition matrix elements between "parity doublets" are indicated by arrows.

7. The collective character of these states is apparent from the enhancement of the transition matrix elements in comparison with the single-particle matrix elements $d_j(=1 \text{ or } 2)$. We see that the main character of the results obtained from the ASCC method are quite similar to those of the exact spectra and transition properties. In view of the very large number of degrees of freedom involved in the model under

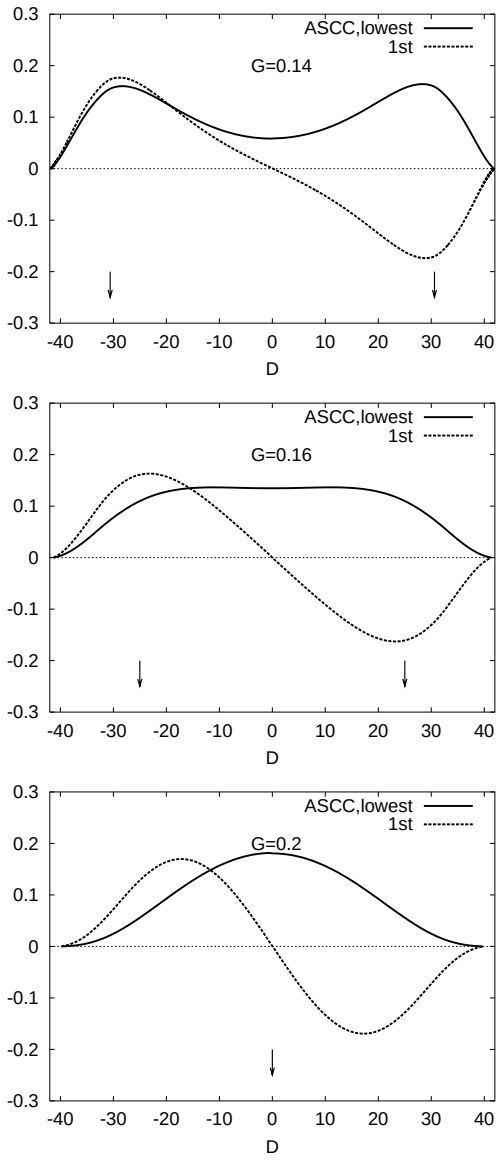

Fig. 6. Collective wave functions $\psi(D)$ for the ground and first excited states, whose energies are plotted in Fig. 5, obtained with the ASCC method for $G = 0.14$ (top), $G = 0.16$ (middle), and $G = 0.20$ (bottom). The equilibrium deformations are indicated by the arrows. The wave functions $\psi(D)$ are defined by $\psi(D) = \psi(q)|\frac{\partial q}{\partial D}|^{\frac{1}{2}}$, where $\psi(q)$ represents wave functions for the collective coordinate q. Thus, they are normalized as $\int |\psi(q)|^2 dq = \int |\psi(q)|^2 |\frac{\partial q}{\partial D}| dD = \int |\psi(D)|^2 dD = 1$.

consideration (the dimension of this shell model space is 1894), it is remarkable that the low-lying states can be described very well in terms of only the single collective coordinate q. In particular, we note that the emergence of the "parity splitting" pattern for smaller values of the strength G of the pairing interaction is clearly

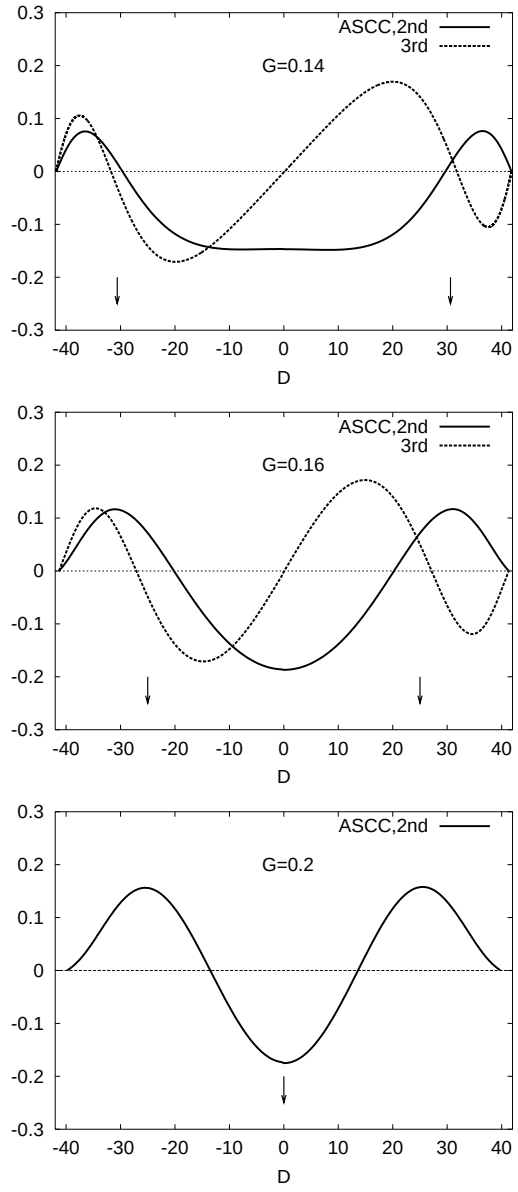

Fig. 7. The same as Fig. 6, but for the second and third excited states. For $G = 0.2$, only the wave function for the second excited state is plotted.

realized in the calculation. This implies that the ASCC method yields a faithful description of the large amplitude tunneling motion through the barrier between the oblate and prolate local minima.

As is well known, the collective mass parameter represents inertia with respect to change of the mean field. It is determined locally and changes as D varies. Because we have set the scale of the collective coordinate q such that the collective mass parameter $M(q) = B^{-1}(q)$ with respect to q is unity, the collective kinetic energy

can be written either in terms of q or D as

$$\frac{1}{2}\dot{q}^2 = \frac{1}{2}\Big(\frac{dq}{dD}\dot{D}\Big)^2 \equiv \frac{1}{2}M(D)\dot{D}^2. \tag{5·7}$$

Thus, we obtain an explicit expression for $M(D)$,

$$M(D) \equiv \Big(\frac{dq}{dD}\Big)^2 = \Big(\frac{d}{dq}\sum_i 2d_i\sigma_i v_i^2(q)\Big)^{-2} = \Big(4\sum_i d_i\sigma_i u_i v_i P_i(q)\Big)^{-2}. \tag{5·8}$$

The collective mass $M(D)$ evaluated in this way is displayed in Fig. 8 as a function of D. It is immediately seen that the ASCC mass $M(D)$ diverges in the limit $D \to D_{\max}$. The reason for this behavior can be clearly understood by examining the relationship between D and the collective coordinate q. This is shown in Fig. 9. We see that the variation of D slows down as D approaches its limiting value, $D_{\max}$. Thus, the derivative dq/dD, which corresponds to the collective mass $M(D)$, according to Eq. (5·8), diverges. Obviously, this divergence is caused by the existence of the maximum value of D, which is an artifact of the model: If we increase the number of shells that are explicitly taken into account, this limit is removed by successive level crossings as D increases.

It is interesting to compare the ASCC mass $M(D)$ with the cranking mass $M_{\rm cr}(D)$,[1)]

$$\begin{aligned} M_{\rm cr}(D) &= 2\sum_n \frac{|\langle\phi_n^{\rm BCS}(D)|\frac{\partial}{\partial D}|\phi_0^{\rm BCS}(D)\rangle|^2}{E_n(D)-E_0(D)} \\ &= 2\sum_i \frac{|2u_iv_i(\chi d_i\sigma_i + \frac{\partial\lambda}{\partial D}) + (u_i^2-v_i^2)\frac{\partial\Delta}{\partial D}|^2}{(2E_i)^3}, \end{aligned} \tag{5·9}$$

where $\phi_0^{\rm BCS}(D)$ and $\phi_n^{\rm BCS}(D)$ represent the ground and excited states, and $E_0(D)$ and $E_n(D)$ are their energies obtained in the BCS approximation. Here, the coefficients of the Bogoliubov transformations (u_i and v_i), the pairing gap Δ, the chemical potential λ, and the quasiparticle energies E_i are evaluated using the single-particle energies defined by $e_i = e_i^0 - \chi d_i\sigma_i D$. It is important to note that the deformation D is treated in the BCS approximation as a phenomenological potential parameter, disregarding the self-consistency condition (4·5). Figure 8 shows that the cranking mass $M_{\rm cr}(D)$ is significantly different from the ASCC mass $M(D)$ over the entire interval of the deformation D, including the spherical point $D = 0$ and the deformed equilibrium points. The difference between the ASCC mass and the cranking mass can be understood in terms of the HB self-consistency.

At the spherical point ($D = 0$), we can make an explicit comparison between the ASCC mass and the cranking mass. There, all terms linear with respect to σ_i in the local harmonic equations vanish after summing over all levels i, so that the pairing and "quadrupole" normal modes are exactly decoupled. Thus, we obtain a simple expression of the ASCC mass,

$$M(D=0) = 2\chi^2\sum_i \frac{2E_i(2d_i\sigma_i u_i v_i)^2}{((2E_i)^2-\omega^2)^2} = 4\chi^2\Delta^2\sum_i \frac{d_i^2}{E_i((2E_i)^2-\omega^2)^2}. \tag{5·10}$$

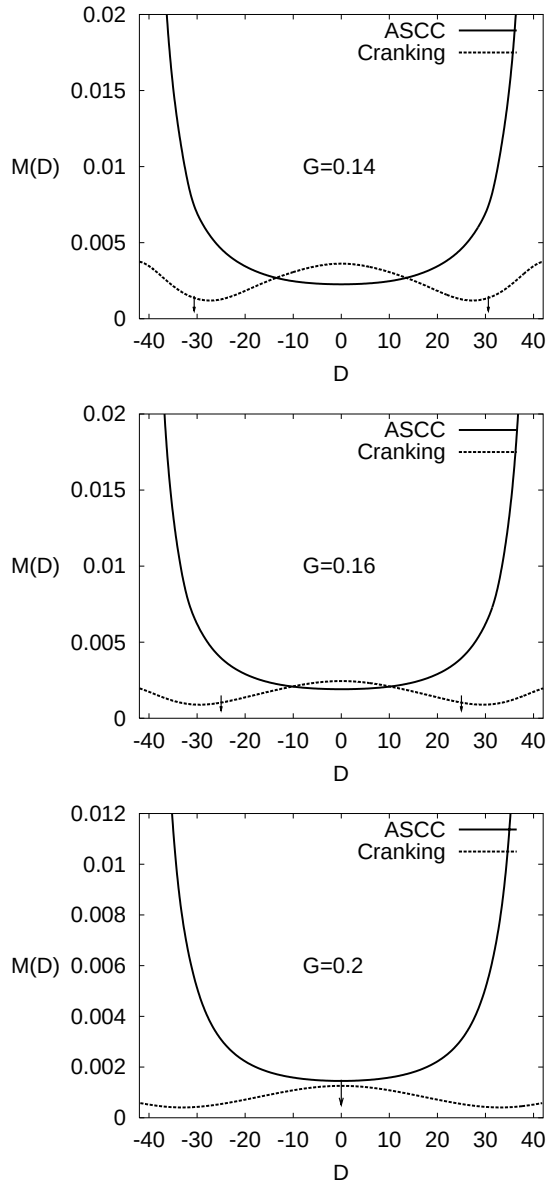

Fig. 8. Collective masses $M(D)$ calculated with the ASCC method for $G = 0.14$ (top), $G = 0.16$ (middle) and $G = 0.20$ (bottom) are plotted by the solid curves as functions of the deformation D. Other parameter values used are the same as in Fig. 2. For comparison, the cranking mass is indicated by dotted curves. The equilibrium deformations are indicated by the arrows.

Also at the spherical point, the expression for the cranking mass $M_{\rm cr}(D)$ reduces to

$$M_{\rm cr}(D=0) = \frac{1}{4}\chi^2\Delta^2 \sum_i \frac{d_i^2}{E_i^5}, \tag{5·11}$$

because the derivatives $\partial\Delta/\partial D$ and $\partial\lambda/\partial D$ vanish at $D = 0$. We see that $M(D = 0)$

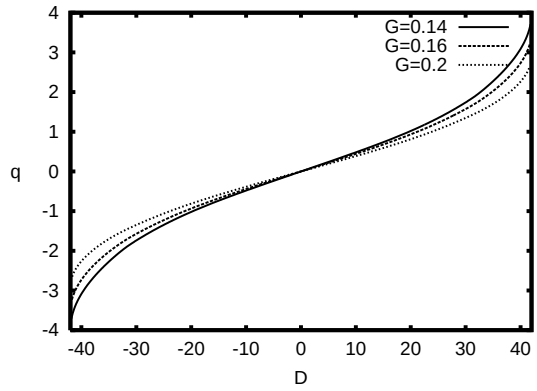

Fig. 9. Relation between the deformation D and the collective coordinate q in the ASCC method. The solid, dashed and dotted curves represent the results of calculations for $G = 0.14, 0.16$ and 0.20, respectively.

reduces to $M_{\rm cr}(D = 0)$ if we set $\omega = 0$ in Eq. (5·10). Actually, the frequency ω is imaginary, and ω^2 is negative when a barrier exists ($G = 0.14$ and 0.16). Accordingly, $M(D = 0) \leq M_{\rm cr}(D = 0)$ in these cases. By contrast, ω is real and ω^2 is positive when the spherical point is stable ($G = 0.20$), so that $M(D = 0) \geq M_{\rm cr}(D = 0)$ in this case. In this way, the difference between the ASCC mass and the cranking mass in the barrier region (near $D \approx 0$), clearly seen in Fig. 8, can be understood in terms of the finite frequency effect of the local harmonic mode, which is connected with the curvature of the collective potential by Eq. (4·38). This finite frequency effect decreases (increases) the collective mass when the barrier increases (decreases). We would like to emphasize that the finite frequency effect in the local harmonic equations represents self-consistent dynamics of the time-dependent mean-field.

We note that, in contrast to the ASCC mass $M(D)$, the cranking mass $M_{\rm cr}(D)$ does not diverge at $D_{\rm max}$. This is because, as emphasized above, the deformation D is treated as a free parameter in the single-particle potential, so that the existence of the limit $D_{\rm max}$ in the self-consistent deformation defined by Eq. (4·5) is disregarded there. In the multi-$O(4)$ model under consideration, the self-consistency of the deformation parameter specifying the single-particle potential and the density deformation evaluated in terms of the wave function becomes extremely important near $D_{\rm max}$.

The comparison between the ASCC mass and the cranking mass made in Fig. 8 thus elucidates the importance of the HB self-consistency in evaluating the collective mass, although it is somewhat exaggerated.

There are various microscopic approaches to deriving the collective mass (also called "inertial functions").[1),2),31)] Certainly, it is important and interesting to make a detailed comparison of different approaches for deriving the collective mass in the multi-$O(4)$ model and to clarify the role of the HB self-consistency in more detail. Such a more systematic and comparative study is beyond the scope of this paper, but it will be carried out in a separate paper.

§6. Conclusions

The ASCC method was applied to an exactly solvable multi-$O(4)$ model that is designed to describe nuclear shape coexistence phenomena. The collective mass and the dynamics of large amplitude collective motion in this model system were analyzed, and it was shown that the method yields a faithful description of tunneling motion through a barrier between the prolate and oblate local minima in the collective potential. The result of numerical analysis seems very promising and encourages us to apply this approach to realistic cases. We plan to investigate the oblate-prolate shape coexistence phenomena in ^{68}Se with use of the P+Q interactions.

References

1) P. Ring and P. Schuck, *The Nuclear Many-Body Problem* (Springer-Verlag, 1980).
2) J.-P. Blaizot and G. Ripka, *Quantum Theory of Finite Systems* (The MIT press, 1986).
3) D. J. Rowe and R. Bassermann, Can. J. Phys. **54** (1976), 1941.
4) K. Goeke, Nucl. Phys. A **265** (1976), 301.
5) F. Villars, Nucl. Phys. A **285** (1977), 269.
6) T. Marumori, Prog. Theor. Phys. **57** (1977), 112.
7) M. Baranger and M. Veneroni, Ann. of Phys. **114** (1978), 123.
8) K. Goeke and P.-G. Reinhard, Ann. of Phys. **112** (1978), 328.
9) T. Marumori, T. Maskawa, F. Sakata and A. Kuriyama, Prog. Theor. Phys. **64** (1980), 1294.
10) M. J. Giannoni and P. Quentin, Phys. Rev. C **21** (1980), 2060.
11) J. Dobaczewski and J. Skalski, Nucl. Phys. A **369** (1981), 123.
12) K. Goeke, P.-G. Reinhard and D. J. Rowe, Nucl. Phys. A **359** (1981), 408.
13) A. K. Mukherjee and M. K. Pal, Phys. Lett. B **100** (1981), 457; Nucl. Phys. A **373** (1982), 289.
14) D. J. Rowe, Nucl. Phys. A **391** (1982), 307.
15) C. Fiolhais and R. M. Dreizler, Nucl. Phys. A **393** (1983), 205.
16) K. Goeke, F. Grümmer and P.-G. Reinhard, Ann. of Phys. **150** (1983), 504.
17) A. Kuriyama and M. Yamamura, Prog. Theor. Phys. **70** (1983), 1675; ibid. **71** (1984), 122.
18) M. Yamamura, A. Kuriyama and S. Iida, Prog. Theor. Phys. **71** (1984), 109.
19) M. Matsuo and K. Matsuyanagi, Prog. Theor. Phys. **74** (1985), 288.
20) M. Matsuo, Prog. Theor. Phys. **76** (1986), 372.
21) Y. R. Shimizu and K. Takada, Prog. Theor. Phys. **77** (1987), 1192.
22) M. Yamamura and A. Kuriyama, Prog. Theor. Phys. Suppl. No. 93 (1987), 1.
23) N. R. Walet, G. Do Dang and A. Klein, Phys. Rev. C **43** (1991), 2254.
24) A. Klein, N. R. Walet and G. Do Dang, Ann. of Phys. **208** (1991), 90.
25) K. Kaneko, Phys. Rev. C **49** (1994), 3014.
26) T. Nakatsukasa and N. R. Walet, Phys. Rev. C **57** (1998), 1192.
27) T. Nakatsukasa and N. R. Walet, Phys. Rev. C **58** (1998), 3397.
28) J. Libert, M. Girod and J.-P. Delaroche, Phys. Rev. C **60** (1999), 054301.
29) E. Kh. Yuldashbaeva, J. Libert, P. Quentin and M. Girod, Phys. Lett. B **461** (1999), 1.
30) T. Nakatsukasa, N. R. Walet and G. Do Dang, Phys. Rev. C **61** (2000), 014302.
31) G. Do Dang, A. Klein and N. R. Walet, Phys. Rep. **335** (2000), 93.
32) J. L. Wood, K. Heyde, W. Nazarewicz, M. Huyse and P. van Duppen, Phys. Rep. **215** (1992), 101.
33) W. Nazarewicz, Phys. Lett. B **305** (1993), 195.
34) W. Nazarewicz, Nucl. Phys. A **557** (1993), 489c.
35) N. Tajima, H. Flocard, P. Bonche, J. Dobaczewski and P.-H. Heenen, Nucl. Phys. A **551** (1993), 409.
36) P. Bonche, E. Chabanat, B. Q. Chen, J. Dobaczewski, H. Flocard, B. Gall, P. H. Heenen, J. Meyer, N. Tajima and M. S. Weiss, Nucl. Phys. A **574** (1994), 185c.
37) P.-G. Reinhard, D. J. Dean, W. Nazarewicz, J. Dobaczewski, J. A. Maruhn and M. R. Strayer, Phys. Rev. C **60** (1999), 014316.

38) A. N. Andreyev et al., Nature **405** (2000), 430; Nucl. Phys. A **682** (2001), 482c.
39) S. M. Fischer et al., Phys. Rev. Lett. **84** (2000), 4064.
40) R. R. Rodríguez-Guzmán, J. L. Egido and L. M. Robledo, Phys. Rev. C **62** (2000), 054319; ibid. **65** (2002), 024304.
41) R. R. Chasman, J. L. Egido and L. M. Robledo, Phys. Lett. B **513** (2001), 325.
42) T. Nikšić, D. Vretenar, P. Ring and G. A. Lalazissis, Phys. Rev. C **65** (2002), 054320.
43) A. Petrovici, K. W. Schmid and A. Faessler, Nucl. Phys. A **710** (2002), 246.
44) T. Duguet, M. Bender, P. Bonche and P.-H. Heenen, nucl-th/0212016.
45) R. Fossion, K. Heyde, G. Thiamova and P. Van Isacker, nucl-th/0301029.
46) M. Matsuo, Prog. Theor. Phys. **72** (1984), 666.
47) M. Matsuo and K. Matsuyanagi, Prog. Theor. Phys. **74** (1985), 1227; ibid. **76** (1986), 93; ibid. **78** (1987), 591.
48) M. Matsuo, Y. R. Shimizu and K. Matsuyanagi, *Proceedings of the Niels Bohr Centennial Conf. on Nuclear Structure*, ed. R. Broglia, G. Hagemann and B. Herskind (North-Holland, 1985), p. 161.
49) K. Takada, K. Yamada and H. Tsukuma, Nucl. Phys. A **496** (1989), 224.
50) K. Yamada, K. Takada and H. Tsukuma, Nucl. Phys. A **496** (1989), 239.
51) K. Yamada and K. Takada, Nucl. Phys. A **503** (1989), 53.
52) H. Aiba, Prog. Theor. Phys. **84** (1990), 908.
53) K. Yamada, Prog. Theor. Phys. **85** (1991), 805; ibid. **89** (1993), 995.
54) J. Terasaki, T. Marumori and F. Sakata, Prog. Theor. Phys. **85** (1991), 1235.
55) J. Terasaki, Prog. Theor. Phys. **88** (1992), 529; ibid. **92** (1994), 535.
56) M. Matsuo, in *New Trends in Nuclear Collective Dynamics*, ed. Y. Abe, H. Horiuchi and K. Matsuyanagi (Springer-Verlag, 1992), p. 219.
57) Y. R. Shimizu and K. Matsuyanagi, Prog. Theor. Phys. Suppl. No. 141 (2001), 285.
58) M. Matsuo, T. Nakatsukasa and K. Matsuyanagi, Prog. Theor. Phys. **103** (2000), 959.
59) M. Baranger and K. Kumar, Nucl. Phys. **62** (1965), 113; Nucl. Phys. A **100** (1967), 490; Nucl. Phys. A **110** (1968), 529; Nucl. Phys. A **122** (1968), 241; Nucl. Phys. A **122** (1968), 273.
60) D. R. Bes and R. A. Sorensen, *Advances in Nuclear Physics* (Prenum Press, 1969), vol. 2, p. 129.
61) K. Matsuyanagi, Prog. Theor. Phys. **67** (1982), 1141; *Proceedings of the Nuclear Physics Workshop*, Trieste, 5-30 Oct. 1981. ed. C. H. Dasso, R. A. Broglia and A. Winther (North-Holland, 1982), p. 29.
62) Y. Mizobuchi, Prog. Theor. Phys. **65** (1981), 1450.
63) T. Suzuki and Y. Mizobuchi, Prog. Theor. Phys. **79** (1988), 480.
64) T. Fukui, M. Matsuo and K. Matsuyanagi, Prog. Theor. Phys. **85** (1991), 281.
65) P. O. Arve and G. F. Bertsch, Phys. Lett. B **215** (1988), 1.

Available online at www.sciencedirect.com
SCIENCE DIRECT®
Nuclear Physics A 728 (2003) 52–64
NUCLEAR PHYSICS A
www.elsevier.com/locate/npe

Superdeformed bands in neutron-rich sulfur isotopes suggested by cranked Skyrme–Hartree–Fock calculations

T. Inakura [a], S. Mizutori [b], M. Yamagami [a], K. Matsuyanagi [a,*]

[a] *Department of Physics, Graduate School of Science, Kyoto University, Kitashirakawa, Kyoto 606-8502, Japan*
[b] *Department of Human Science, Kansai Women's College, Kashiwara City, Osaka 582-0026, Japan*

Received 1 July 2003; received in revised form 4 August 2003; accepted 5 August 2003

Abstract

On the basis of the cranked Skyrme–Hartree–Fock calculations in the three-dimensional coordinate-mesh representation, we suggest that, in addition to the well-known candidate ^{32}S, the neutron-rich nucleus ^{36}S and the drip-line nuclei, ^{48}S and ^{50}S, are also good candidates for finding superdeformed rotational bands in sulfur isotopes. Calculated density distributions for the superdeformed states in ^{48}S and ^{50}S exhibit superdeformed neutron skins.

PACS: 21.60.-n; 21.60.Jz; 27.30.+t

Keywords: Cranked Skyrme–Hartree–Fock method; Superdeformation; Neutron-rich nuclei; High-spin state; Sulfur isotopes

1. Introduction

Recently, superdeformed (SD) rotational bands have been discovered in ^{36}Ar, ^{40}Ca and ^{44}Ti [1–6]. One of the interesting new features of them is that they are built on excited 0^+ states and observed up to high spin, in contrast to the SD bands in heavier mass regions where low-spin portions of them are unknown in almost all cases [7–11]. These excited 0^+ states may be associated with multiparticle–multihole excitations from the spherical closed shells, so that we can hope to learn from such data detailed relationships between spherical

* Corresponding author.
E-mail address: ken@ruby.scphys.kyoto-u.ac.jp (K. Matsuyanagi).

0375-9474/$ – see front matter
doi:10.1016/j.nuclphysa.2003.08.012

shell model and SD configurations. For the mass $A = 30$–50 region, although existence of a SD band in ^{32}S with the SD magic number $N = Z = 16$ has been expected for a long time [12], it has not yet been observed and remains as a great challenge [13–17].

In this paper, as a continuation of the systematic theoretical search [14,18] for SD bands in the mass $A = 30$–50 region by means of the cranked Skyrme–Hartree–Fock (SHF) method [19], we would like to suggest that, in addition to ^{32}S, the neutron-rich nucleus ^{36}S and the nuclei, ^{48}S and ^{50}S, which are situated close to the neutron-drip line [20,21], are also good candidates for finding SD rotational bands in sulfur isotopes. The appearance of the SD band in ^{36}S is suggested in connection with the SD shell structure at $N = 20$ characterizing the observed SD band in ^{40}Ca. The drip-line nuclei, ^{48}S and ^{50}S, are expected to constitute a new "SD doubly closed" region associated with the SD magic numbers, $Z = 16$ for protons and $N \simeq 32$ for neutrons. An interesting theoretical subject for the SD bands in nuclei near the neutron drip line is to understand deformation properties of neutron skins. The calculated density distributions indeed exhibit superdeformed neutron skins.

The calculation has been carried out with the use of the three-dimensional (3D), Cartesian coordinate-mesh representation without imposing any symmetry restriction [14,18]. In parallel, we also carry out the standard calculations [22–25] imposing reflection symmetries. By comparing the symmetry restricted and unrestricted calculations, we can examine the stability of the SD solutions of the SHF equations against reflection-asymmetric deformations. In this way, we have found several cases where the SD minima obtained in the symmetry-restricted calculations are in fact unstable with respect to the reflection-asymmetric deformations. In general, the SD states are rather soft against reflection-asymmetric deformations, so that we need careful study about the stabilities of them against various kinds of deformation breaking the reflection symmetries.

After a brief account of the cranked SHF calculational procedure in Section 2, we present and discuss results of the calculation in Section 3, and give conclusions in Section 4. We shall present deformation energy curves for sulfur isotopes from ^{32}S to ^{50}S, and focus our attention on properties of rotational bands built on the SD 0^+ states, stabilities of the SD local minima against the reflection-asymmetric deformations, and density distributions of the SD states.

A preliminary version of this work was reported in [26].

2. Cranked SHF calculation

Since the cranked SHF method in the 3D coordinate-mesh representation is well known [22–25], we here give only a minimum description about the computational procedure actually adopted. For a recent comprehensive review on selfconsistent mean-field models for nuclear structure, see Ref. [19]. The cranked SHF equation for a system uniformly rotating about the x-axis is given by

$$\delta\langle H - \omega_{\rm rot}\hat{J}_x\rangle = 0, \tag{1}$$

where H, $\omega_{\rm rot}$ and $\hat{J}_x$ mean the Hamiltonian with the Skyrme interaction, the rotational frequency and the x-component of angular momentum, respectively, and the bracket

denotes the expectation value with respect to a Slater determinantal state. We solve the cranked SHF equation by means of the imaginary-time evolution technique [22] in the 3D Cartesian-mesh representation. The algorithm of numerical calculation is the standard one [22–25], except that we allow for both reflection- and axial-symmetry breakings. In this case, it is important to accurately fulfill the center-of-mass and principal-axis conditions. This is done by means of the constrained HF procedure [27]. We solved these equations inside the sphere with radius $R = 10$ fm and mesh size $h = 1$ fm, starting with various initial configurations. The accuracy for evaluating deformation energies with this mesh size was carefully checked by Tajima [25] and was found to be quite satisfactory. When we make a detailed analysis of density distributions, however, we use a smaller mesh size of $h = 1/3$ fm. In addition to the symmetry-unrestricted cranked SHF calculation, we also carry out symmetry-restricted calculations imposing reflection symmetries about the (x, y)-, (y, z)- and (z, x)-planes. Below we call these symmetry-unrestricted and -restricted cranked SHF versions "unrestricted" and "restricted" ones, respectively.

Solutions of the cranked SHF equation give local minima in the deformation energy surface. In order to explore the deformation energy surface around these minima and draw deformation energy curves as functions of deformation parameters, we carry out the constrained HF procedure with relevant constraining operators [27]. For the Skyrme interaction, we adopt the widely used three versions; SIII [28], SkM*[29] and SLy4 [30]. The pairing correlation is not taken into account in this paper. It will be dealt with in future by means of the symmetry-unrestricted Hartree–Fock–Bogoliubov code [31].

3. Results of calculation

3.1. Deformation energy curves

Fig. 1 shows deformation energy curves for sulfur isotopes from ^{32}S to ^{50}S obtained with the use of the SIII interaction. Solid lines with and without filled circles represent the results obtained by the unrestricted and restricted versions, respectively. The result of calculation indicates that the SD minima (with the quadrupole deformation parameter $\beta_2 \approx 0.6$) appear in the neutron-rich nucleus ^{36}S and the drip-line nuclei, ^{48}S and ^{50}S, in addition to the well-known case of ^{32}S. As seen in Figs. 2 and 3, similar results are obtained for the SkM* and SLy4 interactions, except that the SD states in ^{48}S is unstable against the reflection-asymmetric deformation for the SLy4 interaction (see Section 3.3).

As discussed in Refs. [14–18], the SD local minimum in ^{32}S corresponds to the doubly closed shell configuration with respect to the SD magic number $Z = N = 16$ and involves two protons and two neutrons in the down-sloping single-particle levels originating from the $f_{7/2}$ shell. The SD local minimum in ^{36}S results from the coherent combination of the SD magic number, $Z = 16$, and the neutron shell effects occurring at large deformation for $N = 20$. The latter shell effect has been confirmed recently by the discovery of the SD rotation band in ^{40}Ca [4,5]. The SD shell gap at $N = 20$ is associated with the 4p–4h excitation from below the $N = 20$ spherical closed shell to the $f_{7/2}$ shell. Focusing our attention on the occupation numbers of such high-j shells and distinguishing protons (π)

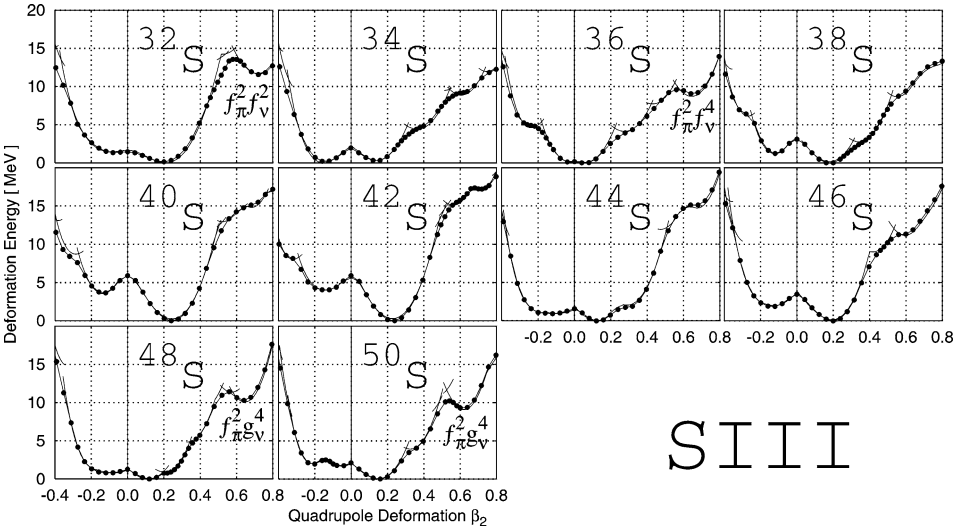

Fig. 1. Deformation energy curves for sulfur isotopes from ^{32}S to ^{50}S calculated at $I = 0$ as functions of the quadrupole deformation β_2 by means of the constrained SHF procedure with the SIII interaction. The deformation parameter is defined as $\beta_2 = \frac{4\pi}{5}\langle\sum_{i=1}^{A} r_i^2 Y_{20}(\theta_i, \phi_i)\rangle/\langle\sum_{i=1}^{A} \boldsymbol{r}_i^2\rangle$. The axial-asymmetry parameter γ is constrained to be zero. Solid curves with and without filled circles represent the results obtained by the unrestricted and restricted versions, respectively. The notation $f_\pi^{n_1} f_\nu^{n_2}$ indicates a configuration in which single-particle levels originating from the $f_{7/2}$ shell are occupied by n_1 protons and n_2 neutrons. Likewise, $f_\pi^{n_1} g_\nu^{n_2}$ indicates that levels from the $f_{7/2}$ shell are occupied by n_1 protons and those from the $g_{9/2}$ shell by n_2 neutrons.

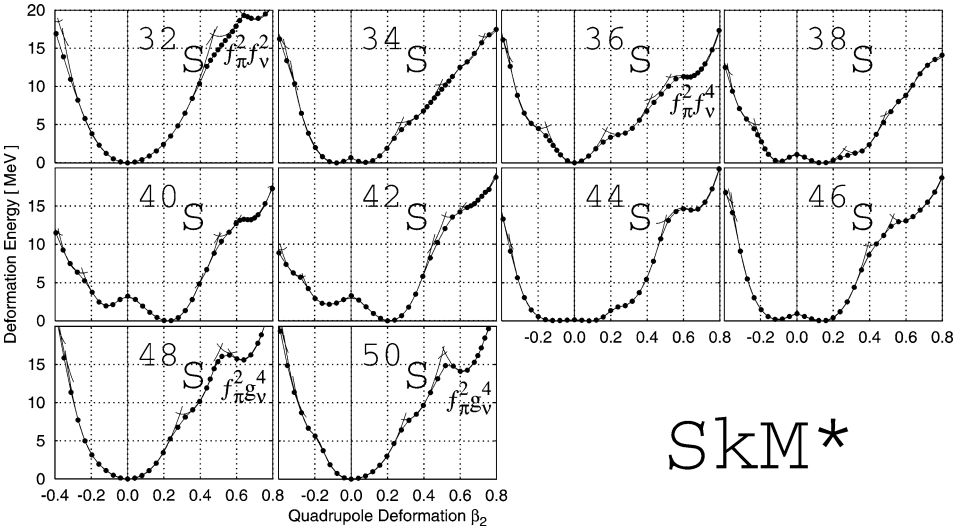

Fig. 2. The same as Fig. 1 but for the SkM* interaction.

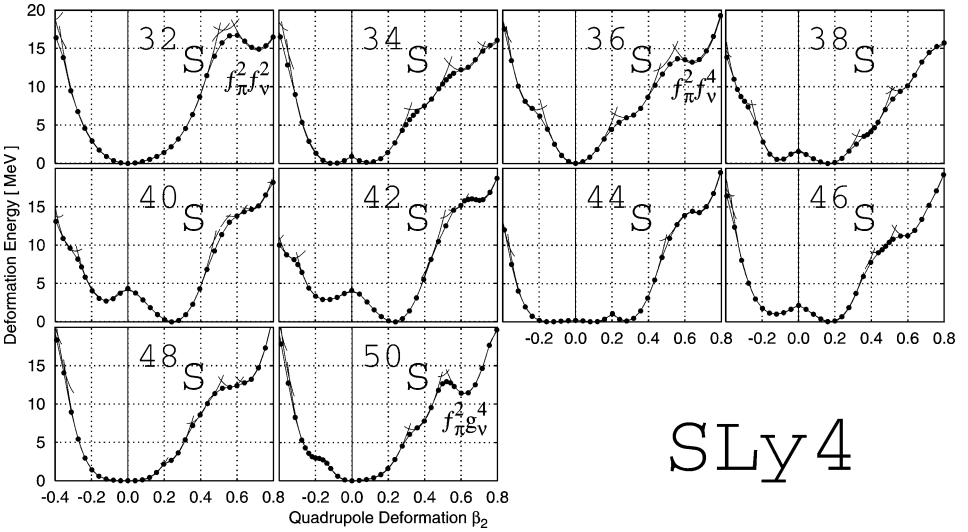

Fig. 3. The same as Fig. 1 but for the SLy4 interaction.

and neutrons (ν), these SD configurations in ^{32}S and ^{36}S are denoted in Figs. 1–3 as $f_\pi^2 f_\nu^2$ and $f_\pi^2 f_\nu^4$, respectively.

The SD local minima in the drip-line nuclei, ^{48}S and ^{50}S, result from the coherent combination of the proton SD shell effect and the neutron shell effects occurring at superdeformation for $N = 32$–34. The neutron configurations in these SD states are similar to those in the known SD bands in ^{60}Zn and ^{62}Zn associated with the SD magic numbers $N = 30$–32 [32,33]. We find that the SD shell effect is strong also for $N = 34$ in the sulfur isotopes under consideration, while the SD local minimum in ^{46}S with $N = 30$ is unstable against the reflection-asymmetric deformation (see Section 3.3). In the drip-line nuclei ^{48}S and ^{50}S, the $f_{7/2}$ shell is fully occupied even in the spherical limit and the SD configurations involve neutron excitations from the fp-shell to the $g_{9/2}$ shell. As before, focusing our attention on the occupation numbers of the high-j shells, let us use the notation $f_\pi^{n_1} g_\nu^{n_2}$ for a configuration in which single-particle levels originating from the $f_{7/2}$ and $g_{9/2}$ shell are occupied by n_1 protons and n_2 neutrons, respectively. With such notations, both the SD local minima in ^{48}S and ^{50}S correspond to the $f_\pi^2 g_\nu^4$ configuration.

The appearance of the SD minimum in ^{36}S suggests that we can expect a SD band associated with the same neutron configuration to appear also in the $N = 20$ isotone, ^{38}Ar, situated between ^{36}S and ^{40}Ca. We examined this point and the result is shown in Fig. 4. We find that the two local minima associated with the configurations $f_\pi^2 f_\nu^2$ and $f_\pi^2 f_\nu^4$ compete in energy and their relative energy differs for different versions of the Skyrme interaction: As clearly seen in the deformation-energy curves obtained by the symmetry-restricted calculations, the former with smaller β_2 is slightly lower for SkM* and SLy4 while the latter with larger β_2 is slightly lower for SIII. Counting both protons and neutrons, these local minima respectively correspond to the 4p–6h and 6p–8h configurations with respect to the spherical doubly closed shell of ^{40}Ca. As we discussed in the previous papers [18,26], the two configurations can mix each other in the crossing region through the reflection-

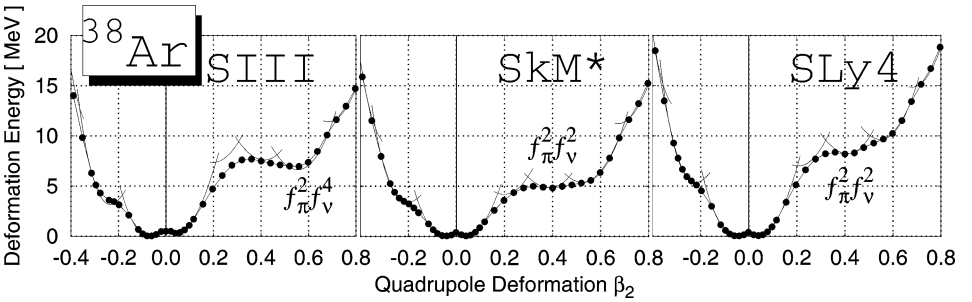

Fig. 4. The same as Fig. 1 but for ^{38}Ar and for the SIII, SkM* and SLy4 interactions.

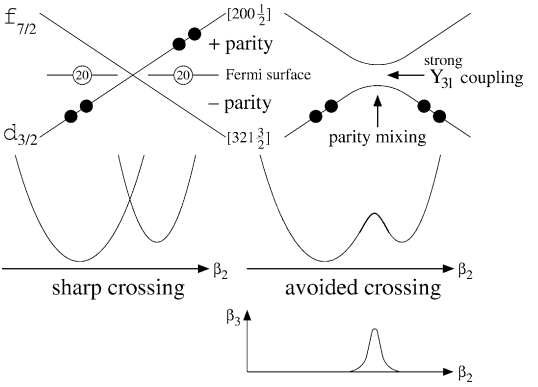

Fig. 5. Schematic illustration of configuration-mixing mechanism through the octupole components of the mean field. When the reflection symmetry is imposed, the positive- and negative-parity single-particle levels sharply cross, and the two configurations (having different number of particles in the $f_{7/2}$ shell) do not mix within the mean-field approximation (left-hand side). In contrast, when such symmetry restriction is removed, smooth crossover between the two configurations is possible via mixing of the positive- and negative-parity levels (right-hand side). Octupole deformation β_3 of the mean field rises in the crossing region. In this figure, the crossing between the two levels with the asymptotic quantum numbers $[321\frac{3}{2}]$ and $[200\frac{1}{2}]$ is illustrated as an example. The two levels satisfy the selection rule, $\Delta n_3 = 2$ and $\Delta\Lambda = 1$, for the matrix elements of the non-axial octupole operator r^3Y_{31}, so that the mixing between them takes place mainly through the r^3Y_{31} component of the mean field.

symmetry breaking components in the mean field. Specifically, around the crossing point between the down-sloping $[321\frac{3}{2}]$ level (coming from the $f_{7/2}$ shell) and the up-sloping $[200\frac{1}{2}]$ level (coming from the $d_{3/2}$ shell below the $N = 20$ spherical magic number), the r^3Y_{31}-type non-axial octupole deformation is generated, and they mix each other through this component of the mean field (see Fig. 5). Note that the matrix element of the operator r^3Y_{31} between the two levels satisfies the selection rules, $\Delta n_3 = 2$ and $\Delta\Lambda = 1$, for the asymptotic quantum numbers n_3 and Λ. As a result of this mixing, the deformation-energy curve becomes rather flat in the symmetry-unrestricted calculation. Recently, the SD band

corresponding to the 4p–6h configuration was found in experiment [34]. The data suggest significant competition between different configurations, which requires further analysis of shape fluctuation dynamics by going beyond the static mean-field approximation.

3.2. SD rotational bands

Let us focus our attention on the SD local minima shown in Figs. 1–3, and investigate properties of the rotational bands built on them. Excitation energies of these SD rotational bands are plotted in Fig. 6 as functions of angular momentum. These rotational bands are calculated by cranking each SHF solution (the SD local minima in Figs. 1–3) and following the same configuration with increasing value of $\omega_{\rm rot}$ until the point where we cannot clearly identify the continuation of the same configuration any more. Thus, the highest values of angular momentum in this figure does not necessarily indicate the band-termination points but merely suggest that drastic changes in their microscopic structure take place around there. Different slopes with respect to the angular momentum between ^{36}S and ^{50}S can be easily understood in terms of the well-known scaling factor $A^{5/3}$ for the rigid-body moment of inertia. This point can be confirmed in Fig. 7 which displays the angular momentum I, the kinematical and dynamical moments of inertia, $\mathcal{J}^{(1)} = I/\omega_{\rm rot}$ and $\mathcal{J}^{(2)} = dI/d\omega_{\rm rot}$, and the rigid-body moments of inertia $\mathcal{J}_{\rm rig} = m\int \rho(\boldsymbol{r})(y^2+z^2)\,d\boldsymbol{r}$ as functions of the rotational frequency $\omega_{\rm rot}$. We see that the calculated moments of inertia are slightly larger than the rigid-body values at $\omega_{\rm rot} = 0$, and smoothly decrease as $\omega_{\rm rot}$ increases until $\omega_{\rm rot} \approx 2.5$ and 1.8 MeV/$\hbar$ for ^{32,36}S and ^{50}S, respectively. The result calculated with the SLy4 interaction is shown here, but we obtained similar results also with the SIII and SkM* interactions.

Calculated quadrupole deformation parameters (β_2, γ) are displayed in the upper portion of Fig. 6. We see that the β_2 values slowly decrease while the axial-asymmetry parameters γ gradually increase with increasing angular momentum for all cases of ^{32}S,

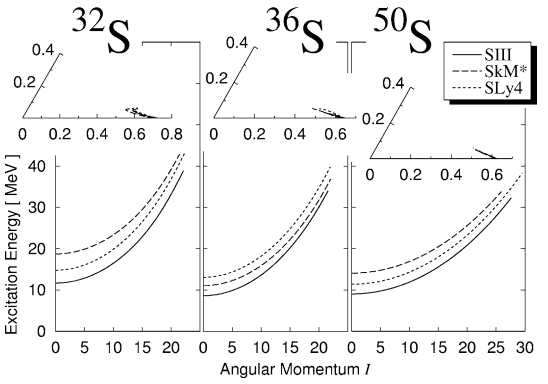

Fig. 6. Plot of the excitation energies versus angular-momentum for the SD rotational bands in ^{32}S, ^{36}S, and ^{50}S calculated by means of the cranked SHF method. Results obtained with the use of the SIII, SkM*, and SLy4 interactions are plotted by solid, dashed, and dotted curves, respectively. Their shape evolutions as functions of angular momentum I in the (β_2, γ) plane are displayed in the upper portions. The β_2 values decrease with increasing I.

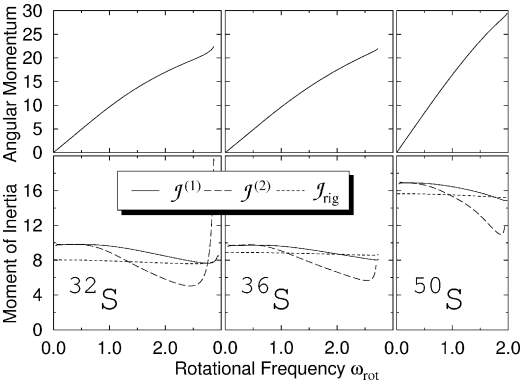

Fig. 7. The angular momenta I and the moments of inertia $\mathcal{J}$ are plotted as functions of rotational frequency $\omega_{\rm rot}$ for the SD rotational bands in ^{32}S, ^{36}S, and ^{50}S. The SLy4 interaction is used. Values of the kinematical and dynamical moments of inertia, $\mathcal{J}^{(1)} = I/\omega_{\rm rot}$ and $\mathcal{J}^{(2)} = dI/d\omega_{\rm rot}$, are plotted in unit of $\hbar^2/$ MeV by solid and dashed curves, respectively. For reference, the rigid-body moments of inertia $\mathcal{J}_{\rm rig} = m\int \rho(\boldsymbol{r})(y^2+z^2)\,d\boldsymbol{r}$ evaluated with the calculated density $\rho(\boldsymbol{r})$ are also indicated.

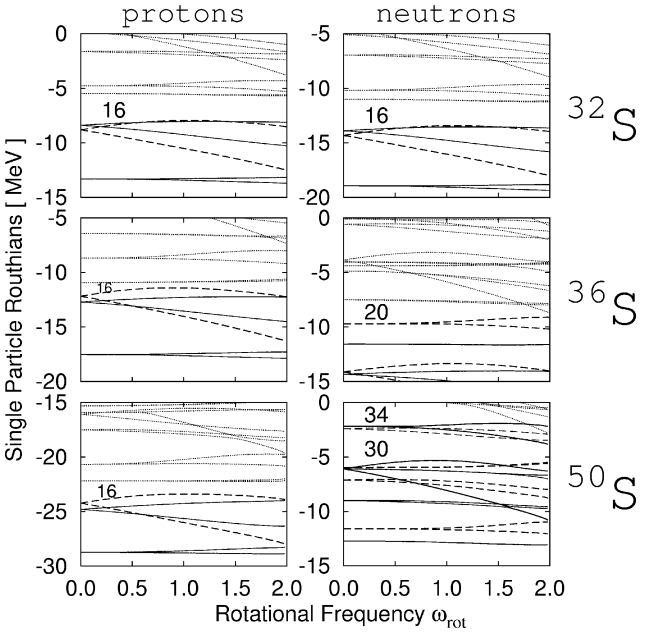

Fig. 8. Single-particle energy diagrams (Routhians) for the SD bands in ^{32}S, ^{36}S, and ^{50}S, plotted as functions of rotational frequency $\omega_{\rm rot}$. The left(right)-hand side displays those for protons(neutrons). The levels associated with the $g_{9/2}$ and $f_{7/2}$ shells are drawn by thick-solid and thick-dashed lines, respectively. Other occupied levels associated with the sd and fp shells are drawn by thin-solid and thin-dashed lines, respectively. Unoccupied levels are drawn by thin-dotted lines. Numbers indicate the Fermi surfaces and total numbers of single-particle states below them. The result calculated with SLy4 is shown here, but we obtained similar results also with SIII and SkM*.

^{36}S and ^{50}S. The variations are rather mild in the range of angular momentum shown in this figure. Single-particle energy diagrams (Routhians) for these SD bands are displayed in Fig. 8 as functions of the rotational frequency $\omega_{\rm rot}$. This figure indicates that level crossings take place in ^{36}S and ^{50}S if we further increase the angular momentum.

3.3. Stabilities of the SD states against reflection-asymmetric deformations

Let us examine stabilities of the SD local minimum against both the axially symmetric and asymmetric octupole deformation ($Y_{30}, Y_{31}, Y_{32}, Y_{33}$). Fig. 9 presents deformation energy curves as functions of the octupole deformation parameters $\beta_{3m} (m = 0, 1, 2, 3)$ for fixed quadrupole deformation parameters (the equilibrium value of β_2 at the SD minimum in each nucleus and $\gamma = 0$). The computation was carried out by means of the constrained HF procedure with the use of the SIII, SkM*, and SLy4 interactions. The result of calculation clearly indicates that the SD states in ^{32}S, ^{36}S and ^{50}S are stable against the octupole deformations and that they are softer for β_{3m} with lower values of m (i.e., for β_{30} and β_{31}), irrespective of the Skyrme interactions used. We obtained a similar result also for ^{48}S (but omitted in this figure).

Although the SD minima in ^{32}S, ^{36}S and ^{50}S are stable with respect to β_{3m} ($m = 0, 1, 2, 3$), we found several cases where the SD minima obtained in the symmetry-restricted calculations become unstable when we allow for reflection-asymmetric defor-

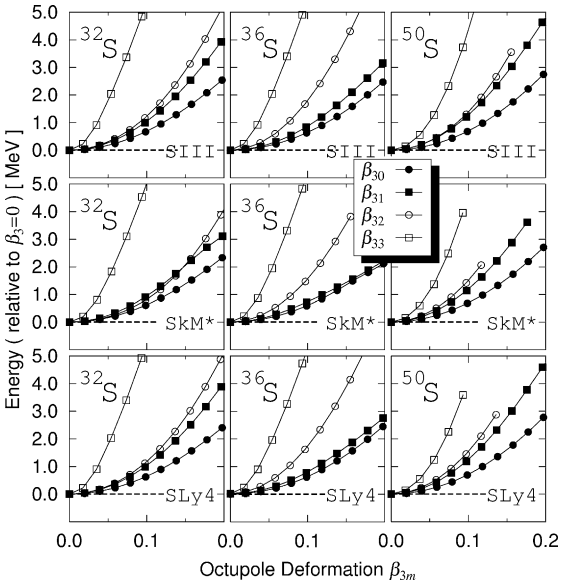

Fig. 9. Deformation energy curves (measured from energies at $\beta_3 = 0$) as functions of the octupole deformation parameters β_{3m} ($m = 0, 1, 2, 3$), calculated for ^{32}S, ^{36}S, and ^{50}S, by means of the constrained HF procedure with the use of the SIII, SkM* and SLy4 interactions. The quadrupole deformation parameters are fixed at the equilibrium value of β_2 in each nucleus and $\gamma = 0$. One of the β_{3m} ($m = 0, 1, 2, 3$) is varied while the other β_{3m}'s are fixed to zero. The deformation parameters β_3 and β_{3m} are defined in terms of the expectation values of the octupole operators (see Ref. [18] for their explicit expressions).

mations of a more general type. As a first example, let us discuss the SD minimum in ^{46}S which appears in the restricted calculation (see Figs. 1–3). In this case, the coupling between the down-sloping $[330\frac{1}{2}]$ level (associated with the $f_{7/2}$ shell) and the up-sloping $[202\frac{5}{2}]$ level (stemming from the $d_{5/2}$ shell) takes place in the proton configuration, when we allow for the breaking of both the axial and reflection symmetries. Thus, the SD configuration $f_\pi^2 g_\nu^2$ mixes with the g_ν^2 configuration (which lacks the proton excitation to the $f_{7/2}$ shell and has a smaller equilibrium value of β_2). As a consequence of this mixing, the barrier between the two configurations disappears and the SD minimum becomes unstable in the unrestricted calculations (see Figs. 1–3). Note that the difference Δn_3 in the asymptotic quantum number n_3 between the two single-particle levels, $[330\frac{1}{2}]$ and $[202\frac{5}{2}]$, is three, so that they cannot be mixed by the octupole operator $r^3 Y_{32}$ which transfers the asymptotic quantum numbers n_3 and Λ by $\Delta n_3 = 1$ and $\Delta\Lambda = 2$. Thus, this mixing may be associated with the reflection-asymmetric deformation of a more higher order like $r^5 Y_{52}$.

As a second example, we take up the SD minimum in ^{48}S. In this case, two configurations, $f_\pi^2 g_\nu^2$ and $f_\pi^2 g_\nu^4$ compete in energy and their relative energy differs for different versions of the Skyrme interaction; the former with smaller β_2 is slightly lower (higher) for SLy4 (SIII and SkM*) (see Figs. 1–3). When we allow for the breaking of both the axial and reflection symmetries, the coupling between the down-sloping $[431\frac{3}{2}]$ level (associated with the $g_{9/2}$ shell) and the $[310\frac{1}{2}]$ level in the fp shell takes place in the neutron configuration, so that they mix each other. Note that the $[431\frac{3}{2}]$ and $[310\frac{1}{2}]$ levels satisfy the selection rules, $\Delta n_3 = 2$ and $\Delta\Lambda = 1$, for the matrix elements of the octupole operator $r^3 Y_{31}$. In the calculation with the SLy4 interaction, since the former configuration with smaller β_2 is situated slightly lower in energy than the latter, the barrier between the two configurations disappears as a result of this mixing. This mixing effect in conjunction with that mentioned above for the $f_\pi^2 g_\nu^2$ configuration in ^{46}S deteriorates the SD minimum for the SLy4 case.

The above examples indicate detailed microscopic mechanisms within the mean-field theory how the stability of the SD local minimum is determined by relative energies between the neighboring configurations and their mixing properties. In this connection, it should be noted that the pairing interaction ignored in this paper might also play an important role in the mixing of crossing configurations. It thus remains to be an interesting future subject to study the competition between the two different mixing mechanisms, i.e., the symmetry breaking in the mean field and the pairing correlation.

3.4. Density distributions

Fig. 10 displays the neutron and proton density profiles for the SD states in ^{32}S, ^{36}S and ^{50}S calculated with the use of the SLy4 interaction. We obtained similar results also for SIII and SkM*. In this figure, equi-density lines with 50% and 1% of the central density in the (x, y)- and (y, z)-planes are drawn for the SD bands at $I = 0$ and at high spins. We can clearly see that superdeformed neutron skin appears in ^{50}S which is situated close to the neutron drip line. The root-mean-square values, $\sqrt{\langle x^2\rangle}$, $\sqrt{\langle y^2\rangle}$, $\sqrt{\langle z^2\rangle}$ and $R_{\rm rms} = \sqrt{\langle \boldsymbol{r}^2\rangle}$, of these density distributions are listed in Table 1. To indicate the deformation properties of the neutron skin in ^{50}S, calculated values for protons and neutrons are separately listed

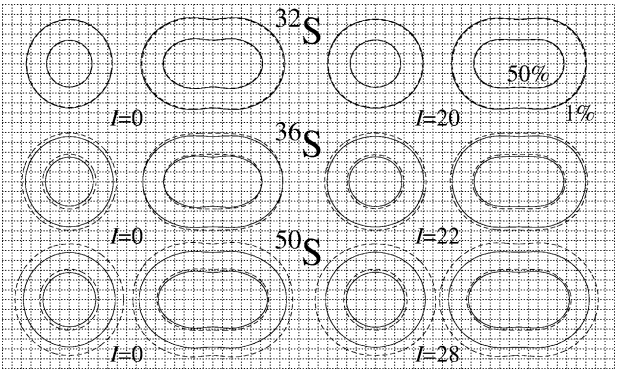

Fig. 10. Left-hand side: Density distributions in the (y,x)- and (z,x)-planes of the SD band at $I=0$ in ^{32}S, ^{36}S, and ^{50}S, calculated with the use of the SLy4 interaction. Neutron (proton) equi-density lines with 50% and 1% of the central density are shown by dashed (solid) lines (the inner and outer lines correspond to the 50% and 1% lines, respectively). Right-hand side: Same as the left-hand side but for $I=20, 22, 28$ for ^{32}S, ^{36}S, and ^{50}S, respectively.

Table 1
Root-mean-square values, $\sqrt{\langle x^2\rangle}$, $\sqrt{\langle y^2\rangle}$, $\sqrt{\langle z^2\rangle}$ and $R_{\rm rms}=\sqrt{\langle \boldsymbol{r}^2\rangle}$, of the density distributions at $I=0$ (second column) and at $I=20, 22, 28$ (third column) of the SD band in ^{32}S, ^{36}S and ^{50}S, calculated with the use of the SLy4 interaction

^{32}S	$I=0$				$I\sim 20$			
	$\sqrt{\langle x^2\rangle}$	$\sqrt{\langle y^2\rangle}$	$\sqrt{\langle z^2\rangle}$	$R_{\rm rms}$	$\sqrt{\langle x^2\rangle}$	$\sqrt{\langle y^2\rangle}$	$\sqrt{\langle z^2\rangle}$	$R_{\rm rms}$
total	1.53	1.53	2.85	3.57	1.53	1.67	2.67	3.50
neutrons	1.52	1.52	2.83	3.55	1.52	1.66	2.65	3.48
protons	1.54	1.54	2.86	3.60	1.54	1.68	2.68	3.52
diff.	−0.02	−0.02	−0.04	−0.04	−0.02	−0.02	−0.04	−0.05
^{36}S	$I=0$				$I\sim 22$			
	$\sqrt{\langle x^2\rangle}$	$\sqrt{\langle y^2\rangle}$	$\sqrt{\langle z^2\rangle}$	$R_{\rm rms}$	$\sqrt{\langle x^2\rangle}$	$\sqrt{\langle y^2\rangle}$	$\sqrt{\langle z^2\rangle}$	$R_{\rm rms}$
total	1.59	1.59	2.78	3.58	1.61	1.73	2.63	3.53
neutrons	1.62	1.62	2.78	3.60	1.64	1.75	2.64	3.57
protons	1.55	1.55	2.78	3.54	1.57	1.69	2.61	3.48
diff.	0.07	0.07	0.00	0.06	0.08	0.06	0.03	0.09
^{50}S	$I=0$				$I\sim 28$			
	$\sqrt{\langle x^2\rangle}$	$\sqrt{\langle y^2\rangle}$	$\sqrt{\langle z^2\rangle}$	$R_{\rm rms}$	$\sqrt{\langle x^2\rangle}$	$\sqrt{\langle y^2\rangle}$	$\sqrt{\langle z^2\rangle}$	$R_{\rm rms}$
total	1.81	1.81	3.11	4.03	1.82	1.96	2.95	3.98
neutrons	1.90	1.90	3.17	4.16	1.91	2.05	3.02	4.12
protons	1.62	1.62	2.96	3.75	1.63	1.75	2.79	3.67
diff.	0.28	0.28	0.20	0.41	0.28	0.31	0.23	0.45

Neutron and proton contributions are separately listed together with their sums (total) and differences (diff.).

together with their sums and differences. We obtained density distributions similar to those for ^{50}S also for the SD state in ^{48}S. A similar result of theoretical calculation exhibiting the superdeformed neutron skin was previously reported in Ref. [35] for the SD state in the very neutron-rich nucleus $^{208}_{66}\mathrm{Dy}_{142}$.

4. Conclusions

On the basis of the cranked SHF calculations in the 3D coordinate-mesh representation, we have suggested that, in addition to the well-known candidate ^{32}S, the neutron-rich ^{36}S and the drip-line nuclei, ^{48}S and ^{50}S, are also good candidates for finding SD rotational bands in sulfur isotopes. Calculated density distributions for the SD states in ^{48}S and ^{50}S, which are situated close to the neutron-drip line, exhibit superdeformed neutron skins.

Acknowledgements

The numerical calculations were performed on the NEC SX-5 supercomputers at RCNP, Osaka University, and at Yukawa Institute for Theoretical Physics, Kyoto University. This work was supported by the Grant-in-Aid for Scientific Research (No. 13640281) from the Japan Society for the Promotion of Science.

References

[1] C.E. Svensson, et al., Phys. Rev. Lett. 85 (2000) 2693.
[2] C.E. Svensson, et al., Phys. Rev. C 63 (2001) 061301(R).
[3] C.E. Svensson, et al., Nucl. Phys. A 682 (2001) 1c.
[4] E. Ideguchi, et al., Phys. Rev. Lett. 87 (2001) 222501.
[5] C.J. Chiara, et al., Phys. Rev. C 67 (2003) 041303(R).
[6] C.D. O'Leary, M.A. Bentley, B.A. Brown, D.E. Appelbe, R.A. Bark, D.M. Cullen, S. Ertürk, A. Maj, A.C. Merchant, Phys. Rev. C 61 (2000) 064314.
[7] P.J. Nolan, P.J. Twin, Annu. Rev. Nucl. Part. Sci. 38 (1988) 533.
[8] S. Åberg, H. Flocard, W. Nazarewicz, Annu. Rev. Nucl. Part. Sci. 40 (1990) 439.
[9] R.V.F. Janssens, T.L. Khoo, Annu. Rev. Nucl. Part. Sci. 41 (1991) 321.
[10] C. Baktash, B. Haas, W. Nazarewicz, Annu. Rev. Nucl. Part. Sci. 45 (1995) 485.
[11] C. Baktash, Prog. Part. Nucl. Phys. 38 (1997) 291.
[12] I. Ragnarsson, S.G. Nilsson, R.K. Sheline, Phys. Rep. 45 (1978) 1.
[13] J. Dobaczewski, in: C. Baktash (Ed.), Proc. Int. Conf. on Nuclear Structure '98, in: AIP Conf. Proc., Vol. 481, 1999, p. 315.
[14] M. Yamagami, K. Matsuyanagi, Nucl. Phys. A 672 (2000) 123.
[15] H. Molique, J. Dobaczewski, J. Dudek, Phys. Rev. C 61 (2000) 044304.
[16] R.R. Rodriguez-Guzmán, J.L. Egido, L.M. Robeldo, Phys. Rev. C 62 (2000) 054308.
[17] T. Tanaka, R.G. Nazmitdinov, K. Iwasawa, Phys. Rev. C 63 (2001) 034309.
[18] T. Inakura, S. Mizutori, M. Yamagami, K. Matsuyanagi, Nucl. Phys. A 710 (2002) 261.
[19] M. Bender, P.-H. Heenen, P.-G. Reinhard, Rev. Mod. Phys. 75 (2003) 121.
[20] T.R. Werner, J.A. Sheikh, W. Nazarewicz, M.R. Strayer, A.S. Umar, M. Misu, Phys. Lett. B 333 (1994) 303.
[21] T.R. Werner, J.A. Sheikh, M. Misu, W. Nazarewicz, J. Rikovska, K. Heeger, A.S. Umar, M.R. Strayer, Nucl. Phys. A 597 (1996) 327.
[22] K.T.R. Davies, H. Flocard, S.J. Krieger, M.S. Weiss, Nucl. Phys. A 342 (1980) 111.
[23] P. Bonche, H. Flocard, P.H. Heenen, S.J. Krieger, M.S. Weiss, Nucl. Phys. A 443 (1985) 39.
[24] P. Bonche, H. Flocard, P.H. Heenen, Nucl. Phys. A 467 (1987) 115.
[25] N. Tajima, Prog. Theor. Phys. Suppl. 142 (2001) 265.
[26] T. Iakura, M. Yamagami, K. Matsuyanagi, S. Mizutori, in: Proc. Int. Symp. "Frontiers of Collective Motions," Aizu-Wakamatsu, Japan, November 6–9, 2002, in press.
[27] H. Flocard, P. Quentin, A.K. Kerman, D. Vautherin, Nucl. Phys. A 203 (1973) 433.

[28] M. Beiner, H. Flocard, N. van Giai, P. Quentin, Nucl. Phys. A 238 (1975) 29.
[29] J. Bartel, P. Quentin, M. Brack, C. Guet, H.-B. Håkansson, Nucl. Phys. A 386 (1982) 79.
[30] E. Chabanat, P. Bonche, P. Haensel, J. Meyer, F. Schaeffer, Nucl. Phys. A 635 (1998) 231.
[31] M. Yamagami, K. Matsuyanagi, M. Matsuo, Nucl. Phys. A 693 (2001) 579.
[32] C.E. Svensson, et al., Phys. Rev. Lett. 82 (1999) 3400.
[33] C.E. Svensson, et al., Phys. Rev. Lett. 79 (1997) 1233.
[34] D. Rudolph, et al., Phys. Rev. C 65 (2002) 034305.
[35] I. Hamamoto, X.Z. Zhang, Phys. Rev. C 52 (1995) R2326.

Nuclear moments of inertia and wobbling motions in triaxial superdeformed nuclei

Masayuki Matsuzaki*
Department of Physics, Fukuoka University of Education, Munakata, Fukuoka 811-4192, Japan

Yoshifumi R. Shimizu†
Department of Physics, Graduate School of Sciences, Kyushu University, Fukuoka 812-8581, Japan

Kenichi Matsuyanagi‡
Department of Physics, Graduate School of Science, Kyoto University, Kyoto 606-8502, Japan
(Received 21 October 2003; published 19 March 2004; publisher error corrected 24 March 2004)

The wobbling motion excited on triaxial superdeformed nuclei is studied in terms of the cranked shell model plus random phase approximation. First, by calculating at a low rotational frequency the γ dependence of the three moments of inertia associated with the wobbling motion, the mechanism of the appearance of the wobbling motion in positive-γ nuclei is clarified theoretically—the rotational alignment of the $\pi i_{13/2}$ quasiparticle(s) is the essential condition. This indicates that the wobbling motion is a collective motion that is sensitive to the single-particle alignment. Second, we prove that the observed unexpected rotational-frequency dependence of the wobbling frequency is an outcome of the rotational-frequency dependent dynamical moments of inertia.

DOI: 10.1103/PhysRevC.69.034325 PACS number(s): 21.10.Re, 21.60.Jz, 23.20.Lv, 27.70.+q

I. INTRODUCTION

Deformation of the nuclear shape from spherical symmetric one has long been one of the most important issues in nuclear structure physics. Among them, searches for evidences of the triaxial (Y_{22} or γ) one have been pursued long time, for example, the even-odd energy staggering in the low-spin part of the γ bands [1], the signature dependence of the energy spectra, and the $E2/M1$ transition rates in medium-spin odd-odd and odd-A nuclei [2–4], properties of the K isomers [5,6], and so on. But their results have not been conclusive; making a clear distinction between the static and the dynamic (vibrational) ones has not been successful up to now. Theoretically, appearance of the wobbling motion, which is well known in classical mechanics of asymmetric tops [7] and whose quantum analog was discussed in terms of a rotor model about 30 years ago [8], is a decisive evidence of static triaxial deformations. Subsequently its microscopic descriptions were developed by several authors [9,10]. Since the small-amplitude wobbling mode carries the same quantum numbers, parity $\pi=+$ and signature $\alpha=1$, as the odd-spin members of the γ band, Ref. [11] anticipated that it would appear as a high-spin continuation of the γ band, but it has not been resolved that in what nuclei, at what spins, and with what γ wobbling modes would be observed.

Shimizu and Matsuyanagi [12] and Onishi [13] performed extensive numerical calculations for normally deformed Er isotopes with relatively small $|\gamma|$. Matsuzaki [14], Shimizu and Matsuzaki [15], and Horibata and Onishi [16] also studied ^{182}Os with relatively large negative γ but their correspondence to experimental information has not been very clear.

These studies indicate the necessity of high-spin states in stably and strongly γ-deformed nuclei. Bengtsson studied high-spin states around ^{164}Hf [17] and found systematic existence of the TSD (triaxial superdeformed or strongly deformed) states with $\epsilon_2 \sim 0.4$ and $|\gamma| \sim 20°$. This confirmed the discussion on the shell gap at $N=94$ in Ref. [18], the work in which the yrast TSD band in ^{163}Lu was reported; in 2000 an excited TSD band was observed in this nucleus and from the strengths of the interband $E2$ transition rates this was unambiguously identified with the wobbling motion [19]. These data were analyzed by using a particle-rotor model [20] and the $E2$ transition rates were reproduced well. Subsequently TSD bands were found in some Lu and Hf isotopes and wobbling excitations were observed also in ^{165,167}Lu [21,22]. A close look at these data, however, tells us that the sign of their γ-deformation seems to contradict to an irrotational motion and that the unexpected behavior of the wobbling frequency has not been explained yet.

Thus in the preceding Rapid Communication [23] we presented an answer to these problems. In the present paper, after summarizing the discussion there we extend numerical analyses to elucidate it. An emphasis is put on the behavior of the calculated dynamic moments of inertia.

II. WOBBLING MOTION IN TERMS OF THE RANDOM PHASE APPROXIMATION

We start from a one-body Hamiltonian in the rotating frame,

$$h' = h - \hbar\omega_{\rm rot} J_x, \tag{1}$$

$$h = h_{\rm Nil} - \Delta_\tau (P_\tau^\dagger + P_\tau) - \lambda_\tau N_\tau, \tag{2}$$

*Email address: matsuza@fukuoka-edu.ac.jp
†Email address: yrsh2scp@mbox.nc.kyushu-u.ac.jp
‡Email address: ken@ruby.scphys.kyoto-u.ac.jp

$$h_{\rm Nil} = \frac{p^2}{2M} + \frac{1}{2}M(\omega_x^2 x^2 + \omega_y^2 y^2 + \omega_z^2 z^2) + v_{ls}\mathbf{l}\cdot\mathbf{s} + v_{ll}(\mathbf{l}^2 - \langle \mathbf{l}^2\rangle_{N_{\rm osc}}). \quad (3)$$

In Eq. (2), $\tau=1$ and 2 stand for neutron and proton, respectively, and chemical potentials λ_τ are determined so as to give correct average particle numbers $\langle N_\tau\rangle$. The oscillator frequencies in Eq. (3) are expressed by the quadrupole deformation parameters ϵ_2 and γ in the usual way. They are treated as parameters as well as pairing gaps Δ_τ. The orbital angular momentum $\mathbf{l}$ in Eq. (3) is defined in the singly stretched coordinates $x'_k=\sqrt{(\omega_k/\omega_0)}x_k$, with $k=1-3$ denoting $x-z$, and the corresponding momenta. By diagonalizing h' at each $\omega_{\rm rot}$, we obtain quasiparticle (QP) orbitals and the nuclear yrast (0QP) state. Since h' conserves parity π and signature α, nuclear states can be labeled by them. Nuclear states with QP excitations are obtained by exchanging the QP energy and wave functions such as

$$(-e'_\mu, \mathbf{V}_\mu, \mathbf{U}_\mu) \to (e'_{\bar\mu}, \mathbf{U}_{\bar\mu}, \mathbf{V}_{\bar\mu}), \quad (4)$$

where $\bar\mu$ denotes the signature partner of μ.

We perform the random phase approximation (RPA) to the residual pairing plus doubly stretched quadrupole-quadrupole ($Q''\cdot Q''$) interaction between QPs. Since we are interested in the wobbling motion that has a definite quantum number, $\alpha=1$, only two components out of five of the $Q''\cdot Q''$ interaction are relevant. They are given by

$$H_{\rm int}^{(-)} = -\frac{1}{2}\sum_{K=1,2}\kappa_K^{(-)} Q_K''^{(-)\dagger} Q_K''^{(-)}, \quad (5)$$

where the doubly stretched quadrupole operators are defined by

$$Q_K'' = Q_K\left(x_k \to x_k'' = \frac{\omega_k}{\omega_0}x_k\right), \quad (6)$$

and those with good signature are

$$Q_K^{(\pm)} = \frac{1}{\sqrt{2(1+\delta_{K0})}}(Q_K \pm Q_{-K}). \quad (7)$$

The residual pairing interaction does not contribute because P_τ is an operator with $\alpha=0$. The equation of motion

$$[h' + H_{\rm int}^{(-)}, X_n^\dagger]_{\rm RPA} = \hbar\omega_n X_n^\dagger \quad (8)$$

for the eigenmode

$$X_n^\dagger = \sum_{\mu<\nu}^{(\alpha=\pm1/2)} [\psi_n(\mu\nu)a_\mu^\dagger a_\nu^\dagger + \varphi_n(\mu\nu)a_\nu a_\mu] \quad (9)$$

leads to a pair of coupled equations for the transition amplitudes

$$T_{K,n} = \langle [Q_K^{(-)}, X_n^\dagger]\rangle. \quad (10)$$

Then, by assuming $\gamma\neq 0$, this can be cast [10] into the form

$$(\omega_n^2 - \omega_{\rm rot}^2)\left[\omega_n^2 - \omega_{\rm rot}^2\frac{[\mathcal{J}_x - \mathcal{J}_y^{(\rm eff)}(\omega_n)][\mathcal{J}_x - \mathcal{J}_z^{(\rm eff)}(\omega_n)]}{\mathcal{J}_y^{(\rm eff)}(\omega_n)\mathcal{J}_z^{(\rm eff)}(\omega_n)}\right] = 0, \quad (11)$$

which is independent of $\kappa_K^{(-)}$s. This expression proves that the spurious (Nambu-Goldstone) mode given by the first factor and all normal modes given by the second are decoupled from each other. Here $\mathcal{J}_x=\langle J_x\rangle/\omega_{\rm rot}$ as usual and the detailed expressions of $\mathcal{J}_{y,z}^{(\rm eff)}(\omega_n)$ are given in Refs. [10,14,15]. Among normal modes, one obtains

$$\omega_{\rm wob}^2 = \omega_{\rm rot}^2\frac{[\mathcal{J}_x - \mathcal{J}_y^{(\rm eff)}(\omega_{\rm wob})][\mathcal{J}_x - \mathcal{J}_z^{(\rm eff)}(\omega_{\rm wob})]}{\mathcal{J}_y^{(\rm eff)}(\omega_{\rm wob})\mathcal{J}_z^{(\rm eff)}(\omega_{\rm wob})} \quad (12)$$

by putting $\omega_n=\omega_{\rm wob}$. Note that this gives a real excitation only when the right-hand side is positive and it is nontrivial whether a collective solution appears or not. Evidently this coincides with the form derived by Bohr and Mottelson in a rotor model [8] and known in classical mechanics [7], aside from the crucial feature that the moments of inertia are $\omega_{\rm rot}$ dependent in the present case.

One drawback in our formulation is that our $\mathcal{J}_x$ tends to be larger than corresponding experimental values because of the spurious velocity dependence of the Nilsson potential as discussed in Refs. [24,25]. A remedy for this was discussed there but that for $\mathcal{J}_{y,z}^{(\rm eff)}$ has not been devised yet. Therefore we assume for the present that a similar discussion holds for the latter, and accordingly the ratio $\mathcal{J}_{y,z}^{(\rm eff)}(\omega_{\rm wob})/\mathcal{J}_x$ which actually determines $\omega_{\rm wob}$ is more reliable than its absolute magnitude.

Interband electric quadrupole transitions between the nth excited band and the yrast are given as

$$B(E2{:}I_n \to (I\pm1)_{\rm yrast}) = \frac{1}{2}(T_{1,n}^{(E)} \pm T_{2,n}^{(E)})^2 \quad (13)$$

in terms of

$$T_{K,n}^{(E)} = e\frac{Z}{A}T_{K,n}. \quad (14)$$

They will be abbreviated as $B(E2)_{\rm out}$ later for simplicity. In-band ones are given as

$$B(E2{:}I \to I-2) = \frac{1}{2}\left(\frac{\sqrt{3}}{2}\langle Q_0^{(+)(E)}\rangle + \frac{1}{2}\langle Q_2^{(+)(E)}\rangle\right)^2 \quad (15)$$

in terms of

$$\langle Q_K^{(+)(E)}\rangle = e\frac{Z}{A}\langle Q_K^{(+)}\rangle, \quad (16)$$

and assumed to be common to all bands. They will be abbreviated as $B(E2)_{\rm in}$. Here we adopted a high-spin approximation [26]. The transition quadrupole moment $Q_{\rm t}$ is extracted from $B(E2)_{\rm in}$ by the usual rotor-model prescription.

To compare collectivities of these two types of $E2$ transitions, we introduce a pair of deformation parameters

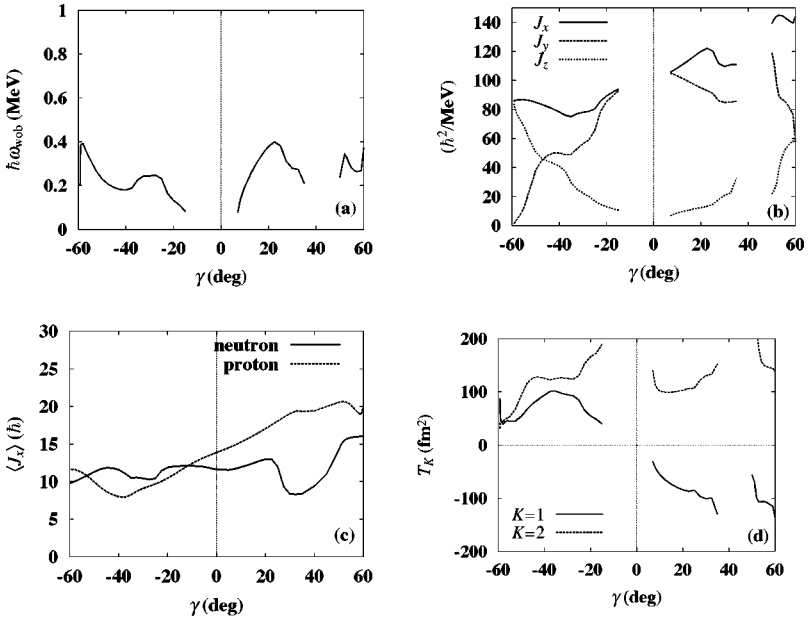

FIG. 1. Triaxiality dependence of (a) excitation energy of the wobbling motion, (b) three moments of inertia associated with it, (c) expectation values of angular momenta in the yrast state, and (d) quadrupole transition amplitudes between the wobbling and the yrast states in ^{168}Hf, calculated at $\hbar\omega_{\rm rot}=0.25$ MeV with $\epsilon_2=0.43$ and $\Delta_n=\Delta_p=0.3$ MeV.

$$R^2\alpha_y=\sqrt{\frac{15}{16\pi}}\langle x^2-z^2\rangle=\left\langle\frac{1}{2}Q_2^{(+)}-\frac{\sqrt{3}}{2}Q_0^{(+)}\right\rangle,$$

$$R^2\alpha_z=\sqrt{\frac{15}{16\pi}}\langle x^2-y^2\rangle=\langle Q_2^{(+)}\rangle. \tag{17}$$

Then it is evident that the in-band one is expressed as

$$B(E2{:}I\to I-2)=\frac{1}{2}R^4(\alpha_y^{(E)}-\alpha_z^{(E)})^2. \tag{18}$$

As for the interband ones, by expanding $Q_K^{(-)}$ by $X_n^\dagger$s and X_ns, where n runs both normal modes and the Nambu-Goldstone mode $X_{\rm NG}^\dagger=1/\sqrt{2I}(J_z+iJ_y)$, we obtain from $[Q_1^{(-)},Q_2^{(-)}]=0$ a kind of sum rule

$$\sum_{n\neq{\rm NG}}T_{1,n}T_{2,n}=-\frac{2}{I}R^4\alpha_y\alpha_z. \tag{19}$$

Consecutively introducing the ratios of the dynamic to static deformations,

$$r_{y,n}=\frac{T_{1,n}}{2R^2\alpha_y},$$

$$r_{z,n}=-\frac{T_{2,n}}{2R^2\alpha_z}, \tag{20}$$

the sum rule above reads

$$\sum_{n\neq{\rm NG}}r_{y,n}r_{z,n}=\frac{1}{2I}. \tag{21}$$

The dynamic amplitudes $T_{K,n}$ describe shape fluctuations associated with the vibrational motion in the uniformly rotating frame. Transformation to the body-fixed (principal axis) frame [10] turns the shape fluctuation into the fluctuation of the angular momentum vector, i.e., the wobbling motion. This transformation relates the ratios $r_{y,n}$ and $r_{z,n}$ to the moments of inertia [15]:

$$r_{y,n}=c_n\frac{1}{\sqrt{2I}}\left(\frac{W_{z,n}}{W_{y,n}}\right)^{1/4},$$

$$r_{z,n}=\sigma_n c_n\frac{1}{\sqrt{2I}}\left(\frac{W_{y,n}}{W_{z,n}}\right)^{1/4}, \tag{22}$$

where c_n is a real amplitude that relates the dynamic amplitude $T_{K,n}$ and the moment of inertia, σ_n is the sign of $(\mathcal{J}_x-\mathcal{J}_y^{(\rm eff)})$ (so $\sigma_n>0$ for wobblinglike RPA solutions), and

$$W_{y,n}=1/\mathcal{J}_z^{(\rm eff)}(\omega_n)-1/\mathcal{J}_x,$$

$$W_{z,n}=1/\mathcal{J}_y^{(\rm eff)}(\omega_n)-1/\mathcal{J}_x. \tag{23}$$

Thus, the interband $B(E2)$ is rewritten as

$$B(E2{:}I_n\to(I\pm1)_{\rm yrast})=\frac{1}{I}R^4c_n^2\left[\alpha_y^{(E)}\left(\frac{W_{z,n}}{W_{y,n}}\right)^{1/4}\mp\sigma_n\alpha_z^{(E)}\times\left(\frac{W_{y,n}}{W_{z,n}}\right)^{1/4}\right]^2, \tag{24}$$

which coincides with the formula given by the rotor model [8], except for the appearance of the amplitude c_n and sign σ_n. Substituting the ratios $r_{y,n}$ and $r_{z,n}$ into Eq. (21), one finds that the amplitudes should satisfy

$$\sum_{n\neq{\rm NG}}\sigma_n c_n^2=1. \tag{25}$$

This form of sum rule clearly indicates that the amplitude c_n is a microscopic correction factor quantifying the collectivity of the wobbling motion, for which $c_n^2\simeq1$ means the full collectivity and reproduces the results of the macro-

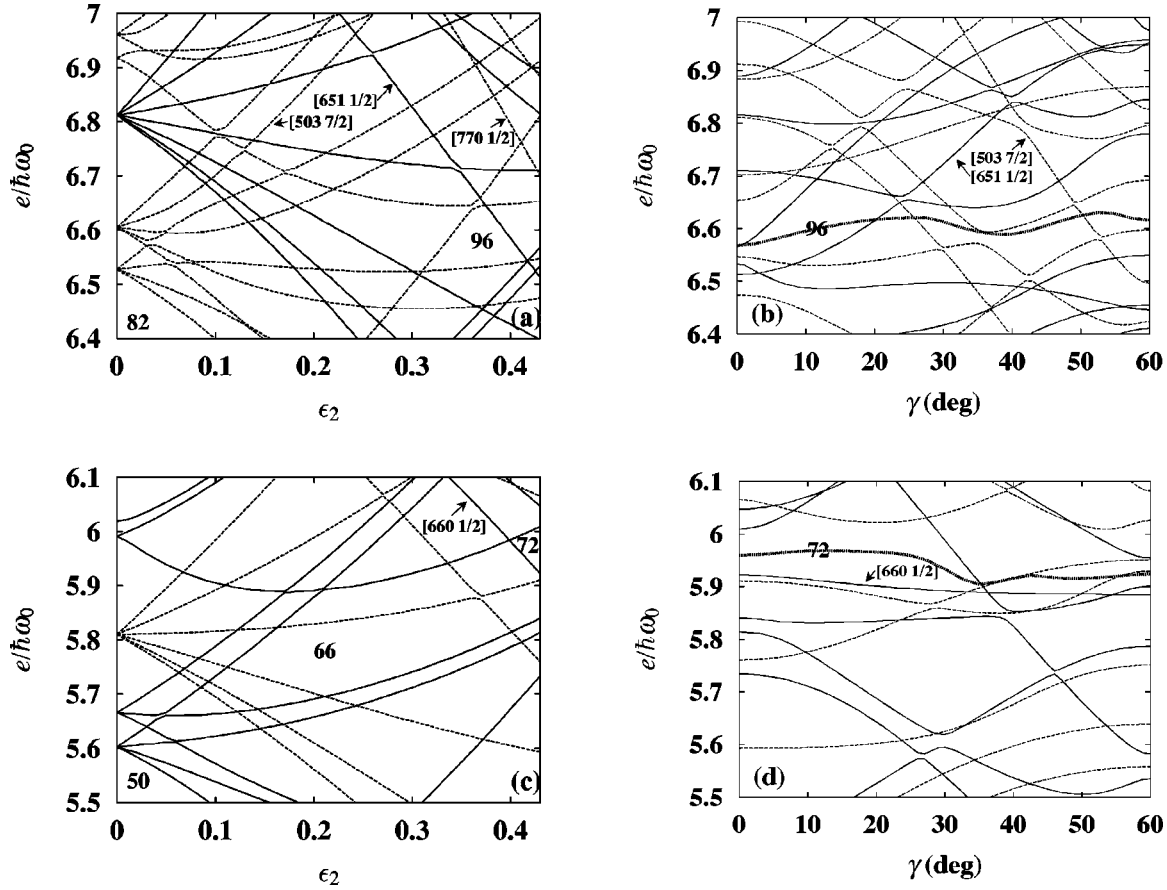

FIG. 2. Nilsson single-particle energy diagrams at $\omega_{\rm rot}=0$, (a) for $0\leqslant\epsilon_2\leqslant 0.43$ with $\gamma=0$ and (b) for $0\leqslant\gamma\leqslant 60°$ with $\epsilon_2=0.43$ for neutrons. (c) and (d) are corresponding ones for protons. Solid and dashed curves represent even and odd parity orbitals, respectively. Asymptotic quantum numbers of some important orbitals are explicitly indicated. Chemical potentials that give particle numbers $N=96$ and $Z=72$ for $\gamma>0$ at $\hbar\omega_{\rm rot}=0.25$ MeV are also indicated in (b) and (d).

scopic rotor model in both the energy and the interband $B(E2)$ values.

III. NUMERICAL CALCULATION AND DISCUSSION

A. Summary of the preceding study

Since the first experimental confirmation of the wobbling excitation in ^{163}Lu [19], $\gamma\simeq+20°$ has been widely accepted as the shape of the TSD states in this region. This is predominantly because the calculated energy minimum for $\gamma\simeq+20°$ is deeper than that for $\gamma\simeq-20°$ [17] according to the shape driving effect of the aligned $\pi i_{13/2}$ quasiparticle. The recent precise measurements of Q_t [27] also support this. On the other hand, the sign of γ deformation leads to different consequences on moments of inertia, which are directly connected to the excitation energy of the wobbling mode through the wobbling frequency formula [8], cf. Eq. (12). Since the RPA is a microscopic formalism, no distinction between the collective rotation and the single-particle degrees of freedom has been made.

Therefore, the moments of inertia calculated in our RPA formalism in Sec. II are those for rotational motions of the whole system. In contrast, the macroscopic irrotational-like moments of inertia are often used in the particle-rotor calculations, where $\mathcal{J}_y>\mathcal{J}_x\gg\mathcal{J}_z$ for $\gamma\simeq+20°$ and they lead to an imaginary wobbling frequency $\omega_{\rm wob}$. It is, however, noted that the moments of inertia of the particle-rotor model are those of the rotor and no effect of the single-particle alignments is included, so that they do not necessarily correspond to those calculated in our RPA formalism.

In the preceding paper [23] we have performed microscopic RPA calculations without dividing the system artificially into the rotor and particles. That work proved that for the calculated moment of inertia, $\mathcal{J}_x=\langle J_x\rangle/\omega_{\rm rot}$, the contribution from the aligned QP(s), $\Delta\mathcal{J}_x=i_{\rm QP}/\omega_{\rm rot}$ with $i_{\rm QP}$ being the aligned angular momentum, is superimposed on an irrotational-like moment of inertia ($\mathcal{J}_y>\mathcal{J}_x$) of the "core." Consequently the total $\mathcal{J}_x$ is larger than $\mathcal{J}_y$, which makes wobbling excitation in $\gamma>0$ nuclei possible.

The second consequence of the formulation adopted in Ref. [23] is that the three moments of inertia are automatically $\omega_{\rm rot}$ dependent even when the mean-field parameters are fixed constant. This is essential in order to explain the observed $\omega_{\rm rot}$ dependence of $\omega_{\rm wob}$—*decreasing* as $\omega_{\rm rot}$ increases. Otherwise $\omega_{\rm wob}$ is proportional to $\omega_{\rm rot}$.

Another important feature of the data is that the interband $B(E2)$ values between the wobbling and the yrast TSD bands are surprisingly large. Our RPA wave function gave ex-

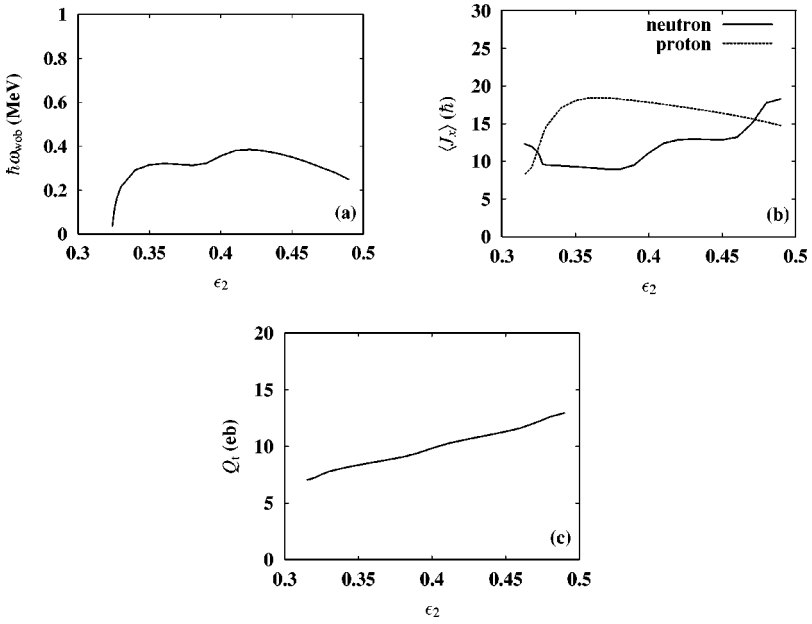

FIG. 3. Deformation dependence of (a) excitation energy of the wobbling motion, (b) expectation values of angular momenta in the yrast state, and (c) transition quadrupole moment in the yrast state in ^{168}Hf, calculated at $\hbar\omega_{\rm rot}=0.25$ MeV with $\gamma=20°$ and $\Delta_n=\Delta_p=0.3$ MeV.

tremely collective $B(E2)_{\rm out}$ that gathered $|c_{n=\rm wob}|\simeq 0.6-0.8$ in the sum rule [Eq. (25)] but the result accounted for only about one-half of the measured one.

To elucidate these findings more, in the following we extend our numerical analyses putting a special emphasis on the γ dependence of the moments of inertia in Sec III B. Dependence on other parameters is also studied in detail. Features in common and different between even-even and odd-A nuclei are also pointed out. In Sec. III C, we discuss $\omega_{\rm rot}$ dependence. In Sec. III D, characteristics of $B(E2)_{\rm out}$ are discussed. Calculations are performed in five major shells; $N_{\rm osc}=3-7$ for neutrons and $N_{\rm osc}=2-6$ for protons. The strengths v_{ls} and v_{ll} in Eq. (3) are taken from Ref. [28].

B. Dependence on the mean-field parameters γ, ϵ_2, and Δ

1. The even-even nucleus ^{168}Hf

Hafnium-168 is the first even-even nucleus in which TSD bands were observed [29]. In this nucleus three TSD bands were observed but interband γ rays connecting them have not been observed yet. This means that the character of the excited bands has not been established, although we expect at least one of them is wobbling excitation. An important feature of the data is that the average transition quadrupole moment was determined as $Q_{\rm t}=11.4^{+1.1}_{-1.2}$ e b. This imposes a moderate constraint on the shape. Referring to the weak parameter dependence discussed later, we choose $\epsilon_2=0.43$, $\gamma=20°$, and $\Delta_n=\Delta_p=0.3$ MeV, which reproduce the observed $Q_{\rm t}$, as a typical mean-field parameter set.

First we study the dependence of various quantities on γ and other mean-field parameters at $\hbar\omega_{\rm rot}=0.25$ MeV. Around this frequency the $(\pi i_{13/2})^2$ alignment that is essential for making wobbling excitation in $\gamma>0$ nuclei possible is completed and therefore the wobbling motion is expected to emerge above this frequency (see Fig. 7 shown later).

Figure 1 shows dependence on γ calculated with keeping $\epsilon_2=0.43$ and $\Delta_n=\Delta_p=0.3$ MeV. Figure 1(a) graphs the calculated excitation energy in the rotating frame, $\hbar\omega_{\rm wob}$. As γ comes close to 0 (symmetric about the z axis) and $-60°$ (symmetric about the y axis), $\omega_{\rm wob}$ approaches 0, see Eq. (12). We did not obtain any low-lying RPA solutions at around $\gamma=40°$ whereas a collective solution appears again for $50°\leqslant\gamma\leqslant 60°$.

Figure 1(b) shows the calculated moments of inertia. Their γ dependence resembles the irrotational, the so-called γ-reversed, and the rigid-body moments of inertia, in $\gamma<0$, $0<\gamma<40°$, and $50°\leqslant\gamma\leqslant 60°$, respectively. These model moments of inertia are given by

$$\mathcal{J}_k^{\rm irr}=4B\beta^2\,\sin^2\left(\gamma+\frac{2}{3}\pi k\right), \tag{26}$$

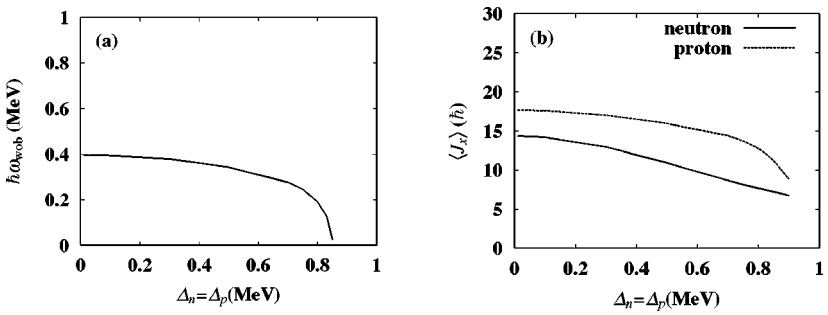

FIG. 4. Pairing gap dependence of (a) excitation energy of the wobbling motion and (b) expectation values of angular momenta in the yrast state in ^{168}Hf, calculated at $\hbar\omega_{\rm rot}=0.25$ MeV with $\epsilon_2=0.43$ and $\gamma=20°$. $\Delta_n=\Delta_p$ is assumed for simplicity.

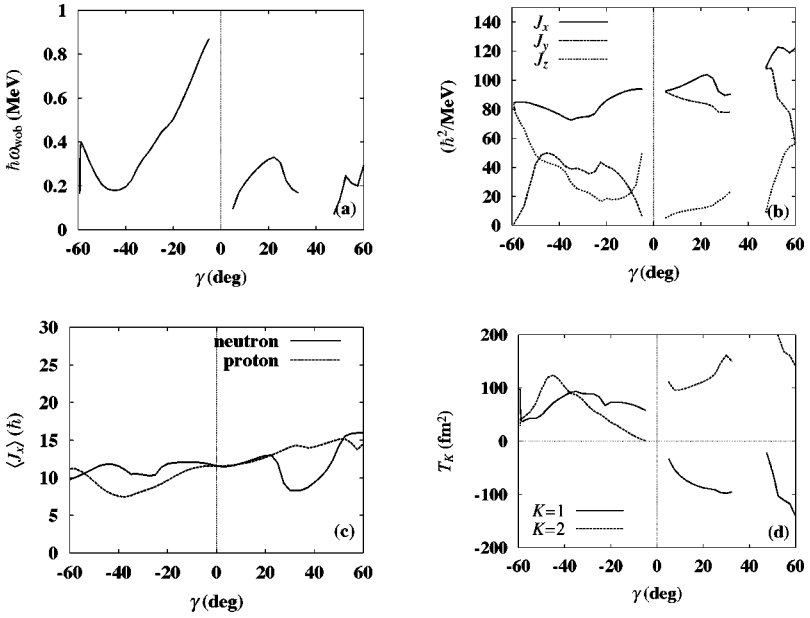

FIG. 5. The same as Fig. 1 but for ^{167}Lu.

$$\mathcal{J}_k^{\rm rev} = 4B\beta^2 \sin^2\left(-\gamma + \frac{2}{3}\pi k\right), \tag{27}$$

and

$$\mathcal{J}_k^{\rm rig} = \mathcal{J}_0\left[1 - \sqrt{\frac{5}{4\pi}}\beta\cos\left(\gamma + \frac{2}{3}\pi k\right)\right], \tag{28}$$

where $k=1-3$ denote the $x-z$ principal axes, B the irrotational mass parameter, $\mathcal{J}_0$ the rigid moment of inertia in the spherical limit, and β is a deformation parameter like ϵ_2. The γ-reversed moment of inertia was introduced to describe positive-γ rotations in the particle-rotor model [3] but its physical meaning has not been very clear; in particular, it does not fulfill the quantum-mechanical requirement that the rotations about the symmetry axis should be forbidden. We have clarified in the preceding paper [23] that the contributions from aligned quasiparticles superimposed on irrotational-like moments of inertia ($\mathcal{J}_x<\mathcal{J}_y$) can realize $\mathcal{J}_x>\mathcal{J}_y$ and this is the very reason why the wobbling excitation [see Eq. (12)] appears in positive-γ nuclei. We also discussed that multiple alignments could eventually lead to a rigid-body-like moment of inertia. Figure 1(c) indicates that, in the present calculation in which configuration is specified as the adiabatic quasiparticle vacuum at each $\omega_{\rm rot}$, two $\pi i_{13/2}$ protons align for $\gamma>0$ as mentioned above while they have not fully aligned for $\gamma<0$ at this $\omega_{\rm rot}$. In other words, these figures cover both regions in which the $(\pi i_{13/2})^2$ alignment is necessary ($\gamma>0$) and that is not necessary ($\gamma<0$) for obtaining wobbling excitations. This aligned angular momentum determines the overall γ dependence of $\mathcal{J}_x$ in Fig. 1(b). As for the neutron part, corresponding to the disappearance of the solution at around $\gamma=40°$, the expectation value of the neutron angular momentum, $\langle J_x\rangle_n$, drops around this region.

To look at this more closely, we investigate the Nilsson single-particle diagram at $\omega_{\rm rot}=0$. Figure 2(a) graphs neutron single-particle energies for $0\leqslant\epsilon_2\leqslant 0.43$ with $\gamma=0$, while Fig. 2(b) for $0\leqslant\gamma\leqslant 60°$ with $\epsilon_2=0.43$. The chemical potential that gives correct neutron number $N=96$ for $\gamma>0$ at $\hbar\omega_{\rm rot}=0.25$ MeV is also drawn in the latter. This figure clearly shows that with this ϵ_2 a shell gap exists for $\gamma \lesssim 20°$ at $N=96$. And by comparing this with Fig. 1 we see that the dropping of $\langle J_x\rangle_n$ is a consequence of the deoccupation of the orbital that is [651 1/2] at $\gamma=0$ (hereafter simply referred to as the [651 1/2] orbital even at $\gamma\neq 0$) originating from the mixed ($g_{9/2}$-$i_{11/2}$) spherical shell. Figure 2(b) also explains the reason why the wobbling excitation revives at around $\gamma=50°$ again; the occupation of other oblate-favoring orbitals such as [503 7/2] makes it possible and leads to a rigid-body-like behavior of the moments of inertia. Figures 2(c) and 2(d) are corresponding ones for protons. This indicates that the proton shell gap is robuster.

Figure 1(d) graphs the quadrupole transition amplitudes $T_K(K=1,2)$ associated with the wobbling mode. [T_K corresponds to $(-1)^{K-1}\mathcal{Q}_K$ in Ref. [15].] This shows that their relative sign changes with that of γ as discussed in Refs. [14,15]. This feature can be understood as follows: $\gamma\sim 0$ is the γ-vibrational region because the $K=2$ component is dominant [see also $\mathcal{J}_x\simeq\mathcal{J}_y^{(\rm eff)}$ and $\mathcal{J}_z^{(\rm eff)}\simeq 0$ in Fig. 1(b)], and the mixing of the $K=1$ component due to triaxiality and ro-

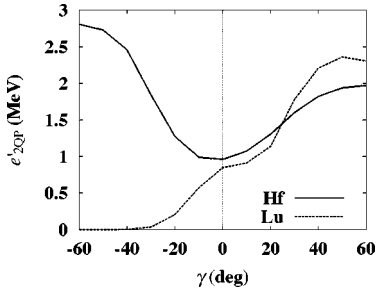

FIG. 6. Energies of the lowest $[\pi(N_{\rm osc}=6)]^2$ two quasiparticle states in ^{168}Hf and ^{167}Lu, calculated at the same time in Figs. 1 and 5, respectively.

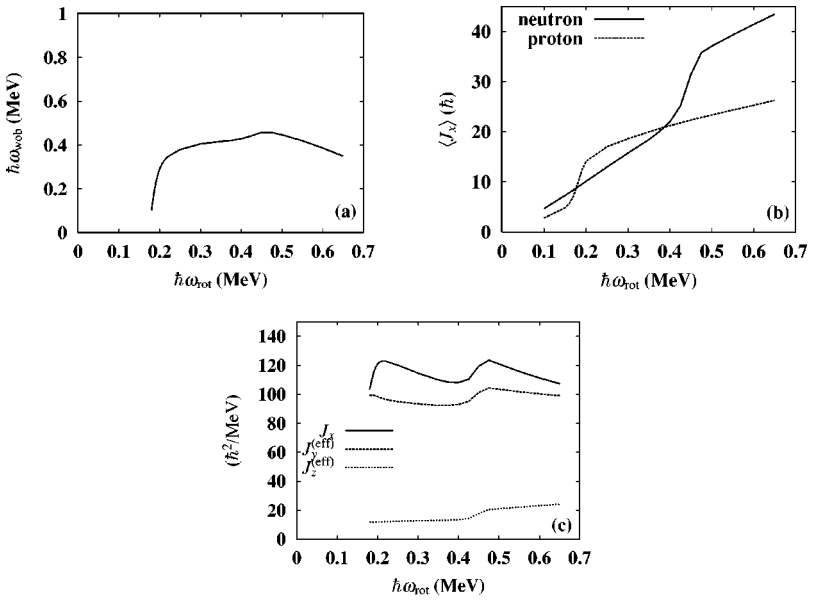

FIG. 7. Rotational frequency dependence of (a) excitation energy of the wobbling motion, (b) expectation values of angular momenta in the yrast state, and (c) three moments of inertia associated with the wobbling motion in ^{168}Hf, calculated with $\epsilon_2=0.43$, $\gamma=20°$, and $\Delta_n=\Delta_p=0.3$ MeV.

tation gives rise to the character of the wobbling motion. This relative sign leads to a selection rule of the interband transition probabilities $B(E2)_{\rm out}$ [15]. In the present case we obtain $B(E2:I\to I-1)_{\rm out} \gtrless B(E2:I\to I+1)_{\rm out}$ for $\gamma \gtrless 0$, and typically their ratio to the in-band ones is $B(E2:I\to I-1)_{\rm out}/B(E2:I\to I-2)_{\rm in}\sim 0.1$.

Figure 3 shows dependence on ϵ_2 calculated with keeping $\gamma=20°$ and $\Delta_n=\Delta_p=0.3$ MeV. The steep rises at around $\epsilon_2=0.33$ in Figs. 3(a) and 3(b) indicate the necessity of the $(\pi i_{13/2})^2$ **[**the [660 1/2] orbital in Fig. 2(c)**]** alignment for the appearance of the wobbling mode although the critical value of ϵ_2 itself is frequency dependent. Aside from this, $\omega_{\rm wob}$ is almost constant in the calculated range. The slight increase at around $\epsilon_2=0.4$ stems from the occupation of the ν[651 1/2] orbital. We have confirmed that in this case the $(\nu j_{15/2})^2$ alignment at around $\epsilon_2=0.47$ seen in Fig. 3(b) does not affect $\omega_{\rm wob}$ visibly since $\Delta\mathcal{J}_y^{(\rm eff)}$ in this case is almost the same as $\Delta\mathcal{J}_x$ although its reason is not clear. Figure 3(c) graphs $Q_{\rm t}$. This figure indicates that the chosen shape $\epsilon_2=0.43$ and $\gamma=20°$ reproduces the measured $Q_{\rm t}$.

Figure 4(a) shows dependence on the pairing gaps. Since we do not have detailed information about the gaps, we assume $\Delta_n=\Delta_p$ for simplicity. This figure shows that the dependence on the gaps is weak unless they are too large. Since the static pairing gap Δ is expected to be small, say, $\Delta \leqslant 0.6$ MeV, in the observed frequency range, $\omega_{\rm wob}$ is not sensitive to the value of Δ. This is a striking contrast to the β and γ vibrations; it is well known that pairing gaps are indispensable for them. Here we note that the behavior of the $\omega_{\rm wob}$ correlates well with $\langle J_x\rangle_p$ presented in Fig. 4(b).

2. The odd-A nucleus ^{167}Lu

Next we study ^{167}Lu in a way similar to the preceding ^{168}Hf case. We choose $\gamma=20°$ and $\Delta_n=\Delta_p=0.3$ MeV as representative mean-field parameters as above. As for ϵ_2, however, we examined various possibilities because $Q_{\rm t}$ has not been measured in this nucleus. Since the sensitive ϵ_2 dependence through the occupation of the ν[651 1/2] orbital appears only at $\hbar\omega_{\rm rot}>0.4$ MeV and therefore the "bandhead" properties do not depend on ϵ_2 qualitatively, first we discuss them adopting $\epsilon_2=0.43$ in order to look at the difference between the even-even and the odd-Z cases.

Figure 5 shows dependence on γ at $\hbar\omega_{\rm rot}=0.25$ MeV with keeping $\epsilon_2=0.43$ and $\Delta_n=\Delta_p=0.3$ MeV constant. Figure 5(a) graphs $\omega_{\rm wob}$. In the $\gamma>0$ region, the solution is quite similar to the ^{168}Hf case. In the $\gamma<0$ region, for $-60° \leqslant \gamma \leqslant -30°$ it is quite similar again but for $-30° \leqslant \gamma < 0$ its character is completely different. In this region the presented solution is the lowest in energy and becomes collective gradually as γ decreases. The largeness of $\omega_{\rm wob}$ corresponds to that of $\mathcal{J}_x - \mathcal{J}_y^{(\rm eff)}$ in Fig. 5(b). Comparison of Figs. 5(c) and 1(c) certifies that the alignment of the $\pi i_{13/2}$ quasiparticle(s) is almost complete for $\gamma>0$ whereas less for $\gamma<0$. This produces quantitative even-odd differences as explained below.

Having confirmed that these features are independent of ϵ_2 and N except that we did not obtain any low-lying solutions for $35° \leqslant \gamma \leqslant 60°$ in the small-ϵ_2 cases, we look into underlying unperturbed 2QP energies to see the even-odd difference. In Fig. 6 we present the energies of the lowest $[\pi(N_{\rm osc}=6)]^2$ states which represent the biggest difference. In the yrast $(\pi i_{13/2})^2$ configuration, A_p and B_p in the usual notation are occupied in the even-Z case, the lowest 2QP

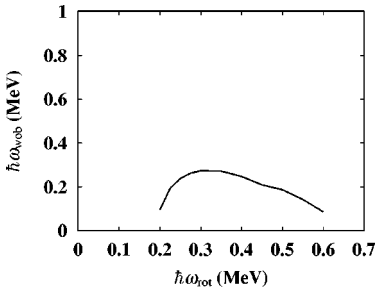

FIG. 8. Rotational frequency dependence of excitation energy of the wobbling motion in ^{174}Hf, calculated with $\epsilon_2=0.453$, $\gamma=16°$, and $\Delta_n=\Delta_p=0.3$ MeV.

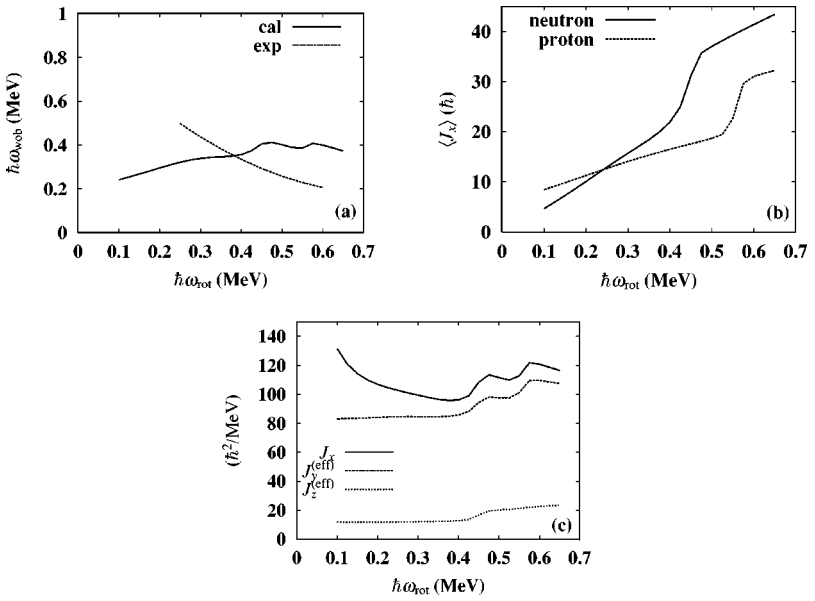

FIG. 9. The same as Fig. 7 but for ^{167}Lu. Experimental values taken from Ref. [22] are also included in (a).

state of signature $\alpha=1$ with respect to this is $\bar{B}_p C_p$ [where $-$ denotes the conjugate state, see Eq. (4)]. In the odd-Z case in which A_p is occupied, the lowest one is $B_p\bar{A}_p$. Since both e'_{B_p} and $e'_{\bar{A}_p}$ decrease as γ decreases, this 2QP state becomes the dominant component in the lowest-energy RPA solution. Note here that the sum $e'_{B_p}+e'_{\bar{A}_p}$ corresponds to the signature splitting between A_p and B_p when they are seen from the usual even-even vacuum. Since both B_p and $\bar{A}_p$ are of $K=1/2$ character, the resulting RPA solution cannot have the $K=2$ collectivity as shown in Fig. 5(d). According to the relation [15]

$$\frac{\mathcal{J}_y^{(\rm eff)}}{\mathcal{J}_x}=\left[1+\frac{\omega_{\rm wob}}{\omega_{\rm rot}}\frac{\sin\gamma}{\sin\left(\gamma+\frac{4}{3}\pi\right)}\frac{T_1}{T_2}\right]^{-1}, \tag{29}$$

$\mathcal{J}_y^{(\rm eff)}$ in Fig. 5(b) becomes small for $-30°\lesssim\gamma<0$. This discussion serves to exclude the possibility of $\gamma\simeq-20°$ for the TSDs that support collective wobbling excitations in the odd-Z cases, whereas the even-odd difference in $\gamma>0$ is merely quantitative.

C. Dependence on the rotational frequency $\omega_{\rm rot}$

1. ^{168}Hf and ^{174}Hf

The analyses above indicate that the chosen mean-field parameters are reasonable, and therefore we proceed to study $\omega_{\rm rot}$ dependence with keeping these parameters constant. Figure 7 shows the result for ^{168}Hf. These figures indicate again the $(\pi i_{13/2})^2$ alignment that makes $\mathcal{J}_x$ larger than $\mathcal{J}_y^{(\rm eff)}$ is indispensable for the formation of the wobbling excitation. At around $\hbar\omega_{\rm rot}=0.45$ MeV the $(\nu j_{15/2})^2$ alignment occurs. In contrast to the low-frequency case reported in Fig. 3, in the present case its effect on $\omega_{\rm wob}$ is visible as a small bump. Although the character of the observed excited TSD bands has not been resolved, some anomaly is seen at around this $\omega_{\rm rot}$ in one of them [29]. We suggest that this is related to the $(\nu j_{15/2})^2$ alignment since this is the only alignable orbital in this frequency region of this shape. However we note that in ^{167}Lu an interaction with a normal deformed state at around this frequency is discussed in Ref. [22].

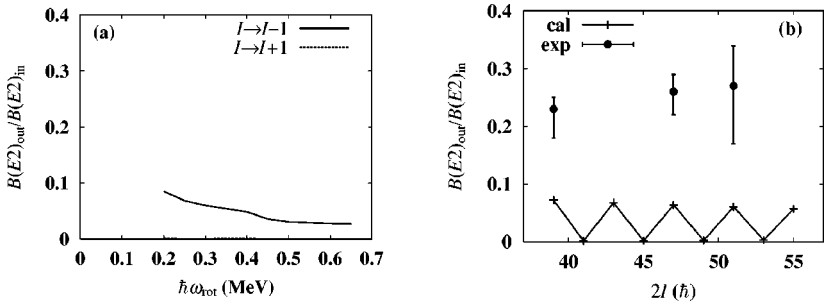

FIG. 10. Interband $E2$ transition rates for I (wobbling on yrast TSD) $\rightarrow I\pm1$ (yrast TSD) transitions in (a) ^{168}Hf and (b) ^{167}Lu. The latter is presented as functions of $2\times$ spin I, while the former is presented as functions of the rotational frequency since experimental spin assignment has not been done for ^{168}Hf. The rotational-frequency range corresponding to (b) is very narrow in comparison to (a). Interband transition rates are divided by the in-band ones. Experimental values [22] are also shown in (b). Noting that, for ^{167}Lu, the states $I+1$ (TSD1) are slightly higher in energy than I (TSD2) at $I>51/2\hbar$ and $B(T_\lambda;I\rightarrow I+1)\simeq B(T_\lambda;I+1\rightarrow I)$ holds at high spins, we plotted those for $I\rightarrow I+1$ at the places with the abscissas $I+1$ in order to show clearly their characteristic staggering behavior.

We performed calculations also for $\gamma=-20°$. In that case, however, wobbling excitation exists only at small $\omega_{\rm rot}$ because $\mathcal{J}_x-\mathcal{J}_y^{(\rm eff)}$ is small as seen from Fig. 1(b).

Very recently TSD bands were observed in another even-even nucleus, ^{174}Hf [30]. It is not trivial if a similar band structure is observed in the nucleus with six neutrons more since the existence of the TSD states depends on the shell gap. Multiple TSD bands were observed but connecting γ rays have not been resolved also in this nucleus. We performed a calculation adopting $\epsilon_2=0.453$ and $\gamma=16°$ suggested in Ref. [30] and $\Delta_n=\Delta_p=0.3$ MeV. The result is presented in Fig. 8. The most striking difference from the case of ^{168}Hf above is that $\omega_{\rm wob}$ decreases steadily as $\omega_{\rm rot}$ increases after the $(\pi i_{13/2})^2$ alignment is completed. This is because the $(\nu j_{15/2})^2$ alignment that causes the small bump in the ^{168}Hf case shifts to very low $\omega_{\rm rot}$ due to the larger neutron number.

2. ^{167}Lu

The wobbling excitation was first observed experimentally in ^{163}Lu [19], later it was also observed in ^{165}Lu [21] and ^{167}Lu [22]. The characteristic features common to these isotopes are (1) $\omega_{\rm wob}$ decreases as $\omega_{\rm rot}$ increases contrary to the consequence of calculations adopting constant moments of inertia and (2) $B(E2:I\rightarrow I-1)_{\rm out}/B(E2:I\rightarrow I-2)_{\rm in}$ is large—typically around 0.2.

Here we concentrate on the isotone of ^{168}Hf discussed above, that is, ^{167}Lu in order to see the even-odd difference. A comparison of Figs. 7 and 9 proves that all the differences are due to the fact that the number of the aligned $\pi i_{13/2}$ quasiparticle is less by one: (1) the $(\pi i_{13/2})^2$ alignment at around $\hbar\omega_{\rm rot}=0.2$ MeV is absent and (2) the B_pC_p crossing occurs at around $\hbar\omega_{\rm rot}=0.55$ MeV, which is proper to the $(\pi i_{13/2})^1$ configuration. Figure 9(a) shows that our calculation does not reproduce the data, although in each frequency range in which the configuration is the same $\omega_{\rm wob}$ decreases at high $\omega_{\rm rot}$ as in the cases of the even-even nuclei presented above. This result might indicate that there is room for improving the mean field. The $\mathcal{J}_x$ in Fig. 9(c) is larger than the experimentally deduced value by about 20–30 %. This is due to the spurious velocity dependence of the Nilsson potential mentioned in Sec. II.

D. Interband $B(E2)$ transitions

Compared to the excitation energy, the interband $B(E2)$ values relative to the in-band ones have been measured in only few cases. In Fig. 10, we report calculated $B(E2)$ ratios for I (wobbling on yrast TSD) $\rightarrow I\pm1$ (yrast TSD) transitions in ^{168}Hf and ^{167}Lu. The measured ones are also included for the latter.

The first point is the magnitude of the larger $(I\rightarrow I-1)$ ones. Apparently, the calculated $B(E2)$ values are smaller by factor 2–3. The measured interband $B(E2)$ values amount almost to the macroscopic rotor value. In the RPA calculations, as summarized in Sec. II, the $B(E2)$ value is reduced by a factor $c^2_{n=\rm wob}$ [see Eq. (24)]: only in the case with the full-strength $c^2_{n=\rm wob}=1$ the rotor value is recovered. Although the obtained RPA wobbling solutions are extremely collective in comparison with the usual low-lying collective vibrations, such as the β or γ vibrations, for which typically $|c_n|\simeq0.3-0.4$, this factor is still $|c_{n=\rm wob}|\simeq0.6-0.8$. This is the main reason why the calculated $B(E2)$ values are a factor 2–3 off the measured ones. As is well known, giant resonances also carry considerable amount of quadrupole strengths, so it seems difficult for the microscopic correction factor $c^2_{n=\rm wob}$ to be unity; it is not impossible, however, because the "sum rule" discussed in Sec. II is not the sum of positive-definite terms. In the RPA formalism, the reduction factor $c^2_{n=\rm wob}$ for the $B(E2)$ value, Eq. (24), comes from the fact that the wobbling motion is composed of the coherent motion of two quasiparticles, and reflects the microscopic structure of collective RPA solutions. The measurement that the $B(E2)$ value suffers almost no reduction may be a challenge to the microscopic RPA theory in the case of the wobbling motion. Calculated $B(E2)$ ratios for ^{174}Hf are slightly smaller than those for ^{168}Hf in Fig. 10(a).

The second point is the staggering, that is, the difference between $I\rightarrow I\pm1$. We clarified [15] its unique correspondence to the sign of γ as mentioned in Sec. III B; that holds for both even-even and odd-A systems. Recently this staggering was discussed from a different point of view [31], but it looks to apply only to $\gamma<0$ cases.

IV. CONCLUSION

The nuclear wobbling motion, which is a firm evidence of stable triaxial deformations, was identified experimentally in the triaxial superdeformed odd-A Lu isotopes. In principle, wobbling excitation is possible both in $\gamma>0$ and $\gamma<0$ nuclei. Every information, theoretical and experimental, suggests $\gamma>0$ for these bands. According to the wobbling frequency formula [8], cf. Eq. (12), its excitation in nuclei rotating principally about the x axis requires $\mathcal{J}_x>\mathcal{J}_y,\mathcal{J}_z$, although irrotational-like model moments of inertia give $\mathcal{J}_x<\mathcal{J}_y$ for $\gamma>0$. To solve this puzzle, we studied the nuclear wobbling motion, in particular, the three moments of inertia associated with it in terms of the cranked shell model plus random phase approximation. This makes it possible to calculate the moments of inertia of the whole system including the effect of aligned quasiparticle(s). The results indicate that the γ dependence of the calculated moment of inertia is basically irrotational-like ($\mathcal{J}_x\gtrless\mathcal{J}_y$ for $\gamma\lessgtr0$) if aligned quasiparticle(s) ($\pi i_{13/2}$ in the present case) does not exist. But once it is excited, it produces an additional contribution, $\Delta\mathcal{J}_x=i_{\rm QP}/\omega_{\rm rot}$, and consequently can lead to $\mathcal{J}_x>\mathcal{J}_y$ even for $\gamma>0$. This is the very reason why wobbling excitation exists in $\gamma>0$ nuclei. In this sense, the wobbling motion is a collective motion that is sensitive to the single-particle alignments.

The resulting moment of inertia for $0<\gamma\lesssim30°$ resembles the γ-reversed one, i.e., the irrotational moment of inertia but with $\mathcal{J}_x$ and $\mathcal{J}_y$ being interchanged. That for $50°\lesssim\gamma\lesssim60°$, where single-particle angular momenta dominate, is rigid-body-like. That for $\gamma<0$ is irrotational-like except for odd-A nuclei with $-30°\lesssim\gamma<0$ where a specific 2QP state determines the lowest RPA solution.

Having studied qualitative features of the three moments of inertia at a low rotational frequency, we calculated wobbling bands up to high $\omega_{\rm rot}$. Experimentally they were confirmed only in odd-A Lu isotopes as mentioned above. The most characteristic feature of the data is that $\omega_{\rm wob}$ decreases as $\omega_{\rm rot}$ increases. This obviously excludes constant moments of inertia. In our calculation three moments of inertia are automatically $\omega_{\rm rot}$ dependent even when mean-field parameters are fixed constant. It should be stressed that the wobblinglike solution in our RPA calculations is insensitive to the mean-field parameters, especially to the pairing gaps, as is shown in Sec. III B 1. This distinguishes the wobblinglike solution from the usual collective vibrations, which are sensitive to the pairing correlations. Thus, our microscopic RPA calculation confirms that the observed band is associated with a new type of collective excitation, although comparisons to the observed excitation energy indicate that there is room for improving the calculation.

As for the interband transition rates, our calculation accounted for only about one-half or less of the measured ones, even though the wobblinglike solution is extremely collective compared to the usual vibrational modes. This issue is independent of the details of choosing parameters. This confronts microscopic theories with a big challenge.

ACKNOWLEDGMENTS

We thank G. B. Hagemann for providing us with some experimental information prior to publication. This work was supported in part by the Grant-in-Aid for scientific research from the Japan Ministry of Education, Science and Culture (Grant Nos. 13640281 and 14540269).

[1] A. S. Davydov and G. F. Filippov, Nucl. Phys. **8**, 237 (1958).
[2] R. Bengtsson, H. Frisk, F. R. May, and J. A. Pinston, Nucl. Phys. **A415**, 189 (1984).
[3] I. Hamamoto and B. Mottelson, Phys. Lett. **132B**, 7 (1983).
[4] M. Matsuzaki, Nucl. Phys. **A519**, 548 (1990).
[5] K. Narimatsu, Y. R. Shimizu, and T. Shizuma, Nucl. Phys. **A601**, 69 (1996).
[6] N. Tajima and N. Onishi, Nucl. Phys. **A491**, 179 (1989).
[7] L. D. Landau and E. M. Lifshitz, *Mechanics* (Pergamon, London, 1960).
[8] A. Bohr and B. R. Mottelson, *Nuclear Structure*, Vol. II (Benjamin, New York, 1975).
[9] D. Janssen and I. N. Mikhailov, Nucl. Phys. **A318**, 390 (1979).
[10] E. R. Marshalek, Nucl. Phys. **A331**, 429 (1979).
[11] I. N. Mikhailov and D. Janssen, Phys. Lett. **72B**, 303 (1978).
[12] Y. R. Shimizu and K. Matsuyanagi, Prog. Theor. Phys. **72**, 799 (1984).
[13] N. Onishi, Nucl. Phys. **A456**, 279 (1986).
[14] M. Matsuzaki, Nucl. Phys. **A509**, 269 (1990).
[15] Y. R. Shimizu and M. Matsuzaki, Nucl. Phys. **A588**, 559 (1995).
[16] T. Horibata and N. Onishi, Nucl. Phys. **A596**, 251 (1996).
[17] R. Bengtsson, http://www.matfys.lth.se/ragnar/TSD.html
[18] W. Schmitz *et al.*, Phys. Lett. B **303**, 230 (1993).
[19] S. W. Ødegård *et al.*, Phys. Rev. Lett. **86**, 5866 (2001).
[20] I. Hamamoto, Phys. Rev. C **65**, 044305 (2002).
[21] G. Schönwaßer *et al.*, Phys. Lett. B **552**, 9 (2003).
[22] H. Amro *et al.*, Phys. Lett. B **553**, 197 (2003).
[23] M. Matsuzaki, Y. R. Shimizu, and K. Matsuyanagi, Phys. Rev. C **65**, 041303(R) (2002).
[24] S.-I. Kinouchi, Ph.D. thesis, University of Tsukuba, 1988.
[25] T. Nakatsukasa, K. Matsuyanagi, S. Mizutori, and Y. R. Shimizu, Phys. Rev. C **53**, 2213 (1996).
[26] E. R. Marshalek, Nucl. Phys. **A275**, 416 (1977).
[27] G. Schönwaßer *et al.*, Eur. Phys. J. A **15**, 435 (2002).
[28] T. Bengtsson and I. Ragnarsson, Nucl. Phys. **A436**, 14 (1985).
[29] H. Amro *et al.*, Phys. Lett. B **506**, 39 (2001).
[30] M. K. Djongolov *et al.*, Phys. Lett. B **560**, 24 (2003).
[31] R. F. Casten, E. A. McCutchan, N. V. Zamfir, C. W. Beausang, and Jing-ye Zhang, Phys. Rev. C **67**, 064306 (2003).

Prog. Theor. Phys. Vol. 112, No. 2, August 2004, Letters

Collective Path Connecting the Oblate and Prolate Local Minima in ^{68}Se

Masato KOBAYASI,[1] Takashi NAKATSUKASA,[2] Masayuki MATSUO[3] and Kenichi MATSUYANAGI[1]

[1]*Department of Physics, Graduate School of Science, Kyoto University, Kyoto 606-8502, Japan*
[2]*Institute of Physics and Center for Computational Science, University of Tsukuba, Tsukuba 305-8571, Japan*
[3]*Graduate School of Science and Technology, Niigata University, Niigata 950-2181, Japan*

(Received May 13, 2004)

By means of the adiabatic self-consistent collective coordinate method and the pairing-plus-quadrupole interaction, we have obtained a self-consistent collective path connecting the oblate and prolate local minima in ^{68}Se for the first time. The result of the calculation indicates the importance of triaxial deformation dynamics in oblate-prolate shape coexistence phenomena.

Shape coexistence phenomena are typical examples of large amplitude collective motion in nuclei. The existence of these phenomena implies that different solutions of the Hartree-Fock-Bogoliubov (HFB) equations (local minima in the deformation energy surface) appear in the same energy region and that the nucleus exhibits large amplitude collective motion connecting these different equilibrium points. The identities and mixings of these different shapes are determined by the dynamics of such collective motion. Some years ago, we proposed a new method of describing such large-amplitude collective motion, called the adiabatic self-consistent collective coordinate (ASCC) method.[1)] This is a new method of solving the basic equations of the SCC method[2)] using an expansion in terms of the collective momentum. It does not assume a single local minimum, and therefore it is believed to be suitable for the description of shape coexistence phenomena. The ASCC method also enables us to include pairing correlations self-consistently, with separating the spurious number fluctuation modes. To examine the feasibility of the ASCC method, we first applied it to an exactly solvable model called the multi-$O(4)$ model, which is a simplified version of the pairing-plus-quadrupole (P+Q) interaction model.[3)] It was also shown that this method yields a faithful description of tunneling motion through a barrier between prolate and oblate local minima in the collective potential.[4)]

In this paper, we give a brief report of our first application of the ASCC method to a realistic P+Q interaction model. We illustrate its practicality, treating as a typical example the oblate-prolate shape coexistence phenomenon in ^{68}Se recently observed in experiments.[5)] The self-consistent collective path obtained by means of the ASCC method is found to run approximately along the valley connecting the oblate and prolate local minima in the collective potential energy landscape. To the

best of our knowledge, this is the first time that a self-consistent collective path has been obtained for a realistic situation starting from the microscopic P+Q Hamiltonian. We note that a similar approach to the study of large amplitude collective motion was recently employed by Almehed and Walet,[6] although they investigated different nuclei and encountered some difficulties in obtaining self-consistent collective paths.

We assume that large amplitude collective motion can be described by a set of time-dependent HFB state vectors $|\phi(q,p,\varphi,N)\rangle$ parametrized by a single collective coordinate q, the collective momentum p conjugate to q, the particle number N, and the gauge angle φ conjugate to N. As discussed in Ref. 1), the state vector can be written

$$|\phi(q,p,\varphi,N)\rangle = e^{-i\varphi\hat{N}}\,|\phi(q,p,N)\rangle = e^{-i\varphi\hat{N}}e^{ip\hat{Q}(q)}|\phi(q)\rangle. \tag{1}$$

Carrying out an expansion with respect to p and requiring the time-dependent variational principle to be satisfied up to second order in p, we obtain the following set of equations to determine $|\phi(q)\rangle$, the infinitesimal generator $\hat{Q}(q)$, and its canonical conjugate $\hat{P}(q)$:

$$\delta\,\langle\phi(q)|\,\hat{H}_M(q)\,|\phi(q)\rangle = 0, \tag{2}$$

$$\delta\,\langle\phi(q)|\,[\hat{H}_M(q),\hat{Q}(q)] - \frac{1}{i}B(q)\hat{P}(q)\,|\phi(q)\rangle = 0, \tag{3}$$

$$\begin{aligned}\delta\,\langle\phi(q)|\,[\hat{H}_M(q),\frac{1}{i}\hat{P}(q)] - C(q)\hat{Q}(q)\\ -\frac{1}{2B(q)}[[\hat{H}_M(q),(\hat{H}-\lambda(q)\hat{N})_A],\hat{Q}(q)] - \frac{\partial\lambda}{\partial q}\hat{N}\,|\phi(q)\rangle = 0.\end{aligned} \tag{4}$$

Here,

$$\hat{H}_M(q) = \hat{H} - \lambda(q)\hat{N} - \frac{\partial V}{\partial q}\hat{Q}(q) \tag{5}$$

is the Hamiltonian in the moving frame,

$$C(q) = \frac{\partial^2 V}{\partial q^2} + \frac{1}{2B(q)}\frac{\partial B}{\partial q}\frac{\partial V}{\partial q} \tag{6}$$

is the local stiffness, $(\hat{H}-\lambda\hat{N})_A$ represents the two-quasiparticle creation and annihilation parts of $(\hat{H}-\lambda\hat{N})$, and $\hat{Q}(q)$ and $\hat{P}(q)$ satisfy the canonical variable condition

$$\langle\phi(q)|\,[\hat{Q}(q),\hat{P}(q)]\,|\phi(q)\rangle = i. \tag{7}$$

Once $|\phi(q)\rangle$ and the infinitesimal generators are determined for every value of q, we obtain the collective Hamiltonian $\mathcal{H}(q,p) = \frac{1}{2}B(q)p^2 + V(q)$ with the collective potential $V(q) = \langle\phi(q)|\,\hat{H}\,|\phi(q)\rangle$ and the inverse mass $B(q) = -\,\langle\phi(q)|\,[[\hat{H},\hat{Q}(q)],\hat{Q}(q)]\,|\phi(q)\rangle$.

We use the P+Q interaction model with the prescriptions of Ref. 3) for the microscopic Hamiltonian $\hat{H}$, but here the pairing and quadrupole force parameters

Table I. Spherical single-particle orbits and their energies used in the calculation. The energies relative to those of $1g_{9/2}$ are given in units of MeV.

orbits	$1f_{7/2}$	$2p_{3/2}$	$1f_{5/2}$	$2p_{1/2}$	$1g_{9/2}$	$2d_{5/2}$	$1g_{7/2}$	$3s_{1/2}$	$2d_{3/2}$
protons	−8.77	−4.23	−2.41	−1.50	0.0	6.55	5.90	10.10	9.83
neutrons	−9.02	−4.93	−2.66	−2.21	0.0	5.27	6.36	8.34	8.80

are chosen as $G = 0.320$ MeV (for both protons and neutrons) and $\chi' = 0.248$ MeV so that the constrained HFB potential energy surface (represented by contour lines in Fig. 1) exhibits two local minima, corresponding to prolate and oblate shapes, whose pairing gaps, quadrupole deformation and energy difference approximately reproduce those obtained in a recent Skyrme-HFB calculation done by Yamagami et al.[7] The spherical single-particle energies are taken from those of the modified oscillator model of Ref. 8) and are listed in Table I. In this way, the effective Hamiltonian provides a suitable situation with which shape coexistence dynamics can be studied, although it may be necessary to make further improvements, e.g., including the quadrupole pairing and/or neutron-proton pairing interactions, in order to allow for quantitative comparison with experimental data.

We have used the following algorithm to solve the set of ASCC equations, (2), (3), (4) and (7). Let the state vector $|\phi(q)\rangle$ be known at a specific value of q. We first solve the local harmonic equations in the moving frame (the moving frame RPA), (3) and (4), under the condition (7) to obtain $\hat{Q}(q)$ and $\hat{P}(q)$. This is done through a straightforward extension of the procedure described in Ref. 4). We then construct a state vector at the neighboring point $q + \delta q$ by using the infinitesimal generator $\hat{P}(q)$ as

$$|\phi(q + \delta q)\rangle = e^{-i\delta q \hat{P}(q)} |\phi(q)\rangle \tag{8}$$

and solve the moving frame RPA with respect to this state to obtain $\hat{Q}(q + \delta q)$ and $\hat{P}(q + \delta q)$. Though the above $|\phi(q + \delta q)\rangle$ does not necessarily satisfy the HFB equation in the moving frame (2), we can use this state vector as an initial solution of (2) at $q + \delta q$. We search for the solution of (2) under the constraints

$$\langle \phi(q + \delta q)|\hat{N}|\phi(q + \delta q)\rangle = N, \tag{9}$$

$$\langle \phi(q + \delta q)|\hat{Q}(q)|\phi(q + \delta q)\rangle = \delta q \tag{10}$$

by means of the gradient method. Here, the nucleon-number constraint (9) is actually applied for both proton and neutron numbers. Equation (10) is the constraint for the increment δq of the collective coordinate. After finding a solution of Eq. (2), we renew $\hat{Q}(q + \delta q)$ and $\hat{P}(q + \delta q)$ by again solving the moving frame RPA equations, (3) and (4), for the new state vector $|\phi(q + \delta q)\rangle$ obtained above. Then we again solve Eq. (2) with the renewed $\hat{Q}(q + \delta q)$. If this iterative procedure converges, we obtain self-consistent solutions that satisfy Eqs. (2), (3), (4) and (7) simultaneously at $q + \delta q$, and we can then proceed to the next point, $q + 2\delta q$. In actual numerical calculations, we start the procedure from one of the HFB local minima and examine whether we arrive at the other local minimum by going along the collective path obtained in the manner described above. We have checked that the same collective path is obtained by starting from the other local minimum and proceeding inversely.

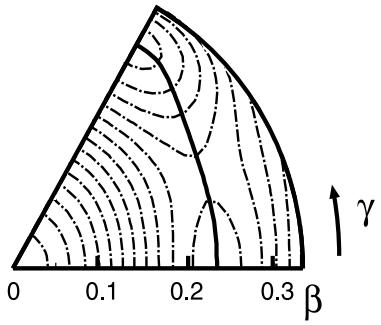

Fig. 1. The bold curve represents the ASCC path connecting the oblate and prolate minima in ^{68}Se projected onto the (β, γ) plane. The contour lines are calculated using the conventional constrained HFB method and plotted for every 100 keV.

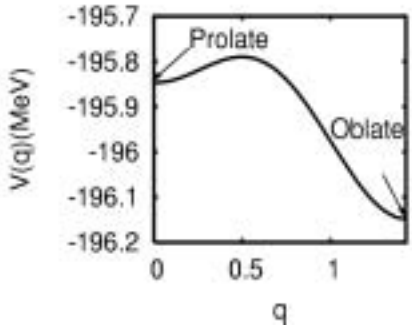

Fig. 2. Collective potential $V(q)$ plotted as a function of the collective coordinate q. Here, the origin of q is chosen to coincide with the prolate local minimum, and its scale is defined such that the collective mass is given by $M(q) = 1$ MeV^{-1}.

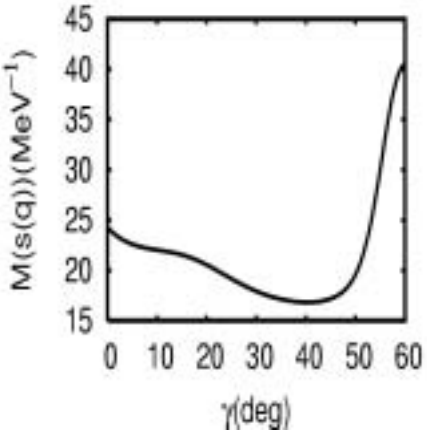

Fig. 3. Collective mass $M(s)$ with respect to the geometrical length s along the collective path in the (β, γ) plane plotted as a function of the triaxiality parameter γ.

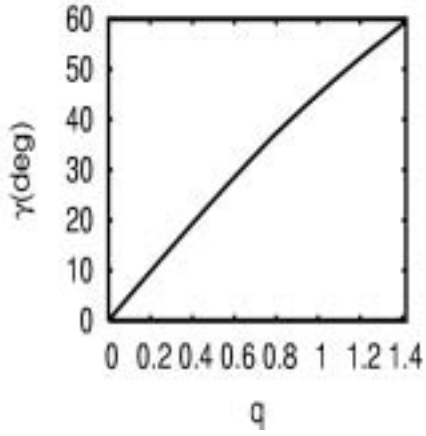

Fig. 4. The triaxiality parameter γ plotted as a function of the collective coordinate q.

Carrying out the above procedure, we have successfully obtained the collective path connecting the oblate and prolate local minima in ^{68}Se. The result is plotted in Fig. 1. The deformation parameters β and γ are defined here as usual, through the expectation values of the quadrupole operators.[7] Roughly speaking, the collective path goes through the valley that exists in the γ direction and connects the oblate and prolate minima. If β is treated as a collective coordinate and the oblate and prolate shapes are connected through the spherical point, the variation of the potential energy would be much greater than that along the collective path we obtained. The potential energy curve $V(q)$ along the collective path evaluated using the ASCC method is shown in Fig. 2. We have defined the scale of the collective coordinate q

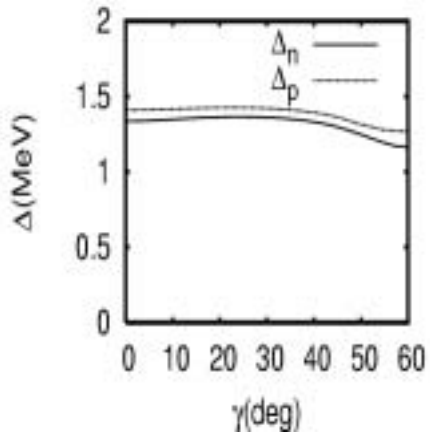

Fig. 5. Neutron and proton pairing gaps, Δ_n and Δ_p, plotted as functions of γ.

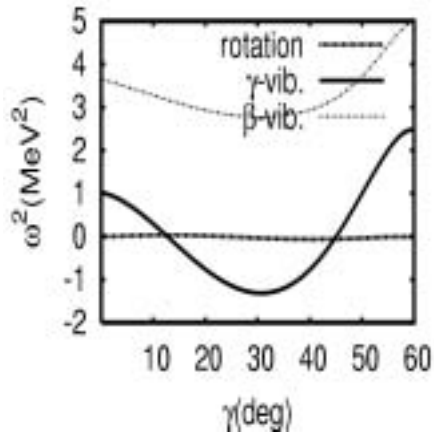

Fig. 6. Lowest three eigen-frequencies squared (i.e. $\omega^2 = BC$) of the moving frame RPA, plotted as functions of γ.

such that the collective mass is given by $M(q) = B(q)^{-1} = 1$ MeV^{-1}. The collective mass as a function of the geometrical length s along the collective path in the (β, γ) plane can be defined by $M(s) = M(q)(ds/dq)^{-2}$, with $ds^2 = d\beta^2 + \beta^2 d\gamma^2$. This quantity is presented in Fig. 3 as a function of γ. The triaxial deformation parameter γ is plotted as a function of q in Fig. 4. Variations of the pairing gaps and of the few lowest eigen-frequencies of the moving frame RPA along the collective path are plotted in Figs. 5 and 6. The solid curve in Fig. 6 represents the frequency squared, $\omega^2(q) = B(q)C(q)$, given by the product of the inverse mass $B(q)$ and the local stiffness $C(q)$, for the moving frame RPA mode that develops from the γ-vibration in the oblate and prolate limits and determines the infinitesimal generators $\hat{Q}(q)$ and $\hat{P}(q)$ along the collective path. The other two curves represent solutions of the moving frame RPA, which possess the characteristics of the collective rotational motion and the β-vibration. These are, however, irrelevant to the collective path. Note that the frequency of the γ mode becomes imaginary in the region $12^\circ < \gamma < 45^\circ$. These results should reveal interesting dynamical properties of the shape coexistence phenomena in ^{68}Se. For instance, the large collective mass in the vicinity of $\gamma = 60^\circ$ (Fig. 3) might increase the stability of the oblate shape in the ground state. Detailed investigation of these quantities as well as solutions of the collective Schrödinger equation will be given in a forthcoming full-length paper.[11)]

In summary, we have applied the ASCC method to the oblate-prolate shape coexistence phenomena in ^{68}Se. It was found that the collective path goes through the valley of the potential energy landscape in the (β, γ) plane, along which the triaxial deformation parameter γ changes between 0° and 60°, while the axially symmetric deformation parameter β remains approximately constant. This is the first time that a self-consistent collective path between the oblate and prolate minima has been obtained for the realistic P+Q interaction model. Recently, the generater coordinate method has often been used to describe a variety of shape coexistence phenomena,

with β employed as the generater coordinate.[9] The triaxial shape vibrational degrees of freedom are also ignored in the extensive microscopic calculation given in Ref. 10). The result of the ASCC calculation, however, strongly indicates the necessity of taking into account the γ degree of freedom, at least for the purpose of describing the oblate-prolate shape coexistence in ^{68}Se. The effects of triaxial deformation dynamics on various properties of shape coexistence, including the results of the calculation for neighboring nuclei, will be studied in a full-length paper.[11]

We thank Drs. D. Almehed and N. R. Walet for useful discussions and kindly pointing out a graphical error in the preprint version of this paper. The numerical calculations were performed on the NEC SX-5 supercomputer at the Yukawa Institute for Theoretical Physics, Kyoto University. This work was supported by Grants-in-Aid for Scientific Research (Nos. 13640281, 14540250 and 14740146) from the Japan Society for the Promotion of Science.

---

1) M. Matsuo, T. Nakatsukasa and K. Matsuyanagi, Prog. Theor. Phys. **103** (2000), 959.
2) T. Marumori, T. Maskawa, F. Sakata and A. Kuriyama, Prog. Theor. Phys. **64** (1980), 1294.
3) M. Baranger and K. Kumar, Nucl. Phys. A **110** (1968), 490.
4) M. Kobayasi, T. Nakatsukasa, M. Matsuo and K. Matsuyanagi, Prog. Theor. Phys. **110** (2003), 65.
5) S. M. Fischer et al., Phys. Rev. Lett. **84** (2000), 4064; Phys. Rev. C **67** (2003), 064318.
6) D. Almehed and N. R. Walet, Phys. Rev. C **69** (2004), 024302.
7) M. Yamagami, K. Matsuyanagi and M. Matsuo, Nucl. Phys. A **693** (2001), 579.
8) T. Bengtsson and I. Ragnarsson, Nucl. Phys. A **436** (1985), 14.
9) T. Duguet, M. Bender, P. Bonche and P.-H. Heenen, Phys. Lett. B **559** (2003), 201.
10) A. Petrovici, K. W. Schmid and A. Faessler, Nucl. Phys. A **710** (2002), 246.
11) M. Kobayasi, T. Nakatsukasa, M. Matsuo and K. Matsuyanagi, in preparation.

Progress of Theoretical Physics, Vol. 113, No. 1, January 2005

Collective Paths Connecting the Oblate and Prolate Shapes in ^{68}Se and ^{72}Kr Suggested by the Adiabatic Self-Consistent Collective Coordinate Method

Masato KOBAYASI,[1] Takashi NAKATSUKASA,[2] Masayuki MATSUO[3] and Kenichi MATSUYANAGI[1]

[1]*Department of Physics, Graduate School of Science, Kyoto University, Kyoto 606-8502, Japan*
[2]*Institute of Physics and Center for Computational Science, University of Tsukuba, Tsukuba 305-8571, Japan*
[3]*Graduate School of Science and Technology, Niigata University, Niigata 950-2181, Japan*

(Received November 15, 2004)

By means of the adiabatic self-consistent collective coordinate method and the pairing-plus-quadrupole interaction, we have for the first time obtained a self-consistent collective path connecting the oblate and prolate local minima in ^{68}Se and ^{72}Kr. This self-consistent collective path is found to run approximately along the valley connecting the oblate and prolate local minima in the collective potential energy landscape. The result of this calculation clearly indicates the importance of triaxial deformation dynamics in oblate-prolate shape coexistence phenomena.

§1. Introduction

The microscopic description of large amplitude collective motion in nuclei is a long-standing fundamental subject of nuclear structure physics.[1)–5)] In spite of the steady development of various theoretical concepts and mathematical formulations, the application of microscopic many-body theory to actual nuclear phenomena still remains a challenging task.[6)–33)] Shape coexistence phenomena are typical examples of large amplitude collective motion in nuclei, and both experimental and theoretical investigations of such phenomena are currently being carried out.[34)–57)] We are particularly interested in the recent discovery of two coexisting rotational bands in ^{68}Se and ^{72}Kr, which are associated with oblate and prolate intrinsic shapes.[41),42)] Clearly, these data strongly call for further development of a theory that is able to describe them and revise our understanding of nuclear structure. From the viewpoint of the microscopic mean-field theory, the coexistence of different shapes implies that different solutions of the Hartree-Fock-Bogoliubov (HFB) equations (local minima in the deformation energy surface) appear in the same energy region and that the nucleus exhibits large amplitude collective motion connecting these different equilibrium points. The identities and mixings of these different shapes are determined by the dynamics of such collective motion.

On the basis of the time-dependent Hartree-Fock (TDHF) theory, the self-consistent collective coordinate (SCC) method was proposed as a microscopic theory

of such large amplitude collective motion.[12] This method was extended to the case of time-dependent HFB (TDHFB) including pairing correlations,[23] and it has been successfully applied to various kinds of anharmonic vibration and high-spin rotational phenomena.[58–69] In order to apply this method to shape coexistence phenomena, however, we need to further develop the theory, because the existing method of solving the basic equations of the SCC method, called the η-expansion method,[12] assumes a single local minima, whereas several local minima of the potential energy surface compete in these systems. Some years ago, we proposed a new method of describing such large-amplitude collective motion, called the adiabatic self-consistent collective coordinate (ASCC) method.[70] This method provides a practical scheme for solving the basic equations of the SCC method[12] using an expansion in terms of the collective momentum. It does not assume a single local minimum, and therefore it is believed to be suitable for the description of shape coexistence phenomena. The ASCC method inherits the major advantages of the adiabatic TDHF (ATDHF) methods and, in addition, enables us to include pairing correlations self-consistently. In this method, the spurious number fluctuation modes are automatically decoupled from the physical modes within the self-consistent framework of the TDHFB theory. This will certainly be a great advantage when the method is applied to realistic nuclear problems. To examine the feasibility of the ASCC method, in Ref. 71), we applied it to an exactly solvable model called the multi-$O(4)$ model,[72–75] which is a simplified version of the pairing-plus-quadrupole (P+Q) interaction model.[76–78] It was shown that this method yields a faithful description of tunneling motion through a barrier between prolate and oblate local minima in the collective potential.[71]

In this paper, we report on our first application of the ASCC method to the P+Q interaction model. The major task here is to develop a practical procedure for solving the basic equations of the ASCC method in order to obtain a self-consistent collective path. We investigate, as typical examples, the oblate-prolate shape coexistence phenomena in ^{68}Se and ^{72}Kr,[41,42] and we find that the self-consistent collective paths run approximately along the valley connecting the oblate and prolate local minima in the collective potential energy landscape. To the best of our knowledge, this is the first time that, starting from the microscopic P+Q Hamiltonian, the collective paths have been fully self-consistently obtained for realistic situations, although a similar approach to the study of large amplitude collective motion was recently employed by Almehed and Walet.[79,80]

This paper is organized as follows. In §2, the basic equations of the ASCC method are summarized. In §3, we present a concrete formulation of the ASCC method for the case of the P+Q Hamiltonian. In §4, an algorithm to solve the basic equations of the ASCC method is discussed. In §5, we present the results of numerical calculations for the oblate-prolate shape coexistence phenomena in ^{68}Se and ^{72}Kr. Concluding remarks are given in §6.

A preliminary version of this work was reported previously in this journal.[81]

§2. Basic equations of the ASCC method

In this section, we summarize the basic equations of the ASCC method.[70] The basic assumption of our approach is that large-amplitude collective motion can be described by a set of time-dependent HFB state vectors $|\phi(q,p,\varphi,N)\rangle$ parameterized by a single collective coordinate q, the collective momentum p conjugate to q, the particle number N and the gauge angle φ conjugate to N. Then, the state vectors can be written in the following form:

$$|\phi(q,p,\varphi,N)\rangle = e^{-i\varphi\hat{N}}\,|\phi(q,p,N)\rangle = e^{-i\varphi\hat{N}}e^{ip\hat{Q}(q)}|\phi(q)\rangle. \tag{2·1}$$

Carrying out an expansion with respect to p and requiring that the time-dependent variational principle be satisfied up to second order in p, we obtain the following set of equations to determine $|\phi(q)\rangle$, the infinitesimal generator $\hat{Q}(q)$, and its canonical conjugate $\hat{P}(q)$. First, we have *the HFB equation in the moving frame*, given by

$$\delta\,\langle\phi(q)|\,\hat{H}_M(q)\,|\phi(q)\rangle = 0, \tag{2·2}$$

where

$$\hat{H}_M(q) = \hat{H} - \lambda(q)\hat{N} - \frac{\partial V}{\partial q}\hat{Q}(q) \tag{2·3}$$

represents the Hamiltonian in the moving frame. Then, we have *the local harmonic equations in the moving frame*,

$$\delta\,\langle\phi(q)|\,[\hat{H}_M(q),\hat{Q}(q)] - \frac{1}{i}B(q)\hat{P}(q)\,|\phi(q)\rangle = 0, \tag{2·4}$$

$$\delta\,\langle\phi(q)|\left[\hat{H}_M(q),\frac{1}{i}\hat{P}(q)\right] - C(q)\hat{Q}(q) - \frac{1}{2B(q)}[[\hat{H}_M(q),(\hat{H}-\lambda(q)\hat{N})_A],\hat{Q}(q)] - \frac{\partial\lambda}{\partial q}\hat{N}\,|\phi(q)\rangle = 0, \tag{2·5}$$

where

$$B(q) = -\,\langle\phi(q)|\,[[\hat{H},\hat{Q}(q)],\hat{Q}(q)]\,|\phi(q)\rangle \tag{2·6}$$

represents the inverse mass,

$$C(q) = \frac{\partial^2 V}{\partial q^2} + \frac{1}{2B(q)}\frac{\partial B}{\partial q}\frac{\partial V}{\partial q} \tag{2·7}$$

the local stiffness, and $(\hat{H}-\lambda\hat{N})_A$ denotes the two-quasiparticle creation and annihilation parts of $(\hat{H}-\lambda\hat{N})$.

The infinitesimal generators, $\hat{Q}(q)$ and $\hat{P}(q)$, satisfy *the canonical variable condition*:

$$\langle\phi(q)|\,[\hat{Q}(q),\hat{P}(q)]\,|\phi(q)\rangle = i. \tag{2·8}$$

Once $|\phi(q)\rangle$ and the infinitesimal generators are determined for every value of q, we obtain the collective Hamiltonian $\mathcal{H}(q,p) = \frac{1}{2}B(q)p^2 + V(q)$ with the collective potential $V(q) = \langle\phi(q)|\,\hat{H}\,|\phi(q)\rangle$.

In the above equations, no distinction is made between protons and neutrons for simplicity in the notation. In the actual calculations described below, however, we explicitly treat the neutron number N and the proton number Z separately.

§3. Application of the ASCC method to the P+Q model

3.1. *The P+Q Hamiltonian and signature quantum number*

Let us start with the well-known P+Q Hamiltonian,[76)–78)]

$$\hat{H} = \sum_k \epsilon_k c_k^\dagger c_k - \sum_\tau \frac{G_\tau}{2}\left(A_\tau^\dagger A_\tau + A_\tau A_\tau^\dagger\right) - \frac{\chi}{2}\sum_{K=-2}^{2} D_{2K}^\dagger D_{2K}, \tag{3·1}$$

where

$$A_\tau^\dagger = \sum_{k\in\tau}{}' c_k^\dagger c_{\tilde{k}}^\dagger, \quad A_\tau = \sum_{k\in\tau}{}' c_{\tilde{k}} c_k,$$
$$D_{2K} = \sum_{\tau=n,p}\sum_{kl\in\tau} D_{2K}^{(\tau)}(kl) c_k^\dagger c_l. \tag{3·2}$$

Here, we have $D_{2K}^{(\tau)}(kl) = \alpha_\tau^2 \langle k| r^2 Y_{2K} |l\rangle$, G_τ and χ denote the pairing and quadrupole force strengths, respectively, and $c_k^\dagger$ and c_k are the nucleon creation and annihilation operators in the single-particle state k, while $c_{\tilde{k}}^\dagger$ and $c_{\tilde{k}}$ denote those in the time-reversed state of k. The index τ indicates protons (with $\tau = p$) and neutrons (with $\tau = n$). Although it is not explicitly mentioned below, it should be kept in mind that the single-particle index k actually includes the index τ. The notation Σ' in the pair operators, $A_\tau^\dagger$ and A_τ, represents a sum over the pairs $(k, \tilde{k})$. The factors $\alpha_n = (2Z/A)^{2/3}$ and $\alpha_p = (2N/A)^{2/3}$, multiplying the quadrupole matrix elements, yield equivalent root-mean-square radii for protons and neutrons. Following Baranger and Kumar,[77)] we take into account two major shells as the model space, and we multiply the quadrupole matrix elements $D_{2K}^{(\tau)}(kl)$ of the upper harmonic-oscillator shell by the reduction factor $\zeta = (N_L + 3/2)/(N_L + 5/2)$, N_L being the total number of oscillator quanta of the lower shell. Following the conventional prescription of the P+Q interaction,[76)–78)] we ignore the exchange (Fock) terms. In other words, we employ the Hartree-Bogoliubov (HB) approximation throughout this paper.

We introduce the following notations:

$$\hat{F}_s^{(\pm)} \equiv \frac{1}{2}(\hat{F}_s \pm \hat{F}_s^\dagger),$$
$$\hat{F}_s^{(\pm)} \equiv \{A_n^{(\pm)}, A_p^{(\pm)}, D_{20}^{(\pm)}, D_{21}^{(\pm)}, D_{22}^{(\pm)}\}. \qquad (s = 1-5) \tag{3·3}$$

We then write the P+Q Hamiltonian in the form

$$\hat{H} = \sum_k \epsilon_k c_k^\dagger c_k - \sum_{s=1}^{5} \frac{\kappa_s}{2}\hat{F}_s^{(+)}\hat{F}_s^{(+)} + \sum_{s=1}^{5} \frac{\kappa_s}{2}\hat{F}_s^{(-)}\hat{F}_s^{(-)}, \tag{3·4}$$

where $\kappa_s = \{2G_n, 2G_p, \chi, 2\chi, 2\chi\}$ for $s = 1-5$. Our Hamiltonian is invariant with respect to a rotation by π about the x axis. The symmetry quantum number associated with it is called the signature, $r = e^{-i\pi\alpha}$. To exploit the signature symmetry,

it is convenient to use nucleon operators with definite signatures defined by

$$d_k \equiv \frac{1}{\sqrt{2}}(c_k + c_{\tilde{k}}), \qquad r = -i \ (\alpha = 1/2),$$
$$d_{\tilde{k}} \equiv \frac{1}{\sqrt{2}}(c_{\tilde{k}} - c_k), \qquad r = +i \ (\alpha = -1/2), \tag{3·5}$$

and their Hermite conjugates, $d_k^\dagger$ and $d_{\tilde{k}}^\dagger$. The operators $\hat{F}_s^{(\pm)}$ are then classified according to the signature quantum numbers, $r = \pm 1$ ($\alpha = 0, 1$), as

$$\{A_n^{(\pm)}, A_p^{(\pm)}, D_{20}^{(+)}, D_{21}^{(-)}, D_{22}^{(+)}\}, \qquad (r = +1)$$
$$\{D_{21}^{(+)}, D_{22}^{(-)}\}. \qquad (r = -1) \tag{3·6}$$

Note that $D_{20}^{(-)} = 0$. The HB local minima corresponding to the oblate and prolate equilibrium shapes possess positive signature, $r = +1(\alpha = 0)$. Therefore, the operators $\hat{Q}(q)$ and $\hat{P}(q)$, generating large amplitude collective motion associated with these shapes, also possess positive signature. In other words, the negative signature degrees of freedom are exactly decoupled from the large amplitude collective motion of interest, and hence we can ignore them. Also, it is readily confirmed that the $K = 1$ components associated with the quadrupole operator $\hat{D}_{21}^{(-)}$ exactly decouple from the $K = 0$ and 2 components in the local harmonic equations, (2·2) and (2·4). As is well known, they are associated with the collective rotational motion, and the large amplitude shape vibrational motion under consideration is exactly decoupled from them in the present framework. We note, however, that it is possible, with a rather straightforward extension, to formulate the ASCC method in a rotating frame of reference. By means of such an extension, we are able to take into account the coupling effects between the two kinds of large amplitude collective motion. It is certainly a very interesting subject to study how the properties of the large-amplitude shape vibrational motion change as a function of the angular momentum, but such an investigation is beyond the scope of this paper. We note, however, that an attempt to treat this subject was recently made by Almehed and Walet.[80)]

Thus, only the components $\{A_n^{(\pm)}, A_p^{(\pm)}, D_{20}^{(+)}, D_{22}^{(+)}\}$ are pertinent to the shape coexistence dynamics of interest presently. They all belong to the positive signature sector, and we are able to adopt a phase convention with which their single-particle matrix elements are real. In the following, we assume that this is the case.

3.2. *Quasiparticle-random-phase approximation (QRPA) at the HB local minima*

As discussed in the introduction, shape coexistence phenomena imply the existence of several local minima in the deformation energy surface, which are solutions of the HB equations. Let us choose one of them and write it $|\phi_0\rangle$. The HB equation is given by

$$\delta\langle\phi_0|\hat{H} - \sum_\tau \lambda_\tau \hat{N}_\tau|\phi_0\rangle = 0, \tag{3·7}$$

where λ_τ represents the chemical potentials for protons ($\tau = p$) and neutrons ($\tau = n$). The quasiparticle creation and annihilation operators, $a_\mu^\dagger$ and a_μ, associated with

the HB local minimum are defined by $a_\mu|\phi_0\rangle = 0$. Similar equations hold for their signature partners, $\bar{\mu}$. They are introduced through the Bogoliubov transformations,

$$\begin{pmatrix} a_\mu^\dagger \\ a_{\bar{\mu}} \end{pmatrix} = \sum_k \begin{pmatrix} U_{\mu k} & V_{\mu\bar{k}} \\ V_{\bar{\mu}k} & U_{\bar{\mu}\bar{k}} \end{pmatrix} \begin{pmatrix} d_k^\dagger \\ d_{\bar{k}} \end{pmatrix}, \tag{3·8}$$

and their Hermite conjugate equations. (Here and hereafter, we do not mix protons and neutrons in these transformations.) In terms of the two quasiparticle creation and annihilation operators,

$$\boldsymbol{A}_{\mu\bar{\nu}}^\dagger \equiv a_\mu^\dagger a_{\bar{\nu}}^\dagger, \quad \boldsymbol{A}_{\mu\bar{\nu}} \equiv a_{\bar{\nu}} a_\mu, \tag{3·9}$$

the RPA normal coordinates and momenta describing small amplitude vibrations about the HB local minimum $|\phi_0\rangle$ are written

$$\hat{Q}_\rho = \sum_{\mu\bar{\nu}} Q_{\mu\bar{\nu}}^\rho (\boldsymbol{A}_{\mu\bar{\nu}}^\dagger + \boldsymbol{A}_{\mu\bar{\nu}}), \tag{3·10}$$

$$\hat{P}_\rho = i \sum_{\mu\bar{\nu}} P_{\mu\bar{\nu}}^\rho (\boldsymbol{A}_{\mu\bar{\nu}}^\dagger - \boldsymbol{A}_{\mu\bar{\nu}}), \tag{3·11}$$

where the sum is taken over the proton and neutron quasiparticle pairs $(\mu\bar{\nu})$, and ρ labels the QRPA modes. The amplitudes $Q_{\mu\nu}^\rho$ and $P_{\mu\nu}^\rho$ are determined by the QRPA equations of motion,

$$\delta \langle\phi_0| \left[\hat{H} - \sum_\tau \lambda_\tau \hat{N}_\tau,\ \hat{Q}_\rho\right] - \frac{1}{i} B_\rho \hat{P}_\rho |\phi_0\rangle = 0, \tag{3·12}$$

$$\delta \langle\phi_0| \left[\hat{H} - \sum_\tau \lambda_\tau \hat{N}_\tau,\ \frac{1}{i}\hat{P}_\rho\right] - C_\rho \hat{Q}_\rho |\phi_0\rangle = 0, \tag{3·13}$$

and the orthonormalization condition $\langle\phi_0| [\hat{Q}_\rho, \hat{P}_{\rho'}] |\phi_0\rangle = i\delta_{\rho,\rho'}$.

3.3. *The HB equation and the quasiparticles in the moving frame*

For the P+Q Hamiltonian, the HB equation (2·2) determining the state vector $|\phi(q)\rangle$ away from the local minimum reduces to

$$\delta \langle\phi(q)| \hat{h}_M(q) |\phi(q)\rangle = 0, \tag{3·14}$$

where $\hat{h}_M(q)$ is the mean-field Hamiltonian in the moving frame,

$$\hat{h}_M(q) = \hat{h}(q) - \sum_\tau \lambda_\tau(q) \hat{N}_\tau - \frac{\partial V}{\partial q} \hat{Q}(q), \tag{3·15}$$

$$\hat{h}(q) = \sum_k \epsilon_k (d_k^\dagger d_k + d_{\bar{k}}^\dagger d_{\bar{k}}) - \sum_s \kappa_s \hat{F}_s^{(+)} \langle\phi(q)| \hat{F}_s^{(+)} |\phi(q)\rangle . \tag{3·16}$$

The state vector $|\phi(q)\rangle$ can be written in terms of a unitary transformation of $|\phi_0\rangle$:

$$|\phi(q)\rangle = e^{\hat{\theta}(q)} |\phi_0\rangle ,$$
$$\hat{\theta}(q) \equiv \sum_{\mu\bar{\nu}} \theta_{\mu\bar{\nu}}(q) \left(\boldsymbol{A}_{\mu\bar{\nu}}^\dagger - \boldsymbol{A}_{\mu\bar{\nu}}\right). \tag{3·17}$$

Here, the sum is taken over the proton and neutron quasiparticle pairs $(\mu\bar{\nu})$. The quasiparticle creation and annihilation operators, $a^\dagger_\mu(q)$ and $a_\mu(q)$, associated with the state $|\phi(q)\rangle$, which satisfy the condition $a_\mu(q)|\phi(q)\rangle = 0$, are written

$$\begin{aligned} a^\dagger_\mu(q) &\equiv e^{\hat{\theta}}(q) a^\dagger_\mu e^{-\hat{\theta}(q)} = \sum_\nu \Big(U_{\mu\nu}(q) a^\dagger_\nu + V_{\mu\bar{\nu}}(q) a_{\bar{\nu}} \Big), \\ a_{\bar{\mu}}(q) &\equiv e^{\hat{\theta}}(q) a_{\bar{\mu}} e^{-\hat{\theta}(q)} = \sum_\nu \Big(V_{\bar{\mu}\nu}(q) a^\dagger_\nu + U_{\bar{\mu}\bar{\nu}}(q) a_{\bar{\nu}} \Big), \end{aligned} \tag{3·18}$$

where

$$\begin{pmatrix} U_{\mu\nu}(q) & V_{\mu\bar{\nu}}(q) \\ V_{\bar{\mu}\nu}(q) & U_{\bar{\mu}\bar{\nu}}(q) \end{pmatrix} = \begin{pmatrix} \cos(\sqrt{\theta\theta^T}) & -\theta \dfrac{\sin(\sqrt{\theta^T\theta})}{\sqrt{\theta^T\theta}} \\ \theta^T \dfrac{\sin(\theta\theta^T)}{\sqrt{\theta\theta^T}} & \cos(\sqrt{\theta^T\theta}) \end{pmatrix}. \tag{3·19}$$

Here, θ on the r.h.s. represents the matrix composed of $\theta_{\mu\nu}(q)$, and it is understood that its elements corresponding to those on the l.h.s. should be taken.

In terms of the quasiparticle operators defined above, the mean-field Hamiltonian in the moving frame $\hat{h}_M(q)$, the neutron and proton number operators $\hat{N}_\tau$, and the pairing and quadrupole operators $\hat{F}^{(\pm)}_s$ are written in the following forms:

$$\hat{h}_M(q) = \langle\phi(q)|\, \hat{h}_M(q)\, |\phi(q)\rangle + \sum_\mu E_\mu(q) \Big(\boldsymbol{B}_{\mu\mu}(q) + \boldsymbol{B}_{\bar{\mu}\bar{\mu}}(q) \Big), \tag{3·20}$$

$$\begin{aligned} \hat{N}_\tau = \langle\phi(q)|\, \hat{N}_\tau\, |\phi(q)\rangle &+ \sum_\mu N_\tau(\mu) \Big(\boldsymbol{A}^\dagger_{\mu\bar{\mu}}(q) + \boldsymbol{A}_{\mu\bar{\mu}}(q) \Big) \\ &+ \sum_\mu N_{B,\tau}(\mu) \Big(\boldsymbol{B}_{\mu\mu}(q) + \boldsymbol{B}_{\bar{\mu}\bar{\mu}}(q) \Big), \end{aligned} \tag{3·21}$$

$$\begin{aligned} \hat{F}^{(\pm)}_s = \langle\phi(q)|\, \hat{F}^{(\pm)}_s\, |\phi(q)\rangle &+ \sum_{\mu\bar{\nu}} F^{(\pm)}_s(\mu\bar{\nu}) \Big(\boldsymbol{A}^\dagger_{\mu\bar{\nu}}(q) \pm \boldsymbol{A}_{\mu\bar{\nu}}(q) \Big) \\ &+ \sum_{\mu\nu} F^{(\pm)}_{B,s}(\mu\nu) \Big(\boldsymbol{B}_{\mu\nu}(q) + \boldsymbol{B}_{\bar{\mu}\bar{\nu}}(q) \Big), \end{aligned} \tag{3·22}$$

where

$$\boldsymbol{A}^\dagger_{\mu\bar{\nu}}(q) \equiv a^\dagger_\mu(q) a^\dagger_{\bar{\nu}}(q), \quad \boldsymbol{A}_{\mu\bar{\nu}}(q) \equiv a_{\bar{\nu}}(q) a_\mu(q), \quad \boldsymbol{B}_{\mu\nu}(q) \equiv a^\dagger_\mu(q) a_\nu(q). \tag{3·23}$$

Note that $E_{\bar{\mu}}(q) = E_\mu(q)$ and also that the equalities $F^{(\pm)}_{B,s}(\bar{\mu}\bar{\nu}) = F^{(\pm)}_{B,s}(\mu\nu)$ hold for the operators under consideration. Explicit expressions for the expectation values and the quasiparticle matrix elements appearing in the above equations are given in Appendix A.

3.4. *Local harmonic equations in the moving frame*

We can represent the infinitesimal generators $\hat{Q}(q)$ and $\hat{P}(q)$ in terms of $\boldsymbol{A}^\dagger_{\mu\bar{\nu}}(q)$ and $\boldsymbol{A}_{\mu\bar{\nu}}(q)$ as

$$\hat{Q}(q) = \sum_{\mu\bar{\nu}} Q_{\mu\bar{\nu}}(q) \Big(\boldsymbol{A}^\dagger_{\mu\bar{\nu}}(q) + \boldsymbol{A}_{\mu\bar{\nu}}(q) \Big), \tag{3·24}$$

$$\hat{P}(q) = i \sum_{\mu\bar{\nu}} P_{\mu\bar{\nu}}(q) \Big(\boldsymbol{A}^{\dagger}_{\mu\bar{\nu}}(q) - \boldsymbol{A}_{\mu\bar{\nu}}(q) \Big), \tag{3·25}$$

where the sum is taken over the proton and neutron quasiparticle pairs $(\mu\bar{\nu})$. For the P+Q Hamiltonian, the local harmonic equations, (2·4) and (2·5), in the moving frame reduce to

$$\delta \langle \phi(q) | \, [\hat{h}_M(q), \hat{Q}(q)] - \sum_s f^{(-)}_{Q,s} \hat{F}^{(-)}_s - \frac{1}{i} B(q) \hat{P}(q) \, | \phi(q) \rangle = 0, \tag{3·26}$$

$$\begin{aligned} \delta \langle \phi(q) | \, \Big[\hat{h}_M(q), \quad \frac{1}{i} B(q) \hat{P}(q) \Big] - \sum_s f^{(+)}_{P,s} \hat{F}^{(+)}_s - B(q) C(q) \hat{Q}(q) - \sum_s f^{(+)}_{R,s} \hat{F}^{(+)}_s \\ + \sum_s f^{(-)}_{Q,s} \hat{R}^{(-)}_s - \sum_\tau f_{N,\tau} \hat{N}_\tau \, | \phi(q) \rangle = 0, \end{aligned} \tag{3·27}$$

where the quantities $f^{(-)}_{Q,s}$, etc., are given by

$$f^{(-)}_{Q,s} \equiv -\kappa_s \langle \phi(q) | \, [\hat{F}^{(-)}_s, \hat{Q}(q)] \, | \phi(q) \rangle = 2\kappa_s (F^{(-)}_s, Q(q)), \tag{3·28}$$

$$f^{(+)}_{P,s} \equiv \kappa_s \langle \phi(q) | \, \Big[\hat{F}^{(+)}_s, \frac{1}{i} B(q) \hat{P}(q) \Big] \, | \phi(q) \rangle = 2\kappa_s B(q) (F^{(+)}_s, P(q)), \tag{3·29}$$

$$f^{(+)}_{R,s} \equiv -\frac{1}{2} \kappa_s \langle \phi(q) | \, [\hat{R}^{(+)}_s, \hat{Q}(q)] \, | \phi(q) \rangle = \kappa_s (R^{(+)}_s, Q(q)), \tag{3·30}$$

$$f_{N,\tau} \equiv B(q) \frac{\partial \lambda_\tau}{\partial q}. \tag{3·31}$$

Here we have introduced the notation

$$\hat{R}^{(\pm)}_s \equiv [\hat{F}^{(\pm)}_{B,s}, \Big(\hat{h}(q) - \sum_\tau \lambda_\tau(q) \hat{N}_\tau \Big)_A] \equiv \sum_{\mu\bar{\nu}} R^{(\pm)}_s(\mu\bar{\nu}) \Big(\boldsymbol{A}^{\dagger}_{\mu\bar{\nu}}(q) \mp \boldsymbol{A}_{\mu\bar{\nu}}(q) \Big), \tag{3·32}$$

where $(\hat{h}(q) - \sum_\tau \lambda_\tau(q) \hat{N}_\tau)_A$ represents the $\boldsymbol{A}^{\dagger}_{\mu\bar{\nu}}(q)$ and $\boldsymbol{A}_{\mu\bar{\nu}}(q)$ parts of the operator in parentheses. We also use the notation

$$(F^{(-)}_s, Q(q)) \equiv \sum_{\mu\bar{\nu}} F^{(-)}_s(\mu\bar{\nu}) Q_{\mu\bar{\nu}}(q), \quad \text{etc.} \tag{3·33}$$

Note that $f^{(-)}_{Q,s}, f^{(+)}_{P,s}$ and $f^{(+)}_{R,s}$ are linear functions of $Q_{\mu\bar{\nu}}(q)$ or $P_{\mu\bar{\nu}}(q)$.

We can easily derive the following expressions for the matrix elements $Q_{\mu\bar{\nu}}(q)$ and $P_{\mu\bar{\nu}}(q)$ from the local harmonic equations in the moving frame, (3·26) and (3·27):

$$\begin{aligned} Q_{\mu\bar{\nu}}(q) = \sum_s g_1(\mu\bar{\nu}) F^{(-)}_s(\mu\bar{\nu}) f^{(-)}_{Q,s} + \sum_s g_2(\mu\bar{\nu}) \Big\{ F^{(+)}_s(\mu\bar{\nu}) f^{(+)}_{PR,s} \\ + R^{(-)}_s(\mu\bar{\nu}) f^{(-)}_{Q,s} + \sum_\tau N_\tau(\mu\bar{\nu}) f_{N,\tau} \Big\} \end{aligned} \tag{3·34}$$

$$\begin{aligned} P_{\mu\bar{\nu}}(q) = \sum_s g_1(\mu\bar{\nu}) \Big\{ F^{(+)}_s(\mu\bar{\nu}) f^{(+)}_{PR,s} + R^{(-)}_s(\mu\bar{\nu}) f^{(-)}_{Q,s} + \sum_\tau N_\tau(\mu\bar{\nu}) f_{N,\tau} \Big\} \\ + \omega^2(q) \sum_s g_2(\mu\bar{\nu}) F^{(-)}_s(\mu\bar{\nu}) f^{(-)}_{Q,s}, \end{aligned} \tag{3·35}$$

where $f^{(+)}_{PR,s} = f^{(+)}_{P,s} + f^{(+)}_{R,s}$ and

$$g_1(\mu\bar{\nu}) \equiv \frac{E_\mu + E_{\bar{\nu}}}{(E_\mu + E_{\bar{\nu}})^2 - \omega^2(q)}, \quad g_2(\mu\bar{\nu}) \equiv \frac{1}{(E_\mu + E_{\bar{\nu}})^2 - \omega^2(q)}. \tag{3·36}$$

Note that ω^2, representing the square of the frequency of the local harmonic mode, $\omega(q) = \sqrt{B(q)C(q)}$, is not necessarily positive. The values of $B(q)$ and $C(q)$ depend on the scale of the collective coordinate q, while $\omega(q)$ does not. In other words, the scale of q can be chosen arbitrarily without affecting the frequency $\omega(q)$. We thus require $B(q) = 1$ everywhere on the collective path to uniquely determine the scale of q.

Inserting expressions (3·34) and (3·35) for $Q_{\mu\bar{\nu}}(q)$ and $P_{\mu\bar{\nu}}(q)$ into Eqs. (3·28)–(3·30) and combining them with the condition of orthogonality to the number operators,

$$\langle\phi(q)|[\hat{N}_\tau, \hat{P}(q)]|\phi(q)\rangle = 2i(P(q), N_\tau) = 0, \tag{3·37}$$

we obtain the linear homogeneous equations

$$\sum_{s'\tau'} \begin{pmatrix} S^{Q,Q}_{ss'} & S^{Q,PR}_{ss'} & S^{Q,N}_{s\tau'} \\ S^{PR,Q}_{ss'} & S^{PR,PR}_{ss'} & S^{PR,N}_{s\tau'} \\ S^{N,Q}_{\tau s'} & S^{N,PR}_{\tau s'} & S^{N,N}_{\tau\tau'} \end{pmatrix} \begin{pmatrix} f^{(-)}_{Q,s'} \\ f^{(+)}_{PR,s'} \\ f_{N,\tau'} \end{pmatrix} = 0 \tag{3·38}$$

for the vectors $\boldsymbol{f}^{(-)}_Q$, $\boldsymbol{f}^{(+)}_{PR}$, and $\boldsymbol{f}_N$ defined by

$$\boldsymbol{f}^{(-)}_Q \equiv \{f^{(-)}_{Q,1},\ f^{(-)}_{Q,1}\}, \tag{3·39}$$

$$\boldsymbol{f}^{(+)}_{PR} \equiv \{f^{(+)}_{PR,1},\ f^{(+)}_{PR,2},\ f^{(+)}_{PR,3},\ f^{(+)}_{PR,5}\}, \tag{3·40}$$

$$\boldsymbol{f}_N \equiv \{f_{N,n},\ f_{N,p}\}. \tag{3·41}$$

Here, we have

$$S^{Q,Q}_{ss'} \equiv 2(F^{(-)}_s, F^{(-)}_{s'})_{g_1} + 2(F^{(-)}_s, R^{(-)}_{s'})_{g_2} - \frac{1}{\kappa_s}\delta_{ss'}, \tag{3·42}$$

$$S^{Q,PR}_{ss'} \equiv 2(F^{(-)}_s, F^{(+)}_{s'})_{g_2}, \tag{3·43}$$

$$S^{Q,N}_{s\tau'} \equiv 2(F^{(-)}_s, N_{\tau'})_{g_2}, \tag{3·44}$$

$$S^{PR,Q}_{ss'} \equiv 2(F^{(+)}_s, R^{(-)}_{s'})_{g_1} + 2\omega^2(q)(F^{(+)}_s, F^{(-)}_{s'})_{g_2} + (R^{(+)}_s, R^{(-)}_{s'})_{g_2}, + (R^{(+)}_s, F^{(-)}_{s'})_{g_1}, \tag{3·45}$$

$$S^{PR,PR}_{ss'} \equiv 2(F^{(+)}_s, F^{(+)}_{s'})_{g_1} + (R^{(+)}_s, F^{(+)}_{s'})_{g_2} - \frac{1}{\kappa_s}\delta_{ss'}, \tag{3·46}$$

$$S^{PR,N}_{s\tau'} \equiv 2(F^{(+)}_s, N_{\tau'})_{g_1} + (R^{(+)}_s, N_{\tau'})_{g_2}, \tag{3·47}$$

$$S^{N,Q}_{\tau s'} \equiv \omega^2(q)(N_\tau, F^{(-)}_{s'})_{g_2} + (N_\tau, R^{(-)}_{s'})_{g_1}, \tag{3·48}$$

$$S^{N,PR}_{\tau s'} \equiv (N_\tau, F^{(+)}_{s'})_{g_1}, \tag{3·49}$$

$$S^{N,N}_{\tau\tau'} \equiv (N_\tau, N_{\tau'})_{g_1}, \tag{3·50}$$

with the notations

$$(F_s^{(-)}, F_{s'}^{(-)})_{g_1} \equiv \sum_{\mu\bar{\nu}} F_s^{(-)}(\mu\bar{\nu}) g_1(\mu\bar{\nu}) F_{s'}^{(-)}(\mu\bar{\nu}), \quad \text{etc.} \tag{3·51}$$

Equation (3·38) takes the form

$$\sum_{\sigma'=1}^{8} S_{\sigma\sigma'}(\omega^2(q)) f_{\sigma'} = 0 \tag{3·52}$$

for the vector $\boldsymbol{f}$ composed of

$$\{f_{\sigma=1-8}\} \equiv \{\boldsymbol{f}_Q^{(-)},\ \boldsymbol{f}_{PR}^{(+)},\ \boldsymbol{f}_N\} \tag{3·53}$$

$$\equiv \{f_{Q,1}^{(-)},\ f_{Q,2}^{(-)},\ f_{PR,1}^{(+)},\ f_{PR,2}^{(+)},\ f_{PR,3}^{(+)},\ f_{PR,5}^{(+)},\ f_{N,n},\ f_{N,p}\}. \tag{3·54}$$

Thus, the frequency ω of the local harmonic mode is determined by the condition $\det S = 0$. The normalizations of $\boldsymbol{f}$ are fixed by

$$\langle\phi(q)|[\hat{Q}(q), \hat{P}(q)]|\phi(q)\rangle = 2i(Q(q), P(q)) = i. \tag{3·55}$$

Note that ω^2 represents the curvature of the collective potential,

$$\omega^2 = \frac{\partial^2 V}{\partial q^2}, \tag{3·56}$$

for the choice of coordinate scale with which the mass is unity, i.e., $B(q) = 1$.

In concluding this section, we mention that the reduction of the local harmonic equations to linear homogeneous equations like (3·52) can be done for any effective interaction that can be written as a sum of separable terms. Below, we call the local harmonic equations in the moving frame the "moving frame QRPA" for brevity.

§4. Procedure of the calculation

4.1. *Algorithm to find collective paths*

In order to find the collective path connecting the oblate and prolate local minima, we have to determine the state vectors $|\phi(q)\rangle$ and the infinitesimal generators $\hat{Q}(q)$ and $\hat{P}(q)$ by solving the moving frame HB equation (3·14) and the moving frame QRPA equations, (3·26) and (3·27). Because $\hat{Q}(q)$ and $|\phi(q)\rangle$ are mutually dependent, we have to resort to some iterative procedure. We carry this out through the following algorithm.

Let us assume that the state vector $|\phi(q)\rangle$ and the infinitesimal generators $\hat{Q}(q)$ and $\hat{P}(q)$ are known at a specific point of q. We then find the state vector $|\phi(q+\delta q)\rangle$ and the infinitesimal generators $\hat{Q}(q+\delta q)$ and $\hat{P}(q+\delta q)$ at a neighboring point $q+\delta q$ through the following steps.

Step 1: Construct a state vector at the neighboring point $q + \delta q$ using $\hat{P}(q)$:

$$|\phi(q+\delta q)\rangle^{(0)} = e^{-i\delta q \hat{P}(q)}|\phi(q)\rangle. \tag{4·1}$$

Though $|\phi(q+\delta q)\rangle^{(0)}$ does not necessarily satisfy the moving frame HB equation, (3·14), we can use this state vector as an initial guess for $q+\delta q$.
Step 2: Solve the moving frame HB equation (3·14) using $\hat{Q}^{(0)}(q+\delta q)=\hat{Q}(q)$ as an initial guess for $\hat{Q}(q+\delta q)$ and obtain an improved state vector $|\phi(q+\delta q)\rangle^{(1)}$. Doing this, we find it important to impose the constraint

$$\langle\phi(q+\delta q)|\hat{Q}(q)|\phi(q+\delta q)\rangle=\delta q \tag{4·2}$$

for the increment δq of the collective coordinate q, together with the constraints

$$\langle\phi(q+\delta q)|\hat{N}_\tau|\phi(q+\delta q)\rangle=N_\tau, \qquad \tau=p,n \tag{4·3}$$

for the proton and neutron numbers ($N_p=Z,\ N_n=N$). The constraint (4·2) is easily derived by combining Eq. (4·1) with the canonical variable condition (2·8). The details of this step are described in Appendix B.
Step 3: Solve the moving frame QRPA equations, (3·26) and (3·27), with the use of $|\phi(q+\delta q)\rangle^{(1)}$ to obtain $\hat{Q}^{(1)}(q+\delta q)$ and $\hat{P}^{(1)}(q+\delta q)$.
Step 4: Return to *Step 2* and solve Eq. (3·14) using $\hat{Q}^{(1)}(q+\delta q)$.

If the iterative procedure, *Steps 2-4*, converges, we obtain self-consistent solutions, $\hat{Q}(q+\delta q)$, $\hat{P}(q+\delta q)$ and $|\phi(q+\delta q)\rangle$, that satisfy Eqs. (3·14), (3·26) and (3·27) simultaneously at $q+\delta q$. Then, we return to *Step 1* to construct an initial guess $|\phi(q+2\delta q)\rangle^{(0)}$ for the next point, $q+2\delta q$, and repeat the above procedure. In this way, we proceed step by step along the collective path.

The above is a brief summary of the basic algorithm. In actual numerical calculations, we start the procedure from one of the HB local minima and choose the lowest frequency QRPA mode as an initial condition for the infinitesimal generators $\hat{Q}$ and $\hat{P}$ at $q=0$. Under ordinary conditions, we can proceed along the collective path following the procedure described above. In some special situations, however, we need additional considerations concerning the choice of the initial guess, $\hat{Q}^{(0)}(q+\delta q)$, in *Step 2*. Actually, we encounter such situations in some special regions of the collective path for ^{72}Kr. We give detailed discussion of this point in §5.3.

We have checked that the same collective path is obtained by starting from the other local minimum and proceeding in the inverse manner.

4.2. *Details of the calculation*

In the numerical calculation, we use the spherical single-particle energies of the modified oscillator model of Ref. 83), which are listed in Table I, and follow the conventional prescriptions of the P+Q interaction model,[77] except that the pairing and quadrupole interaction strengths, G_τ and χ, are chosen to approximately reproduce the pairing gaps and quadrupole deformations obtained in the Skyrme-HFB calculation carried out by Yamagami et al.[82] The values they obtained are $G_n=0.320$ (0.299) $G_p=0.320$ (0.309) and $\chi'\equiv\chi b^4=0.248$ (0.255) in units of MeV for ^{68}Se (^{72}Kr), where b is the length parameter given by $b^2=\frac{4}{5}\left(\frac{2}{3}\right)^{1/3}r_0^2A^{1/3}$. The pairing gaps, $\Delta_{\tau=p,n}$, and deformation parameters, β and γ, are defined as usual through the expectation values of the pairing and quadrupole operators:

$$\Delta_\tau(q)=G_\tau\langle\phi(q)|\sum_{k\in\tau}d_k^\dagger d_{\bar{k}}^\dagger|\phi(q)\rangle, \tag{4·4}$$

Table I. Spherical single-particle orbits and their energies used in the calculation. The energies relative to those of $1g_{9/2}$ are given in units of MeV.

orbits	$1f_{7/2}$	$2p_{3/2}$	$1f_{5/2}$	$2p_{1/2}$	$1g_{9/2}$	$2d_{5/2}$	$1g_{7/2}$	$3s_{1/2}$	$2d_{3/2}$
protons	−8.77	−4.23	−2.41	−1.50	0.0	6.55	5.90	10.10	9.83
neutrons	−9.02	−4.93	−2.66	−2.21	0.0	5.27	6.36	8.34	8.80

$$\beta\cos\gamma = \chi'\langle\phi(q)|\hat{D}^{(+)}_{20}|\phi(q)\rangle/(\hbar\omega_0 b^2), \tag{4·5}$$

$$\beta\sin\gamma = \sqrt{2}\chi'\langle\phi(q)|\hat{D}^{(+)}_{22}|\phi(q)\rangle/(\hbar\omega_0 b^2). \tag{4·6}$$

Here, $\hbar\omega_0$ denotes the frequency of the harmonic oscillator potential.

§5. Results of the calculation

5.1. *Properties of the QRPA modes at the local minima in ^{68}Se and ^{72}Kr*

For the P+Q Hamiltonian described in §4, the lowest HB solution corresponds to a oblate shape, while the second lowest HB solution possesses a prolate shape for both ^{68}Se and ^{72}Kr (see Table II). Their energy differences are 0.30 and 0.82 MeV for ^{68}Se and ^{72}Kr, respectively. In the QRPA calculations at these local minima, we obtain strongly collective quadrupole modes with low frequencies. They correspond to the β and γ vibrations in deformed nuclei with axial symmetry. Although the former in fact contains pairing vibrational components, we call it a β vibration, because the transition matrix elements for the quadrupole operator $D^{(+)}_{20}$ are enhanced. (A neutron pairing vibrational mode appears as the second QRPA mode at the oblate minimum in ^{72}Kr; see Table II.) We note that there is an important difference between ^{68}Se and ^{72}Kr concerning the relative excitation energies of the β and γ vibrational modes: In the case of ^{68}Se, the frequencies of the γ vibrational QRPA mode are lower than those of the β vibrational one for both the oblate and prolate local minima. The situation is opposite in the case of ^{72}Kr; that is, the frequencies of the β vibrations are lower than those of the γ vibrations. As we see in the succeeding subsections, this difference leads to an important difference in the properties of the collective path connecting the two local minima.

Table II. The equilibrium quadrupole deformation parameters (β, γ), the pairing gaps (Δ_τ) in units of MeV, the QRPA eigenenergies $\hbar\omega_{\rho=1,2}$ in units of MeV, and the relevant quadrupole transition matrix elements squared, $|M_\rho|^2 \equiv |\langle\rho|D^{(+)}_{2K}|0\rangle|^2$ ($\rho = 1, 2$). Here, $|\rho\rangle$ and $|0\rangle$ denote the QRPA one-phonon and the ground states. The symbols β, γ and Δ_n in the eighth column respectively indicate the β-, γ- and neutron-pairing vibrational modes; the $|M_\rho|^2$ values for $K = 0,\ 2$ and 0 are presented in Weisskopf units.

	β	γ	Δ_n	Δ_p	ω_1	$\lvert M_1\rvert^2$	ω_2	$\lvert M_2\rvert^2$
^{68}Se (prolate)	0.234	0°	1.34	1.42	1.02(γ)	33.66	1.91(β)	12.19
^{68}Se (oblate)	0.284	60°	1.17	1.27	1.55(γ)	13.64	2.25(β)	7.67
^{72}Kr (prolate)	0.376	0°	1.15	1.29	1.60(β)	12.97	1.67(γ)	14.61
^{72}Kr (oblate)	0.354	60°	0.86	1.00	1.15(β)	5.37	1.91(Δ_n)	0.19

5.2. *Collective path connecting the oblate and prolate minima in* ^{68}Se

As the γ vibrational mode is the lowest frequency and most collective QRPA mode at the prolate local minimum, we have chosen this mode as the initial condition for solving the basic equations of the ASCC method and carried out the procedure described in §4.1. We thus obtained the collective path connecting the oblate and prolate local minima in ^{68}Se, which is plotted in Fig. 1(a). As we have extracted the collective path in the TDHB phase space, which has a very large number of degrees of freedom, the path drawn in this figure should be regarded as a projection of the collective path onto the (β, γ)-plane. Roughly speaking, the collective path goes through the valley that exists in the γ direction and connects the oblate and prolate minima. If β is treated as a collective coordinate and the oblate and prolate shapes are connected through the spherical point, the variation of the potential energy would be much greater than that along the collective path we obtained. The potential energy curve $V(q)$ along the collective path evaluated using the ASCC method is displayed in Fig. 1(b). Because we have defined the scale of the collective coordinate q such that the collective mass is given by $M(q) = B(q)^{-1} = 1$ MeV^{-1}, the collective mass as a function of the geometrical length s along the collective path in the (β, γ) plane can be defined by

$$M(s(q)) = M(q)\Big(\frac{ds}{dq}\Big)^{-2}, \tag{5·1}$$

with $ds^2 = d\beta^2 + \beta^2 d\gamma^2$. This quantity is presented in Fig. 1(c) as a function of q. The triaxial deformation parameter γ is plotted as a function of q in Fig. 1(d). Variations of the pairing gaps, $\Delta_\tau(q)$, and of the eigen-frequencies of the moving frame QRPA equations along the collective path are plotted in Figs. 1(e) and (f). The solid curve in Fig. 1(f) represents the frequencies squared, $\omega^2(q) = B(q)C(q)$, given by the product of the inverse mass $B(q)$ and the local stiffness $C(q)$ of the solutions of the moving frame QRPA equations, which correspond to the γ-vibration in the oblate and prolate limits. These QRPA solutions determine the infinitesimal generators $\hat{Q}(q)$ and $\hat{P}(q)$ along the collective path. For reference, we also present in Fig. 1(f) another solution of the moving frame QRPA equations, which possesses the β-vibrational properties and is irrelevant to the collective path in the case of ^{68}Se. Note that the frequency of the γ-vibrational mode becomes imaginary in the region $12^\circ < \gamma < 45^\circ$. These results should reveal interesting dynamical properties of the shape coexistence phenomena in ^{68}Se. For instance, the large collective mass in the vicinity of $\gamma = 60^\circ$ [Fig. 1(c)] might increase the stability of the oblate shape in the ground state. A detailed investigation of these quantities as well as solutions of the collective Schrödinger equation will be given in a succeeding paper.[84)]

5.3. *Collective path connecting the oblate and prolate minima in* ^{72}Kr

In contrast to ^{68}Se, the lowest-frequency QRPA mode is the β vibration at the prolate local minimum in ^{72}Kr. For this reason, we have chosen this mode as the initial condition at the prolate minimum and started the procedure of extracting the collective path. Then, the collective path first goes in the direction of the β axis in the (β, γ)-plane. As we go along the β axis, we eventually encounter a situation in

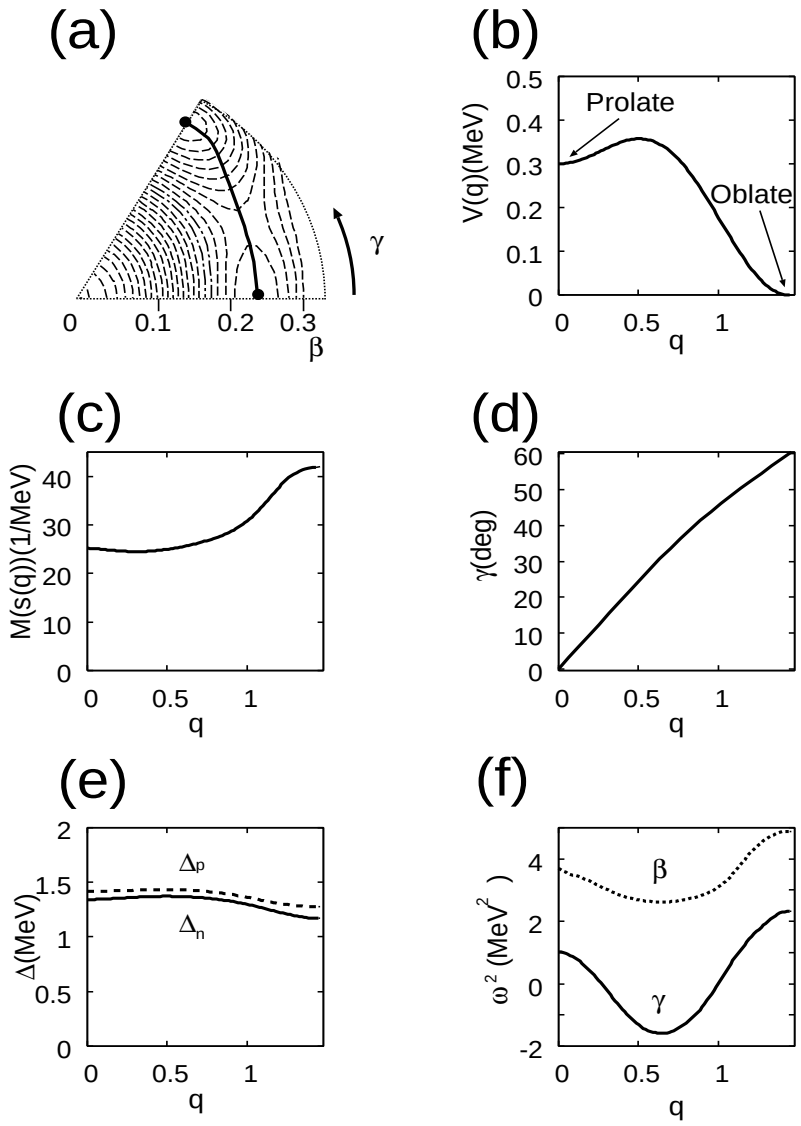

Fig. 1. Results of the calculation for ^{68}Se. (a) The bold curve represents the ASCC path projected onto the (β, γ) plane, which connects the oblate and the prolate minima designated by filled circles. The contour lines were calculated using the conventional constrained HB method and plotted at intervals of 50 keV. (b) Collective potential $V(q)$ plotted as a function of the collective coordinate q. Here the origin of q is chosen to coincide with the prolate local minimum, and its scale is defined such that the collective mass is given by $M(q) = 1$. (c) Collective mass $M(s(q))$ with respect to the geometrical length $s(q)$ along the collective path in the (β, γ)-plane, plotted as a function of q. (d) The triaxiality parameter γ as a function of q. (e) Neutron and proton pairing gaps, Δ_n and Δ_p, as functions of q. (f) The lowest two eigen-frequencies squared (i.e., $\omega^2 = BC$) of the moving frame RPA, plotted as functions of q. These modes at triaxial deformed shapes are more general than the ordinary β- and γ-vibrations in the oblate and prolate limits and contain both components. The symbols β and γ are used, however, to indicate the major components of the moving frame RPA modes.

which the two solutions of the moving frame QRPA equations compete in energy, and they eventually cross. Thus, we see that the properties of the solution with the lowest value of $\omega^2 = BC$ change from those of the β vibrational to those of the γ vibrational case at some point on the collective path. If only the solution $\hat{Q}_1(q)$ with the lowest

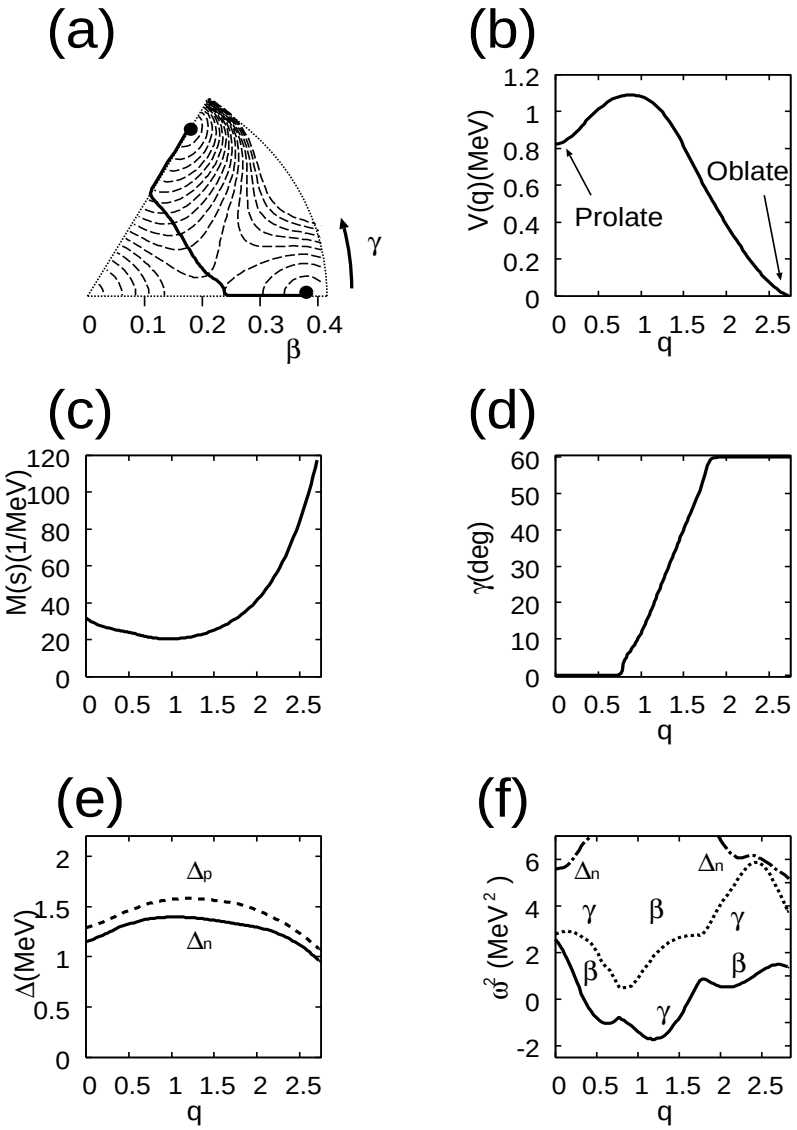

Fig. 2. Results of the calculation for ^{72}Kr. The details here are the same as in Fig. 1, except for the following: In (a), the contour lines are plotted at intervals of 100 keV. In (f), the lowest three eigen-frequencies squared (i.e., $\omega^2 = BC$) of the moving frame RPA are plotted as functions of q. As mentioned in the caption to Fig. 1, these modes at triaxial deformed shapes are more general than the ordinary β- and γ-vibrations in the oblate and prolate limits and contain both components. The symbols β and γ are used, however, in order to indicate the major components of the moving frame RPA modes. Similarly, the symbol Δ_n is used to indicate that the major component is the neutron pairing vibrational mode.

value of ω^2 at the previous point q is always chosen as an initial guess for $\hat{Q}(q+\delta q)$ in *Step 2* of the algorithm described in §4.1, then the direction of the collective path in the (β, γ) plane changes abruptly from the β direction to the γ direction immediately after the crossing point (in the vicinity of the point C' in Fig. 3 presented below), and the numerical algorithm outlined in §4.1 fails at this point: During the iterative procedure of solving the moving frame HB equation, we encounter a situation in which the overlap $(Q(q), Q(q+\delta q))$ between the infinitesimal generators $\hat{Q}$ at the neighboring points q and $q+\delta q$ vanishes, because K=0 for the former, whereas K=2 for the latter. The numerical algorithm (whose details are described in Appendix B) then is no longer effective at this point, where the overlaps $(N_\tau, Q(q+\delta q))$ also vanish for the same reason. This problem exists even if we decrease the step size δq. We find, however, that we can avoid this difficulty by employing a more suitable initial guess for $\hat{Q}(q+\delta q)$. Specifically, we take a linear combination of the two solutions $\hat{Q}_1(q)$ and $\hat{Q}_2(q)$ at the previous point q, $\hat{Q}^{(0)}(q+\delta q) = (1-\varepsilon)\hat{Q}_1(q) + \varepsilon \hat{Q}_2(q)$, with a small coefficient ε, as an initial guess. This improvement is just for the purpose of starting the iterative procedure at the next point, $q+\delta q$, on the collective path, so that the self-consistent solution, $\hat{Q}(q+\delta q)$, obtained upon the convergence of the iterative procedure, of course, does not depend on the values of ε. For instance, we obtain an axially symmetric solution $|\phi(q+\delta q)\rangle$ and a generator $\hat{Q}(q+\delta q)$ preserving the K quantum number in the region satisfying $\beta > 0.24$ around the prolate minimum, even when we start the iterative procedure using an initial guess for $\hat{Q}(q+\delta q)$ that breaks the axial symmetry. We confirmed that this is indeed the case as long as ε is a small finite value around 0.1. This special care is needed only near such crossing points (as shown below in Figs. 3–5), where two solutions of the moving frame QRPA equations with different K quantum numbers compete in energy.

With the improved algorithm mentioned above, we have successfully obtained the smooth deviation of the direction of the collective path from the β axis toward the γ direction [see Fig. 2(a)]. We note that the properties of the lowest ω^2 solution of the local harmonic equations also gradually change from those of the β vibrational to those of the γ vibrational case [see Fig. 2(f)]. The details of the turnover region are presented in Fig. 3. It can clearly be seen in Fig. 3(a) that there is a gradual onset of axial-symmetry breaking in the solutions $|\phi(q)\rangle$ of the moving frame HB equation. It can also be seen in Fig. 3(b) that there is an avoided crossing between the lowest two solutions of the moving frame QRPA equations associated with mixing of the components with K=0 and 2. After a smooth turn in the γ direction, the γ value increases, with the value of β roughly constant, and the collective path eventually approaches the $\gamma = 60^\circ$ axis. Then, we again encounter a similar situation. Adopting the improved algorithm, we have confirmed that the properties of the lowest ω^2 solution change smoothly this time, from those of the γ vibrational to those of the β vibrational case. The collective path thus merges with the $\gamma = 60^\circ$ axis, and it finally reaches the oblate minimum.

We have also carried out a calculation starting from the oblate minimum and proceeded in the inverse manner, obtaining the same collective path. This should be regarded as a crucial test of the consistency of our calculation. Figure 4 presents the details of this test: The collective path that started from the prolate minimum

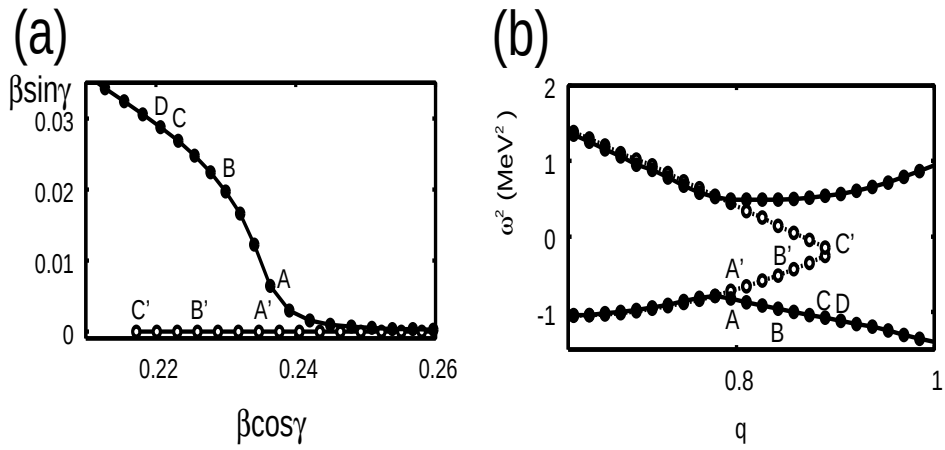

Fig. 3. Enlargement of the turnover region of Figs. 2(a) and (f) for ^{72}Kr, where the collective path turns in the γ direction. A step size $\delta q = 0.0157$ and the value $\varepsilon = 0.1$ were used in the numerical calculation. Every step δq is represented by a filled circle and connected by a solid curve. The points designated A, B, C, D on the collective path in (a) correspond to those in (b), which displays the squared frequencies, ω^2, of the lowest two solutions of the moving frame QRPA equations as functions of the collective coordinate q. The open circles represent those obtained in the calculation with $\varepsilon = 0$, where the mixing effects between the K=0 and 2 components are ignored. The points designated A', B', C' in the latter calculation correspond to the points A, B, C in the former calculation. In the latter calculation, we could not obtain the point corresponding to D, because the problem discussed in the main text is encountered in the numerical algorithm. It was checked that the same collective path is obtained with use of $\delta q = 0.0314$, except that the distances between the successive points are doubled.

and turned in the γ direction gradually merges with the $\gamma = 60^\circ$ axis. Moving in the opposite direction, we see a gradual onset of axial symmetry breaking in the collective path that started from the oblate minimum. We see that the two results of the calculation for the collective path agree nicely. The importance of taking account of the mixing between the β- and γ-vibrational degrees of freedom in solving the moving frame HB and QRPA equations is again demonstrated in Fig. 5, which displays the details of the turnover region from the $\gamma = 60^\circ$ axis.

Although the collective path plotted in Fig. 2(a) should be regarded as its projection onto the (β, γ)-plane, the result of calculation indicates that the collective path runs roughly along the valley in this plane. The potential energy curve $V(q)$, the collective mass $M(s(q))$, and the variations of the pairing gaps, $\Delta_\tau(q)$, are presented in Figs. 2(b), (c) and (e), respectively. Their properties are similar to those for ^{68}Se. In particular, we notice again a significant increase of $M(s(q))$ in the vicinity of the oblate minimum.

Quite recently, Almehed and Walet studied the oblate-prolate shape coexistence phenomenon in ^{72}Kr by means of an approach similar to the ASCC method but with some additional approximations[80] and found a collective path going from the oblate minimum over a spherical energy maximum into the prolate secondary minimum. We have also obtained such a collective path when we impose axial symmetry on the solutions $|\phi(q)\rangle$ of the moving frame HB equation and always use only K=0 solutions

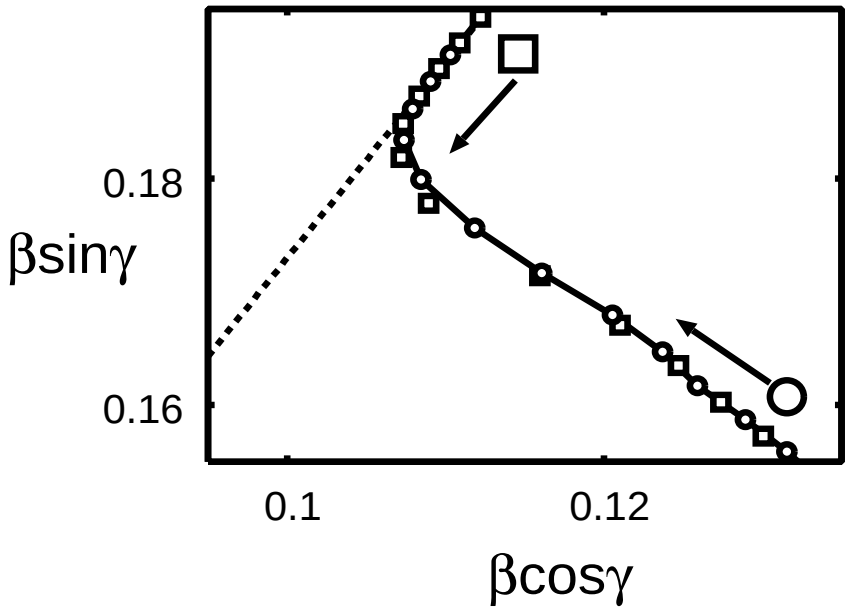

Fig. 4. Enlargement of the turnover region of Figs. 2(a) for ^{72}Kr, where the collective path (solid curve) coming from the prolate minimum merges with the $\gamma = 60^\circ$ axis (dotted line). Every step δq is represented by an open circle and connected by a solid curve. For comparison, the result of calculation starting from the oblate minimum and moving in the opposite direction is represented by open squares. Slight deviations from the solid curve indicate the degree of precision of the present numerical calculation. The step size $\delta q = 0.0157$ and the value $\varepsilon = 0.1$ were used in both cases. The collective path obtained with these different calculations agree well.

of the moving frame QRPA equations. However, when we relax such symmetry restrictions and follow the lowest ω^2 solution of the moving frame QRPA equations, we obtain the collective path presented in Fig. 2, which breaks the axial symmetry. The reason for this disagreement is not clear at present. With the parameter values they used for the P+Q Hamiltonian, they did not encounter the change in properties of the lowest moving-frame-QRPA mode on the collective path from those of the β vibrational to those of the γ vibrational case. However, it is interesting that they in fact encountered the avoided crossing with a γ-vibrational mode, similar to the one shown in Fig. 2(f), and obtained a collective path that turns into the triaxial plane in their calculation for states with angular momentum $I = 2$.

§6. Concluding remarks

We have applied the ASCC method to the oblate-prolate shape coexistence phenomena in ^{68}Se and ^{72}Kr. It was found that the self-consistent collective paths run approximately along the valley connecting the oblate and prolate local minima in the collective potential energy landscape. This is the first time that the self-consistent collective paths between the oblate and prolate minima have been obtained in realistic situations starting from the microscopic P+Q Hamiltonian. Recently, the gen-

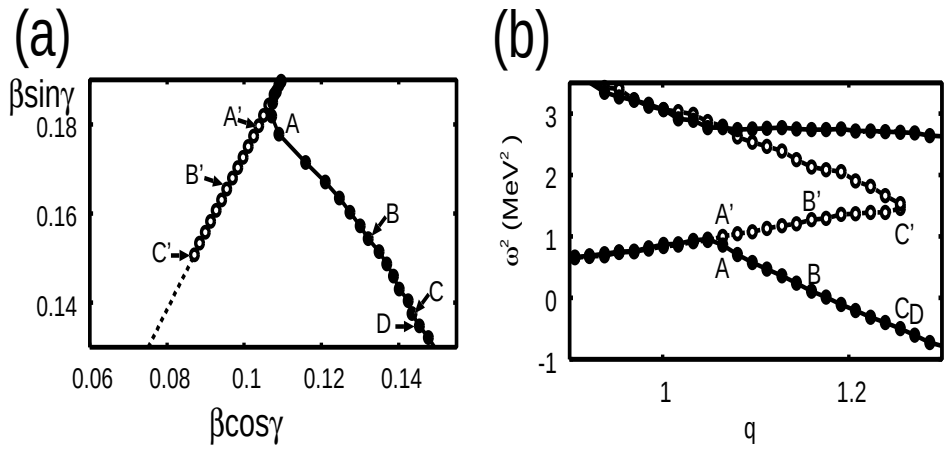

Fig. 5. Enlargement of the turnover region of Figs. 2(a) and (f) for ^{72}Kr, where the collective path (solid curve) coming from the oblate minimum starts to deviate from the $\gamma = 60^\circ$ axis (dotted line). The numerical calculation was done starting from the oblate minimum and using the step size $\delta q = 0.0157$ and the value $\varepsilon = 0.1$. Every step δq is represented by a filled circle and connected by a solid curve. The points designated A, B, C, D on the collective path in (a) correspond to those in (b), which displays the squared frequencies, ω^2, of the lowest two solutions of the moving frame QRPA equations as functions of the collective coordinate q. Note that the values of q in this figure are measured from the oblate minimum. The open circles represent those obtained in the calculation with $\varepsilon = 0$, where the mixing effects between the K=0 and 2 components are ignored. The points designated A', B', C' in the latter calculation correspond to the points A, B, C in the former calculation. In the latter calculation, we cannot get the point corresponding to D, because the problem discussed in the main text is encountered in the numerical algorithm. The slight wiggles along the successive points seen in (b) are due to numerical error, and they indicate the degree of precision of the present numerical calculation. It was checked that the same collective path is obtained with use of $\delta q = 0.0314$, except that the distances between the successive points are doubled.

erator coordinate method has been used in a number of cases to describe a variety of shape coexistence phenomena, with β employed as the generator coordinate.[47),48)] The triaxial shape vibrational degrees of freedom were also ignored in the extensive variational calculations by the Tübingen group.[49),50)] The result of the ASCC calculation, however, strongly indicates the necessity of taking into account the γ degree of freedom, at least for the purpose of describing the oblate-prolate shape coexistence in ^{68}Se and ^{72}Kr. In order to evaluate the mixing effects between the oblate and prolate shapes, taking into account the triaxial deformation dynamics, we have to quantize the classical collective Hamiltonian obtained in this paper and solve the resulting collective Schrödinger equation. This will be the subject of a subsequent paper.[84)]

Acknowledgements

This work was done as a part of the Japan-U.S. Cooperative Science Program "Mean-Field Approach to Collective Excitations in Unstable Medium-Mass

and Heavy Nuclei", and is supported by a Grant-in-Aid for the 21st Century COE "Center for Diversity and Universality in Physics" from the Ministry of Education, Culture, Sports, Science and Technology (MEXT) of Japan and also by Grants-in-Aid for Scientific Research (Nos. 14540250 and 14740146) from the Japan Society for the Promotion of Science. The numerical calculations were performed on the NEC SX-5 supercomputer at Yukawa Institute for Theoretical Physics, Kyoto University.

Appendix A

Explicit Expressions of the Quasiparticle Matrix Elements

Combining the successive Bogoliubov transformations, (3·8) and (3·18), the quasiparticles, $a^\dagger_\mu(q)$ and $a_\mu(q)$, associated with the state $|\phi(q)\rangle$, can be written in terms of the nucleon operator, $d^\dagger_k$ and $d_{\bar{k}}$, as

$$\begin{pmatrix} a^\dagger_\mu(q) \\ a_{\bar{\mu}}(q) \end{pmatrix} = \sum_k \begin{pmatrix} U_{\mu k}(q) & V_{\mu\bar{k}}(q) \\ V_{\bar{\mu}k}(q) & U_{\bar{\mu}\bar{k}}(q) \end{pmatrix} \begin{pmatrix} d^\dagger_k \\ d_{\bar{k}} \end{pmatrix}. \tag{A·1}$$

Making use of the inverse transformation,

$$\begin{pmatrix} d^\dagger_k \\ d_{\bar{k}} \end{pmatrix} = \sum_\mu \begin{pmatrix} U_{k\mu}(q) & V_{k\bar{\mu}}(q) \\ V_{\bar{k}\mu}(q) & U_{\bar{k}\bar{\mu}}(q) \end{pmatrix} \begin{pmatrix} a^\dagger_\mu(q) \\ a_{\bar{\mu}}(q) \end{pmatrix}, \tag{A·2}$$

one can easily derive explicit expressions for the expectation values and the matrix elements of the operators $\hat{F}^{(\pm)}_s$ appearing in Eq. (3·22):

$$\begin{aligned}
\langle\phi(q)|\,\hat{F}^{(+)}_{s=1,2}\,|\phi(q)\rangle &= -2\sum_\mu\sum_k (k\bar{k}|A^{(+)}_{\tau=n,p}|0)U_{k\mu}(q)V_{\bar{k}\mu}(q), \\
F^{(\pm)}_{s=1,2}(\mu\bar{\nu}) &= \sum_k (k\bar{k}|A^{(\pm)}_{\tau=n,p}|0)\Big(U_{k\mu}(q)U_{\bar{k}\bar{\nu}}(q) \pm V_{k\bar{\nu}}(q)V_{\bar{k}\mu}(q)\Big), \\
F^{(\pm)}_{B,s=1,2}(\mu\nu) &= \sum_k (k\bar{k}|A^{(\pm)}_{\tau=n,p}|0)\Big(U_{k\mu}(q)V_{\bar{k}\nu}(q) \pm U_{k\nu}(q)V_{\bar{k}\mu}(q)\Big), \\
\langle\phi(q)|\,\hat{F}^{(+)}_{s=3,5}\,|\phi(q)\rangle &= 2\sum_{\bar{\mu}}\sum_{kl} (k|D^{(+)}_{2,K=0,2}|l)V_{k\bar{\mu}}(q)V_{l\bar{\mu}}(q), \\
F^{(+)}_{s=3,5}(\mu\bar{\nu}) &= \sum_{kl} (k|D^{(+)}_{2,K=0,2}|l)\Big(U_{k\mu}(q)V_{l\bar{\nu}}(q) + U_{k\nu}(q)V_{l\bar{\mu}}(q)\Big), \\
F^{(+)}_{B,s=3,5}(\mu\nu) &= \sum_{kl} (k|D^{(+)}_{2,K=0,2}|l)\Big(U_{k\mu}(q)U_{l\nu}(q) - V_{k\bar{\nu}}(q)V_{l\bar{\mu}}(q)\Big).
\end{aligned} \tag{A·3}$$

The expectation values of the anti-Hermitian operators $A^{(-)}_{\tau=n,p}$ vanish. The quantities $(k|D^{(+)}_{2K}|l)$, etc., appearing in the above expressions are the matrix elements between the single-particle states defined by Eq. (3·5):

$$\begin{aligned}
(k|D^{(+)}_{2K}|l) &\equiv (0|d_k D^{(+)}_{2K} d^\dagger_l|0), \\
(k\bar{k}|A^{(\pm)}_\tau|0) &\equiv (0|d_{\bar{k}} d_k A^{(\pm)}_\tau|0), \quad \text{etc.},
\end{aligned} \tag{A·4}$$

where $|0)$ is the vacuum for the nucleon operators $(d^\dagger, d)$. The matrix elements of the Bogoliubov transformations, (A·1) and (A·2), possess the following symmetries:

$$U_{\mu k} = U_{\bar{\mu}\bar{k}} = U_{k\mu} = U_{\bar{k}\bar{\mu}}, \quad V_{\mu\bar{k}} = -V_{\bar{\mu}k} = V_{k\bar{\mu}} = -V_{\bar{k}\mu}. \tag{A·5}$$

It is also easily seen that equalities

$$(\bar{k}|D^{(+)}_{2,K=0,2}|\bar{l}) = (k|D^{(+)}_{2,K=0,2}|l), \tag{A·6}$$

$$F^{(\pm)}_{B,s}(\bar{\mu}\bar{\nu}) = F^{(\pm)}_{B,s}(\mu\nu), \quad F^{(\pm)}_{B,s}(\nu\mu) = \pm F^{(\pm)}_{B,s}(\mu\nu) \tag{A·7}$$

hold for the pairing and quadrupole operators under consideration $\{A^{(\pm)}_n, A^{(\pm)}_p, D^{(+)}_{20}, D^{(+)}_{22}\}$. The expectation values $\langle\phi(q)|\,\hat{N}_\tau\,|\phi(q)\rangle$ and the matrix elements $N_\tau(\mu)$ and $N_{B,\tau}(\mu)$ of the neutron and proton number operators are readily obtained from those of $\hat{F}^{(+)}_{s=3}$ by replacing $(k|D^{(+)}_{20}|l)$ with δ_{kl} and restricting the sum over the single-particle index k to neutrons or protons.

Appendix B
—— *Solving the Moving Frame HB Equation* ——

We solve the moving frame HB equation using a method similar to the imaginary time method.[85] Let $\left|\phi^{(i)}(q)\right\rangle$ be the state vector at the iterative step i. We first calculate the mean-field Hamiltonian associate with it:

$$\begin{aligned}
\hat{h}^{(i)}(q) &= \sum_k \epsilon_k (d^\dagger_k d_k + d^\dagger_{\bar{k}} d_{\bar{k}}) - \sum_s \kappa_s \langle \hat{F}^{(+)}_s \rangle^{(i)} \hat{F}^{(+)}_s, \\
\langle \hat{F}^{(+)}_s \rangle^{(i)} &\equiv \left\langle \phi^{(i)}(q) \right| \hat{F}^{(+)}_s \left| \phi^{(i)}(q) \right\rangle .
\end{aligned} \tag{B·1}$$

Using the quasiparticle operators $b^{(i)\dagger}_\mu$ and $b^{(i)}_\mu$ defined by

$$b^{(i)}_\mu \left|\phi^{(i)}(q)\right\rangle = 0, \tag{B·2}$$

we then generate the state vector at the $(i+1)$th step as

$$\begin{aligned}
\left|\phi^{(i+1)}(q)\right\rangle &\equiv \exp \hat{X}^{(i+1)} \left|\phi^{(i)}(q)\right\rangle \\
\hat{X}^{(i+1)} &= -\varepsilon\Big(\hat{h}^{(i)}(q) - \sum_\tau \lambda^{(i+1)}_\tau(q)\hat{N}_\tau - \mu^{(i+1)}(q)\hat{Q}(q)\Big)_+ \\
&\quad + \varepsilon\Big(\hat{h}^{(i)}(q) - \sum_\tau \lambda^{(i+1)}_\tau(q)\hat{N}_\tau - \mu^{(i+1)}(q)\hat{Q}(q)\Big)_- \\
&\equiv \sum_{\mu\bar{\nu}} x^{(i+1)}_{\mu\bar{\nu}} \Big(\boldsymbol{X}^{(i)\dagger}_{\mu\bar{\nu}} - \boldsymbol{X}^{(i)}_{\mu\bar{\nu}} \Big),
\end{aligned} \tag{B·3}$$

where ε is a small parameter,

$$\boldsymbol{X}^{(i)\dagger}_{\mu\bar{\nu}} = b^{(i)\dagger}_\mu b^{(i)\dagger}_{\bar{\nu}}, \quad \boldsymbol{X}^{(i)}_{\mu\bar{\nu}} = b^{(i)}_{\bar{\nu}} b^{(i)}_\mu, \tag{B·4}$$

and the subscripts + and − denote the two-quasiparticle creation and annihilation parts of the operator in the parentheses, respectively. It should be noted that, in contrast to the conventional imaginary time method, the unitary operator $\exp \hat{X}^{(i+1)}$ is used here so that the normalization is preserved during the iteration. The Lagrange multipliers $\lambda_\tau^{(i+1)}(q)$ and $\mu^{(i+1)}(q)$ are determined by the constraint equations

$$\begin{aligned} \left\langle \phi^{(i+1)}(q) \right| \hat{N}_\tau \left| \phi^{(i+1)}(q) \right\rangle &= N_\tau^{(0)}, \\ \left\langle \phi^{(i+1)}(q) \right| \hat{Q}(q-\delta q) \left| \phi^{(i+1)}(q) \right\rangle &= \delta q, \end{aligned} \tag{B·5}$$

where $N_n^{(0)}$ and $N_p^{(0)}$ are the neutron and proton numbers of the nucleus under consideration. Similar but slightly different constraints were utilized by Almehed and Walet.[79] Expanding the left-hand sides up to first order in $x^{(i+1)}$, we obtain equations determining them:

$$\begin{aligned} &\begin{pmatrix} (N_n,N_n) & (N_n,N_p) & (N_n,Q(q)) \\ (N_p,N_n) & (N_p,N_p) & (N_p,Q(q)) \\ (Q(q-\delta q),N_n) & (Q(q-\delta q),N_p) & (Q(q-\delta q),Q(q)) \end{pmatrix} \begin{pmatrix} \lambda_n^{(i+1)}(q) \\ \lambda_p^{(i+1)}(q) \\ \mu^{(i+1)}(q) \end{pmatrix} \\ &\qquad = \begin{pmatrix} (N_n^{(0)} - \langle \hat{N}_n \rangle^{(i)})/2\varepsilon + (h^{(i)}(q), N_n) \\ (N_p^{(0)} - \langle \hat{N}_p \rangle^{(i)})/2\varepsilon + (h^{(i)}(q), N_p) \\ (\delta q - \langle \hat{Q}(q-\delta q) \rangle^{(i)})/2\varepsilon + (h^{(i)}(q), Q(q-\delta q)), \end{pmatrix}, \end{aligned} \tag{B·6}$$

where the quantities $(N_\tau, N_{\tau'}), (N_\tau, Q(q))$, etc., are defined by (3.33), except that the coefficients $N_\tau(\mu), Q_{\mu\bar{\nu}}(q)$, etc., involved in these quantities are here defined with respect to the two-quasiparticle creation and annihilation operators, $\boldsymbol{X}^{(i)\dagger}_{\mu\bar{\nu}}$ and $\boldsymbol{X}^{(i)}_{\mu\bar{\nu}}$. Using the state vector $\left|\phi^{(i+1)}(q)\right\rangle$, we calculate the mean-field Hamiltonian $\hat{h}^{(i+1)}(q)$ at the $(i+1)$th step, and repeat the above procedure until convergence is attained. The mean-field Hamiltonian thus obtained takes the following form:

$$\begin{aligned} \hat{h}_M(q) &= \hat{h}(q) - \sum_\tau \lambda_\tau(q)\hat{N}_\tau - \mu(q)\hat{Q}(q) \\ &= \langle \phi(q)| \hat{h}_M(q) |\phi(q)\rangle + \sum_{\mu\nu} h_{\mu\nu}(q) \Big(b_\mu^\dagger(q) b_\nu(q) + b_{\bar{\mu}}^\dagger(q) b_{\bar{\nu}}(q) \Big). \end{aligned} \tag{B·7}$$

Finally we introduce the quasiparticle operators $a_\mu^\dagger(q)$ and $a_\mu(q)$ that diagonalize $\hat{h}_M(q)$:

$$\hat{h}_M(q) = \langle \phi(q)| \hat{h}_M(q) |\phi(q)\rangle + \sum_\mu E_\mu(q) \Big(a_\mu^\dagger(q) a_\mu(q) + a_{\bar{\mu}}^\dagger(q) a_{\bar{\mu}}(q) \Big). \tag{B·8}$$

It is easy to see that $\mu(q) = \partial V/\partial q$. In actual calculations, the above procedure is a part of the double iterative algorithm described in §4. Specifically, we carry out the above iterative procedure using the constraint operator $\hat{Q}(q)^{(n)}$ that is obtained in the n-th iteration step determining the infinitesimal generators, $\hat{Q}(p)$ and $\hat{P}(q)$.

References

1) P. Ring and P. Schuck, *The Nuclear Many-Body Problem* (Springer-Verlag, 1980).
2) J.-P. Blaizot and G. Ripka, *Quantum Theory of Finite Systems* (The MIT press, 1986).
3) A. Klein and E. R. Marshalek, Rev. Mod. Phys. **63** (1991), 375.
4) G. Do Dang, A. Klein and N. R. Walet, Phys. Rep. **335** (2000), 93.
5) A. Kuriyama, K. Matsuyanagi, F. Sakata, K. Takada and M. Yamamura (ed.), Prog. Theor. Phys. Suppl. No. 141 (2001).
6) D. J. Rowe and R. Bassermann, Can. J. Phys. **54** (1976), 1941.
7) K. Goeke, Nucl. Phys. A **265** (1976), 301.
8) F. Villars, Nucl. Phys. A **285** (1977), 269.
9) T. Marumori, Prog. Theor. Phys. **57** (1977), 112.
10) M. Baranger and M. Veneroni, Ann. of Phys. **114** (1978), 123.
11) K. Goeke and P.-G. Reinhard, Ann. of Phys. **112** (1978), 328.
12) T. Marumori, T. Maskawa, F. Sakata and A. Kuriyama, Prog. Theor. Phys. **64** (1980), 1294.
13) M. J. Giannoni and P. Quentin, Phys. Rev. C **21** (1980), 2060.
14) J. Dobaczewski and J. Skalski, Nucl. Phys. A **369** (1981), 123.
15) K. Goeke, P.-G. Reinhard and D. J. Rowe, Nucl. Phys. A **359** (1981), 408.
16) A. K. Mukherjee and M. K. Pal, Phys. Lett. B **100** (1981), 457; Nucl. Phys. A **373** (1982), 289.
17) D. J. Rowe, Nucl. Phys. A **391** (1982), 307.
18) C. Fiolhais and R. M. Dreizler, Nucl. Phys. A **393** (1983), 205.
19) K. Goeke, F. Grümmer and P.-G. Reinhard, Ann. of Phys. **150** (1983), 504.
20) A. Kuriyama and M. Yamamura, Prog. Theor. Phys. **70** (1983), 1675; ibid. **71** (1984), 122.
21) M. Yamamura, A. Kuriyama and S. Iida, Prog. Theor. Phys. **71** (1984), 109.
22) M. Matsuo and K. Matsuyanagi, Prog. Theor. Phys. **74** (1985), 288.
23) M. Matsuo, Prog. Theor. Phys. **76** (1986), 372.
24) Y. R. Shimizu and K. Takada, Prog. Theor. Phys. **77** (1987), 1192.
25) M. Yamamura and A. Kuriyama, Prog. Theor. Phys. Suppl. No. 93 (1987), 1.
26) N. R. Walet, G. Do Dang and A. Klein, Phys. Rev. C **43** (1991), 2254.
27) A. Klein, N. R. Walet and G. Do Dang, Ann. of Phys. **208** (1991), 90.
28) K. Kaneko, Phys. Rev. C **49** (1994), 3014.
29) T. Nakatsukasa and N. R. Walet, Phys. Rev. C **57** (1998), 1192.
30) T. Nakatsukasa and N. R. Walet, Phys. Rev. C **58** (1998), 3397.
31) J. Libert, M. Girod and J.-P. Delaroche, Phys. Rev. C **60** (1999), 054301.
32) E. Kh. Yuldashbaeva, J. Libert, P. Quentin and M. Girod, Phys. Lett. B **461** (1999), 1.
33) T. Nakatsukasa, N. R. Walet and G. Do Dang, Phys. Rev. C **61** (2000), 014302.
34) J. L. Wood, K. Heyde, W. Nazarewicz, M. Huyse and P. van Duppen, Phys. Rep. **215** (1992), 101.
35) W. Nazarewicz, Phys. Lett. B **305** (1993), 195.
36) W. Nazarewicz, Nucl. Phys. A **557** (1993), 489c.
37) N. Tajima, H. Flocard, P. Bonche, J. Dobaczewski and P.-H. Heenen, Nucl. Phys. A **551** (1993), 409.
38) P. Bonche, E. Chabanat, B. Q. Chen, J. Dobaczewski, H. Flocard, B. Gall, P. H. Heenen, J. Meyer, N. Tajima and M. S. Weiss, Nucl. Phys. A **574** (1994), 185c.
39) P.-G. Reinhard, D. J. Dean, W. Nazarewicz, J. Dobaczewski, J. A. Maruhn and M. R. Strayer, Phys. Rev. C **60** (1999), 014316.
40) A. N. Andreyev et al., Nature **405** (2000), 430; Nucl. Phys. A **682** (2001), 482c.
41) S. M. Fischer et al., Phys. Rev. Lett. **84** (2000), 4064; Phys. Rev. C **67** (2003), 064318.
42) E. Bouchez et al., Phys. Rev. Lett. **90** (2003), 082502.
43) R. R. Rodríguez-Guzmán, J. L. Egido and L. M. Robledo, Phys. Rev. C **62** (2000), 054319; ibid. C **65** (2002), 024304; ibid. C **69** (2004), 054319.
44) J. L. Egido, L. M. Robledo and R. R. Rodríguez-Guzmán, Phys. Rev. Lett. **93** (2004), 082502.
45) R. R. Chasman, J. L. Egido and L. M. Robledo, Phys. Lett. B **513** (2001), 325.
46) T. Nikšić, D. Vretenar, P. Ring and G. A. Lalazissis, Phys. Rev. C **65** (2002), 054320.
47) T. Duguet, M. Bender, P. Bonche and P.-H. Heenen, Phys. Lett. B **559** (2003), 201.
48) M. Bender, P. Bonche, T. Duguet and P.-H. Heenen, Phys. Rev. C **69** (2004), 064303.

49) A. Petrovici, K. W. Schmid, A. Faessler, J. H. Hamilton and A. V. Ramayya, Prog. in Part. Nucl. Phys. **43** (1999), 485.
50) A. Petrovici, K. W. Schmid and A. Faessler, Nucl. Phys. A **665** (2000), 333; ibid. **710** (2002), 246.
51) R. Fossion, K. Heyde, G. Thiamova and P. Van Isacker, Phys. Rev. C **67** (2003), 024306.
52) A. Frank, P. Van Isacker and C. E. Vargas, Phys. Rev. C **69** (2004), 034323.
53) C. D. Dracoulis et al. Phys. Rev. C **69** (2004), 054318.
54) K. Kaneko, M. Hasegawa and T. Mizusaki, Phys. Rev. C **66** (2002), 051306(R); nucl-th/0410046.
55) M. Hasegawa, K. Kaneko, T. Mizusaki and S. Tazaki, Phys. Rev. C **69** (2004), 034324.
56) M. Hasegawa, K. Kaneko and T. Mizusaki, nucl-th/0408062; nucl-th/0408063.
57) Y. Sun, Eur. Phys. J. A **20** (2004), 133.
58) M. Matsuo, Prog. Theor. Phys. **72** (1984), 666.
59) M. Matsuo and K. Matsuyanagi, Prog. Theor. Phys. **74** (1985), 1227; ibid. **76** (1986), 93; ibid. **78** (1987), 591.
60) M. Matsuo, Y. R. Shimizu and K. Matsuyanagi, *Proceedings of the Niels Bohr Centennial Conf. on Nuclear Structure*, ed. R. Broglia, G. Hagemann and B. Herskind (North-Holland, 1985), p. 161.
61) K. Takada, K. Yamada and H. Tsukuma, Nucl. Phys. A **496** (1989), 224.
62) K. Yamada, K. Takada and H. Tsukuma, Nucl. Phys. A **496** (1989), 239.
63) K. Yamada and K. Takada, Nucl. Phys. A **503** (1989), 53.
64) H. Aiba, Prog. Theor. Phys. **84** (1990), 908.
65) K. Yamada, Prog. Theor. Phys. **85** (1991), 805; ibid. **89** (1993), 995.
66) J. Terasaki, T. Marumori and F. Sakata, Prog. Theor. Phys. **85** (1991), 1235.
67) J. Terasaki, Prog. Theor. Phys. **88** (1992), 529; ibid. **92** (1994), 535.
68) M. Matsuo, in *New Trends in Nuclear Collective Dynamics*, ed. Y. Abe, H. Horiuchi and K. Matsuyanagi (Springer-Verlag, 1992), p. 219.
69) Y. R. Shimizu and K. Matsuyanagi, Prog. Theor. Phys. Suppl. No. 141 (2001), 285.
70) M. Matsuo, T. Nakatsukasa and K. Matsuyanagi, Prog. Theor. Phys. **103** (2000), 959.
71) M. Kobayasi, T. Nakatsukasa, M. Matsuo and K. Matsuyanagi, Prog. Theor. Phys. **110** (2003), 65.
72) K. Matsuyanagi, Prog. Theor. Phys. **67** (1982), 1441; *Proceedings of the Nuclear Physics Workshop, Trieste, 5-30 Oct. 1981.* ed. C. H. Dasso, R. A. Broglia and A. Winther (North-Holland, 1982), p. 29.
73) Y. Mizobuchi, Prog. Theor. Phys. **65** (1981), 1450.
74) T. Suzuki and Y. Mizobuchi, Prog. Theor. Phys. **79** (1988), 480.
75) T. Fukui, M. Matsuo and K. Matsuyanagi, Prog. Theor. Phys. **85** (1991), 281.
76) M. Baranger and K. Kumar, Nucl. Phys. **62** (1965), 113; Nucl. Phys. A **110** (1968), 529; Nucl. Phys. A **122** (1968), 241; Nucl. Phys. A **122** (1968), 273.
77) M. Baranger and K. Kumar, Nucl. Phys. A **110** (1968), 490.
78) D. R. Bes and R. A. Sorensen, *Advances in Nuclear Physics* (Prenum Press, 1969), vol. 2, p. 129.
79) D. Almehed and N. R. Walet, Phys. Rev. C **69** (2004), 024302.
80) D. Almehed and N. R. Walet, Phys. Lett. B **604** (2004), 163.
81) M. Kobayasi, T. Nakatsukasa, M. Matsuo and K. Matsuyanagi, Prog. Theor. Phys. **112** (2004), 363.
82) M. Yamagami, K. Matsuyanagi and M. Matsuo, Nucl. Phys. A **693** (2001), 579.
83) T. Bengtsson and I. Ragnarsson, Nucl. Phys. A **436** (1985), 14.
84) M. Kobayasi, T. Nakatsukasa, M. Matsuo and K. Matsuyanagi, in preparation.
85) K. T. R. Davies, H. Flocard, S. Krieger and M. S. Weiss, Nucl. Phys. A **342** (1980), 111.

Progress of Theoretical Physics, Vol. 113, No. 6, June 2005

Comparative Study of Octupole Excitations on Superdeformed States in ^{32}S, ^{36}S, ^{40}Ca and ^{50}S

Kenichi YOSHIDA,[1] Masayuki YAMAGAMI[2] and Kenichi MATSUYANAGI[1]

[1]*Department of Physics, Graduate School of Science, Kyoto University, Kyoto 606-8502, Japan*
[2]*Heavy Ion Nuclear Physics Laboratory, RIKEN, Wako 351-0198, Japan*

(Received January 27, 2005)

By means of an RPA calculation based on the deformed Woods-Saxon potential in the coordinate-mesh representation, we make a comparative study of octupole excitations built on superdeformed states in the ^{40}Ca region and those in ^{50}S. For the $N = Z$ stable nuclei, ^{32}S and ^{40}Ca, enhancement of octupole transition strengths results from the coherence of the proton and neutron excitations. Contrastingly, for ^{50}S close to the neutron drip line, we find that the low-lying state created by the excitation of a single neutron from a loosely bound low Ω state to a high Ω resonance state acquires an extremely large transition strength. A similar enhancement of the octupole strength is also found in oblately deformed ^{40}Mg close to the neutron drip line.

§1. Introduction

In recent years, the physics of unstable nuclei close to the drip line has become one of the most active fields in nuclear structure physics. New features, such as neutron skins and shell structure near the continuum, are currently being actively investigated both theoretically and experimentally.[1)–3)] Although, at present, drip-line nuclei that allow for relevant experiments are largely restricted to light nuclei, the region of unstable nuclei that can be explored experimentally will soon be significantly extended to medium-mass regions, when new facilities for radioactive ion beams start running. To investigate the possibility of the emergence of excitation modes unique to unstable nuclei in heavier-mass regions, many attempts have been made using the self-consistent RPA based on the Skyrme-Hartree-Fock (SHF) method[4)–6)] and its extensions, including pairing correlations.[7)–10)] A number of similar approaches using different mean fields have also been employed.[11)–14)] (See Refs. 10) and 15) for extensive lists of references concerning the self-consistent RPA and mean-field theories.) To describe such weakly bound systems for which the Fermi energy is close to zero, it is essential to properly treat the particle-hole excitations into the continuum. Thus, the continuum RPA method employing the Green functions that satisfy the scattering boundary condition has been widely used.[4)–7),16),17)] Quite recently, this method was extended to the continuum quasiparticle-RPA, taking into account pairing correlations.[18)–22)] However, most of these investigations are restricted to spherical nuclei. For deformed unstable nuclei, although low-lying Gamow-Teller β-decay strengths have been investigated[23)] by means of the standard matrix formulation of the RPA, other low-frequency RPA modes remain largely unexplored, except some recent attempts to describe low-frequency isovector dipole modes using

the time-dependent Hartree-Fock method with absorbing boundary conditions[24),25)] and gamma vibrations using the quasiparticle-RPA with the BCS approximation.[26)]

In order to clearly see the deformation effects in unstable nuclei, Inakura et al.[27),28)] investigated properties of negative-parity collective excitations built on superdeformed (SD) states in neutron-rich sulfur isotopes by means of the mixed representation RPA[29)–32)] based on the SHF mean field, and found many low-energy modes possessing strongly enhanced isoscalar octupole transition strengths. They also studied excitation modes built on the SD states in the ^{40}Ca region with $N = Z$, for which the SD yrast states have been discovered in recent experiments.[33),34)] In the mixed representation RPA, the *particle* states are treated using the coordinate-mesh representation, while the HF basis is used for the *hole* states. This approach is fully self-consistent in that the same effective interaction is used in both the mean-field and RPA calculations. Also, it is unnecessary to introduce an upper cutoff with respect to the energies of the *particle* states. On the other hand, it is not easy in this method to identify microscopic particle-hole configurations generating individual RPA modes. Therefore, using the deformed Woods-Saxon potential and the conventional matrix formulation of the RPA, we have made a detailed analysis of the microscopic structure of octupole excitation modes built on the SD states in the ^{40}Ca region with $N = Z$ and the ^{50}S region close to the neutron drip line. In this approach, we can easily obtain a simple and transparent understanding of the particle-hole configurations generating the RPA eigenmodes.

This paper is organized as follows. In the next section, the frameworks of the mean-field and RPA calculations are described. In §3.1, the results of the RPA calculation for the SD states in ^{32}S, ^{36}S and ^{40}Ca are presented and discussed. In §3.2, we present the result for ^{50}S close to the neutron drip line and suggest that some low-lying states associated with excitations of a single neutron from a loosely bound state to a resonance state acquire extremely strong transition strengths. In §3.3, we discuss excitation modes in the oblately deformed ^{40}Mg and suggest that the results obtained for ^{50}S are not restricted to the SD states but are rather general phenomena. Conclusions are given in §4.

§2. Method of calculation

2.1. *Mean-field calculation*

We consider the single-particle motion in an axially symmetric deformed potential. Using the standard notation, the Schrödinger equation is written

$$\left\{-\frac{\hbar^2}{2m}\nabla^2 + V_{WS}f(\boldsymbol{r}) + V_{SO}\nabla f(\boldsymbol{r})\cdot(\boldsymbol{\sigma}\times\boldsymbol{p}) + V_C(\boldsymbol{r})\frac{(1-\tau_3)}{2}\right\}\Phi_i = e_i\Phi_i. \quad (2\cdot1)$$

The solutions to this equation take the following form:

$$\Phi_i(x) = \Phi_i(\boldsymbol{r},\sigma,\tau) = \chi_{q_i}(\tau)\left[\phi_i^+(\rho,z)e^{i\Lambda_i^-\varphi}\chi_{\frac{1}{2}}(\sigma) + \phi_i^-(\rho,z)e^{i\Lambda_i^+\varphi}\chi_{-\frac{1}{2}}(\sigma)\right]. \quad (2\cdot2)$$

Here, $\Lambda_i^\pm = \Omega_i \pm 1/2$, where Λ_i and Ω_i are the z-components of the total and orbital angular momenta, respectively, and (ρ, z, φ) are the cylindrical coordinates

of $\boldsymbol{r} = (x, y, z)$:

$$x = \rho\cos\varphi, \quad y = \rho\sin\varphi, \quad z = z. \tag{2·3}$$

The subscript $q_i = +1/2$ $(-1/2)$ denotes neutrons (protons). In terms of the wave functions given in (2·2), the nucleon density is given by

$$\varrho(\rho, z) = \sum_i [|\phi_i^+(\rho, z)|^2 + |\phi_i^-(\rho, z)|^2], \tag{2·4}$$

and the mean-square radii of protons and neutrons are calculated as

$$\langle r^2\rangle_\tau = \frac{\int \rho d\rho dz r^2 \varrho_\tau(\rho, z)}{\int \rho d\rho dz \varrho_\tau(\rho, z)}, \tag{2·5}$$

where $r = \sqrt{\rho^2 + z^2}$ and $\tau{=}\pi$ or ν, with $\varrho_\pi(\rho, z)$ and $\varrho_\nu(\rho, z)$ being the proton and neutron densities.

We employ the phenomenological Woods-Saxon potential

$$f(\boldsymbol{r}) = (1 + \exp[(r - R(\theta))/a])^{-1}, \tag{2·6}$$

$$R(\theta) = c(1 + \beta_2 Y_{20}(\theta)), \tag{2·7}$$

where c is determined by the volume conservation condition. Though an angle dependent diffuseness parameter $a(\theta)$ is better for a more accurate calculation,[35] we use a constant $a = 0.67$ fm for simplicity. We also use the standard parameter values[36] for the central and spin-orbit potentials,

$$V_{WS} = -51 + 33\frac{N - Z}{A}\tau_3, \tag{2·8}$$

$$V_{SO} = \frac{1}{2}r_0^2\left(-22 + 14\frac{N - Z}{A}\tau_3\right), \tag{2·9}$$

with $r_0 = 1.27$ fm. The spin-orbit term is written

$$\hat{V}_{ls} = -\frac{1}{2}V_{SO}\left[\sigma_+ e^{-i\varphi}\left\{\frac{\partial f}{\partial\rho}\frac{\partial}{\partial z} - \frac{\partial f}{\partial z}\left(\frac{\partial}{\partial\rho} + \frac{\hat{l_z}}{\rho}\right)\right\}\right.$$
$$\left. + \sigma_- e^{i\varphi}\left\{-\frac{\partial f}{\partial\rho}\frac{\partial}{\partial z} + \frac{\partial f}{\partial z}\left(\frac{\partial}{\partial\rho} - \frac{\hat{l_z}}{\rho}\right)\right\} + \sigma_z 2\frac{\partial f}{\partial\rho}\frac{\hat{l_z}}{\rho}\right], \tag{2·10}$$

where $\sigma_\pm = \sigma_x \pm i\sigma_y$ and $\hat{l}_z = -i\partial/\partial\varphi$. For protons, we solve the Poisson equation, $\nabla^2 V_C(\boldsymbol{r}) = 4\pi e\varrho_\pi(\boldsymbol{r})$, to obtain the Coulomb potential V_C. In the present calculation, we approximate the proton density $\varrho_\pi(\boldsymbol{r})$ by a Woods-Saxon form.

We can rewrite the Schrödinger equation (2·1) in the matrix form

$$h\boldsymbol{\phi} = \begin{pmatrix} h_{\uparrow\uparrow} & h_{\uparrow\downarrow} \\ h_{\downarrow\uparrow} & h_{\downarrow\downarrow} \end{pmatrix}\begin{pmatrix} \phi_i^+(\rho, z) \\ \phi_i^-(\rho, z) \end{pmatrix} = e_i \begin{pmatrix} \phi_i^+(\rho, z) \\ \phi_i^-(\rho, z) \end{pmatrix}, \tag{2·11}$$

where

$$h_{\uparrow\uparrow} = -\frac{\hbar^2}{2m}\left[\frac{\partial^2}{\partial\rho^2} + \frac{1}{\rho}\frac{\partial}{\partial\rho} + \frac{\partial^2}{\partial z^2} - \left(\frac{\Lambda^-}{\rho}\right)^2\right] + V_{WS}f(\rho,z) - V_{SO}\frac{\partial f(\rho,z)}{\partial\rho}\frac{\Lambda^-}{\rho}, \tag{2·12a}$$

$$h_{\downarrow\downarrow} = -\frac{\hbar^2}{2m}\left[\frac{\partial^2}{\partial\rho^2} + \frac{1}{\rho}\frac{\partial}{\partial\rho} + \frac{\partial^2}{\partial z^2} - \left(\frac{\Lambda^+}{\rho}\right)^2\right] + V_{WS}f(\rho,z) + V_{SO}\frac{\partial f(\rho,z)}{\partial\rho}\frac{\Lambda^+}{\rho}, \tag{2·12b}$$

$$h_{\uparrow\downarrow} = -\frac{1}{2}V_{SO}\left[\frac{\partial f(\rho,z)}{\partial\rho}\frac{\partial}{\partial z} - \frac{\partial f(\rho,z)}{\partial z}\left(\frac{\partial}{\partial\rho} + \frac{\Lambda^+}{\rho}\right)\right], \tag{2·12c}$$

$$h_{\downarrow\uparrow} = -\frac{1}{2}V_{SO}\left[-\frac{\partial f(\rho,z)}{\partial\rho}\frac{\partial}{\partial z} + \frac{\partial f(\rho,z)}{\partial z}\left(\frac{\partial}{\partial\rho} - \frac{\Lambda^-}{\rho}\right)\right]. \tag{2·12d}$$

Because this equation possesses time-reversal symmetry, we know that if $\Phi_i = \{\phi_i^+, \phi_i^-, \Omega_i\}$ is a solution, then $\Phi_{\bar{i}} = \{-\phi_i^-, \phi_i^+, -\Omega_i\}$ is also a solution with the same eigenvalue e_i, and thus it is sufficient to solve it for positive Ω only. We also assume reflection symmetry with respect to the x-y plane. Then, the wave function $\phi^\pm$ possesses z-parity $\pi(-1)^{\Lambda^\mp}$ as a good quantum number (π being the parity), and therefore it is sufficient to consider only positive z.

We solve Eq. (2·11) directly in coordinate space. In comparison to the conventional method of using a deformed harmonic oscillator basis,[37] this method is believed to be more effective in the treatment of spatially extended wave functions, like loosely bound states, resonant states and continuum states. The Hamiltonian matrix (2·11) is discretized by use of a coordinate mesh in the (ρ, z) plane. The mesh points are chosen as

$$\rho_i = \left(i - \frac{1}{2}\right)\Delta, \qquad i = 1, 2, \cdots N, \tag{2·13}$$

to avoid division by zero, where Δ represents the lattice mesh size. The mesh points in the z direction are taken as

$$z_j = (j-1)\Delta, \qquad j = 1, 2, \cdots M. \tag{2·14}$$

The boundary conditions are set as

$$\phi_{i,M} = \phi_{N,j} = 0, \tag{2·15}$$

where $\phi_{i,j} = \phi(\rho, z)$. We construct the discretized Hamiltonian matrix by use of the finite difference method for derivatives and then diagonalize the matrix to obtain the single-particle wave functions on the two-dimensional lattice. The kinetic energy term is evaluated using the 9-points formula; its explicit expression is given in Appendix A.

2.2. *RPA calculation*

Using the single-particle basis obtained in the previous subsection, we solve the RPA equation in the standard matrix formulation,[38]

$$\sum_{p'h'} \begin{pmatrix} A_{php'h'} & B_{php'h'} \\ B^*_{php'h'} & A^*_{php'h'} \end{pmatrix} \begin{pmatrix} f^\lambda_{p'h'} \\ g^\lambda_{p'h'} \end{pmatrix} = \hbar\omega_\lambda \begin{pmatrix} 1 & 0 \\ 0 & -1 \end{pmatrix} \begin{pmatrix} f^\lambda_{ph} \\ g^\lambda_{ph} \end{pmatrix}, \tag{2·16}$$

where

$$A_{php'h'} = (e_p - e_h)\delta_{pp'}\delta_{hh'} + \bar{v}_{ph'hp'}, \qquad B_{php'h'} = \bar{v}_{pp'hh'}. \tag{2·17}$$

Here, the subscripts p and h denote the single-particle states above and below the Fermi energy (particles and holes), respectively. The antisymmetrized matrix elements of the residual interaction v are denoted $\bar{v}_{ph'hp'}$ and $\bar{v}_{pp'hh'}$. For v, we employ the Skyrme-type interaction[16] without momentum-dependent terms,

$$v(\boldsymbol{r}, \boldsymbol{r}') = \Big[t_0(1 + x_0P_\sigma) + \frac{1}{6}t_3(1 + x_3P_\sigma)\varrho(\boldsymbol{r})\Big]\delta(\boldsymbol{r} - \boldsymbol{r}'), \tag{2·18}$$

with $t_0 = -1100$ MeV·fm^3, $t_3 = 16000$ MeV·fm^6, $x_0 = 0.5$, and $x_3 = 1.0$, P_σ being the spin exchange operator. Because our calculation is not self-consistent in the sense that the residual interaction is not related to the mean-field potential, we renormalize the residual interaction by multiplying it by a factor f to obtain the spurious modes at zero excitation energy: $v \to f \cdot v$.

The intrinsic matrix elements $\langle 0|Q_{3K}|\lambda\rangle$ of the octupole operator Q_{3K} between the excited state $|\lambda\rangle$ and the ground state $|0\rangle$ are given by

$$\langle 0|Q_{3K}|\lambda\rangle = \sum_{ph}\Big(Q^{hp}_{3K}f^\lambda_{ph} + Q^{ph}_{3K}g^\lambda_{ph}\Big) = \sum_{ph} M^{ph}_{3K}, \tag{2·19}$$

and

$$Q^{ph}_{3K} = 2\pi\delta_{K,\Omega_p-\Omega_h}\int\rho d\rho dz\Big(\phi^+_p(\rho,z)\phi^+_h(\rho,z) + \phi^-_p(\rho,z)\phi^-_h(\rho,z)\Big)Q_{3K}(\rho,z) \tag{2·20}$$

$$\equiv 2\pi\delta_{K,\Omega_p-\Omega_h}\int d\rho dz Q^{ph}_{3K}(\rho,z), \tag{2·21}$$

where $Q_{3K}(\rho,z) = Q_{3K}(\boldsymbol{r})e^{-iK\varphi} = r^3Y_{3K}(\theta,\varphi)e^{-iK\varphi}$.

The isoscalar octupole strength function is

$$S^{\rm IS}(\omega) = \sum_\lambda |\langle 0|Q^{\rm IS}_{3K}|\lambda\rangle|^2\delta(\hbar\omega - \hbar\omega_\lambda), \tag{2·22}$$

where $Q^{\rm IS}_{3K} = Q^\pi_{3K} + Q^\nu_{3K}$, and Q^π_{3K} and Q^ν_{3K} are the proton and neutron octupole operators. The reduced isoscalar octupole transition probability is defined by $B(Q^{\rm IS}3) = |\langle 0|Q^{\rm IS}_{3K}|\lambda\rangle|^2$. The reduced proton and neutron octupole transition probabilities, $B(E3)$ and $B(Q^\nu 3)$, are obtained by replacing $Q^{\rm IS}_{3K}$ with eQ^π_{3K} and Q^ν_{3K}, respectively. Note that these quantities represent intrinsic transition strengths, and hence the appropriate Clebsh-Gordan coefficients should be multiplied to obtain transition probabilities in the laboratory frame.

2.3. *Details of numerical calculation*

We numerically solved the Schrödinger equation (2·11) in a rectangular box, using a lattice mesh size $\Delta = 0.5$ fm. The size of the box used was 2.5 (3.5) times the half density radii in the directions of the major and minor axes for ^{32,36}S and ^{40}Ca (^{50}S). Bode's rule was used for the numerical integrations of the RPA matrix elements (see Appendix B). The deformation parameters β_2 were determined so as to approximately reproduce the shell structure near the Fermi level obtained in the SHF calculation by Inakura et al.[39] Their values for protons and neutrons are not necessarily the same. The actual values of the box size used in the calculations are indicated in the figure captions for individual cases, together with the β_2 values adopted. The RPA matrix (2·17) was diagonalized with the cutoff at 30 MeV for the particle-hole excitation energy. In spherical systems, there is only one spurious $J^\pi = 1^-$ mode associated with the center-of-mass motion. In deformed systems, this mode splits into the $K^\pi = 0^-$ and 1^- modes. We find that, e.g., for ^{32}S, the factors $f_0 = 0.7545$ and $f_1 = 0.7723$ are needed to obtain the spurious $K^\pi = 0^-$ and $K^\pi = 1^-$ modes at zero energy. Using these f_0 and f_1 values, we obtain low-lying $K^\pi = 2^-$ states at 2.653 and 2.557 MeV, respectively. This difference of about 0.1 MeV indicates the magnitude of the numerical uncertainty caused by ignoring self-consistency in our calculation. In the following, we choose the factor f such that the excitation energy of the spurious $K^\pi = 1^-$ mode becomes zero.

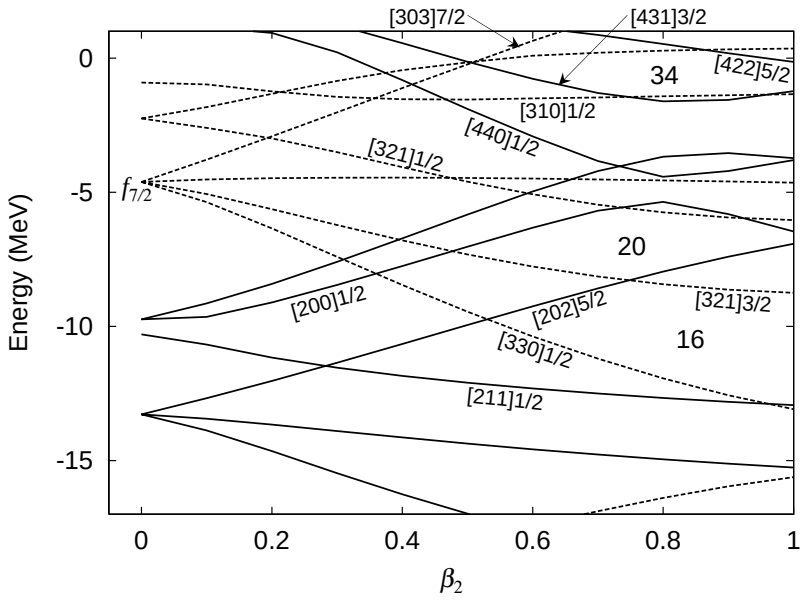

Fig. 1. Neutron single-particle levels in the deformed Woods-Saxon potential, plotted as functions of the quadrupole deformation parameter β_2. The solid and dotted curves denote positive- and negative-parity levels, respectively. The SD magic numbers are $N = 16$, 20 and 34. They are responsible for the appearance of the SD states in ^{32}S, ^{36}S, ^{40}Ca and ^{50}S.

§3. Results and discussion

3.1. *The SD states in ^{32}S, ^{36}S and ^{40}Ca*

We first discuss the result of the RPA calculation for the SD state in ^{32}S. Although the existence of the SD band in ^{32}S has been conjectured for a long time,[40] it has not yet been observed, and this remains a great challenge: As discussed in Refs. 41)–45), the SD local minimum in ^{32}S corresponds to the doubly closed shell configuration with respect to the SD magic number $Z = N = 16$. It involves two protons and two neutrons in the down-sloping single-particle levels originating from the $f_{7/2}$ shell (see Fig. 1). The calculated octupole transition strengths with $K^\pi = 2^-$ are displayed in Fig. 2. A prominent peak is seen at about 2.6 MeV with a strongly enhanced transition strength of about 23 Weisskopf units (1 W.u. $\simeq$ 61 fm^6 for ^{32}S). There are no peaks representing strengths greater than 1 W.u. for other values of K in this energy region. As shown in Table I, the major component of this RPA mode is the particle-hole excitation from the [211]1/2 state to the [321]3/2 state. The proton and neutron excitations act coherently. Other particle-hole configurations also contribute coherently. Here we note that, although the RPA amplitude f_{ph} for the particle-hole excitation from the [330]1/2 state to the [202]5/2 state is appreciable, its contribution to the transition matrix element M_{32}^{ph} is very small. This can be understood from the asymptotic selection rules[47] for low-energy octupole transitions in the SD harmonic-oscillator potential with the axis ratio 2:1:

$$Q_{30}: \quad \Delta N_{\rm sh} = 1,\ \Delta n_3 = 1,\ \Delta\Lambda = 0, \tag{3·1a}$$

$$Q_{31}: \quad \Delta N_{\rm sh} = 0,\ \Delta n_3 = 2,\ \Delta\Lambda = 1, \tag{3·1b}$$

$$Q_{32}: \quad \Delta N_{\rm sh} = 1,\ \Delta n_3 = 1,\ \Delta\Lambda = 2, \tag{3·1c}$$

$$Q_{33}: \quad \Delta N_{\rm sh} = 2,\ \Delta n_3 = 0,\ \Delta\Lambda = 3. \tag{3·1d}$$

Here, the shell quantum number is defined as $N_{\rm sh} = 2n_\perp + n_3$. These selection rules hold approximately also for the SD Wood-Saxon potential under consideration. Accordingly, the [330]1/2 $\rightarrow$ [202]5/2 octupole matrix element is very small, while that of the [211]1/2 $\rightarrow$ [321]3/2 excitation is large. Thus, the coherent proton and neutron excitations from the [211]1/2 hole state to the [321]3/2 particle state are the major origin of the large octupole transition strength for this RPA mode.

Next, let us discuss the result of the RPA calculation for the SD state in ^{40}Ca. As mentioned in §1, for this nucleus, the SD yrast band has been discovered in recent experiments.[33),34)] The SD shell gap at $Z = N = 20$ is associated with the $4p$-$4h$ excitation (for both protons and neutrons) from below the spherical closed shell to the $f_{7/2}$ shell. Figure 3 presents the calculated octupole transition strengths with $K^\pi = 1^-$. It is seen that there are no peaks representing strengths greater than 1.5 W.u. for other values of K in this energy region. There is a prominent peak at 2.2 MeV with an isoscalar strength of about 6 W.u. (1 W.u. $\simeq$ 95 fm^6 for ^{40}Ca). As shown in Table II, this RPA eigenstate consists of components from the coherent proton and neutron excitations from [321]3/2 to [200]1/2, which satisfy the asymptotic selection rule (3·1b).

The SD states in ^{32}S and ^{40}Ca are associated with the SD magic numbers $N =$

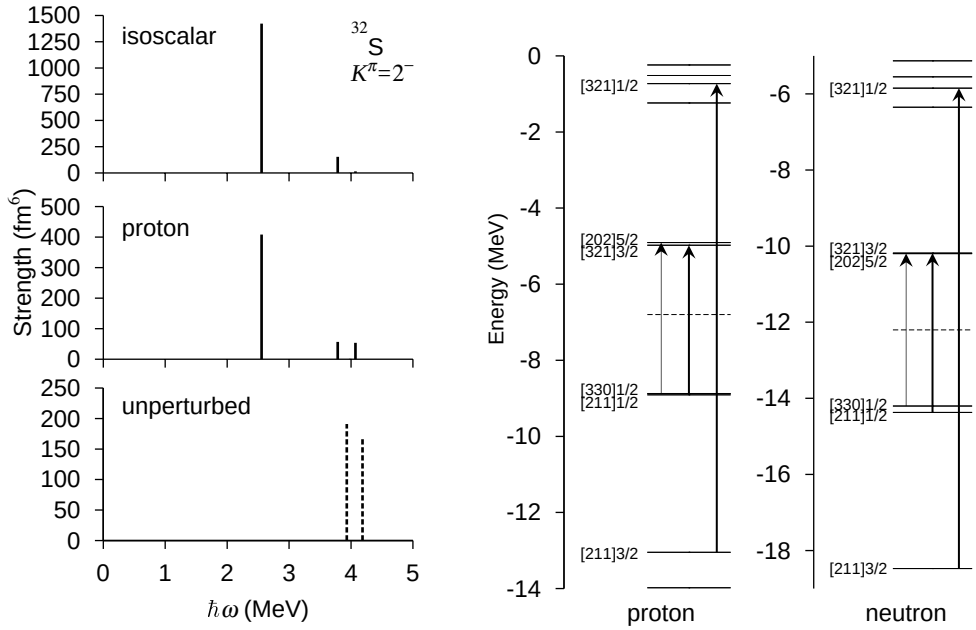

Fig. 2. *Left*: The isoscalar and proton octupole strengths, $B(Q^{\rm IS}3)$ and $B(E3)/e^2$, for the $K^\pi = 2^-$ excitations on the SD state in ^{32}S are plotted in the top and middle panels as functions of the excitation energy. These were obtained using an RPA calculation with $\beta_2 = 0.78$ for both protons and neutrons, using a box of size $\rho_{\max} \times z_{\max} = 8.25$ fm $\times 14.0$ fm. The unperturbed particle-hole strengths are also plotted with dashed lines in the bottom panel. *Right*: Particle-hole configurations generating the lowest $K^\pi = 2^-$ state at 2.6 MeV. Excitations satisfying the asymptotic selection rule Eq. (3·1) are indicated by thick arrows. The asymptotic quantum numbers $[Nn_3\Lambda]\Omega$ are displayed for pertinent levels. The Fermi surfaces for protons and neutrons are indicated by the dashed lines.

Table I. RPA amplitudes for the 2^- state at 2.6 MeV in ^{32}S, calculated with $\beta_2 = 0.78$ for both protons and neutrons. It is characterized by $B(E3) = 408\ e^2$fm^6, $B(Q^\nu 3) = 306$ fm^6, $B(Q^{\rm IS}3) = 1422$ fm^6, and $\sum |g_{ph}|^2 = 1.86 \times 10^{-1}$. The single-particle levels are labeled with the asymptotic quantum numbers $[Nn_3\Lambda]\Omega$. Only components with $|f_{ph}| > 0.1$ are listed.

particle	hole	$\epsilon_p - \epsilon_h$(MeV)	f_{ph}	Q_{32}^{ph} (fm^3)	M_{32}^{ph} (fm^3)
ν[202]5/2	ν[330]1/2	4.01	−0.293	−0.101	0.040
ν[321]3/2	ν[211]1/2	4.19	−0.631	−13.0	11.5
ν[321]1/2	ν[211]3/2	12.6	−0.141	−11.2	2.27
π[202]5/2	π[330]1/2	3.97	−0.282	−0.248	0.096
π[321]3/2	π[211]1/2	3.93	−0.733	−13.8	13.7
π[321]1/2	π[211]3/2	12.3	−0.138	−11.8	2.35

Table II. RPA amplitudes for the 1^- state at 2.2 MeV in ^{40}Ca, calculated with $\beta_2 = 0.6$ for both protons and neutrons. It is characterized by $B(E3) = 122\ e^2$fm^6, $B(Q^\nu 3) = 153$ fm^6, $B(Q^{\rm IS}3) = 549$ fm^6, and $\sum |g_{ph}|^2 = 4.69 \times 10^{-2}$. Only components with $|f_{ph}| > 0.1$ are listed.

particle	hole	$\epsilon_p - \epsilon_h$(MeV)	f_{ph}	Q_{31}^{ph} (fm^3)	M_{31}^{ph} (fm^3)
ν[200]1/2	ν[321]3/2	2.46	0.836	9.08	8.87
π[200]1/2	π[321]3/2	2.59	0.568	10.1	7.06

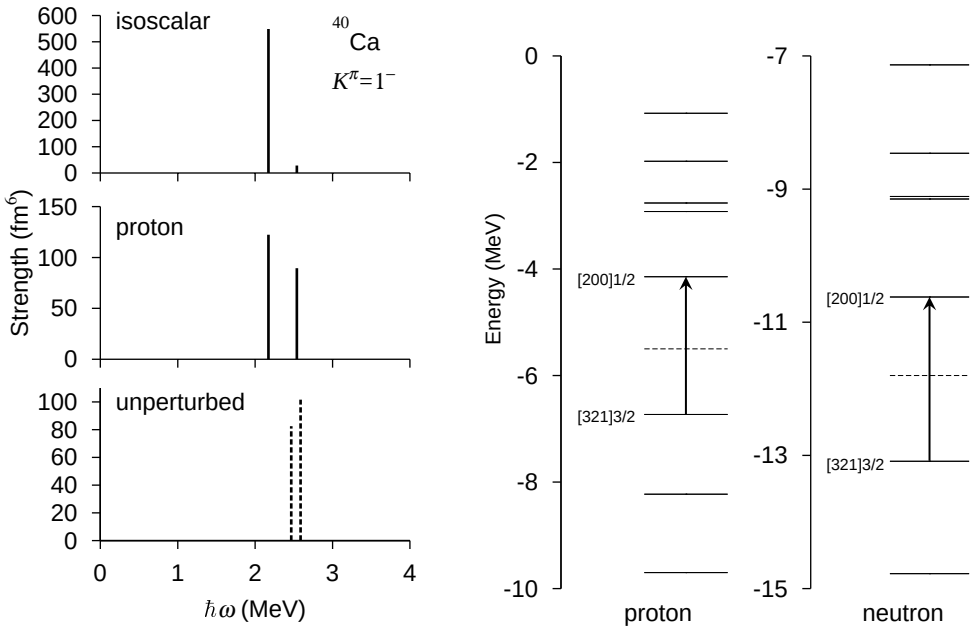

Fig. 3. *Left*: The isoscalar and proton octupole strengths, $B(Q^{\rm IS}3)$ and $B(E3)/e^2$, for the $K^\pi = 1^-$ excitations on the SD state in ^{40}Ca are plotted in the top and middle panels as functions of the excitation energy. These were obtained using an RPA calculation with $\beta_2 = 0.6$ for both protons and neutrons, using a box of size $\rho_{\max} \times z_{\max} = 8.25$ fm $\times 14.0$ fm. The unperturbed particle-hole strengths are also plotted with dashed lines in the bottom panel. *Right*: Particle-hole configurations generating the lowest $K^\pi = 1^-$ state at 2.2 MeV. The notation here is the same as in Fig. 2.

Table III. RPA amplitudes for the 1^- state 2.6 MeV in ^{36}S, calculated with $\beta_2 = 0.565$ and 0.685 for protons and neutrons, respectively. It is characterized by $B(E3) = 5.95$ e^2fm^6, $B(Q^\nu 3) = 189$ fm^6, $B(Q^{\rm IS}3) = 262$ fm^6, and $\sum |g_{ph}|^2 = 9.18 \times 10^{-3}$. Only components with $|f_{ph}| > 0.03$ are listed.

particle	hole	$\epsilon_p - \epsilon_h$(MeV)	f_{ph}	Q_{31}^{ph} (fm^3)	M_{31}^{ph} (fm^3)
ν[200]1/2	ν[321]3/2	2.71	−0.999	9.71	−10.5
ν[200]1/2	ν[330]1/2	6.11	−0.038	4.46	−0.22
π[200]1/2	π[330]1/2	5.23	−0.062	3.62	−0.28

Table IV. RPA amplitudes for the 2^- state 3.9 MeV in ^{36}S, calculated with $\beta_2 = 0.565$ and 0.685 for protons and neutrons, respectively. It is characterized by $B(E3) = 352$ e^2fm^6, $B(Q^\nu 3) = 97.0$ fm^6, $B(Q^{\rm IS}3) = 819$ fm^6, and $\sum |g_{ph}|^2 = 3.52 \times 10^{-2}$. Only components with $|f_{ph}| > 0.1$ are listed.

particle	hole	$\epsilon_p - \epsilon_h$(MeV)	f_{ph}	Q_{32}^{ph} (fm^3)	M_{32}^{ph} (fm^3)
ν[321]1/2	ν[202]5/2	4.75	−0.141	−8.37	1.34
ν[440]1/2	ν[321]3/2	5.19	0.137	6.34	1.01
ν[321]1/2	ν[211]3/2	11.7	−0.114	−12.5	1.85
π[321]3/2	π[211]1/2	4.45	−0.970	−12.5	14.2
π[321]1/2	π[211]3/2	12.9	−0.101	−10.8	1.43

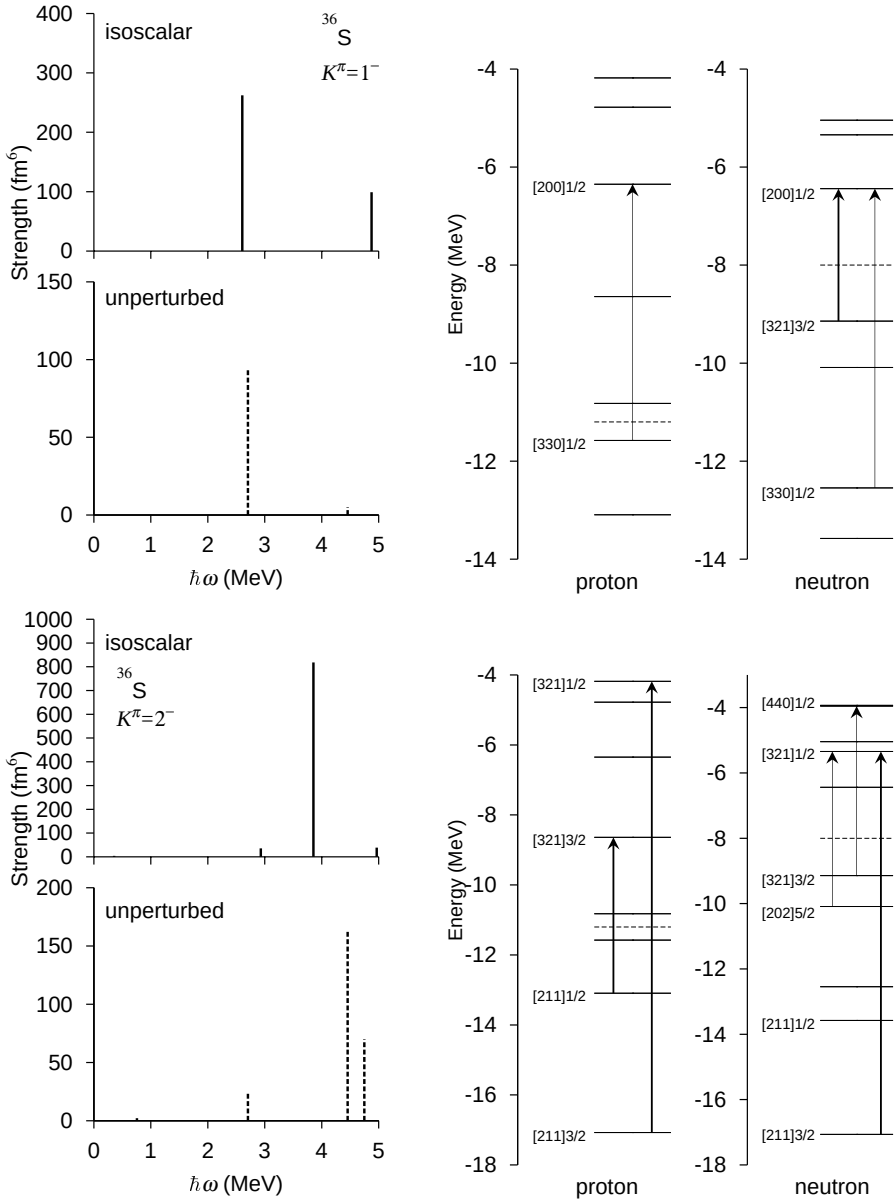

Fig. 4. *Upper left*: The isoscalar octupole strength $B(Q^{\rm IS}3)$ distribution for the $K^\pi = 1^-$ excitations on the SD state in ^{36}S is plotted in the top panel as a function of the excitation energy. This was obtained using an RPA calculation with $\beta_2 = 0.565$ and 0.685 for protons and neutrons, respectively, using a box of size $\rho_{\rm max} \times z_{\rm max} = 8.25$ fm $\times 14.0$ fm. The unperturbed particle-hole strength distribution is also plotted with dashed lines in the bottom panel. *Upper right*: Particle-hole configurations generating the lowest $K^\pi = 1^-$ state at 2.5 MeV. The notation is the same as in Fig. 2. *Lower left*: Same as above, but for the $K^\pi = 2^-$ excitations. *Lower right*: Same as above, but for the $K^\pi = 2^-$ excitation at 3.9 MeV.

$Z = 16$ and 20, respectively. It is thus interesting to consider the SD state in ^{36}S, which has $Z = 16$ and $N = 20$. Evidence for the existence of the SD band in this nucleus has been obtained from an SHF calculation.[39] The result of the RPA calculation is presented in Fig. 4, Table III and Table IV. There is a peak corresponding to $K^\pi = 1^-$ at 2.6 MeV with an isoscalar strength of about 3.4 W.u. and another peak corresponding to $K^\pi = 2^-$ at 3.9 MeV with an isoscalar strength of about 11 W.u. (1 W.u. $\simeq$ 77 fm^6 for ^{36}S). The $K^\pi = 1^-$ peak is associated with the particle-hole excitation from [321]3/2 to [200]1/2, while the $K^\pi = 2^-$ peak corresponds to the [211]1/2 $\rightarrow$ [321]3/2 excitation. These particle-hole configurations are the same as for the $K^\pi = 1^-$ state in ^{40}Ca and the $K^\pi = 2^-$ in ^{32}S discussed above. However, in contrast to the $N = Z$ nuclei, ^{32}S and ^{40}Ca, the coherence of proton and neutron excitations is absent in the case of ^{36}S. Thus, these RPA modes in ^{36}S are dominated by specific particle-hole configurations, although appreciable amounts of other particle-hole configurations collectively contribute to the $K^\pi = 2^-$ mode (see Table IV). The collectivity of these modes is apparently weak in comparison with the octupole vibrations built on the SD states in heavy nuclei,[48),49] because the number of particle-hole configurations contributing to the RPA modes is rather small in the nuclei under consideration. It should be mentioned, however, that transition strengths much larger than those in our results are obtained for these nuclei in the mixed representation RPA calculation carried out by Inakura et al.,[27),28] where no cutoff is imposed in the particle-hole excitation energy. The major cause of this difference may be the rather severe energy cutoff in the present RPA calculation. (See Ref. 50) for a numerical analysis of the contributions from very high-lying particle-hole configurations to the transition strengths of the low-lying RPA modes.)

3.2. *The SD state in ^{50}S*

In this subsection, we discuss the result for ^{50}S, which is, according to the SHF calculations,[39),46] close to the neutron drip line. The existence of the SD band in this nucleus is suggested in Ref. 39). The isoscalar octupole strength distribution with $K^\pi = 2^-$ calculated with the RPA is presented in Fig. 5. There are no peaks at any values of K in this energy region other than those corresponding to excitations to the discretized continuum. As we explain in detail below, the highest peak, at 3.1 MeV, with $K^\pi = 2^-$ is associated with the excitation of a single neutron from the loosely bound [310]1/2 state to the resonance [422]5/2 state. We obtain a peak of similar nature but with a smaller strength at 2.9 MeV. It is associated with the excitation

Table V. RPA amplitudes for the 2^- state at 3.1 MeV in ^{50}S, calculated with $\beta_2 = 0.54$ and 0.73 for protons and neutrons, respectively. It is characterized by $B(E3) = 19.4\ e^2\text{fm}^6$, $B(Q^\nu 3) = 5359$ fm^6, $B(Q^{\text{IS}}3) = 6023$ fm^6, and $\sum |g_{ph}|^2 = 6.42 \times 10^{-3}$. Only components with $|f_{ph}| > 0.1$ are listed.

particle	hole	$\epsilon_p - \epsilon_h$(MeV)	f_{ph}	Q_{32}^{ph} (fm^3)	M_{32}^{ph} (fm^3)
ν[303]7/2	ν[431]3/2	3.01	0.133	-11.6	-1.49
ν[422]5/2	ν[310]1/2	3.20	0.967	65.7	66.1
π[321]3/2	π[211]1/2	4.69	-0.138	-12.4	2.26

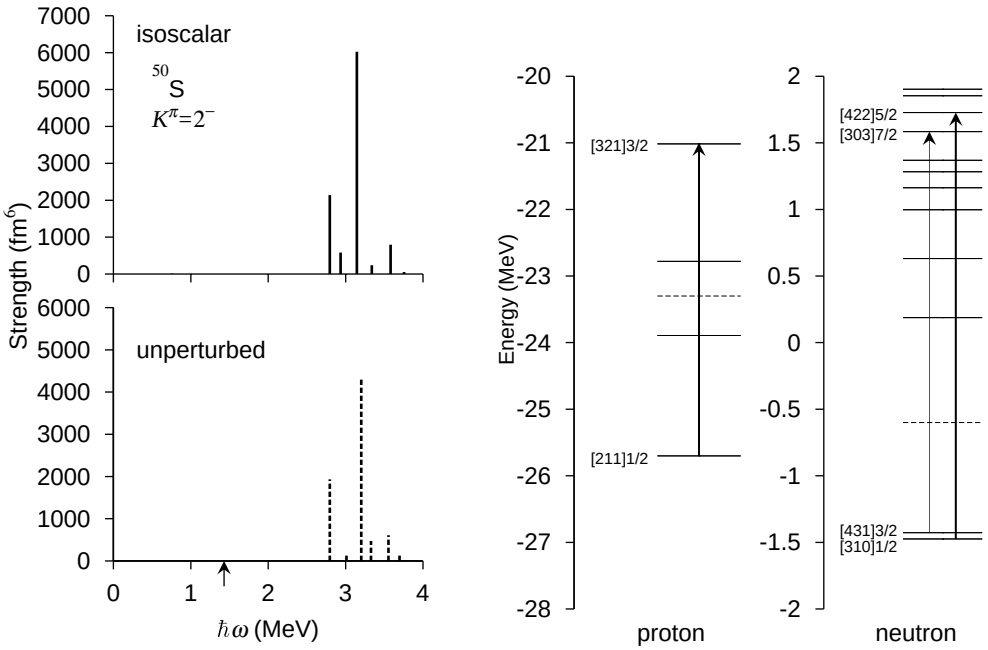

Fig. 5. *Left*: The isoscalar octupole strength $B(Q^{\rm IS}3)$ distribution for the $K^\pi = 2^-$ excitations built on the SD state in ^{50}S is plotted in the top panel as a function of the excitation energy. This was obtained using an RPA calculation with $\beta_2 = 0.54$ and 0.73 for protons and neutrons, respectively, using a box of size $\rho_{\rm max} \times z_{\rm max} = 14.25$ fm $\times 22.0$ fm. The unperturbed particle-hole strengths are also plotted with dashed lines in the bottom panel. The arrow indicates the threshold energy, $E_{\rm th} = 1.4$ MeV. *Right*: Particle-hole configurations generating the lowest $K^\pi = 2^-$ state at 3.1 MeV. The notation here is the same as in Fig. 2.

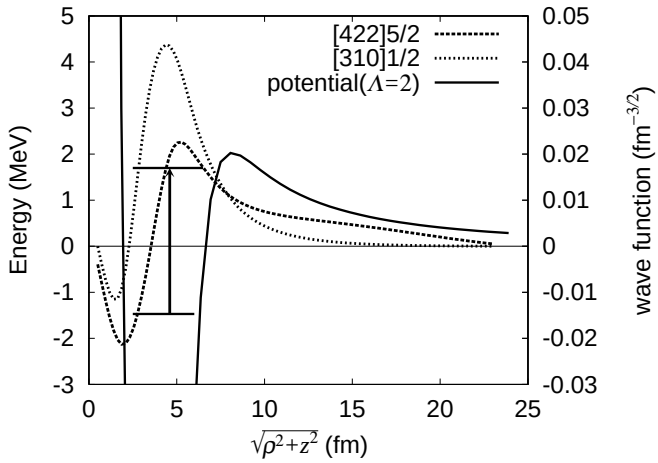

Fig. 6. The neutron particle-hole excitation contributing to the strongly enhanced transition strength of the $K^\pi = 2^-$ state at 3.1 MeV in superdeformed ^{50}S. The particle and hole states are labeled by their asymptotic quantum numbers. Their wave functions are plotted by the dotted curves. The solid curve denotes the neutron single-particle potential including the centrifugal barrier for $\Lambda = 2$. The horizontal axis represents $\sqrt{\rho^2 + z^2}$ along the $\theta = 45^\circ$ line.

of a single neutron from the loosely bound [431]3/2 state to the resonance [303]7/2 state. This difference in strength between the two peaks can be understood from the asymptotic selection rule (3·1c): The former particle-hole excitation satisfies it, whereas the latter does not. On the other hand, the second highest peak, at 2.8 MeV, is due to a neutron excitation from the [431]3/2 state to a discretized continuum state with $\Omega^\pi = 1/2^-$.

We now discuss the microscopic structure of the $K^\pi = 2^-$ excitation at 3.1 MeV in detail. It has an extremely strong isoscalar strength of $B(Q^{\rm IS}3) = 41$ W.u. and a weak electric strength of $B(E3) = 0.13$ W.u. (1 W.u. $\simeq 149$ fm^6 for ^{50}S). As shown in Table V, the major component of this RPA mode is the [310]1/2 $\rightarrow$ [422]5/2 excitation of a neutron. Their wave functions are plotted in Fig. 6. Because the [310]1/2 state is loosely bound and the [422]5/2 state is a resonance state, their wave functions extend significantly outside of the half-density radius of this nucleus. Together with the fact that this particle-hole configuration satisfies the asymptotic selection rule (3·1c), the very extended spatial structures of their wave functions are the main reason why it has the extremely large transition strength.

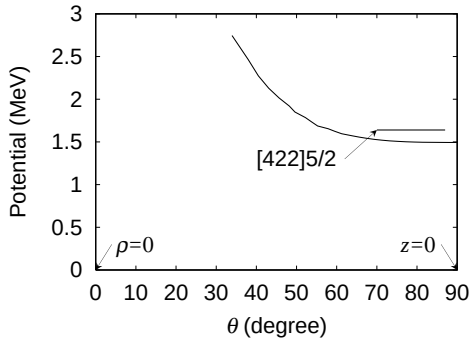

Fig. 7. Angle dependence of the centrifugal barrier height for the $\Lambda = 2$ states in superdeformed ^{50}S. The z- and ρ-axes correspond to $\theta = 0^\circ$ and 90°, respectively.

This [422]5/2 state has an interesting property: Because the centrifugal barrier is angle dependent, it lies below the barrier along the z-axis and 0.2 MeV above it along the ρ-axis (see Fig. 7). To determine whether or not the resonance interpretation of this state is valid, we first examined the box size dependence of calculated single-particle energies. As shown in Fig. 8, the energy of the [422]5/2 state is found to be stable with respect to variation of the box size. We next evaluated the sum of the eigenphase, $\Delta(E) = \sum_a \delta_a(E)$, following the procedure of Ref. 51). The eigenphase is obtained through eigenvalues of the S-matrix, and their sum has the same

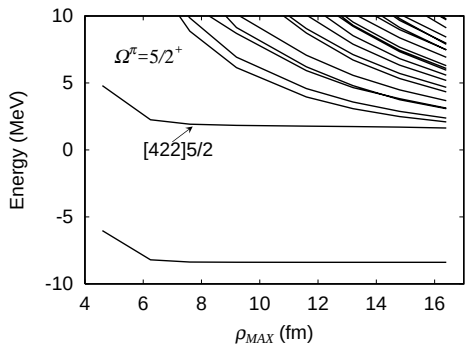

Fig. 8. Box size dependence of single-particle levels with $\Omega^\pi = 5/2^+$ in superdeformed ^{50}S. The [422]5/2 level is stable with respect to variation of the box size.

energy dependence around a resonance as the phase shift in a spherical system,[52]

$$\tan(\Delta(E) - \Delta_0(E)) = \frac{\Gamma}{2(E - E_R)}, \tag{3·2}$$

where E_R and Γ denote the resonance energy and the total width, respectively. The sum of the background eigenphases, $\Delta_0(E)$, is considered a slowly-varying quantity. The result of this calculation, presented in Fig. 9, confirms that the [422]5/2 state can be regarded as a resonance. Its width is estimated to be about 0.14 MeV. Furthermore, we confirmed that the root-mean-square radius of this state is clearly distinguishable from those of discretized continuum states (see Fig. 10). In this figure, the root-mean-square radius of various single-particle states are plotted. We find that not only the resonance [422]5/2 state but also the weakly bound [310]1/2 state has a root-mean-square radius about 2 fm larger than the average value for neutrons, $\sqrt{\langle r^2 \rangle}_\nu = 4.44$ fm. This is because the low angular momentum $p_{1/2}$ component that has a spatially extended structure becomes dominant in such a $\Omega^\pi = 1/2^-$ neutron level as the binding energy approaches zero.[53),54)]

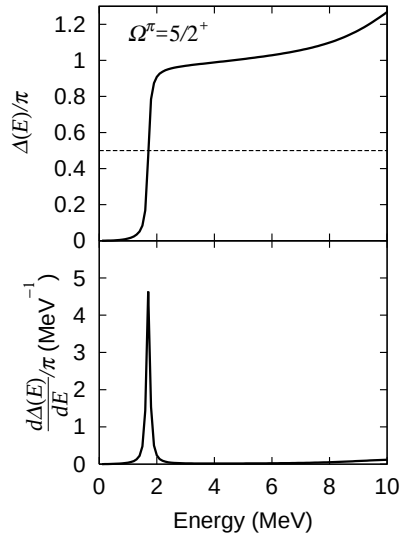

Fig. 9. The eigenphase sum (upper panel) and its derivative (lower panel) for the $\Omega^\pi = 5/2^+$ state in superdeformed ^{50}S are plotted as functions of energy.

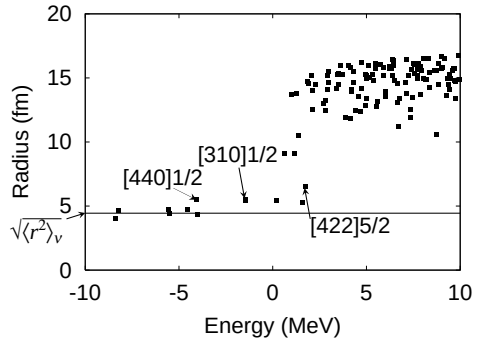

Fig. 10. Root-mean-square radii $\sqrt{\langle r^2 \rangle}$ of neutron single-particle states in superdeformed ^{50}S, obtained in a calculation using a box of size $\rho_{\max} \times z_{\max} = 14.25$ fm $\times$ 22.0 fm. Here, the root-mean-square radius of neutrons $\sqrt{\langle r^2 \rangle_\nu}$ is 4.44 fm.

In contrast to the peak at 3.1 MeV discussed above, the peak at 2.8 MeV corresponds to the excitation of the loosely bound [431]3/2 neutron to a discretized continuum state with $\Omega^\pi = 1/2^-$. Therefore, its position and height do not have definite physical meanings. In fact, these values change as the box size is varied. This peak even disappears when smaller boxes are used in the numerical calculation (see Fig. 11), whereas the peak position and the height associated with the [310]1/2 $\rightarrow$ [422]5/2 excitation is stable, as long as a box larger than $\rho_{\max} \times z_{\max} = 12.25$ fm $\times 20.0$ fm is used. We should also mention

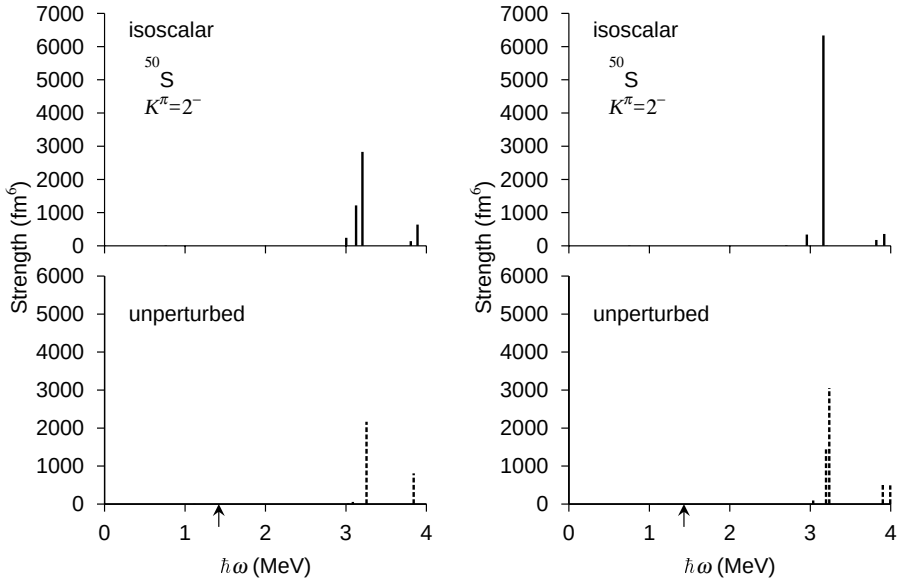

Fig. 11. The isoscalar octupole strength $B(Q^{\rm IS}3)$ distributions for the $K^\pi = 2^-$ excitations on the SD state in ^{50}S, obtained using an RPA calculation with $\beta_2 = 0.54$ and 0.73 for protons and neutrons, respectively, using a box of size $\rho_{\rm max} \times z_{\rm max} = 10.25$ fm $\times 16.0$ fm (left) and 12.25 fm $\times 20.0$ fm (right). The neutron root-mean-square radii $\sqrt{\langle r^2 \rangle_\nu}$ are 4.42 fm and 4.44 fm. The unperturbed particle-hole strengths are also plotted with dashed lines in the bottom panels. The arrows indicate the threshold energy, $E_{\rm th} = 1.4$ MeV.

that the convergence of the numerical calculation is insufficient for the unperturbed strength of the $[310]1/2 \rightarrow [422]5/2$ transition, because the root-mean-square radius of the $[422]5/2$ state still increases from 5.90 fm to 6.54 fm for a larger box, with $\rho_{\rm max} \times z_{\rm max} = 14.25$ fm $\times 22.0$ fm. Therefore, the calculated transition strength has only qualitative meaning.

Finally, let us make a comparison between the spatial distributions of the $K^\pi = 2^-$ octupole strength associated with individual particle-hole excitations on the SD state in the drip line nucleus ^{50}S and those in the stable nucleus ^{32}S. Figure 12 plots the spatial distribution functions $Q^{ph}_{3K}(\rho, z)$ for some major configurations generating the low-lying $K^\pi = 2^-$ modes in ^{32}S and ^{50}S. It is clear that the particle-hole excitations in ^{50}S have spatial distributions significantly extended outside of the nucleus, while those in ^{32}S are peaked around the surface region. This spatially extended structure brings about a strong enhancement of the octupole strength in ^{50}S. This can be regarded as one of the unique properties of excitation modes in nuclei close to the drip line. Note that this mechanism of transition strength enhancement is different from the threshold effect associated with the excitation of a loosely bound neutron into the non-resonant continuum.[55)]

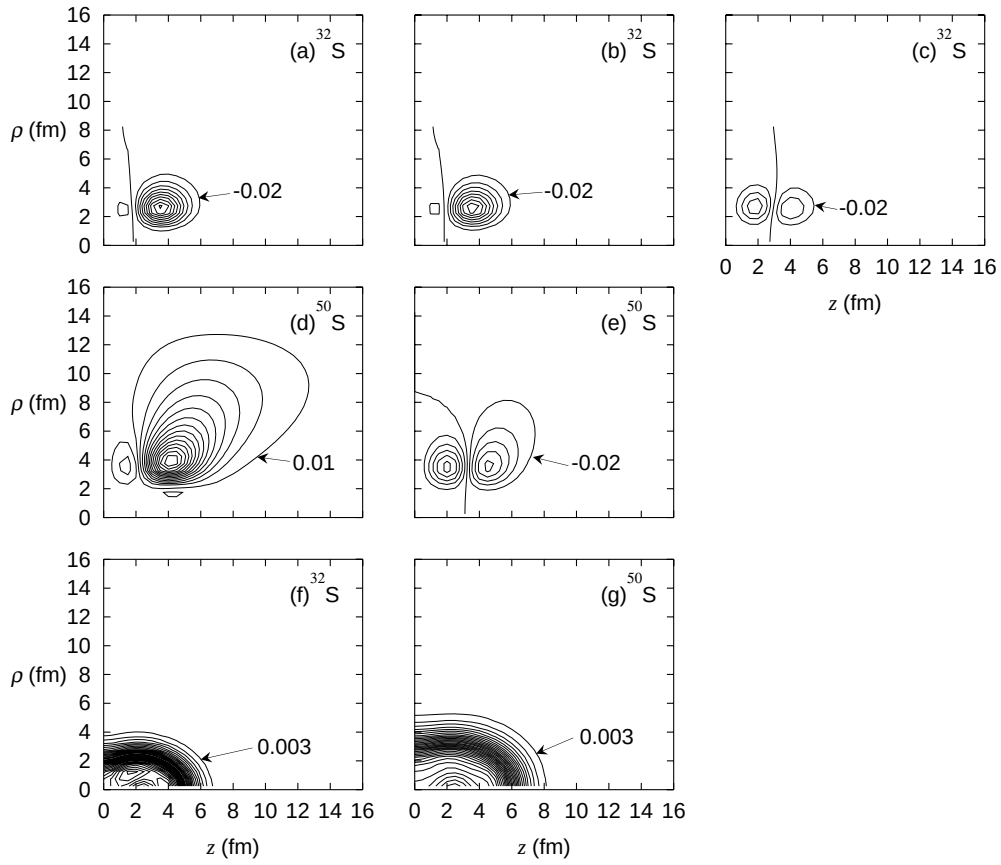

Fig. 12. Spatial distribution functions $Q_{32}^{ph}(\rho, z)$ for some particle-hole excitations generating the low-lying $K^\pi = 2^-$ states in superdeformed ^{32}S and ^{50}S. The contour lines are plotted at intervals of 0.02 fm. The panels denoted (a), (b) and (c) correspond to the $[211]1/2 \rightarrow [321]3/2$, $[211]3/2 \rightarrow [321]1/2$, and $[330]1/2 \rightarrow [202]5/2$ excitations in ^{32}S, respectively, while (d) and (e) correspond to the $[310]1/2 \rightarrow [422]5/2$ and $[431]3/2 \rightarrow [303]7/2$ excitations in ^{50}S. The bottom panels, (f) and (g), display the neutron density distributions of the SD states in ^{32}S and ^{50}S, respectively. The contour lines are plotted at intervals of 0.003 fm^{-3}. The neutron root-mean-square radii, $\sqrt{\langle r^2 \rangle_\nu}$, are 3.49 and 4.44 fm for ^{32}S and ^{50}S, respectively.

3.3. *The oblately deformed state in ^{40}Mg*

To show that the strong enhancement of the transition strength for an excitation from a loosely bound state to a resonance state is not restricted to the SD states but expected to be a rather general phenomenon in nuclei close to the drip line, we present in this subsection another example of the RPA calculation for ^{40}Mg. According to the HF-Bogoliubov calculations,[56),57)] this nucleus is situated close to the neutron drip line and possesses both prolate and oblate local minima.

Figure 13 displays the octupole transition strengths for the $K^\pi = 3^-$ excita-

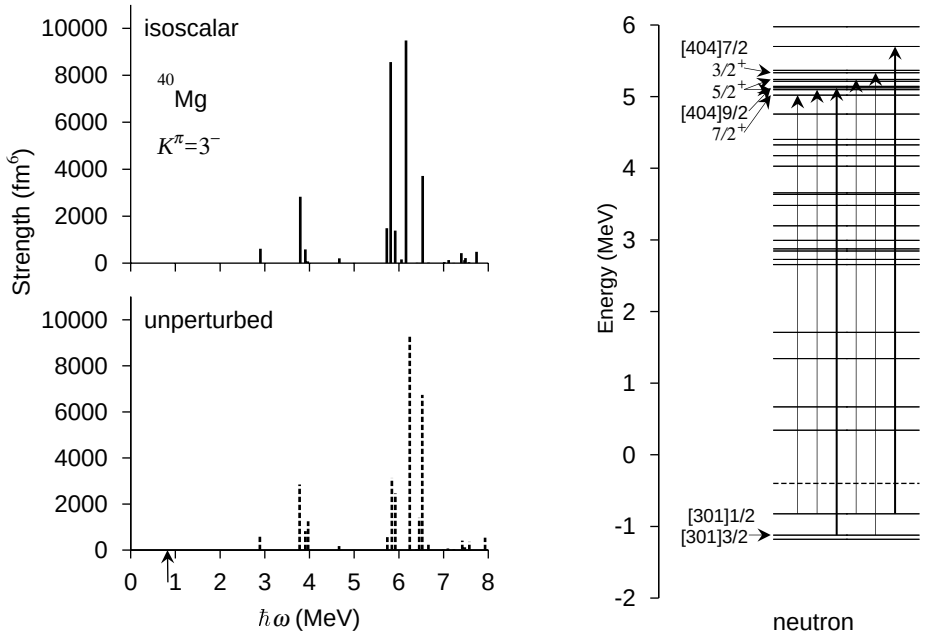

Fig. 13. *Left*: The isoscalar octupole strength $B(Q^{\rm IS}3)$ distribution for the $K^\pi = 3^-$ excitations on the oblate state in ^{40}Mg is plotted in the top panel as a function of the excitation energy. This was obtained using an RPA calculation with $\beta_2 = -0.2$ for both protons and neutrons, using a box of size $\rho_{\max} \times z_{\max} = 14.25$ fm $\times 12.0$ fm. The unperturbed particle-hole strengths are also plotted with dashed lines in the bottom panel. The arrow indicates the threshold energy $E_{\rm th} = 0.82$ MeV. *Right*: Particle-hole configurations of neutrons generating the $K^\pi = 3^-$ state at 6.2 MeV. The levels denoted [404]9/2 and [404]7/2 correspond to resonances, while other levels in the positive energy region represent discretized continuum states.

Table VI. RPA amplitudes for the 3^- state at 6.2 MeV in the oblately deformed ^{40}Mg, calculated with $\beta_2 = -0.2$ for both protons and neutrons. It is characterized by $B(E3) = 1.09\ e^2{\rm fm}^6$, $B(Q^\nu 3) = 9280$ fm^6, $B(Q^{\rm IS}3) = 9482$ fm^6, and $\sum |g_{ph}|^2 = 1.46 \times 10^{-3}$. The particle states other than the ν[404]9/2 and ν[404]7/2 resonances represent discretized continuum states. Only components with $|f_{ph}| > 0.1$ are listed.

particle	hole	$\epsilon_p - \epsilon_h$(MeV)	f_{ph}	Q^{ph}_{33} (fm^3)	M^{ph}_{33} (fm^3)
ν 7/2$^+$	ν[301]1/2	5.84	−0.142	−56.0	7.81
ν 5/2$^+$	ν[301]1/2	5.92	0.156	49.6	7.58
ν 5/2$^+$	ν[301]1/2	6.06	0.211	−0.526	−0.109
ν[404]9/2	ν[301]3/2	6.24	0.909	−96.7	−89.5
ν 3/2$^+$	ν[301]3/2	6.45	0.171	−37.4	−6.51
ν[404]7/2	ν[301]1/2	6.52	0.160	−82.1	−13.3

tions on the oblately deformed state in ^{40}Mg. Among several peaks in the isoscalar strength distribution, we can give a clear physical interpretation for the two prominent peaks at 6.2 and 6.6 MeV: The former is created by the excitation of a neutron from the loosely bound [301]3/2 state to the resonance [404]9/2 state, while the latter is from the loosely bound [301]3/2 state to the resonance [404]7/2 state. These

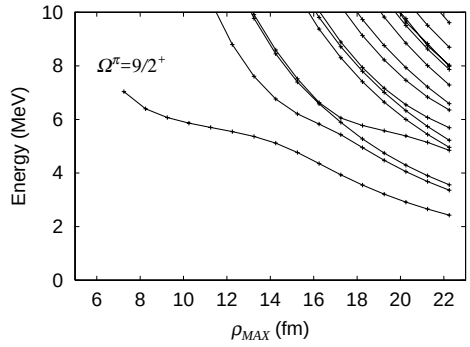

Fig. 14. Box size dependence of single-particle levels with $\Omega^\pi = 9/2^+$ in the oblately deformed ^{40}Mg.

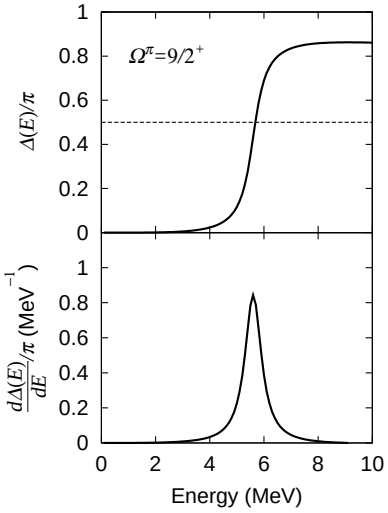

Fig. 15. The eigenphase sum (upper panel) and its derivative (lower panel) for the $\Omega^\pi = 9/2^+$ state in the oblately deformed ^{40}Mg are plotted as functions of energy.

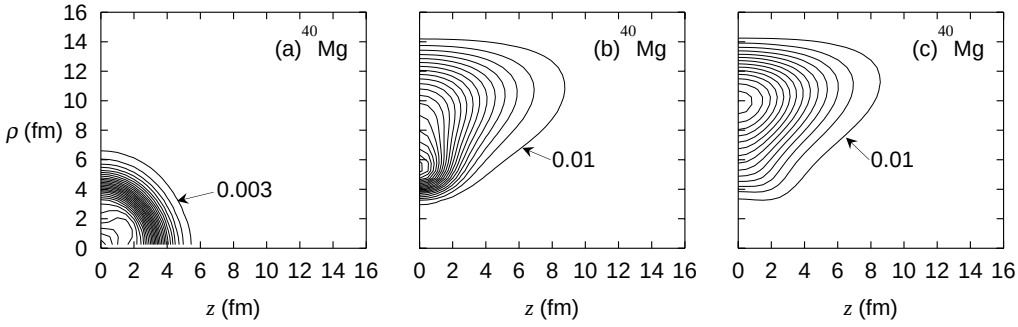

Fig. 16. (a) The neutron density distribution of the oblately deformed state in ^{40}Mg. The contour lines are plotted at intervals of 0.003 fm^{-3}. The root-mean-square radius of neutrons, $\sqrt{\langle r^2\rangle_\nu}$, is 4.06 fm. (b) Spatial distribution function $Q_{33}^{ph}(\rho, z)$ for the [301]3/2 $\rightarrow$ [404]9/2 excitation on the oblately deformed state in ^{40}Mg. The contour lines are plotted at intervals of 0.02 fm. (c) Same as (b), but for the [301]1/2 $\rightarrow$ [404]7/2 excitation.

resonance states are associated with the $g_{9/2}$ orbit, which has a high centrifugal barrier. Due to the spatially extended structure of this type of particle-hole excitation, they acquire extremely large transition strengths; the isoscalar octupole strength of the former (latter) is about 90 (39) W.u. (1 W.u. $\simeq$ 95 fm^6 for ^{40}Mg). The major components of the RPA amplitudes of the $K^\pi = 3^-$ mode at 6.2 MeV are presented in Table VI. Other peaks in this figure are due to excitations to discretized continuum states; e.g., the peak at 3.8 (5.8) MeV is associated with the excitation from the [301]3/2 ([301]1/2) state to the discretized continuum Ω^π=3/2$^+$ (7/2$^+$)

state. Therefore, their positions and peak heights do not have definite physical meanings. This conclusion was obtained by examining the box size dependence of single-particle energies and their eigenphase sums. Typical results of these calculations are presented in Figs. 14 and 15. The widths of the resonant [404]9/2 and [404]7/2 states are estimated to be about 0.8 and 1.2 MeV, respectively.

Finally, we show in Fig. 16 the spatial distribution functions $Q_{33}^{ph}(\rho, z)$ for the $[301]3/2 \rightarrow [404]9/2$ and $[301]1/2 \rightarrow [404]7/2$ excitations, together with the neutron density distribution of the oblately deformed state in ^{40}Mg. It is clearly seen that the strengths of these particle-hole excitations extend far from the nuclear surface. Furthermore, we notice that the peak positions of the two distributions, shown in (b) and (c), differ considerably. This can be regarded as the major reason that the two particle-hole configurations do not strongly mix with each other in the RPA eigenmodes, despite the fact that their unperturbed energies are fairy close (see Table VI). This is quite different from the familiar situations for low-frequency RPA modes in stable nuclei, in which the strength distribution functions of many particle-hole configurations have peaks near the nuclear surface and tend to mix with each other, generating collective vibrational modes.

§4. Conclusions

By means of the RPA calculation based on the deformed Woods-Saxon potential in the coordinate-mesh representation, we have carried out a comparative study of octupole excitations built on the SD states in the ^{40}Ca region and those in ^{50}S. In the $N = Z$ stable nuclei, ^{32}S and ^{40}Ca, the enhancement of the octupole transition strength results from the coherence between the proton and neutron excitations. By contrast, in ^{50}S close to the neutron drip line, we have found that the low-lying state created by the excitation of a single neutron from a loosely bound low Ω state to a high Ω resonance state acquires an extremely large transition strength. We have made a detailed study of the spatial distributions of particle-hole transition strengths and confirmed that this enhancement of the strength is a natural consequence of the fact that these particle and hole wave functions extend significantly outside of the nuclear surface. To show that this kind of enhancement phenomenon is not restricted to the SD states, we have also presented another example for oblately deformed ^{40}Mg close to the neutron drip line.

The present calculation indicates that, as we approach the drip line, it becomes increasingly difficult to generate collective modes of excitation by coherent superpositions of many particle-hole excitations. This is because the bound particle states disappear and individual resonance wave functions possess different spatial structures. It should be emphasized, however, that the pairing correlation is not taken into account in the present calculation. Quite recently, one of the authors (M. Y.) showed[58] that collectivity emerges in nuclei close to the drip line, owing to the pairing anti-halo effect:[59] The self-consistent pairing correlation in the continuum brings about spatial localization of particle-hole excitations, which helps in generating the collective modes of excitation. Thus, it is an important next step to investigate how

the results presented in this paper are modified by the pairing correlation.

Acknowledgements

We thank S. Mizutori and T. Inakura for valuable discussions and comments. We are grateful to K. Hagino for useful suggestions and for providing us with a computer program for calculation of the eigenphase sum. This work was done as a step in our long-range plan to explore exotic modes of excitation unique in deformed nuclei close to the drip line, and it is supported by the Japan-U.S. Cooperative Science Program "Mean-Field Approach to Collective Excitations in Unstable Medium-Mass and Heavy Nuclei", a Grant-in-Aid for the 21st Century COE "Center for Diversity and Universality in Physics" from the Ministry of Education, Culture, Sports, Science and Technology (MEXT) of Japan, and a Grant-in-Aid for Scientific Research No. 16540249 from the Japan Society for the Promotion of Science. The numerical calculations were performed on the NEC SX-5 supercomputer at Yukawa Institute for Theoretical Physics, Kyoto University.

Appendix A
—— Numerical Derivative ——

For wave functions of the form $\Phi(\rho,\varphi,z)=\phi(\rho,z)e^{i\Lambda\varphi}$, we have

$$\nabla^2\phi(\rho,z)e^{i\Lambda\varphi}=\left(\frac{1}{\rho}\frac{\partial}{\partial\rho}+\frac{\partial^2}{\partial\rho^2}-\frac{\Lambda^2}{\rho^2}+\frac{\partial^2}{\partial z^2}\right)\phi(\rho,z)e^{i\Lambda\varphi}. \tag{A·1}$$

Using the coordinate-mesh representation and the 9-points formula, the derivative parts can be written as

$$\begin{aligned}
&\left(\frac{1}{\rho}\frac{\partial}{\partial\rho}+\frac{\partial^2}{\partial\rho^2}+\frac{\partial^2}{\partial z^2}\right)\phi_{i,j}\\
&=\frac{1}{\Delta^2}\left[\frac{287000}{5040}\phi_{i,j}+\left(\frac{8064}{5040}+\frac{672}{840(i-1/2)}\right)\phi_{i+1,j}+\left(\frac{8064}{5040}-\frac{672}{840(i-1/2)}\right)\phi_{i-1,j}\right.\\
&\quad-\left(\frac{1008}{5040}+\frac{168}{840(i-1/2)}\right)\phi_{i+2,j}-\left(\frac{1008}{5040}-\frac{168}{840(i-1/2)}\right)\phi_{i-2,j}\\
&\quad+\left(\frac{128}{5040}+\frac{32}{840(i-1/2)}\right)\phi_{i+3,j}+\left(\frac{128}{5040}-\frac{32}{840(i-1/2)}\right)\phi_{i-3,j}\\
&\quad-\left(\frac{9}{5040}+\frac{3}{840(i-1/2)}\right)\phi_{i+4,j}-\left(\frac{9}{5040}-\frac{3}{840(i-1/2)}\right)\phi_{i-4,j}\\
&\qquad+\frac{8064}{5040}(\phi_{i,j+1}+\phi_{i,j-1})-\frac{1008}{5040}(\phi_{i,j+2}+\phi_{i,j-2})\\
&\qquad\left.+\frac{128}{5040}(\phi_{i,j+3}+\phi_{i,j-3})-\frac{9}{5040}(\phi_{i,j+4}+\phi_{i,j-4})\right].
\end{aligned} \tag{A·2}$$

Appendix B
Numerical Quadrature

For numerical integration, we use Bode's rule given by

$$\int_{x_i}^{x_{i+4}} f(x)dx = \frac{2\Delta}{45}(7f_i + 32f_{i+1} + 12f_{i+2} + 32f_{i+3} + 7f_{i+4}) + O(\Delta^7). \qquad \text{(B·1)}$$

This formula is a generalization of the well-known Simpson's rule, and it is derived by taking into account polynomials up to quartic order in the Taylor expansion for interpolation between the mesh points.[60)]

References

1) Ed. I. Tanihata, Nucl. Phys. A **693** (2001), Issues 1, 2.
2) Ed. H. Horiuchi, T. Otsuka and Y. Suzuki, Prog. Theor. Phys. Suppl. No. 142 (2001).
3) Ed. K. Hagino, H. Horiuchi, M. Matsuo and I. Tanihata, Prog. Theor. Phys. Suppl. No. 146 (2002).
4) I. Hamamoto, H. Sagawa and X. Z. Zhang, Phys. Rev. C **53** (1996), 765; ibid. **55** (1997), 2361; ibid. **56** (1997), 3121; ibid. **57** (1998), R1064; ibid. **64** (2001), 024313.
5) I. Hamamoto and H. Sagawa, Phys. Rev. C **60** (1999), 064314; ibid. **62** (2000), 024319; ibid. **66** (2002), 044315.
6) S. Shlomo and B. Agrawal, Nucl. Phys. A **722** (2003), C98.
7) K. Hagino and H. Sagawa, Nucl. Phys. A **695** (2001), 82.
8) M. Bender, J. Dobaczewski, J. Engel and W. Nazarewicz, Phys. Rev. C **65** (2002), 054322.
9) M. Yamagami and Nguyen Van Giai, Phys. Rev. C **69** (2004), 034301.
10) J. Terasaki, J. Engel, M. Bender, J. Dobaczewski, W. Nazarewicz and M. Stoitsov, nucl-th/0407111.
11) D. Vretenar, T. Nikšić, N. Paar and P. Ring, Nucl. Phys. A **731** (2004), 281.
12) N. Paar, P. Ring, T. Nikšić and D. Vretenar, Phys. Rev. C **67** (2003), 034312.
13) N. Paar, T. Nikšić, D. Vretenar and P. Ring, Phys. Rev. C **69** (2004), 054303.
14) G. Giambrone, S. Scheit, F. Barranco, P. F. Bortignon, G. Colò, D. Sarchi and E. Vigezzi, Nucl. Phys. A **726** (2003), 3.
15) M. Bender, P.-H. Heenen and P.-G. Reinhard, Rev. Mod. Phys. **75** (2003) 121.
16) S. Shlomo and G. F. Bertsch, Nucl. Phys. A **243** (1975), 507.
17) G. F. Bertsch and S. F. Tsai, Phys. Rep. **18** (1975), 125.
18) M. Matsuo, Nucl. Phys. A **696** (2001), 371.
19) M. Matsuo, Prog. Theor. Phys. Suppl. No. 146 (2002), 110.
20) M. Matsuo, K. Mizuyama and Y. Serizawa, nucl-th/0408052.
21) E. Khan, N. Sandulescu, M. Grasso and N. V. Giai, Phys. Rev. C **66** (2002), 024309.
22) E. Khan, N. Sandulescu, N. V. Giai and M. Grasso, Phys. Rev. C **69** (2004), 014314.
23) P. Urkedal, X. Z. Zhang and I. Hamamoto, Phys. Rev. C **64** (2001), 054304.
24) T. Nakatsukasa and K. Yabana, *Proc. Int. Symp. "A New Era of Nuclear Structure Physics", Niigata 2003*, ed. Y. Suzuki, S. Ohta, M. Matsuo and T. Ohtsubo (Word Scientific, 2004), p. 251.
25) T. Nakatsukasa and K. Yabana, Phys. Rev. C **71** (2005), 024301.
26) K. Hagino, Nguyen Van Giai and H. Sagawa, Nucl. Phys. A **731** (2004), 264.
27) T. Inakura, M. Yamagami, K. Matsuyanagi, S. Mizutori, H. Imagawa and Y. Hashimoto, *Proc. the 10th Marie and Pierre Curie Nuclear Physics Workshop, 24-28 September, 2003, Kazimierz Dolny, Poland*, Int. J. Mod. Phys. E **13** (2004), 157.
28) T. Inakura, Doctor Thesis (Kyoto University, 2004).
29) R. H. Lemmer and M. Véneroni, Phys. Rev. **170** (1968), 883.
30) A. Muta, J.-I. Iwata, Y. Hashimoto and K. Yabana, Prog. Theor. Phys. **108** (2002), 1065.
31) H. Imagawa and Y. Hashimoto, Phys. Rev. C **67** (2003), 037302.
32) H. Imagawa, Doctor Thesis, University of Tsukuba (2003).
33) E. Ideguchi et al., Phys. Rev. Lett. **87** (2001), 222501.
34) C. J. Chiara et al., Phys. Rev. C **67** (2003), 041303(R).

35) H. C. Pauli, Phys. Rep. **7** (1973), 35.
36) A. Bohr and B. R. Motteleson, *Nuclear Structure*, vol. I (Benjamin, 1969).
37) S. Cwiok, J. Dudek, W. Nazarewicz, J. Skalski and T. Werner, Comput. Phys. Commun. **46** (1987), 379.
38) P. Ring and P. Schuck, *The Nuclear Many-Body Problem* (Springer, 1980).
39) T. Inakura, M. Yamagami, S. Mizutori and K. Matsuyanagi, Nucl. Phys. A **728** (2003), 52.
40) I. Ragnarsson, S. G. Nilsson and R. K. Sheline, Phys. Rep. **45** (1978), 1.
41) J. Dobaczewski, AIP Conf. Proc. **481** (1999), 315.
42) M. Yamagami and K. Matsuyanagi, Nucl. Phys. A **672** (2000), 123.
43) H. Molique, J. Dobaczewski and J. Dudek, Phys. Rev. C **61** (2000), 044304.
44) R. R. Rodriguez-Guzmán, J. L. Egido and L. M Robeldo, Phys. Rev. C **62** (2000), 054308.
45) T. Tanaka, R. G. Nazmitdinov and K. Iwasawa, Phys. Rev. C **63** (2001), 034309.
46) T. R. Werner, J. A. Sheikh, M. Misu, W. Nazarewicz, J. Rikovska, K. Heeger, A. S. Umar and M. R. Strayer, Nucl. Phys. A **597** (1996), 327.
47) S. Mizutori, T. Nakatsukasa, K. Arita, Y. R. Shimizu and K. Matsuyanagi, Nucl. Phys. A **557** (1993), 125.
48) T. Nakatsukasa, K. Matsuyanagi, S. Mizutori and Y. R. Shimizu, Phys. Rev. C **53** (1996), 2213.
49) T. Nakatsukasa, K. Matsuyanagi, S. Mizutori and W. Nazarewicz, Phys. Lett. B **343** (1995), 19.
50) J. P. Blaizot and D. Gogny, Nucl. Phys. A **284** (1977), 429.
51) K. Hagino and Nguyen Van Giai, Nucl. Phys. A **735** (2004), 55.
52) A. U. Hazi, Phys. Rev. A **19** (1979), 920.
53) T. Misu, W. Nazarewicz and S. Åberg, Nucl. Phys. A **614** (1997), 44.
54) I. Hamamoto, Phys. Rev. C **69** (2004), 041306.
55) F. Catara, E. G. Lanza, M. A. Nagarajan and A. Vitturi, Nucl. Phys. A **624** (1997), 449.
56) J. Terasaki, H. Flocard, P.-H. Heenen and P. Bonche, Nucl. Phys. A **621** (1997), 706.
57) M. V. Stoitsov, J. Dobaczewski, W. Nazarewicz, S. Pittel and D. J. Dean, Phys. Rev. C **68** (2003), 054312.
58) M. Yamagami, *Proceedings of the Fifth Japan China Joint Nuclear Physics Symposium, 7-10 March, 2004, Kyushu University, Japan*; nucl-th/0404030.
59) K. Bennaceur, J. Dobaczewski and M. Ploszajczak, Phys. Lett. B **496** (2000), 154.
60) S. E. Koonin, *Computational Physics* (Addison-Wesley, 1986).

High-K precession modes: Axially symmetric limit of wobbling motion in the cranked random-phase approximation description

Yoshifumi R. Shimizu,[1] Masayuki Matsuzaki,[2] and Kenichi Matsuyanagi[3]
[1]*Department of Physics, Graduate School of Sciences, Kyushu University, Fukuoka 812-8581, Japan*
[2]*Department of Physics, Fukuoka University of Education, Munakata, Fukuoka 811-4192, Japan*
[3]*Department of Physics, Graduate School of Science, Kyoto University, Kyoto 606-8502, Japan*
(Received 19 December 2004; published 14 July 2005)

The rotational band built on the high-K multi-quasiparticle state can be interpreted as a multi-phonon band of the precession mode, which represents the precessional rotation about the axis perpendicular to the direction of the intrinsic angular momentum. By using the axially symmetric limit of the random-phase approximation (RPA) formalism developed for the nuclear wobbling motion, we study the properties of the precession modes in ^{178}W: the excitation energies, $B(E2)$ and $B(M1)$ values. We show that the excitations of such a specific type of rotation can be well described by the RPA formalism, which gives new insight into the wobbling motion in the triaxial superdeformed nuclei from a microscopic viewpoint.

DOI: 10.1103/PhysRevC.72.014306 PACS number(s): 21.10.Re, 21.60.Jz, 23.20.Lv, 27.70.+q

I. INTRODUCTION

Rotation is a typical collective motion in atomic nuclei. It manifests itself as a rotational band, a sequence of states connected by strong electromagnetic (e.g., $E2$) transitions. Most of the rotational bands observed so far are based on the uniform rotation about an axis perpendicular to the symmetry axis of axially symmetric deformation. The well-known ground state rotational bands and the superdeformed rotational bands with axis ratios about 2:1 are typical examples of this type of rotational motion. Quite recently, exotic rotational motions, in contrast to the normal ones mentioned above, have been under discussion. They are generally neither uniform nor rotating about one of three principal axes of deformation, and they clearly indicate the possible existence of *three-dimensional* rotations in atomic nuclei. The recently observed wobbling rotational bands [1–5] and the chiral rotation/vibration bands [6–9] are such examples.

Such exotic rotations are very interesting because they give hints to answering a fundamental question: How does an atomic nucleus rotate as a three-dimensional object? They may also shed light on collective motions in nuclei with triaxial deformation, which are characteristic in these rotational bands and are very scarce near the ground state region. Although the triaxial deformation is crucial for those exotic rotations, it is not a necessary condition for three-dimensional rotations to occur. For example, the chiral rotation is a kind of "magnetic rotation" or "tilted axis rotation" [10], where the axis of rotation is neither along a principal axis of deformation nor in the plane of two principal axes, but is pointing inside a triangle composed of three principal axes. In the case of the typical magnetic rotation observed in the Pb region, the so-called shears band [10], the deformation is axially symmetric and weakly oblate. Similarly, one can think of an axially symmetric limit of the wobbling motion: the so-called "precession band", which is nothing but a rotational band excited on a high-K isomeric state, in analogy to the classical motion of the symmetric top. The main purpose of the present paper is to investigate the precession band from a microscopic viewpoint.

In recent publications [11,12], we studied the nuclear wobbling motions associated with the triaxial superdeformed (TSD) bands in Lu and Hf isotopes on the basis of the microscopic framework: the cranked mean-field and the random-phase approximation (RPA) [13–19]. It has been found that RPA eigenmodes, which can be interpreted as the wobbling motions, appear naturally if appropriate mean-field parameters are chosen. The deformation of the mean-field is large ($\epsilon_2 > 0.35$) with a positive triaxial shape ($\gamma \approx +20^\circ$ in the Lund convention), i.e., mainly rotating about the shortest axis, and the static pairing is small ($\Delta_{n,p} < 0.6$ MeV), both of which properties are in accordance with the potential energy surface calculation [20]. It should be stressed that the solution of the RPA eigenvalue is uniquely determined, once the mean field is fixed, as long as the "minimal coupling" residual interaction is adopted (see Sec. III). Therefore, it is highly nontrivial that we could obtain wobbling-like RPA solutions at correct excitation energies. However, the detailed rotational frequency dependence of the observed excitation energy in Lu isotopes, monotonically decreasing with frequency, could not be reproduced, and the out-of-band $B(E2)$ values from the wobbling band were considerably underestimated in our RPA calculation.

In the axially symmetric deformation with a uniform rotation about a principal axis, the angular momentum of high-spin states is built up either by a collective rotation, i.e., the rotation axis is perpendicular to the symmetry axis, or by alignments of single-particle angular momenta, i.e., the rotation axis is the same as the symmetry axis. Thus, four rotation schemes are possible: oblate noncollective, prolate collective, oblate collective, and prolate noncollective rotations, corresponding to the triaxiality parameter $\gamma = 60^\circ$, $\gamma = 0^\circ$, $\gamma = -60^\circ$, and $\gamma = -120^\circ$ in the Lund convention, respectively. The axially symmetric limit of the RPA wobbling formalism can be taken for the so-called noncollective rotation schemes with oblate or prolate deformation, namely $\gamma = 60^\circ$ or $\gamma = -120^\circ$

cases. In both cases, long-lived isomers are observed, but the rotational bands starting from the isomers have not been observed in the oblate noncollective case. On the other hand, the high-K isomers and the associated rotational bands have been known for many years in the Hf and W region with prolate deformation. Making full use of the axial symmetry, the RPA formalism has been developed [21–24], which is capable of describing the rotational band based on the high-K state as a multi-phonon band, i.e., the precession band. Recently, the same kind of rotational bands built on high-K isomers have also been studied by means of the tilted axis cranking model [25–28].

In this paper, we would like to make a link between the two RPA formalisms, the one for the (triaxial) wobbling and the one for the (axially symmetric) precession motions. In fact, we will show that the precession mode can be naturally obtained as the axially symmetric limit of the noncollective rotation in the cranked-RPA description for the wobbling mode. Moreover, applying the formalism to a typical nucleus ^{178}W, where many high-K isomers have been observed, allows us to study the properties of the precession bands in detail, not only the excitation energies but also the $B(E2)$ and $B(M1)$ values. This kind of study for the precession band sheds new light on understanding the recently observed wobbling motion. For completeness of explanation in the following sections, we review the wobbling and precession bands in the rotor model in Sec. II, while in Sec. III the RPA wobbling formalism and the connection to the precession band in the axially symmetric limit are considered. The result of calculations for ^{178}W is presented and discussed in Sec. IV. Section V is devoted to some concluding remarks. Preliminary results for the magnetic property of the precession band were already reported [29].

II. WOBBLING AND PRECESSION IN SCHEMATIC ROTOR MODEL

The macroscopic rotor model is a basic tool for studying the nuclear collective rotation, and its high-spin properties have been investigated within a harmonic approximation [30] or by including higher order effects [31–33]. In this section, we review the consequences of the simple rotor model according to Ref. [30]. We use $\hbar = 1$ unit throughout this paper. The Hamiltonian of the simplest triaxial rotor model is given by

$$H_{\rm rot} = \frac{I_x^2}{2\mathcal{J}_x} + \frac{I_y^2}{2\mathcal{J}_y} + \frac{I_z^2}{2\mathcal{J}_z}, \tag{1}$$

where I's are angular momentum operators in the body-fixed coordinate frame, and the three moments of inertia, $\mathcal{J}_x, \mathcal{J}_y$, and $\mathcal{J}_z$, are generally different. We assume, for definiteness, the rotor describes the even-even nucleus (integer spins).

Following the argument of Ref. [30], let us consider the high-spin limit, $I \gg 1$, and assume that the main rotation is about the x axis; namely, the yrast band is generated by a uniform rotation about the x axis. Then, the excited band at spin I can be described by the excitation of the wobbling phonon,

$$X^\dagger_{\rm wob} = \frac{a}{\sqrt{2I}} i I_y + \frac{b}{\sqrt{2I}} I_z, \tag{2}$$

where a and b are the amplitudes determined by the eigenmode equation, $[H_{\rm rot}, X^\dagger_{\rm wob}] = \omega_{\rm wob}(I) X^\dagger_{\rm wob}$, at each spin I in the harmonic approximation. The resultant eigenvalue $\omega_{\rm wob}(I)$ is given by the well-known formula

$$\begin{aligned}\omega_{\rm wob}(I) &= I\sqrt{(1/\mathcal{J}_y - 1/\mathcal{J}_x)(1/\mathcal{J}_z - 1/\mathcal{J}_x)} \\ &= \omega_{\rm rot}(I)\sqrt{\frac{(\mathcal{J}_x - \mathcal{J}_y)(\mathcal{J}_x - \mathcal{J}_z)}{\mathcal{J}_y\,\mathcal{J}_z}},\end{aligned} \tag{3}$$

with the rotational frequency of the main rotation

$$\omega_{\rm rot}(I) \equiv \frac{I}{\mathcal{J}_x}. \tag{4}$$

It should be noted that the triaxial deformation of the nuclear shape is directly related to the intrinsic quadrupole moments, e.g., $\tan\gamma = -\sqrt{2}Q_{22}/Q_{20}$, but does not give a definite relation between three moments of inertia. One has to introduce a model, e.g., the irrotational flow model, in order to relate the triaxiality parameter γ of deformation to three inertia. However, the simple irrotational moment of inertia is inconsistent with the existence of wobbling mode if the positive γ shape is assumed, since then $\mathcal{J}_y > \mathcal{J}_x, \mathcal{J}_z$ and therefore the wobbling frequency (3) becomes imaginary.

The spectra of the rotor near the yrast line are given in the harmonic approximation by

$$E_{\rm rot}(I, n) = \frac{I(I+1)}{2\mathcal{J}_x} + \omega_{\rm wob}(I)\Big(n + \frac{1}{2}\Big), \tag{5}$$

and are composed of two sequences, the $\Delta I = 2$ horizontal one,

$$E^{\rm (hor)}_n(I) = E_{\rm rot}(I, n), \quad I = n, n+2, n+4, \ldots \tag{6}$$

with given phonon numbers $n = 0, 1, 2, \ldots$, and the $\Delta I = 1$ vertical sequence,

$$E^{\rm (ver)}_{I_0}(I) = E_{\rm rot}(I, I - I_0), \quad I = I_0, I_0 + 1, I_0 + 2, \ldots \tag{7}$$

with given bandhead spins $I_0 = 0, 2, 4, \ldots$, both of which are connected by $E2$ transitions. The horizontal sequences are conventional rotational bands with transition energies $E_\gamma \approx 2\omega_{\rm rot}$, and the $\Delta I = -2$ in-band $B(E2)$ values are proportional to the square of the quadrupole moment about the x axis. The vertical sequences look like phonon bands with transition energies $E_\gamma \approx (\omega_{\rm wob} + \omega_{\rm rot})$, and the $\Delta I = -1$ vertical $B(E2)$ values are $O(1/I)$ smaller than the horizontal $B(E2)$. These features are summarized schematically in Fig. 1. In fact, the $\Delta I = -1$ out-of-band transition was crucial to identifying the wobbling motion in Lu isotopes [1]. If the wobbling-phonon energy $\omega_{\rm wob}(I)$ is larger than the $\Delta I = 2$ rotational energy $\Delta E_{\rm rot}(I) = E_{\rm rot}(I+1, n) - E_{\rm rot}(I-1, n) = (2I+1)/\mathcal{J}_x$, both the $\Delta I = \pm 1$ transitions are possible. The $\Delta I = -1$ transition is much stronger than the $\Delta I = +1$ one for the positive γ shape, and *vice versa* for the negative γ shape, which also supports that the TSD bands in the Lu region have positive γ shape.

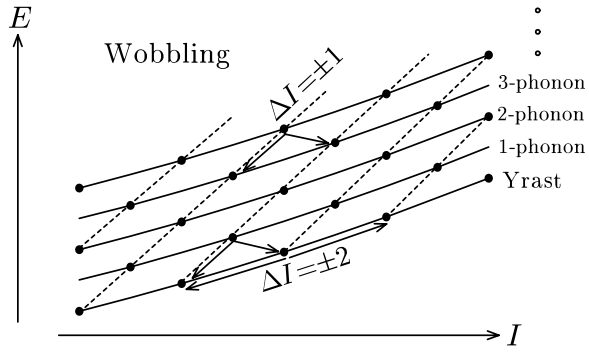

FIG. 1. Rotational spectra of a triaxial rotor Hamiltonian. Horizontal rotational bands are connected by solid lines; vertical phonon bands, by dotted lines.

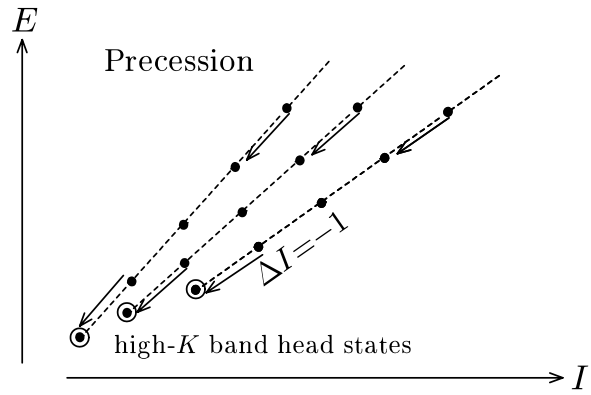

FIG. 2. Precession bands excited on high-K isomeric states. All $|\Delta I| = 2$ horizontal sequences shown in Fig. 1 disappear, leaving only one $|\Delta I| = 1$ vertical band in the case of the noncollective rotation.

Next, let us consider the precession band [22] built on a high-K isomeric state. In this case, the spin $I_x \approx I = K$ is composed of single-particle alignments, and the deformation is axially symmetric about the x axis. Since no collective rotation exists about the x axis, the rotational energy spectra are given simply by [30]

$$E_{\text{high-}K}(I) = \frac{1}{2\mathcal{J}_\perp}[I(I+1) - K^2], \tag{8}$$

where $\mathcal{J}_\perp$ is the moment of inertia with respect to the perpendicular axis ($\mathcal{J}_\perp \equiv \mathcal{J}_y = \mathcal{J}_z$). The excitation energy of this band can be rewritten, by putting $I = K + n$, as

$$E_{\text{high-}K}(I) = \omega_{\text{prec}}\left(n + \frac{1}{2} + \frac{n(n+1)}{K}\right), \tag{9}$$

with

$$\omega_{\text{prec}} \equiv \frac{K}{\mathcal{J}_\perp}, \tag{10}$$

leading to a harmonic phonon band structure with a one-phonon energy (10), when K is sufficiently large. The spectra in this limit are drawn in Fig. 2. The harmonic picture holds not only for the energy spectra but also for the $B(E2)$ values; for example, by using $B(E2) \propto \langle I_f K 20 | I_i K\rangle^2$, one finds, in the leading order, $B(E2; n \to n-1) \propto 3(n/K)$ and $B(E2; n \to n-2) \propto (3/2)(n(n-1)/K^2)$, where $n = I - K$ is the number of the precession phonon quanta, so that the two-phonon transition is hindered when K is large.

Now, let us discuss the relation [22] between the wobbling phonon energy (3) and the precession phonon energy (10). By putting $\mathcal{J}_y = \mathcal{J}_z \equiv \mathcal{J}_\perp$ with keeping $\mathcal{J}_x > \mathcal{J}_y, \mathcal{J}_z$ in Eq. (3), the wobbling frequency reduces to

$$\omega_{\text{wob}}(I) = \frac{I}{\mathcal{J}_\perp} - \omega_{\text{rot}}(I). \tag{11}$$

Namely, at the bandhead $I = K$, the precession phonon energy $\omega_{\text{prec}} = \omega_{\text{wob}} + \omega_{\text{rot}}$ coincides with the vertical $\Delta I = 1$ transition energy in the wobbling spectra in such a case. This result can be interpreted to mean that each horizontal band (6) in the wobbling spectra disappears (no collective rotations), leaving one vertical band, whose transition energy is ω_{prec}. This interpretation is possible in the microscopic cranked-RPA description [14] in the next section, where the rotational frequency ω_{rot} is replaced by the cranking frequency ω_{cr} about the x axis and the moment of inertia about this axis is defined by $\mathcal{J}_x \equiv \langle J_x\rangle/\omega_{\text{cr}}$; i.e., it is the kinematic moment of inertia containing the contribution from the quasiparticle alignments, so that the condition $\mathcal{J}_x > \mathcal{J}_y, \mathcal{J}_z$ can be satisfied. The cranking frequency ω_{cr} is a redundant variable in this case of the noncollective rotation, but all physical observables do not depend on it. In this way, both the wobbling and precession bands can be treated in a unified manner in the framework of the RPA wobbling formalism, which is shown in more detail in the next section (see Sec. III B).

III. AXIALLY SYMMETRIC LIMIT OF RPA WOBBLING FORMALISM

A. Minimal coupling and RPA wobbling equation

Microscopic RPA theories for nuclear wobbling motion have been developed in Refs. [14,15,17]. The most important among them is that of Marshalek [14], where the transformation to the principal axis frame (body-fixed frame) is performed and the theory is formulated in that frame. Moreover, it is shown that the RPA equation for the wobbling mode can be cast into the same form as Eq. (3) if three moments of inertia are replaced with those appropriately defined in the microscopic framework; we call this equation the wobbling form equation. The adopted microscopic Hamiltonian in Ref. [14] is composed of the spherical mean-field and the quadrupole-quadrupole interaction (with the monopole pairing if necessary). In Ref. [17], however, it was pointed out that the RPA equation could not be reduced to the wobbling form equation if a most general residual interaction is used. A closer look into the argument in Ref. [17] shows, however, that the following "minimal coupling," being used as a residual interaction, leads to the wobbling form equation as the RPA dispersion equation.

In Marshalek's theory the rotational Nambu-Goldstone (NG) modes (or spurious modes as conventionally called), J_y and J_z, play a crucial role. The RPA guarantees the

decoupling of these modes if the self-consistency of the mean field is satisfied in the Hartree-Fock sense. In many cases, however, non-self-consistent mean fields are necessary; for example, the deformation is more properly determined by the Strutinsky procedure than by the Hartree-Fock calculations with simple interactions, or one wants to study the system by hypothetically changing the mean-field parameters, as has been done in our previous calculations [12] for the nuclear wobbling motions. Thus, we consider that the mean field h rather than the interaction is given, and we look for the residual interaction $H_{\rm res}^{(m)}$, which fulfills the decoupling condition of the NG modes within the RPA [34]. The same idea has been formulated in the context of the particle-vibration coupling theory [30], where the rotational invariance is restored by considering the coupling resulting from a small rotation about the x, y, or z axis. Thus the minimum requirement is what we call the "minimal coupling" given by

$$H_{\rm res}^{(m)} = -\frac{1}{2}\sum_{k,l=x,y,z}\chi_{kl}F_kF_l. \tag{12}$$

Here, the Hermitian operator F_k and the 3×3 symmetric force-strength matrix χ_{kl} are defined as

$$F_k = i[h, J_k], \tag{13}$$

$$(\chi^{-1})_{kl} = -\langle\Phi|[[h, J_k], J_l]|\Phi\rangle, \tag{14}$$

with the mean-field vacuum state $|\Phi\rangle$ (the Slater determinant if no pairing is included), on which RPA eigenmodes are created. If the mean field is given by the anisotropic harmonic oscillator potential, the minimal coupling leads to the doubly stretched $Q''Q''$ interaction combined with the Landau prescription [21,35–41]. One has to include the monopole pairing interaction in realistic calculations. It should be stressed that the minimal coupling can be used for any type of mean fields, e.g., the Woods-Saxon potential.

For the wobbling modes in the yrast region, the mean-field vacuum state $|\Phi(\omega_{\rm cr})\rangle$ is obtained as the lowest eigenstate of the cranked mean-field Hamiltonian,

$$h' = h - \omega_{\rm cr}J_x, \tag{15}$$

as a function of the cranking frequency $\omega_{\rm cr}$. Assuming the signature symmetry (with respect to a π rotation about the x axis) of the mean field and the conventional phase convention that the matrix elements of the single-particle operators iJ_y and J_z are real in the mean-field basis, it can be shown that the force-strength matrix χ_{kl} is diagonal. The excitation of the wobbling phonon corresponds to the vertical $\Delta I = \pm 1$ transitions in Sec. II, therefore only the part of the RPA equations which transfer the signature quantum number by $\alpha = 1$ is relevant; i.e., only $k, l = y, z$ parts of $H_{\rm res}^{(m)}$ in Eq. (12) contribute. It is now straightforward to follow the same procedure as has been done in Ref. [14], but with the modification that the quadrupole field of the interaction is replaced with F_k in Eq. (12). Then one finds that the same RPA dispersion equation can be derived as

$$\left(\omega^2 - \omega_{\rm cr}^2\right)\begin{vmatrix} A_y(\omega) & B_z(\omega) \\ B_y(\omega) & A_z(\omega)\end{vmatrix} = 0, \tag{16}$$

where

$$\begin{aligned} A_y(\omega) &= I - \omega_{\rm cr}\mathcal{J}_y(\omega) + \omega\mathcal{J}_{yz}(\omega),\\ A_z(\omega) &= I - \omega_{\rm cr}\mathcal{J}_z(\omega) + \omega\mathcal{J}_{yz}(\omega),\\ B_y(\omega) &= \omega\mathcal{J}_y(\omega) - \omega_{\rm cr}\mathcal{J}_{yz}(\omega),\\ B_z(\omega) &= \omega\mathcal{J}_z(\omega) - \omega_{\rm cr}\mathcal{J}_{yz}(\omega), \end{aligned} \tag{17}$$

with the following definitions:

$$\begin{aligned} I &= \langle\Phi(\omega_{\rm cr})|J_x|\Phi(\omega_{\rm cr})\rangle \\ &= \sum_{\mu<\nu} 2J_y(\mu\nu)J_z(\mu\nu),\\ \mathcal{J}_y(\omega) &= \sum_{\mu<\nu}\frac{2E_{\mu\nu}J_y(\mu\nu)^2}{E_{\mu\nu}^2-(\omega)^2},\\ \mathcal{J}_z(\omega) &= \sum_{\mu<\nu}\frac{2E_{\mu\nu}J_z(\mu\nu)^2}{E_{\mu\nu}^2-(\omega)^2},\\ \mathcal{J}_{yz}(\omega) &= \sum_{\mu<\nu}\frac{2\omega J_y(\mu\nu)J_z(\mu\nu)}{E_{\mu\nu}^2-(\omega)^2}. \end{aligned} \tag{18}$$

In these expressions, ω is the phonon excitation energy, $E_{\mu\nu} = E_\mu + E_\nu$ are two-quasiparticle energies with $\alpha = 1$, and $J_y(\mu\nu) = \langle\mu\nu|iJ_y|\Phi\rangle (J_z(\mu\nu) = \langle\mu\nu|J_z|\Phi\rangle)$ are two-quasiparticle matrix elements of the operator iJ_y (J_z), which are associated with the vacuum state $|\Phi(\omega_{\rm cr})\rangle$ and determined by the mean-field Hamiltonian h' in the rotating frame. It is now clear that once the mean-field Hamiltonian is given and the vacuum state $|\Phi(\omega_{\rm cr})\rangle$ is obtained, the RPA eigenmodes can be calculated without any ambiguity. This is precisely the consequence of the minimal coupling given by Eq. (12).

The rotational NG mode appears as a decoupled $\omega = \omega_{\rm cr}$ solution in the RPA dispersion equation (16);

$$\Gamma^\dagger = \frac{1}{\sqrt{2I}}(iJ_y + J_z)_{\rm RPA} = \frac{1}{\sqrt{2I}}(iJ_-)_{\rm RPA}, \tag{19}$$

$$J_\pm \equiv J_y \pm iJ_z, \quad (x\text{-axis quantization}), \tag{20}$$

where the subscript RPA means the two-quasiparticle transfer part (the particle-hole part if no pairing is included) of the operator. Note that it is normalizable, $[\Gamma, \Gamma^\dagger]_{\rm RPA} = 1$, because $\langle\Phi|[J_z, iJ_y]|\Phi\rangle = \langle\Phi|J_x|\Phi\rangle = I \neq 0$. The cranked mean field (15) describes the rotating state, which has an angular momentum vector aligned with the x axis, and this NG mode plays a role to tilt the whole system by changing the x component of the angular momentum by -1 unit. The reason why the NG mode has a finite excitation energy is that there is a cranking term in the Hamiltonian (15) (the Higgs mechanism).

Finally, Marshalek [14] has shown that the non-NG part of the RPA dispersion equation (16) is reduced to the wobbling form, where the rotational frequency $\omega_{\rm rot}$ is replaced by the cranking frequency $\omega_{\rm cr}$:

$$(\omega)^2 = (\omega_{\rm cr})^2\frac{\left[\mathcal{J}_x - \mathcal{J}_y^{(\rm eff)}(\omega)\right]\left[\mathcal{J}_x - \mathcal{J}_z^{(\rm eff)}(\omega)\right]}{\mathcal{J}_y^{(\rm eff)}(\omega)\,\mathcal{J}_z^{(\rm eff)}(\omega)}, \tag{21}$$

if three moments of inertia are replaced with microscopically defined ones in the following way:

$$\begin{aligned}\mathcal{J}_x &= \frac{I}{\omega_{\rm cr}} = \frac{\langle\Phi(\omega_{\rm cr})|J_x|\Phi(\omega_{\rm cr})\rangle}{\omega_{\rm cr}},\\ \mathcal{J}_y^{(\rm eff)}(\omega) &= \mathcal{J}_y(\omega) - \mathcal{J}_{yz}(\omega)\frac{A_y(\omega)}{B_z(\omega)},\\ \mathcal{J}_z^{(\rm eff)}(\omega) &= \mathcal{J}_z(\omega) - \mathcal{J}_{yz}(\omega)\frac{A_z(\omega)}{B_y(\omega)}.\end{aligned} \tag{22}$$

Since the y- and z-effective inertia are ω dependent, the equation is non-linear and they are determined only after solving it.

As for the electromagnetic transition probabilities, Marshalek proposed a $1/I$-expansion technique by utilizing the perturbative boson expansion method [13]. The $\Delta I = \mp 1$ $E2$ and $M1$ vertical transitions from the one-phonon wobbling band to the yrast band, discussed in Sec. II, can be calculated within the RPA, which is the lowest order in $1/I$, as

$$B(E2; I \pm 1 \to I) \approx |\langle\Phi|[Q_{2\mp1}, X^\dagger_{\rm wob}]|\Phi\rangle|^2, \tag{23}$$

$$B(M1; I \pm 1 \to I) \approx |\langle\Phi|[\mu_{1\mp1}, X^\dagger_{\rm wob}]|\Phi\rangle|^2, \tag{24}$$

where $X^\dagger_{\rm wob}$ is the wobbling phonon creation operator, and the $E2$ and $M1$ operators quantized with respect to the x axis,

$$Q_{2\pm1} = \frac{i}{\sqrt{2}}\left(Q^{(-)}_{21} \pm Q^{(-)}_{22}\right), \tag{25}$$

$$\mu_{1\pm1} = \pm\frac{i}{\sqrt{2}}(i\mu_y \mp \mu_z), \tag{26}$$

are introduced (see also Ref. [19]). Here $Q^{(\pm)}_{2K}$ $(K = 0, 1, 2)$ are electric quadrupole operators (z-axis quantization) with a good signature,

$$\begin{aligned}Q^{(-)}_{21} &= -\sqrt{\frac{15}{4\pi}}\, e \sum_{a=1}^{Z} (xz)^{(\pi)}_a,\\ Q^{(-)}_{22} &= i\sqrt{\frac{15}{4\pi}}\, e \sum_{a=1}^{Z} (xy)^{(\pi)}_a,\end{aligned} \tag{27}$$

and μ_k $(k = x, y, z)$ are magnetic dipole operators,

$$\mu_k = \sqrt{\frac{3}{4\pi}}\,\mu_N \sum_{a=1}^{A}\left(g^{(\tau)}_l l_k + g^{(\tau)}_s s_k\right)_a, \quad (\tau = \pi, \nu). \tag{28}$$

B. Axially symmetric limit and RPA precession equation

If the deformation is axially symmetric about the x axis, the angular momentum is generated not by the collective rotation, but by the alignment of the angular momenta of quasiparticles along the symmetry axis. The mean-field vacuum state $|\Phi\rangle$, a high-K state, is a multiple-quasiparticle excited state, and its spin value is the sum of the projections, Ω_μ, of their angular momenta on the symmetry axis; $I = K = \sum_\mu^{(\rm occ)} \Omega_\mu$, i.e., the time reversal invariance is spontaneously broken in $|\Phi\rangle$. In this case, the cranking term in Eq. (15) does not change the vacuum state $|\Phi\rangle$, so that the cranking frequency $\omega_{\rm cr}$ is a redundant variable. All observables should not depend on $\omega_{\rm cr}$. It is reflected in the fact that the quasiparticle energies linearly depend on the rotational frequency:

$$E_\mu(\omega_{\rm cr}) = E^0_\mu - \omega_{\rm cr}\Omega_\mu, \tag{29}$$

where E^0_μ are quasiparticle energies for the non-cranked mean-field Hamiltonian h. Since the eigenvalue of J_x, Ω, is a good quantum number, it is convenient to rewrite the RPA dispersion equation (16) in terms of the matrix elements of $J_\pm$ rather than iJ_y and J_z. After a little algebra, the equation decouples into two equations,

$$(\omega \pm \omega_{\rm cr})S_{\pm1}(\omega \pm \omega_{\rm cr}) = 0, \tag{30}$$

where the functions $S_\rho(\omega)$ with $\rho = \pm1$ determine the $\Delta\Omega = \pm1$ solutions, respectively, and are given by

$$\begin{aligned}S_{\pm1}(\omega) = \frac{1}{2}\sum_{\mu<\nu}\Bigg\{&\frac{(E_{\mu\nu} \pm \omega_{\rm cr})|J_\pm(\mu\nu)|^2}{E_{\mu\nu} \pm \omega_{\rm cr} - \omega}\\ &- \frac{(E_{\mu\nu} \mp \omega_{\rm cr})|J_\mp(\mu\nu)|^2}{E_{\mu\nu} \mp \omega_{\rm cr} + \omega}\Bigg\}.\end{aligned} \tag{31}$$

The precession is a $\Delta\Omega = +1$ mode, as is clear from the rotor model in Sec. II, and then only the $\Delta I = -1$ $E2$ and $M1$ transitions are allowed; i.e., their $\Delta I = +1$ probabilities vanish in Eqs. (23) and (24) because the two RPA transition amplitudes, $\langle\Phi|[Q^{(-)}_{21}, X^\dagger_{\rm wob}]|\Phi\rangle$ and $\langle\Phi|[Q^{(-)}_{22}, X^\dagger_{\rm wob}]|\Phi\rangle$, are the same in their absolute value with the opposite sign; a corresponding relation holds for the $M1$ amplitudes.

On the other hand, the y and z inertia are the same due to the axial symmetry about the x axis, and then, just like Eq. (11), Eq. (21) reduces to

$$\omega = \pm\frac{K}{\mathcal{J}^{(\rm eff)}_\perp(\omega)} \mp \omega_{\rm cr} \quad (\Delta\Omega = \pm1), \tag{32}$$

where $I = \langle\Phi|J_x|\Phi\rangle$ is denoted by K, and the perpendicular inertia $\mathcal{J}^{(\rm eff)}_\perp(\omega) \equiv \mathcal{J}^{(\rm eff)}_y(\omega) = \mathcal{J}^{(\rm eff)}_z(\omega)$ is simply written as

$$\mathcal{J}^{(\rm eff)}_\perp(\omega) = \mathcal{J}_\perp(\omega) \mp \mathcal{J}_{yz}(\omega) \quad (\Delta\Omega = \pm1), \tag{33}$$

with $\mathcal{J}_\perp(\omega) \equiv \mathcal{J}_y(\omega) = \mathcal{J}_z(\omega)$.

The vibrational treatment of the rotational band built on the high-K isomeric state in terms of the RPA has been done for a harmonic oscillator model in Refs. [21,22], and for realistic nuclei by employing the Nilsson potential in Ref. [23], followed by calculations with the Woods-Saxon potential in Ref. [24]. The residual interaction adopted in Refs. [23,24] is derived by applying the vibrating potential model of Bohr-Mottelson [30] to an infinitesimal rotation about the perpendicular axis, and is equivalent to the minimal coupling (12). In the axially symmetric case,

$$H_{\rm int} = -\tfrac{1}{4}\kappa(F^\dagger_+F_+ + F^\dagger_-F_-), \tag{34}$$

with $F_\pm$ being defined by using $J_\pm$ in Eq. (20),

$$F_\pm = \frac{i}{\kappa}[h, J_\pm], \quad \kappa = -\frac{1}{2}\langle\Phi|[[h, J_-], J_+]|\Phi\rangle. \tag{35}$$

Note that the mean-field state $|\Phi\rangle$ is now a multi-quasiparticle excited state for the noncranked mean-field Hamiltonian h, and so $\omega_{\rm cr}$ does not appear, although it can be used as the "sloping

Fermi surface" to obtain optimal states [42]. The cranking procedure is totally unnecessary in this approach.

The resultant RPA dispersion equations are given for the parts associated with the fields $F_\pm$ separately,

$$\omega\, S_{\pm 1}(\omega) = 0, \tag{36}$$

where the functions $S_{\pm 1}(\omega)$ are defined by

$$S_{\pm 1}(\omega) = \frac{1}{2}\sum_{\mu<\nu}\left\{\frac{E^0_{\mu\nu}|J_\pm(\mu\nu)|^2}{E^0_{\mu\nu}-\omega} - \frac{E^0_{\mu\nu}|J_\mp(\mu\nu)|^2}{E^0_{\mu\nu}+\omega}\right\}, \tag{37}$$

which turn out to be the same functions as Eq. (31) because of the property (29) of quasiparticle energies in the noncollective rotation scheme. It is worth mentioning that $S_{+1}(\omega) = -S_{-1}(-\omega)$, so that $\Delta\Omega = -1$ modes are obtained as negative energy solutions of the $\Delta\Omega = +1$ dispersion equation and *vice versa*. For the physical $\Delta\Omega = +1$ modes, the eigenenergies of the wobbling dispersion equation (30) and the precession one (36) are related as

$$\omega_{\rm wob} = \omega_{\rm prec} - \omega_{\rm cr}. \tag{38}$$

By comparing it with Eq. (32), we obtain

$$\omega_{\rm prec} = \frac{K}{\mathcal{J}^{(\rm eff)}_\perp}, \tag{39}$$

with $\mathcal{J}^{(\rm eff)}_\perp$ being written as

$$\mathcal{J}^{(\rm eff)}_\perp = \frac{1}{2}\sum_{\mu<\nu}\left\{\frac{|J_+(\mu\nu)|^2}{E^0_{\mu\nu}-\omega_{\rm prec}} + \frac{|J_-(\mu\nu)|^2}{E^0_{\mu\nu}+\omega_{\rm prec}}\right\}, \tag{40}$$

which is the microscopic RPA version of Eq. (10) in Sec. II. This $\mathcal{J}^{(\rm eff)}_\perp$ does not depend on $\omega_{\rm cr}$, while both $\mathcal{J}_\perp = \mathcal{J}_y = \mathcal{J}_z$ and $\mathcal{J}_{yz}$ in Eq. (33) do. This result can also be obtained directly from the precession dispersion Eq. (36). Note that the perpendicular inertia (40) reduces to the Inglis cranking inertia (or that of Belyaev if pairing is included) in the adiabatic limit $\omega_{\rm prec} \to 0$.

The reason why the $\omega_{\rm cr}$-dependent wobbling eigenenergy and the $\omega_{\rm cr}$-independent precession eigenenergy is related in a simple way (38) is that the RPA treatment in Refs. [21–24] is formulated in the laboratory frame, while Marshalek's wobbling theory is in the principal axis frame (body-fixed frame). The energies in the laboratory frame $E^{(\rm L)}$ and in the uniformly rotating frame described by the cranked mean-field $E^{(\rm UR)}$ are related by $E^{(\rm UR)} = E^{(\rm L)} - \Omega\omega_{\rm cr}$ for the state which has a projection Ω of angular momentum on the cranking axis. Moreover, the energies in the principal axis and the uniformly rotating frames are the same under the small amplitude approximation in the RPA. Thus the difference of phonon energies in (38) comes from the difference of coordinate frames where the two approaches are formulated. The rotational NG mode $\Gamma^\dagger$ (20) appears at zero energy in the precession dispersion Eq. (36) by the same reason. The transformation between the laboratory and the principal axis frames have been discussed more thoroughly in Refs. [14,22].

As for the electromagnetic transition probabilities in the precession formalism [23,24], the RPA vacuum state $|\mathrm{RPA}\rangle$ is considered to be a stretched eigenstate of the angular momentum $|I = K, M = K\rangle$, because $\Gamma|\mathrm{RPA}\rangle = 0$ for the NG mode (20) [$\Gamma \propto (J_+)_{\rm RPA}$]. In the same way, the $\Delta\Omega = +1$ one-phonon precession state $X^\dagger_{\rm prec}|\mathrm{RPA}\rangle$ corresponds to $|I = K+1, M = K+1\rangle$, because $\Gamma X^\dagger_{\rm prec}|\mathrm{RPA}\rangle = [\Gamma, X^\dagger_{\rm prec}]|\mathrm{RPA}\rangle = 0$. Then, by using the Wigner-Eckart theorem, we obtain, for example,

$$\begin{aligned}\langle I = K||\mathcal{M}(E2)||I = K+1\rangle &= \sqrt{2K+1}\frac{\langle \mathrm{RPA}|Q_{2-1}X^\dagger_{\rm prec}|\mathrm{RPA}\rangle}{\langle K+1\, K+1\, 2\, -1|K\, K\rangle}.\end{aligned} \tag{41}$$

Thus, by inserting explicit expressions of the Clebsch-Gordan coefficients, one finds

$$B(E2; K+1 \to K) = \frac{K+2}{K}|\langle\Phi|[Q_{2-1}, X^\dagger_{\rm prec}]|\Phi\rangle|^2, \tag{42}$$

$$B(M1; K+1 \to K) = |\langle\Phi|[\mu_{1-1}, X^\dagger_{\rm prec}]|\Phi\rangle|^2, \tag{43}$$

which coincide, within the lowest order in $1/K$, with Eqs. (23) and (24) in the wobbling formalism.

IV. RESULT AND DISCUSSION

A. Calculation of precession bands in ^{178}W

In the previous papers [11,12], we studied the wobbling motions in the triaxial superdeformed bands in Hf and Lu isotopes. As demonstrated in the previous section, the precession mode can be described as an axially symmetric limit of the RPA wobbling formalism. Thus we have performed calculations of the precession bands in ^{178}W, for which the richest experimental information is available [43–45]. Exactly the same wobbling formalism is used, but taking the prolate noncollective limit suitable for high-K isomers, i.e., the triaxiality parameter $\gamma = -120^\circ$ in the Lund convention. The first result for this nucleus, concentrating on the magnetic property, was reported already in Ref. [29].

The procedure of the calculation is the same as in Refs. [11,12,29]. The standard Nilsson potential [46] is employed as a mean field with the monopole pairing being included,

$$h = h_{\rm Nils}(\epsilon_2, \gamma) - \sum_{\tau=\nu,\pi}\Delta_\tau(P^\dagger_\tau + P_\tau) - \sum_{\tau=\nu,\pi}\lambda_\tau N_\tau. \tag{44}$$

Here the ϵ_4 deformation is neglected, and all the mean-field parameters are fixed for simplicity. There are a few refinements of calculation, however: (1) the difference of the oscillator frequencies for neutrons and protons in the Nilsson potential is taken into account, and the correct electric quadrupole operator is used, while Z/A times the mass quadrupole operator was used previously, and (2) the model space is fully enlarged; $N_{\rm osc} = 3$–8 for neutrons and 2–7 for protons, which guarantees the NG mode decoupling with sufficient accuracy in numerical calculations. As for point (1), $Q^{(\pi)} \approx (Z/A)(Q^{(\nu)} + Q^{(\pi)})$ usually, holds for static and RPA transitional quadrupole moments in stable nuclei, and therefore the simplification in the previous paper was a good approximation. It is, however, found that $Q^{(\pi)}$ is appreciably smaller, by about $4-8\%$, than $(Z/A)(Q^{(\nu)} + Q^{(\pi)})$ in ^{178}W. Thus, in this paper, we make a more precise calculation using the electric (proton) part of the quadrupole operator.

TABLE I. Configurations assigned for high-K isomers in ^{178}W [43–45], which are used in the RPA calculations for the precession bands excited on them. The experimental values of the precession one-phonon energy, $\omega_{\rm prec}^{\rm exp} = E_K(I = K + 1) - E_K(I = K)$, are also tabulated in the last column. The neutron states are $1/2^-[521]$, $5/2^-[512]$, $7/2^-[514]$, $\mathbf{7/2}^+[633]$, $\mathbf{9/2}^+[624]$, and $7/2^{-a}[503]$. The proton states are $\mathbf{1/2}^-[541]$, $5/2^+[402]$, $7/2^+[404]$, $9/2^-[514]$, and $11/2^-[505]$. The bold letters indicate the $h_{9/2}$ proton and the $i_{13/2}$ neutron quasiparticles.

K^π	Neutron configuration	Proton configuration	$\omega_{\rm prec}^{\rm exp}$(keV)
13^-	$\mathbf{7/2}^+, 7/2^-$	$5/2^+, 7/2^+$	164
14^+	$\mathbf{7/2}^+, 7/2^-$	$5/2^+, 9/2^-$	150
15^+	$\mathbf{7/2}^+, 7/2^-$	$7/2^+, 9/2^-$	207
18^-	$\mathbf{7/2}^+, 7/2^-$	$\mathbf{1/2}^-, 5/2^+, 7/2^+, 9/2^-$	184
21^-	$5/2^-, \mathbf{7/2}^+, 7/2^-, \mathbf{9/2}^+$	$5/2^+, 9/2^-$	362
22^-	$5/2^-, \mathbf{7/2}^+, 7/2^-, \mathbf{9/2}^+$	$7/2^+, 9/2^-$	373
25^+	$5/2^-, \mathbf{7/2}^+, 7/2^-, \mathbf{9/2}^+$	$\mathbf{1/2}^-, 5/2^+, 7/2^+, 9/2^-$	288
28^-	$5/2^-, \mathbf{7/2}^+, 7/2^-, \mathbf{9/2}^+$	$\mathbf{1/2}^-, 7/2^+, 9/2^-, 11/2^-$	328
29^+	$5/2^-, \mathbf{7/2}^+, 7/2^-, \mathbf{9/2}^+, 1/2^-, 7/2^{-a}$	$\mathbf{1/2}^-, 5/2^+, 7/2^+, 9/2^-$	437
30^+	$5/2^-, \mathbf{7/2}^+, 7/2^-, \mathbf{9/2}^+$	$5/2^+, 7/2^+, 9/2^-, 11/2^-$	559
34^+	$5/2^-, \mathbf{7/2}^+, 7/2^-, \mathbf{9/2}^+, 1/2^-, 7/2^{-a}$	$5/2^+, 7/2^+, 9/2^-, 11/2^-$	621

The calculation is performed for the high-K isomeric configurations listed in Table I; they cover almost all the multi-quasiparticle states higher than or equal to four (more than or equal to two quasineutrons and two quasiprotons), on which rotational bands are observed. The quadrupole deformation is chosen to be $\epsilon_2 = 0.240$, which reproduces in a rough average the value $Q_0 = 7.0$ b for the configurations in Table I assumed in the experimental analyses [44,45]. The pairing gap parameters are taken, for simplicity, to be 0.5 MeV for two-quasiparticle configurations, and 0.01 MeV for those with more than or equal to four quasiparticles, both for neutrons and protons. Chemical potentials λ_τ ($\tau = \nu, \pi$) are always adjusted so as to give correct neutron and proton numbers. These mean that the choice of parameters in this work is semiquantitative. As explained in detail in Sec. III, the final results do not depend on the cranking frequency $\omega_{\rm cr}$ at all for the noncollective rotation about the x axis. We have confirmed this fact numerically and used $\omega_{\rm cr} = 0.001$ MeV in actual calculations. (Note that the RPA wobbling formalism requires a finite frequency in numerical calculations.) No effective charge is used for the $E2$ transitions, and $g_s^{\rm (eff)} = 0.7 g_s^{\rm (free)}$ is used for the $M1$ transitions as usual.

We have checked the dependences of the results on the variations of the deformation parameter ϵ_2 and pairing gaps. Those on the pairing gaps are shown in Fig. 3. In this figure, the excitation energy ω and the RPA transition amplitude for the electric $Q_{22}^{(-)}$ operator (28), $\mathcal{Q} \equiv |\langle [Q_{22}^{(-)}, X_{\rm prec}^\dagger] \rangle|$, which is a measure of the $E2$ collectivity, for the precession modes excited on the $K = 25^+$ and $K = 30^+$ configurations, are shown as functions of the pairing gap, $\Delta = \Delta_\pi = \Delta_\nu$ (the common value for protons and neutrons). For reference sake, the results are also included for the γ vibrations on the ground states, i.e., the $\Delta K = \pm 2$ vibrational mode excited on the $\gamma = 0^\circ$ prolate mean field (without cranking), for ^{166}Er, ^{168}Yb, and ^{178}Hf nuclei. Note that the meaning of the operator $Q_{22}^{(-)}$ is different for $\gamma = -120^\circ$ and $\gamma = 0^\circ$ shapes, so that the comparison of the magnitude of the amplitude $\mathcal{Q}$ is not meaningful between the precession mode and the γ-vibrational mode. As stressed in Sec. III A, the precession mode is calculated without any ambiguity once the mean field is fixed; we have just used the same parameters explained above with the exception that the pairing gaps are varied. The situation for the γ vibration is different; one has to include

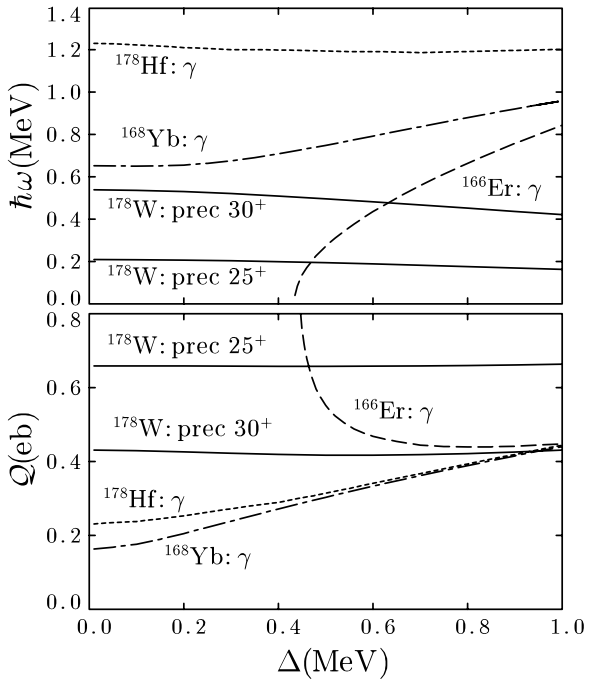

FIG. 3. Dependence of numerical results on the pairing gap parameter $\Delta = \Delta_\pi = \Delta_\nu$. Upper panel shows the excitation energies; lower panel, the RPA transition amplitudes for the electric $Q_{22}^{(-)}$ operator (28). Solid curves show results for the precession modes excited on the 25^+ and 30^+ high-K states in ^{178}W; dotted, dashed, and dot-dashed curves represent those for the γ vibrations in ^{166}Er, ^{168}Yb, and ^{178}Hf, respectively.

TABLE II. Mean-field parameters used in the calculation for the γ vibrations on the ground states ($\gamma = 0^\circ$), and observed excitation energies of γ vibrations [47]. ϵ_2 values are taken from Ref. [48], where they are deduced from the measured $B(E2: 0_g^+ \to 2_g^+)$ values. Even-odd mass differences are calculated by the third-order difference formula using the binding energy data in Ref. [49].

Nucleus	ϵ_2	Δ_ν (MeV)	Δ_π (MeV)	$\omega_\gamma^{\rm exp}$ (MeV)
^{166}Er	0.272	0.966	0.877	0.786
^{168}Yb	0.258	1.039	0.983	0.984
^{178}Hf	0.227	0.694	0.824	1.175

components other than the minimal coupling, (12) or (34). We use the $K = 2$ part of the doubly stretched $Q''Q''$ force, and the force strength is determined in such a way that the calculations with adopting the even-odd mass differences as pairing gap parameters reproduce the experimental energies of the γ vibration; see Table II for the parameters and data used. Then, with the use of the force strength thus fixed, calculations are performed while varying the pairing gaps.

As clearly seen in Fig. 3, the reduction of pairing gaps makes the excitation energies of γ vibration change in various ways depending on the shell structure near the Fermi surface; i.e., the distribution of the $\Delta\Omega = \pm 2$ quasiparticle excitations, which have large quadrupole matrix elements. The energy becomes smaller and smaller in the case of ^{166}Er, and finally leads to an instability ($\omega_\gamma \to 0$); accordingly, the transition amplitude $\mathcal{Q}$ diverges. No instability takes place in the case of ^{168}Yb, and the excitation energy decreases with decreasing Δ, while it is almost constant for the γ vibration in ^{178}Hf. However, the transition amplitudes $\mathcal{Q}$ reduce by about 40–60% with decreasing Δ except for ^{166}Er. These are well-known features for the low-lying collective vibrations; namely, the collectivities of the vibrational mode are sensitive to the pairing correlations and especially enhanced by them. In contrast, for the case of the precession modes, the excitation energies are stable and transition amplitudes are surprisingly constant against the change of the pairing gap. This is a feature common to the wobbling mode excited on the triaxial superdeformed band [12]. Although both the precession (or the wobbling) and the γ vibration are treated as vibrational modes in the RPA, the structures of their vacua are quite different; the time reversal invariance is kept in the ground state while it is spontaneously broken in the high-spin intrinsic states. Since the precession or the wobbling is a part of rotational degrees of freedom, this symmetry-breaking may be an important factor to generate these modes. It should be mentioned that the transition amplitude $\mathcal{Q}$ for ^{166}Er leads to about a factor of 2 larger $B(E2: 2_\gamma^+ \to 0_g^+)$ value than the observed one in the present calculation, in which the model space employed is large enough. The RPA calculation overestimates the $B(E2)$ transition probability for the low-lying γ vibration if the Nilsson potential is used as a mean field and the simple pairing plus $Q''Q''$ force is used as a residual interaction [50].

There are many RPA solutions in general, and it is not always guaranteed that the collective solution exists. In some cases, collective solutions split into two or more, whose energies are close, and the collectivity is fragmented (the Landau damping), or the character of the collective solution is exchanged. Moreover, in the case of precession-like solutions, the $\Omega = \pm 1$ modes interact with each other, as shown in Ref. [23]. In fact, when the deformation is changed, it is found that the precession mode on the $K^\pi = 15^+$ configuration disappears for $\epsilon_2 > 0.250$, and that on the $K^\pi = 14^-$ splits into two for $\epsilon_2 > 0.245$. Similar situations also occur when changing the pairing gap parameters in a few cases. Apart from these changes, the results are rather stable against the change of the mean-field parameters. The fact that we have been able to obtain collective solutions for all the cases listed in Table I indicates that our choice of mean-field parameters are reasonable if not the best.

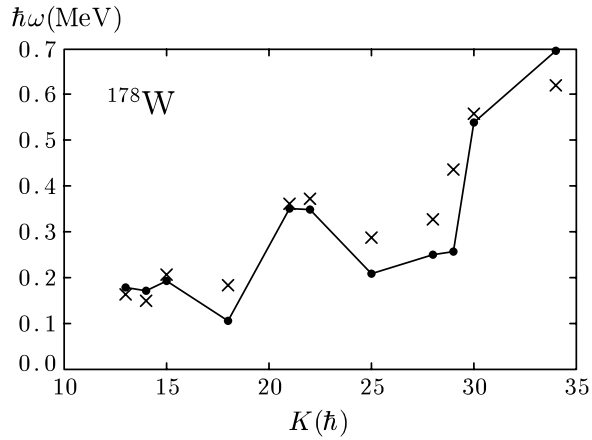

FIG. 4. Excitation energies of the one-phonon precession modes excited on high-K configurations. Calculated energies are denoted by filled circles connected by solid lines; experimental data, by crosses. Data are from Refs. [44,45].

Figure 4 presents the calculated and observed relative excitation energies of the first rotational band member, $E_{I=K+1} - E_{I=K}$, i.e., the one-phonon precession energies. Corresponding perpendicular moments of inertia, Eq. (39), are shown in Fig. 5, where the contributions to the inertia from protons and neutrons are also displayed. Our RPA calculation reproduces the observed trend rather well in a wide range of isomeric configurations, from four- to ten-quasiparticle excitations. This is highly nontrivial because, as stressed in Sec. III, we have no adjustable parameter in the RPA for the calculation of the precession modes once the mean-field vacuum state is given. With a closer look, however, one finds deviations, especially at $K^\pi = 18^-, 25^+, 28^-$, and 29^+. The precession energies on them are smaller in comparison with others, but the calculated ones are too small. Low calculated energies correspond to large perpendicular moments of inertia as clearly seen in Fig. 5. These four configurations contain the proton high-j decoupled orbital (i.e., with $\Omega = \pm 1/2$) $\pi[541]1/2^-$ originating from the $h_{9/2}$, whose decoupling parameter is large. Occupation of such an orbital makes the Inglis moment of inertia, which is given by Eq. (40) with setting $\omega_{\rm prec} = 0$, diverge due to the zero-energy excitation from an occupied $\Omega = +1/2$ quasiparticle state to an empty

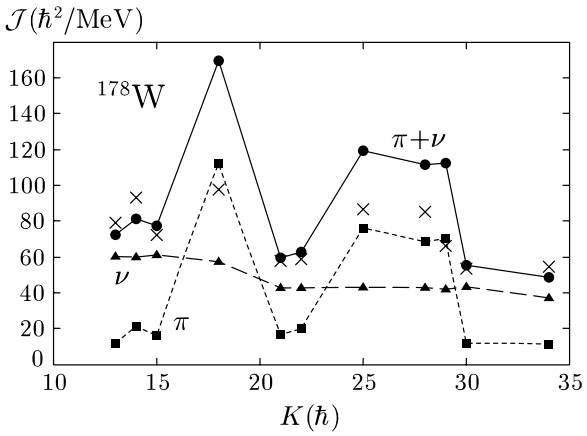

FIG. 5. Moments of inertia associated with the precession bands built on high-K configurations. The RPA effective inertia (40) are shown by filled circles connected by solid lines, the proton part of them by filled squares connected by dotted lines, and the neutron part by filled triangles connected by dashed lines. The crosses are values extracted from the experimental spectra according to the simple relation (39).

$-1/2$ state. The reason for a too large moment of inertia may be overestimation of this effect for the proton contribution in the calculation. The large effect of this $\pi h_{9/2}$ orbital on the moment of inertia has been pointed out also in Refs. [25,51].

Except for the case of four configurations including the $\pi[541]1/2^-$ orbital, the values of moments of inertia are about 50–80 $\hbar^2$/MeV, which are smaller than the rigid-body value, $\mathcal{J}_{\rm rig} = 87.8\ \hbar^2$/MeV, and considerably larger than the ground state value, $\mathcal{J}_{\rm gr} = 28.3\,\hbar^2$/MeV. Here $\mathcal{J}_{\rm rig}$ is calculated by assuming the ^{178}W nucleus as an ellipsoidal body with $\epsilon_2 = 0.240$ and $r_0 = 1.2$ fm, and $\mathcal{J}_{\rm gr}$ by $3/E_{2^+}$. The pairing gaps are already quenched in the calculation for more than or equal to eight-quasiparticle (four-quasiprotons and four-quasineutrons) configurations ($K \geqslant 25^+$). The value 0.5 MeV of the pairing gap used for two-quasiparticle configurations is already small enough to make the moment of inertia quite large. It is also noticed that the moment of inertia decreases with increasing K, which is opposite to intuition and clearly indicates the importance of the shell effect to the moment of inertia [52]. In Refs. [25,44], the angular momentum of the precession band is divided into the collective and aligned ones; the inertia defined in Eq. (39) includes both of them. It is shown that the collective inertia, in which the effect of the aligned angular momentum of the high-j decoupled orbital is removed, takes the value 50–60 $\hbar^2$/MeV consistent with the other configurations. As shown in Fig. 5, the proton contribution to the inertia is about 20–30% (except for the four configurations above), which is considerably smaller than Z/A but consistent with the calculated value for the g_R factor in the ground state rotational band (see below).

As for the electromagnetic transitions in the rotational bands built on high-K isomers, the strong coupling rotational model [30] is utilized as a good description. The expressions for $B(E2)$ and $B(M1)$ are well known:

$$B(E2: I = K+1 \to K)_{\rm rot} = \frac{5}{16\pi}\, e^2 Q_0^2 \langle K+1\, K\, 20 | K\, K\rangle^2 \tag{45}$$

$$\approx \frac{15}{16\pi}\frac{1}{K} e^2 Q_0^2, \tag{46}$$

$$B(M1: I = K+1 \to K)_{\rm rot} = \frac{3}{4\pi}\mu_N^2 (g_K - g_R)^2 K^2 \langle K+1\, K\, 10 | K\, K\rangle^2 \tag{47}$$

$$\approx \frac{3}{4\pi}\mu_N^2 (g_K - g_R)^2 K, \tag{48}$$

where, in the last lines, the Clebsch-Gordan coefficients are replaced with their lowest order expressions in $1/K$. Q_0 and $(g_K - g_R)$ can be extracted from experiments; the sign of the mixing ratio is necessary to determine the relative sign of them. These quantities are calculated within the mean-field approximation,

$$Q_0 = \sqrt{\frac{16\pi}{5}}\frac{1}{e}\langle Q_{20}\rangle = \left\langle \sum_{a=1}^{Z} (2x^2 - y^2 - z^2)_a^{(\pi)} \right\rangle, \tag{49}$$

$$g_K = \sqrt{\frac{4\pi}{3}}\frac{\langle \mu_x\rangle}{\mu_N \langle J_x\rangle}, \quad g_R = \sqrt{\frac{4\pi}{3}}\frac{\langle \mu_x\rangle_{\rm gr}}{\mu_N \langle J_x\rangle_{\rm gr}}, \tag{50}$$

where $\langle\,\rangle$ means that the expectation value is taken with respect to the high-K configuration ($\gamma = -120^\circ$), e.g., $\langle J_x\rangle = K$; and $\langle\,\rangle_{\rm gr}$, with respect to the ground state rotational band ($\gamma = 0^\circ$). The latter expectation value is calculated by the cranking prescription (15), with the same ϵ_2 and with the even-odd mass differences as pairing gaps. The value of g_R is thus $\omega_{\rm cr}$ dependent, but its dependence is weak at low frequencies, so we take the value $g_R = 0.227$ obtained at $\omega_{\rm cr} \to 0$, which is much smaller than the standard value, $Z/A = 0.416$.

On the other hand, $B(E2)$ and $B(M1)$ are calculated by Eqs. (23) and (24), respectively, in the RPA wobbling formalism which is in the lowest order in $1/K$. By equating these expressions with those of the rotational model (46) and (48), we define the corresponding quantities in the RPA formalism by ($K = \langle J_x\rangle$)

$$(Q_0)_{\rm RPA} = \sqrt{\frac{16\pi K}{15}}\frac{1}{e}\,\langle [X^\dagger_{\rm prec}, Q_{2-1}]\rangle, \tag{51}$$

$$(g_K - g_R)_{\rm RPA} = \sqrt{\frac{4\pi}{3K}}\frac{1}{\mu_N}\,\langle [X^\dagger_{\rm prec}, \mu_{1-1}]\rangle. \tag{52}$$

Only their relative phase is meaningful, and the overall phase is chosen in such a way that $(Q_0)_{\rm RPA}$ is positive. We compare calculated values of Q_0 in the usual mean-field approximation (49) and in the RPA formalism (51) in Fig. 6 for all high-K configurations listed in Table I. These two calculated Q_0's roughly coincide with each other, but appreciable deviations are seen for the $K^\pi = 18^-, 25^+, 28^-$, and 29^+ isomers. The high-j decoupled orbital $\pi[541]1/2^-$ has a large prolate quadrupole moment, so its occupation generally leads to a

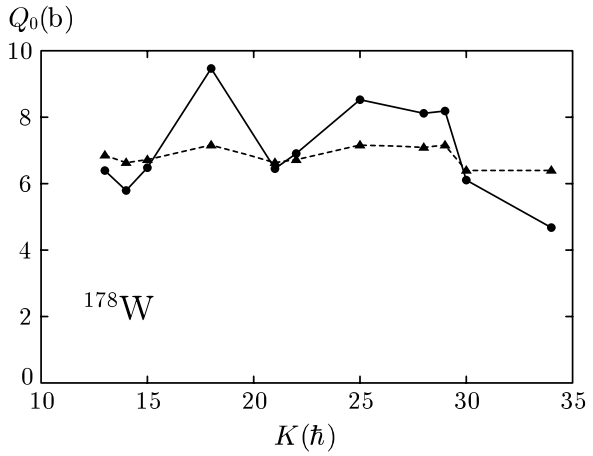

FIG. 6. Quadrupole moments Q_0 for high-K configurations. Those calculated by the RPA, Eq. (51), are denoted by filled circles connected by solid lines; those by the mean-field approximation (49), by filled triangles connected by dotted lines.

larger value of Q_0. This is clearly seen in Fig. 6 even if ϵ_2 is fixed in our calculation. See Ref. [53], for example, for the polarization effect of this high-j orbital on Q_0. Notice, however, that the effect is even larger in the RPA calculation, just as in the case of the excitation energy in Fig. 4. For the 34^+ isomer, we have found a less collective RPA solution at a lower energy, 560 keV, which has about 80% of the $(Q_0)_{\rm RPA}$ value of the most collective one presented in the figure. The reason why $(Q_0)_{\rm RPA}$ for the 34^+ isomer is considerably small is traced back to this fragmentation of the precession mode in this particular case. This kind of fragmentation sometimes happens in the RPA calculation.

In Fig. 7, we compare the effective $(g_K - g_R)$ factors extracted from the experimental data and those calculated in two ways, Eq. (50) and Eq. (52). As for the observed ones, they were determined [44,45] from the branching ratios of available lowest transitions in respective rotational bands, by using the rotational model expressions (45) and (47) with $Q_0 = 7.0$ b being assumed. In this way, absolute value $|g_K - g_R|$ is obtained, and we assume that its sign is determined by that of the calculated $E2/M1$ mixing ratio in the RPA result. Accordingly, some care is necessary to compare the experimentally extracted g factors with calculations. The agreement between the observed and calculated ones is semiquantitative, but the RPA result follows the observed trend rather well. Compared to the RPA g factors, those calculated by the mean-field approximation are poorer. Again, the two calculations deviate appreciably for the $K^\pi = 18^-, 25^+, 28^-$, and 29^+ configurations, where the high-j decoupled orbital $\pi[541]1/2^-$, which has a large positive g factor, is occupied. The difference between the mean-field $(g_K - g_R)$ and $(g_K - g_R)_{\rm RPA}$ is further discussed in the next subsection by studying the adiabatic limit of the precession mode in the RPA.

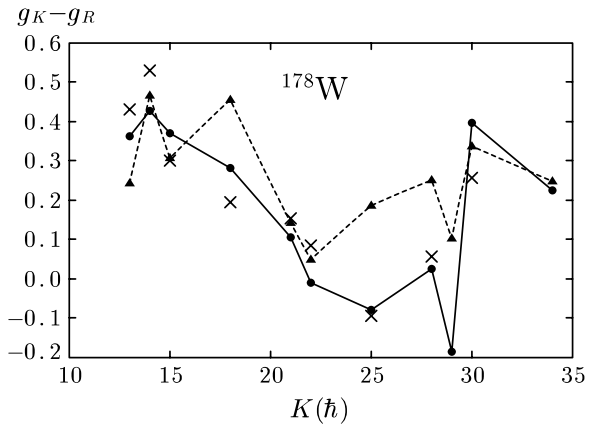

FIG. 7. Effective $(g_K - g_R)$ factors for high-K configurations. Those calculated by the RPA, Eq. (52), are denoted by filled circles connected by solid lines; those by the mean-field approximation (49), by filled triangles connected by dotted lines. Those extracted from the experimental data [44,45] are shown by crosses.

B. Interpretation of the result in the adiabatic limit

As demonstrated in the previous subsection, the RPA calculation reproduces the precession phonon energies without any kind of adjustments. The electromagnetic properties obtained through the RPA wobbling formalism are in good agreement with those of the strong coupling rotational model, where the quadrupole moments and the effective g factors are calculated within the mean-field approximation. Since the rotational band is described as multi-phonon excitations in the RPA wobbling (or precession) model, it is not apparent that two models lead to similar results for observables. Our results indicate, however, that the RPA treatment of the rotational excitations is valid; it especially gives a reliable microscopic framework for studying the wobbling motion recently observed.

The reason why the RPA precession mode gives the $B(E2)$ and $B(M1)$ similar to those calculated according to the rotational model is inferred by taking the adiabatic limit $(\omega_{\rm prec} \to 0)$ of the RPA phonon creation operator. It has been shown in Ref. [22] that the precession phonon can be explicitly written up to the first order in $\omega_{\rm prec}$ as

$$X^\dagger_{\rm prec} \approx \frac{1}{\sqrt{2K}}\left(J_+ + \omega_{\rm prec}\mathcal{J}^{\rm cr}_\perp i\Theta_+\right)_{\rm RPA} \approx \frac{1}{\sqrt{2K}}(J_+ + K\, i\Theta_+)_{\rm RPA}. \quad (53)$$

Here the angle operator Θ_+ is defined by

$$\Theta_\pm = \Theta_y \pm i\Theta_z, \quad [h, i\Theta_k] = \frac{1}{\mathcal{J}^{\rm cr}_\perp}J_k, \quad (k = y, z), \quad (54)$$

where $\mathcal{J}^{\rm cr}_\perp$ is the Inglis cranking inertia and given from the effective inertia (40) by setting $\omega_{\rm prec} = 0$. These angle operators possess desired properties,

$$\langle[\Theta_k, J_l]\rangle = i\delta_{kl}. \quad (55)$$

For the $E2$ transitions, the contribution of the Θ_+ part in Eq. (53) proves to be negligible if the harmonic oscillator potential is taken as a mean field that is,

$$\langle[X^\dagger_{\rm prec}, Q_{2-1}]\rangle \approx \frac{1}{\sqrt{2K}}\langle[J_+, Q_{2-1}]\rangle = \sqrt{\frac{3}{K}}\,\langle Q_{20}\rangle, \quad (56)$$

which precisely means $Q_0 \approx (Q_0)_{\rm RPA}$ in the adiabatic limit.

As for the $M1$ transitions, however, the Θ_+ part also contributes:

$$\langle [X^\dagger_{\rm prec}, \mu_{1-1}]\rangle \approx \frac{1}{\sqrt{2K}}(\langle [J_+, \mu_{1-1}]\rangle + K\,\langle [i\Theta_+, \mu_{1-1}]\rangle) = \frac{1}{\sqrt{K}}\Big(\langle \mu_x\rangle - \frac{K}{\sqrt{2}}\,\langle [\mu_{1-1}, i\Theta_+]\rangle\Big), \quad (57)$$

which gives $(g_K - g_R) \approx (g_K - g_R)_{\rm RPA}$ if we identify

$$g_R \leftrightarrow \hat{g}_R \equiv \sqrt{\frac{2\pi}{3}}\frac{1}{\mu_N}\,\langle [\mu_{1-1}, i\Theta_+]\rangle. \quad (58)$$

This identification is reasonable. The magnetic moment operator μ_{1-1} possesses a property of angular momentum and is approximately proportional to J_-. Then the expectation value of the right-hand side of Eq. (58) is expected to depend only weakly on the high-K configuration because of Eq. (55). More precisely, if the operators J_-, Θ_+, and μ_{1-1} are divided into the neutron and proton parts like

$$J_- = J_-^{(\pi)} + J_-^{(\nu)}, \quad \Theta_+ = \Theta_+^{(\pi)} + \Theta_+^{(\nu)}, \qquad \mu_{1-1} \approx \sqrt{\frac{3}{8\pi}}\,\mu_N\big(g^{(\pi)}J_-^{(\pi)} + g^{(\nu)}J_-^{(\nu)}\big), \quad (59)$$

then the following relation is derived,

$$\hat{g}_R \approx \frac{g^{(\pi)}\mathcal{J}_\perp^{{\rm cr}(\pi)} + g^{(\nu)}\mathcal{J}_\perp^{{\rm cr}(\nu)}}{\mathcal{J}_\perp^{{\rm cr}(\pi)} + \mathcal{J}_\perp^{{\rm cr}(\nu)}}, \quad (60)$$

because of $\langle [J_-^{(\tau)}, i\Theta_+^{(\tau)}]\rangle = 2\mathcal{J}_\perp^{{\rm cr}(\tau)}/\mathcal{J}_\perp^{\rm cr}$ with $\mathcal{J}_\perp^{\rm cr} = \mathcal{J}_\perp^{{\rm cr}(\pi)} + \mathcal{J}_\perp^{{\rm cr}(\nu)}$ $(\tau = \pi, \nu)$. With a cruder estimate $\langle [J_-^{(\tau)}, i\Theta_+^{(\tau)}]\rangle \approx 2N_\tau/A$ $(\tau = \pi, \nu)$, one finds a constant $g_R \approx \sum_\tau N_\tau g^{(\tau)}/A$, which gives a classical result, Z/A, by setting $g^{(\pi)} = 1$ and $g^{(\nu)} = 0$.

An approximate relation $g_R = \mathcal{J}^{(\pi)}/(\mathcal{J}^{(\pi)} + \mathcal{J}^{(\nu)})$, which corresponds to Eq. (60) with $g^{(\pi)} = 1$ and $g^{(\nu)} = 0$, has been used for the ground state rotational band, i.e., the case of collective rotations [54]. It seems, however, difficult to justify a similar relation, $g_R = Z\mathcal{J}^{(\pi)}/(Z\mathcal{J}^{(\nu)} + N\mathcal{J}^{(\pi)})$, which is used in Ref. [44]. Thus, the "rotor g factor" g_R is not a common constant, but it also depends on the high-K configurations as the intrinsic g factor g_K does. To see how the approximate relation (60) holds, we compare, in Fig. 8, the two calculated quantities, $g_K - (g_K - g_R)_{\rm RPA}$ and $\mathcal{J}_\perp^{({\rm eff},\pi)}/(\mathcal{J}_\perp^{({\rm eff},\pi)} + \mathcal{J}_\perp^{({\rm eff},\nu)})$, where the cranking inertia $\mathcal{J}_\perp^{{\rm cr}(\tau)}$, which diverges when the $\pi[541]1/2^-$ orbital is occupied, is replaced with the neutron or proton part of the effective inertia (40), see also Fig. 5. As seen in the figure, these two quantities are in good agreement with each other, again, except for the $K^\pi = 18^-, 25^+, 28^-$, and 29^+ configurations, where the high-j decoupled orbital is occupied and $\mathcal{J}_\perp^{({\rm eff},\pi)}/(\mathcal{J}_\perp^{({\rm eff},\pi)} + \mathcal{J}_\perp^{({\rm eff},\nu)})$ is very large. The excitation energies are underestimated for these high-K configurations. Therefore, the proton moments of inertia are overestimated for them; in fact the proton contributions are considerably larger than the neutron ones in these configurations, as shown in Fig. 5. Apart from these four configurations, the deduced g_R factors in Fig. 8 are similar to

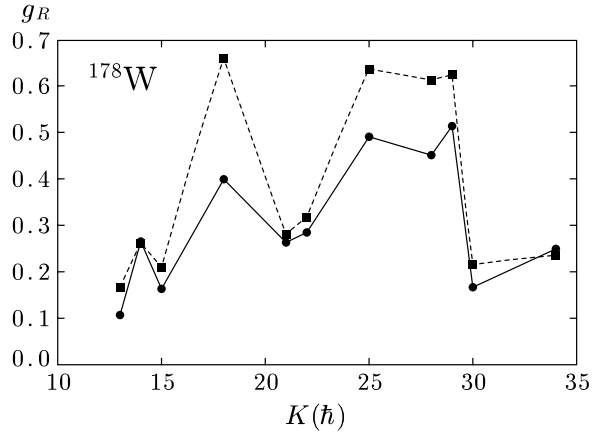

FIG. 8. Comparison of deduced g_R from two calculations. One from $g_K - (g_K - g_R)_{\rm RPA}$ is denoted by filled circles connected by solid lines; the quantity $\mathcal{J}_\perp^{({\rm eff},\pi)}/(\mathcal{J}_\perp^{({\rm eff},\pi)} + \mathcal{J}_\perp^{({\rm eff},\nu)})$, by filled squares connected by dotted lines.

the ground state value, 0.227, though it is appreciably different from the standard value, $Z/A = 0.416$. For reference, the cranking moment of inertia for the ground state rotational band calculated using the even-odd mass differences as pairing gaps is $\mathcal{J}_\perp^{\rm cr} = 22.7\,\hbar^2$/MeV (about 80% of the experimental value, see the previous subsection). The proton contribution to it is $6.1\,\hbar^2$/MeV and $\mathcal{J}_\perp^{({\rm cr})(\pi)}/(\mathcal{J}_\perp^{({\rm cr})(\pi)} + \mathcal{J}_\perp^{({\rm cr})(\nu)}) = 0.269$, which is slightly larger but consistent with the calculated ground state g_R value, 0.227.

The above results indicate that the rotor g_R should be considered to depend also on the intrinsic configurations, but the dependence is conspicuous only for those including the high-j decoupled orbit, which has a large decoupling parameter as well as a large g factor. The reason why the effective $(g_K - g_R)$ factors of the RPA calculation reproduce the experimentally extracted ones better than those of the mean-field g factors is inferred as follows. Since, as is well known, the g factors of proton orbitals are much larger than those of neutron orbitals, the amount of the proton contribution is overwhelming for the mean value $\langle \mu_x\rangle$ in comparison with that for $\langle J_x\rangle$. Considering this fact together with the overestimation of the proton moments of inertia mentioned in the previous paragraph, it is likely that the calculated values of g_K (50) for the $K^\pi = 18^-, 25^+, 28^-$, and 29^+ configurations with a proton high-j decoupled orbital are also overestimated. In the mean-field calculation, the calculated values of $(g_K - g_R)$ for those configurations are thus relatively large, because the common ground state g_R factor (50) is used. This trend can be seen also in the similar type of mean-field calculations in Refs. [44,45]. (Note that different g_R factors are used in [44] and [45].) In the RPA calculation, however, the rotor g factor is given by $\hat{g}_R$, (58) or (60), which is overestimated for these four configurations (see Fig. 8). Thus, the overestimation of two g factors may largely cancel out in the resulting $(g_K - g_R)_{\rm RPA}$ values, yielding a reasonable agreement with the experimental data seen in Fig. 7.

The realistic mean field is not very different from the harmonic oscillator potential, so the approximate equality (56)

for the $E2$ operator is expected to hold in general cases. However, it is not very clear to what extent this equality holds. It is a subtle problem of whether the adiabatic approximation holds because the precession phonon energies are 200 to 600 keV, which are not negligible compared to the quasiparticle excitation energies. (Note that the pairing gap is quenched in high-K conconfigurations.) In addition to the deviations caused by the nonadiabatic effects, the adiabatic approximation itself breaks down if one quasiparticle in a pair of high-j decoupling orbits ($\Omega_\mu = \pm 1/2$) is occupied, because the Inglis cranking moment of inertia diverges due to the zero denominator. In such cases, the present RPA calculation eventually overestimates the moment of inertia, although it does not diverge. This effect is also reflected in the calculated transition moments $(Q_0)_{\rm RPA}$ and the effective g factors, which are rather different from the values given by the mean fields. Whether the RPA calculation gives reliable results for such cases where the nonadiabatic effect is large is an important future issue. The direct measurement of Q_0 [i.e., $B(E2)$ value] for the precession band is desirable for this purpose.

V. CONCLUDING REMARKS

We have investigated the precession bands, i.e., the strongly coupled rotational bands excited on high-K intrinsic configurations, by means of the RPA, the microscopic theory for vibrations. It is demonstrated that the observed trend of the precession phonon energies in ^{178}W is well reproduced by the RPA calculation. This is highly nontrivial because we have employed the minimal coupling interaction, which is determined by the mean field and the vacuum state based on it, and so there are no adjustable force parameters whatsoever.

It is emphasized that this precession mode is related to the three-dimensional motion of the angular momentum vector in the principal axis frame (body-fixed frame), where a collective rotation about the perpendicular axis is superimposed on the large noncollective rotation about the symmetry axis (high-K quasiparticle alignments). It has been shown that such a precession mode can be obtained by taking an axially symmetric limit of more general wobbling motions in the microscopic framework of the cranked-RPA theory. The unique feature of the ideal wobbling motion is the triaxiality of deformation, which means that the system can rotate collectively around all three principal axes. It is, however, noticed that the single-particle alignments are known to contribute equally well to high-spin states in real nuclei. Actually, in the case of Lu, Hf nuclei, where the wobbling phonon bands are observed, the $\pi i_{13/2}$ quasiparticle alignments play important roles [11,12,20]. The angular momentum along the main rotation (cranking) axis is composed of the collective and the single-particle degrees of freedom in the microscopic cranking formalism. Then the axially symmetric limit of the non-collective rotation scheme can be naturally taken from the case of triaxial deformation; the portion of the single-particle alignments increases in the course of taking the limit, and finally it describes the high-K isomeric state (100% alignments). Although the unique feature of the triaxial wobbling motion is lost in this limit, the precession mode is still interesting because it corresponds to the eigenmode of a nonuniform rotational motion of a classical symmetric top. It gives us a hint as to how a nucleus rotates as a three-dimensional object.

The electromagnetic properties, the $E2$ and $M1$ transition probabilities, are also important for this kind of collective excitation modes. We have shown that the calculated $B(E2)$ and $B(M1)$ in terms of the RPA correspond to those given by the conventional rotational model expressions, where the intrinsic quadrupole moment and the effective g factors are calculated within the mean-field approximation. The link between the RPA and the rotational model expressions is given in the adiabatic limit, where the precession phonon energy goes to zero. Then the rotor g_R factor is not a common factor any more, but depends on the configurations, especially on the occupation of the high-j decoupled proton orbital. Since the RPA formalism includes this effect properly, the calculated $B(M1)$ values reproduce the experimentally deduced ones rather well. It is, however, noticed that the adiabatic approximation is not necessarily a good approximation because the precession energies are not very small; more crucially, if a high-j decoupled orbital with $\Omega = 1/2$ is occupied, the approximation breaks down completely. Therefore, it is an important future task to examine how the nonadiabatic effect plays a role in the realistic cases. More experimental data, especially $B(E2)$ and $B(M1)$ values, are necessary for this purpose.

Finally, it is worth mentioning the similar RPA calculations for the wobbling motion in the Lu and Hf region. We have presented the result in recent papers [11,12]. Although we obtained the RPA solutions, which have expected properties of the wobbling motion, the calculated out-of-band over in-band $B(E2)$ ratios were smaller than the measured ones by about a factor 2 to 3; this was the most serious problem in our microscopic calculation. The measured ratio is almost reproduced by the simple rotor model. Both the out-of-band and in-band $B(E2)$, which are vertical and horizontal transitions discussed in Sec. II, are expressed in terms of the intrinsic quadrupole moments Q_{20} and Q_{22} [30] [or e.g., deformation parameters (ϵ_2, γ)], combined with the wobbling phonon amplitudes. In the RPA wobbling formalism, on the other hand, the in-band transition is calculated by the intrinsic moments; while the out-of-band transition is calculated by the RPA phonon transition in Eq. (23). Thus the underestimation of the $B(E2)$ ratio above means that the RPA phonon transition amplitudes are smaller by about 50−70% than the expected ones.

The adiabatic approximation can also be considered for the case of the wobbling phonon [14]. Similar correspondence between the intrinsic moments and the RPA transition amplitudes, like $Q_0 \approx (Q_0)_{\rm RPA}$ in the present paper, is obtained with a nontrivial modification: two amplitudes are related to the operators $Q_{21}^{(-)}$ and $Q_{22}^{(-)}$ in Eq. (28), and $B(E2)$ is calculated by a linear combination of them with coefficients involving the three moments of inertia. Therefore, incorrect coefficients of amplitudes would make $B(E2)$ values deviate considerably, even though the adiabatic approximation is applicable and two amplitudes are obtained in a good approximation. There is, of course, another possibility that the adiabatic approximation

itself is no longer valid. It should be noted that the wobbling excitation energies observed in Lu isotopes are about 200−500 keV, which are not small if translated to the transition phonon energy in the laboratory frame, $\omega_{\rm wob} + \omega_{\rm cr}$; see Eq. (38). In light of the present investigation, it may be possible that the RPA approach yields the correct magnitude of out-of-band transitions also for the case of the wobbling mode, because it actually does in the case of the precession phonon bands. Thus, it is a very important future issue to examine whether the RPA wobbling formalism can describe the observed $B(E2)$ ratio in the Lu and Hf region.

ACKNOWLEDGMENTS

This work was supported by the Grant-in-Aid for Scientific Research (No. 16540249) from the Japan Society for the Promotion of Science.

[1] S. W. Ødegård *et al*., Phys. Rev. Lett. **86**, 5866 (2001).
[2] D. R. Jensen *et al*., Nucl. Phys. **A703**, 3 (2002).
[3] D. R. Jensen *et al*., Phys. Rev. Lett. **89**, 142503 (2002).
[4] I. Hamamoto, Phys. Rev. C **65**, 044305 (2002).
[5] I. Hamamoto and G. B. Hagemann, Phys. Rev. C **67**, 014319 (2003).
[6] S. Frauendorf and J. Meng, Nucl. Phys. **A617**, 131 (1997).
[7] K. Starosta *et al*., Phys. Rev. Lett. **86**, 971 (2001).
[8] T. Koike, K. Starosta, C. J. Chiara, D. B. Fossan, and D. R. LaFosse, Phys. Rev. C **67**, 044319 (2003).
[9] T. Koike, K. Starosta, and I. Hamamoto, Phys. Rev. Lett. **93**, 172502 (2004).
[10] S. Frauendorf, Rev. Mod. Phys. **73**, 463 (2001).
[11] M. Matsuzaki, Y. R. Shimizu, and K. Matsuyanagi, Phys. Rev. C **65**, 041303(R) (2002).
[12] M. Matsuzaki, Y. R. Shimizu, and K. Matsuyanagi, Phys. Rev. C **69**, 034325 (2004).
[13] E. R. Marshalek, Nucl. Phys. **A275**, 416 (1977).
[14] E. R. Marshalek, Nucl. Phys. **A331**, 429 (1979).
[15] D. Janssen and I. N. Mikhailov, Nucl. Phys. **A318**, 390 (1979).
[16] J. L. Egido, H. J. Mang, and P. Ring, Nucl. Phys. **A339**, 390 (1980).
[17] V. G. Zelevinsky, Nucl. Phys. **A344**, 109 (1980).
[18] Y. R. Shimizu and K. Matsuyanagi, Prog. Theor. Phys. **70**, 144 (1983).
[19] Y. R. Shimizu and M. Matsuzaki, Nucl. Phys. **A588**, 559 (1995). There are misprints in Ref. [19]: − sign is missing in front of $\frac{1}{2}Q_0^{(+)}$ in Eq. (2.3a), and factors $\frac{1}{2}$ should be deleted in Eq. (4.1).
[20] R. Bengtsson, http://www.matfys.lth.se/ragnar/TSD.html.
[21] H. Kurasawa, Prog. Theor. Phys. **64**, 2055 (1980).
[22] H. Kurasawa, Prog. Theor. Phys. **68**, 1594 (1982).
[23] C. G. Andersson, J. Krumlinde, G. Leander, and Z. Szymański, Nucl. Phys. **A361**, 147 (1981).
[24] J. Skalski, Nucl. Phys. **A473**, 40 (1987).
[25] S. Frauendorf, K. Neergård, J. A. Sheikh, and P. M. Walker, Phys. Rev. C **61**, 064324 (2000).
[26] S. Frauendorf, Nucl. Phys. **A677**, 115 (2000).
[27] D. Almehed, S. Frauendorf, and F. Dönau, Phys. Rev. C **63**, 044311 (2001).
[28] S.-I. Ohtsubo and Y. R. Shimizu, Nucl. Phys. **A714**, 44 (2003).
[29] M. Matsuzaki and Y. R. Shimizu, Prog. Theor. Phys. **114** (2005) in press.
[30] A. Bohr and B. R. Mottelson, *Nuclear Structure Vol. II* (Benjamin, New York, 1975).
[31] K. Tanabe and K. Sugawara-Tanabe, Phys. Lett. **B34**, 575 (1971).
[32] E. R. Marshalek, Phys. Rev. C **11**, 1426 (1975).
[33] M. Yamamura, Prog. Theor. Phys. **64**, 101 (1980).
[34] N. I. Pyatov and D. I. Salamov, Nukleonika **22**, 127 (1977).
[35] T. Kishimoto *et al*., Phys. Rev. Lett. **35**, 552 (1975).
[36] H. Sakamoto and T. Kishimoto, Nucl. Phys. **A501**, 205 (1989); **A501**, 242 (1989).
[37] T. Suzuki and D. J. Rowe, Nucl. Phys. **A289**, 461 (1977).
[38] E. R. Marshalek, Phys. Rev. Lett. **51**, 1534 (1983).
[39] E. R. Marshalek, Phys. Rev. C **29**, 640 (1984).
[40] Y. R. Shimizu and K. Matsuyanagi, Prog. Theor. Phys. **72**, 799 (1984).
[41] S. Åberg, Phys. Lett. **B157**, 9 (1985).
[42] G. Andersson, S. E. Larsson, G. Leander, P. Möller, S. G. Nilsson, I. Ragnarsson, S. Åberg, J. Dudek, B. Nerlo-Pomorska, K. Pomorski, and Z. Szymański, Nucl. Phys. **A268**, 205 (1976).
[43] C. S. Purry *et al*., Phys. Rev. Lett. **75**, 406 (1995).
[44] C. S. Purry *et al*., Nucl. Phys. **A632**, 229 (1998).
[45] D. M. Cullen *et al*., Phys. Rev. C **60**, 064301 (1999).
[46] T. Bengtsson and I. Ragnarsson, Nucl. Phys. **A436**, 14 (1985).
[47] R. B. Firestone *et al*., *Table of Isotopes,* 8th ed. (Wiley, New York, 1999).
[48] K. E. G. Löbner, M. Vetter, and V. Hönig, Nucl. Data Tables **A7**, 496 (1970).
[49] G. Audi and A. Wapstra, Nucl. Phys. **A595**, 409 (1995).
[50] T. S. Dumitrescu and I. Hamamoto, Nucl. Phys. **A383**, 205 (1982).
[51] G. D. Dracoulis, F. G. Kondev, and P. M. Walker, Phys. Lett. **B419**, 7 (1998).
[52] M. A. Deleplanque, S. Frauendorf, V. V. Pashkevich, S. Y. Chu, and A. Unzhakova, Phys. Rev. C **69**, 044309 (2004).
[53] F. R. Xu, P. M. Walker, J. A. Sheikh, and R. Wyss, Phys. Lett. **B435**, 257 (1998).
[54] R. Bengtsson and S. Åberg, Phys. Lett. **B172**, 277 (1986).

Progress of Theoretical Physics, Vol. 115, No. 3, March 2006

Effects of Time-Odd Components in Mean Field on Large Amplitude Collective Dynamics

Nobuo HINOHARA,[1] Takashi NAKATSUKASA,[2] Masayuki MATSUO[3] and Kenichi MATSUYANAGI[1]

[1]*Department of Physics, Graduate School of Science, Kyoto University, Kyoto 606-8502, Japan*
[2]*Institute of Physics and Center for Computational Sciences, University of Tsukuba, Tsukuba 305-8571, Japan*
[3]*Department of Physics, Faculty of Science, Niigata University, Niigata 950-2181, Japan*

(Received November 30, 2005)

We apply the adiabatic self-consistent collective coordinate (ASCC) method to the multi-$O(4)$ model and study the collective mass (inertia function) of many-body tunneling motion. Comparing the results with those obtained from the exact diagonalization, we show that the ASCC method is capable of describing the gradual change of the excitation spectra from an anharmonic vibration about a spherical shape to a doublet pattern associated with a deformed double-well potential possessing oblate-prolate symmetry. It is found that the collective mass is significantly increased by the quadrupole-pairing contribution to time-odd components of the moving mean field. In contrast, the cranking (Inglis-Belyaev) mass based on the constrained mean field, which ignores the time-odd components, is smaller than the ASCC mass and fails to reproduce the exact spectra.

§1. Introduction

Microscopic theories of large-amplitude collective dynamics are a long-standing and fundamental subject of nuclear structure physics.[1)–3)] Though many theories have been proposed and tested with regard to a variety of phenomena involving the large-amplitude collective motion,[4)–35)] many theoretical problems remain unsolved.[36)–38)] In particular, the microscopic determination of the collective mass (i.e., the inertia of the collective motion) has been the subject of much debate.

The Inglis-Belyaev cranking mass,[1)] which is derived using adiabatic perturbation theory, has been widely used in the literature. It is known that values of the cranking mass are systematically too low to account for experimental data for the low-frequency $K^\pi = 0^+$ vibrational modes in deformed nuclei.[39)] The Inglis-Belyaev cranking mass does not take account of the contributions of the residual interactions. In particular, the effects of the time-odd components of the moving mean-field are completely neglected. The importance of such time-odd contributions to the collective mass has been investigated in connection with the Thouless-Valatin moment of inertia for rotational motion[40),41)] and in the context of the adiabatic time-dependent Hartree-Fock (ATDHF) theory.[5),8),11),12),17)] It is also well known that, without taking into account the time-odd components, one cannot obtain the correct mass for the center of mass motion of a nucleus. In Ref. 11), the contributions from the time-odd

components were evaluated on the basis of the ATDHF theory, and its importance was demonstrated for the isoscalar giant quadrupole modes. In this work, however, the pairing correlations were not taken into account. It should be noted that, in the time-dependent Hartree-Fock-Bogoliubov (TDHFB) theory for nuclei with superfluidity, the pairing correlations also cause the appearance of the time-odd components in the moving mean field. To the best of our knowledge, however, there are very few papers[12] seeking to evaluate the time-odd effects of the pairing correlations on large-amplitude collective dynamics. This is rather surprising, because we know that the pairing correlations play crucial roles in low-energy nuclear collective dynamics (see, e.g., Refs. 42) and 43)). For this reason, in this paper, we develop a microscopic theory of large-amplitude collective motion in nuclei with superfluidity and study the time-odd mean-field effects, associated with the pairing correlations, on the inertia mass of collective motion.

We approach this goal on the basis of the self-consistent collective coordinate (SCC) method[10] and its extension to include the pairing correlations.[21] This method is based on the TDHFB theory, and it enables us to extract, in a fully self-consistent manner, the optimum collective coordinate and the collective momentum from the huge dimensional TDHFB phase space. This feature of the SCC method is in marked contrast to the widely used generator coordinate method,[1] in which the collective coordinate (generator coordinate) is chosen in a phenomenological manner. The SCC method has been successfully applied to various kinds of low-frequency anharmonic vibration and high-spin rotational motion.[44–55] However, for genuine large-amplitude cases, such as the nuclear fission and the shape coexistence phenomena,[56–58] a practical scheme for solving its basic equations does not exist. A possible solution to this problem was proposed in Ref. 59), an adiabatic approximation of the SCC method, called the adiabatic SCC (ASCC) method. The ASCC method was first applied to the solvable multi-$O(4)$ model and its feasibility was tested.[60] The multi-$O(4)$ model can be regarded as a simplified version of the pairing plus quadrupole (P+Q) interaction model,[61–63] and it has been used as a testing ground of microscopic theories of nuclear collective motion.[64–67] Recently, Kobayasi et al. applied the ASCC method to the oblate-prolate shape coexistence phenomena in ^{68}Se and ^{72}Kr[57,58] and extracted a collective path connecting the oblate and prolate equilibrium points.[68] It was found that the collective path runs through the triaxially deformed region, and it almost coincides with the valley line in the deformation-energy surface obtained with the constrained Hartree-Bogoliubov (HB) calculation. Similar studies have also been carried out by Almehed and Walet.[34,35] In those works, the P+Q interaction Hamiltonian was adopted. In order to study the time-odd contributions to the collective mass, however, we need to use a more general Hamiltonian, including, for instance, the quadrupole-pairing interaction, because the time-odd contributions from the P+Q interactions are known to vanish.[8,12,69] The importance of the quadrupole-pairing interaction in low-frequency collective excitations is well known (see references listed in Ref. 55)).

In this paper, we extend the multi-$O(4)$ model to include a quadrupole-type pairing interaction. Varying its strength within a range consistent with the exper-

imental data for the ratio Δ_2/Δ_0 of the quadrupole and monopole pairing gaps,[55] we evaluate its effect on the collective mass through the time-odd part of the mean field.

This paper is organized as follows. In §2, the basic equations of the ASCC method are briefly reviewed. In §3, we apply the ASCC method to a new version of the multi-$O(4)$ model with the quadrupole-type pairing interaction. Also there, a numerical algorithm to solve the ASCC equations for the multi-$O(4)$ model is presented. In §4, we present results of the numerical analysis. Conclusions are given in §5. A preliminary version of this work appears in Ref. 70).

§2. Basic equations of the ASCC method

The SCC method enables us to extract the "optimal" collective subspace from the huge dimensional TDHFB space.[10] The large amplitude collective motion takes place in this collective subspace. In the case that the collective subspace is parametrized by a pair of collective variables (a single collective coordinate q and a momentum p), it is called the "collective path". In superconducting nuclei, we need an additional set of collective variables to take into account the pairing rotational degrees of freedom, which recovers the particle number symmetry broken by the mean field approximation.[21] The pairing rotation is described by the particle-number variable N and its canonically conjugate gauge angle φ. Thus, a TDHFB state vector on the collective path is parametrized by four collective variables, (q, p, φ, N). In the SCC method, the large-amplitude collective motion is assumed to be approximately decoupled from the non-collective degrees of freedom. This assumption is called "the maximal decoupling condition of the collective submanifold". The time dependence of the TDHFB state on the collective path is then determined in terms of this set of collective variables.

The time-dependent variational principle for the collective motion is given by

$$\delta \left\langle \phi(q,p,\varphi,N) \right| i\frac{\partial}{\partial t} - \hat{H} \left| \phi(q,p,\varphi,N) \right\rangle = 0, \tag{2·1}$$

where $|\phi(q,p,\varphi,N)\rangle$ represents a TDHFB state vector on the collective path, and the variation is taken over all possible deviations around it. The intrinsic state $|\phi(q,p,N)\rangle$ in the gauge space (associated with the pairing rotation) is defined by

$$|\phi(q,p,\varphi,N)\rangle = e^{-i\varphi\hat{N}} \left| \phi(q,p,N) \right\rangle . \tag{2·2}$$

These four collective variables are required to satisfy the following canonical variable conditions:

$$\left\langle \phi(q,p,N) \right| i\frac{\partial}{\partial q} \left| \phi(q,p,N) \right\rangle = p, \qquad \left\langle \phi(q,p,N) \right| \frac{\partial}{i\partial p} \left| \phi(q,p,N) \right\rangle = 0, \tag{2·3}$$

$$\left\langle \phi(q,p,N) \right| \hat{N} \left| \phi(q,p,N) \right\rangle = N \equiv N_0 + n, \quad \left\langle \phi(q,p,N) \right| \frac{\partial}{i\partial N} \left| \phi(q,p,N) \right\rangle = 0. \tag{2·4}$$

Here, N_0 denotes the number of particles in the system (we assume a single kind of fermion, for simplicity), and the difference $n = N - N_0$ represents the dynamical number fluctuation.

We now apply the adiabatic approximation to the TDHFB state $|\phi(q,p,N)\rangle$ by assuming that the collective momentum and the number fluctuation are small and that the moving state $|\phi(q,p,N)\rangle$ is close to $|\phi(q)\rangle = |\phi(q,p=0,N=N_0)\rangle$. Using the fact that an arbitrary TDHFB state vector can be constructed from a given TDHFB state vector by a unitary transformation (generalized Thouless theorem),[1),2)] we construct the moving TDHFB state vector $|\phi(q,p,N)\rangle$ from the static state vector $|\phi(q)\rangle$ in the form

$$|\phi(q,p,N)\rangle = e^{i\hat{G}(q,p,N)}\,|\phi(q)\rangle = e^{ip\hat{Q}(q)+in\hat{\Theta}(q)}|\phi(q)\rangle, \tag{2·5}$$

where $\hat{Q}(q)$ and $\hat{\Theta}(q)$ are one-body operators. Substituting the moving state vector $|\phi(q,p,N)\rangle$ of this form into Eqs. (2·3) and (2·4), and comparing the coefficients of the first order in p and n, we obtain

$$\langle\phi(q)|\,[\hat{Q}(q),\hat{P}(q)]\,|\phi(q)\rangle = i, \tag{2·6}$$

$$\langle\phi(q)|\,[\hat{\Theta}(q),\hat{N}]\,|\phi(q)\rangle = i, \tag{2·7}$$

where $\hat{P}(q)$ is the local shift operator of the collective coordinate q, defined by

$$\hat{P}(q)\,|\phi(q)\rangle = i\frac{\partial}{\partial q}\,|\phi(q)\rangle\,. \tag{2·8}$$

The other commutators, such as $\langle\phi(q)|\,[\hat{Q}(q),\hat{N}]\,|\phi(q)\rangle$ and $\langle\phi(q)|\,[\hat{N},\hat{P}(q)]\,|\phi(q)\rangle$, are zero.

The collective Hamiltonian is also expanded up to second order in p, and we have

$$\begin{aligned}\mathcal{H}(q,p,N) &\equiv \langle\phi(q,p,N)|\,\hat{H}\,|\phi(q,p,N)\rangle \\ &= V(q) + \frac{1}{2}B(q)p^2 + \lambda(q)n,\end{aligned} \tag{2·9}$$

where

$$V(q) = \mathcal{H}(q,p,N)|_{p=0,N=N_0} = \langle\phi(q)|\,\hat{H}\,|\phi(q)\rangle\,, \tag{2·10}$$

$$B(q) = \frac{\partial^2\mathcal{H}}{\partial p^2}\,\Big|_{p=0,N=N_0} = -\,\langle\phi(q)|\,[[\hat{H},\hat{Q}(q)],\hat{Q}(q)]\,|\phi(q)\rangle\,, \tag{2·11}$$

$$\lambda(q) = \frac{\partial\mathcal{H}(q,p,N)}{\partial N}\,\Big|_{p=0,N=N_0} = \langle\phi(q)|\,[\hat{H},i\hat{\Theta}(q)]\,|\phi(q)\rangle\,. \tag{2·12}$$

The collective potential $V(q)$ embodies the static properties of the collective path, while the mass function $B(q)$ represents the dynamical properties, i.e., the inertia of the collective motion. The quantity $\lambda(q)$ is regarded as the locally defined chemical potential.

The basic equations of the ASCC method are obtained by performing an adiabatic expansion of the equation of the collective path (2·1) with respect to the collective momentum p and requiring the variations to be zero at each order in p. At zero-th order, we obtain the moving-frame HFB equation,

$$\delta\,\langle\phi(q)|\,\hat{H}_M(q)\,|\phi(q)\rangle = 0, \tag{2·13}$$

where

$$\hat{H}_M(q) = \hat{H} - \lambda(q)\hat{N} - \frac{\partial V}{\partial q}\hat{Q}(q) \tag{2·14}$$

is the moving-frame Hamiltonian.

The first and second orders of the adiabatic expansion of Eq. (2·1) yield the local harmonic equations (also called the moving-frame quasiparticle RPA equation).[59] They are composed of the following two equations:

$$\delta \langle\phi(q)| [\hat{H}_M(q), \hat{Q}(q)] - \frac{1}{i}B(q)\hat{P}(q) |\phi(q)\rangle = 0, \tag{2·15}$$

$$\delta \langle\phi(q)| \left[\hat{H}_M(q), \frac{1}{i}\hat{P}(q)\right] - C(q)\hat{Q}(q) - \frac{1}{2B(q)}\left[\left[\hat{H}_M(q), \frac{\partial V}{\partial q}\hat{Q}(q)\right], \hat{Q}(q)\right] - \frac{\partial \lambda}{\partial q}\hat{N} |\phi(q)\rangle = 0, \tag{2·16}$$

where $C(q)$ represents the local stiffness defined on the collective path,

$$C(q) = \frac{\partial^2 V}{\partial q^2} + \frac{1}{2B(q)}\frac{\partial B}{\partial q}\frac{\partial V}{\partial q}. \tag{2·17}$$

The collective variables (q, p) and the collective Hamiltonian $\mathcal{H}(q, p, N)$ are determined by solving the ASCC equations, (2·13), (2·15), and (2·16).

§3. Application of the ASCC to the multi-$O(4)$ model

In this section, we present an explicit form of the ASCC equations for the multi-$O(4)$ model Hamiltonian. The ASCC equations take a very simple form for the case of separable interactions. A numerical algorithm for finding a collective path is also explained.

3.1. *Multi-$O(4)$ model*

The multi-$O(4)$ model Hamiltonian has been used to test the validity of various kinds of theories of nuclear collective motion.[64)–67)] In this paper, we extend this model Hamiltonian such that it includes the quadrupole-type pairing interaction in addition to the monopole-pairing interaction. We write the model Hamiltonian in the following form:

$$\hat{H} = \hat{h}_0 - \frac{1}{2}G_0(\hat{A}^\dagger\hat{A} + \hat{A}\hat{A}^\dagger) - \frac{1}{2}G_2(\hat{B}^\dagger\hat{B} + \hat{B}\hat{B}^\dagger) - \frac{1}{2}\chi\hat{D}^2, \tag{3·1}$$
$$\hat{h}_0 = \sum_j e_j^0 \hat{N}_j.$$

The first term on the right-hand side of Eq. (3·1) is the single-particle Hamiltonian, giving a spherical single-particle energy e_j^0 for each j-shell which possesses $(2\Omega_j)$-fold degeneracy $(2\Omega_j = 2j + 1)$. The other terms represent the residual two-body

interactions: the monopole-pairing interaction, the quadrupole-type pairing interaction, and the quadrupole-type particle-hole interaction. Their interaction strengths are denoted by G_0, G_2, and χ, respectively. The operators appearing in this model Hamiltonian are defined in terms of the nucleon creation and the annihilation operators $(c^\dagger_{jm}, c_{jm})$ by

$$\hat{A}^\dagger = \sum_j \hat{A}^\dagger_j, \quad \hat{B}^\dagger = \sum_j d_j \hat{B}^\dagger_j, \quad \hat{N} = \sum_j \hat{N}_j, \quad \hat{D} = \sum_j d_j \hat{D}_j, \tag{3·2}$$

where

$$\hat{A}^\dagger_j = \sum_{m>0} c^\dagger_{jm} c^\dagger_{j-m}, \qquad \hat{B}^\dagger_j = \sum_{m>0} \sigma_{jm} c^\dagger_{jm} c^\dagger_{j-m}, \tag{3·3}$$

$$\hat{N}_j = \sum_m c^\dagger_{jm} c_{jm}, \qquad \hat{D}_j = \sum_m \sigma_{jm} c^\dagger_{jm} c_{jm}, \tag{3·4}$$

with

$$\sigma_{jm} = \begin{cases} 1 & |m| < \Omega_j/2, \\ -1 & |m| > \Omega_j/2. \end{cases} \tag{3·5}$$

Here, the operators $\hat{A}$ and $\hat{N}$ are the monopole-pair and the number operators, while $\hat{B}$ and $\hat{D}$ represent the simplified quadrupole-pair and quadrupole particle-hole operators, respectively. These operators contain the factors $d_j\sigma_{jm}$, which simulate the basic property of the quadrupole matrix elements $\langle jm| r^2 Y_{20} |jm\rangle$ in a schematic way. Although they are not real quadrupole operators, we call them "quadrupole" for brevity. Exact solutions (eigen-energies and eigen-functions) of the multi-$O(4)$ model are easily obtained by means of the matrix diagonalization method (see Appendix A).

3.2. *Quasiparticle representation*

To solve the ASCC equations, it is convenient to use the quasiparticle basis locally defined with respect to the state $|\phi(q)\rangle$ on the collective path. For the multi-$O(4)$ model, the Bogoliubov transformation to the quasiparticle creation and annihilation operators, $a^\dagger_i(q)$ and $a_i(q)$, satisfying the vacuum condition, $a_i(q)\,|\phi(q)\rangle = 0$, is written

$$\begin{pmatrix} a^\dagger_i(q) \\ a_{-i}(q) \end{pmatrix} \equiv \begin{pmatrix} u_i(q) & -v_i(q) \\ v_i(q) & u_i(q) \end{pmatrix} \begin{pmatrix} c^\dagger_i \\ c_{-i} \end{pmatrix}. \tag{3·6}$$

Here, the indices $\pm i$ represent the set of angular momentum quantum numbers $(j, \pm m)$.

Using the quasiparticle bilinear operators

$$\boldsymbol{A}^\dagger_i(q) = a^\dagger_i(q) a^\dagger_{-i}(q), \tag{3·7}$$

$$\boldsymbol{N}_i(q) = a^\dagger_i(q) a_i(q) + a^\dagger_{-i}(q) a_{-i}(q), \tag{3·8}$$

the nucleon bilinear operators $\hat{A}_i^\dagger$ and $\hat{N}_i$ are rewritten as

$$\hat{A}_i^\dagger = u_i(q)v_i(q) + u_i^2(q)\boldsymbol{A}_i^\dagger(q) - v_i^2(q)\boldsymbol{A}_i(q) - u_i(q)v_i(q)\boldsymbol{N}_i(q), \tag{3·9}$$

$$\hat{N}_i = 2v_i^2(q) + 2u_i(q)v_i(q)(\boldsymbol{A}_i^\dagger(q) + \boldsymbol{A}_i(q)) + (u_i^2(q) - v_i^2(q))\boldsymbol{N}_i(q). \tag{3·10}$$

The quasiparticle bilinear operators $\boldsymbol{A}_i^\dagger(q), \boldsymbol{A}_i(q)$, and $\boldsymbol{N}_i(q)$ satisfy the following commutation relations:

$$\left[\boldsymbol{A}_i(q), \boldsymbol{A}_{i'}^\dagger(q)\right] = \delta_{ii'}(1 - \boldsymbol{N}_i(q)), \tag{3·11}$$

$$\left[\boldsymbol{N}_i(q), \boldsymbol{A}_{i'}^\dagger(q)\right] = 2\delta_{ii'}\boldsymbol{A}_{i'}^\dagger(q). \tag{3·12}$$

The particle number N_0, the quadrupole deformation $D(q)$, the monopole-pairing gap $\Delta_0(q)$, and the quadrupole-pairing gap $\Delta_2(q)$ are given by the expectation values with respect to the mean-field state vector $|\phi(q)\rangle$:

$$N_0 = \langle\phi(q)|\,\hat{N}\,|\phi(q)\rangle = 2\sum_{i>0} v_i^2(q), \tag{3·13}$$

$$D(q) = \langle\phi(q)|\hat{D}|\phi(q)\rangle = 2\sum_{i>0} d_i\sigma_i v_i^2(q), \tag{3·14}$$

$$\Delta_0(q) = G_0\,\langle\phi(q)|\,\hat{A}^\dagger\,|\phi(q)\rangle = G_0\sum_{i>0} u_i(q)v_i(q), \tag{3·15}$$

$$\Delta_2(q) = G_2\,\langle\phi(q)|\,\hat{B}^\dagger\,|\phi(q)\rangle = G_2\sum_{i>0} d_i\sigma_i u_i(q)v_i(q). \tag{3·16}$$

Below, we often omit the q-dependence in expressions, for example, writing $\boldsymbol{A}_i(q)$ as $\boldsymbol{A}_i$. It should be kept in mind that all of these quantities are locally defined with respect to the quasiparticle vacuum $|\phi(q)\rangle$ and depend on q.

3.3. *ASCC equations for separable interactions*

The ASCC equations can be easily solved when the effective interactions in the microscopic Hamiltonian are separable. We can always write such a separable Hamiltonian in the following form:

$$\hat{H} = \hat{h}_0 - \frac{1}{2}\sum_s \kappa_s \hat{F}_s^{(+)}\hat{F}_s^{(+)} + \frac{1}{2}\sum_s \kappa_s \hat{F}_s^{(-)}\hat{F}_s^{(-)}, \tag{3·17}$$

where

$$\hat{F}_s^{(\pm)} \equiv (\hat{F}_s \pm \hat{F}_s^\dagger)/2 = \pm\hat{F}_s^{(\pm)\dagger}. \tag{3·18}$$

The superscripts $(\pm)$ indicate the Hermitian or anti-Hermitian nature of the bilinear operator $\hat{F}$. The multi-$O(4)$ model Hamiltonian under consideration contains three kinds of residual interactions. The indices s =1, 2, and 3 on the operators $\hat{F}$ and the interaction strengths κ_s indicate the monopole-pairing, the quadrupole-pairing and the quadrupole particle-hole interactions, respectively: $\hat{F}_{s=1} = A, \hat{F}_{s=2} = B$, $\hat{F}_{s=3} = \hat{D}$, $\kappa_1 = 2G_0, \kappa_2 = 2G_2$, and $\kappa_3 = \chi$.

For the separable Hamiltonian, it is possible to directly derive the ASCC equations from the time-dependent variational principle,

$$\delta \langle\phi(t)| i\frac{\partial}{\partial t} - \hat{h}(t) |\phi(t)\rangle = 0, \tag{3·19}$$

for the self-consistent mean-field Hamiltonian defined by

$$\hat{h}(t) = \hat{h}_0 - \sum_s \kappa_s \hat{F}_s^{(+)} \langle\phi(t)| \hat{F}_s^{(+)} |\phi(t)\rangle + \sum_s \kappa_s \hat{F}_s^{(-)} \langle\phi(t)| \hat{F}_s^{(-)} |\phi(t)\rangle . \tag{3·20}$$

Here, the exchange terms are omitted as is usually done for the separable interactions.[61),63)] The second and third terms on the right-hand side of $\hat{h}(t)$ represent the time-even and time-odd components, respectively. Note that the expectation values $\langle\phi(t)| \hat{F}_s^{(-)} |\phi(t)\rangle$ are purely imaginary, indicating that the third term is odd under time reversal. Substituting $|\phi(t)\rangle = e^{ip\hat{Q}(q)} |\phi(q)\rangle$ and expanding Eq. (3·19) up to second order in p, we obtain the ASCC equations for the separable Hamiltonian,

$$\delta \langle\phi(q)| \hat{h}_M(q) |\phi(q)\rangle = 0, \tag{3·21}$$

$$\delta \langle\phi(q)| [\hat{h}_M(q), \hat{Q}(q)] - \sum_s f_{Q,s}^{(-)} \hat{F}_s^{(-)} - \frac{1}{i} B(q)\hat{P}(q) |\phi(q)\rangle = 0, \tag{3·22}$$

$$\begin{aligned}\delta \langle\phi(q)| \left[\hat{h}_M(q), \frac{1}{i}B(q)\hat{P}(q)\right] - \sum_s f_{P,s}^{(+)}(q)\hat{F}_s^{(+)} - B(q)C(q)\hat{Q}(q) - \sum_s f_{R,s}^{(+)}(q)\hat{F}_s^{(+)} \\ + \sum_s [\hat{F}_s^{(-)}, (\hat{h}(q) - \lambda(q)\hat{N})_A] f_{Q,s}^{(-)} - f_N(q)\hat{N} |\phi(q)\rangle = 0,\end{aligned} \tag{3·23}$$

where $\hat{h}_M(q)$ denotes the self-consistent mean-field Hamiltonian in the moving frame, defined by

$$\hat{h}_M(q) = \hat{h}(q) - \lambda(q)\hat{N} - \frac{\partial V}{\partial q}\hat{Q}(q), \tag{3·24}$$

with

$$\hat{h}(q) = \hat{h}_0 - \sum_s \kappa_s \hat{F}_s^{(+)} \langle\phi(q)| \hat{F}_s^{(+)} |\phi(q)\rangle . \tag{3·25}$$

The quantity $(\hat{h}(q) - \lambda(q)\hat{N})_A$ represents the $\boldsymbol{A}_i^\dagger$ and $\boldsymbol{A}_i$ parts of the operator in the parentheses, and we have

$$f_{Q,s}^{(-)}(q) = -\kappa_s \langle\phi(q)| [\hat{F}_s^{(-)}, \hat{Q}(q)] |\phi(q)\rangle , \tag{3·26}$$

$$f_{P,s}^{(+)}(q) = \kappa_s \langle\phi(q)| [\hat{F}_s^{(+)}, \frac{1}{i}B(q)\hat{P}(q)] |\phi(q)\rangle , \tag{3·27}$$

$$f_{R,s}^{(+)}(q) = -\frac{1}{2}\kappa_s \langle\phi(q)| [[\hat{F}_s^{(+)}, (\hat{h}(q) - \lambda(q)\hat{N})_A], \hat{Q}(q)] |\phi(q)\rangle , \tag{3·28}$$

$$f_N(q) = B(q)\frac{\partial \lambda}{\partial q}. \tag{3·29}$$

Note that all matrix elements are real, so that $\langle\phi(q)|\,\hat{F}_s^{(-)}\,|\phi(q)\rangle = 0$. In the above equations, the quantities $f_{Q,s}^{(-)}$ represent the effects of the time-odd components of the mean field, which introduce important effects, discussed in the next section.

The above ASCC equations can be obtained also by inserting the expression (3·17) into Eqs. (2·15) and (2·16). In this derivation, the exchange terms of the residual interactions should be omitted.[61),63)] This implies that here we adopt the Hartree-Bogoliubov (HB) approximation in place of the HFB approximation.

3.4. *The moving-frame HB equation*

The moving-frame HB equation (3·21) at a given q determines the static TDHB state, $|\phi(q)\rangle$. If we know the operator $\hat{Q}(q)$, we can solve this equation using the gradient method. The quantities $\lambda(q)$ and $\frac{\partial V}{\partial q}$ are regarded as Lagrange multipliers, which are determined by the following two constraints. The first constraint is placed on the particle number:

$$\langle\phi(q)|\,\hat{N}\,|\phi(q)\rangle = N_0. \tag{3·30}$$

This constraint specifies the location in particle number space. The second constraint is

$$\langle\phi(q)|\,\hat{Q}(q-\delta q)\,|\phi(q)\rangle = \delta q, \tag{3·31}$$

which can be readily derived from the canonical variable conditions,

$$\langle\phi(q)|\,\hat{Q}(q)\,|\phi(q)\rangle = 0 \tag{3·32}$$

and

$$\langle\phi(q)|\,\frac{\partial\hat{Q}}{\partial q}(q)\,|\phi(q)\rangle = -1. \tag{3·33}$$

Equation (3·31) is the condition on the collective coordinate q that the "distance" from $|\phi(q-\delta q)\rangle$ to $|\phi(q)\rangle$ be equal to δq. In numerical calculations, the quantity δq corresponds to the mesh size of the discretized collective path. Provided that $\hat{Q}(q-\delta q)$ and $\hat{Q}(q)$ are known, we can solve the moving-frame HB equation. Because the variation in Eq. (3·21) is taken with respect to arbitrary creations of two quasiparticles,

$$\delta\,|\phi(q)\rangle = a_i^\dagger a_j^\dagger\,|\phi(q)\rangle\,, \tag{3·34}$$

the two-quasiparticle terms proportional to $\boldsymbol{A}_i^\dagger$ and $\boldsymbol{A}_i$ in the moving-frame Hamiltonian $\hat{h}_M(q)$ should vanish.

We solve the moving-frame HB equation with the above two constraints by means of an algorithm analogous to the gradient method.[1)] Details of this algorithm are given in Appendix B.

3.5. *The local harmonic equations*

In order to obtain the collective path, we need to solve the local harmonic equations, (3·22) and (3·23), and find the operators $\hat{Q}(q)$ and $\hat{P}(q)$ which determine the

direction of the collective path in the TDHB space. In solving the local harmonic equations, we note that the moving-frame Hamiltonian $\hat{h}_M(q)$ is expressed in terms of the quasiparticle bilinear operators $\boldsymbol{A}_i^\dagger, \boldsymbol{A}_i$, and $\boldsymbol{N}_i$ in the following manner:

$$\hat{h}_M(q) = V(q) - \lambda(q)N_0 + \sum_{i>0} E_i(q)\boldsymbol{N}_i, \tag{3·35}$$

$$\begin{aligned}\hat{F}_s^{(+)} &= \langle\phi(q)|\,\hat{F}_s^{(+)}\,|\phi(q)\rangle + \hat{F}_{A,s}^{(+)} + \hat{F}_{B,s}^{(+)} \\ &= \langle\phi(q)|\,\hat{F}_s^{(+)}\,|\phi(q)\rangle + \sum_{i>0} F_{A,s}^{(+)}(i)(\boldsymbol{A}_i^\dagger + \boldsymbol{A}_i) + \sum_{i>0} F_{B,s}^{(+)}(i)\boldsymbol{N}_i,\end{aligned} \tag{3·36}$$

$$\hat{F}_s^{(-)} = \sum_{i>0} F_{A,s}^{(-)}(i)(\boldsymbol{A}_i^\dagger - \boldsymbol{A}_i). \tag{3·37}$$

Here, we have the following:

$$F_{A,1}^{(+)}(i) = \frac{1}{2}(u_i^2 - v_i^2), \quad F_{A,2}^{(+)}(i) = \frac{1}{2}d_i\sigma_i(u_i^2 - v_i^2), \quad F_{A,3}^{(+)}(i) = 2d_i\sigma_i u_i v_i, \tag{3·38}$$

$$F_{A,1}^{(-)}(i) = -\frac{1}{2}, \qquad F_{A,2}^{(-)}(i) = -\frac{1}{2}d_i\sigma_i, \qquad F_{A,3}^{(-)}(i) = 0, \tag{3·39}$$

$$F_{B,1}^{(+)}(i) = -u_i v_i, \qquad F_{B,2}^{(+)}(i) = -d_i\sigma_i u_i v_i, \qquad F_{B,3}^{(+)}(i) = d_i\sigma_i(u_i^2 - v_i^2), \tag{3·40}$$

$$E_i(q) = (u_i^2 - v_i^2)\,(e_i - \chi d_i\sigma_i D(q) - \lambda(q)) - 2(\Delta_0(q) + d_i\sigma_i\Delta_2(q))u_i v_i. \tag{3·41}$$

These quantities are determined by solving the moving-frame HB equation, (3·21). For later convenience, we define the following quasiparticle bilinear operator:

$$\hat{R}_s^{(+)} \equiv [\hat{F}_{B,s}^{(+)}, (\hat{h}(q) - \lambda(q)\hat{N})_A] = 2\sum_{i>0} R_s^{(+)}(i)(\boldsymbol{A}_i^\dagger - \boldsymbol{A}_i), \tag{3·42}$$

with

$$\begin{aligned}R_s^{(+)}(i) =& \big\{2u_i(q)v_i(q)(e_i - \chi d_i\sigma_i D(q) - \lambda(q)) \\ &- (\Delta_0(q) + d_i\sigma_i\Delta_2(q))(u_i^2(q) - v_i^2(q))\big\}F_{B,s}^{(+)}(i).\end{aligned} \tag{3·43}$$

The infinitesimal generators can be written as

$$\hat{Q}(q) = \sum_{i>0} Q_i(\boldsymbol{A}_i^\dagger + \boldsymbol{A}_i), \tag{3·44}$$

$$\hat{P}(q) = i\sum_{i>0} P_i(\boldsymbol{A}_i^\dagger - \boldsymbol{A}_i). \tag{3·45}$$

We can express the matrix elements Q_i and P_i in terms of $f_{Q,s}^{(-)}$, $f_{P,s}^{(+)}$, $f_{R,s}^{(+)}$ and f_N by substituting Eqs. (3·44) and (3·45) into Eqs. (3·22) and (3·23):

$$Q_i = \frac{2E_i}{(2E_i)^2 - \omega^2}\sum_s F_{A,s}^{(-)}(i)f_{Q,s}^{(-)} + \frac{1}{(2E_i)^2 - \omega^2}\sum_s (F_{A,s}^{(+)}(i)f_{PR,s}^{(+)} + N_i f_N), \tag{3·46}$$

$$P_i = \frac{2E_i}{(2E_i)^2 - \omega^2}\sum_s (F_{A,s}^{(+)}(i)f_{PR,s}^{(+)} + N_i f_N) + \frac{\omega^2}{(2E_i)^2 - \omega^2}\sum_s F_{A,s}^{(-)}(i)f_{Q,s}^{(-)}, \tag{3·47}$$

where

$$N_i = 2u_i(q)v_i(q), \tag{3·48}$$

$$f^{(+)}_{PR,s} = f^{(+)}_{P,s}(q) + f^{(+)}_{R,s}(q), \tag{3·49}$$

$$\omega = \sqrt{B(q)C(q)}. \tag{3·50}$$

Substituting Eqs. (3·42), (3·44) and (3·45) into Eqs. (3·26), (3·27) and (3·28), we also have the following relations:

$$f^{(-)}_{Q,s} = 2\kappa_s \sum_{i>0} F^{(-)}_{A,s}(i) Q_i, \tag{3·51}$$

$$f^{(+)}_{PR,s} = 2\kappa_s \sum_{i>0} \left\{ F^{(+)}_{A,s}(i) P_i + R^{(+)}_s(i) Q_i \right\}. \tag{3·52}$$

Note that $f^{(-)}_{Q,3} = 0$. From the canonical variable condition, the orthogonality of the collective and number fluctuation modes is required:

$$\langle \phi(q) | [\hat{N}, \hat{P}(q)] | \phi(q) \rangle = 2i \sum_{i>0} N_i P_i = 0. \tag{3·53}$$

Eliminating Q_i and P_i from Eqs. (3·51), (3·52), and (3·53) with the use of Eqs. (3·46) and (3·47), we finally obtain the dispersion equation

$$\boldsymbol{S}(\omega^2) \cdot \boldsymbol{f} = 0, \tag{3·54}$$

for the quantity $\boldsymbol{f} = \boldsymbol{f}(q) = \{f^{(-)}_{Q,1},\ f^{(-)}_{Q,2},\ f^{(+)}_{PR,1},\ f^{(+)}_{PR,2},\ f^{(+)}_{PR,3},\ f_N\}$. Here $\boldsymbol{S} = \{S_{ij}\}$ is a 6×6 matrix whose elements are given by

$$S_{11} = 4G_0 S^{(1)}(F^{(-)}_{A,1}, F^{(-)}_{A,1}) - 1, \qquad S_{12} = 4G_0 S^{(1)}(F^{(-)}_{A,1}, F^{(-)}_{A,2}), \tag{3·55a}$$

$$S_{13} = 4G_0 S^{(2)}(F^{(-)}_{A,1}, F^{(+)}_{A,1}), \qquad S_{14} = 4G_0 S^{(2)}(F^{(-)}_{A,1}, F^{(+)}_{A,2}), \tag{3·55b}$$

$$S_{15} = 4G_0 S^{(2)}(F^{(-)}_{A,1}, F^{(+)}_{A,3}), \qquad S_{16} = 4G_0 S^{(2)}(F^{(-)}_{A,1}, N), \tag{3·55c}$$

$$S_{21} = 4G_2 S^{(1)}(F^{(-)}_{A,2}, F^{(-)}_{A,1}), \qquad S_{22} = 4G_2 S^{(1)}(F^{(-)}_{A,2}, F^{(-)}_{A,2}) - 1, \tag{3·56a}$$

$$S_{23} = 4G_2 S^{(2)}(F^{(-)}_{A,2}, F^{(+)}_{A,1}), \qquad S_{24} = 4G_2 S^{(2)}(F^{(-)}_{A,2}, F^{(+)}_{A,2}), \tag{3·56b}$$

$$S_{25} = 4G_2 S^{(2)}(F^{(-)}_{A,2}, F^{(+)}_{A,3}), \qquad S_{26} = 4G_2 S^{(2)}(F^{(-)}_{A,2}, N), \tag{3·56c}$$

$$S_{31} = 4G_0 \{ S^{(1)}(R^{(+)}_1, F^{(-)}_{A,1}) + \omega^2 S^{(2)}(F^{(+)}_{A,1}, F^{(-)}_{A,1}) \}, \tag{3·57a}$$

$$S_{32} = 4G_0 \{ S^{(1)}(R^{(+)}_1, F^{(-)}_{A,2}) + \omega^2 S^{(2)}(F^{(+)}_{A,1}, F^{(-)}_{A,2}) \}, \tag{3·57b}$$

$$S_{33} = 4G_0 \{ S^{(1)}(F^{(+)}_{A,1}, F^{(+)}_{A,1}) + S^{(2)}(R^{(+)}_1, F^{(+)}_{A,1}) \} - 1, \tag{3·57c}$$

$$S_{34} = 4G_0 \{ S^{(1)}(F^{(+)}_{A,1}, F^{(+)}_{A,2}) + S^{(2)}(R^{(+)}_1, F^{(+)}_{A,2}) \}, \tag{3·57d}$$

$$S_{35} = 4G_0 \{ S^{(1)}(F^{(+)}_{A,1}, F^{(+)}_{A,3}) + S^{(2)}(R^{(+)}_1, F^{(+)}_{A,3}) \}, \tag{3·57e}$$

$$S_{36} = 4G_0 \{ S^{(1)}(F^{(+)}_{A,1}, N) + S^{(2)}(R^{(+)}_1, N) \}, \tag{3·57f}$$

$$S_{41} = 4G_2\{S^{(1)}(R_2^{(+)}, F_{A,1}^{(-)}) + \omega^2 S^{(2)}(F_{A,2}^{(+)}, F_{A,1}^{(-)})\}, \tag{3·58a}$$
$$S_{42} = 4G_2\{S^{(1)}(R_2^{(+)}, F_{A,2}^{(-)}) + \omega^2 S^{(2)}(F_{A,2}^{(+)}, F_{A,2}^{(-)})\}, \tag{3·58b}$$
$$S_{43} = 4G_2\{S^{(1)}(F_{A,2}^{(+)}, F_{A,1}^{(+)}) + S^{(2)}(R_2^{(+)}, F_{A,1}^{(+)})\}, \tag{3·58c}$$
$$S_{44} = 4G_2\{S^{(1)}(F_{A,2}^{(+)}, F_{A,2}^{(+)}) + S^{(2)}(R_2^{(+)}, F_{A,2}^{(+)})\} - 1, \tag{3·58d}$$
$$S_{45} = 4G_2\{S^{(1)}(F_{A,2}^{(+)}, F_{A,3}^{(+)}) + S^{(2)}(R_2^{(+)}, F_{A,3}^{(+)})\}, \tag{3·58e}$$
$$S_{46} = 4G_2\{S^{(1)}(F_{A,2}^{(+)}, N) + S^{(2)}(R_2^{(+)}, N)\}, \tag{3·58f}$$

$$S_{51} = 2\chi\{S^{(1)}(R_3^{(+)}, F_{A,1}^{(-)}) + \omega^2 S^{(2)}(F_{A,3}^{(+)}, F_{A,1}^{(-)})\}, \tag{3·59a}$$
$$S_{52} = 2\chi\{S^{(1)}(R_3^{(+)}, F_{A,2}^{(-)}) + \omega^2 S^{(2)}(F_{A,3}^{(+)}, F_{A,2}^{(-)})\}, \tag{3·59b}$$
$$S_{53} = 2\chi\{S^{(1)}(F_{A,3}^{(+)}, F_{A,1}^{(+)}) + S^{(2)}(R_3^{(+)}, F_{A,1}^{(+)})\}, \tag{3·59c}$$
$$S_{54} = 2\chi\{S^{(1)}(F_{A,3}^{(+)}, F_{A,2}^{(+)}) + S^{(2)}(R_3^{(+)}, F_{A,2}^{(+)})\}, \tag{3·59d}$$
$$S_{55} = 2\chi\{S^{(1)}(F_{A,3}^{(+)}, F_{A,3}^{(+)}) + S^{(2)}(R_3^{(+)}, F_{A,3}^{(+)})\} - 1, \tag{3·59e}$$
$$S_{56} = 2\chi\{S^{(1)}(F_{A,3}^{(+)}, N) + S^{(2)}(R_3^{(+)}, N)\}, \tag{3·59f}$$

$$S_{61} = \omega^2 S^{(2)}(N, F_{A,1}^{(-)}), \qquad S_{62} = \omega^2 S^{(2)}(N, F_{A,2}^{(-)}), \tag{3·60a}$$
$$S_{63} = S^{(1)}(N, F_{A,1}^{(+)}), \qquad S_{64} = S^{(1)}(N, F_{A,2}^{(+)}), \tag{3·60b}$$
$$S_{65} = S^{(1)}(N, F_{A,3}^{(+)}), \qquad S_{66} = S^{(1)}(N, N). \tag{3·60c}$$

Here, the quantities $S^{(1)}$ and $S^{(2)}$ are defined by

$$S^{(1)}(X, Y) = \sum_{i>0} \frac{2E_i(q)}{(2E_i(q))^2 - \omega^2(q)} X_i Y_i, \tag{3·61}$$
$$S^{(2)}(X, Y) = \sum_{i>0} \frac{1}{(2E_i(q))^2 - \omega^2(q)} X_i Y_i. \tag{3·62}$$

The unknown quantities in the dispersion equation (3·54) are $\boldsymbol{f}(q)$ and $\omega^2(q)$. The squared frequency $\omega^2(q)$ can be determined by the condition that the matrix $\boldsymbol{S}(\omega^2(q))$ has no inverse:

$$\det \boldsymbol{S}(\omega^2(q)) = 0. \tag{3·63}$$

In the case that there are many solutions $\omega^2(q)$ satisfying this equation, we choose the smallest of these (including negative values) as the collective mode. Once the value of $\omega^2(q)$ and, consequently, the matrix $\boldsymbol{S}(q)$ is specified, the direction of the vector $\boldsymbol{f}(q)$ is found. Then, its absolute value is fixed by the normalization condition for the collective mode, i.e.,

$$\langle \phi(q) | [\hat{Q}(q), \hat{P}(q)] | \phi(q) \rangle = 2i \sum_{i>0} Q_i(q) P_i(q) = i. \tag{3·64}$$

Note that we can use an arbitrary scale for the collective coordinate q. This means that we can set $B(q) = 1$ on the collective path without loss of generality. We adopt this choice. Then, $\omega^2(q)$ is identically the curvature of the collective potential:

$$\omega^2(q) = \frac{\partial^2 V(q)}{\partial q^2}. \tag{3·65}$$

The choice of the sign of $\hat{Q}(q)$ and $\hat{P}(q)$ is still arbitrary, however. This sign specifies the "rear" and "front" of the one-dimensional collective path.

3.6. *Numerical algorithm for solving the ASCC equations*

The infinitesimal generators $\hat{Q}(q)$ and $\hat{P}(q)$, which depend on the quasiparticle vacuum $|\phi(q)\rangle$, represent a solution of the local harmonic equations, while the quasiparticle vacuum $|\phi(q)\rangle$, which depends on $\hat{Q}(q)$, is a solution of the moving-frame HB equation. Thus, the set of ASCC equations requires self-consistency and an iterative solution. In fact, we need a double iteration for each value of q, because the gradient method itself used to solve the moving-frame HB equation is an iterative procedure. The numerical algorithm utilized in the present work is summarized as follows:

Step 0: HB state (starting point)

Solve the static HB equation and choose one of the solutions. Then, solve the quasiparticle RPA equations and select the collective excitation mode that has the lowest frequency, $\omega(q_0)$. This provides the solution of the ASCC equations at $q = q_0$.

Step 1: Initial setting

Assume that we have solved the ASCC equations at a position q at which we have the self-consistent generator $\hat{Q}(q)$ and the state $|\phi(q)\rangle$.

Set $\hat{Q}^{(0)}(q+\delta q) = \hat{Q}(q)$ as the initial guess for $\hat{Q}(q+\delta q)$, and then start the following iteration to find the self-consistent solution at $q + \delta q$. [Below, the superscript (n) indicates the number of iterations.]

Step 2: Moving-frame HB equation

Using the operator $\hat{Q}^{(n-1)}(q + \delta q)$ $(n \geq 1)$, solve the moving-frame HB equation at $q + \delta q$,

$$\delta \left\langle \phi^{(n)}(q+\delta q) \right| \hat{H} - \lambda^{(n)}\hat{N} - \mu^{(n)}\hat{Q}^{(n-1)}(q+\delta q) \left| \phi^{(n)}(q+\delta q) \right\rangle = 0. \tag{3·66}$$

Here, the constraints Eqs. (3·30) and (3·31) determine the Lagrange multipliers, $\lambda^{(n)}$ and $\mu^{(n)}$. We use the gradient method described in Appendix B to solve Eq. (3·66). This determines the moving-frame HB state, $\left|\phi^{(n)}(q+\delta q)\right\rangle$.

Step 3: Local harmonic equation

Using $\left|\phi^{(n)}(q+\delta q)\right\rangle$ with the Lagrange multipliers $\lambda(q+\delta q) = \lambda^{(n)}$, solve the local harmonic equations (3·22) and (3·23). This determines the infinitesimal generator $\hat{Q}^{(n)}(q+\delta q)$.

Step 4: Self-consistency

Updating the infinitesimal generator $\hat{Q}^{(n)}(q+\delta q)$, return to *Step 2*, and repeat *Steps 2* and *3* until all quantities at $q+\delta q$ converge.

Step 5: Repetition

Change q to $q+\delta q$ and return to *Step 1*.

Carrying out these iterations, *Steps 1-5*, we obtain the collective path starting from the HB equilibrium point in one direction ($q > q_0$). The collective path in the opposite direction is obtained by changing the sign of δq and repeating the same procedure, *Steps 1-5*. In this way, we determine the self-consistent collective path passing through the HB equilibrium point.

We should give an additional remark concerning *Step 3*. When we solve the local harmonic equations, we set $f^{(-)}_{Q,1}(q) = 0$ in the iteration procedure to avoid a numerical instability problem.[70] We have confirmed that the solutions obtained under this assumption satisfy the required self-consistency. Quite recently, we have found that this prescription is valid generally. This recent progress in the ASCC method, including the proof of this validity, will be reported in another paper.[72]

The solution of the ASCC equations yields the classical collective Hamiltonian (for a constant particle number $N = N_0$):

$$\mathcal{H}(q,p) = \frac{1}{2}p^2 + V(q). \tag{3·67}$$

We then obtain the quantum collective Hamiltonian by carrying out the canonical quantization $\mathcal{H}(q,p) \to \mathcal{H}\left(q, \frac{1}{i}\frac{\partial}{\partial q}\right)$. Note that, in this quantization step, there is no ambiguity associated with the ordering of q and p, because the coordinate scale is chosen such that the inverse mass function is unity, i.e., $B(q) = 1$.

§4. Numerical calculations and discussion

4.1. *Details of the numerical calculation*

We solve the ASCC equations following the algorithm described in the previous section and determine the collective path embedded in the TDHB phase space. In order to investigate the effects of the quadrupole-pairing interaction on the large-amplitude collective dynamics, we use the same parameters as in Ref. 60), except for the quadrupole-pairing strength, G_2. We consider a system composed of three shells, with the spherical single-particle energies $e^0_{j_1} = 0$, $e^0_{j_2} = 1.0$, $e^0_{j_3} = 3.5$, the pair degeneracies $\Omega_{j_1} = 14$, $\Omega_{j_2} = 10$, $\Omega_{j_3} = 4$, and the single-particle quadrupole moments $d_{j_1} = 2$, $d_{j_2} = d_{j_3} = 1$ for each shell. One kind of fermion is considered in this model, and the number of particles N_0 is set to 28. This value is half of the total number of shell model states. The quadrupole particle-hole interaction strength χ is fixed to 0.04, while three values, 0.20, 0.16 and 0.14, are employed for the monopole pairing interaction strength G_0. For each case, the effects of the quadrupole-pairing interaction are studied for three values of its strength G_2, 0.00, 0.02 and 0.04. This parameter range is adopted so that the calculated ratios of the monopole and quadrupole pairing gaps are approximately equal to the value found

in realistic analysis.[55] The HB calculation yields a single spherical minimum for the $G_0 = 0.20$ case and two local minima, corresponding to the oblate and prolate equilibrium shapes, for the $G_0 = 0.16$ and 0.14 cases. For the latter cases, we present below the results obtained by starting from the prolate equilibrium point ($D > 0$). Of course, we obtain the identical collective path even if we start the calculation from the oblate equilibrium point ($D < 0$). Note that the multi-$O(4)$ Hamiltonian possesses "parity" symmetry (invariance under the transformation $\sigma_{jm} \to -\sigma_{jm}$, that is, $\hat{D} \to -\hat{D}$ and $\hat{B} \to -\hat{B}$). Therefore, all the quantities are either even or odd functions of the quadrupole deformation parameter D.

4.2. *Collective path and collective potential*

A nice property of the multi-$O(4)$ model is that by changing the ratio G_0/χ, we can simulate the phase transition in a finite quantum system from a single-well to a double-well potential. This is analogous to the nuclear shape phase transition and shape coexistence phenomena. The collective potential V and the pairing gaps Δ_0 and Δ_2 are displayed in Figs. 1 and 2. In the ASCC method, these quantities are calculated as functions of the collective coordinate q, but they are easily converted to those as functions of D. (See the relation between q and D shown in the left panels of Fig. 3.) We see that the collective potential changes from a single well to a double well as the ratio G_0/χ decreases, i.e., as the effect of the monopole-pairing interaction is weakened. When oblate and prolate shapes coexist (for $G_0 = 0.14, 0.16$), the collective path calculated from one local minimum passes through the other local minimum. In this case it is seen that $\Delta_0(D)$ decreases while $|\Delta_2(D)|$ increases as D increases. Both gaps vanish in the limits, $D \to D_{\min} = -42$ and $D \to D_{\max} = 42$. This behavior is due to the smallness of the model space and does not exist in realistic situations. The quadrupole-pairing gap $|\Delta_2(D)|$ is maximal at the prolate and oblate HB equilibrium points. Because of the energy gain associated with the quadrupole pairing, the oblate and prolate local minima in the collective potential $V(D)$ decrease as G_2 increases.

Significant effects of the quadrupole-pairing interaction are obviously seen in the solutions of the local harmonic equations. The squared frequencies $\omega^2(q)$, representing the curvature of the collective potential, are shown in the right column of Fig. 3, while the sums $\sum_{i>0} |Q_i(q)|^2$ and $\sum_{i>0} |P_i(q)|^2$ of the two quasiparticle components, $Q_i(q)$ and $P_i(q)$, are displayed in Fig. 4. They are again plotted as functions of D. It is clearly seen that the absolute magnitudes of $Q_i(q)$ increase significantly, while those of $P_i(q)$ decrease with increasing G_2. (To avoid complication, their sums, rather than individual values, are presented in Fig. 4.) These changes in the microscopic structure of $\hat{Q}(q)$ and $\hat{P}(q)$ lead to the increase of the derivative dq/dD with increasing G_2 (Fig. 3). This results in a significant enhancement of the collective mass $M(D(q))$ with respect to the coordinate of the quadrupole deformation parameter D. These interesting properties of the collective mass are the main subject of this paper and are discussed in the next subsection.

We have also carried out constrained HB (CHB) calculations, choosing the quadrupole operator $\hat{D}$ as the constraint. The calculated values of $V(D)$, $\Delta_0(D)$ and $\Delta_2(D)$ were almost indistinguishable from those obtained with the ASCC method

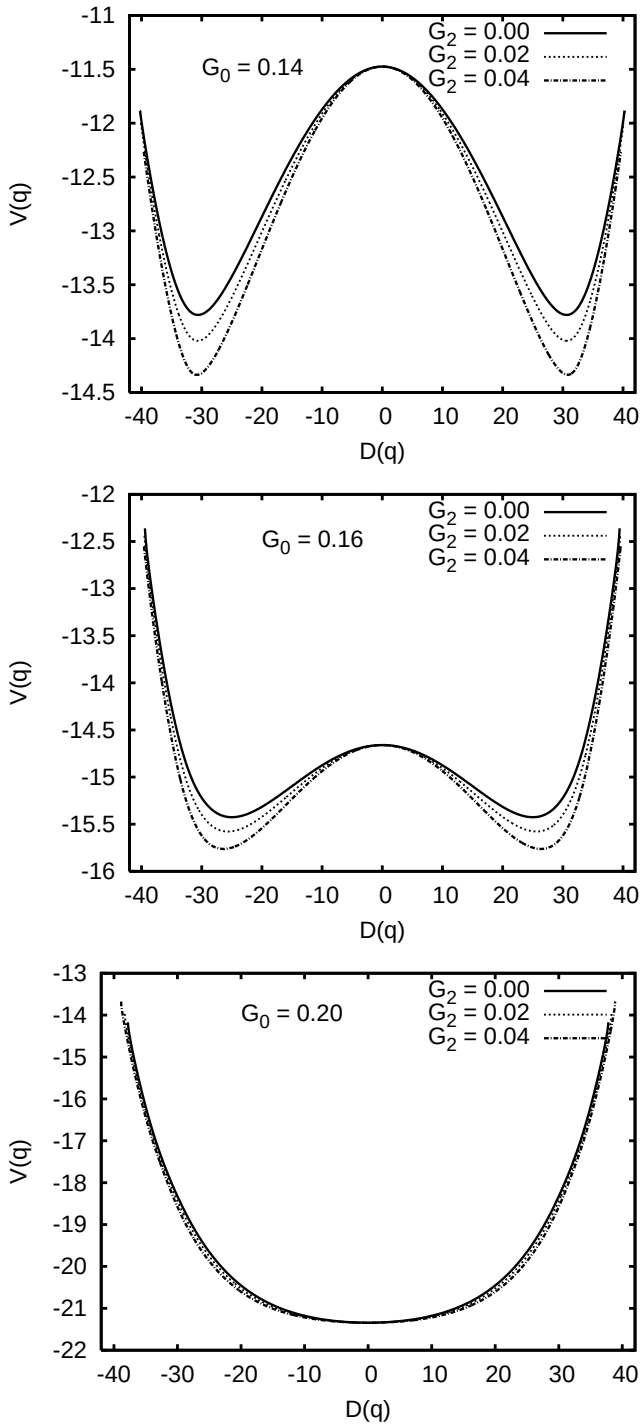

Fig. 1. Collective potentials plotted as functions of the quadrupole deformation D. The upper, middle and lower panels display the results for $G_0 = 0.14, 0.16$ and 0.20, respectively. In each panel, the results for $G_2 = 0.00, 0.02$ and 0.04 are compared.

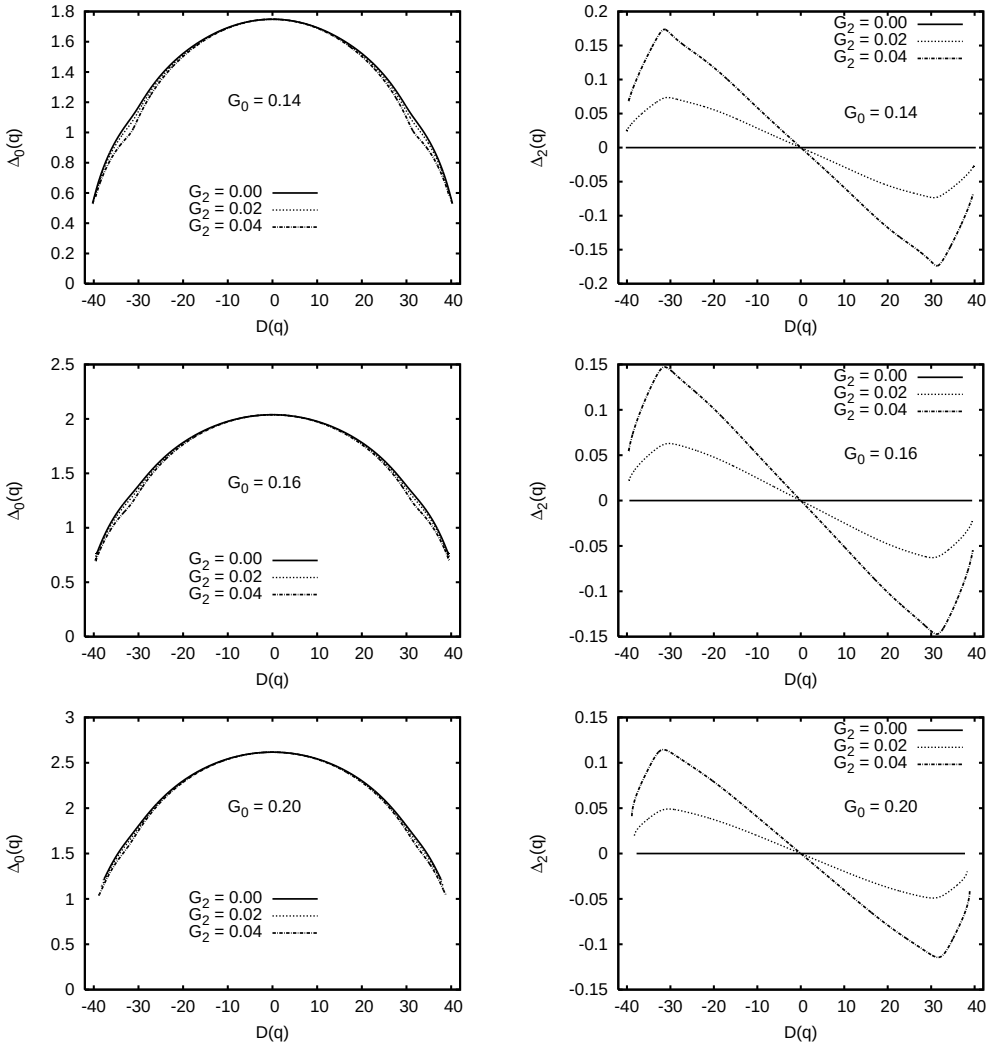

Fig. 2. Monopole-pairing gaps Δ_0 (*left column*) and quadrupole-pairing gaps Δ_2 (*right column*), plotted as functions of D. The upper, middle and lower rows display the results for $G_0 = 0.14, 0.16$ and 0.20, respectively. In each panel, the results for $G_2 = 0.00, 0.02$ and 0.04 are compared.

displayed in Figs. 1 and 2. Thus, with regard to these static mean-field quantities, we find no difference between the ASCC and the CHB calculations. It should be noted, however, that this good agreement is due to the simplicity of the multi-$O(4)$ model; i.e., it contains only one degree of freedom, $\hat{D}$, relevant to the large-amplitude collective motion. In reality, many degrees of freedom (a variety of particle-hole excitations associated with shell structures, triaxial deformations, various multipolarities, low and high frequency excitations, etc.) would be interwoven to generate the large-amplitude collective motion. In fact, it has been shown that the self-consistently determined collective coordinate operators for low-frequency quadrupole-type col-

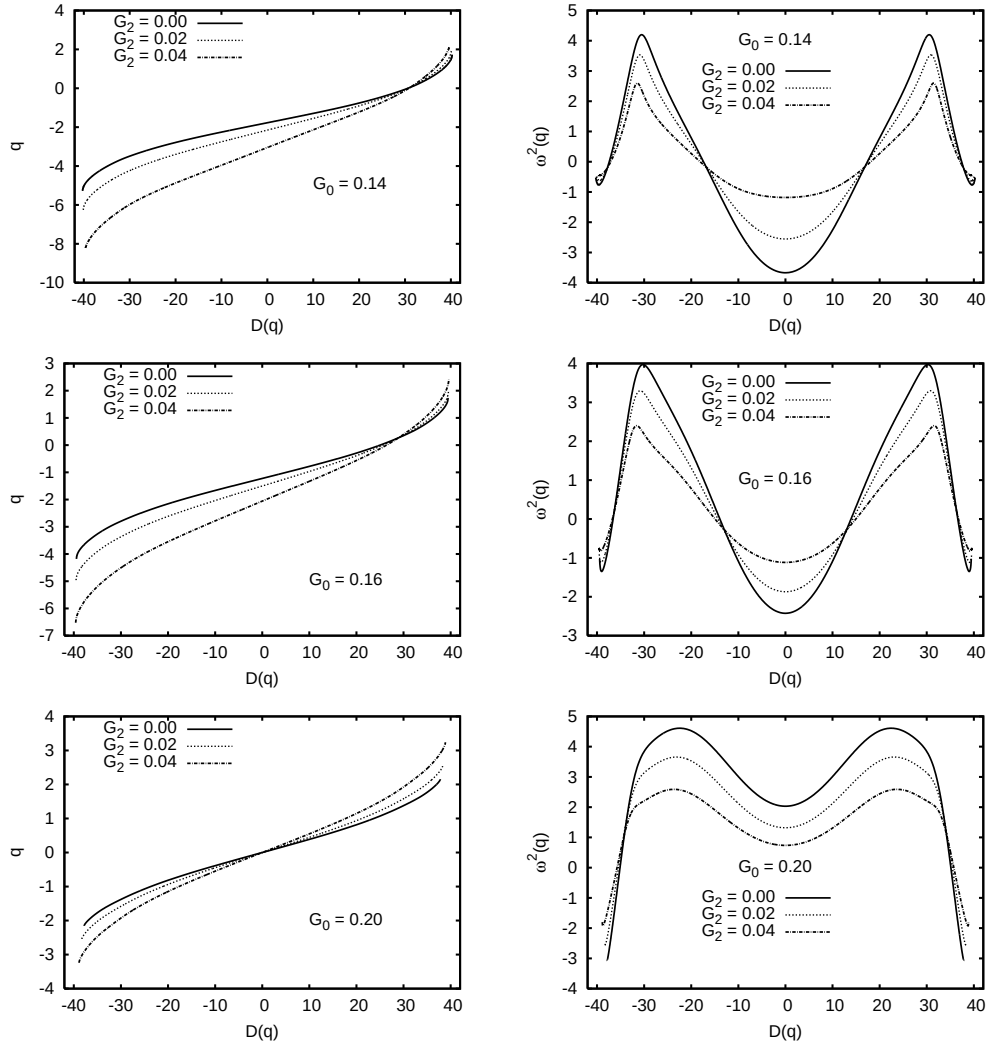

Fig. 3. *Left column*: Relation between the collective coordinate q and the quadrupole deformation $D(q) = \langle\phi(q)|\,\hat{D}\,|\phi(q)\rangle$. The point $q = 0$ corresponds to the HB equilibrium, which is the starting point of the numerical calculation. *Right column*: Squared frequencies $\omega^2(q)$ of the local harmonic equation, plotted as functions of D. Note that they are negative; i.e., $\omega(q)$ is purely imaginary in the region where the curvature of the collective potential is negative. The upper, middle and lower rows display the results for $G_0 = 0.14, 0.16$ and 0.20, respectively. In each panel, the results for $G_2 = 0.00, 0.02$ and 0.04 are compared.

lective vibration differ significantly from the quadrupole operators (see, for instance, Ref. 30)). Let us now consider the collective mass, where we can clearly see the merits of the ASCC method.

4.3. *Collective mass*

As mentioned in §3.5, we set the scale of the collective coordinate q so as to make the collective mass unity. In order to compare the collective mass obtained using the

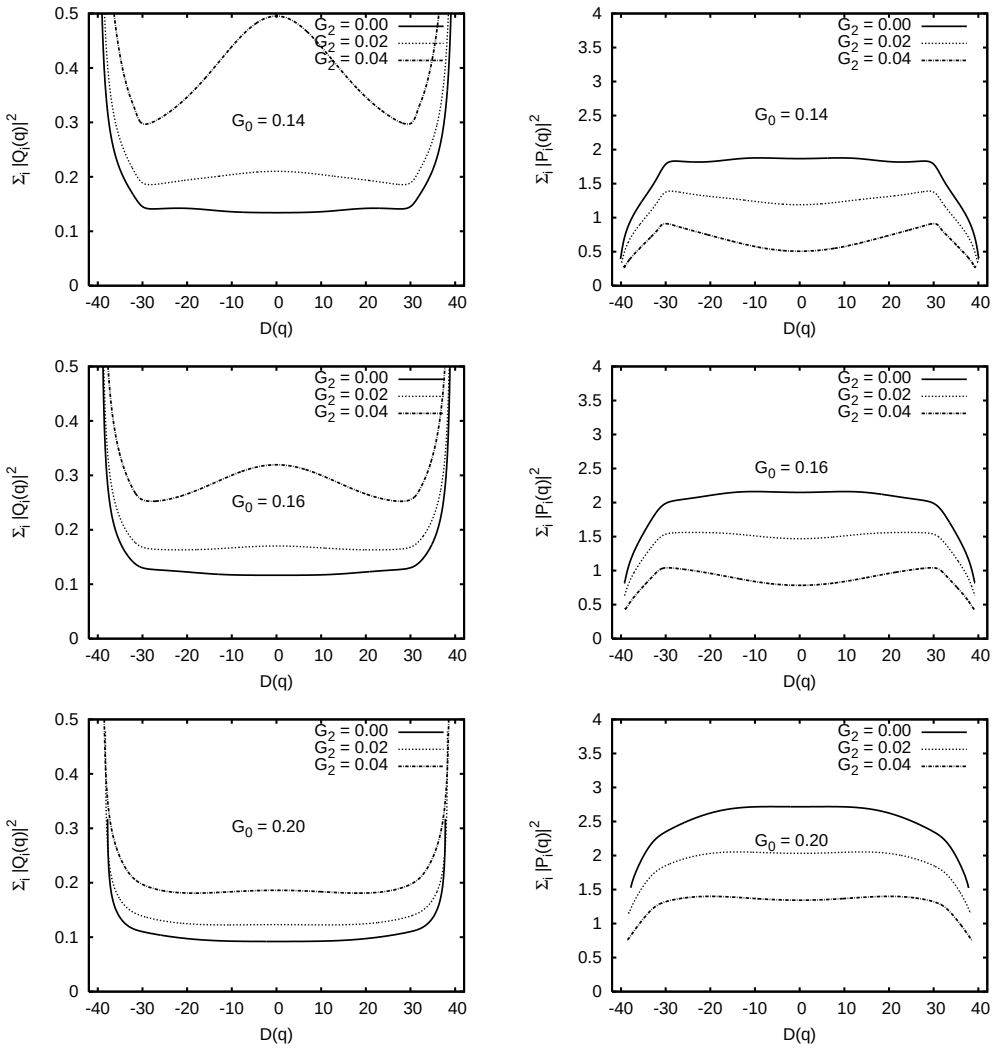

Fig. 4. The sums $\sum_{i>0}|Q_i(q)|^2$ and $\sum_{i>0}|P_i(q)|^2$ of the two quasi-particle components, $Q_i(q)$ and $P_i(q)$, of the infinitesimal generators $\hat{Q}(q)$ and $\hat{P}(q)$, plotted as functions of the quadrupole deformation D. The upper, middle and lower rows display the results for $G_0 = 0.14$, 0.16 and 0.20, respectively. In each panel, the results for $G_2 = 0.00, 0.02$ and 0.04 are compared.

ASCC method with the conventional cranking mass, let us evaluate the collective mass as a function of the quadrupole deformation D. This quantity, $M(D(q))$, is readily obtained by transforming the collective kinetic energy as a function of the velocity $\dot{D}$:

$$\frac{1}{2}B(q)p^2 = \frac{1}{2}p^2 = \frac{1}{2}\dot{q}^2 = \frac{1}{2}M(D(q))\dot{D}^2, \tag{4·1}$$

$$M(D(q)) = \left(\frac{dq}{dD}\right)^2 = \left(4\sum_{i>0} d_i\sigma_i u_i v_i P_i(q)\right)^{-2}. \tag{4·2}$$

As is well known, the Inglis-Belyaev cranking mass is derived by means of adiabatic perturbation theory[1] and is given by

$$M_{\rm cr}(D) = 2\sum_n \frac{|\,\langle\phi_n(D)|\,\dfrac{\partial}{\partial D}\,|\phi_0(D)\rangle\,|^2}{E_n(D)-E_0(D)}. \tag{4·3}$$

Here, $|\phi_0(D)\rangle$ and $E_0(D)$ represent the ground state and its energy at the deformation D, while $|\phi_n(D)\rangle$ and $E_n(D)$ represent the (two-quasiparticle) excited states and their energies. We can use this formula either treating the deformation D as a phenomenological parameter or a self-consistently determined quantity. If the ground states are calculated at every point of D by means of the CHB method, i.e., using

$$\delta\,\langle\phi_0(D)|\,\hat{H}-\lambda(D)\hat{N}-\mu(D)\hat{D}\,|\phi_0(D)\rangle = 0, \tag{4·4}$$

with the self-consistency conditions for the particle number and the quadrupole deformation,

$$\langle\phi_0(D)|\,\hat{N}\,|\phi_0(D)\rangle = N_0, \quad \langle\phi_0(D)|\,\hat{D}\,|\phi_0(D)\rangle = D, \tag{4·5}$$

then we obtain the following explicit expression for $M_{\rm cr}(D)$:

$$M_{\rm cr}(D) = 2\sum_{i>0}\frac{1}{(2E_i(D))^3}\Big|\,2u_i(D)v_i(D)\left(\left(\chi+\frac{\partial\mu}{\partial D}\right)d_i\sigma_i+\frac{\partial\lambda}{\partial D}\right) + (u_i^2(D)-v_i^2(D))\left(\frac{\partial\Delta_0}{\partial D}+d_i\sigma_i\frac{\partial\Delta_2}{\partial D}\right)\Big|^2. \tag{4·6}$$

Hereafter, we call this the "CHB-cranking mass". Note that here we have used a slightly different definition of the cranking mass than in Ref. 60), in which the CHB self-consistency is ignored.

In Fig. 5, the ASCC mass $M(D(q))$ is plotted as a function of D and compared with the CHB-cranking mass $M_{\rm cr}(D)$ for various combinations of the pairing-interaction strengths, G_0 and G_2. It is seen that these quantities diverge near $D_{\rm min} = -42$ and $D_{\rm max} = 42$. This behavior indicates that, in the multi-$O(4)$ model under consideration, it becomes harder and harder to increase D as either of these limits is approached. For this reason, we focus our attention on the region of intermediate values of D. This is the region important for the quantum mechanical tunneling motion through the barrier (small G_0/χ case) and for the vibrational motion about the spherical equilibrium (large G_0/χ case). It is seen that when the quadrupole-pairing interaction is absent ($G_2 = 0$), the magnitudes of the ASCC mass are almost the same as those of the CHB-cranking mass. They also exhibit similar deformation dependence. When the quadrupole-pairing interaction is switched on, however, a significant difference between the ASCC and the CHB-cranking masses appears: The ASCC mass increases significantly as G_2 increases, while the CHB-cranking mass changes very little.

The origin of this different behavior of $M(D(q))$ and $M_{\rm cr}(D)$ can be understood in the following way. The CHB-cranking mass is derived by ignoring the contribution of the residual interaction to the collective mass, and thus the effects of the

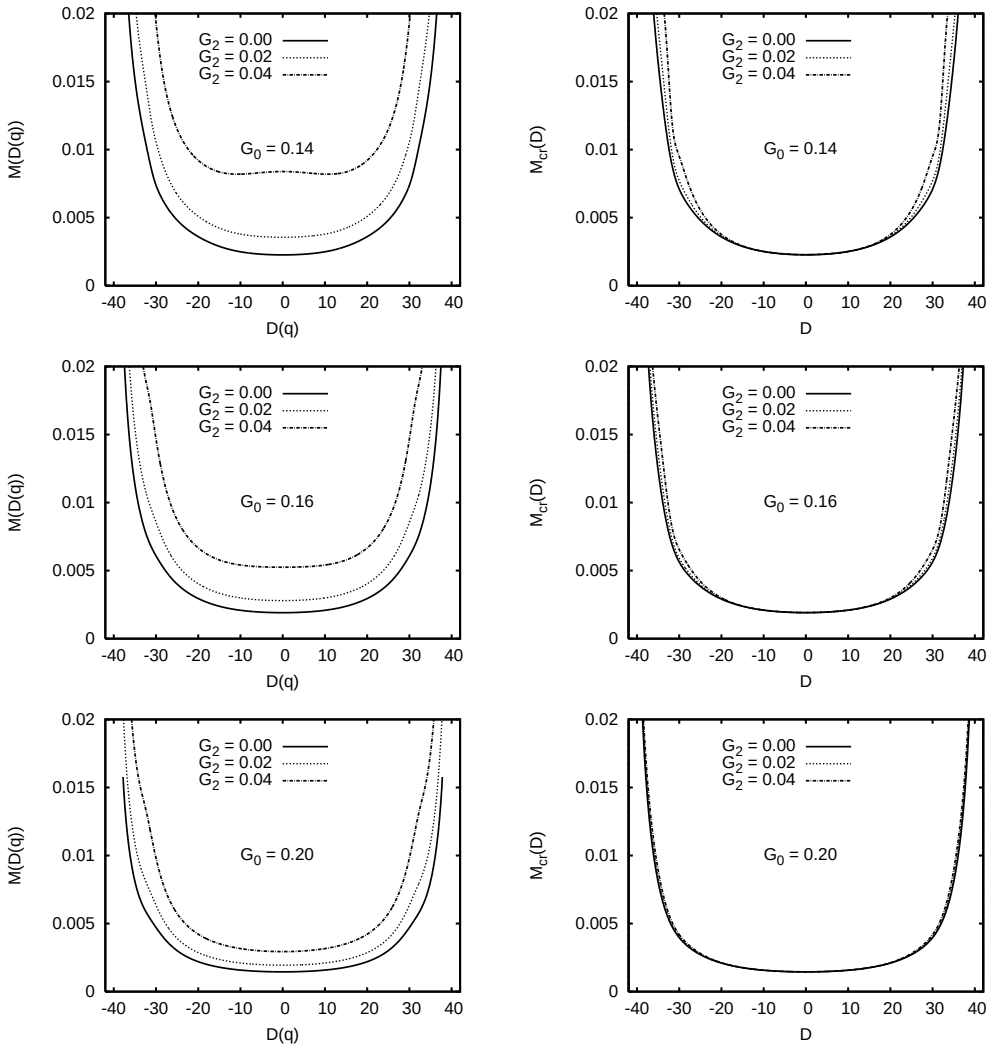

Fig. 5. The ASCC collective mass $M(D(q))$ (*left column*) and the CHB-cranking mass $M_{\rm cr}(D)$ (*right column*) as functions of the deformation D. The upper, middle and lower rows display the results for $G_0 = 0.14, 0.16$ and 0.20, respectively. In each panel, the results for $G_2 = 0.00, 0.02$ and 0.04 are compared.

quadrupole-pairing interaction are taken into account only in the static quantities, like the quadrupole-pairing gap $\Delta_2(D)$. Contrastingly, the effects of the residual interaction on the dynamics are taken into account in the ASCC method through the time-odd components of the mean-field, which change sign under time reversal, $p \to -p$. The time-odd part of the mean-field Hamiltonian, $\hat{h}(t)$, represents the change in the self-consistent mean-field associated with the dynamical motion. It is well known that this part is necessary to obtain the correct center of mass for the translational motion.[8] On the other hand, it is also known that neither the monopole-pairing interaction nor the quadrupole particle-hole interaction con-

tributes to the time-odd part.[8),12),69)] Thus, only the quadrupole-pairing interaction contributes to the time-odd part in the case of the multi-$O(4)$ model Hamiltonian under consideration.

The significant difference between the ASCC mass and the CHB-cranking mass displayed in Fig. 5 clearly indicates the importance of the quadrupole-pairing interaction on the collective dynamics. This is in striking contrast to its effect on static properties. In that case, the important properties of the collective potential energy curve $V(D)$ are determined by the competition between the monopole-pairing and quadrupole particle-hole correlations. There, $\Delta_2(D)$ is much smaller than $\Delta_0(D)$, and therefore the quadrupole pairing plays only a minor role. However, it plays a major role in determining the dynamical properties of collective motion.

4.4. *Excitation spectra and transition matrix elements*

We calculate the eigen-energies E_k and wave functions $\Psi_k(q)$ for the quantized large-amplitude collective motion by solving the collective Schrödinger equation,

$$\left(-\frac{1}{2}\frac{\partial^2}{\partial q^2} + V(q)\right)\Psi_k(q) = E_k\Psi_k(q), \tag{4·7}$$

with the orthonormalization

$$\int_{q_{\min}}^{q_{\max}} \Psi_k^*(q)\Psi_l(q)dq = \delta_{kl}, \tag{4·8}$$

and the boundary conditions $\Psi_k(q_{\min}) = \Psi_k(q_{\max}) = 0$, where $q_{\min}$ and $q_{\max}$ are the minimum and maximum values of q along the collective path (see Fig. 3). The quadrupole transition matrix elements are evaluated as

$$\langle\Psi_k|\,\hat{D}\,|\Psi_l\rangle = \int_{q_{\min}}^{q_{\max}} \Psi_k^*(q)D(q)\Psi_l(q)dq, \tag{4·9}$$

where the deformation $D(q)$ is defined on the collective path by Eq. (3·14).

Figure 6 displays the results of the ASCC calculation for excitation spectra and quadrupole transition matrix elements between low-lying states. For $G_0 = 0.20$ we obtain anharmonic vibrational spectra about the spherical equilibrium. By contrast, the collective potential $V(D)$ for $G_0 = 0.14$ and 0.16 possesses two local minima, corresponding to the oblate and prolate shapes, and the spherical point ($D = 0$) becomes the top of the barrier. In the $G_0 = 0.14$ case, this barrier is high. Consequently, a ground state doublet similar to the well-known parity doublet in the double well potential appears. In the present multi-$O(4)$ model, the doublet corresponds to the symmetric and anti-symmetric superpositions of the oblate and prolate ground states, and its energy splitting provides a sensitive measure of the quantum tunneling effect through the potential barrier. Contrastingly, in the $G_0 = 0.16$ case, the barrier is rather low, and therefore the spectrum exhibits a transient feature toward the doublet pattern mentioned above. In the quantum spectra displayed in Fig. 6, we can clearly identify the effects of the increase of the collective mass due to the quadrupole pairing. First, the vibrational excitation energy decreases as G_2

increases. Second, the energy splitting of the doublet decreases with increasing G_2, indicating that tunneling becomes more difficult as the collective mass increases. Thus, for the combination $G_0 = 0.14$ and $G_2 = 0.04$, we obtain a doublet of excited states in addition to the ground-state doublet. The wave functions of the excited-state doublet as well as the ground-state doublet are displayed in Fig. 9. This figure clearly indicates that the excited doublet corresponds to symmetric and anti-symmetric linear combinations of vibrational excitations about the oblate and prolate local minima. We also confirm that the amplitude in the barrier region indeed decreases with increasing G_2.

In Fig. 7, the results of the exact matrix diagonalization of the microscopic multi-$O(4)$ Hamiltonian are presented. It is found that for every combination of the interaction strengths G_0, G_2 and χ, the excitation spectra and the transition matrix elements obtained with the ASCC method agree to very good approximation with the results of the exact calculation. It is a significant result that the ASCC calculation can describe the gradual change of the quantum spectra associated with the phase transition of the finite system from a spherical shape to oblate-prolate shape coexistence.

We now carry out a thorough quantitative comparison concerning the energy splitting of the ground-state doublet in the $G_0 = 0.14$ case. The splittings obtained in the ASCC method are 0.043, 0.012, and 5×10^{-4} for $G_2 = 0.00, 0.02$ and 0.04, respectively. The corresponding values obtained by the exact diagonalization are 0.091, 0.020 and 3×10^{-4}. It should be noted here that the energy splitting under discussion is a very small quantity associated with the barrier penetration for which even a slight error in the collective mass can result in an error similar in size to the magnitude of the energy splitting itself. Therefore, the obtained agreement within a factor of 2 indicates that the collective mass evaluated using the ASCC method is very reliable. It should also be emphasized that this tunneling motion is large-amplitude collective motion associated with the rearrangement of microscopic configurations of many particles and that the collective mass represents the inertia of this motion of the many-body system as a whole. Thus, the accurate evaluation of the collective mass is a highly non-trivial task.

Let us now investigate how the difference between the ASCC mass and the CHB-cranking mass discussed in the previous subsection affects the excitation spectra and the transition matrix elements. Adopting the Pauli quantization prescription, we obtain the collective Schrödinger equation

$$\left(-\frac{1}{2M_{\rm cr}(D)^{1/4}}\frac{\partial}{\partial D}\frac{1}{\sqrt{M_{\rm cr}(D)}}\frac{\partial}{\partial D}\frac{1}{M_{\rm cr}(D)^{1/4}} + V_{\rm CHB}(D)\right)\Psi_k^{(\rm cr)}(D) = E_k^{(\rm cr)}\Psi_k^{(\rm cr)}(D) \tag{4·10}$$

for the wave functions $\Psi_k^{(\rm cr)}(D)$ that incorporate the metric factor $M_{\rm cr}(D)^{1/4}$ such that the orthonormalizations are given by[71]

$$\int_{D_{\rm min}}^{D_{\rm max}} \Psi_k^{(\rm cr)*}(D)\Psi_l^{(\rm cr)}(D)dD = \delta_{kl}. \tag{4·11}$$

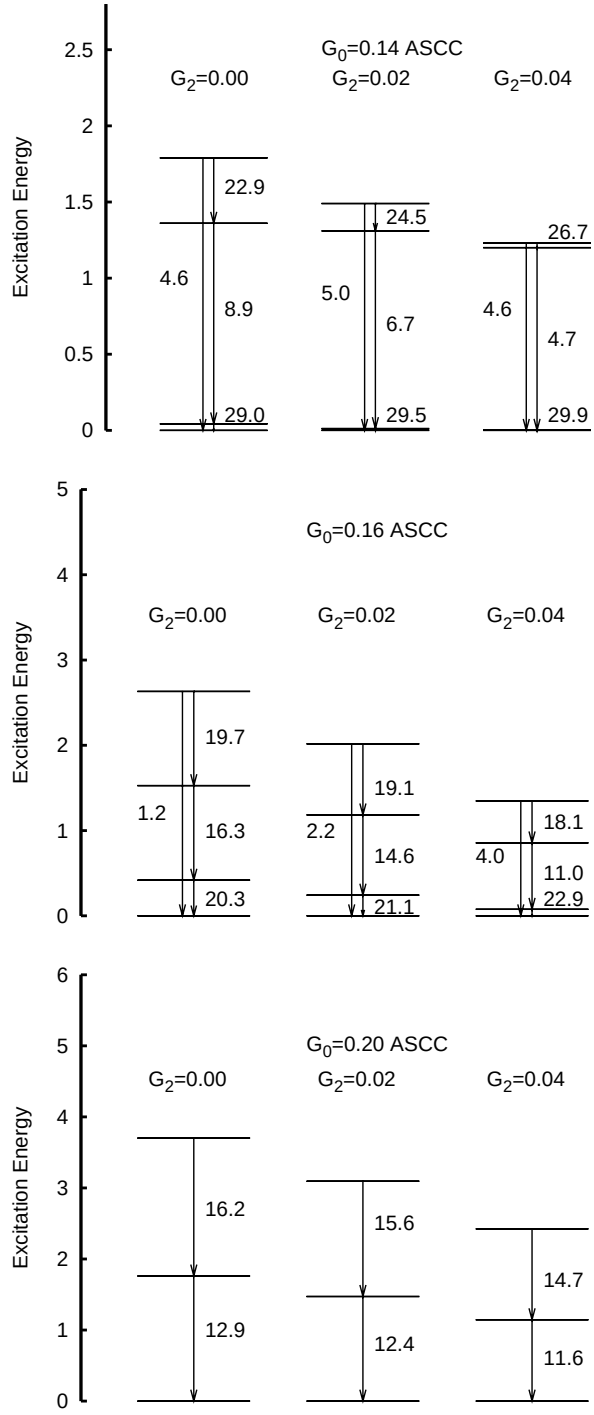

Fig. 6. Excitation spectra calculated with the ASCC method. The upper, middle and lower rows display the results for $G_0 = 0.14$, 0.16 and 0.20, respectively. In each row, the results for $G_2 = 0.00, 0.02$ and 0.04 are compared. The numbers adjacent to the vertical lines are the absolute values of the transition matrix elements. The matrix elements between the doublets are indicated beside them.

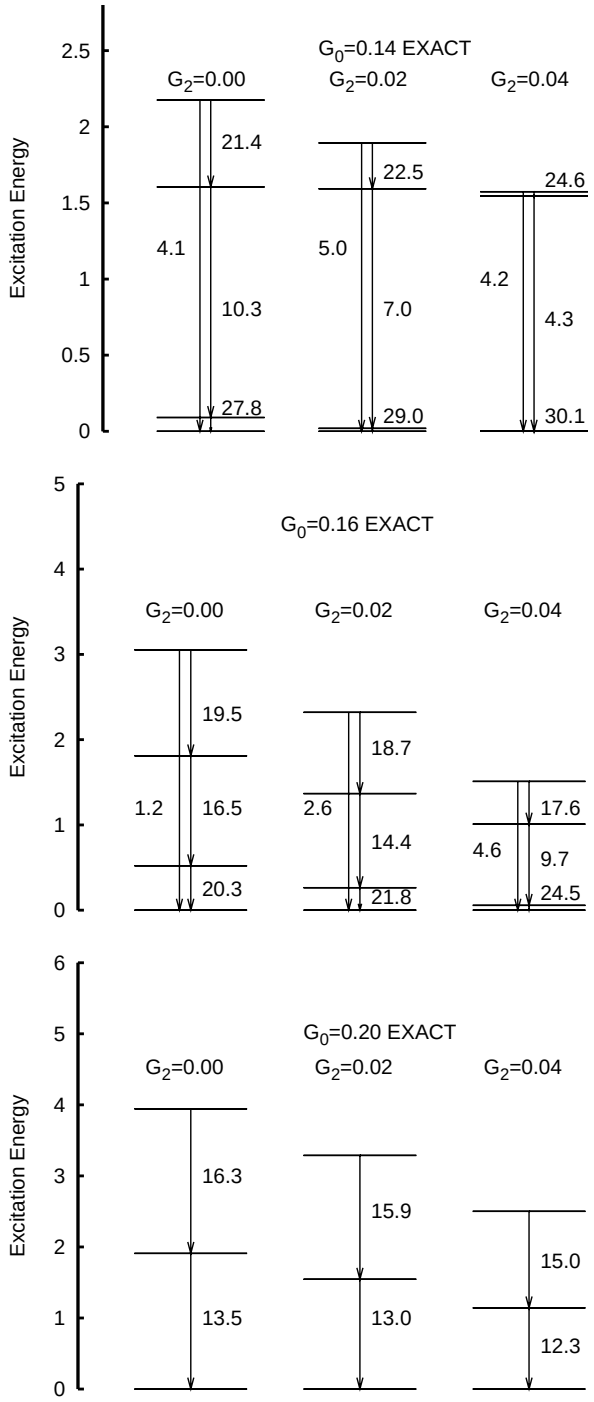

Fig. 7. Excitation spectra calculated with the exact diagonalization. (See the caption of Fig. 6.)

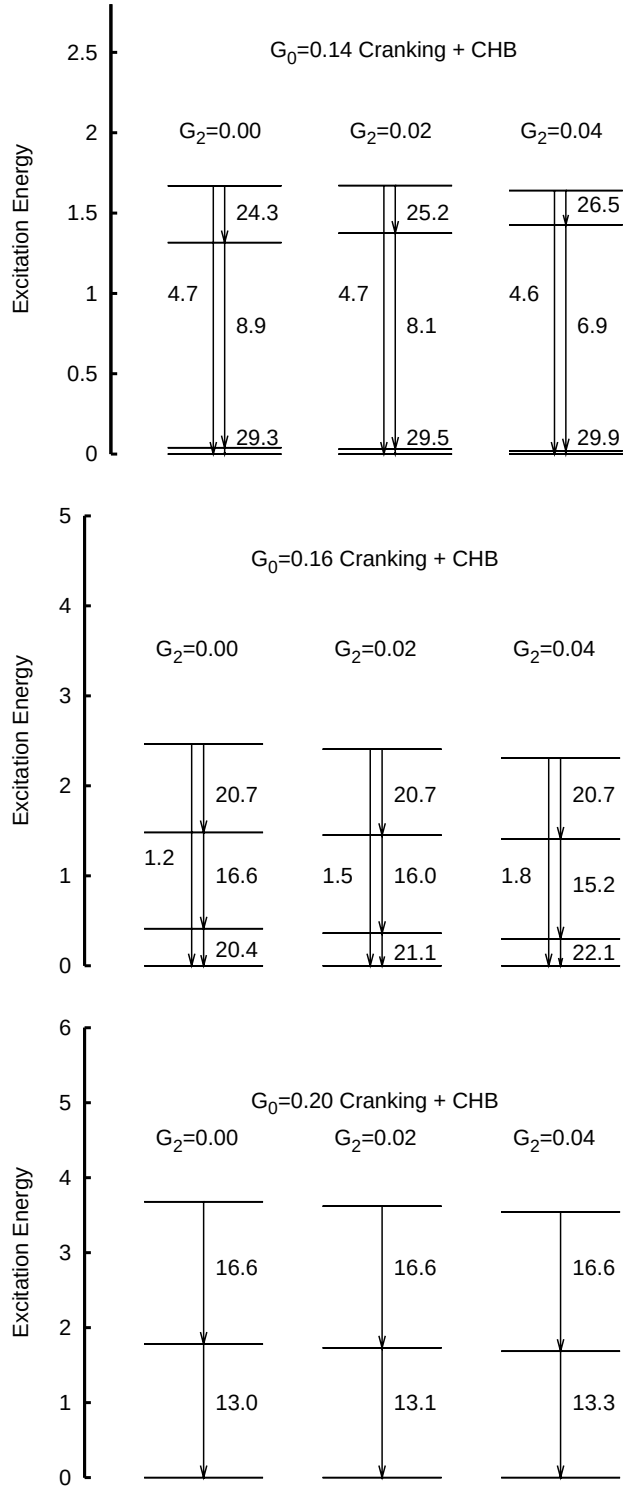

Fig. 8. Excitation spectra calculated with the CHB-cranking procedure. (See the caption of Fig. 6.)

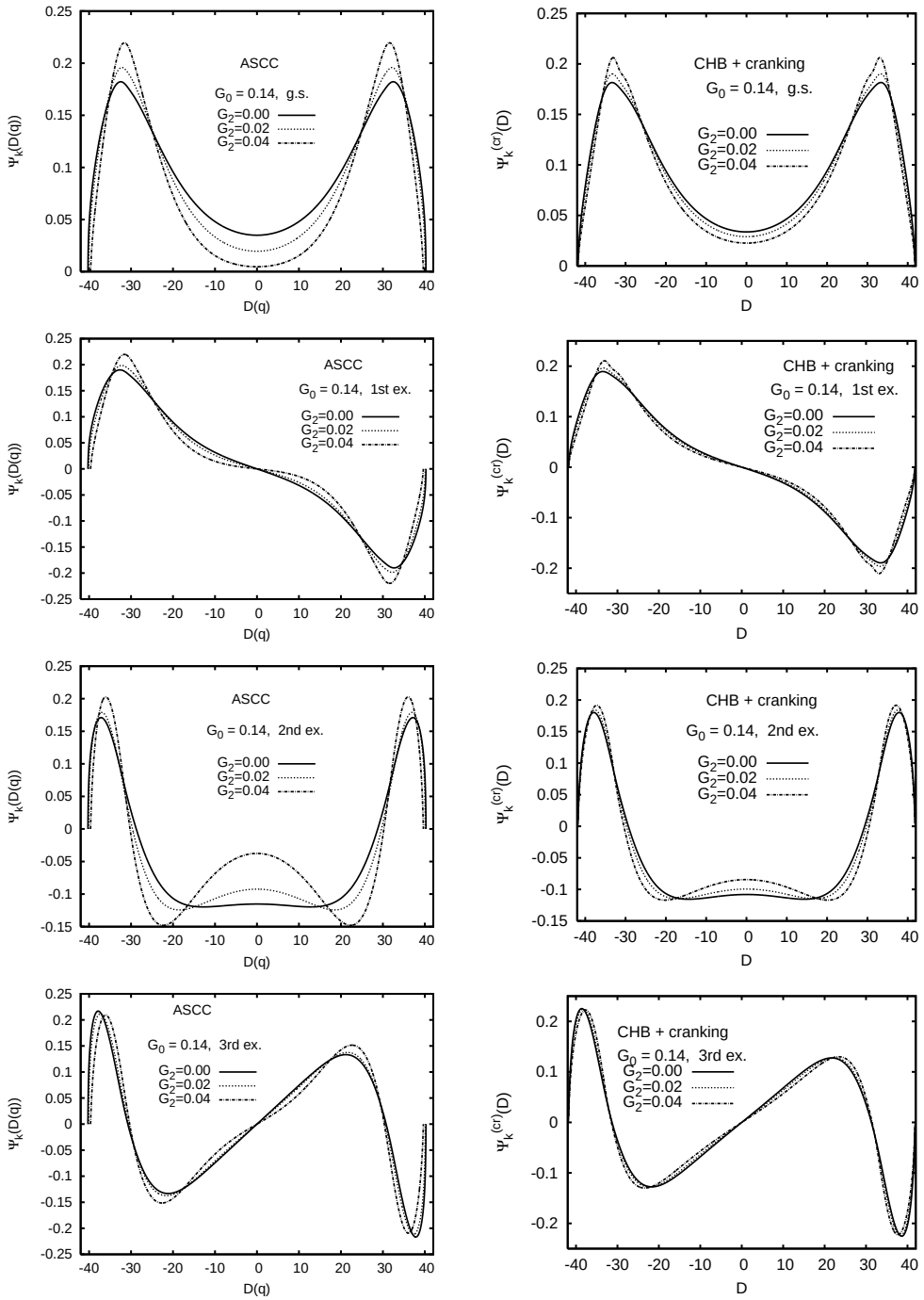

Fig. 9. Wave functions of eigenstates of the collective Schrödinger equation, Eq. (4·10), for $G_0 = 0.14$. The wave functions obtained with the ASCC (CHB-cranking) method are plotted in the left (right) column. In order to allow comparison, they are both plotted as functions of the parameter D. Specifically, those of the ASCC method are defined by $\Psi_k(D(q)) \equiv \Psi_k(q)\sqrt{dq/dD} = \Psi_k(q)M(D(q))^{1/4}$ and normalized as $\int |\Psi_k(D)|^2 dD = 1$. The first, second, third and fourth rows display the wave functions for the ground state, the first, second, and third excited states, respectively. In each panel, the results for $G_2 = 0.00, 0.02$ and 0.04 are compared.

We solve this Schrödinger equation under the boundary conditions $\Psi_k^{(\mathrm{cr})}(D_{\min}) = \Psi_k^{(\mathrm{cr})}(D_{\max}) = 0$. The quadrupole transition matrix elements are evaluated by

$$\left\langle \Psi_k^{(\mathrm{cr})} \middle| \hat{D} \middle| \Psi_l^{(\mathrm{cr})} \right\rangle = \int_{D_{\min}}^{D_{\max}} \Psi_k^{(\mathrm{cr})*}(D) D \Psi_l^{(\mathrm{cr})}(D) dD. \tag{4·12}$$

As mentioned in §4.2, the ASCC collective potential $V(q)$ almost coincides with the potential $V_{\mathrm{CHB}}(D)$ calculated by means of the CHB method, and hence the difference between the quantum spectra can be mainly attributed to the difference between the collective masses. The results are displayed in Fig. 8. When the quadrupole pairing is absent ($G_2 = 0$), we find rather good agreement between the CHB-cranking results and the exact solutions. However, the excitation spectra and transition matrix elements are almost unchanged when the quadrupole-pairing interaction is switched on and G_2 increases. This represents a significant difference between the ASCC method and the CHB-cranking calculation. We can confirm this point also by considering the wave functions displayed in Fig. 9. The amplitudes in the barrier region change only little when G_2 increases, in contrast to the ASCC wave functions. It is obvious that this failure to take into account the effect of the quadrupole pairing originates from the fact that the CHB-cranking procedure ignores the time-odd mean-field contribution to the collective mass.

§5. Conclusions

The multi-$O(4)$ model is a simple model to simulate phase transitions in finite quantum systems from a spherical shape to oblate-prolate shape coexistence. We have applied the ASCC method to this model and studied the collective mass of the many-body tunneling motion through the potential barrier between the oblate and prolate local minima. Comparing our results with those obtained from the exact diagonalization, we have shown that the ASCC method succeeds in describing the gradual change of the excitation spectra from anharmonic vibration about the spherical equilibrium to the doublet pattern associated with the deformed double-well potential possessing oblate-prolate symmetry. It was found that the collective mass increases significantly due to the quadrupole-pairing contribution to the time-odd component of the moving mean field. We have also shown that the CHB-cranking procedure underestimates the collective mass, because the contribution from the time-odd component is disregarded there.

Employing the approach developed in this paper, in a forthcoming paper[72] we will evaluate the contribution of the time-odd components to the collective mass of the large amplitude collective motion associated with the oblate-prolate shape coexistence in the ^{68}Se and ^{72}Kr regions.

Acknowledgements

This work is supported by a Grant-in-Aid for the 21st Century COE "Center for Diversity and Universality in Physics" from the Ministry of Education, Culture,

Sports, Science and Technology (MEXT) of Japan and also by Grants-in-Aid for Scientific Research (Nos. 16540249, 17540231 and 17540244) from the Japan Society for the Promotion of Science. We thank the Yukawa Institute for Theoretical Physics at Kyoto University, discussions during the YITP workshop YITP-W-05-01, on "New Developments in Nuclear Self-Consistent Mean-Field Theories" were useful in completing this work. We also thank the Institute for Nuclear Theory at the University of Washington for its hospitality and the Department of Energy for partial support during the completion of this work.

Appendix A

—— *Exact Diagonalization of the Multi-$O(4)$ Model Hamiltonian* ——

It is possible to construct the following two sets of $SU(2)$ generators for each j-shell from the basic operators of the multi-$O(4)$ model:

$$K_j^+ = \frac{1}{2}(\hat{A}_j^\dagger + \hat{B}_j^\dagger), \qquad L_j^+ = \frac{1}{2}(\hat{A}_j^\dagger - \hat{B}_j^\dagger), \tag{A·1}$$

$$K_j^- = \frac{1}{2}(\hat{A}_j + \hat{B}_j), \qquad L_j^- = \frac{1}{2}(\hat{A}_j - \hat{B}_j), \tag{A·2}$$

$$K_j^0 = \frac{1}{2}(\hat{N}_j + \hat{D}_j - \Omega_j), \qquad L_j^0 = \frac{1}{2}(\hat{N}_j - \hat{D}_j - \Omega_j). \tag{A·3}$$

The operators $\{K_{j+}, K_{j-}, K_{j0}\}$ and $\{L_{j+}, L_{j-}, L_{j0}\}$ satisfy the commutation relations of the $SU(2)$ algebra:

$$[K_j^+, K_{j'}^-] = 2K_j^0\delta_{jj'}, \qquad [L_j^+, L_{j'}^-] = 2L_j^0\delta_{jj'}, \tag{A·4}$$

$$[K_j^0, K_{j'}^\pm] = \pm K_j^\pm\delta_{jj'}, \qquad [L_j^0, L_{j'}^\pm] = \pm L_j^\pm\delta_{jj'}. \tag{A·5}$$

All commutation relations between the K and L operators are zero. Thus, we can construct the orthogonal basis vectors of the model space as

$$|\boldsymbol{n_K}, \boldsymbol{n_L}\rangle \equiv \prod_j |n_{K_j}, n_{L_j}\rangle \equiv \prod_j (K_j^+)^{n_{K_j}} (L_j^+)^{n_{L_j}} |0\rangle, \tag{A·6}$$

where (n_{K_j}, n_{L_j}) are integers satisfying the relations $0 \le n_{K_j}, n_{L_j} \le \Omega_j/2$ and $\sum_j (n_{K_j} + n_{L_j}) = N_0/2$.

In terms of these $SU(2)$ generators, the multi-$O(4)$ Hamiltonian is expressed as

$$\begin{aligned}\hat{H} = &\sum_j e_j^0\{2(K_j^0 + L_j^0) + \Omega_j\} - 2\chi \sum_{ij} d_i d_j (K_i^0 - L_i^0)(K_j^0 - L_j^0) \\ &- \frac{1}{2}\sum_{ij}(G_0 + G_2 d_i d_j)(K_i^+ K_j^- + K_i^+ K_j^- + L_i^+ L_j^- + L_i^- L_j^+) \\ &- \frac{1}{2}\sum_{ij}(G_0 - G_2 d_i d_j)(K_i^- L_j^+ + K_i^+ L_j^- + L_i^- K_j^+ + L_i^+ K_j^-).\end{aligned} \tag{A·7}$$

The operators K_j^+, K_j^- and K_j^0 act on the basis $\left|n_{K_j}, n_{L_j}\right\rangle$ as

$$K_j^0 \left|n_{K_j}, n_{L_j}\right\rangle = \left(n_{K_j} - \frac{\Omega_j}{4}\right) \left|n_{K_j}, n_{L_j}\right\rangle, \tag{A·8a}$$

$$K_j^+ \left|n_{K_j}, n_{L_j}\right\rangle = \sqrt{(n_{K_j}+1)\left(\frac{\Omega_j}{2} - n_{K_j}\right)}\left|n_{K_j}+1, n_{L_j}\right\rangle, \tag{A·8b}$$

$$K_j^- \left|n_{K_j}, n_{L_j}\right\rangle = \sqrt{n_{K_j}\left(\frac{\Omega_j}{2} - n_{K_j}+1\right)}\left|n_{K_j}-1, n_{L_j}\right\rangle. \tag{A·8c}$$

Similar equations hold for L_j^+, L_j^-, and L_j^0. The matrix elements of the multi-$O(4)$ Hamiltonian, $\langle \boldsymbol{n_K}', \boldsymbol{n_L}'| \hat{H} |\boldsymbol{n_K}, \boldsymbol{n_L}\rangle$, can be calculated by using Eqs. (A·7) and (A·8). Diagonalizing this matrix, we obtain the exact eigen-energies and eigen-states. For the parameters given in the text, the dimension of this Hamiltonian matrix is 1894. The quadrupole transition matrix elements between the eigen-states $|\phi_\alpha\rangle$ and $|\phi_\beta\rangle$ are given by

$$\langle \phi_\alpha | \hat{D} | \phi_\beta \rangle = \sum_{\boldsymbol{n_K}, \boldsymbol{n_L}} 2d_j (n_{K_j} - n_{L_j}) C^{\alpha *}_{\boldsymbol{n_K}, \boldsymbol{n_L}} C^{\beta}_{\boldsymbol{n_K}, \boldsymbol{n_L}}, \tag{A·9}$$

where the quantities $C^{\alpha}_{\boldsymbol{n_K}, \boldsymbol{n_L}}$ are the expansion coefficients in the $SU(2)$ basis:

$$|\phi_\alpha\rangle = \sum_{\boldsymbol{n_K}, \boldsymbol{n_L}} C^{\alpha}_{\boldsymbol{n_K}, \boldsymbol{n_L}} |\boldsymbol{n_K}, \boldsymbol{n_L}\rangle. \tag{A·10}$$

Appendix B

—— *Gradient Method for the Moving-Frame HB Equation* ——

In this appendix, we solve the variational equation of the form

$$\delta \langle \phi(q)| \hat{H} - \lambda \hat{N} - \mu \hat{Q} |\phi(q)\rangle = 0, \tag{B·1}$$

using the gradient method,[1)] with the following constraint conditions for the number operator $\hat{N}$ and the one-body operators $\hat{R}$:

$$\langle \phi(q)| \hat{N} |\phi(q)\rangle = N_0, \quad \langle \phi(q)| \hat{R} |\phi(q)\rangle = R_0. \tag{B·2}$$

Here, $\hat{R}$ is an arbitrary one-body operator which, in general, may be different from $\hat{Q}$.

Let $\left|\phi^{(k)}(q)\right\rangle$ be the state vector at the iterative step k. Using the quasiparticle bilinear operators $\boldsymbol{A}_i^\dagger(q)$ and $\boldsymbol{A}_i(q)$, which satisfy $\boldsymbol{A}_i(q)\left|\phi^{(k)}(q)\right\rangle = 0$, we then generate the state vector at the $(k+1)$-th step in the form of a unitary transform of $\left|\phi^{(k)}(q)\right\rangle$ as

$$\left|\phi^{(k+1)}(q)\right\rangle = e^{\hat{Z}(q)}\left|\phi^{(k)}(q)\right\rangle, \tag{B·3}$$

with the anti-Hermitian operator

$$\hat{Z}(q) = \sum_{i>0} Z_i^{20}(q)(\boldsymbol{A}_i^\dagger(q) - \boldsymbol{A}_i(q)). \tag{B·4}$$

It should be noted that the normalization is preserved during the iteration. Then, assuming that $\hat{Z}(q)$ is small, we expand the difference between the energies of $\left|\phi^{(k+1)}(q)\right\rangle$ and $\left|\phi^{(k)}(q)\right\rangle$ as follows:

$$\begin{aligned}\Delta E &= \left\langle \phi^{(k+1)}(q)\right| \hat{H} - \lambda\hat{N} - \mu\hat{Q} \left|\phi^{(k+1)}(q)\right\rangle - \left\langle \phi^{(k)}(q)\right| \hat{H} - \lambda\hat{N} - \mu\hat{Q} \left|\phi^{(k)}(q)\right\rangle \\ &= \left\langle \phi^{(k)}(q)\right| [\hat{H} - \lambda\hat{N} - \mu\hat{Q}, \hat{Z}(q)] \left|\phi^{(k)}(q)\right\rangle + O(\hat{Z}^2) \\ &= \sum_{i>0} (H_i^{20}(q) - \lambda N_i^{20}(q) - \mu Q_i^{20}(q)) Z_i^{20}(q) + O(\hat{Z}^2). \end{aligned} \tag{B·5}$$

If $Z_i^{20}(q)$ is chosen as

$$Z_i^{20}(q) = -\Delta T (H_i^{20}(q) - \lambda N_i^{20}(q) - \mu Q_i^{20}(q)), \tag{B·6}$$

with a positive step size ΔT, ΔE is negative in each iteration. The constraint conditions (B·2) can also be expanded up to first order in $\hat{Z}(q)$, and we find

$$\begin{aligned}\left\langle \phi^{(k+1)}(q)\right| \hat{R} \left|\phi^{(k+1)}(q)\right\rangle &= \left\langle \phi^{(k)}(q)\right| \hat{R} \left|\phi^{(k)}(q)\right\rangle + \left\langle \phi^{(k)}(q)\right| [\hat{R}, \hat{Z}(q)] \left|\phi^{(k)}(q)\right\rangle \\ &\quad + O(\hat{Z}^2), \end{aligned} \tag{B·7a}$$

$$\begin{aligned}\left\langle \phi^{(k+1)}(q)\right| \hat{N} \left|\phi^{(k+1)}(q)\right\rangle &= \left\langle \phi^{(k)}(q)\right| \hat{N} \left|\phi^{(k)}(q)\right\rangle + \left\langle \phi^{(k)}(q)\right| [\hat{N}, \hat{Z}(q)] \left|\phi^{(k)}(q)\right\rangle \\ &\quad + O(\hat{Z}^2). \end{aligned} \tag{B·7b}$$

Substituting Eq. (B·6) into Eq. (B·7), we obtain the following equation, which determines the Lagrange multipliers λ and μ:

$$\begin{bmatrix} \sum_i R_i^{20} N_i^{20} & \sum_i R_i^{20} Q_i^{20} \\ \sum_i N_i^{20} N_i^{20} & \sum_i N_i^{20} Q_i^{20} \end{bmatrix} \begin{bmatrix} \lambda \\ \mu \end{bmatrix} = \begin{bmatrix} \dfrac{R_0 - \bar{R}}{2\Delta T} + \sum_i R_i^{20} H_i^{20} \\ \dfrac{N_0 - \bar{N}}{2\Delta T} + \sum_i N_i^{20} H_i^{20} \end{bmatrix}. \tag{B·8}$$

Here $N_i^{20}, R_i^{20}, Q_i^{20}$ and H_i^{20} are the coefficients of the two-quasiparticle creation and annihilation parts of the operators $\hat{N}, \hat{R}, \hat{Q}$ and $\hat{H}$, while the quantities $\bar{R}$ and $\bar{N}$ represent $\left\langle \phi^{(k)}(q)\right| \hat{R} \left|\phi^{(k)}(q)\right\rangle$ and $\left\langle \phi^{(k)}(q)\right| \hat{N} \left|\phi^{(k)}(q)\right\rangle$.

When solving the moving-frame HFB equation (3·21) with the constraint conditions (3·30) and (3·31), we use $\hat{Q}(q - \delta q)$ for $\hat{R}(q)$. This operator is defined at $q - \delta q$ in terms of the quasiparticle bilinear operators $\boldsymbol{A}_i^\dagger(q - \delta q)$ and $\boldsymbol{A}_i(q - \delta q)$, which satisfy $\boldsymbol{A}_i(q - \delta q) \left|\phi(q - \delta q)\right\rangle = 0$. Thus, at each iteration step, it is necessary to rewrite $\hat{Q}(q - \delta q)$ in terms of $\boldsymbol{A}_i^\dagger(q)$, $\boldsymbol{A}_i(q)$ and $\boldsymbol{N}_i(q)$, defined with respect to $\left|\phi^{(k)}(q)\right\rangle$ at q:

$$\begin{aligned}\hat{R}(q) = \hat{Q}(q - \delta q) &= \sum_{i>0} Q_i^{20}(q - \delta q)(\boldsymbol{A}_i^\dagger(q - \delta q) + \boldsymbol{A}_i(q - \delta q)) \\ &= R^{00}(q) + \sum_{i>0} R_i^{11}(q) \boldsymbol{N}_i(q) + R_i^{20}(q)(\boldsymbol{A}_i^\dagger(q) + \boldsymbol{A}_i(q)). \end{aligned} \tag{B·9}$$

The explicit expression for the coefficients $R_i^{20}(q)$, which we need to solve Eq. (B·8), is

$$R_i^{20}(q) = Q_i^{20}(q-\delta q)\left[(u_i(q-\delta q)^2 - v_i(q-\delta q)^2)(u_i^2(q) - v_i^2(q)) \right. \\ \left. +4u_i(q-\delta q)v_i(q-\delta q)u_i(q)v_i(q)\right]. \qquad \text{(B·10)}$$

The above procedure is repeated until convergence is realized. In fact, this is *Step 2* in the iterative algorithm described in §3.6.

References

1) P. Ring and P. Schuck, *The Nuclear Many-Body Problem* (Springer-Verlag, 1980).
2) J.-P. Blaizot and G. Ripka, *Quantum Theory of Finite Systems* (The MIT press, 1986).
3) Ed. A. Abe and T. Suzuki, Prog. Theor. Phys. Suppl. Nos. 74 & 75 (1983).
4) D. J. Rowe and R. Bassermann, Can. J. Phys. **54** (1976), 1941.
5) D. M. Brink, M. J. Giannoni and M. Veneroni, Nucl. Phys. A **258** (1976), 237.
6) F. Villars, Nucl. Phys. A **285** (1977), 269.
7) T. Marumori, Prog. Theor. Phys. **57** (1977), 112.
8) M. Baranger and M. Veneroni, Ann. of Phys. **114** (1978), 123.
9) K. Goeke and P.-G. Reinhard, Ann. of Phys. **112** (1978), 328.
10) T. Marumori, T. Maskawa, F. Sakata and A. Kuriyama, Prog. Theor. Phys. **64** (1980), 1294.
11) M. J. Giannoni and P. Quentin, Phys. Rev. C **21** (1980), 2060; Phys. Rev. C **21** (1980), 2076.
12) J. Dobaczewski and J. Skalski, Nucl. Phys. A **369** (1981), 123.
13) K. Goeke, P.-G. Reinhard and D. J. Rowe, Nucl. Phys. A **359** (1981), 408.
14) A. K. Mukherjee and M. K. Pal, Phys. Lett. B **100** (1981), 457; Nucl. Phys. A **373** (1982), 289.
15) D. J. Rowe, Nucl. Phys. A **391** (1982), 307.
16) C. Fiolhais and R. M. Dreizler, Nucl. Phys. A **393** (1983), 205.
17) P.-G. Reinhard, F. Grümmer and K. Goeke, Z. Phys. A **317** (1984), 339.
18) A. Kuriyama and M. Yamamura, Prog. Theor. Phys. **70** (1983), 1675; Prog. Theor. Phys. **71** (1984), 122.
19) M. Yamamura, A. Kuriyama and S. Iida, Prog. Theor. Phys. **71** (1984), 109.
20) M. Matsuo and K. Matsuyanagi, Prog. Theor. Phys. **74** (1985), 288.
21) M. Matsuo, Prog. Theor. Phys. **76** (1986), 372.
22) Y. R. Shimizu and K. Takada, Prog. Theor. Phys. **77** (1987), 1192.
23) M. Yamamura and A. Kuriyama, Prog. Theor. Phys. Suppl. No. 93 (1987), 1.
24) A. Bulgac, A. Klein, N. R. Walet and G. Do Dang, Phys. Rev. C **40** (1989), 945.
25) N. R. Walet, G. Do Dang and A. Klein, Phys. Rev. C **43** (1991), 2254.
26) A. Klein, N. R. Walet and G. Do Dang, Ann. of Phys. **208** (1991), 90.
27) K. Kaneko, Phys. Rev. C **49** (1994), 3014.
28) T. Nakatsukasa and N. R. Walet, Phys. Rev. C **57** (1998), 1192.
29) T. Nakatsukasa and N. R. Walet, Phys. Rev. C **58** (1998), 3397.
30) T. Nakatsukasa, N. R. Walet and G. Do Dang, Phys. Rev. C **61** (2000), 014302.
31) J. Libert, M. Girod and J.-P. Delaroche, Phys. Rev. C **60** (1999), 054301.
32) E. Kh. Yuldashbaeva, J. Libert, P. Quentin and M. Girod, Phys. Lett. B **461** (1999), 1.
33) L. Próchniak, P. Quentin, D. Samsoen and J. Libert, Nucl. Phys. A **730** (2004), 59.
34) D. Almehed and N. R. Walet, Phys. Rev. C **69** (2004), 024302.
35) D. Almehed and N. R. Walet, Phys. Lett. B **604** (2004), 163.
36) A. Klein and E. R. Marshalek, Rev. Mod. Phys. **63** (1991), 375.
37) G. Do Dang, A. Klein, and N. R. Walet, Phys. Rep. **335** (2000), 93.
38) Ed. A. Kuriyama, K. Matsuyanagi, F. Sakata, K. Takada and M. Yamamura, Prog. Theor. Phys. Suppl. No. 141 (2001).
39) J. Dudek, W. Dudek, E. Ruchowska and J. Skalski, Z. Phys. A **294** (1980), 341.
40) D. J. Thouless and J. G. Valatin, Nucl. Phys. **31** (1962), 211.
41) J. Dobaczewski and J. Dudek, Phys. Rev. C **52** (1995), 1827.

42) F. Barranco, G. F. Bertsch, R. A. Broglia and E. Vigezzi, Nucl. Phys. A **512** (1990), 253.
43) G. F. Bertsch, Nucl. Phys. A **574** (1994), 169.
44) M. Matsuo, Prog. Theor. Phys. **72** (1984), 666.
45) M. Matsuo and K. Matsuyanagi, Prog. Theor. Phys. **74** (1985) 1227; Prog. Theor. Phys. **76** (1986), 93; Prog. Theor. Phys. **78** (1987), 591.
46) M. Matsuo, Y. R. Shimizu and K. Matsuyanagi, *Proceedings of The Niels Bohr Centennial Conf. on Nuclear Structure*, ed. R. Broglia, G. Hagemann and B. Herskind (North-Holland, 1985), p. 161.
47) K. Takada, K. Yamada and H. Tsukuma, Nucl. Phys. A **496** (1989), 224.
48) K. Yamada, K. Takada and H. Tsukuma, Nucl. Phys. A **496** (1989), 239.
49) K. Yamada and K. Takada, Nucl. Phys. A **503** (1989), 53.
50) H. Aiba, Prog. Theor. Phys. **84** (1990), 908.
51) K. Yamada, Prog. Theor. Phys. **85** (1991), 805; Prog. Theor. Phys. **89** (1993), 995.
52) J. Terasaki, T. Marumori and F. Sakata, Prog. Theor. Phys. **85** (1991), 1235.
53) J. Terasaki, Prog. Theor. Phys. **88** (1992), 529; Prog. Theor. Phys. **92** (1994), 535.
54) M. Matsuo, in *New Trends in Nuclear Collective Dynamics*, ed. Y. Abe, H. Horiuchi and K. Matsuyanagi (Springer-Verlag, 1992), p. 219.
55) Y. R. Shimizu and K. Matsuyanagi, Prog. Theor. Phys. Suppl. No. 141 (2001), 285.
56) J. L. Wood, K. Heyde, W. Nazarewicz, M. Huyse and P. van Duppen, Phys. Rep. **215** (1992), 101.
57) S. M. Fischer et al., Phys. Rev. Lett. **84** (2000), 4064; Phys. Rev. C **67** (2003), 064318.
58) E. Bouchez et al., Phys. Rev. Lett. **90** (2003), 082502.
59) M. Matsuo, T. Nakatsukasa and K. Matsuyanagi, Prog. Theor. Phys. **103** (2000), 959.
60) M. Kobayasi, T. Nakatsukasa, M. Matsuo and K. Matsuyanagi, Prog. Theor. Phys. **110** (2003), 65.
61) M. Baranger and K. Kumar, Nucl. Phys. **62** (1965), 113; Nucl. Phys. A **110** (1968), 529; Nucl. Phys. A **122** (1968), 241; Nucl. Phys. A **122** (1968), 273.
62) M. Baranger and K. Kumar, Nucl. Phys. A **110** (1968), 490.
63) D. R. Bes and R. A. Sorensen, *Advances in Nuclear Physics*, vol. 2 (Prenum Press, 1969), p. 129.
64) K. Matsuyanagi, Prog. Theor. Phys. **67** (1982), 1441; *Proceedings of the Nuclear Physics Workshop*, Trieste, 5-30 Oct. 1981. ed. C. H. Dasso, R. A. Broglia and A. Winther (North-Holland, 1982), p. 29.
65) Y. Mizobuchi, Prog. Theor. Phys. **65** (1981), 1450.
66) T. Suzuki and Y. Mizobuchi, Prog. Theor. Phys. **79** (1988), 480.
67) T. Fukui, M. Matsuo and K. Matsuyanagi, Prog. Theor. Phys. **85** (1991), 281.
68) M. Kobayasi, T. Nakatsukasa, M. Matsuo and K. Matsuyanagi, Prog. Theor. Phys. **112** (2004), 363; Prog. Theor. Phys. **113** (2005), 129.
69) S. T. Belyaev, Nucl. Phys. **64** (1965), 17.
70) N. Hinohara, *Proceedings of the YITP workshop on New Developments in Nuclear Self-Consistent Mean-Field Theories*, Yukawa Institute, Kyoto, May 30-June 1, 2005; Master Thesis, Kyoto University, 2005.
71) J. M. Eisenberg and W. Greiner, *Nuclear Theory* (North-Holland, 1970) [3rd revised version (1988)], vol. 1.
72) N. Hinohara, T. Nakatsukasa, M. Matsuo and K. Matsuyanagi, in preparation.